UNIVERSITY OF CALIFORNIA

Santa Barbara

Synthesis and Characterization of Atomically Precise Copper Nanoclusters

A dissertation submitted in partial satisfaction of the

requirements for the degree Doctor of Philosophy

in Chemistry

by

Thùy-Ái Đăng Nguyễn

Committee in charge:

Professor Trevor W. Hayton, Chair

Professor Peter C. Ford

Professor R. Daniel Little

Professor Ram Seshadri

September 2017

The dissertation of Thuy-Ai D. Nguyen is approved.

_____

Professor Peter C. Ford

_____

Professor R. Daniel Little

_____

Professor Ram Seshadri

_____

Professor Trevor W. Hayton, Committee Chair

September 2017

Synthesis and Characterization of Atomically Precise Copper Nanoclusters

Acknowledgements

I have been very fortunate to be surrounded by people throughout my academic career who have made my time in graduate school rewarding, and at times, quite enjoyable! Going chronologically, I would first like to thank my mother, holder of the first PhD in our family, for setting me on this path and teaching me "how to learn." I am grateful to my family for their love, guidance and support throughout my life, and especially my mother, uncle "Cậu Ngoãn," little brother, and grandpa for all the shipments of food from the farm. I was the best fed graduate student in Santa Barbara. My first chemistry professor in college, Dr. Steve Borick, was instrumental in sparking my interest in chemistry with his constant enthusiasm for the subject. I am grateful for his mentorship, even after I finished his courses, and the time he took outside of class to help me catch up with lectures when I had to be absent for tennis matches. Prof. Anne K. Jones was my undergraduate research advisor, as well as my inorganic chemistry professor. I'd like to thank her for taking me into her lab and letting me explore inorganic synthesis. She was a tremendous help with writing and editing my graduate school applications and I would not be where I am today without her intervention. I also thank her former graduate students Dr. Souvik Roy and Prof. Arnab Dutta for being good mentors and convincing me that inorganic chemistry is "cool," and for dealing with all of my rookie mistakes in lab.

Foremost, I would like to thank my advisor Prof. Trevor Hayton for his guidance and support, which have been essential to my successes in graduate school. I needed a lot of help, especially during the first few years, and I was never once turned away without useful information. He has encouraged me to do chemistry that I found interesting and I've been able to discover a rainbow of new colored complexes, which has been a dream of mine since

a child. He has also pragmatically guided me through trying times with more challenging projects and I have great respect for his scientific intuition and integrity. I am also grateful for his support of my non academic endeavors and for giving me time to be outside and enjoy Santa Barbara. For example, he brought his surfboard in to my office to use after seeing me in a wetsuit one day. My committee members, Prof. Peter Ford, Prof. Ram Seshadri, and Prof. R. Dan Little, also deserve my thanks for their input and support over the years. Prof. Susannah Scott and her graduate student Zach Jones have also played an important role in my research as collaborators. I value their input and my work is better off for their contributions.

My labmates have made the last 5 years a unique experience and I can't imagine doing graduate school with any other group. Peter "Grouchy" Damon who started at the same time I did was an especially close companion because we shared the "Closet Office," and a penchant for nicknames. We call ourselves Pouchy and Grouchy and have been dubbed "The Wonder Twins." We were the only two students in the transition metal lab/glovebox for a time as second years and together, managed to keep it relatively intact and not blown up as Drs. Ash Wright and Richard Lewis, who we inherited the Closet Office and glovebox from, predicted we would. I'd like to thank Ash and Richard for their mentorship when we were first starting out, and especially Richard for continuing to answer phone calls and HeyTells full of questions on chemistry, lab maintenance, and life. Dr. Danil "Rainbow" Smiles was another person I often looked to for help in lab, as well as a listening ear who always found the humor in my bad day ventings. He has also managed to pull off some prodigious pranks, including filling my office with balloons and my car with boxes ("more boxes??!). The younger students Nate "Mr. Sunshine" Hartman and Andrew "New New

Guy/Cheeseless" Cook have also been an integral part of the transition metal glovebox and we have had all kinds of differents types of fun. The days spent trying to fix Mr. Edwards pump are especially memorable and their good natures made it all a little less painful. I'd like to thank Nate, Andrew, and Alex "Newerest Guy 2" Touchton for checking in on me while I was writing this thesis in my closet isolation chamber. NG2 is rotating and not yet an official Haytonian, but I hope he stays for the clusters.

I don't have room to list by name all the people who deserve it. However, I would like to acknowledge all the friends who have made it a point to keep in contact and see me when I'm in town, who tell me they're proud of me and listen to my troubles. I am exceedingly grateful for all of my friends in Santa Barbara, especially my roommate Tracy Chuong, who have made it feel like home and I am sad that I will be leaving them soon.

I would like to acknowledge CenSURF, a NSF Center for Chemical Innovation (NSF CHE-1240194), for funding, for providing a valuable network of research collaborations, as well as for sending me to Australia ("Pouchyland," the land of pouches big and small) to collect neutron diffraction data at ANSTO. I also thank UCSB, the UCSB Shoreliners, and Mellichamp for fellowships that allowed me freedom to do more research, and UCSB, DowMI/MRL, and the ACS Division of Inorganic Chemistry for giving me various travel grants to go present my work at conferences. Finally, my NMR spectra were collected on an instrument supported by an NIH Shared Instrumentation Grant (SIG, 1S10OD012077-01A1), and my ESI mass spectra were acquired at the MRL Shared Experimental Facilities, supported by the MRSEC Program of the NSF under Award No. DMR 1121053 and a member of the NSF-funded Materials Research Facilities Network.

Vita of Thuy-Ai D. Nguyen

September 2017

EDUCATION

Doctor of Philosophy in Chemistry (expected) Sept 2017
University of California, Santa Barbara
Advisor: Professor Trevor W. Hayton
Dissertation: "Synthesis and Characterization of Atomically Precise Copper Nanoclusters"

Bachelor of Science, Biochemistry May 2012
Arizona State University
Advisor: Professor Anne K. Jones

Associates in Science May 2010
Scottsdale Community College

PROFESSIONAL EMPLOYMENT

08/12-Present	Graduate Student Researcher, Department of Chemistry & Biochemistry / Center for Sustainable Use of Renewable Feedstocks, University of California, Santa Barbara
06/17	Graduate Student Researcher, Los Alamos National Laboratory
08/15	Guest Researcher, Bragg Institute Neutron Beam Facility, Australian Nuclear Science and Technology Organisation
03/15-06/15, 09/12-06/13	Teaching Assistant, Department of Chemistry & Biochemistry, University of California, Santa Barbara
01/11-05/12	Undergraduate Researcher, Department of Chemistry & Biochemistry, Arizona State University
06/11-08/11	Helios Scholar Intern, Center for Proteomics, Translational Genomics Research Institute

PUBLICATIONS

Thuy-Ai D. Nguyen; Andrew W. Cook; Guang Wu; Trevor W. Hayton. Subnanometer-Sized Copper Clusters: A Critical Re-evaluation of the Synthesis and Characterization of $Cu_8(MPP)_4$ (HMPP = 2-Mercapto-5-*n*-propylpyrimidine). *Inorg. Chem.* **2017**, 56, 8390-8396. Link

Kai Yu; Ping Lu; Jeffrey Jackson; Thuy-Ai D. Nguyen; Joseph Alvarado; Craig E. Stivala; Yun Ma; Kyle A. Mack; Trevor W. Hayton; David B. Collum; Armen Zakarian. Lithium Enolates in the Enantioselective Construction of Tetrasubstituted Carbon Centers with Chiral Lithium Amides as Noncovalent Stereodirecting Auxiliaries, *J. Am. Chem. Soc.* **2017**, 139, 527-533. Link

Andrew W. Cook; Thuy-Ai D. Nguyen; William R. Buratto; Guang Wu; Trevor W. Hayton. Synthesis, Characterization, and Reactivity of the Group 11 Hydrido Clusters $[Ag_6H_4(dppm)_4(OAc)_2]$ and $[Cu_3H(dppm)_3(OAc)_2]$, *Inorg. Chem.* **2016**, 55, 12435-12440. Link

Thuy-Ai D. Nguyen; Zachary J. Jones; Domenick F. Leto; Guang Wu; Susannah L. Scott; Trevor W. Hayton. Ligand Exchange Mediates the Growth of an Atomically Precise Cu_{29} Nanocluster from a Smaller Cluster. *Chem. Mater.* **2016**, 28, 8385-8390. Link

Thuy-Ai D. Nguyen; Zachary J. Jones; Bryan R. Goldsmith; William R. Buratto; Guang Wu; Susannah L. Scott; Trevor W. Hayton. A Cu_{25} Nanocluster with Partial Cu(0) Character. *J. Am. Chem. Soc*. **2015**, 137, 13319–13324. Link

Souvik Roy; Thuy-Ai D. Nguyen; Lu Gan; Anne K. Jones. Biomimetic peptide-based models of [FeFe]-hydrogenases: utilization of phosphine-containing peptides. *Dalton Trans*. **2015**, 44, 14865-14876. Link

Thuy-Ai D. Nguyen; Bryan R. Goldsmith; Homaira T. Zaman; Guang Wu; Baron Peters; Trevor W. Hayton. Synthesis and Characterization of a Cu_{14} Hydride Cluster Supported by Neutral Donor Ligands. *Chem. Eur. J.* **2015**, 21, 5341-5344. Link

Thuy-Ai D. Nguyen; Ashley M. Wright; Joshua S. Page; Guang Wu; Trevor W. Hayton. Oxidation of Alcohols and Activated Alkanes with Lewis Acid-Activated TEMPO. *Inorg. Chem*. **2014**, 53, 11377-11387. Link

PRESENTATIONS

Thuy-Ai D. Nguyen; Zachary J. Jones; Domenick F. Leto; Guang Wu; Susannah L. Scott; Trevor W. Hayton. Bottom-up Assembly of Copper Nanoclusters as Models for the Cu-PMO Catalyst. Mellichamp Academic Initiative in Sustainability Renewable Carbon Workshop. Santa Barbara, CA, Sept 21, 2016 (Oral presentation).

Thuy-Ai D. Nguyen; Guang Wu; Trevor W. Hayton. Synthesis and Reactivity of a Cu_{26} Hydride Nanocluster. 252nd ACS National Meeting, Div. Inorg. Chem. Philadelphia, PA, Aug 21, 2016 (Oral presentation).

Thuy-Ai D. Nguyen; Guang Wu; Trevor W. Hayton. Synthesis and Reactivity of Copper Hydride Nanoclusters. 251th ACS National Meeting, Div. Inorg. Chem. San Diego, CA, March 17, 2016 (Oral presentation).

Thuy-Ai D. Nguyen; Guang Wu; Trevor W. Hayton. Synthesis and Reactivity of Copper Hydride Nanoclusters. SoCal Organometallics Meeting, December 5, 2015 (Oral presentation).

Thuy-Ai D. Nguyen; Guang Wu; Trevor W. Hayton. Oxidation of Lignin Models with Lewis acid-activated TEMPO. 248th ACS National Meeting, Div. Inorg. Chem. San Francisco CA, August 10, 2014 (Oral presentation).

Thuy-Ai D. Nguyen; Stephen Springer; Robert Francke; William R. Buratto; Alison Butler; Trevor W. Hayton; R. Daniel Little. Chemical and Electrochemical Approaches Towards Oxidative Lignin Disassembly. 248th ACS National Meeting, Div. Inorg. Chem. San Francisco CA, August 10, 2014 (Poster presentation).

Jason T. Tillman; **Thuy-Ai D. Nguyen**; Homaira T. Zaman; Trevor W. Hayton; Clifford P. Kubiak. Towards Electrocatalytic CO_2 Reduction with Homogeneous Copper. 248th ACS National Meeting, Div. Inorg. Chem. San Francisco, CA, August 10, 2014 (Poster presentation)

Thuy-Ai D. Nguyen; Trevor W. Hayton. Oxidation of Lignin Models with Lewis acid-activated TEMPO. SoCal Organometallics Meeting, November 17, 2013 (Oral presentation).

Thuy-Ai D. Nguyen; Tony Tegeler; Konstantinos Petritis. A Modified Liquid Chromatography Method for Applications in Proteomics. 2011 Helios Scholars Program at TGen, Helios Scholars Symposium. Phoenix Ballroom, Sheraton Phoenix Downtown Hotel, July 20, 2011 (Poster presentation)

AWARDS

- ACS Division of Inorganic Chemistry Travel Award, 2016
- DowMI/MRL Summer-Fall 2016 Travel Fellowship, UCSB, 2016
- Broida-Hirschfelder Fellowship, UCSB, 2016
- Mellichamp Academic Initiative in Sustainability Fellowship, UCSB, 2016
- Roche Bioscience Distinguished Teaching Fellowship, UCSB, 2016
- Graduate Student Association Travel Grant, UCSB, 2016
- Doctoral Student Travel Grant 2015-16, UCSB, 2016
- Graduate Research Mentorship Program Fellowship, UCSB, 2015, 2016
- Outstanding Service to the Department Award, UCSB, 2014
- ACS Division of Inorganic Chemistry Undergraduate Award, ASU, 2012
- NJCAA Distinguished Academic All American, SCC, 2010
- NJCAA Academic All American Team of the Year, SCC, 2009, 2010
- President's Scholarship, SCC, 2008, 2009, 2010
- Academic Excellence in Chemistry – First Year "Excellence Under the Stars," SCC, 2010
- Who's Who Among Students in American Junior Colleges, SCC, 2009

Major Field: Inorganic Chemistry

Studies in Copper Hydride Cluster Chemistry

Abstract

Synthesis and Characterization of Atomically Precise Copper Nanoclusters

by

Thuy-Ai D. Nguyen

The reactivity of $MCl_3(\eta^1$-TEMPO) (M = Fe, Al; TEMPO = 2,2,6,6-tetramethylpiperidine-*N*-oxyl) with a variety of lignin models, including 3,4-dimethoxybenzyl alcohol, 1-phenyl-2-phenoxyethanol and 1,2-diphenyl-2-methoxyethanol is investigated. $FeCl_3(\eta^1$-TEMPO) is effective in cleanly converting these substrates to the corresponding aldehyde or ketone. $AlCl_3(\eta^1$-TEMPO) is also able to oxidize these substrates, however in a few instances the products of over-oxidation are also observed. In contrast, 2-phenoxyethanol is not oxidized by $MCl_3(\eta^1$-TEMPO); instead it likely coordinates to the metal center, forming a 2-phenoxyethoxide complex. Oxidation of activated alkanes by $MCl_3(\eta^1$-TEMPO) suggests that the reactions proceed via an initial 1-electron concerted proton-electron transfer (CPET) event. Finally, reaction of TEMPO with $FeBr_3$ in Et_2O results in oxidation of the solvent.

The copper hydride clusters $[Cu_{14}H_{12}(phen)_6(PPh_3)_4][X]_2$ (X = Cl, OTf) are obtained in good yields by reaction of $[(Ph_3P)CuH]_6$ with 1,10-phenanthroline, in the presence of a halide or pseudohalide source. $[Cu_{14}H_{12}(phen)_6(PPh_3)_4][Cl]_2$ reacts with CO_2 in CH_2Cl_2, in

the presence of excess Ph_3P, to form the formate complex, $[(Ph_3P)_2Cu(\kappa^2\text{-}O_2CH)]$, along with [(phen)($Ph_3P$)CuCl].

$[Cu_{25}H_{22}(PPh_3)_{12}]Cl$ and $[Cu_{18}H_{17}(PPh_3)_{10}]Cl$, are isolated from the reaction of Cu(OAc) and CuCl with Ph_2SiH_2, in the presence of PPh_3. $[Cu_{25}H_{22}(PPh_3)_{12}]Cl$ formally features partial Cu(0) character. Subsequent reaction with Ph_2phen resulted in the isolation of $[Cu_{29}Cl_4H_{22}(Ph_2phen)_{12}]Cl$ (Ph_2phen = 4,7-diphenyl-1,10-phenanthroline), in good yields. A time-resolved kinetic evaluation of the formation of $[Cu_{29}Cl_4H_{22}(Ph_2phen)_{12}]Cl$ reveals that the mechanism of cluster growth is initiated by rapid ligand exchange, followed by slower extrusion of CuCl monomer, transport, and subsequent capture by intact clusters.

Two Cu_{26} nanoclusters, tentatively formulated as $[Cu_{26}H_{17}(PPh_3)_9(OAc)_3]$ and $[Cu_{26}H_{22}(PPh_3)_{10}(OAc)_2]$, are isolated from the reaction of Cu(OAc) with Ph_2SiH_2, in the presence of PPh_3. As formulated, $[Cu_{26}H_{17}(PPh_3)_9(OAc)_3]$ features a magic number $N^* = 6$, which is unprecedented for a copper nanocluster. XANES supports an assignment of more Cu(0) character than $[Cu_{25}H_{22}(PPh_3)_{12}]Cl$ ($N^* = 2$) for this complex.

A critical reevaluation of the synthesis and characterization of $Cu_8(MPP)_4$ is reported. This product was reportedly formed by reaction of $Cu(NO_3)_2$ with 2-mercapto-5-*n*-propylpyrimidine (HMPP) and $NaBH_4$, in ethanol, in the presence of $[N(C_8H_{17})_4][Br]$. However, upon reevaluation, no experimental evidence to support the existence of $Cu_8(MPP)_4$ was found. Instead, the material isolated from this reaction is a complex mixture containing $[N(C_8H_{17})_4]^+$, Br^-, NO_3^-, 2-mercapto-5-*n*-propyl-1,6-dihydropyrimidine (H_2MPP^*), along with the Cu(I) coordination polymer, $[Cu(MPP)]_n$. H_2MPP^* and $[Cu(MPP)]_n$, as well as the related Cu(I) coordination complexes, $[Cu(HMPP^*)]_n$ and $[Cu_2(MPP^*)]_n$ are independently synthesized to support these conclusions.

Table of Contents

List of Figures

List of Schemes

List of Tables

There’s something that doesn’t make sense.

Let’s go and poke it with a stick!

-The Doctor

Chapter 1. **Introduction**

1.1 Lignin as a Sustainable Feedstock

Lignin, a major component of nonedible biomass (25-35%),[1] has the potential to be a sustainable source of aromatic chemical feedstocks.[2,3] Approximately 50 million tons of lignin are generated each year by the pulp and paper industry; however, only about 2% of this is used commercially,[3,4] while the remainder is burned. The inefficient use of ligand is due, in part, to the challenges associated with efficiently converting lignin into value-added chemical feedstocks, and despite the fact that there is high demand for aromatics in the chemical industry. For example, the market for benzene, toluene, and xylenes (BTX) is 45 billion pounds per year in the US, currently almost exclusively supplied from fossil carbon sources.[1,5-7]

Lignin is formed by the radical-radical coupling reaction of three primary monomers (monolignols): *p*-coumaryl, coniferyl, and sinapyl alcohol.[3] This process creates a complex and highly cross-linked heterogeneous polymer, making lignin disassembly a challenge, as its robust structure is resistant to chemical and biological degradation.[3,8,9] In spite of extensive research, there are very few reports of effective methods for depolymerizing lignin to valuable aromatic products.[10] In terms of chemical processes, reduction and oxidation are two major pathways employed for lignin disassembly. During reductive depolymerization, the aromatic rings are often saturated before hydrogenolysis and cleavage of the C-O and C-C bonds.[11] The substrates also undergo deoxygenation in this process. In catalytic lignin reduction, the focus is mainly on making and upgrading bio-oils and fuels, although, less functionalized aromatics such as phenols and BTX are also viable targets. While reductive reactions usually remove functionality in lignin, oxidative lignin disassembly generally

forms more complex aromatic compounds with added functionality. Under oxidative conditions, the alcohol substituents are oxidized to the corresponding ketones or aldehydes, prior to depolymerization of lignin *via* radical processes.[11] One challenge, however, is that this radical process can actually cause repolymerization, as well.[11] However, the potential products may be useful as platform chemicals for organic synthesis, or they can be used as fine chemicals.[3] For example, Stahl and co-workers demonstrated that lignin de-polymerization can be achieved by initial oxidation of its primary or secondary alcohol functionalities, which prepares the lignin for a subsequent C-C/C-O bond cleavage process.[10] The optimal catalyst for this system consists of 4-acetamido-TEMPO/HNO_3/HCl (TEMPO = 2,2,6,6-tetramethylpiperidine-*N*-oxyl), wherein the active oxidant is likely [4-acetamido-TEMPO]$^+$. Stephenson and co-workers report a similar two-stage lignin degradation process, in which the benzylic alcohol functionalities are first oxidized by [4-acetamido-TEMPO][BF_4].[12]

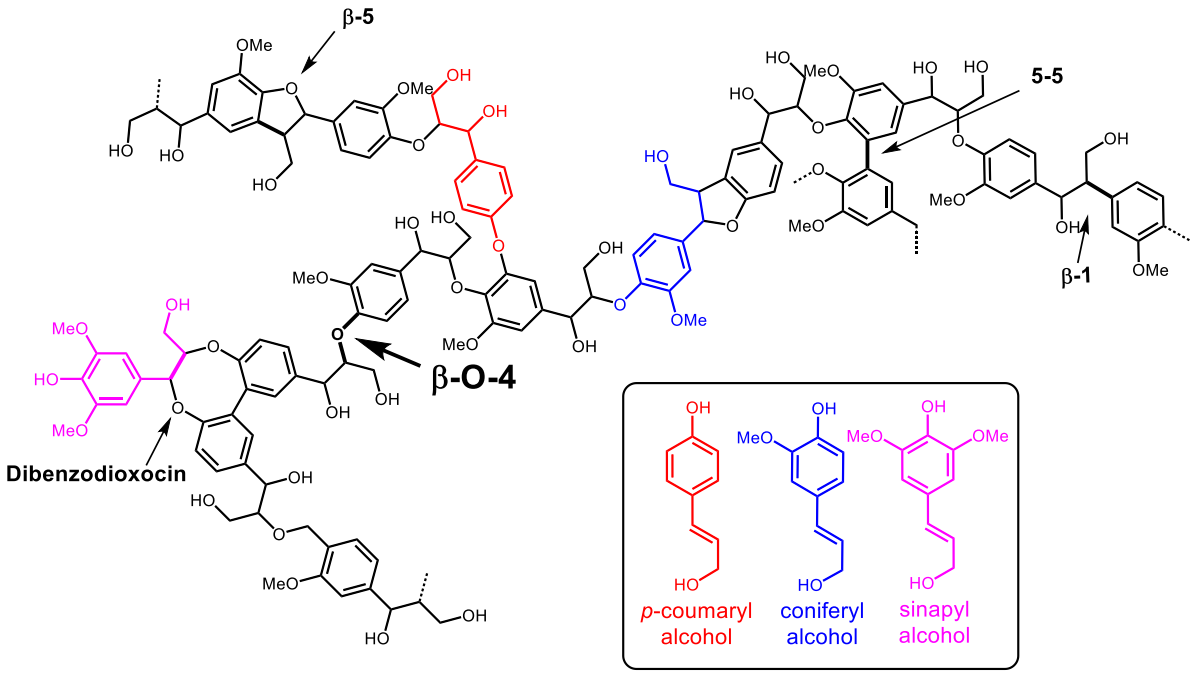

Figure 1.1. Schematic representation of the lignin structure with various linkages labeled and an example of each monomer being incorporated into the structure, highlighted in color. Inset: the three monolignols. Image adapted from Ref. 3.

In 2011, the UCSB Process to catalytically produce liquid fuel from woody biomass was published by Ford and co-workers.[13] This reduction process is a one-pot procedure that occurs in supercritical methanol (sc-MeOH) with a copper-doped porous metal oxide (Cu20-PMO) catalyst. In addition to acting as the catalyst for biomass breakdown, Cu20-PMO catalyzes methanol reforming and the water gas shift, which produces the reducing equivalents in the form of H_2, required to depolymerize, reduce and deoxygenate lignin and cellulose. Previous work by the Ford group had used this system to depolymerize dihydrobenzofuran, a lignin model compound, as well as organosolv lignin.[14,15] However, their ability to start directly from sawdust is an even more impressive result.[13] This process is unique in that it produces little to no intractable carbon waste / char. Interestingly, control reactions show that when the PMO support is not doped with copper, the sawdust remains

largely unreacted and significant amounts of char forms.[13] Copper clearly plays a key role in catalyzing lignin depolymerization. Ford and co-workers have continued developing this protocol by modifying the catalyst with various additives to control selectivity during lignin disassembly. They have also mapped out the organic products formed during depolymerization to gain an understanding of the operative reaction pathways.[16-19] In addition, they have collaborated with the Scott group at UCSB to study the catalyst in more detail through techniques that include X-ray absorption spectroscopy (XAS), transmission electron microscopy (TEM), X-ray photoelectron spectroscopy (XPS), energy dispersive X-ray spectroscopy (EDX), and chemisorption with N_2O. While these results have not been published, they are relevant to this work, because they have found that the copper in the active catalyst is present as small copper nanoparticles (~1-2 nm).

1.2 Copper Nanomaterial Based Applications

Copper nanomaterials play important roles in catalysis, medicine, imaging, devices, and water purification.[20] Nanoparticles possess very high surface to volume ratios, a property that is useful in many applications such as catalysis and drug delivery.[21] They have been used as a major component of conductive inks for low-cost inkjet printing of electronic components.[22] Compared to bulk copper, copper nanoparticles are more easily dispersed and have lower melting points because of their size. In addition, copper inks are superior to various silver conductive inks that have been used in microscale patterning, due to less ion migration at high-temperature and humidity, as well as being significantly cheaper for comparable bulk conductivities. However, the challenges for using copper for this application include the difficulty of reducing copper ions under mild reaction conditions. There has also been research towards the synthesis of air-stable copper nanoparticles for

inkjet printing, generally through encapsulation of the reactive copper core by inert materials.[23-27] Copper nanoparticles have also been found to have antimicrobial properties and are interesting because of their large active surface area and high chemical and biological reactivity.[28,29] They can also be used as additives to make antimicrobial surfaces and materials.[30,31]

Copper nanoparticles have been used as catalysts in a wide variety of chemical transformations. These reactions include reduction, oxidation, coupling, photocatalysis, electrocatalysis, and gas phase reactions.[32] For instance, copper nanoparticles are good catalysts for many organic transformations, including the Huisgen 1,3-dipolar cycloaddition "click" reaction between azides and terminal alkynes.[32] This reaction can be conducted under ambient conditions in the presence of air and water, and is compatible with a wide range of functional groups.[16-18,33-35] Copper-based nanoparticles are a cost-effective and reliable "drop-in" substitute for many reported catalytic protocols, replacing rarer metals such as palladium.[32]

Copper nanoparticles also play a role in CO_2 reduction as photocatalysts and electrocatalysts. There are examples of photocatalytic CO_2 reduction in which copper nanomaterials serve as a co-catalyst. Grimes and co-workers reported solar conversion of CO_2 and water vapor to methane and other hydrocarbon fuels using nitrogen-doped titania nanotube arrays loaded with copper nanoparticle co-catalysts.[33] Mesoporous Cu/TiO_2/SBA-15 composite photocatalysts were successful in converting CO_2 and H_2O to methanol, where the material without copper was less efficient.[34] Photocatalytic CO_2 conversion can also be achieved over a double-walled TiO_2 nanotube array that is modified with Cu-Pt nanoalloy.[35] This room temperature reaction produces CH_4, C_2H_4, and C_2H_6 as the main products.

In the electrochemical reduction of CO_2, copper is a unique and selective catalyst because it can promote the formation of hydrocarbons and form C-C bonds.[36,37] Thus, reduction of CO_2 on copper electrodes can lead to the production of important compounds such as ethylene, acetylene, and ethanol. A major challenge in this process is the large overpotential required in order to compete with hydrogen formation from water. Thus, the catalyst must inhibit hydrogen evolution from water, as well as promote CO_2 reduction.[38] In 2015, Yeo *et al.* reported a remarkable relationship between the faradic yield of ethylene and ethanol, with copper oxide film thickness.[39] Further characterization demonstrated that the copper oxide catalyst was reduced to metallic particles during the reduction process and Cu(0) was claimed to be the active site. Finally, CO_2 reduction over copper nanocube electrocatalysts has shown enhanced selectivity for ethylene formation.[40] Despite these successes, all of these examples are of relatively poorly defined nanomaterials, and there are still many unanswered questions regarding the origins of catalytic activity and the nature of electron transfer within the systems.[32] Additional studies must be undertaken to understand the mechanisms of copper nanoparticle reactivity.

1.3 Nanoparticles vs Nanoclusters

Although many advances have been made on the application of nanoparticles, it is still largely unclear what the surface chemistries of these systems are; an issue inherent to their large sizes, polydispersity, and ill-defined structures and surfaces.[41] The surface layer of conventional nanoparticles, which includes the capping ligands as well as the inorganic-organic interface, remains poorly understood because transmission electron microscopy (TEM) cannot provide a direct image. Spectroscopic tools typically used to study molecular compounds such as nuclear magnetic resonance spectroscopy (NMR), mass spectrometry

(MS), and infrared spectroscopy (IR) are of less utility in characterizing nanoparticles because of their polydispersity and heterogeneity. In addition, there is often excess ligand, surfactant, residual reactants, and side products present in these mixtures of nanoparticles. Thus, there is fundamental interest in building better particles where the exact composition and structure of the surfaces can be probed, because applications such as catalysis occur at the surfaces of the particles and understanding these surfaces is critically important for guiding further improvement. This goal can be achieved through the development of ultra-small nanoparticles, or nanoclusters, which we define to be smaller than ~2 nm (~10-300 metal atoms) and that can be purified to be perfectly monodisperse.[41] In addition, while nanoclusters are not always fully metallic like larger nanoparticles, we define nanoclusters to possess at least a small degree of M(0) character, differentiating them from clusters that are simple coordination polymers. Of the group 11 metals, gold nanoclusters are the most developed due to their high stability in comparison to silver, and especially copper. Nanoclusters are unique by virtue of their atomically precise, truly uniform nature, which is possible due to their relatively small size. This level of atomic precision is particularly important at this size because strong quantum size effects start to play a role and the particles can become sensitive to even a single atom difference.[42] Nanoclusters also have more surface sites, relative to their total volune, and may be more reactive. Molecular purity is also necessary for determination of the total structures of these clusters by single crystal X-ray diffraction, which is the most reliable technique for structure determination.[41]

1.4 Group 11 Nanoclusters

Among the structurally characterized nanoclusters presently known, the most common are thiolate protected gold nanoclusters because they are unusually robust. $Au_{25}(SR)_{18}^{q}$ (q =

-1, 0, +1), synthesized with a variety of different thiolate ligands, is a classic example of a gold thiolate system that has been reported in high purity and well characterized.[41,43-45] Au_{25} is built around an icosahedron with a Au_{13} core, one of the most widely observed structural motifs in nanoclusters.[41] The total structure determination of $[Au_{102}(p\text{-MBA})_{44}]$ (*p*-MBA = *p*-mercaptobenzoic acid) by Kornberg *et al.* in 2007 is another impressive result.[46]

Since 2007, there have only been a handful of crystal structures with a larger gold core reported. These include $Au_{130}(p\text{-MBT})_{50}$ (*p*-MBT = 4-methylbenzenethiolate) and $Au_{133}(SPh\text{-}^tBu)_{52}$, both reported in 2015.[47,48] While thiolate ligands are the principal focus in gold nanocluster chemistry, other ligands have also been used, including phosphines, mixed phosophine/thiolate, selenolate, and alkynyl ligands.[41] Examples include the first Au_{14} cluster, $[Au_{14}(PPh_3)_8(NO_3)_4]$, $[Au_{24}(PPh_3)_{10}(SC_2H_4Ph)_5X_2]^+$ (X = Cl, Br), $Au_{24}(SeR)_{20}$ (R = C_6H_5), and $[Au_{24}(C{\equiv}CPh)_{14}(PPh_3)_4](SbF_6)_2$.[49-52] Although less advanced, the chemistry of Ag nanoclusters has also seen recent developments, the first crystal structures of a silver thiolate nanocluster being $[Ag_{44}(p\text{-MBA})_{30}]^{4-}$ (*p*-MBA = *p*-mercaptobenzoic acid) and $[Ag_{44}(SPhF_2)_{30}]^{4-}$, reported around the same time, in 2013, in *Nature* by Bigioni *et al.* and *Nature Communications* by Zheng and Häkkinen *et al*., respectively.[53,54] Interestingly, these Ag_{44} structures are quite different from the corresponding $Au_{44}(SR)_{28}$ nanoclusters. However, there are also Au and Ag nanoclusters that are essentially identical structurally, such as $M_{25}(SR)_{18}$ (M = Au, Ag). In general, silver nanoclusters feature more complex surface structures than gold.[41] Au/Ag and Au/Cu intermetallic nanoclusters are also known. For example, $[Au_{12}Ag_{32}(SPhF_2)_{30}]^{4-}$ has the same structural framework as $[Ag_{44}(SPhF_2)_{30}]^{4-}$, but with a Ag_{12} icosahedral shell replaced by a Au_{12} layer.[54] There are also series of Au/Cu intermetallic nanoclusters, including $Au_{13}Cu_n$ (n = 2, 4, 8) ligated by 2-

pyridylthiolate (2-SPy).[55] In contrast, nanoclusters containing only copper are exceptionally rare. To our knowledge, the only one not reported in this dissertation is $[Cu_{13}\{S_2CN^nBu_2\}_6(C{\equiv}CR)_4]^+$ (R = C(O)OMe, C_6H_4F), reported by Liu and coworkers in 2016.[56]

1.4.1 Superatoms

NCs often have specific numbers of metal-metal bonded electrons (magic numbers: N^* = 2, 8, 18, 20, 34, 58, 92, 138…) that correspond to a closed shell diamagnetic electronic structure, which imparts stability to the cluster. These mixed-valent NCs have partial M(0) character and are termed superatoms.[57] Superatom electronic theory parallels atomic theory in that it predicts the stability and chemical nature of simple metal clusters and nanoclusters. The free electrons in superatoms are delocalized and occupy molecular orbitals that resemble atomic orbitals. For spherical metal clusters, the "superatomic orbitals" are as follows: $1S^2 \mid 1P^6 \mid 1D^{10} \mid 2S^2\ 1F^{14} \mid 2P^6\ 1G^{18} \mid 2D^{10}\ 3S^2\ 1H^{22} \mid$…, where S, P, D, F, G, H, denote the angular-momentum characters.[57] Thus, a closed shell superatom can be thought of as the nanocluster equivalent of a noble gas. The equation to determine the magic number (N^*) for a ligand protected NC is $N^* = Nv_A - M - z$, where N is the number of core metal atoms, v_A is the atomic valence of the core metal atoms (v_A = 1 for group 11 metals), M is the number of anionic ligands (assuming ligands with a -1 charge), and z is the overall charge on the cluster.[57] For example, for $[Au_{102}(p\text{-MBA})_{44}]$, N = 102, v_A = 1, M = 44, and z = 0, resulting in a magic number, N^*, of 58, which is one of the shell closing magic numbers.

1.5 General Remarks

This work started as a study of lignin depolymerization. However, the need for more well-defined catalysts shifted the goal of this research to improving the understanding of

nanocluster chemistry through the synthesis and characterization of new copper hydride nanoclusters.

Chapter 2 describes the oxidation of a variety of simple alcohol lignin model compounds and activated alkanes using Lewis acid activated TEMPO. This system is able to oxidize both primary and secondary alcohols to the corresponding aldehyde or ketone, however, in some instances over oxidation of the substrate and incorporation of TEMPO is observed. The reactivity of TEMPO when activated by a stronger Lewis acid is also explored.

Chapter 3 details the synthesis of a Cu_{14} cluster from Stryker's reagent, $[(Ph_3P)CuH]_6$, in a high yielding ligand exchange reaction. This cluster was characterized by X-ray crystallography, NMR spectroscopy, and mass spectrometry. DFT analysis was performed to locate probable locations for the hydride ligands, because they cannot be located by X-ray crystallography. The cluster's reactivity with CO_2 is also described.

Chapter 4 describes the synthesis of a rare Cu_{25} superatom with magic number $N^* = 2$, showing that cluster size can be controlled by adjusting the metal to ligand ratio in the reaction mixture. A Cu_{18} cluster containing all Cu(I) is also isolated in this reaction. X-ray crystallography, NMR spectroscopy, ESI mass spectrometry, and DFT were used to study these complexes. In addition, XANES and EXAFS data were collected to probe the average oxidation state and gain structural information for these clusters.

Chapter 5 describes the ligand exchange induced growth of the Cu_{25} superatom to a larger Cu_{29} cluster. The kinetics of this transformation were monitored by UV-vis spectroscopy and a mechanism for the reaction is discussed. This cluster was characterized

by X-ray crystallography, NMR spectroscopy, and mass spectrometry, as well as XANES and EXAFS.

Chapter 6 details the synthesis of two new Cu_{26} clusters by expansion of the strategy used to generate the Cu_{25} cluster. One of them tentatively has the highest Cu(0) character observed in a copper nanocluster. Pure material has been isolated. However, the characterization has proven challenging.

Chapter 7 details a critical re-evaluation of a previously published complex, $Cu_8(MPP)_4$, which struck us as highly unusual because it is a mixed valent Cu(0)/Cu(I) complex. Through NMR spectroscopy and mass spectrometry, it is demonstrated that the reported complex does not exist and its probable identity is described. A discussion on the danger of over reliance on only one characterization technique, such as mass spectrometry is also included.

1.6 References

(1) Chen, P.; Peng, L. In *Biological Conversion of Biomass for Fuels and Chemicals: Explorations from Natural Utilization Systems*; The Royal Society of Chemistry: 2014, p 83.

(2) Collinson, S. R.; Thielemans, W. The catalytic oxidation of biomass to new materials focusing on starch, cellulose and lignin. *Coord. Chem. Rev.* **2010**, *254*, 1854.

(3) Zakzeski, J.; Bruijnincx, P. C. A.; Jongerius, A. L.; Weckhuysen, B. M. The Catalytic Valorization of Lignin for the Production of Renewable Chemicals. *Chem. Rev.* **2010**, *110*, 3552.

(4) Chakar, F. S.; Ragauskas, A. J. Review of current and future softwood kraft lignin process chemistry. *Ind. Crop. Prod.* **2004**, *20*, 131.

(5) Besson, M.; Gallezot, P.; Pinel, C. Conversion of Biomass into Chemicals over Metal Catalysts. *Chem. Rev.* **2014**, *114*, 1827.

(6) Feghali, E.; Cantat, T. Unprecedented organocatalytic reduction of lignin model compounds to phenols and primary alcohols using hydrosilanes. *Chem. Commun.* **2014**, *50*, 862.

(7) Bozell, J. J.; Holladay, J. E.; Johnson, D.; White, J. F. *Top Value Added Chemicals From Biomass - II: Results of Screening for Potential Candidates from Biorefinery Lignin*, Pacific Northwest National Laboratory, 2007.

(8) Wong, D. S. Structure and Action Mechanism of Ligninolytic Enzymes. *Appl Biochem Biotechnol* **2009**, *157*, 174.

(9) Martinez, A. T.; Speranza, M.; Ruiz-Duenas, F. J.; Ferreira, P.; Camarero, S.; Guillen, F.; Martinez, M. J.; Gutierrez, A.; del Rio, J. C. Biodegradation of lignocellulosics: microbial, chemical, and enzymatic aspects of the fungal attack of lignin. *International microbiology : the official journal of the Spanish Society for Microbiology* **2005**, *8*, 195.

(10) Rahimi, A.; Azarpira, A.; Kim, H.; Ralph, J.; Stahl, S. S. Chemoselective Metal-Free Aerobic Alcohol Oxidation in Lignin. *J. Am. Chem. Soc.* **2013**, *135*, 6415.

(11) Zhao, C.; Lercher, J. A. In *The Role of Catalysis for the Sustainable Production of Bio-fuels and Bio-chemicals*; Lappas, A. A., Stöcker, M., Eds.; Elsevier: Amsterdam, 2013, p 289.

(12) Nguyen, J. D.; Matsuura, B. S.; Stephenson, C. R. J. A Photochemical Strategy for Lignin Degradation at Room Temperature. *J. Am. Chem. Soc.* **2013**, *136*, 1218.

(13) Matson, T. D.; Barta, K.; Iretskii, A. V.; Ford, P. C. One-Pot Catalytic Conversion of Cellulose and of Woody Biomass Solids to Liquid Fuels. *J. Am. Chem. Soc.* **2011**, *133*, 14090.

(14) Macala, G. S.; Matson, T. D.; Johnson, C. L.; Lewis, R. S.; Iretskii, A. V.; Ford, P. C. Hydrogen Transfer from Supercritical Methanol over a Solid Base Catalyst: A Model for Lignin Depolymerization. *ChemSusChem* **2009**, *2*, 215.

(15) Barta, K.; Matson, T. D.; Fettig, M. L.; Scott, S. L.; Iretskii, A. V.; Ford, P. C. Catalytic disassembly of an organosolv lignin via hydrogen transfer from supercritical methanol. *Green Chem.* **2010**, *12*, 1640.

(16) Barta, K.; Ford, P. C. Catalytic Conversion of Nonfood Woody Biomass Solids to Organic Liquids. *Acc. Chem. Res.* **2014**, *47*, 1503.

(17) Bernt, C. M.; Bottari, G.; Barrett, J. A.; Scott, S. L.; Barta, K.; Ford, P. C. Mapping reactivities of aromatic models with a lignin disassembly catalyst. Steps toward controlling product selectivity. *Catal. Sci. Technol.* **2016**, *6*, 2984.

(18) Barrett, J. A.; Gao, Y.; Bernt, C. M.; Chui, M.; Tran, A. T.; Foston, M. B.; Ford, P. C. Enhancing Aromatic Production from Reductive Lignin Disassembly: in Situ O-Methylation of Phenolic Intermediates. *ACS Sustainable Chem. Eng.* **2016**, *4*, 6877.

(19) Chui, M.; Metzker, G.; Bernt, C. M.; Tran, A. T.; Burtoloso, A. C. B.; Ford, P. C. Probing the Lignin Disassembly Pathways with Modified Catalysts Based on Cu-Doped Porous Metal Oxides. *ACS Sustainable Chem. Eng.* **2017**, *5*, 3158.

(20) Din, M. I.; Rehan, R. Synthesis, Characterization, and Applications of Copper Nanoparticles. *Anal. Lett.* **2017**, *50*, 50.

(21) Lohse, S. E.; Murphy, C. J. Applications of Colloidal Inorganic Nanoparticles: From Medicine to Energy. *J. Am. Chem. Soc.* **2012**, *134*, 15607.

(22) Youngil, L.; Jun-rak, C.; Kwi Jong, L.; Nathan, E. S.; Donghoon, K. Large-scale synthesis of copper nanoparticles by chemically controlled reduction for applications of inkjet-printed electronics. *Nanotechnology* **2008**, *19*, 415604.

(23) Grouchko, M.; Kamyshny, A.; Magdassi, S. Formation of air-stable copper-silver core-shell nanoparticles for inkjet printing. *J. Mater. Chem.* **2009**, *19*, 3057.

(24) Norman, A. L.; Evagelos, K. A.; Wendelin, J. S. Graphene-stabilized copper nanoparticles as an air-stable substitute for silver and gold in low-cost ink-jet printable electronics. *Nanotechnology* **2008**, *19*, 445201.

(25) Tang, X.-F.; Yang, Z.-G.; Wang, W.-J. A simple way of preparing high-concentration and high-purity nano copper colloid for conductive ink in inkjet printing technology. *Colloids and Surfaces A: Physicochem. Eng. Aspects* **2010**, *360*, 99.

(26) Kang, J. S.; Kim, H. S.; Ryu, J.; Thomas Hahn, H.; Jang, S.; Joung, J. W. Inkjet printed electronics using copper nanoparticle ink. *J. Mater. Sci: Mater. Electron.* **2010**, *21*, 1213.

(27) Magdassi, S.; Grouchko, M.; Kamyshny, A. Copper Nanoparticles for Printed Electronics: Routes Towards Achieving Oxidation Stability. *Materials* **2010**, *3*, 4626.

(28) Camacho-Flores, B. A.; Martinez-Alvarez, O.; Arenas-Arrocena, M. C.; Garcia-Contreras, R.; Argueta-Figueroa, L.; de la Fuente-Hernandez, J.; Acosta-Torres, L. S. Copper: Synthesis Techniques in Nanoscale and Powerful Application as an Antimicrobial Agent. *J. Nanomater.* **2015**, *2015*, 10.

(29) Zarschler, K.; Rocks, L.; Licciardello, N.; Boselli, L.; Polo, E.; Garcia, K. P.; De Cola, L.; Stephan, H.; Dawson, K. A. Ultrasmall inorganic nanoparticles: State-of-the-art and perspectives for biomedical applications. *Nanomedicine* **2016**, *12*, 1663.

(30) Palza, H. Antimicrobial Polymers with Metal Nanoparticles. *Int. J. Mol. Sci.* **2015**, *16*, 2099.

(31) Anton, N.; Xiaolong, D.; Qing, X.; Cvelbar, U.; DeGeyter, N.; Morent, R.; Christophe, L. Non-thermal plasma technology for the development of antimicrobial surfaces: a review. *J. Phys. D: Appl. Phys.* **2016**, *49*, 204002.

(32) Gawande, M. B.; Goswami, A.; Felpin, F.-X.; Asefa, T.; Huang, X.; Silva, R.; Zou, X.; Zboril, R.; Varma, R. S. Cu and Cu-Based Nanoparticles: Synthesis and Applications in Catalysis. *Chem. Rev.* **2016**, *116*, 3722.

(33) Varghese, O. K.; Paulose, M.; LaTempa, T. J.; Grimes, C. A. High-Rate Solar Photocatalytic Conversion of CO_2 and Water Vapor to Hydrocarbon Fuels. *Nano Lett.* **2009**, *9*, 731.

(34) Yang, H.-C.; Lin, H.-Y.; Chien, Y.-S.; Wu, J. C.-S.; Wu, H.-H. Mesoporous TiO_2/SBA-15, and Cu/TiO_2/SBA-15 Composite Photocatalysts for Photoreduction of CO_2 to Methanol. *Catal. Lett.* **2009**, *131*, 381.

(35) Zhang, X.; Han, F.; Shi, B.; Farsinezhad, S.; Dechaine, G. P.; Shankar, K. Photocatalytic Conversion of Diluted CO_2 into Light Hydrocarbons Using Periodically Modulated Multiwalled Nanotube Arrays. *Angew. Chem. Int. Ed.* **2012**, *51*, 12732.

(36) Schouten, K. J. P.; Pérez Gallent, E.; Koper, M. T. M. The influence of pH on the reduction of CO and CO_2 to hydrocarbons on copper electrodes. *J. Electroanal. Chem.* **2014**, *716*, 53.

(37) Kas, R.; Kortlever, R.; Milbrat, A.; Koper, M. T. M.; Mul, G.; Baltrusaitis, J. Electrochemical CO_2 reduction on Cu_2O-derived copper nanoparticles: controlling the catalytic selectivity of hydrocarbons. *Phys. Chem. Chem. Phys.* **2014**, *16*, 12194.

(38) Nakata, K.; Ozaki, T.; Terashima, C.; Fujishima, A.; Einaga, Y. High-Yield Electrochemical Production of Formaldehyde from CO_2 and Seawater. *Angew. Chem. Int. Ed.* **2014**, *53*, 871.

(39) Ren, D.; Deng, Y.; Handoko, A. D.; Chen, C. S.; Malkhandi, S.; Yeo, B. S. Selective Electrochemical Reduction of Carbon Dioxide to Ethylene and Ethanol on Copper(I) Oxide Catalysts. *ACS Catal.* **2015**, *5*, 2814.

(40) Roberts, F. S.; Kuhl, K. P.; Nilsson, A. High selectivity for ethylene from carbon dioxide reduction over copper nanocube electrocatalysts. *Angew. Chem. Int. Ed.* **2015**, *54*, 5179.

(41) Jin, R.; Zeng, C.; Zhou, M.; Chen, Y. Atomically Precise Colloidal Metal Nanoclusters and Nanoparticles: Fundamentals and Opportunities. *Chem. Rev.* **2016**, *116*, 10346.

(42) Qian, H.; Zhu, M.; Wu, Z.; Jin, R. Quantum Sized Gold Nanoclusters with Atomic Precision. *Acc. Chem. Res.* **2012**, *45*, 1470.

(43) Zhu, M.; Aikens, C. M.; Hollander, F. J.; Schatz, G. C.; Jin, R. Correlating the Crystal Structure of A Thiol-Protected Au_{25} Cluster and Optical Properties. *J. Am. Chem. Soc.* **2008**, *130*, 5883.

(44) Heaven, M. W.; Dass, A.; White, P. S.; Holt, K. M.; Murray, R. W. Crystal Structure of the Gold Nanoparticle $[N(C_8H_{17})_4][Au_{25}(SCH_2CH_2Ph)_{18}]$. *J. Am. Chem. Soc.* **2008**, *130*, 3754.

(45) Dainese, T.; Antonello, S.; Gascón, J. A.; Pan, F.; Perera, N. V.; Ruzzi, M.; Venzo, A.; Zoleo, A.; Rissanen, K.; Maran, F. $Au_{25}(SEt)_{18}$, a Nearly Naked Thiolate-Protected Au_{25} Cluster: Structural Analysis by Single Crystal X-ray Crystallography and Electron Nuclear Double Resonance. *ACS Nano* **2014**, *8*, 3904.

(46) Jadzinsky, P. D.; Calero, G.; Ackerson, C. J.; Bushnell, D. A.; Kornberg, R. D. Structure of a Thiol Monolayer-Protected Gold Nanoparticle at 1.1 Å Resolution. *Science* **2007**, *318*, 430.

(47) Chen, Y.; Zeng, C.; Liu, C.; Kirschbaum, K.; Gayathri, C.; Gil, R. R.; Rosi, N. L.; Jin, R. Crystal Structure of Barrel-Shaped Chiral Au_{130}(*p*-MBT)$_{50}$ Nanocluster. *J. Am. Chem. Soc.* **2015**, *137*, 10076.

(48) Dass, A.; Theivendran, S.; Nimmala, P. R.; Kumara, C.; Jupally, V. R.; Fortunelli, A.; Sementa, L.; Barcaro, G.; Zuo, X.; Noll, B. C. $Au_{133}(SPh\text{-}^tBu)_{52}$ Nanomolecules: X-ray Crystallography, Optical, Electrochemical, and Theoretical Analysis. *J. Am. Chem. Soc.* **2015**, *137*, 4610.

(49) Gutrath, B. S.; Oppel, I. M.; Presly, O.; Beljakov, I.; Meded, V.; Wenzel, W.; Simon, U. $[Au_{14}(PPh_3)_8(NO_3)_4]$: An Example of a New Class of $Au(NO_3)$-Ligated Superatom Complexes. *Angew. Chem. Int. Ed.* **2013**, *52*, 3529.

(50) Das, A.; Li, T.; Nobusada, K.; Zeng, Q.; Rosi, N. L.; Jin, R. Total Structure and Optical Properties of a Phosphine/Thiolate-Protected Au_{24} Nanocluster. *J. Am. Chem. Soc.* **2012**, *134*, 20286.

(51) Song, Y.; Wang, S.; Zhang, J.; Kang, X.; Chen, S.; Li, P.; Sheng, H.; Zhu, M. Crystal Structure of Selenolate-Protected $Au_{24}(SeR)_{20}$ Nanocluster. *J. Am. Chem. Soc.* **2014**, *136*, 2963.

(52) Wan, X.-K.; Xu, W. W.; Yuan, S.-F.; Gao, Y.; Zeng, X.-C.; Wang, Q.-M. A Near-Infrared-Emissive Alkynyl-Protected Au_{24} Nanocluster. *Angew. Chem. Int. Ed.* **2015**, *54*, 9683.

(53) Desireddy, A.; Conn, B. E.; Guo, J.; Yoon, B.; Barnett, R. N.; Monahan, B. M.; Kirschbaum, K.; Griffith, W. P.; Whetten, R. L.; Landman, U.; Bigioni, T. P. Ultrastable silver nanoparticles. *Nature* **2013**, *501*, 399.

(54) Yang, H.; Wang, Y.; Huang, H.; Gell, L.; Lehtovaara, L.; Malola, S.; Häkkinen, H.; Zheng, N. All-thiol-stabilized Ag_{44} and $Au_{12}Ag_{32}$ nanoparticles with single-crystal structures. *Nature Commun.* **2013**, *4*, 2422.

(55) Yang, H.; Wang, Y.; Lei, J.; Shi, L.; Wu, X.; Mäkinen, V.; Lin, S.; Tang, Z.; He, J.; Häkkinen, H.; Zheng, L.; Zheng, N. Ligand-Stabilized $Au_{13}Cu_x$ (x = 2, 4, 8)

Bimetallic Nanoclusters: Ligand Engineering to Control the Exposure of Metal Sites. *J. Am. Chem. Soc.* **2013**, *135*, 9568.

(56) Chakrahari, K. K.; Liao, J.-H.; Kahlal, S.; Liu, Y.-C.; Chiang, M.-H.; Saillard, J.-Y.; Liu, C. W. $[Cu_{13}\{S_2CN^nBu_2\}_6(acetylide)_4]^+$: A Two-Electron Superatom. *Angew. Chem. Int. Ed.* **2016**, *55*, 14704.

(57) Walter, M.; Akola, J.; Lopez-Acevedo, O.; Jadzinsky, P. D.; Calero, G.; Ackerson, C. J.; Whetten, R. L.; Grönbeck, H.; Häkkinen, H. A unified view of ligand-protected gold clusters as superatom complexes. *Proc. Natl. Acad. Sci.* **2008**, *105*, 9157.

Chapter 2. **Oxidation of Alcohols and Activated Alkanes with Lewis Acid-Activated TEMPO**

Portions of this work were published in:

Thuy-Ai D. Nguyen; Ashley M. Wright; Joshua S. Page; Guang Wu; Trevor W. Hayton. Oxidation of Alcohols and Activated Alkanes with Lewis Acid-Activated TEMPO. *Inorg. Chem*. **2014**, 53, 11377-11387.

2.1 Introduction

N-oxyl radicals, such as TEMPO (TEMPO = 2,2,6,6-tetramethylpiperidine-*N*-oxyl) and ABNO (ABNO = 9-azabicyclo[3.3.1]nonane *N*-oxyl), are widely used in a variety of organic oxidations. In particular, they have proven excellent reagents for the selective oxidation of primary alcohols,[1-5] secondary alcohols,[6,7] primary amines,[8] and the α-oxyamination of aldehydes.[9] More recently, TEMPO has also found use in the depolymerization of lignin. For example, Stahl and co-workers demonstrated that efficient oxidation of the alcohol functionalities in lignin[10] can be achieved with the 4-acetamido-TEMPO/HNO_3/HCl system, wherein the active oxidant is likely [4-acetamido-TEMPO]$^+$. Stephenson and co-workers report a similar lignin oxidation process, in which the benzylic alcohol functionalities are oxidized by [4-acetamido-TEMPO][BF_4].[11] Hanson and co-workers have also had considerable success in effecting the degradation of lignin model compounds by using a TEMPO-based oxidant.[12,13] For example, they reported that the CuCl/TEMPO and CuOTf/2,6-lutidine/TEMPO catalyst systems could oxidatively cleave both a β-O-4 lignin model and β-1 lignin model, using oxygen as the terminal oxidant. While promising, these

Cu/TEMPO protocols required harsh conditions and long reaction times, which is significant because several lignin functional groups are not stable at elevated temperatures.[11]

Previously, our research group reported the use of the Lewis acids $FeCl_3$ and $AlCl_3$, to activate TEMPO towards the oxidation of alcohols.[14] The resulting $MCl_3(\eta^1$-TEMPO) (M = Fe, **2.1**; Al, **2.2**) adducts were observed to quickly oxidize both 1° and 2° alcohols, forming the corresponding carbonyl compounds under mild conditions. Complexes **2.1** and **2.2** are also capable of oxidizing 9,10-dihydroanthracene, although this oxidation is much slower than those performed with alcohol substrates. Importantly, complexes **2.1** and **2.2** appear to be more reactive than other TEMPO-based systems, oxidizing alcohols within minutes at room temperature. While the $MCl_3(\eta^1$-TEMPO) system appears to have some advantages over other TEMPO protocols, there are still several mechanistic questions that remain unanswered. In particular, previous work on the Cu/TEMPO system suggests that the reaction proceeds via a concerted $2e^-$ oxidation, wherein a Cu-bound alcohol is simultaneously oxidized by TEMPO and Cu(II).[15] In contrast, preliminary mechanistic experiments with $MCl_3(\eta^1$-TEMPO) suggest that the reaction proceeds via an initial $1e^-$ hydrogen atom transfer event, which apparently makes this system unique amongst TEMPO-containing oxidants. As a result, I wanted to solidify our proposed mechanism by exploring the reactivity of $MCl_3(\eta^1$-TEMPO) with a variety of mechanistic probes, including activated alkanes and radical clocks. Herein, is reported the reactivity of **2.1** and **2.2** towards a variety of alcohols and activated alkanes, including xanthene.[10,16-24] The latter substrate is significant, because its reactivity confirms that these oxidations can proceed via a concerted proton coupled electron transfer (CPET) step, as was previously surmised.[14] To

test the role of the Lewis acid in activating the TEMPO moiety, I also explored the reactivity of TEMPO with $FeBr_3$ in Et_2O.

2.2 Results and Discussion

2.2.1 Exploration of Substrate Scope

Reaction of $MCl_3(\eta^1$-TEMPO) (M = Fe, **2.1**; Al, **2.2**) with 3,4-dimethoxybenzyl alcohol (**2.3**), in Et_2O (for **2.1**) or CD_2Cl_2 (for **2.2**), results in the complete consumption of the alcohol within 10 min at room temperature and formation of 3,4-dimethoxybenzaldehyde (**2.4**) in good yields (Table 2.1, Entry 1). For both reactions, compound **2.4** is the only organic product observable in the reaction mixture by ^{1}H NMR spectroscopy.[25] Similarly, oxidation of 1-phenyl-2-phenoxyethanol (**2.5**), which has been previously employed as a β-O-4 lignin model compound,[21-23] with complex **2.1** results in complete consumption of the alcohol within 3 h, and formation of 2-phenoxyacetophenone (**2.6**) in 65% yield (Table 2.1, Entry 2). Complex **2.2** also oxidizes **2.5** to **2.6** (75% yield); however, a small amount of a new product is also observed in this transformation, namely, 2-(2,2,6,6-tetramethylpiperidine-*N*-oxyl)-2-phenoxyacetophenone (**2.7**), which is produced in 5% yield (Table 2.1, Entry 2). This product is likely formed through further oxidation of compound **2.6** by complex **2.2**, which results in formation of an α-keto radical, via H-atom abstraction. The α-keto radical is subsequently quenched by coupling to free TEMPO, resulting in the formation of the new C-O bond. The formation of **2.7** is perhaps not surprising considering that the strength of the C-H bond abstracted in **2.6** (80.6 kcal/mol in DMSO)[26] is identical to the benzylic C-H bond enthalpy of 9,10-dihydroanthracene (80.6 kcal/mol in DMSO),[14,27] which both complexes **2.1** and **2.2** can readily oxidize. Interestingly, a related α-

oxyamination using TEMPO has been previously described for enamines, and likely occurs via a similar mechanism.[9]

I also explored the reaction of complexes **2.1** and **2.2** with 1,2-diphenyl-2-methoxyethanol (**2.8**), a common β-1 lignin model compound.[10,12,21] Oxidation of **2.8** with complex **2.1** results in complete consumption of the starting material and formation of 2-methoxy-1,2-diphenylethanone (**2.9**) in 75% yield (Table 2.1, Entry 3). No other oxidation products were observed in the reaction mixture, according to ^{1}H NMR spectroscopy. In contrast, reaction of **2.2** with **2.8** does not result in the formation of **2.9**. Instead, the major organic product formed in the reaction is benzil (**2.10**) in 54% yield (77% conversion; Table 2.1, Entry 3). I suggest that formation of benzil occurs via hydrogen abstraction of the transiently formed **2.9** by complex **2.2**, which results in the formation of an α-keto radical stabilized by the captodative effect.[28] The α-keto radical is then quenched by TEMPO, resulting in the formation of a new C-O bond. This species then forms benzil by release of methoxy and piperidyl radicals. Interestingly, TEMPO is known to function as an O-atom source via N-O bond cleavage and release of the piperidyl radical.[29] For comparison, Hanson and co-workers reported that oxidation of **2.8** with O_2, in the presence of 10 mol% CuCl and 30 mol% TEMPO at 100 °C in pyridine, resulted in formation of benzaldehyde (84%) and methyl benzoate (88%).[12] I do not observe either of these products, which suggests that different mechanisms are operative in the two systems.

Table 2.1. Oxidation of lignin models by complexes **2.1** and **2.2**

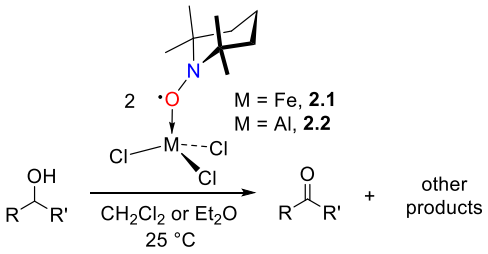

Entry	Substrate	% Conversion Fe	% Conversion Al	Product	% Yield Fe	% Yield Al
1	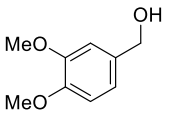 **2.3**	100	100	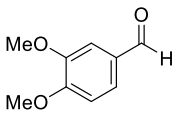 **2.4**	75	99
2	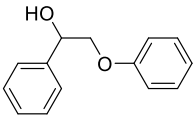 **2.5**	100	100	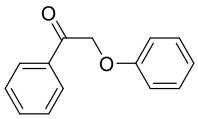 **2.6**	65	75
				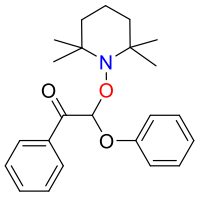 **2.7**	0	5
3	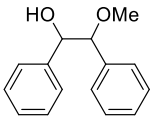 **2.8**	100	77	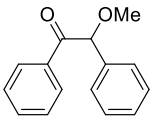 **2.9**	75	0
				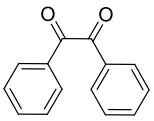 **2.10**	0	54

*Yields determined by ^{1}H NMR spectroscopy

The viability of ketones **2.6** and **2.9** to act as the substrates for the formation of **2.7** and **2.10** was confirmed by their independent reaction with complexes **2.1** and **2.2**. Thus, reaction of 2 equiv of **2.2** with **2.6** in CH_2Cl_2 results in almost complete consumption of the starting material (96% conversion) after only 3 h, and production of the α-oxyamination

product in 48% yield (Table 2.2, Entry 4). In contrast, reaction of **2.6** with 2 equiv of **2.1** in Et_2O for 18 h left the starting material largely unreacted and produced **2.7** in only 3% yield, according to ^1H NMR spectroscopy (Table 2.2, Entry 4). Oxidation of **2.9** by complex **2** in CH_2Cl_2 at room temperature for 15 h results in the formation of benzil (**2.10**) (53% yield) and 2,2-dimethoxy-2-phenylacetophenone (**2.11**) (16% yield), demonstrating that 2-methoxy-1,2-diphenylethanone (**2.9**) is a viable precursor to compound **2.10** (Table 2.2, Entry 5). Compound **2.11** is probably formed by a Lewis-acid catalyzed reaction of **2.10** with methanol.[30-32] Notably, there is no reaction observed between complex **2.1** and **2.9** in CH_2Cl_2 after 15 h of stirring (Table 2.2, Entry 5), which is consistent with the reactivity observed between **2.1** and **2.8** (Table 2.1, Entry 3). I also explored the reaction of complexes **2.1** and **2.2** with 2,3-dihydrobenzofuran (**2.12**), a model for the β-5 phenylcoumaran linkage,[24,33] and the only lignin model compound examined that did not contain an alcohol substituent. Solutions of **2.12** with 2 equiv of either complex **2.1** or **2.2** in CD_2Cl_2 were monitored by ^1H NMR spectroscopy for 18 h at room temperature. However, no consumption of **2.12** was observed in either case (Table 2.2, Entry 6).

Table 2.2. Oxidation of selected substrates by complexes **2.1** and **2.2**

Entry	Substrate	% Conversion Fe	% Conversion Al	Product	% Yield Fe	% Yield Al
4	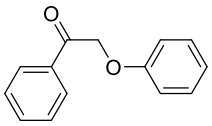 **2.6**	27	96	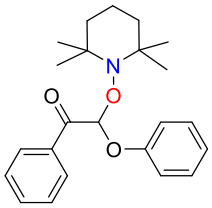 **2.7**	3	48
5	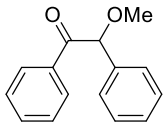 **2.9**	0	89	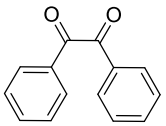 **2.10**	0	53
				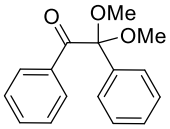 **2.11**	0	16
6	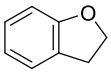 **2.12**	0	0	-	0	0

*Yields determined by ^{1}H NMR spectroscopy

I also examined the reaction of complexes **2.1** and **2.2** with 2-phenoxyethanol (**2.14**), another β-O-4 lignin model compound.[21] Interestingly, the reaction of complexes **2.1** or **2.2** with **2.14** results in complete consumption of **2.14**, according to ^{1}H NMR spectroscopy, yet yields no 2-phenoxyacetaldehyde after filtration through a basic alumina column. To explain these results, I hypothesized that **2.14** coordinates with either the Fe or Al metal centers in **2.1** and **2.2**, respectively, to form an alkoxide complex, thus inhibiting substrate oxidation. To test this hypothesis, 1.5 equiv of **2.14** was added to a solution of $FeCl_3(\eta^1$-TEMPOH) (**2.13**) in CH_2Cl_2. Complex **2.13**, which features the TEMPO ligand in its -1 oxidation state, was chosen as a model for complexes **2.1** and **2.2** to simplify the reactivity because of its reduced temperature sensitivity. Upon addition, an immediate color change from purple to

orange is observed, and upon work-up, the 2-phenoxyethoxide-bridged dimer, $[FeCl_2(\eta^1$-TEMPOH)(μ-$OCH_2CH_2OPh)]_2$ (**2.15**), was isolated in 30% yield as red-brown crystals (Scheme 2.1). The ^{1}H NMR spectrum of **2.15** in CD_2Cl_2/py-d_5 features broad singlets at -14.66 and -27.62 ppm, in a 12:4 ratio, which I have assigned to the methyl and β-methylene protons of the TEMPOH ligand, respectively. In addition, broad singlets at 7.21, 7.26, and 7.64 ppm were assigned to the three phenyl environments of the phenoxyethoxide moiety (Figures A2.1 and A2.2).

Complex **2.15** crystallizes in the triclinic space group $P\bar{1}$ as the Et_2O solvate, **2.15**·Et_2O, and its solid state molecular structure is shown in Figure 2.1. Complex **2.15** features two independent molecules in the asymmetric unit; however, only one will be discussed in detail. In the solid state complex **2.15** exists as a bimetallic species. Each Fe center in **2.15** exhibits a distorted trigonal bipyramidal coordination environment, wherein one chloride ligand and the phenoxyethoxide ligand occupy the axial positions. The phenoxyethoxide ligand also coordinates to an equatorial site of the neighboring Fe center. The Fe-O(ethoxide) bond lengths in **2.15** are 1.9341(14) and 2.0398(14) Å, which are consistent with the presence of an Fe(III)-alkoxide linkage. For comparison, related Fe(III) ethoxide complexes feature bridging Fe-O bond lengths that range from 1.965-1.991 Å.[34-36] In addition, the Fe-O(TEMPOH) bond length (Fe1-O1 = 1.9244(14) Å) is comparable to that of **2.1** (Fe-O = 1.8996(12) Å),[14] suggesting the presence of Fe^{3+} centers in **2.15**. Finally, the metrical parameters of the TEMPOH ligand in **2.15** are consistent with the presence of $[TEMPO]^-$, suggesting no change in oxidation state of this moiety has occurred.[14,37] In particular, the N1-O1 bond length in **2.15** is 1.399(2) Å, while the sum of the angles around N1 is 325.3°. For comparison, the N-O bond length in **2.13** is 1.4006(11) Å, while the sum of the angles

around the TEMPO nitrogen atom is 339.2°.[37] Additionally, a hydrogen atom was located in the difference map and successfully refined on N1.

To rationalize the formation of **2.15** I suggest that 2-phenoxyethanol (**2.14**) protonates a chloride ligand in **2.13**, generating HCl. Consistent with this hypothesis, the isolation of complex **2.15** requires that the reaction mixture be exposed to vacuum, which presumably removes the volatile HCl by-product. The formation of complex **2.15** also rationalizes the inability of complexes **2.1** and **2.2** to oxidize **2.14**, as coordination of the 2-phenoxyethanol substrate to the metal center likely protects it from oxidation, or, alternately, renders the metal center less Lewis acidic, decreasing the oxidizing power of the bound TEMPO moiety. It is interesting to note that the other alcohol substrates that we investigated (**2.3**, **2.5**, and **2.8**) do not appear to undergo the chloride protonation pathway. This may be because the alcohol substituent in 2-phenoxyethanol is less sterically hindered compared to the other lignin models studied.

Scheme 2.1. Reaction of $FeCl_3(\eta^1$-TEMPOH) with 2-phenoxyethanol

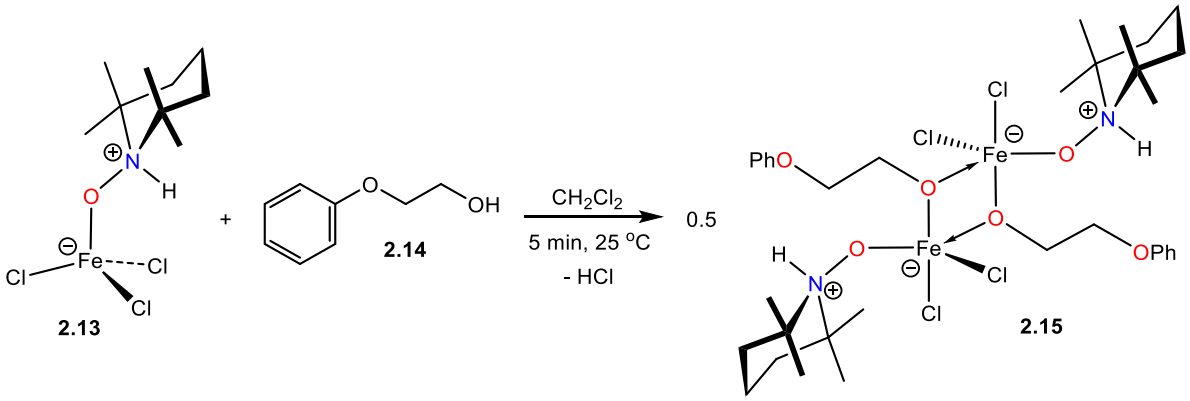

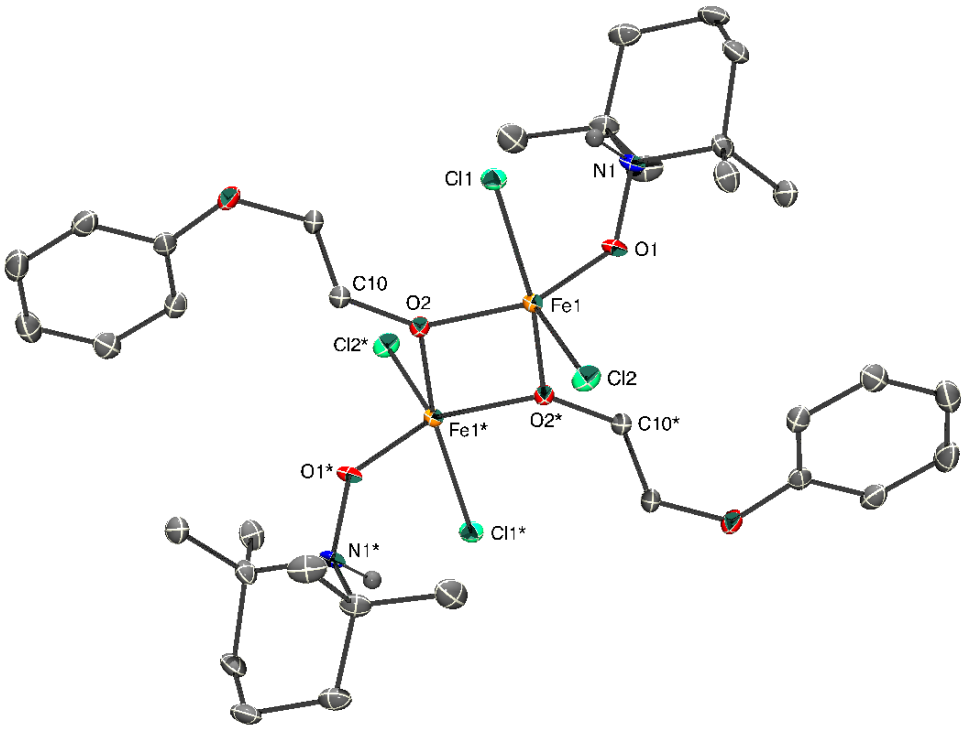

Figure 2.1. ORTEP Diagram of $[FeCl_2(\eta^1\text{-TEMPOH})(\mu\text{-}OCH_2CH_2OPh)]_2 \cdot Et_2O$ (**2.15**$\cdot Et_2O$) with 50% probability ellipsoids. One Et_2O solvent molecule, a second molecule of **2.15**, and all hydrogen atoms, except the N-H hydrogen atom, are omitted for clarity. Atoms labelled with an asterisk are generated by symmetry. Selected bond lengths (Å) and angles (deg): Fe1-O2 = 1.9341(14), Fe1-O2* = 2.0398(14), Fe1-Cl1 = 2.3211(7), Fe1-Cl2 = 2.2354(7), Fe1-O1 = 1.9244(14), N1-O1 = 1.399(2), ∑(E-O2-E) = 359.6, ∑(E-N1-E) = 325.3.

2.2.2 Mechanistic Studies

Previously, it was argued that the first step in the oxidation of substrate by complexes **2.1** and **2.2** was a concerted proton-electron transfer (CPET) event.[14,27] To further evaluate this hypothesis, and better understand the reactivity of complexes **2.1** and **2.2** toward alcohols, I explored the reactivity of $MCl_3(\eta^1\text{-TEMPO})$ with a variety of activated alkanes.

Reaction of 1,4-cyclohexadiene (**2.16**) with 2 equiv of **2.1** in toluene-d_8 results in almost complete consumption of **2.16** within 2 h, and formation of benzene in 82% yield (Table 2.3, Entry 7). Similarly, reaction of **2.16** with 2 equiv of **2.2** in CD_2Cl_2 results in the complete conversion of **2.16** into benzene within 15 min (Table 2.3, Entry 7), according to ^{1}H NMR spectroscopy. Oxidation of xanthene (**2.18**) with 2 equiv of **2.1** in CH_2Cl_2 yields bixanthenyl[38] (**2.19**) and xanthone[39] (**2.20**), in 18% and 33% yield, respectively, after 2 d at room temperature (Table 2.3, Entry 8). Similarly, oxidation of **2.18** with 2 equiv of **2.2** in CH_2Cl_2 yields **2.19** and **2.20**, in 51% and 4% yield, respectively, after 3 d at room temperature (Table 2.3, Entry 8). The presence of bixanthenyl in each reaction mixture can be rationalized by invoking the formation of the xanthenyl radical, which subsequently dimerizes to give the final product. Importantly, its presence provides evidence for an initial one-electron CPET event upon oxidation of xanthene.[40] The presence of xanthone in the reaction mixture can be similarly rationalized. However, instead of coupling to another xanthenyl radical, the xanthenyl radical instead reacts with TEMPO, forming the C-O bond. This TEMPO-xanthenyl intermediate then forms xanthone by release of the piperidyl radical.[29] The reactivity of complexes **2.1** and **2.2** with fluorene (**2.21**) and triphenylmethane (**2.22**), substrates with slightly stronger C-H bonds than xanthene, was also examined (Table 2.3, Entries 9 and 10). However, no reaction was observed upon addition of 1 equiv of **2.1** or **2.2** to either substrate in CD_2Cl_2, even after prolonged reaction times (4 d). Finally, a control reaction between TEMPO and 1,4-cyclohexadiene reveals some reactivity. However, the reaction is extremely slow, only reaching 22% conversion after 4 d at room temperature. Similarly, TEMPO will react with xanthene in the absence of a Lewis acid, but the reaction is slow, only achieving 9% conversion after 4 d. In line with this observation, Gunnoe and

co-workers reported that TEMPO will oxidize 1,4-cyclohexadiene at elevated temperatures.[41]

The experiments outlined in Table 2.3 reveal a clear correlation between the BDE (or BDFE) of the cleaved C-H bond in the substrate and its ability to react with **2.1** and **2.2**. The strongest C-H bonds that **2.1** and **2.2** are able to activate appear to be those of xanthene (BDE = 77.9 kcal/mol in DMSO) and 9,10-dihydroanthracene (BDE = 80.6 kcal/mol in DMSO),[14,27] which we tested in an earlier study. For comparison, other TEMPO/Lewis acid systems appear to be more reactive. For example, the TEMPO/$Co(OAc)_2$/NaOCl system is capable of oxidizing a variety of benzylic C-H bonds, including those of toluene (BDE = 92 kcal/mol in DMSO).[27,42] While the mechanism in the $Co(OAc)_2$ system is not entirely clear, it is possible that these oxidations proceed via the formation of a $[TEMPO]^+$ intermediate and not a TEMPO-Lewis acid adduct, as is likely the case for our system.

Table 2.3. Oxidation of activated alkanes, cyclobutanol, and cyclopropylcarbinol by complexes **2.1** and **2.2**

Entry	Substrate	% Conversion Fe	% Conversion Al	Product	% Yield[b] Fe	% Yield[b] Al	BDE[a] (kcal/mol)	BDFE[a] (kcal/mol)
7	 **2.16**	99	100	 **2.17**	82	96	76.0	67.8
8	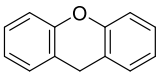 **2.18**	100	99	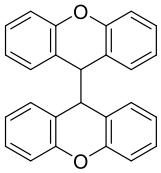 **2.19**	18	51	77.9	73.3
				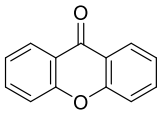 **2.20**	33	4		
9	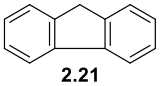 **2.21**	0	0	-	N.R.	N.R.	82.0	77.4
10	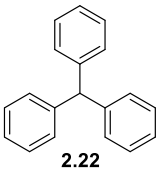 **2.22**	0	0	-	N.R.	N.R.	83.4	78.8
[c]11	 **2.23**	100	100	 **2.24**	75	100	-	-
[d]12	 **2.25**	100	100	 **2.26**	84	91	-	-
[e]13	 **2.25**	100	100	 **2.26**	98	95	-	-

[a]BDE and BDFE from ref. 27. [b]Yields determined by ^{1}H NMR spectroscopy. [c]Concentrations of **2.1** and **2.2** were 385 mM and 200 mM, respectively. [d]Concentrations of **2.1** and **2.2** were 260 mM and 190 mM, respectively. [e]Concentrations of **2.1** and **2.2** were 6.3 mM and 4.4 mM, respectively.

Finally, the reactions of complexes **2.1** and **2.2** with cyclobutanol (**2.23**) and cyclopropylcarbinol (**2.25**) were investigated. Both reagents are common mechanistic probes used to distinguish between oxidations that proceed in one- or two-electron redox steps.[43,44] This discrimination is possible because one-electron oxidants favor the formation of ring-opened products, such as butyraldehyde, or 2- and 3-butenaldehyde, while two-electron oxidants convert **2.23** and **2.25** into cyclobutanone (**2.24**) and cyclopropanecarboxaldehyde (**2.26**), respectively.[44-47] All the available evidence suggests that complexes **2.1** and **2.2** react via an initial 1-electron CPET step. Accordingly, we hypothesized that reaction of complexes **2.1** or **2.2** with **2.23** and **2.25** would result in formation of ring opened products. Thus, addition of **2.23** to 2 equiv of **2.1** or **2.2** in C_6D_6 results in complete consumption of the alcohol within 10 min at room temperature, according to ^{1}H NMR spectroscopy. Surprisingly, the only oxidation product observed in the reaction mixture is the ring-closed product **2.24** (Table 2.3, Entry 11). The reactions of **2.25** with 2 equiv of **2.1** or **2.2** in CD_2Cl_2 also yielded the ring-closed product, **2.26** as the only oxidation product (100% conversion; 84 and 91% yield, respectively; Table 2.3, Entry 12). Performing the oxidation of **2.25** at lower concentrations also only resulted in formation of the ring-closed product, **2.26** (Table 2.3, Entry 13). These observations are puzzling for several reasons. For one, complex **2.2** does not contain a redox-active metal center and should only be capable of a one-electron oxidation. Secondly, this selectivity is at odds with the reactivity observed for the other substrates investigated in this study, such as 2-phenoxyacetophenone (**2.6**) and xanthene (**2.18**). These data suggest that multiple pathways could be operative upon reaction of substrate with $MCl_3(\eta^1$-TEMPO), including a two-electron pathway involving the intermediacy of $[TEMPO]^+$ (which can function as a $2e^-$ oxidant). In this regard, we have

recently demonstrated that coordination of TEMPO to BBr_3 can generate $[TEMPO]^+$ via disproportionation of the neutral TEMPO radical.[48] In addition, $[TEMPO]^+$ is known to oxidize substituted cyclobutanols to cyclobutanone, without the formation of ring-opened products.[49] Alternately, it is possible that the ring opening rate constants for cyclobutanol and cyclopropylcarbinol are not large enough to allow for the discrimination between the $1e^-$ and $2e^-$ oxidation pathways in our system. In support of this suggestion, we note that the oxidation of cyclobutanol by $Fe(aq)^{2+}$ / O_3 results in the formation of both ring-closed and ring-opened products, demonstrating that the rates of oxidation and ring-opening are comparable in magnitude.[50] Therefore, it is apparent that care must be taken in interpreting results derived from radical clock experiments, and on balance, we still suggest that for our system the $1e^-$ mechanism is most consistent with available evidence.

2.2.3 Activation of TEMPO with $FeBr_3$

Previously, we speculated that activation of TEMPO with stronger Lewis acids would allow us to expand the substrate scope to unactivated alkanes.[14,48] To test this hypothesis I explored the reaction of $FeBr_3$ with TEMPO. While a quantitative evaluation of the Lewis acidity of $FeBr_3$ has not been performed,[51] it is likely to be a stronger Lewis acid than $FeCl_3$. I based this conclusion on the knowledge that bromide salts are often better Lewis acids that their chloride congeners. For example, it is well established than BBr_3 is a stronger Lewis acid that BCl_3.[52-54] Likewise, thermochemical data suggest that $AlBr_3$ is a stronger Lewis acid than $AlCl_3$.[51] Given these considerations, I rationalized that $FeBr_3$ would likely follow the same trend as the Group 13 Lewis acids. Accordingly, addition of 1 equiv of TEMPO to an Et_2O solution of $FeBr_3$ results in the immediate formation of an orange precipitate. A subsequent ^1H NMR analysis of this solid reveals the presence of two major species,

identified as $FeBr_3(\eta^1$-TEMPOH) (**2.27**) and $[FeBr_2(\eta^1$-TEMPOH)$]_2(\mu$-O) (**2.28**) (Scheme 2.3). These species are present in an approximate 3:2 ratio, respectively.

Scheme 2.2. Reaction of $FeBr_3$ with TEMPO

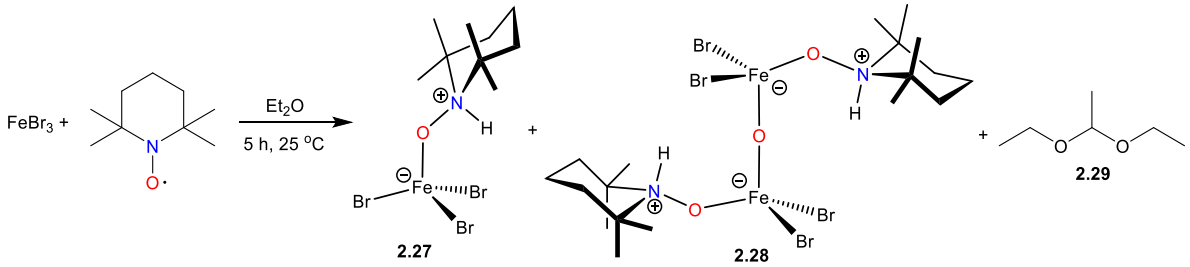

The identity of complex **2.27** was determined by comparison of its ^{1}H NMR spectral parameters with those of chloride congener, $FeCl_3(\eta^1$-TEMPOH).[14] In particular, **2.27** features a diagnostic resonance at δ 59.20 ppm, assignable to a TEMPO β-H resonance, in its ^{1}H NMR spectrum in CD_2Cl_2 (Figure A2.11). This chemical shift is nearly identical to the analogous TEMPO β-H resonance observed for $FeCl_3(\eta^1$-TEMPOH).[14] Unfortunately, I have been unable to cleanly separate complex **2.27** from **2.28**, and so was unable to complete its characterization. However, Joshua Page, a former undergraduate student in our group, along with Ashley Wright, a former graduate student in our group, were able to isolate a few X-ray quality crystals of **2.27**, which has permitted its characterization by X-ray crystallography. Complex **2.27** crystallizes in the orthorhombic space group Pnma, and its solid state molecular structure is shown in Figure 2.2. Complex **2.27** is isostructural with $MCl_3(\eta^1$-TEMPOH) (M = Fe, Al).[14] It features an N1-O1 bond length of 1.406(3) Å, consistent with the presence of the reduced $[TEMPO]^-$ moiety. In addition, the sum of the angles around N1 is 339.2°, while a hydrogen atom was located in the difference map and successfully refined on N1. Finally, the Fe1-O1 bond length in **2.27** is 1.882(2) Å, which is similar to that exhibited by $FeCl_3(\eta^1$-TEMPOH).[14] Interestingly, addition of 1 equiv of

TEMPOH to an Et_2O solution of $FeBr_3$ also generates a mixture of **2.27** and **2.28**. Under these conditions, **2.27** and **2.28** are formed in a 1:1 ratio, according to ^1H NMR spectroscopy (Figure A2.12).

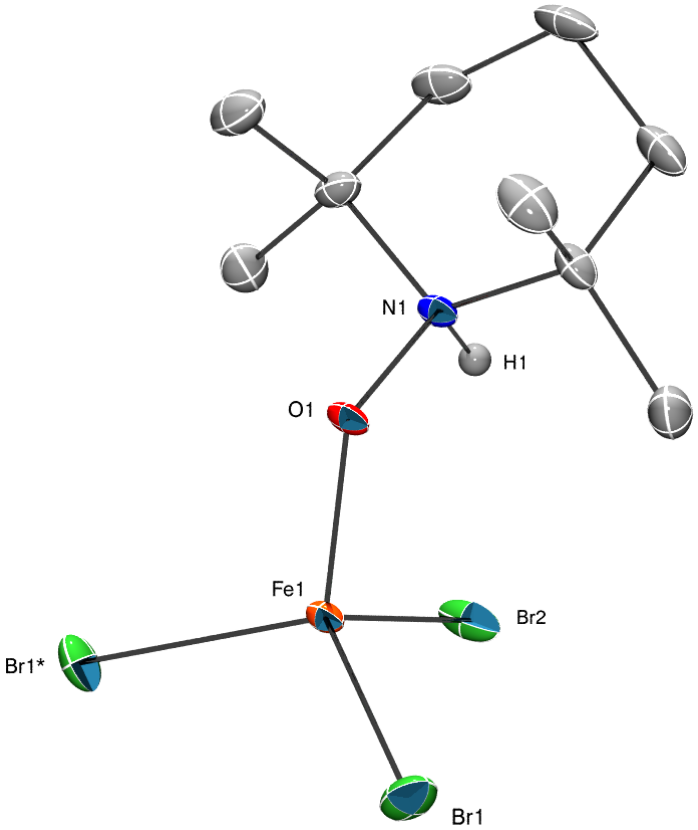

Figure 2.2. ORTEP Diagram of $FeBr_3(\eta^1$-TEMPOH) (**2.27**) with 50% probability ellipsoids. All hydrogen atoms, except the N-H hydrogen atom, are omitted for clarity. Atoms labelled with an asterisk are generated by symmetry. Selected bond lengths (Å) and angles (deg): Fe1-Br1 = 2.3184(3), Fe1-Br2 = 2.3396(5), Fe1-O1 = 1.882(2), N1-O1 = 1.406(3), ∑(E-N1-E) = 339.2.

Complex **2.28** can be generated in higher yield by reaction of 1 equiv of TEMPO with $FeBr_3$ in Et_2O, in the presence of 1 equiv of 1,4-cyclohexadiene. When formed in this manner, it can then be separated from the small amount of **2.27** that is also generated in the

reaction by recrystallization twice from CH_2Cl_2/Et_2O. Generated in this fashion, **2.28** can be isolated as an orange crystalline solid in 32% yield. Its ^1H NMR spectrum in CD_2Cl_2 exhibits two broad resonances at δ 3.72 and 1.86 ppm, assignable to the methyl protons of TEMPOH, and three broad resonances at δ 6.39, 2.36, and 1.64 ppm, assignable to the methylene protons of TEMPOH. The resonance assignable to the NH proton is observed at δ 47.21 ppm. I suggest that the bridged oxo ligand in complex **2.28** is derived from the TEMPO moiety, based on the well-established ability of TEMPO to act as an oxygen atom source in both transition metal and actinide systems.[29,55-58] For example, reaction of $Fe(hfac)_2(H_2O)_2$ with TEMPO results in O-atom transfer and formation of an Fe(III) oxo-bridged dimer, along with formation of the piperidinium ion.[59]

Complex **2.28** crystallizes in the orthorhombic space group Pccn, and its solid state molecular structure is shown in Figure 2.3. In the solid state, complex **2.28** exists as a bimetallic oxo-bridged complex. The Fe-O(oxo) bond length in **2.28** is 1.7702(7) Å, which is consistent with the presence of a Fe(III)-bridged oxo linkage. For comparison, the closely related Fe(III) complex, $[FeBr_2(HNP(^tBu)_3)]_2(\mu\text{-}O)$, features Fe-O(oxo) bond lengths of 1.768(7) and 1.760(7) Å.[60] The Fe-O(TEMPOH) bond length in **2.28** (Fe1-O2 = 1.889(2) Å) is comparable to that of **1** (Fe-O = 1.8996(12) Å),[14] while the metrical parameters of the TEMPOH ligand in **2.28** are consistent with the presence of $[TEMPO]^-$, indicating that reduction of this moiety has occurred.[14,37] In particular, the N1-O2 bond length in **2.28** is 1.396(3) Å, while the sum of the angles around N1 is 330.0°. Additionally, a hydrogen atom was located in the difference map and successfully refined on N1. Finally, the Fe-Br bond lengths in **2.28** (av. 2.34 Å) are consistent with those of **2.27** and other Fe^{3+} bromide complexes.[60]

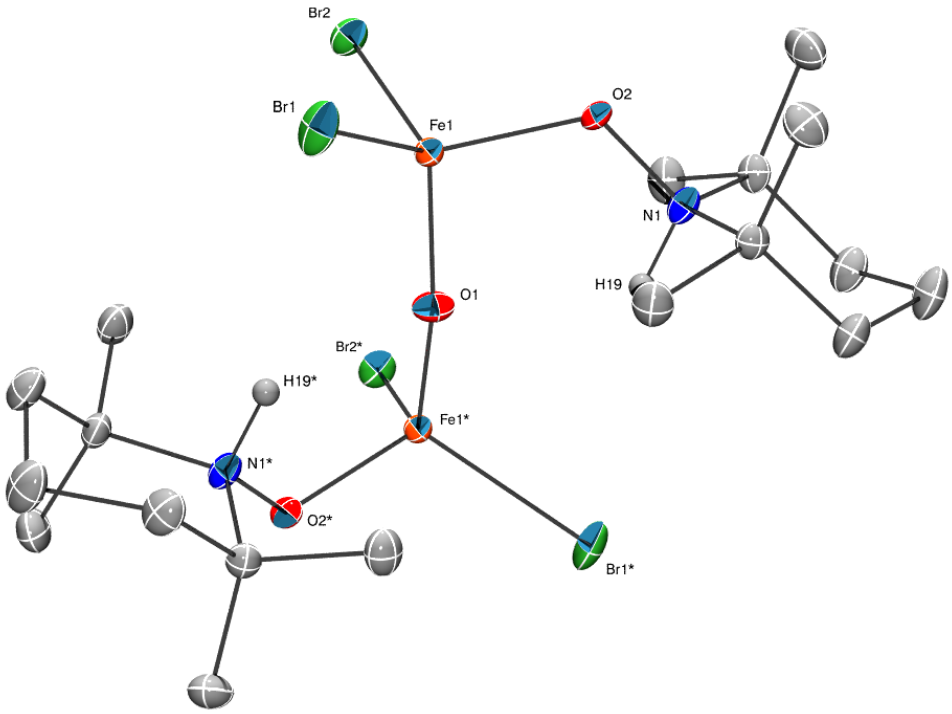

Figure 2.3. ORTEP Diagram of $[FeBr_2(\eta^1\text{-TEMPOH})]_2(\mu\text{-O})$ (**24**) with 50% probability ellipsoids. All hydrogen atoms, except the N-H hydrogen atom, are omitted for clarity. Atoms labelled with an asterisk are generated by symmetry. Selected bond lengths (Å) and angles (deg): Fe1-Br1 = 2.3565(4), Fe1-Br2 = 2.3312(5), Fe1-O1 = 1.7702(7), Fe1-O2 = 1.889(2), N1-O2 = 1.396(3), ∑(E-N1-E) = 330.0.

I have also attempted to identify the organic products formed during the formation of **2.27** and **2.28**. Thus, the supernatant formed upon addition of 1 equiv of TEMPO to an Et_2O solution of $FeBr_3$ was filtered through basic alumina to remove the metal containing products. A GC/MS trace of the resulting filtrate reveals the presence of 1,1-diethoxyethane (**2.29**) (Figure A2.13). Its formation can be rationalized by invoking the formation of an Et_2O methylene radical, which subsequently reacts with a molecule of Et_2O, resulting in C-O bond cleavage, formation of 1,1-diethoxyethane, and ejection of an ethyl radical. It is unlikely that **2.29** is the only oxidation product generated in the reaction; however, other

possible Et_2O oxidation products, such as acetaldehyde,[61-63] ethylene, or ethane, were not observed in the GC trace, likely because of their greater volatility vs. that of Et_2O. Ethanol, another possible oxidation product,[61] was also not observed. Interestingly, however, unreacted TEMPO was observed in the GC/MS trace. The GC/MS analysis is significant because it confirms that $FeBr_3$/TEMPO can oxidize the methylene C-H bond in Et_2O, which is a stronger C-H bond (BDE = 92.5 kcal/mol) than the other substrates that we have probed.[27,64]

2.3 Summary

In summary, I have shown that the Lewis acid-TEMPO adducts, $MCl_3(\eta^1$-TEMPO) (M = Fe, **2.1**; Al, **2.2**), can oxidize the lignin models 3,4-dimethoxybenzyl alcohol (**3.3**), 1-phenyl-2-phenoxyethanol (**2.5**), and 1,2-diphenyl-2-methoxyethanol (**2.8**) at room temperature. I also demonstrate that complexes **2.1** and **2.2** are unable to oxidize 2-phenoxyethanol (**2.14**); instead they likely form a 2-phenoxyethoxide complex via protonation of a chloride ligand by the alcohol substituent. While these simple molecules are not very accurate models of lignin, they nonetheless represent a good starting point for further studies with lignin itself. Their oxidations likely proceed via an initial 1-electron CPET event, a hypothesis which is supported by the isolation of 2-(2,2,6,6-tetramethylpiperidyl-*N*-oxyl)-2-phenoxyacetophenone (**2.7**) upon oxidation of either **2.5** or 2-phenoxyacetophenone (**2.6**) by complex **2.2**. The isolation of bixanthenyl (**2.19**) upon oxidation of xanthene (**2.18**) by complexes **2.1** or **2.2** also supports this premise. The reaction of TEMPO with $FeBr_3$ in Et_2O results in the formation of a mixture of $FeBr_3(\eta^1$-TEMPOH) and $[FeBr_2(\eta^1$-TEMPOH)$]_2(\mu$-O), via oxidation of the solvent, Et_2O. This results

further confirms the hypothesis that the strength of the Lewis acid can modulate the oxidation potential of TEMPO and result in an expanded substate scope.

2.4 Experimental

2.4.1 General Procedures

All reactions and subsequent manipulations were performed under anaerobic and anhydrous conditions under an atmosphere of nitrogen. Hexanes, diethyl ether, and toluene were dried by passage over activated molecular sieves using a Vacuum Atmospheres solvent purification system, while methylene chloride, C_6D_6, CD_2Cl_2, and toluene-d_8 were dried over 3 Å molecular sieves for 24 h prior to use. Mesitylene, 3,4-dimethoxybenzyl alcohol (**2.3**), 2-phenoxyethanol (**2.14**), 2,3-dihydrobenzofuran (**2.12**), cyclobutanol (**2.23**), and cyclopropylcarbinol (**2.25**) were degassed and dried over 3 Å molecular sieves for 24 h prior to use. $AlCl_3(\eta^1$-TEMPO) (**2.2**),[14] $FeCl_3(\eta^1$-TEMPO) (**2.1**),[14] 1-phenyl-2-phenoxyethanol (**2.5**),[65] 2-phenoxyacetophenone (**2.6**),[66] 1,2-diphenyl-2-methoxyethanol (**2.8**) (mixture of 85:15 u (R,S + S,R): l (R,R + S,S) diastereomers),[21] and anhydrous TEMPOH[67] were prepared according to the previously reported procedures. NMR spectral data for these compounds were consistent with those reported in the literature (Note: the ^{1}H NMR spectral data for TEMPOH in C_6D_6 differ substantially between ref. 67 and 68. Our data were consistent with those in ref. 68).[14,65,43,68] Compound **8** was recrystallized from a concentrated CH_2Cl_2 solution at -25 °C and washed with cold Et_2O (3 × 1 mL) before use. All other reagents were purchased from commercial suppliers and used as received.

All NMR spectra were collected at 25 °C. ^{1}H NMR spectra were recorded on a Varian UNITY INOVA 400 MHz spectrometer, an Agilent Technologies 400-MR DD2 400 MHz Spectrometer, a Varian UNITY INOVA 500 MHz spectrometer, or an actively shielded

Varian UNITY INOVA 600 MHz spectrometer. $^{13}C\{^{1}H\}$ NMR spectra were recorded on a Varian UNITY INOVA 500 MHz spectrometer. ^{1}H and $^{13}C\{^{1}H\}$ NMR spectra are referenced to external $SiMe_4$ using the residual protio solvent peaks as internal standards (^{1}H NMR experiments) or the characteristic resonances of the solvent nuclei ($^{13}C\{^{1}H\}$ NMR experiments). All ^{1}H NMR spectra containing mesitylene as an internal standard were recorded with a relaxation delay time (d1) of 60 s. IR spectra were recorded on a Nicolet 6700 FT-IR spectrometer with a NXR FT Raman Module. GC/MS traces were collected on a Hewlett-Packard 5890A GC coupled to a Hewlett Packard 5970B Mass Selective Detector (MSD), equipped with a J&W DB-5ms capillary column (30 m × 0.25 mm I.D. with 0.25 μm film thickness). The MSD has a dedicated electron ionization (EI) source and a quadrupole mass analyzer. All other mass spectra were collected by the Mass Spectrometry Facility at the University of California, Santa Barbara. Elemental analyses were performed by the Micro-Mass Facility at the University of California, Berkeley.

2.4.2 Synthesis of 2-methoxy-1,2-diphenylethanone (2.9)

2-methoxy-1,2-diphenylethanone was prepared according to a previously reported procedure[69] for using Dess-Martin periodinane (DMP) to oxidize alcohols: To a stirring CH_2Cl_2 (3 mL) solution of 1,2-diphenyl-2-methoxyethanol (149.8 mg, 656.2 μmol) was added dropwise a CH_2Cl_2 (10 mL) solution of DMP (337.5 mg, 795.7 μmol). The reaction mixture was allowed to stir for 2.5 h, whereupon it was transferred to a separatory funnel containing 5% NaOH (aq) (10 mL) and Et_2O (20 mL). The organic layer was separated and rinsed with H_2O (2 × 30 mL), dried with anhydrous $MgSO_4$, and filtered to give a colorless solution. The solvent was then removed in vacuo to provide a white solid that was recrystallized from a concentrated CH_2Cl_2/Et_2O (1:1) solution at -25 °C and washed with

cold Et_2O (3 × 1 mL). 133.2 mg, 90% yield of **2.9**. ^{1}H NMR (500 MHz, 25 °C, CD_2Cl_2): δ 3.43 (s, 3H, OC*H*$_3$), 5.52 (s, 1 H, C*H*), 7.30 (m, 1H, *p*-Ph), 7.35 (m, 2H, *m*-Ph), 7.39-7.45 (m, 4H, Ph), 7.53 (m, 1H, *p*-Ph), 7.97 (m, 2H, *o*-Ph). ^{13}C{^{1}H} NMR (126 MHz, 25 °C, CD_2Cl_2): δ 57.91 (*C*H$_3$), 87.00 (H*C*OMe), 128.21 (Ar), 129.01 (Ar), 129.04 (Ar), 129.31 (Ar), 129.44 (Ar), 133.75 (Ar), 135.78 (Ar), 136.95 (Ar), 197.46 (*C*O). FI-MS: *m/z* 226.10 [M]$^+$, 121.08 [$C_6H_5CHOCH_3$ fragment]$^+$, 105.04 [C_6H_5CO fragment]$^+$.

2.4.3 Oxidation of 3,4-dimethoxybenzyl alcohol by $FeCl_3(\eta^1$-TEMPO)

3,4-dimethoxybenzyl alcohol (5 μL, 34.4 μmol) was added via microsyringe to a stirring Et_2O solution (2 mL) of $FeCl_3(\eta^1$-TEMPO) (23.9 mg, 75.1 μmol). The purple solution immediately lightened upon addition of the alcohol, concomitant with the deposition of a reddish tan precipitate. The reaction mixture was allowed to stir for 10 min, whereupon it was filtered through a basic alumina column (1 cm × 0.5 cm) supported on glass wool. The column was subsequently rinsed with Et_2O (5 mL) to provide a colorless filtrate. The solvent was removed in vacuo and the resulting residue was dissolved in C_6D_6 (700 μL) and transferred to an NMR tube. Mesitylene (5 μL, 35.9 μmol) was added via microsyringe and a ^{1}H NMR spectrum was recorded. Analysis of the chemical shifts and comparison of the product peak integrations with those of the internal standard revealed complete consumption of the alcohol and formation of 3,4-dimethoxybenzaldehyde in 75% yield. NMR spectral data of the product are consistent with those reported in the literature for 3,4-dimethoxybenzaldehyde.[10] ^{1}H NMR (400 MHz, 25 °C, C_6D_6) δ 3.21 (s, 3H, OC*H*$_3$), 3.25 (s, 3H, OC*H*$_3$), 6.34 (d, *J* = 8.1 Hz, 1H, Ph), 7.08 (dd, *J* = 8.1, 1.9 Hz, 1H, Ph), 7.35 (d, *J* = 1.9 Hz, 1H, Ph), 9.75 (s, 1H, C*H*O).

2.4.4 Oxidation of 3,4-dimethoxybenzyl alcohol by $AlCl_3(\eta^1$-TEMPO)

$AlCl_3(\eta^1$-TEMPO) (26.3 mg, 90.8 μmol) was dissolved in CD_2Cl_2 (700 μl) and transferred to an NMR tube. 3,4-dimethoxybenzyl alcohol (5 μL, 34.4 μmol) was then added via microsyringe. Within 3 min, the clear yellow solution lightened to a very faint yellow. After 2 h, mesitylene (5 μL, 35.9 μmol) was added via microsyringe and a ^{1}H NMR spectrum was recorded. Analysis of the chemical shifts and comparison of the product peak integrations with those of the internal standard revealed complete consumption of the alcohol and formation of 3,4-dimethoxybenzaldehyde in 99% yield. NMR spectral data of the product are consistent with those reported in the literature for 3,4-dimethoxybenzaldehyde.[10] ^{1}H NMR (600 MHz, 25 °C, CD_2Cl_2): 3,4-dimethoxybenzaldehyde: δ 3.90 (s, 3H, OCH_3), 3.93 (s, 3H, OCH_3), 7.01 (d, J = 8.2 Hz, 1H, Ph), 7.39 (s, 1H, Ph), 7.48 (d, J = 7.9 Hz, 1H, Ph), 9.83 (s, 1H, CHO); $AlCl_3(\eta^1$-TEMPOH): δ 1.43 (s, 6H, CH_3), 1.55 (s, 6H, CH_3), 1.63 – 1.85 (m, 4H, CH_2), 1.99 (d, J = 14.5 Hz, 2H, CH_2), 7.15 (br s, 1H, N-H).

2.4.5 Oxidation of 1-phenyl-2-phenoxyethanol by $FeCl_3(\eta^1$-TEMPO)

An Et_2O solution (1.5 mL) of $FeCl_3(\eta^1$-TEMPO) (18.9 mg, 59.3 μmol) was added to a stirring Et_2O solution (0.5 mL) of 1-phenyl-2-phenoxyethanol (5.2 mg, 24.3 μmol), resulting in the immediate conversion of the deep purple solution to a red-brown suspension. The reaction mixture was allowed to stir for 18 h, whereupon it was filtered through a basic alumina column (1.5 cm × 0.5 cm) supported on glass wool. The column was then rinsed with Et_2O (6 mL) to provide a colorless filtrate. The solvent was removed in vacuo and the resulting white solid was dissolved in CD_2Cl_2 (700 μL). This solution was transferred to an NMR tube, mesitylene (5 μL, 35.9 μmol) was added via microsyringe, and a ^{1}H NMR

spectrum was recorded. Analysis of the chemical shifts and comparison of the product peak integrations with those of the internal standard revealed complete consumption of the alcohol and formation of 2-phenoxyacetophenone in 65% yield. This was confirmed by comparison of the NMR spectral data to that of an authentic sample of 2-phenoxyacetophenone.[65] ^{1}H NMR (600 MHz, 25 °C, CD_2Cl_2): δ 5.32 (s, 2H, C*H*$_2$), 6.94 (d, *J* = 8.2 Hz, 2H, *o*-Ph), 7.00 (t, *J* = 7.4 Hz, 1H, *p*-Ph), 7.31 (t, *J* = 7.8 Hz, 2H, *m*-Ph), 7.54 (t, *J* = 7.7 Hz, 2H, *m*-Ph), 7.65 (t, *J* = 7.5 Hz, 1H, *p*-Ph), 8.01 (d, *J* = 7.6 Hz, 2H, *o*-Ph).

2.4.6 Oxidation of 1-phenyl-2-phenoxyethanol by $AlCl_3(\eta^1$-TEMPO)

$AlCl_3(\eta^1$-TEMPO) (15.1 mg, 52.1 μmol) was added to a solution of 1-phenyl-2-phenoxyethanol (5.0 mg, 23.3 μmol) dissolved in CH_2Cl_2 (1 mL). The yellow solution was allowed to stand without stirring for 3 h. The color of the solution gradually lightened over this time. The solvent was removed in vacuo and the resulting solid was extracted into Et_2O (3 mL) and filtered through a basic alumina column (1.5 cm × 0.5 cm) supported on glass wool. The column was then rinsed with Et_2O (6 mL) to provide a colorless filtrate. The solvent was removed in vacuo and the resulting white solid was dissolved in CD_2Cl_2 (700 μL). This solution was transferred to an NMR tube, mesitylene (5 μL, 35.9 μmol) was added via microsyringe, and a ^{1}H NMR spectrum was recorded. Analysis of the chemical shifts and comparison of the product peak integrations with those of the internal standard revealed complete consumption of 1-phenyl-2-phenoxyethanol, and formation of 2-phenoxyacetophenone (**2.6**) and 2-(2,2,6,6-tetramethylpiperidine-*N*-oxyl)-2-phenoxyacetophenone (**2.7**) in 75% yield and 5% yield, respectively. The identities of these products were confirmed by comparison of the NMR spectral data to that of authentic material. ^{1}H NMR (500 MHz, 25 °C, CD_2Cl_2): Compound **2.6**: δ 5.31 (s, 2H, C*H*$_2$), 6.93 (d,

J = 8.8 Hz, 2H, *o*-Ph), 6.99 (t, *J* = 6.9 Hz, 1H, *p*-Ph), 7.30 (m, 2H, *m*-Ph), 7.53 (t, *J* = 7.8 Hz, 2H, *m*-Ph), 7.65 (t, *J* = 7.4 Hz, 1H, *p*-Ph), 7.99 (d, *J* = 8.0 Hz, 2H, *o*-Ph); Compound **2.7**: δ 1.03 (s, 3H, C*H*$_3$), 1.23 (s, 3H, C*H*$_3$), 1.36 (s, 3H, C*H*$_3$), 6.02 (s, 1H, C*H*), 8.26 (d, *J* = 7.98 Hz, 2H, *o*-Ph), missing methyl resonance overlapping with solvent, missing aryl resonances overlap with those of compound **2.6**.

2.4.7 Oxidation of 2-phenoxyacetophenone by $FeCl_3(\eta^1$-TEMPO)

An Et_2O solution (1.5 mL) of $FeCl_3(\eta^1$-TEMPO) (49.2 mg, 154.5 μmol) was added to a stirring Et_2O solution (0.5 mL) of 2-phenoxyacetophenone (15.1 mg, 71.1 μmol). The reaction mixture was allowed to stir for 18 h, whereupon a small amount of dark solid precipitated. The solution remained dark purple. This reaction mixture was filtered through a basic alumina column (2 cm × 0.5 cm) supported on glass wool. The column was then rinsed with Et_2O (6 mL) to provide a pale orange filtrate. The solvent was removed in vacuo and the resulting pale orange solid was dissolved in CD_2Cl_2 (700 μL). This solution was transferred to an NMR tube, mesitylene (5 μL, 35.9 μmol) was added via microsyringe, and a ^{1}H NMR spectrum was recorded. Analysis of the chemical shifts and comparison of the product peak integrations with those of the internal standard revealed the formation of **2.7** (3% yield) and the presence of unreacted 2-phenoxyacetophenone (73% yield). ^{1}H NMR (600 MHz, 25 °C, CD_2Cl_2): Compound **2.6**: δ 5.32 (s, 2H, C*H*$_2$), 6.95 (d, *J* = 7.63 Hz, 2H, *o*-Ph), 7.01 (t, *J* = 6.86 Hz, 1H, *p*-Ph), 7.32 (t, *J* = 7.12 Hz, 2H, *m*-Ph), 7.54 (t, *J* = 7.03 Hz, 2H, *m*-Ph), 7.66 (t, *J* = 6.74 Hz, 1H, *p*-Ph), 8.01 (d, *J* = 7.2 Hz, 2H, *o*-Ph); Compound **2.7**: δ 1.05 (s, 3H, C*H*$_3$), 1.25 (s, 3H, C*H*$_3$), 1.38 (s, 3H, C*H*$_3$), 6.04 (s, 1H, C*H*), 8.28 (d, *J* = 7.45 Hz, 2H, *o*-Ph), missing aryl resonances overlap with those of compound **2.6**, and unassigned CH_2 and CH_3 resonances of **2.7** overlap with C*H*$_3$ resonances and minor impurities.

2.4.8 Oxidation of 2-phenoxyacetophenone by $AlCl_3(\eta^1$-TEMPO)

$AlCl_3(\eta^1$-TEMPO) (22.7 mg, 78.4 μmol) was added to a solution of 2-phenoxyacetophenone (7.0 mg, 33.0 μmol) dissolved in CH_2Cl_2 (1 mL). The yellow solution was allowed to stand without stirring for 3 h. The solvent was removed in vacuo and the resulting solid was extracted into Et_2O (4 mL) and filtered through a basic alumina column (1.5 cm × 0.5 cm) supported on glass wool. The column was then rinsed with Et_2O (6 mL) to provide a colorless filtrate. The solvent was removed in vacuo and the resulting colorless oil was dissolved in CD_2Cl_2 (700 μL). This solution was transferred to an NMR tube, mesitylene (5 μL, 35.9 μmol) was added via microsyringe, and ^{1}H and $^{13}C\{^1H\}$ NMR spectra were recorded. Analysis of the chemical shifts and comparison of the product peak integrations with those of the internal standard revealed the formation of **2.7** in 48% yield and the presence of unreacted 2-phenoxyacetophenone in 4% yield. Compound **2.7**: ^{1}H NMR (400 MHz, 25 °C, CD_2Cl_2): δ 1.02 (s, 3H, C*H*$_3$), 1.15 (s, 3H, C*H*$_3$), 1.22 (s, 3H, C*H*$_3$), 1.32 (s, 2H, γ-C*H*$_2$ overlapping with CH_3 resonance), 1.36 (s, 3H, C*H*$_3$), 1.43-1.67 (m, 4H, β-CH_2 overlapping with impurities, 6.01 (s, 1H, C*H*), 6.95 – 7.05 (m, 3H, Ph), 7.25 (t, *J* = 8.0 Hz, 2H, *m*-Ph), 7.50 (t, *J* = 7.6 Hz, 2H, *m*-Ph), 7.60 (t, *J* = 7.4 Hz, 1H, *p*-Ph), 8.26 (d, *J* = 7.9 Hz, 2H, *o*-Ph). $^{13}C\{^1H\}$ NMR (126 MHz, 25 °C, CD_2Cl_2) δ 17.62 (γ-*C*H$_2$), 20.46 (*C*H$_3$), 21.19 (*C*H$_3$), 33.41 (*C*H$_3$), 34.14 (*C*H$_3$), 40.35 (β-*C*H$_2$), 40.73 (β-*C*H$_2$), 60.54 (α-*C*), 61.71 (α-*C*), 110.35 (*C*HO), 117.31 (*o*-*C*H), 122.70 (*p*-*C*H), 128.85 (*m*-*C*H), 130.02 (*m*-*C*H), 130.86 (*o*-*C*H), 133.69 (*i*-*C*), 134.06 (*p*-*C*H), 157.30 (*i*-*C*), 192.98 (*C*O). ESI-MS: *m/z* 390.21 $[M + Na]^+$, 757.44 $[2M + Na]^+$.

2.4.9 Oxidation of 1,2-diphenyl-2-methoxyethanol by $FeCl_3(\eta^1$-TEMPO)

A CH_2Cl_2 (0.5 mL) solution of $FeCl_3(\eta^1$-TEMPO) (23.7 mg, 74.4 μmol) was added to a CH_2Cl_2 (0.5 mL) solution of 1,2-diphenyl-2-methoxyethanol (6.4 mg, 28.0 μmol). The deep purple solution immediately lightened to maroon. This solution was allowed to stand without stirring for 2 h. The reaction mixture was filtered through a basic alumina column (2 cm × 0.5 cm) supported on glass wool. The column was then rinsed with Et_2O (6 mL) to provide a pale orange filtrate. The solvent was removed in vacuo and the resulting light orange oil was dissolved in CD_2Cl_2 (700 μl). This solution was transferred to an NMR tube, mesitylene (5 μL, 35.9 μmol) was added via microsyringe, and a ^{1}H NMR spectrum was recorded. Analysis of the chemical shifts and comparison of the product peak integrations with those of the internal standard revealed complete consumption of the alcohol and formation of 2-methoxy-1,2-diphenylethanone in 75% yield. The identity of this product was confirmed by comparison of the NMR spectral data to that of authentic material.[10] ^{1}H NMR (600 MHz, 25 °C, CD_2Cl_2): δ 3.43 (s, 3H, C*H*$_3$), 5.52 (s, 1H, C*H*), 7.31 (t, *J* = 7.3 Hz, 1H, Ph), 7.36 (t, *J* = 7.4 Hz, 2H, Ph), 7.39 – 7.45 (m, 4H, Ph), 7.53 (t, *J* = 7.4 Hz, 1H, Ph), 7.97 (d, *J* = 7.4 Hz, 2H, Ph). FI-MS: *m/z* 226.10 $[M]^+$, 121.08 $[C_6H_5CHOCH_3$ fragment$]^+$, 105.04 $[C_6H_5CO$ fragment$]^+$.

2.4.10 Oxidation of 1,2-diphenyl-2-methoxyethanol by $AlCl_3(\eta^1$-TEMPO)

$AlCl_3(\eta^1$-TEMPO) (58.6 mg, 202.4 μmol) was added to a CH_2Cl_2 (1 mL) solution of 1,2-diphenyl-2-methoxyethanol (22.0 mg, 96.4 μmol). This orange reaction mixture was allowed to stand without stirring for 3 h. The solvent was then removed in vacuo and the resulting solid was extracted into Et_2O (3 mL) and filtered through a basic alumina column

(2 cm × 0.5 cm) supported on glass wool. The column was rinsed with Et_2O (6 mL) to provide a pale yellow filtrate. The solvent was removed in vacuo and the resulting light yellow oil was dissolved in CD_2Cl_2 (700 µl). This solution was transferred to an NMR tube, mesitylene (5 µL, 35.9 µmol) was added via microsyringe, and a ^1H NMR spectrum was recorded. Analysis of the chemical shifts and comparison of the product peak integrations with those of the internal standard revealed the presence of unreacted 1,2-diphenyl-2-methoxyethanol (**2.8**) in 23% yield, the formation of benzil (**2.10**) in 54% yield (based on **2.2**), and the formation of a minor unidentified product, as evidenced by a methoxy resonance at 3.51 ppm. The identity of benzil was confirmed by comparison of the NMR spectral data to that of authentic material.[70] ^1H NMR (600 MHz, 25 °C, CD_2Cl_2): δ 3.21 (s, 3H, OC*H*$_3$, **2.8**), 3.51 (s, 3H, OC*H*$_3$, unknown minor product), 4.35 (s, 1H, C*H*, **2.8**), 4.88 (s, 1H, C*H*, **2.8**), 7.14 – 7.32 (m, Ar, **2.8**, overlapping with unknown minor product), 7.55 (t, *J* = 7.83 Hz, 4H, *m*-Ph, **2.10**, overlapping with unknown minor product), 7.70 (t, *J* = 7.1 Hz, 2H, *p*-Ph, **2.10**), 7.97 (d, *J* = 8.22 Hz, 4H, *o*-Ph, **2.10**, overlapping with unknown minor product). ESI-MS: *m/z* 251.11 [**2.8** + Na]$^+$. FI-MS: *m/z* 228.11 [**2.8**]$^+$, 210.07 [**2.10**]$^+$.

2.4.11 Attempted oxidation of 2-methoxy-1,2-diphenylethanone by $FeCl_3(\eta^1$-TEMPO)

$FeCl_3(\eta^1$-TEMPO) (22.8 mg, 71.6 µmol) was added to a solution of 2-methoxy-1,2-diphenylethanone (7.1 mg, 31.4 µmol) dissolved in CH_2Cl_2 (1 mL). This dark purple reaction mixture was allowed to stand without stirring for 15 h. No color change or formation of precipitate was observed over this timeframe. Et_2O (2 mL) was added to the reaction mixture. This solution was then filtered through a basic alumina column (2 cm × 0.5 cm) supported on glass wool and rinsed with Et_2O (10 mL) to provide a pale orange filtrate.

The solvent was removed in vacuo and the resulting oil was dissolved in CD_2Cl_2 (700 μL). This solution was transferred to an NMR tube, mesitylene (5 μL, 35.9 μmol) was added via microsyringe, and a ^{1}H NMR spectrum was recorded. Analysis of the chemical shifts and comparison of the product peak integrations with those of the internal standard revealed a 98% recovery of the starting 2-methoxy-1,2-diphenylethanone and no formation of oxidation products.

2.4.12 Oxidation of 2-methoxy-1,2-diphenylethanone by $AlCl_3(\eta^1$-TEMPO)

$AlCl_3(\eta^1$-TEMPO) (32.6 mg, 112.6 μmol) was added to a solution of 2-methoxy-1,2-diphenylethanone (11.4 mg, 50.4 μmol) dissolved in CH_2Cl_2 (1 mL). The dark yellow reaction mixture was allowed to stand without stirring for 15 h, whereupon the solvent was removed in vacuo. The resulting solid was extracted into Et_2O (3 mL) and filtered through a basic alumina column (2 cm × 0.5 cm) supported on glass wool. The column was then rinsed with Et_2O (6 mL) to provide a pale yellow filtrate. The solvent was removed in vacuo and the resulting solid was dissolved in CD_2Cl_2 (700 μL). This solution was transferred to an NMR tube, mesitylene (5 μL, 35.9 μmol) was added via microsyringe, and a ^{1}H NMR spectrum was recorded. Analysis of the chemical shifts and comparison of the product peak integrations with those of the internal standard revealed the presence of 2-methoxy-1,2-diphenylethanone (**2.9**) in 11% yield, and the formation of benzil (**2.10**) and 2,2-dimethoxy-2-phenylacetophenone (**2.11**) in 53% and 16% yields, respectively. The identities of the products were confirmed by comparison of the NMR and mass spectral data to those of authentic sample.[70,71] ^{1}H NMR (600 MHz, 25 °C, CD_2Cl_2): δ 3.20 (s, 3H, OC*H*$_3$, **2.11**), 3.44 (s, 3H, OC*H*$_3$, **2.9**), 5.52 (s, 1H, C*H*, **2.9**), 7.27 – 7.48 (m, overlapping aryl CH of **2.9** and **2.11**), 7.54 (t, *J* = 7.7 Hz, Ar of **2.10,** overlapping aryl CH of **2.9**), 7.59 (d, *J* = 7.7 Hz, 2H,

o-Ph, **2.11**), 7.69 (t, *J* = 7.5 Hz, 2H, *p*-Ph, **2.10**), 7.97 (d, *J* = 7.8 Hz, *o*-Ph of **2.10,** overlapping aryl CH of **2.9**), 8.04 (d, *J* = 7.9 Hz, 2H, *o*-Ph, **2.11**). ESI-MS: *m/z* 249.09 [**2.9** + Na]$^+$, 279.11 [**2.11** + Na]$^+$. FI-MS: *m/z* 226.10 [**2.9**]$^+$, 210.07 [**2.10**]$^+$.

2.4.13 Reaction of $FeCl_3(\eta^1$-TEMPOH) and 2-phenoxyethanol

2-phenoxyethanol (35 µL, 279.2 µmol) was added to a CH_2Cl_2 (4 mL) solution of $FeCl_3(\eta^1$-TEMPO) (59.3 mg, 185.6 µmol) via microsyringe. The purple solution immediately became orange. The reaction mixture was allowed to stir for 10 min, with intermittent application of vacuum. The orange solution was filtered through a Celite column supported on glass wool (1 cm × 0.5 cm) and subsequently layered with Et_2O (5 mL). Storage of this solution at -25 °C for 13 days resulted in the deposition of reddish brown crystals. The orange supernatant was decanted and the red-brown blocks were washed with Et_2O (3 × 1 mL) and dried in vacuo. 23.7 mg, 30% yield of complex **2.15**. Anal. Calcd for $C_{38}H_{66}Cl_4Fe_2N_2O_7$ (**2.15**·Et_2O): C, 49.80, H, 7.26, N, 3.06. Found: C, 49.58, H, 7.09, N, 3.06. ^{1}H NMR (500 MHz, 25 °C, CD_2Cl_2/py-d_5): δ -27.62 (br s, 4H, TEMPO β-CH_2), -14.66 (br s, 12H, CH_3), 1.55 (br s, 2H, TEMPO CH_2 or phenoxyethoxide *CH₂*), 2.20 (br s, 1H, N*H*), 4.43 (br s, 2H, TEMPO CH_2 or phenoxyethoxide CH_2), 7.21 (br s, 1H, *p*-C*H*), 7.26 (br s, 2H, aryl C*H*), 7.64 (br s, 2H, aryl C*H*), 15.30 (br s, 2H, TEMPO CH_2 or phenoxyethoxide CH_2). IR (KBr, cm^{-1}): 3015 (s), 2986 (s), 2950 (s), 2880 (m), 1599 (s), 1586 (m), 1497 (s), 1471 (m), 1396 (m), 1385 (s), 1371 (m), 1338 (w), 1329 (w), 1298 (m), 1249 (s), 1218 (m), 1171 (w), 1117 (s), 1081 (m), 1036 (s), 1021 (s), 992 (w), 974 (w), 945 (w), 888 (w), 817 (w), 757 (s), 696 (m), 630 (m), 590 (w), 515 (s), 426 (w), 408 (w).

2.4.14 Oxidation of 1,4-cyclohexadiene by $FeCl_3(\eta^1$-TEMPO)

$FeCl_3(\eta^1$-TEMPO) (36.4 mg, 114.3 μmol) was dissolved in toluene-d_8 (700 μl) and 1,4-cyclohexadiene (5 μL, 52.9 μmol) was added via microsyringe. The dark purple solution immediately lightened. The reaction was allowed to stand for 2 h without stirring. The solution was then filtered through a basic alumina column (1 cm × 0.5 cm) supported on glass wool into an NMR tube. The column was rinsed with toluene-d_8 (0.5 mL), mesitylene (5 μL, 35.9 μmol) was added to the NMR tube via microsyringe, and a ^{1}H NMR spectrum was recorded. Analysis of the chemical shifts and comparison of the product peak integrations with those of the internal standard revealed the presence of unreacted 1,4-cyclohexadiene in 1% yield, and formation of benzene in 82% yield. ^{1}H NMR (600 MHz, 25 °C, toluene-d_8): benzene: δ 7.14 (s, 6H, C*H*); 1,4-cyclohexadiene: δ 2.52 (s, 4H, CH_2), 5.59 (s, 4H, C*H*).

2.4.15 Oxidation of 1,4-cyclohexadiene by $AlCl_3(\eta^1$-TEMPO)

$AlCl_3(\eta^1$-TEMPO) (35.8 mg, 123.6 μmol) was dissolved in CD_2Cl_2 (700 μl) and transferred to an NMR tube. An initial ^{1}H NMR spectrum was recorded. 1,4-cyclohexadiene (5 μL, 52.9 μmol) was then added via microsyringe, whereupon the yellow solution immediately lightened. After 15 min, mesitylene (5 μL, 35.9 μmol) was added via microsyringe and a ^{1}H NMR spectrum was recorded. Analysis of the chemical shifts and comparison of the product peak integrations with those of the internal standard revealed the complete consumption of 1,4-cyclohexadiene and the formation of benzene in 96% yield. ^{1}H NMR (400 MHz, 25 °C, CD_2Cl_2): benzene: δ 7.36 (s, 6H, C*H*); $AlCl_3(\eta^1$-TEMPOH): δ 1.43 (s, 6H, CH_3), 1.55 (s, 6H, CH_3), 1.63 – 1.85 (m, 4H, CH_2), 1.99 (d, J = 14.29 Hz, 2H, CH_2), 7.14 (br s, 1H, N-*H*).

2.4.16 Oxidation of xanthene by $FeCl_3(\eta^1$-TEMPO)

$FeCl_3(\eta^1$-TEMPO) (109.6 mg, 344.2 μmol) was added to a CH_2Cl_2 (3 mL) solution of xanthene (28.5 mg, 156.4 μmol). After 48 h, the orange reaction mixture was filtered through a basic alumina column (2.5 cm × 0.5 cm) supported on glass wool and the column was rinsed with Et_2O (6 mL) to provide a nearly colorless filtrate. The solvent was removed in vacuo and the resulting white solid was dissolved in CD_2Cl_2 (700 μL). This solution was transferred to an NMR tube, mesitylene (5 μL, 35.9 μmol) was added via microsyringe, and a ^{1}H NMR spectrum was recorded. Analysis of the chemical shifts and comparison of the product peak integrations with those of the internal standard revealed the absence of xanthene, and formation of bixanthenyl (**2.19**) and xanthone (**2.20**) in 18% yield and 33% yield, respectively. The NMR spectral data of the products are consistent with those previously reported for bixanthenyl and xanthone.[38,39] ^{1}H NMR (500 MHz, 25 °C, CD_2Cl_2): Compound **2.20**: δ 7.40 (m, 2H, Ar), 7.50 – 7.54 (m, 2H, Ar), 7.75 (m, 2H, Ar), 8.30 (dd, *J* = 7.9, 1.8 Hz, 2H, Ar); Compound **2.19**: δ 4.26 (s, 2H, C*H*), 6.70 (dd, *J* = 7.6, 1.6 Hz, 4H, Ar), 6.83 (dd, *J* = 8.1, 1.2 Hz, 4H, Ar), 6.95 (td, *J* = 7.4, 1.2 Hz, 4H, Ar), 7.21 (m, 4H, Ar). ^{13}C{^{1}H} NMR (126 MHz, 25 °C, CD_2Cl_2): Compound **2.20**: δ 118.56 (*C*H), 122.36 (*C*(C=O)*C*), 124.46 (*C*H), 126.99 (*C*H), 135.39 (*C*H), 156.77 (*C*O*C*), 177.36 (*C*=O); Compound **2.19**: δ 49.99 (*C*H), 116.23 (Ar *C*H), 122.43 (*C*), 123.23 (Ar *C*H), 128.63 (Ar *C*H), 129.74 (Ar *C*H), 153.56 (*C*O*C*).

2.4.17 Oxidation of xanthene by $AlCl_3(\eta^1$-TEMPO)

$AlCl_3(\eta^1$-TEMPO) (77.3 mg, 266.9 μmol) was added to a CH_2Cl_2 (700 μL) solution of xanthene (24.1 mg, 132.3 μmol) and transferred to a J. Young NMR tube. Mesitylene (5 μL,

35.9 μmol) was added via microsyringe and the yellow solution was monitored by ^{1}H NMR spectroscopy for 72 h, whereupon it gradually darkened to orange. The solvent was removed in vacuo and the resulting solid was extracted into toluene (2 mL) and filtered through a basic alumina column (1.5 cm × 0.5 cm) supported on glass wool. The column was then rinsed with toluene (6 mL) to provide a colorless filtrate. The solvent was removed in vacuo and the white solid was dissolved in CD_2Cl_2 (700 μL). This solution was transferred to an NMR tube, mesitylene (5 μL, 35.9 μmol) was added via microsyringe, and a ^{1}H NMR spectrum was recorded. Analysis of the chemical shifts and comparison of the product peak integrations with those of the internal standard revealed the presence of unreacted xanthene (**2.18**) in 1% yield, and formation of bixanthenyl (**2.19**) and xanthone (**2.20**) in 51% and 4% yields, respectively. The NMR spectral data of the products are consistent with those previously reported for bixanthenyl and xanthone.[38,39] ^{1}H NMR (600 MHz, 25 °C, CD_2Cl_2): Compound **2.19**: δ 4.26 (s, 2H, C*H*), 6.71 (dd, *J* = 7.4, 1.6 Hz, 4H, Ar), 6.83 (d, *J* = 8.1 Hz, 4H, Ar), 6.95 (t, *J* = 7.4 Hz, 4H, Ar), 7.20 – 7.23 (m, 4H, Ar overlapping with Ar from xanthene starting material); Compound **2.20**: δ 7.40 (t, *J* = 7.5 Hz, 2H, Ar), 7.53 (d, *J* = 8.5 Hz, 2H, Ar), 7.76 (m, 2H, Ar), 8.30 (dd, *J* = 7.9, 1.7 Hz, 2H, Ar).

2.4.18 Oxidation of cyclobutanol by $FeCl_3(\eta^1$-TEMPO) (385 mM concentration)

$FeCl_3(\eta^1$-TEMPO) (85.9 mg, 269.7 μmol) was dissolved in C_6D_6 (700 μL) to provide a purple solution. This corresponded to a $FeCl_3(\eta^1$-TEMPO) concentration of 385 mM. Addition of cyclobutanol (10 μl, 127.7 μmol) via microsyringe resulted in the immediate lightening of the solution, concomitant with the deposition of a maroon precipitate. The reaction mixture was allowed to stand without stirring for 10 min, whereupon it was filtered into an NMR tube through a basic alumina column (1 cm × 0.5 cm) supported on glass wool.

The column was rinsed with C_6D_6 (0.5 mL), mesitylene (5 μL, 35.9 μmol) was added to the NMR tube via microsyringe, and a ^{1}H NMR spectrum was recorded. Analysis of the chemical shifts and comparison of the product peak integrations with those of the internal standard revealed the complete consumption of cyclobutanol and formation of cyclobutanone in 75% yield. The NMR spectral data of the product were consistent with that previously reported for cyclobutanone.[72] ^{1}H NMR (600 MHz, 25 °C, C_6D_6) δ 1.20 (quintet, *J* = 8.2 Hz, 2H, C*H*$_2$), 2.47 (t, *J* = 8.2 Hz, 4H, C*H*$_2$).

2.4.19 Oxidation of cyclobutanol by $AlCl_3(\eta^1$-TEMPO) (200 mM concentration)

$AlCl_3(\eta^1$-TEMPO) (40.6 mg, 140.2 μmol) was dissolved in CD_2Cl_2 (700 μL) and transferred to an NMR tube to provide a yellow solution. This corresponded to a $AlCl_3(\eta^1$-TEMPO) concentration of 200 mM. Addition of cyclobutanol (5 μl, 63.9 μmol) via microsyringe resulted in an immediate color change to orange, which then lightened to a very pale yellow within 30 min. Mesitylene (5 μL, 35.9 μmol) was added via microsyringe and a ^{1}H NMR spectrum was recorded. Analysis of the chemical shifts and comparison of the product peak integrations with those of the internal standard revealed complete consumption of cyclobutanol and formation of cyclobutanone in 100% yield. The NMR spectral data of the product were consistent with that previously reported for cyclobutanone.[72] ^{1}H NMR (500 MHz, 25 °C, CD_2Cl_2): cyclobutanone: δ 1.98 (quintet, *J* = 8.2 Hz, 2H, C*H*$_2$ overlapping with $AlCl_3(\eta^1$-TEMPOH)), 3.05 (t, *J* = 8.2 Hz, 4H, C*H*$_2$); $AlCl_3(\eta^1$-TEMPOH): δ 1.42 (s, 6H, C*H*$_3$), 1.54 (s, 6H, C*H*$_3$), 1.63 – 1.86 (m, 4H, C*H*$_2$), 1.95-2.02 (m, 2H, C*H*$_2$ overlapping with cyclobutanone), 7.14 (br s, 1H, N-*H*).

2.4.20 Oxidation of cyclopropylcarbinol by $FeCl_3(\eta^1$-TEMPO) (260 mM concentration)

$FeCl_3(\eta^1$-TEMPO) (41.6 mg, 130.6 μmol) was dissolved in C_6D_6 (500 μL) to provide a purple solution. This corresponded to a $FeCl_3(\eta^1$-TEMPO) concentration of 260 mM. Addition of cyclopropylcarbinol (5 μl, 61.7 μmol) via microsyringe resulted in the immediate lightening of the solution, concomitant with the deposition of a maroon precipitate. The reaction mixture was allowed to stand without stirring for 30 min, whereupon it was filtered into an NMR tube through a basic alumina column (1 cm × 0.5 cm) supported on glass wool. The column was rinsed with C_6D_6 (0.5 mL), mesitylene (5 μL, 35.9 μmol) was added to the NMR tube via microsyringe, and a ^{1}H NMR spectrum was recorded. Analysis of the chemical shifts and comparison of the product peak integrations with those of the internal standard revealed the complete consumption of cyclopropylcarbinol and formation of cyclopropanecarboxaldehyde in 84% yield. The NMR spectral data of the product were consistent with that previously reported for cyclopropanecarboxaldehyde (Figure S27).[73] ^{1}H NMR (400 MHz, 25 °C, C_6D_6) δ 0.28 (m, 2H, CH_2), 0.47 (m, 2H, CH_2), 1.27 (m, 1H, C*H*), 8.53 (d, *J* = 5.5 Hz, 1H, C*H*O).

2.4.21 Oxidation of cyclopropylcarbinol by $FeCl_3(\eta^1$-TEMPO) (6.3 mM concentration)

$FeCl_3(\eta^1$-TEMPO) (1.0 mg, 3.14 μmol) was dissolved in C_6D_6 (500 μL) to provide a purple solution. This corresponded to a $FeCl_3(\eta^1$-TEMPO) concentration of 6.3 mM. Addition of cyclopropylcarbinol (1 μl of a 1.23 M stock solution, 1.23 μmol) via microsyringe resulted in the immediate lightening of the solution. The reaction mixture was allowed to stand without stirring for 30 min, whereupon it was filtered into an NMR tube

through a basic alumina column (1 cm × 0.5 cm) supported on glass wool. The column was rinsed with C_6D_6 (0.5 mL), mesitylene (1 µl of a 0.72 M stock solution, 0.72 µmol) was added to the NMR tube via microsyringe, and a ^{1}H NMR spectrum was recorded. Analysis of the chemical shifts and comparison of the product peak integrations with those of the internal standard revealed the complete consumption of cyclopropylcarbinol and formation of cyclopropanecarboxaldehyde in 98% yield. The NMR spectral data of the product were consistent with that previously reported for cyclopropanecarboxaldehyde.[73] No evidence for the formation of any ring opened product was observed in the ^{1}H NMR spectrum of the reaction mixture. ^{1}H NMR (400 MHz, 25 °C, C_6D_6) δ 0.26 (m, 2H, C*H*$_2$), 0.45 (m, 2H, C*H*$_2$), 1.25 (m, 1H, C*H*), 8.52 (d, *J* = 5.5 Hz, 1H, C*H*O).

2.4.22 Oxidation of cyclopropylcarbinol by $AlCl_3(\eta^1$-TEMPO) (190 mM concentration)

$AlCl_3(\eta^1$-TEMPO) (38.7 mg, 133.6 µmol) was dissolved in CD_2Cl_2 (700 µL) and transferred to an NMR tube to provide a yellow solution. This corresponded to a $AlCl_3(\eta^1$-TEMPO) concentration of 190 mM). Addition of cyclopropylcarbinol (5 µl, 61.7 µmol) via microsyringe resulted in an immediate color change to orange, which slowly lightened to a pale yellow over the course of 45 min. Mesitylene (5 µL, 35.9 µmol) was added via microsyringe and a ^{1}H NMR spectrum was recorded. Analysis of the chemical shifts and comparison of the product peak integrations with those of the internal standard revealed complete consumption of cyclopropylcarbinol and formation of cyclopropanecarboxaldehyde in 91% yield. The NMR spectral data of the products were consistent with that previously reported for cyclopropanecarboxaldehyde (Figure S28).[73] ^{1}H NMR (400 MHz, 25 °C, CD_2Cl_2): cyclopropanecarboxaldehyde: δ 1.04 – 1.11 (m, 4H, C*H*$_2$),

8.84 (d, *J* = 6.0 Hz, 1H, C*H*O), unassigned C*H* resonance overlaps with CH_2 resonance from $AlCl_3(\eta^1$-TEMPOH); $AlCl_3(\eta^1$-TEMPOH): δ 1.42 (s, 6H, CH_3), 1.54 (s, 6H, CH_3), 1.61 – 1.87 (m, 4H, CH_2 overlapping with cyclopropanecarboxaldehyde), 1.94-2.04 (m, 2H, CH_2), 7.15 (br s, 1H, N*H*).

2.4.23 Oxidation of cyclopropylcarbinol by $AlCl_3(\eta^1$-TEMPO) (4.4 mM concentration)

$AlCl_3(\eta^1$-TEMPO) (0.9 mg, 3.11 μmol) was dissolved in CD_2Cl_2 (700 μL) and transferred to an NMR tube to provide a pale yellow solution. This corresponded to a $AlCl_3(\eta^1$-TEMPO) concentration of 190 mM. Addition of cyclopropylcarbinol (1 μl of a 1.23 M stock solution, 1.23 μmol) via microsyringe resulted in a color change to colorless over the course of 45 min. Mesitylene (1 μl of a 0.72 M stock solution, 0.72 μmol) was then added via microsyringe and a ^{1}H NMR spectrum was recorded. Analysis of the chemical shifts and comparison of the product peak integrations with those of the internal standard revealed complete consumption of cyclopropylcarbinol and formation of cyclopropanecarboxaldehyde in 95% yield. The NMR spectral data of the products were consistent with that previously reported for cyclopropanecarboxaldehyde.[73] No evidence for the formation of any ring opened product was observed in the ^{1}H NMR spectrum of the reaction mixture. ^{1}H NMR (400 MHz, 25 °C, CD_2Cl_2): cyclopropanecarboxaldehyde: δ 1.05 – 1.12 (m, 4H, CH_2), 8.85 (d, *J* = 6.0 Hz, 1H, C*H*O), unassigned C*H* resonance overlaps with CH_2 resonance from $AlCl_3(\eta^1$-TEMPOH); $AlCl_3(\eta^1$-TEMPOH): δ 1.43 (s, 6H, CH_3), 1.55 (s, 6H, CH_3), 1.62 – 1.88 (m, 4H, CH_2 overlapping with cyclopropanecarboxaldehyde), 1.95-2.05 (m, 2H, CH_2), 7.14 (br s, 1H, N*H*).

2.4.24 Reaction of $FeBr_3$ with TEMPO in Et_2O

An Et_2O solution (1 mL) of TEMPO (105.2 mg, 0.673 mmol) was added to a solution of $FeBr_3$ (204.1 mg, 0.691 mmol) in Et_2O (1 mL). An orange precipitate immediately formed. The reaction mixture was allowed to stand at room temperature for 5 h, whereupon the supernatant was filtered through a basic alumina column (1 cm × 0.5 cm) supported on glass wool to remove the metal containing products. The column was rinsed with Et_2O (1 mL). Analysis of the filtrate by GC-MS revealed the presence of 1,1-diethoxyethane and TEMPO (Figure A2.13). The retention times of 1,1-diethoxyethane and TEMPO were consistent with that of authentic material, recorded using the same conditions. The orange precipitate was the dissolved in CH_2Cl_2 (3 mL), and the resulting orange solution was filtered through a Celite plug supported on glass wool (1 cm × 0.5 cm). The dark orange filtrate was then layered with hexanes (5 mL), and subsequent storage at –25 ºC for 12 h resulted in the deposition of an orange powder (236.0 mg). Analysis of this powder by ^{1}H NMR spectroscopy revealed the presence of complexes **2.27** and **2.28** in an approximate 3:2 ratio. ^{1}H NMR (400 MHz, 25 °C, CD_2Cl_2): Complex **2.27**: δ -1.14 (s, 2H, β-H), 8.18 (s, 1H, γ-H), 10.89 (s, 1H, γ-H), 12.47 (br s, 6H, C*H*$_3$), 16.02 (br s, 6H, C*H*$_3$), 59.20 (s, 2H, β-H), a resonance assignable to NH was not observed, likely due to paramagnetic broadening; Complex **2.28**: δ 1.72 (sh, 4H, C*H*$_2$), 2.02 (s, 12H, C*H*$_3$), 2.50 (s, 4H, C*H*$_2$), 3.73 (s, 12H, C*H*$_3$), 6.58 (s, 4H, C*H*$_2$), 47.18 (s, 2H, N*H*). GC-MS: *m/z* 1,1-diethoxyethane: 117 $[M-H]^+$, 103 $[C_5H_{11}O_2$ fragment$]^+$, 73 $[C_4H_9O$ fragment$]^+$, 45 $[C_2H_5O$ fragment$]^+$; TEMPO: 156 $[M]^+$.

2.4.25 Synthesis of $[FeBr_2(\eta^1\text{-TEMPOH})]_2(\mu\text{-O})$ (2.28)

An Et_2O solution (1 mL) of TEMPO (131 mg, 0.838 mmol) and 1,4-cyclohexadiene (80 μL, 0.846 mmol) was layered on to an Et_2O solution (2 mL) of $FeBr_3$ (229 mg, 0.774 mmol) that was previously filtered through a Celite plug supported on glass wool (1 cm × 0.5 cm). An orange precipitate immediately formed. The reaction mixture was allowed to stand at room temperature for 18 h, whereupon the resulting orange precipitate was isolated by decanting off the supernatant. This solid was recrystallized twice from CH_2Cl_2 solutions layered with Et_2O, which were stored at –25 ºC for 12 h. 68.7 mg, 32% yield. ^{1}H NMR (400 MHz, 25 ˚C, CD_2Cl_2) δ 1.64 (sh, 4H, CH_2), 1.86 (s, 12H, CH_3), 2.36 (s, 4H, CH_2), 3.72 (br s, 12H, CH_3), 6.39 (s, 4H, CH_2), 47.21 (br s, 2H, N*H*). Anal. Calcd for $C_{18}H_{38}Br_4Fe_2N_2O_3$: C, 28.38, H, 5.03, N, 3.68. Found: C, 28.36, H, 5.29, N, 3.60. IR (KBr pellet, cm^{-1}): 3077 (s), 3021 (m), 2989 (m), 2970 (s), 2950 (s), 2876 (m), 1461 (m), 1397 (s), 1384 (s), 1367 (m), 1357 (m), 1336 (w), 1299 (w), 1246 (w), 1226 (m), 1204 (m), 1170 (m), 1117 (m), 1086 (w), 1062 (w), 1054 (w), 1026 (s), 988 (w), 974 (m), 945 (m), 870 (s), 744 (m), 712 (w), 635 (s), 565 (w), 499 (m), 427 (m), 412 (w).

2.4.26 Reaction of $FeBr_3$ with TEMPOH in Et_2O

An Et_2O solution (1 mL) of TEMPOH (57.8 mg, 0.368 mmol) was added to a solution of $FeBr_3$ (102.0 mg, 0.345 mmol) in Et_2O (3 mL). An orange precipitate immediately formed. Storage of this mixture at –25 ºC for 12 h resulted in the deposition of more orange powder. The solid was then collected by decanting off the supernatant (101.5 mg). Analysis of this material by ^{1}H NMR spectroscopy revealed the presence of complexes **2.27** and **2.28**, in an approximate 1:1 ratio. ^{1}H NMR (400 MHz, 25 °C, CD_2Cl_2): Complex **2.27**: δ -1.37 (s, 2H, β-H), 7.89 (s, 1H, γ-H), 10.69 (s, 1H, γ-H), 12.31 (br s, 6H, CH_3), 15.75 (br s, 6H, CH_3),

58.60 (s, 2H, β-H), a resonance assignable to NH was not observed, likely due to paramagnetic broadening; Complex **2.28**: δ 1.70 (sh, 4H, CH_2), 1.93 (s, 12H, CH_3), 2.46 (s, 4H, CH_2), 3.69 (s, 12H, CH_3), 6.48 (s, 4H, CH_2), 47.09 (s, 2H, N*H*).

2.4.27 Control Reactions

TEMPO (14.2 mg, 90.9 μmol) was added to a solution of 3,4-dimethoxybenzyl alcohol (5 μL, 34.4 μmol) in CD_2Cl_2 (700 μL) and transferred to an NMR tube. The reaction was monitored by ^{1}H NMR spectroscopy for 18 h. No formation of 3,4-dimethoxybenzaldehyde was observed.

TEMPO (15.0 mg, 96.0 μmol) was added to a solution of 2-phenoxyethanol (5 μL, 40.1 μmol) in CD_2Cl_2 (700 μL) and transferred to an NMR tube. The reaction was monitored by ^{1}H NMR spectroscopy for 18 h. No formation of 2-phenoxyacetaldehyde was observed.

TEMPO (24.7 mg, 158.1 μmol) was added to a solution of 1-phenyl-2-phenoxyethanol (15.6 mg, 72.8 μmol) in CD_2Cl_2 (700 μL) and transferred to an NMR tube. The reaction was monitored by ^{1}H NMR spectroscopy for 18 h. No formation of 2-phenoxyacetophenone was observed.

TEMPO (12.0 mg, 76.8 μmol) was added to a solution of 2-phenoxyacetophenone (7.1 mg, 33.5 μmol) in CD_2Cl_2 (700 μL) and transferred to an NMR tube. The reaction was monitored by ^{1}H NMR spectroscopy for 48 h. No consumption of 2-phenoxyacetophenone or formation of any oxidation products was observed.

TEMPO (28.2 mg, 180.5 μmol) was added to a solution of 1,2-diphenyl-2-methoxyethanol (16.6 mg, 72.7 μmol) in CD_2Cl_2 (700 μL) and transferred to an NMR tube. The reaction was monitored by ^{1}H NMR spectroscopy for 18 h. No formation of 2-methoxy-1,2-diphenylethanone or any other oxidation products were observed.

TEMPO (17.4 mg, 111.4 μmol) was added to a solution of 2,3-dihydrobenzofuran (16.6 mg, 72.7 μmol) in CD_2Cl_2 (700 μL) and transferred to an NMR tube. The reaction was monitored by ^1H NMR spectroscopy for 18 h. No reaction was observed.

TEMPO (16.9 mg, 108.2 μmol) was added to a solution of 1,4-cyclohexadiene (5 μL, 52.9 μmol) in CD_2Cl_2 (700 μL) and transferred to a J. Young NMR tube. Mesitylene (5 μL, 35.9 μmol) was then added via microsyringe. The reaction was monitored by ^1H NMR spectroscopy for 4 days, revealing the slow formation of 1,4-cyclohexadiene to benzene, along with formation of TEMPOH.[74] The reaction was still not complete after 4 days (20% yield, 22% conversion). ^1H NMR (500 MHz, 25 °C, CD_2Cl_2): TEMPO: δ -28.84 (br s, 4H, β-C*H*$_2$), -15.48 (br s , 12H, C*H*$_3$), 15.33 (br s, 2H, γ-C*H*$_2$); 1,4-cyclohexadiene: δ 2.73 (s, 4H, C*H*$_2$), 5.76 (s, 4H, C*H*); TEMPOH: δ 1.19 (s, 12H, C*H*$_3$), 1.54 (s, 6H, overlapping C*H*$_2$), O*H* resonance is not observed; Benzene: δ 7.43 (s, 6H, C*H*).

Xanthene (7.4 mg, 40.6 μmol) was added to a solution of TEMPO (7.0 mg, 44.8 μmol) in CD_2Cl_2 (700 μL) and transferred to a J. Young NMR tube, then mesitylene (5 μL, 35.9 μmol) was added via microsyringe. The reaction was monitored by ^1H NMR spectroscopy for 4 days. Comparison of the integrations of the resonances assignable to xanthene in the initial spectrum and the 4 d spectrum revealed 9% conversion of xanthene, and formation of a new, as-yet-unidentified product. Resonances assignable to bixanthenyl or xanthone were not observed in the spectrum. ^1H NMR (500 MHz, 25 °C, CD_2Cl_2): xanthene: δ 4.09 (s, 2H, C*H*$_2$), 7.05-7.10 (m, 4H, C*H*), 7.17-7.27 (m, 4H, C*H* overlapping with unidentified product); New product: δ 6.01 (s), 7.17-7.27 (m, C*H* overlapping with xanthene C*H*), 7.41 (t, *J* = 6.2, C*H*), 7.68 (d, *J* = 7.2 Hz, C*H*).

TEMPO (21.2 mg, 135.7 μmol) was added to a solution of cyclobutanol (5 μL, 63.9 μmol) in C_6D_6 (700 μL) and transferred to an NMR tube. The reaction was monitored by ^{1}H NMR spectroscopy for 20 h. No formation of cyclobutanone was observed. ^{1}H NMR (400 MHz, 25 °C, C_6D_6): cyclobutanol: δ 1.29 (s, 2H, C*H*$_2$), 1.53 (s, 1H, C*H*), 1.86 (s, 2H, C*H*$_2$), 2.18 (s, 2H, C*H*$_2$), 4.78 (s, 1H, O*H*).

TEMPO (19.4 mg, 124.2 μmol) was added to a solution of cyclopropylcarbinol (5 μL, 63.9 μmol) in CD_2Cl_2 (700 μL) and transferred to an NMR tube. The reaction was monitored by ^{1}H NMR spectroscopy for 24 h. No formation cyclopropanecarboxaldehyde was observed. ^{1}H NMR (400 MHz, 25 °C, CD_2Cl_2): cyclopropylcarbinol: δ 0.62 (br s, 1H, O*H*), 0.31 (s, 2H, C*H*$_2$), 0.63 (s, 2H, C*H*$_2$), 1.20 (s, 1H, C*H*), 3.75 (s, 2H, C*H*$_2$).

2.4.28 X-ray Crystallography

Data for **2.15**·Et_2O, **2.27,** and **2.28** were collected on a Bruker KAPPA APEX II diffractometer equipped with an APEX II CCD detector using a TRIUMPH monochromater with a MoKα X-ray source (α = 0.71073 Å). Crystals were mounted on a cryoloop under Paratone-N oil, and all data were collected at 100(2) K using an Oxford nitrogen gas cryostream system. X-ray data for **15**·Et_2O were collected utilizing frame exposures of 2 seconds, while data for both **2.27** and **2.28** were collected utilizing frame exposures of 10 (low angle) and 15 s (high angle). Data collection and cell parameter determination were conducted using the SMART program.[75] Integration of the data frames and final cell parameter refinement were performed using SAINT software.[76] Absorption correction of the data were carried out using the multi-scan method SADABS.[77] Subsequent calculations were carried out using SHELXTL.[78] Structure determination was done using direct methods

and difference Fourier techniques. All hydrogen atom positions were idealized, and rode on the atom of attachment with the exception of the NH hydrogen atom. Structure solution, refinement, graphics, and creation of publication materials were performed using SHELXTL.[78]

Table 2.4. Crystallographic details for complexes **2.15**·Et_2O, **2.27** and **2.28**

	2.15·Et_2O	**2.27**	**2.28**
empirical formula	$C_{38}H_{66}Cl_4Fe_2N_2O_7$	$C_9H_{19}Br_3FeNO$	$C_{18}H_{38}Br_4Fe_2N_2O_3$
crystal habit, color	Block, brown	block, orange	block, orange
crystal size (mm)	0.25 × 0.25 × 0.05	0.11 × 0.05 × 0.03	0.25 × 0.15 × 0.12
crystal system	triclinic	orthorhombic	orthorhombic
space group	$P\bar{1}$	Pnma	Pccn
volume ($Å^3$)	2243.6(10)	1467.1(2)	2711.6(4)
a (Å)	9.693(2)	11.8901(9)	12.3267(9)
b (Å)	10.744(3)	13.0806(10)	13.7288(10)
c (Å)	22.420(7)	9.4327(8)	16.0229(13)
α (deg)	86.333(10)	90.00	90.00
β (deg)	86.445(7)	90.00	90.00
γ (deg)	74.565(5)	90.00	90.00
Z	2	4	4
formula weight (g/mol)	916.42	452.83	761.82
density (calculated) (Mg/m^3)	1.357	2.050	1.866
absorption coefficient (mm^{-1})	0.930	9.177	6.985
F_{000}	968	976	1504
total no. reflections	30564	6350	17333
unique reflections	9888	2301	4170
final R indices [I >2σ(I)]	R_1 = 0.0352 wR_2 = 0.0805	R_1 = 0.0220 wR_2 = 0.0441	R_1 = 0.0315 wR_2 = 0.0663
largest diff. peak and hole ($e^- A^{-3}$)	0.506 and −0.351	0.775 and −0.522	0.815 and −0.643
GOF	1.020	1.032	1.022

2.5 Appendix

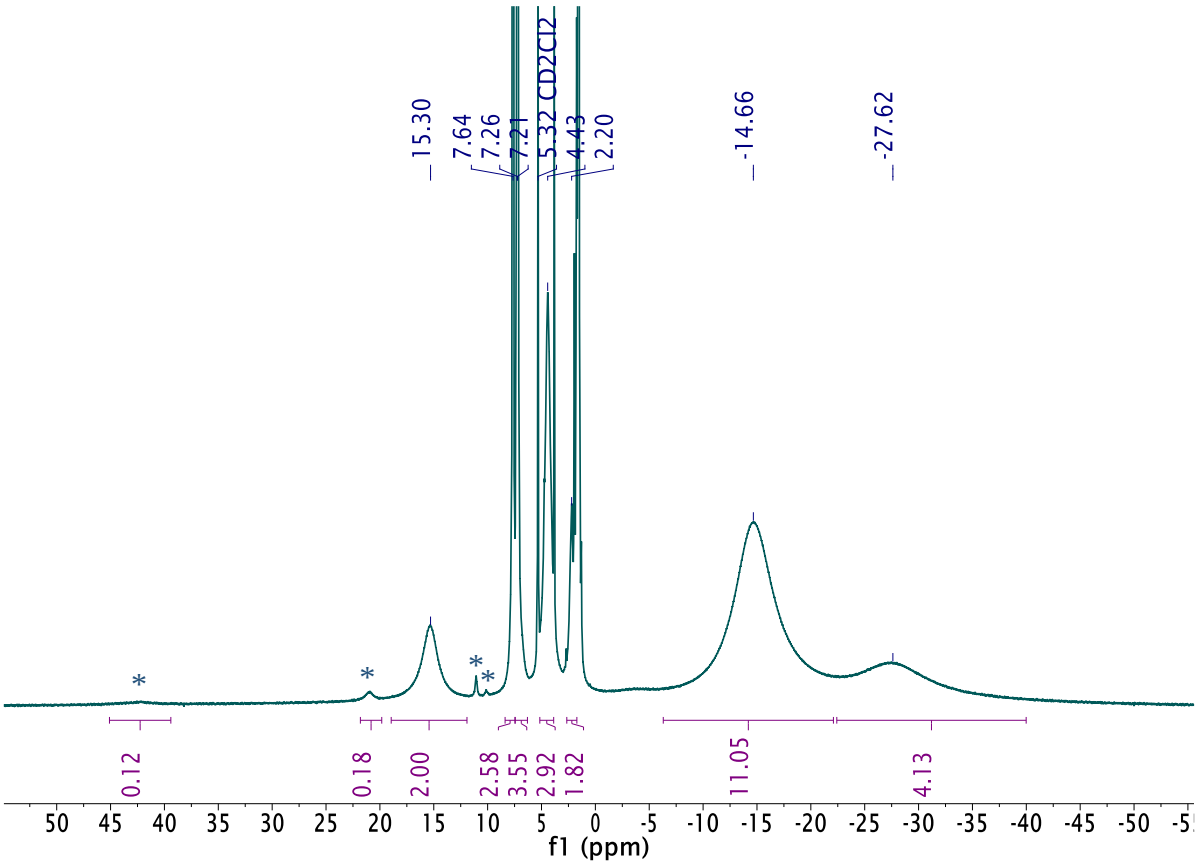

Figure A2.1. ^{1}H NMR spectrum of single crystals of complex **2.15** in CD_2Cl_2/pyridine-d_5. Blue asterisks denote the presence of a minor impurity.

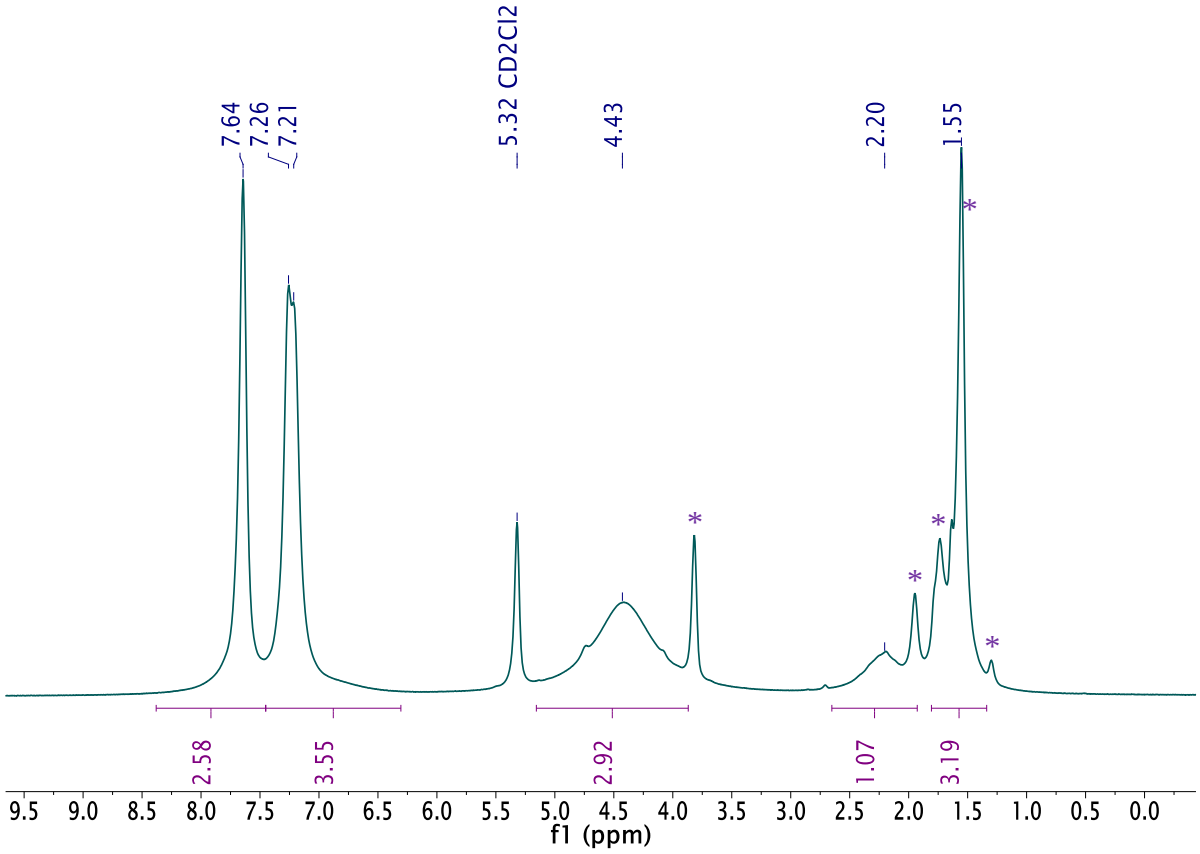

Figure A2.2. Partial ^{1}H NMR spectrum of single crystals of complex **2.15** in CD_2Cl_2/pyridine-d_5. Purple asterisks denote the presence of hexanes and lattice Et_2O.

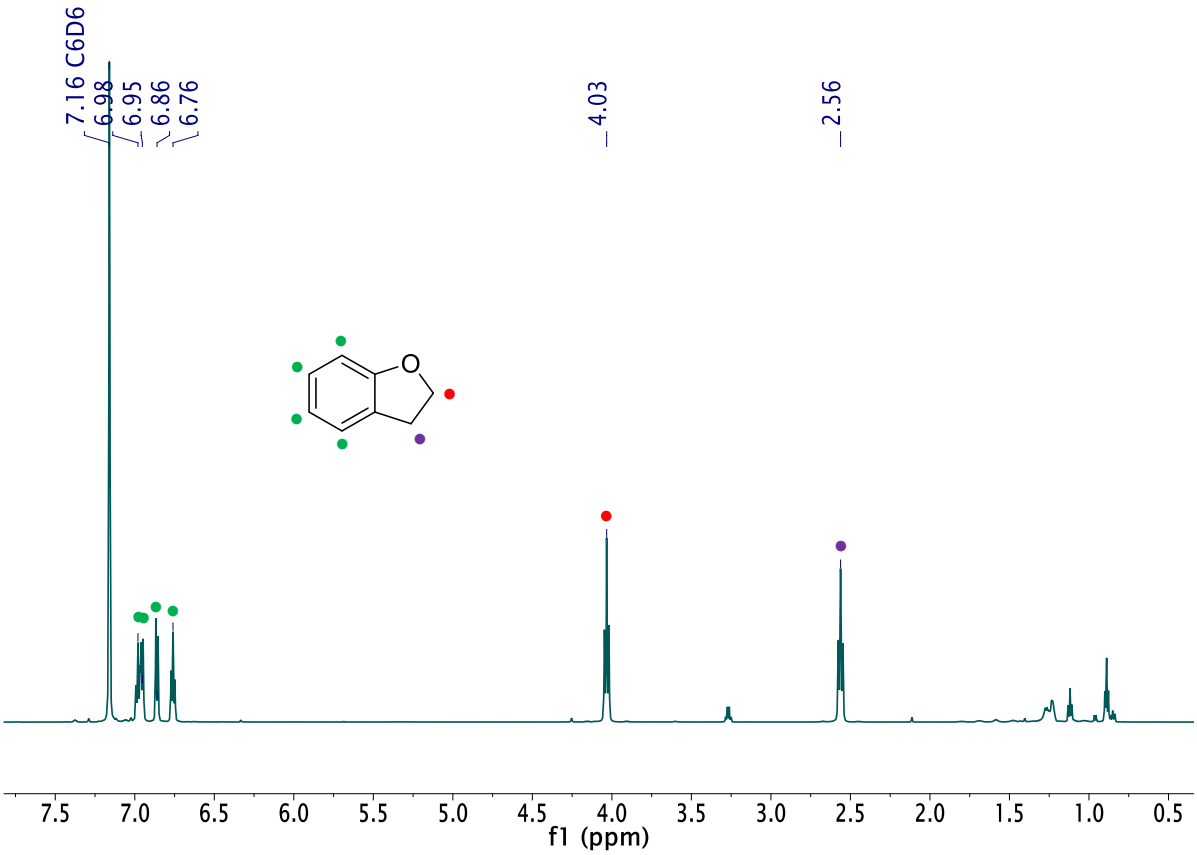

Figure A2.3. ^{1}H NMR spectrum of the reaction products of 2,3-dihydrobenzofuran and $FeCl_3(\eta^1$-TEMPO) after 24 h. • indicate resonances assignable to 2,3-dihydrobenzofuran. Unlabeled resonances are assignable to solvent impurities. **Experimental Details:** $FeCl_3(\eta^1$-TEMPO) (61.8 mg, 194.1 μmol) was dissolved in C_6D_6 (700 μl) and transferred to an NMR tube. 2,3-dihydrobenzofuran (10 μl, 88.6 μmol) was added via microsyringe and the dark purple solution was allowed to stand without stirring for 18 h. No color change was observed. The reaction mixture was filtered through a basic alumina column (2 cm × 0.5 cm) supported on glass wool into an NMR tube. A ^{1}H NMR spectrum of the yellow orange solution was recorded. Analysis of the spectrum revealed only recovery of starting material.

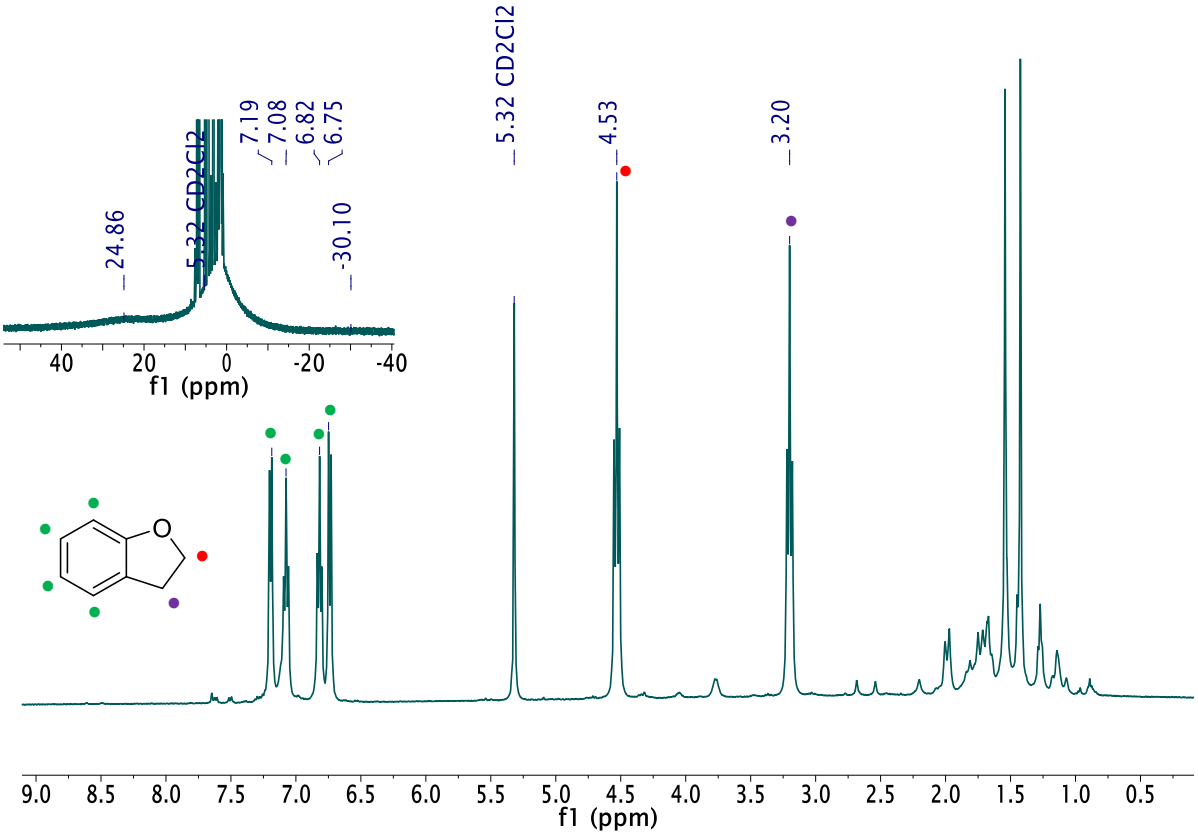

Figure A2.4. *In situ* ^{1}H NMR spectrum of the reaction of 2,3-dihydrobenzofuran and $AlCl_3(\eta^1$-TEMPO) after 24 h. • indicate resonances assignable to 2,3-dihydrobenzofuran. The full spectrum shows three broad resonances assignable to unreacted $AlCl_3(\eta^1$-TEMPO). The small amount of $AlCl_3(\eta^1$-TEMPOH) generated in the reaction is likely formed by decomposition of $AlCl_3(\eta^1$-TEMPO), and not by oxidation of 2,3-dihydrobenzofuran. **Experimental Details:** $AlCl_3(\eta^1$-TEMPO) (27.7 mg, 95.7 μmol) was dissolved in CD_2Cl_2 (700 μl) and transferred to an NMR tube. 2,3-dihydrobenzofuran (5 μl, 44.3 μmol) was added via microsyringe. The reaction was monitored by ^{1}H NMR spectroscopy for 24 h. Analysis of the NMR spectra revealed that no oxidation of 2,3-dihydrobenzofuran has occurred.

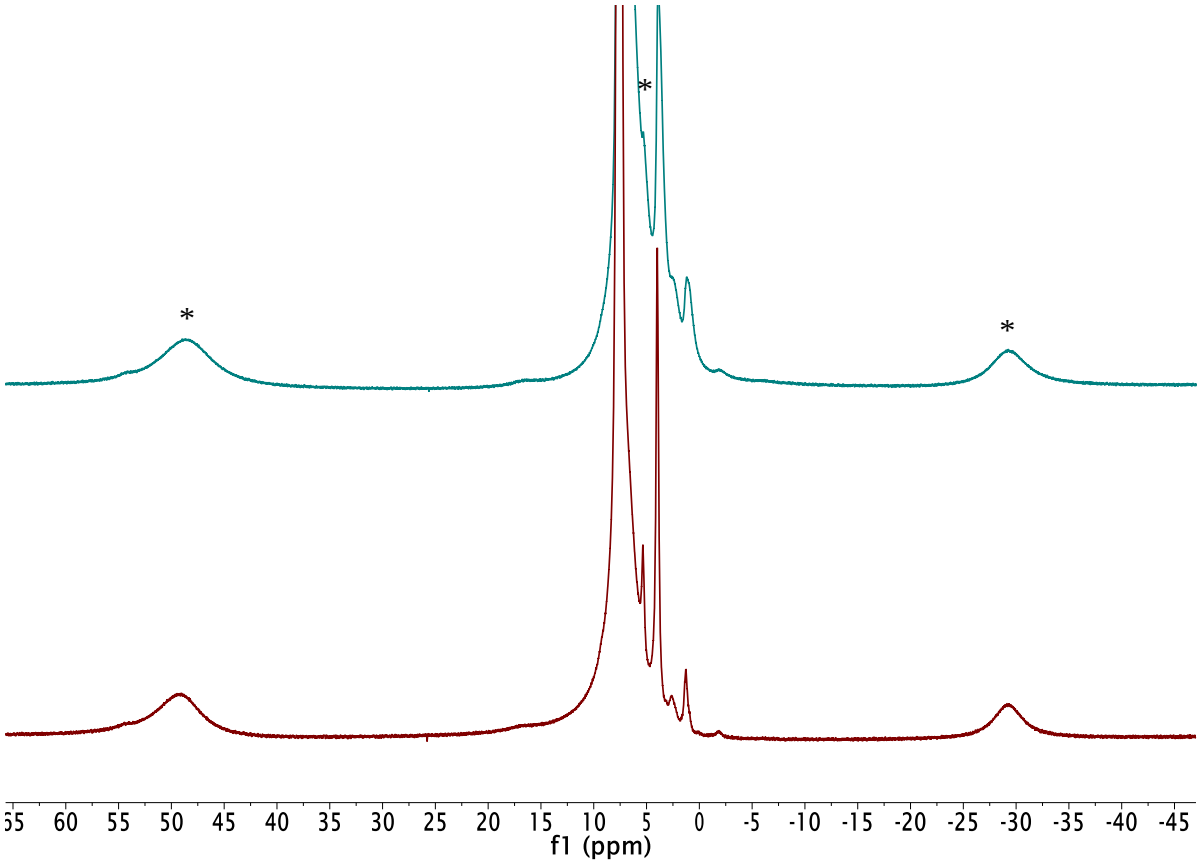

Figure A2.5. *In situ* ^{1}H NMR spectra of the attempted oxidation of fluorene by $FeCl_3(\eta^1$-TEMPO) in CD_2Cl_2 at 10 min (bottom) and 4 d (top). Black asterisks indicate resonances assignable to unreacted $FeCl_3(\eta^1$-TEMPO). **Experimental Details:** $FeCl_3(\eta^1$-TEMPO) (20.7 mg, 65.0 μmol) was dissolved in CD_2Cl_2 (700 μL). This solution was transferred to an NMR tube and an initial ^{1}H NMR spectrum was recorded. Fluorene (9.2 mg, 55.3 μmol) was added to the deep purple solution and the reaction mixture was monitored by ^{1}H NMR spectroscopy for 4 days. No oxidation of fluorene was observed.

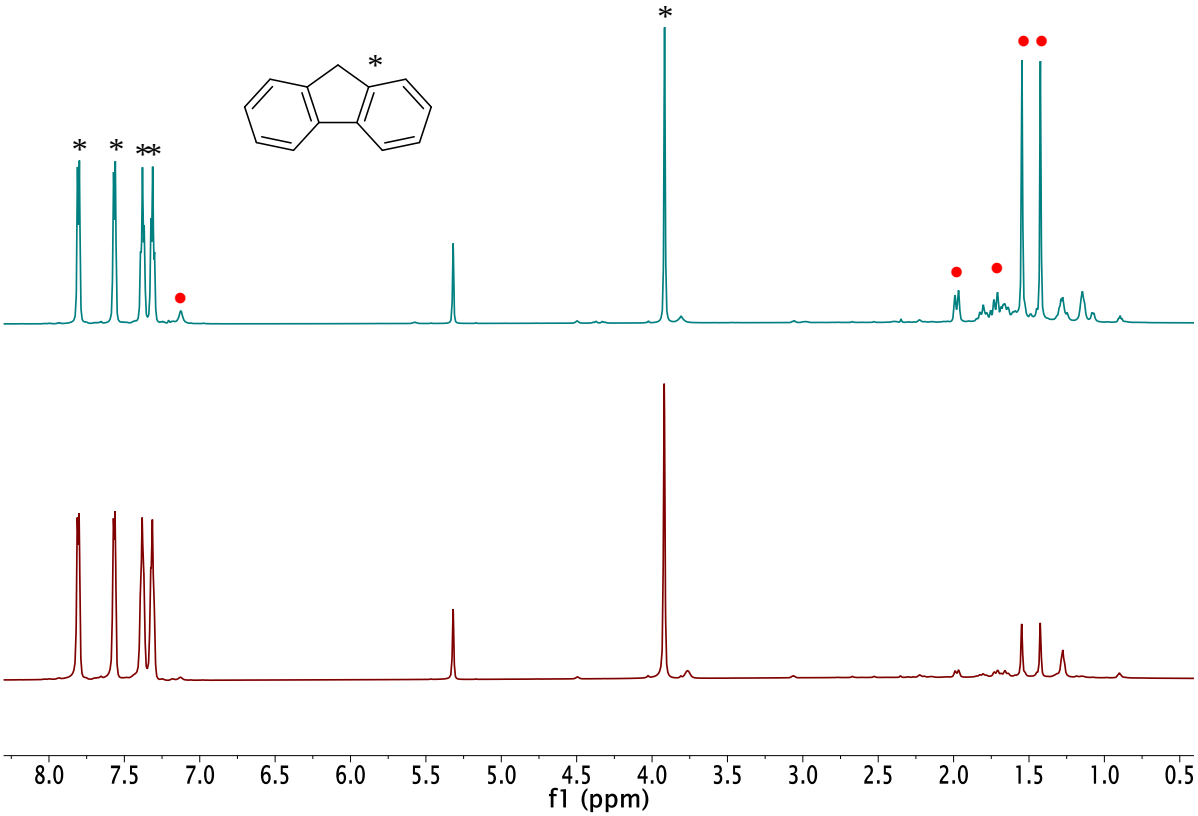

Figure A2.6. In situ ^{1}H NMR spectra of the attempted oxidation of fluorene by $AlCl_3(\eta^1$-TEMPO) in CD_2Cl_2 at 10 min (bottom) and 4 d (top). Black asterisks indicate resonances assignable to unreacted fluorene while • indicate resonances assignable to $AlCl_3(\eta^1$-TEMPOH). The three broad resonances assignable to unreacted $AlCl_3(\eta^1$-TEMPO) are not shown. The small amount of $AlCl_3(\eta^1$-TEMPOH) generated in the reaction is likely formed by decomposition of $AlCl_3(\eta^1$-TEMPO), and not by oxidation of fluorene. **Experimental Details:** $AlCl_3(\eta^1$-TEMPO) (13.9 mg, 48.0 μmol) was dissolved in CD_2Cl_2 (700 μL). This solution was transferred to an NMR tube and an initial ^{1}H NMR spectrum was recorded. Fluorene (7.6 mg, 45.7 μmol) was then added to the yellow solution and the reaction mixture was monitored by ^{1}H NMR spectroscopy for 4 days. No oxidation of fluorene was observed.

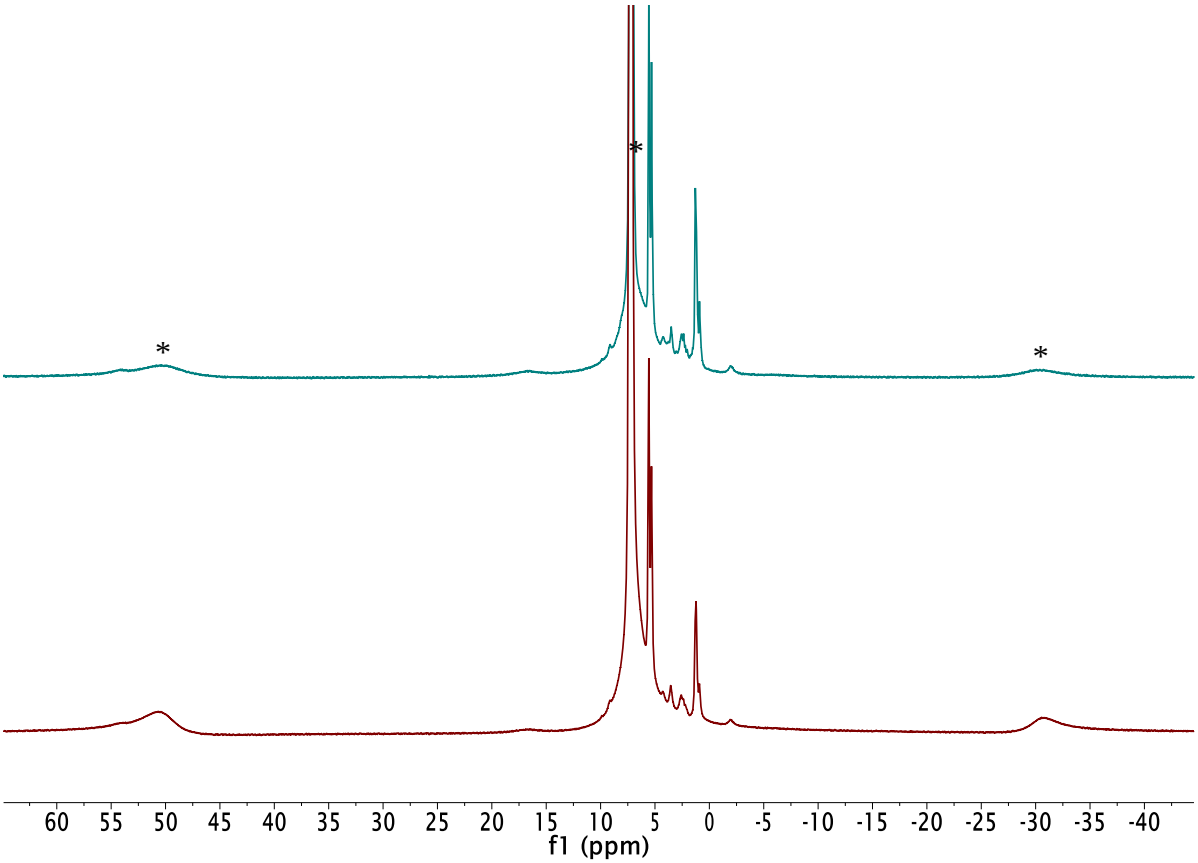

Figure A2.7. In situ ^{1}H NMR spectra of the attempted oxidation of triphenylmethane by $FeCl_3(\eta^1$-TEMPO) (2 equiv) in CD_2Cl_2 at 10 min (bottom) and 4 d (top). Black asterisks indicate resonances assignable to unreacted $FeCl_3(\eta^1$-TEMPO). **Experimental Details:** $FeCl_3(\eta^1$-TEMPO) (8.2 mg, 25.7 μmol) was dissolved in CD_2Cl_2 (700 μL). This solution was transferred to an NMR tube and an initial ^{1}H NMR spectrum was recorded. Ph_3CH (4.8 mg, 19.6 μmol) was added to the deep purple solution and the reaction mixture was monitored by ^{1}H NMR spectroscopy for 4 days. No oxidation of Ph_3CH was observed.

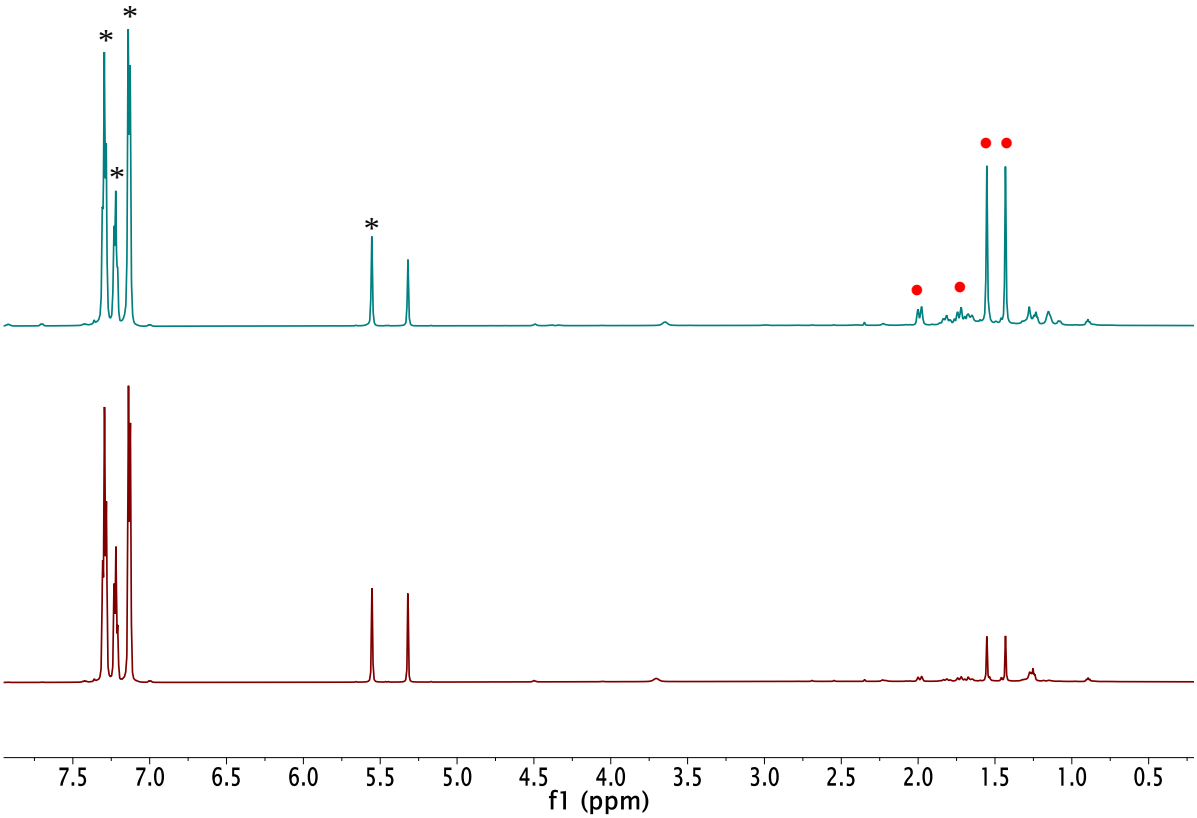

Figure A2.8. In situ ^{1}H NMR spectra of the attempted oxidation of triphenylmethane by $AlCl_3(\eta^1$-TEMPO) in CD_2Cl_2 at 10 min (bottom) and 4 d (top). Black asterisks indicate resonances assignable to unreacted triphenylmethane while • indicate resonances assignable to $AlCl_3(\eta^1$-TEMPOH). The three broad resonances assignable to unreacted $AlCl_3(\eta^1$-TEMPO) are not shown. The small amount of $AlCl_3(\eta^1$-TEMPOH) generated in the reaction is likely formed by decomposition of $AlCl_3(\eta^1$-TEMPO), and not by oxidation of triphenylmethane. **Experimental Details:** $AlCl_3(\eta^1$-TEMPO) (10.9 mg, 37.6 μmol) was dissolved in CD_2Cl_2 (700 μL). This solution was transferred to an NMR tube and an initial ^{1}H NMR spectrum was recorded. Ph_3CH (7.3 mg, 29.9 μmol) was then added to the yellow solution and the reaction mixture was monitored by ^{1}H NMR spectroscopy for 4 days. No oxidation of Ph_3CH was observed.

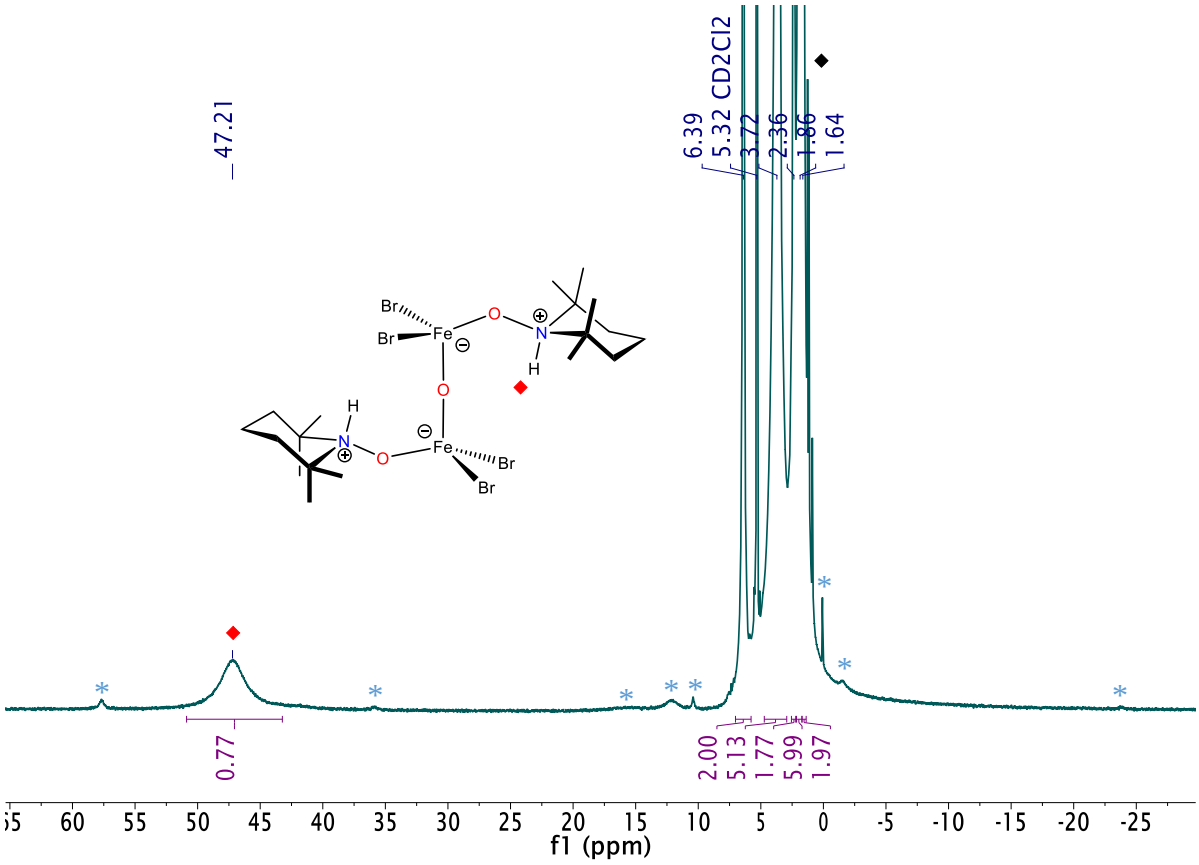

Figure A2.9. ^{1}H NMR spectrum of complex **2.28** in CD_2Cl_2. ◆ indicate resonances assignable to **2.28**. Blue asterisks denote the presence of minor impurities.

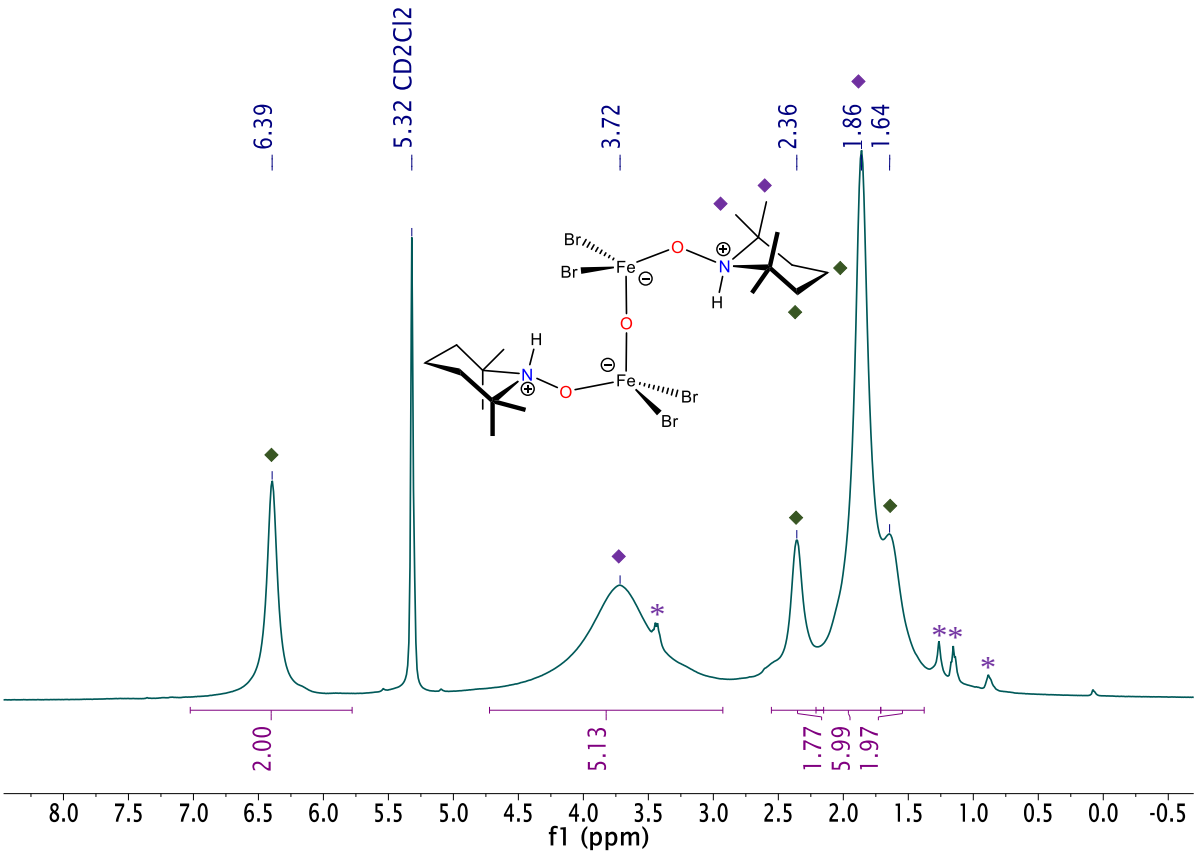

Figure A2.10. Partial ^{1}H NMR spectrum of complex **2.28** in CD_2Cl_2. ◆ indicate resonances assignable to **2.28**. Purple asterisks denote the presence of hexanes and Et_2O.

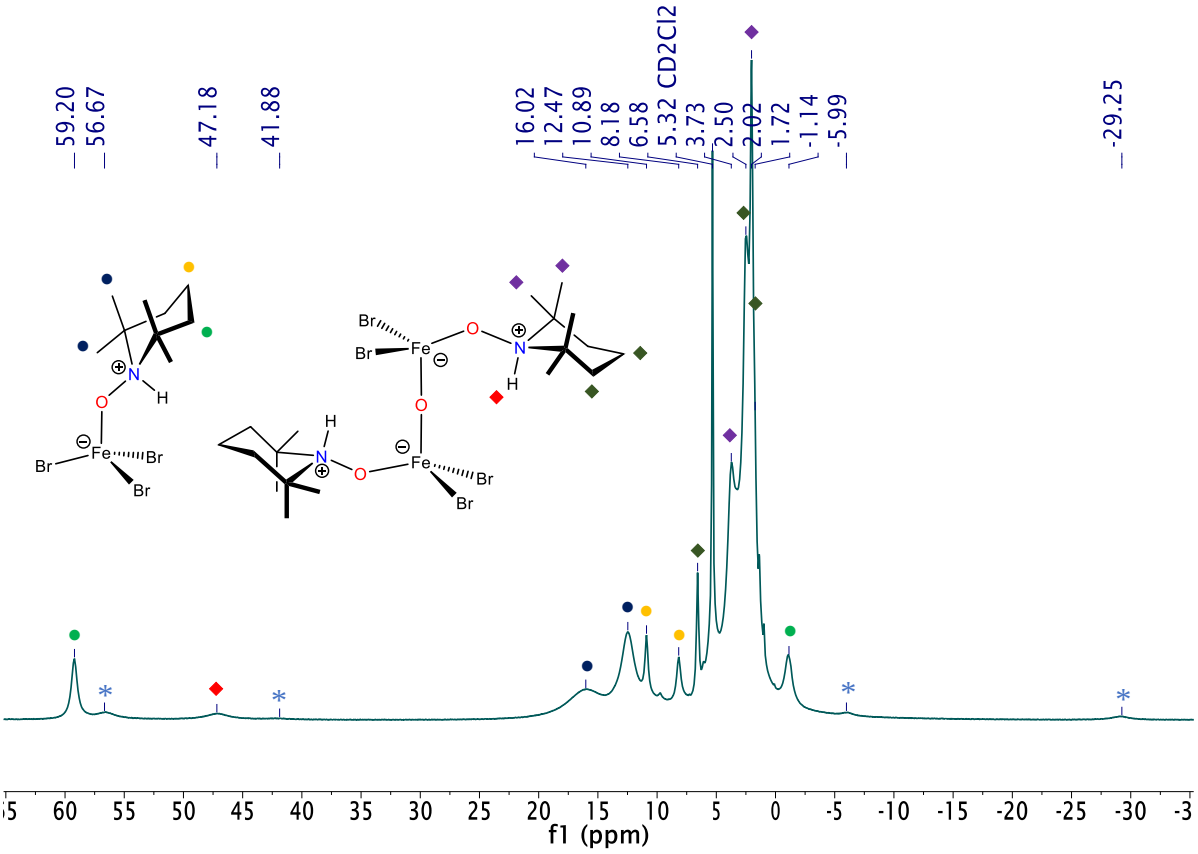

Figure A2.11. ^{1}H NMR spectrum in CD_2Cl_2 of a mixture of complexes **2.27** and **2.28** from the reaction of $FeBr_3$ and TEMPO in Et_2O. • and ◆ indicate resonances assignable to **2.27** and **2.28**, respectively. Blue asterisks denote the presence of a minor unidentified product. The identity of complex **2.27** was determined by comparison of the ^{1}H NMR spectral parameters with those of the chloride congener, $FeCl_3(\eta^1$-TEMPOH).[14]

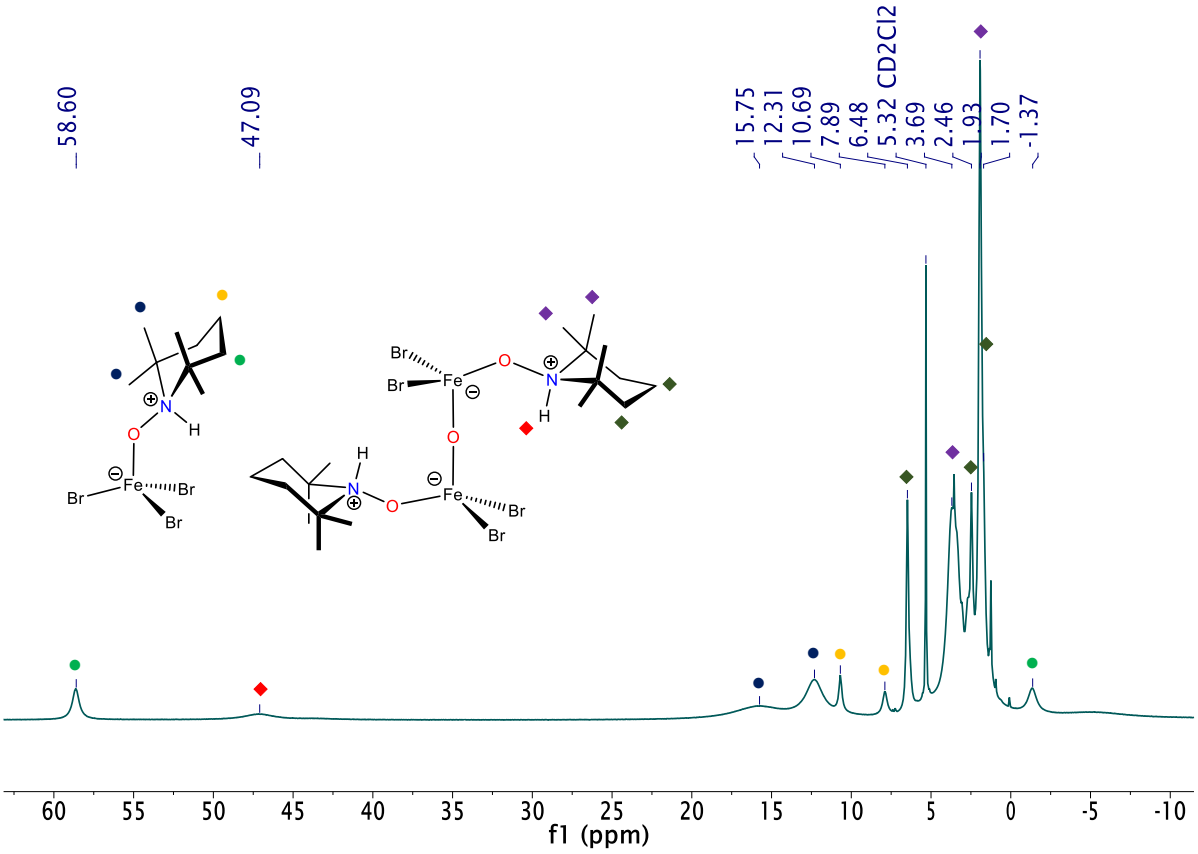

Figure A2.12. ^{1}H NMR spectrum in CD_2Cl_2 of a mixture of complexes **2.27** and **2.28** from the reaction of $FeBr_3$ and TEMPOH in Et_2O. • and ◆ indicate resonances assignable to **2.27** and **2.28**, respectively. The identity of complex **2.27** was determined by comparison of the ^{1}H NMR spectral parameters with those of the chloride congener, $FeCl_3(\eta^1$-TEMPOH).[14]

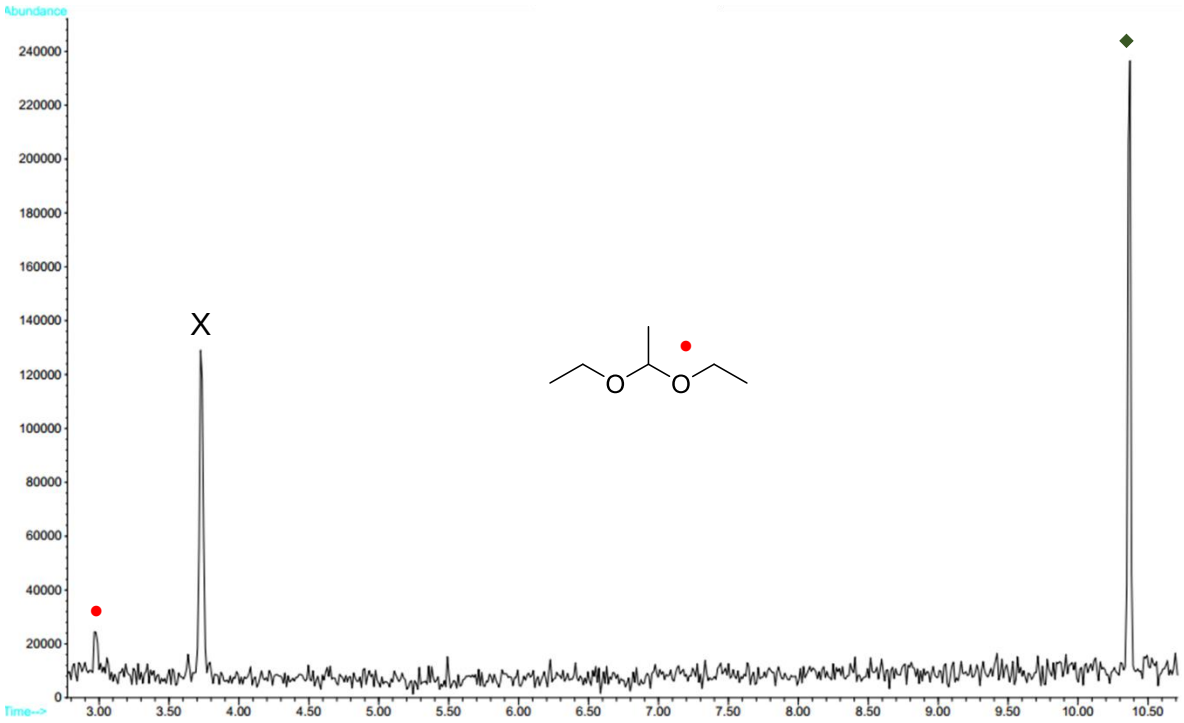

Figure A2.13. GC/MS trace of the supernatant from the reaction of $FeBr_3$ and TEMPO in Et_2O following filtration through a basic alumina column. • and ◆ indicate peaks assignable to 1,1-diethoxyethane and TEMPO, respectively. X indicates the presence of toluene, which is also present in the control trace of Et_2O alone.

2.6 References

(1) Vogler, T.; Studer, A. Applications of TEMPO in Synthesis. *Synthesis* **2008**, *2008*, 1979.

(2) Sheldon, R. A.; Arends, I. W. C. E. Organocatalytic Oxidations Mediated by Nitroxyl Radicals. *Adv. Synth. Catal.* **2004**, *346*, 1051.

(3) Hoover, J. M.; Stahl, S. S. Highly Practical Copper(I)/TEMPO Catalyst System for Chemoselective Aerobic Oxidation of Primary Alcohols. *J. Am. Chem. Soc.* **2011**, *133*, 16901.

(4) Gamez, P.; Arends, I. W. C. E.; Reedijk, J.; Sheldon, R. A. Copper(II)-catalysed aerobic oxidation of primary alcohols to aldehydes. *Chem. Commun.* **2003**, 2414.

(5) Dijksman, A.; Arends, I.; Sheldon, R. A. Cu(II)-nitroxyl radicals as catalytic galactose oxidase mimics. *Org. Biomol. Chem.* **2003**, *1*, 3232.

(6) Lauber, M. B.; Stahl, S. S. Efficient Aerobic Oxidation of Secondary Alcohols at Ambient Temperature with an ABNO/NOx Catalyst System. *ACS Catal.* **2013**, *3*, 2612.

(7) Steves, J. E.; Stahl, S. S. Copper(I)/ABNO-Catalyzed Aerobic Alcohol Oxidation: Alleviating Steric and Electronic Constraints of Cu/TEMPO Catalyst Systems. *J. Am. Chem. Soc.* **2013**, *135*, 15742.

(8) Kim, J.; Stahl, S. S. Cu/Nitroxyl-Catalyzed Aerobic Oxidation of Primary Amines into Nitriles at Room Temperature. *ACS Catal.* **2013**, *3*, 1652.

(9) Van Humbeck, J. F.; Simonovich, S. P.; Knowles, R. R.; MacMillan, D. W. C. Concerning the Mechanism of the $FeCl_3$-Catalyzed α-Oxyamination of Aldehydes: Evidence for a Non-SOMO Activation Pathway. *J. Am. Chem. Soc.* **2010**, *132*, 10012.

(10) Rahimi, A.; Azarpira, A.; Kim, H.; Ralph, J.; Stahl, S. S. Chemoselective Metal-Free Aerobic Alcohol Oxidation in Lignin. *J. Am. Chem. Soc.* **2013**, *135*, 6415.

(11) Nguyen, J. D.; Matsuura, B. S.; Stephenson, C. R. J. A Photochemical Strategy for Lignin Degradation at Room Temperature. *J. Am. Chem. Soc.* **2014**, *136*, 1218.

(12) Sedai, B.; Díaz-Urrutia, C.; Baker, R. T.; Wu, R.; Silks, L. A. P.; Hanson, S. K. Comparison of Copper and Vanadium Homogeneous Catalysts for Aerobic Oxidation of Lignin Models. *ACS Catal.* **2011**, *1*, 794.

(13) Sedai, B.; Díaz-Urrutia, C.; Baker, R. T.; Wu, R.; Silks, L. A. P.; Hanson, S. K. Aerobic Oxidation of β-1 Lignin Model Compounds with Copper and Oxovanadium Catalysts. *ACS Catal.* **2013**, *3*, 3111.

(14) Scepaniak, J. J.; Wright, A. M.; Lewis, R. A.; Wu, G.; Hayton, T. W. Tuning the Reactivity of TEMPO by Coordination to a Lewis Acid: Isolation and Reactivity of $MCl_3(\eta^1$-TEMPO) (M = Fe, Al). *J. Am. Chem. Soc.* **2012**, *134*, 19350.

(15) Hoover, J. M.; Ryland, B. L.; Stahl, S. S. Copper/TEMPO-Catalyzed Aerobic Alcohol Oxidation: Mechanistic Assessment of Different Catalyst Systems. *ACS Catal.* **2013**, *3*, 2599.

(16) Haikarainen, A.; Sipilä, J.; Pietikäinen, P.; Pajunen, A.; Mutikainen, I. Salen complexes with bulky substituents as useful tools for biomimetic phenol oxidation research. *Bioorgan. Med. Chem.* **2001**, *9*, 1633.

(17) Fabbrini, M.; Galli, C.; Gentili, P.; Macchitella, D. An oxidation of alcohols by oxygen with the enzyme laccase and mediation by TEMPO. *Tetrahedron Lett.* **2001**, *42*, 7551.

(18) Sonar, S.; Ambrose, K.; Hendsbee, A. D.; Masuda, J. D.; Singer, R. D. Synthesis and application of Co(salen) complexes containing proximal imidazolium ionic liquid cores. *Can. J. Chem.* **2011**, *90*, 60.

(19) Ferreira, P.; Hernandez-Ortega, A.; Herguedas, B.; Rencoret, J.; Gutierrez, A.; Martinez, M. J.; Jimenez-Barbero, J.; Medina, M.; Martinez, A. T. Kinetic and chemical characterization of aldehyde oxidation by fungal aryl-alcohol oxidase. *Biochem J* **2010**, *425*, 585.

(20) Crestini, C.; Caponi, M. C.; Argyropoulos, D. S.; Saladino, R. Immobilized methyltrioxo rhenium (MTO)/H_2O_2 systems for the oxidation of lignin and lignin model compounds. *Bioorgan. Med. Chem.* **2006**, *14*, 5292.

(21) Hanson, S. K.; Baker, R. T.; Gordon, J. C.; Scott, B. L.; Thorn, D. L. Aerobic Oxidation of Lignin Models Using a Base Metal Vanadium Catalyst. *Inorg. Chem.* **2010**, *49*, 5611.

(22) Fabbri, C.; Bietti, M.; Lanzalunga, O. Generation and Reactivity of Ketyl Radicals with Lignin Related Structures. On the Importance of the Ketyl Pathway in the Photoyellowing of Lignin Containing Pulps and Papers. *J. Org. Chem.* **2005**, *70*, 2720.

(23) Nichols, J. M.; Bishop, L. M.; Bergman, R. G.; Ellman, J. A. Catalytic C−O Bond Cleavage of 2-Aryloxy-1-arylethanols and Its Application to the Depolymerization of Lignin-Related Polymers. *J. Am. Chem. Soc.* **2010**, *132*, 12554.

(24) Jongerius, A. L.; Jastrzebski, R.; Bruijnincx, P. C. A.; Weckhuysen, B. M. CoMo sulfide-catalyzed hydrodeoxygenation of lignin model compounds: An extended reaction network for the conversion of monomeric and dimeric substrates. *J. Catal.* **2012**, *285*, 315.

(25) Interestingly, oxidations with complex **2.1** appear to result in lower observed yields overall. However, this is likely an artifact of the reaction work-up procedure. In particular, the products formed in the reaction with **2.1** are only observable by ^{1}H NMR spectroscopy after filtration through a basic alumina column, which is required to remove the paramagnetic by-product, $FeCl_3(\eta^1$-TEMPOH) (see Experimental section for more details). This filtration procedure likely results in some product loss on the alumina column. While this procedure is obviously not ideal, it was the only protocol we discovered that was able to separate the organic products from the paramagnetic iron-containing by-products. In comparison, in most instances the analogous oxidations with **2.2** do not require removal of metal-containing products via filtration through a basic alumina column for analysis by ^{1}H NMR spectroscopy. As a result, reactions with **2.2** often feature higher yields.

(26) Bordwell, F. G.; Zhang, X. M. Polarizability effects of alkyl groups in RCH_2, R, RS, RSO_2, RO, and R_2N moieties in families of weak acids on the stabilities of adjacent anions and radicals in DMSO solution. *J. Am. Chem. Soc.* **1994**, *116*, 973.

(27) Warren, J. J.; Tronic, T. A.; Mayer, J. M. Thermochemistry of Proton-Coupled Electron Transfer Reagents and its Implications. *Chem. Rev.* **2010**, *110*, 6961.

(28) Viehe, H. G.; Janousek, Z.; Merenyi, R.; Stella, L. The captodative effect. *Acc. Chem. Res.* **1985**, *18*, 148.

(29) Lippert, C. A.; Soper, J. D. Deoxygenation of Nitroxyl Radicals by Oxorhenium(V) Complexes with Redox-Active Ligands. *Inorg. Chem.* **2010**, *49*, 3682.

(30) Wuts, P. G. M.; Greene, T. W. In *Greene's Protective Groups in Organic Synthesis*; John Wiley & Sons, Inc.: 2006, p 431.

(31) Lee, S. H.; Lee, J. H.; Yoon, C. M. An efficient protection of carbonyls and deprotection of acetals using decaborane. *Tetrahedron Lett.* **2002**, *43*, 2699.

(32) Tateiwa, J.; Horiuchi, H.; Uemura, S. Ce3+-Exchanged Montmorillonite (Ce3+-Mont) as a Useful Substrate-Selective Acetalization Catalyst. *J. Org. Chem.* **1995**, *60*, 4039.

(33) Macala, G. S.; Matson, T. D.; Johnson, C. L.; Lewis, R. S.; Iretskii, A. V.; Ford, P. C. Hydrogen Transfer from Supercritical Methanol over a Solid Base Catalyst: A Model for Lignin Depolymerization. *ChemSusChem.* **2009**, *2*, 215.

(34) Le Gall, F.; Fabrizi de Biani, F.; Caneschi, A.; Cinelli, P.; Cornia, A.; Fabretti, A. C.; Gatteschi, D. Synthesis, crystal structures and magnetic characterization of four β-diketonate-alkoxide iron(III) dimers. Dependence of the magnetic properties on geometrical and electronic parameters. *Inorg. Chim. Acta.* **1997**, *262*, 123.

(35) Kovacs, T.; Speier, G.; Reglier, M.; Giorgi, M.; Vertes, A.; Vanko, G. Preparation and characterization of homoleptic and ethoxy-bridged nitronato iron(III) complexes. *Chem. Commun.* **2000**, 469.

(36) Chiari, B.; Piovesana, O.; Tarantelli, T.; Zanazzi, P. F. Exchange interaction in multinuclear transition-metal complexes. 6. Nature of metal-metal coupling in dinuclear iron(III) systems containing FeOFeO bridging units. *Inorg. Chem.* **1984**, *23*, 3398.

(37) Stefan, S.; Belaj, F.; Madl, T.; Pietschnig, R. A Radical Approach to Hydroxylaminotrichlorosilanes: Synthesis, Reactivity, and Crystal Structure of TEMPO-$SiCl_3$ (TEMPO = 2,2,6,6-Tetramethylpiperidine-*N*-oxyl). *Eur. J. Inorg. Chem.* **2010**, *2010*, 289.

(38) Li, P.-C.; Wang, T.-S.; Lee, G.-H.; Liu, Y.-H.; Wang, Y.; Chen, C.-T.; Chao, I. Theoretical Study and X-ray Determination of Bianthrones: Long C−C Bond Length and Preferred Gauche Conformation. *J. Org. Chem.* **2002**, *67*, 8002.

(39) Shan, G.; Yang, X.; Ma, L.; Rao, Y. Pd-Catalyzed C-H Oxygenation with TFA/TFAA: Expedient Access to Oxygen-Containing Heterocycles and Late-Stage Drug Modification. *Angew. Chem. Int. Ed.* **2012**, *124*, 13247.

(40) Larsen, A. S.; Wang, K.; Lockwood, M. A.; Rice, G. L.; Won, T.-J.; Lovell, S.; Sadílek, M.; Tureček, F.; Mayer, J. M. Hydrocarbon Oxidation by Bis-μ-oxo Manganese Dimers: Electron Transfer, Hydride Transfer, and Hydrogen Atom Transfer Mechanisms. *J. Am. Chem. Soc.* **2002**, *124*, 10112.

(41) Feng, Y.; Gunnoe, T. B.; Grimes, T. V.; Cundari, T. R. Octahedral $[TpRu(PMe_3)_2OR]^{n+}$ Complexes (Tp = hydridotris(pyrazolyl)borate; R = H or Ph; n = 0 or 1): Reactions at Ru(II) and Ru(III) Oxidation States with Substrates that Possess Carbon−Hydrogen Bonds. *Organometallics* **2006**, *25*, 5456.

(42) Jin, C.; Zhang, L.; Su, W. Direct Benzylic Oxidation with Sodium Hypochlorite Using a New Efficient Catalytic System: TEMPO/$Co(OAc)_2$. *Synlett* **2011**, *2011*, 1435.

(43) Hanson, S. K.; Baker, R. T.; Gordon, J. C.; Scott, B. L.; Silks, L. A. P.; Thorn, D. L. Mechanism of Alcohol Oxidation by Dipicolinate Vanadium(V): Unexpected Role of Pyridine. *J. Am. Chem. Soc.* **2010**, *132*, 17804.

(44) Griller, D.; Ingold, K. U. Free-radical clocks. *Acc. Chem. Res.* **1980**, *13*, 317.

(45) Rocek, J.; Aylward, D. E. One-electron vs. two-electron oxidations. Vanadium(V) oxidation of cyclobutanols. *J. Am. Chem. Soc.* **1975**, *97*, 5452.

(46) Bowry, V. W.; Ingold, K. U. A radical clock investigation of microsomal cytochrome P-450 hydroxylation of hydrocarbons. Rate of oxygen rebound. *J. Am. Chem. Soc.* **1991**, *113*, 5699.

(47) Rozantzev, E. G.; Neiman, M. B. Organic radical reactions involving no free valence. *Tetrahedron* **1964**, *20*, 131.

(48) Wright, A. M.; Page, J. S.; Scepaniak, J. J.; Wu, G.; Hayton, T. W. Divergent Reactivity of TEMPO with MBr_3 (M = B, Al). *Eur. J. Inorg. Chem.* **2013**, *2013*, 3817.

(49) Yang, G.; Ghosez, L. Synthesis of Enantiopure α-Chlorocyclobutanones and Cyclobutanols as Scaffolds for the Diverted Synthesis of Serine Protease Inhibitors. *Eur. J. Org. Chem.* **2009**, *2009*, 1738.

(50) Pestovsky, O.; Bakac, A. Reactivity of Aqueous Fe(IV) in Hydride and Hydrogen Atom Transfer Reactions. *J. Am. Chem. Soc.* **2004**, *126*, 13757.

(51) Satchell, D. P. N.; Satchell, R. S. Quantitative aspects of the Lewis acidity of covalent metal halides and their organo derivatives. *Chem. Rev.* **1969**, *69*, 251.

(52) Swanson, B.; Shriver, D. F.; Ibers, J. A. Nature of the donor-acceptor bond in acetonitrile-boron trihalides. The structures of the boron trifluoride and boron trichloride complexes of acetonitrile. *Inorg. Chem.* **1969**, *8*, 2182.

(53) Bessac, F.; Frenking, G. Why Is BCl_3 a Stronger Lewis Acid with Respect to Strong Bases than BF_3? *Inorg. Chem.* **2003**, *42*, 7990.

(54) Rowsell, B. D.; Gillespie, R. J.; Heard, G. L. Ligand Close-Packing and the Lewis Acidity of BF_3 and BCl_3. *Inorg. Chem.* **1999**, *38*, 4659.

(55) Fortier, S.; Brown, J. L.; Kaltsoyannis, N.; Wu, G.; Hayton, T. W. Synthesis, Molecular and Electronic Structure of $U^{V}(O)[N(SiMe_3)_2]_3$. *Inorg. Chem.* **2012**, *51*, 1625.

(56) Lucarini, M.; Marchesi, E.; Pedulli, G. F.; Chatgilialoglu, C. Homolytic Reactivity of Group 14 Organometallic Hydrides toward Nitroxides. *J. Org. Chem.* **1998**, *63*, 1687.

(57) Fortier, S.; Kaltsoyannis, N.; Wu, G.; Hayton, T. W. Probing the Reactivity and Electronic Structure of a Uranium(V) Terminal Oxo Complex. *J. Am. Chem. Soc.* **2011**, *133*, 14224.

(58) Lu, E.; Cooper, O. J.; McMaster, J.; Tuna, F.; McInnes, E. J. L.; Lewis, W.; Blake, A. J.; Liddle, S. T. Synthesis, Characterization, and Reactivity of a Uranium(VI) Carbene Imido Oxo Complex. *Angew. Chem.* **2014**, *126*, 6814.

(59) Ahlers, C.; Dickman, M. H. Iron-Mediated Cleavage of Coordinated 1,1,1,5,5,5-Hexafluoropentane-2,4-dione by the 2,2,6,6-Tetramethylpiperidine-1-oxyl Nitroxyl Radicalâ€ *Inorg. Chem.* **1998**, *37*, 6337.

(60) LePichon, L.; Stephan, D. W.; Gao, X.; Wang, Q. Iron Phosphinimide and Phosphinimine Complexes: Catalyst Precursors for Ethylene Polymerization. *Organometallics* **2002**, *21*, 1362.

(61) Waddington, D. J. The Gaseous Oxidation of Diethyl Ether. *Proc. R. Soc. A* **1959**, *252*, 260.

(62) Suib, S. L.; Tanguay, J. F.; Occelli, M. L. Comparison of the photochemical and photophysical properties of clays, pillared clays, and zeolites. *J. Am. Chem. Soc.* **1986**, *108*, 6972.

(63) Di Tommaso, S.; Rotureau, P.; Crescenzi, O.; Adamo, C. Oxidation mechanism of diethyl ether: a complex process for a simple molecule. *Phys. Chem. Chem. Phys.* **2011**, *13*, 14636.

(64) Burkey, T. J.; Majewski, M.; Griller, D. Heats of formation of radicals and molecules by a photoacoustic technique. *J. Am. Chem. Soc.* **1986**, *108*, 2218.

(65) Kandanarachchi, P. H.; Autrey, T.; Franz, J. A. Model Compound Studies of the β-O-4 Linkage in Lignin: Absolute Rate Expressions for β-Scission of Phenoxyl Radical from 1-Phenyl-2-phenoxyethanol-1-yl Radical. *J. Org. Chem.* **2002**, *67*, 7937.

(66) Dorrestijn, E.; Hemmink, S.; Hulstman, G.; Monnier, L.; van Scheppingen, W.; Mulder, P. The reduction of alpha-X-acetophenones (X = PhO, Br, Cl) in hydrogen-donating solvents at elevated temperatures. *Eur. J. Org. Chem.* **1999**, 607.

(67) Giffin, N. A.; Makramalla, M.; Hendsbee, A. D.; Robertson, K. N.; Sherren, C.; Pye, C. C.; Masuda, J. D.; Clyburne, J. A. C. Anhydrous TEMPO-H: reactions of a good hydrogen atom donor with low-valent carbon centres. *Org. Biomol. Chem.* **2011**, *9*, 3672.

(68) Williams, U. J.; Mahoney, B. D.; Lewis, A. J.; DeGregorio, P. T.; Carroll, P. J.; Schelter, E. J. Single Crystal to Single Crystal Transformation and Hydrogen-Atom

Transfer upon Oxidation of a Cerium Coordination Compound. *Inorg. Chem.* **2013**, *52*, 4142.

(69) Dess, D. B.; Martin, J. C. A useful 12-I-5 triacetoxyperiodinane (the Dess-Martin periodinane) for the selective oxidation of primary or secondary alcohols and a variety of related 12-I-5 species. *J. Am. Chem. Soc.* **1991**, *113*, 7277.

(70) Zhang, L.; Bi, X.; Guan, X.; Li, X.; Liu, Q.; Barry, B.; Liao, P. Chemoselective Oxidative C(CO)-C(methyl) Bond Cleavage of Methyl Ketones to Aldehydes Catalyzed by CuI with Molecular Oxygen. *Angew. Chem. Int. Ed.* **2013**, *52*, 11303.

(71) Gebeyehu, G.; McNelis, E. Oxidation of diphenylacetylene by I7+ and I5+ compounds. *J. Org. Chem.* **1980**, *45*, 4280.

(72) Lee, D. G.; Chen, T. The oxidation of alcohols by permanganate. A comparison with other high-valent transition-metal oxidants. *J. Org. Chem.* **1991**, *56*, 5341.

(73) Trost, B. M.; Nguyen, H. M.; Koradin, C. Synthesis of a tricyclic core of rameswaralide. *Tetrahedron Lett.* **2010**, *51*, 6232.

(74) Wu, A.; Mader, E. A.; Datta, A.; Hrovat, D. A.; Borden, W. T.; Mayer, J. M. Nitroxyl Radical Plus Hydroxylamine Pseudo Self-Exchange Reactions: Tunneling in Hydrogen Atom Transfer. *J. Am. Chem. Soc.* **2009**, *131*, 11985.

(75) *SMART Apex II*; Bruker AXS Inc.: Madison, WI, 2005.

(76) *SAINT Software User's Guide*; Bruker AXS Inc.: Madison, WI, 2005.

(77) Sheldrick, G. M. *SADABS*; University of Göttingen: Göttingen, Germany, 2005.

(78) *SHELXTL PC*; Bruker AXS Inc.: Madison, WI, 2005.

Chapter 3. **A Cu_{14} Hydride Cluster Supported by Neutral Donor Ligands**

Portions of this work were published in:

Thuy-Ai D. Nguyen; Bryan R. Goldsmith; Homaira T. Zaman; Guang Wu; Baron Peters; Trevor W. Hayton. Synthesis and Characterization of a Cu_{14} Hydride Cluster Supported by Neutral Donor Ligands. *Chem. Eur. J.* **2015**, 21, 5341-5344.

3.1 Introduction

For several decades, copper hydrides have attracted widespread interest for their ability to catalyze the reduction of α,β-unsaturated carbonyls, electron deficient alkenes, alkynes, and even CO_2.[1-10] More recently, the structural chemistry of copper hydrides has seen increased attention, partly in an effort to better understand their reactivity.[11] For example, several large Cu(I) hydride clusters have been structurally characterized in recent years, including $[(Me_3\text{-tach})_3Cu_6(\mu_6\text{-}H)Cl_4]^{2+}$, $[Cu_7H(S_2P(O^iPr)_2)_6]$, $[Cu_{18}H_7(1,2\text{-}S(C_6H_4)PPh_2)_{10}(I)]$, $[Cu_{20}H_{11}(S_2P(O^iPr)_2)_9]$, and $[Cu_{28}H_{15}(S_2CN^nPr_2)_{12}]^+$.[12-18] A common feature of these materials is the presence of anionic supporting ligands. In contrast, copper hydride clusters that feature neutral co-ligands appear to be less common.[19-22] This distinction is significant because each anionic ligand reduces the total number of possible hydrides that can be present in a Cu(I) cluster, which has consequences for both reactivity and structure. Herein, I describe the synthesis of an unsual Cu_{14} hydride cluster, which features neutral donor ligands, and describe its reactivity with CO_2.

3.2 Results and Discussion

Addition of 26 equiv of 1,10-phenanthroline (phen) to $[(Ph_3P)CuH]_6$ in CH_2Cl_2 results in immediate formation of a dark red solution. On standing, this solution undergoes a color change to dark green and then to dark blue. Work-up of this solution after 18 h results in the isolation of the copper hydride cluster, $[Cu_{14}H_{12}(phen)_6(PPh_3)_4][Cl]_2$ (**3.1**), as a dark blue crystalline material in 80% yield (Scheme 3.1). Homaira Zaman, an undergraduate in our group, helped with the development of this synthesis. While only 2.6 equiv of phen is required to form **3.1**, according to the stoichiometry of the reaction, reasonable yields were only achieved when a large excess of phen was added to the $[(Ph_3P)CuH]_6$. If excess phen was not added, then substantial quantities of starting material were recovered from the reaction mixture. For comparison, the related copper hydride cluster, $[(Cp^*AlCu)_6H_4]$ is also formed by displacement of Ph_3P in $[(Ph_3P)CuH]_6$; however, addition of excess $[(Cp^*Al)_4]$ is not required to achieve a high yield, possibly because it has a stronger affinity to Cu(I) than does phen.[23,24] Complex **3.1** crystallizes in the orthorhombic space group $P2_12_12_1$, as a dichloromethane and benzene solvate, **3.1**$\cdot 3CH_2Cl_2 \cdot C_6H_6$ (Figure 3.3a). In the solid state, $[Cu_{14}H_{12}(phen)_6(PPh_3)_4][Cl]_2$ features a tetrahedral $[Cu_4]^{4+}$ core (Figure 3.3d), which is connected, via Cu-Cu bonds, to a diamondoid arrangement of ten Cu(I) centers (Figure 3.3c). These 10 copper centers are coordinated by four PPh_3 ligands, which are arranged at the corners of a tetrahedron, and six phen ligands, which are arranged in the corners of an octahedron. As a result of this arrangement, complex **3.1** features four hexagonal faces, wherein each face is situated opposite to a Ph_3P ligand. The average Cu_{tet}–Cu_P (av. 2.655 Å), Cu_{tet}–Cu_N (av. 2.514 Å), and Cu_P–Cu_N (2.663 Å) bond lengths (Table 3.1) are comparable to the Cu–Cu distances in $[(Ph_3P)CuH]_6$ (av. 2.630 Å),[25] $[(Me_3\text{-tach})_3Cu_6(\mu_6\text{-H})Cl_4]^{2+}$ (av. 2.580 Å),[12] and the outer Cu–Cu distances in $[Cu_{20}H_{11}(S_2P(O^iPr)_2)_9]$ (2.5284(9)–2.7542(7)

Å).[14] The Cu_P–P bond length (av. 2.298 Å) is typical of Cu(I)–P bonds.[25,26] Similarly, the Cu_N–N bond length (av. 2.100 Å) is comparable to Cu-N bonds in $[(Me_3\text{-tach})_3Cu_6(\mu_6\text{-H})Cl_4]^{2+}$ (2.11 Å) and $[(Me_3\text{-tach})_2Cu_3Cl_2]_2^{2+}$ (2.03 Å).[12] Interestingly, the metrical parameters of the tetrahedral $[Cu_4]^{4+}$ core in **3.1** (av. Cu_{tet}–Cu_{tet} = 2.893 Å) are nearly identical to those of the $[Cu_4(\mu_4\text{-H})]^{3+}$ core in $[Cu_8H\{S_2CN^nPr_2\}_6]^+$ (2.894(2)–2.989(2) Å).[13] Lastly, the two Cl^- counterions in **3.1** were observed to be disordered, and were modelled over 8 positions with partial occupancies.

Scheme 3.1. Syntheses of complexes **3.1** and **3.2**

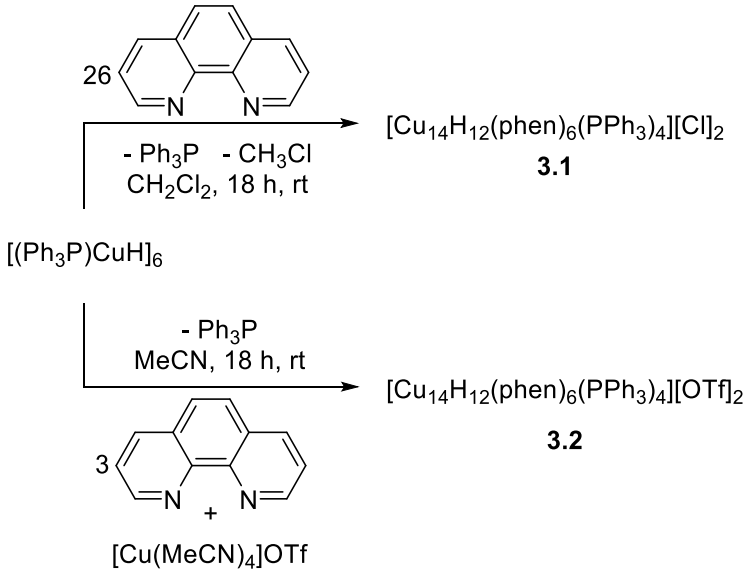

Consistent with the high symmetry observed in the solid-state, complex **3.1** features a single resonance in its $^{31}P\{^1H\}$ NMR spectrum at -5.35 ppm in CD_2Cl_2. Likewise, complex **3.1** features resonances at 6.67, 7.88, and 8.10, and 8.85 ppm in its ^1H NMR spectrum, which are assignable to the six magnetically equivalent phen ligands. Also present in the ^1H NMR spectrum is a broad resonance (FWHM = 31 Hz) at 3.45 ppm, which integrates for 12H, and is assignable to the μ_3-hydride ligand environments.

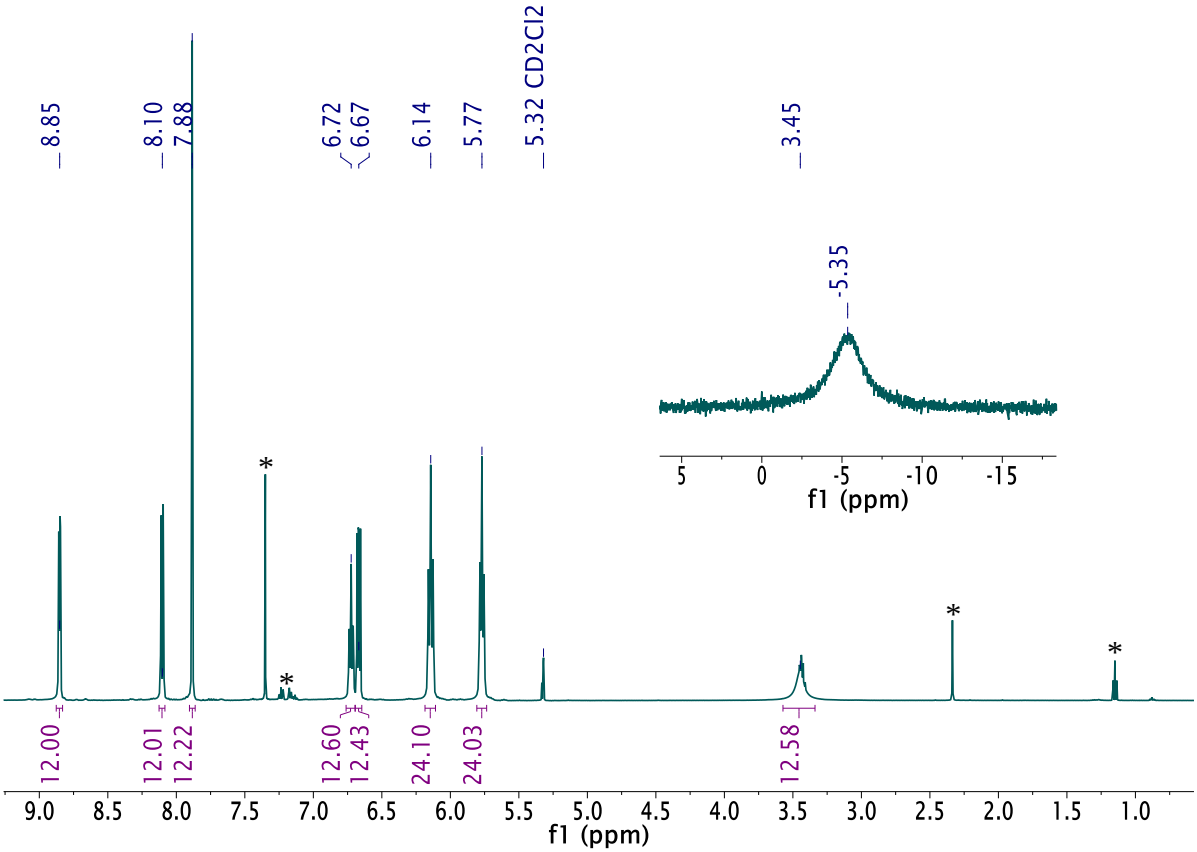

Figure 3.1. ^{1}H NMR and ^{31}P{^{1}H} NMR (inset) spectra of $[Cu_{14}H_{12}(phen)_6(PPh_3)_4][Cl]_2$ (**3.1**) in CD_2Cl_2. (*) denote the presence of benzene, toluene, and Et_2O. The resonance at 3.45 ppm overlaps with Et_2O.

Complex **3.1** features a signal at *m/z* 1515.93 in its ESI mass spectrum, which corresponds to the parent $[M]^{2+}$ ion (calcd *m/z* 1515.94). Conductivity measurements also support the proposed formulation. In MeCN, **3.1** exhibits a Λ_M of 220.5 $ohm^{-1}\cdot cm^2\cdot mol^{-1}$ at 25 °C, which is in excellent agreement with expected molar conductivity for a 2:1 electrolyte in MeCN (220–300 $ohm^{-1}\cdot cm^2\cdot mol^{-1}$).[27]

As previously mentioned, the metrical parameters of the tetrahedral $[Cu_4]^{4+}$ core in **3.1** (av. Cu_{tet}–Cu_{tet} = 2.893 Å) are nearly identical to those of the tetrahedral $[Cu_4(\mu_4\text{-H})]^{3+}$ core in $[Cu_8H\{S_2CN^nPr_2\}_6]^+$ (2.894(2)–2.989(2) Å).[13] To rule out the presence of a μ_4-H ligand

in complex **3.1**, I synthesized the deuteride analogue, **3.1-*d*$_{12}$**, by reaction of phen with [(Ph$_3$P)CuD]$_6$. As anticipated, complex **3.1-*d*$_{12}$** features a singlet at 3.58 ppm in its ^{2}H NMR spectrum, which is assignable to the 12 μ_3-deuteride ligands. Most importantly, though, no resonance assignable to a μ_4-D ligand was observed in the ^{2}H NMR spectrum. Finally, complex **3.1-*d*$_{12}$** features a signal at *m/z* 1522.04 in its ESI mass spectrum, which corresponds to the $[M]^{2+}$ parent ion (calcd. *m/z* 1521.98), a shift of 6 *m/z* versus the signal observed for **3.1-*h*$_{12}$**.

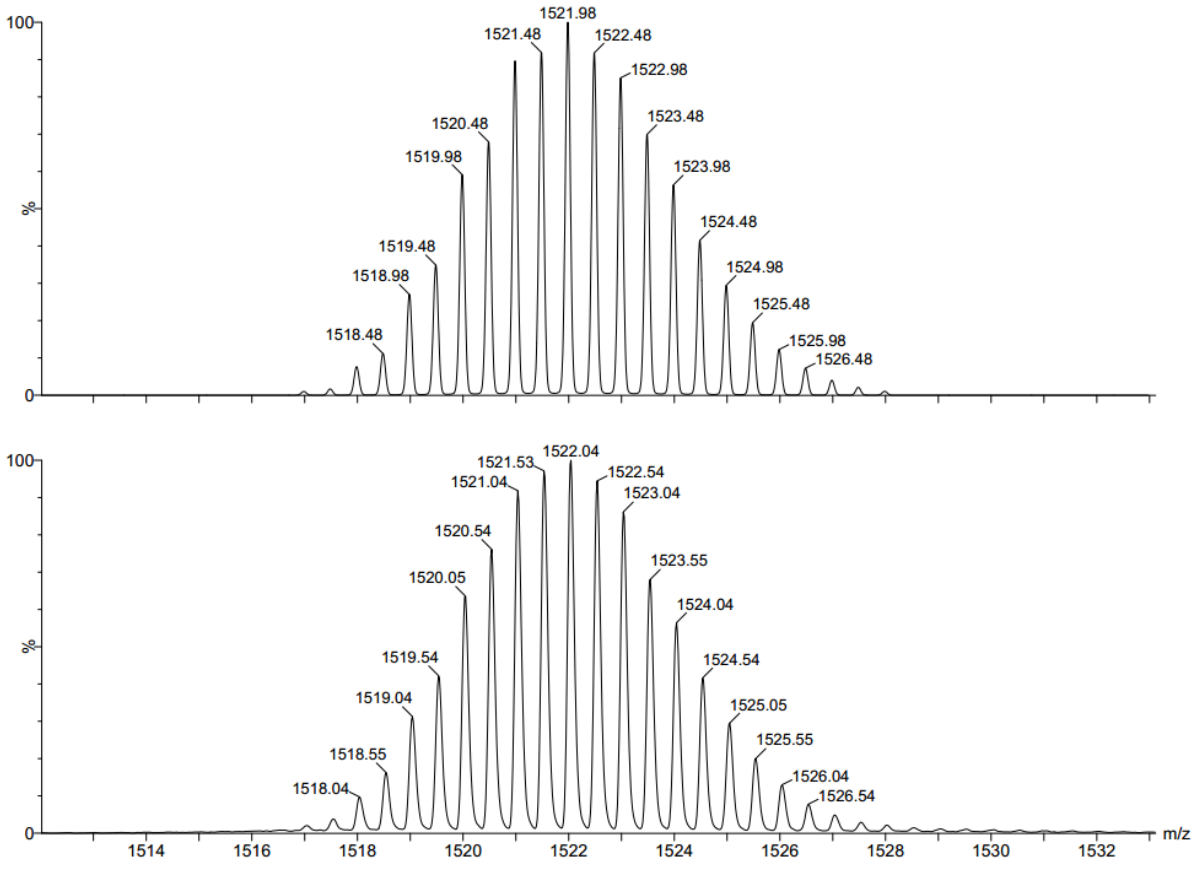

Figure 3.2. Partial ESI-MS of [Cu$_{14}$D$_{12}$(phen)$_6$(PPh$_3$)$_4$][Cl]$_2$ (**3.1-*d*$_{12}$**). The experimental (bottom) and calculated (top) peaks assignable to $[M]^{2+}$ ion are shown.

Table 3.1. Comparison of bond lengths (Å) between **3.1**·$3CH_2Cl_2$·C_6H_6 and the calculated structures for both **3.1** and **3.1-*h*$_{13}$**.

	Expt.	PBE (**3.1**)	PW91 (**3.1**)	PBE (**3.1-*h*$_{13}$**)	PW91 (**3.1-*h*$_{13}$**)
Cu_{tet} – Cu_{tet}	2.893[a]	2.809	2.826	2.828	2.832
Cu_{tet} – Cu_P	2.655	2.681	2.684	2.700	2.704
Cu_{tet} – Cu_N	2.514	2.557	2.559	2.596	2.596
Cu_P – Cu_N	2.663	2.710	2.711	2.743	2.745
Cu_P – P	2.298	2.335	2.333	2.318	2.318
Cu_N – N	2.100	2.101	2.101	2.090	2.090

[a] All lengths are average bond lengths.

To further support the proposed formulation, and rule out the alternate $[Cu_{14}H_{13}(phen)_6(PPh_3)_4][Cl]$ (**3.1-*h*$_{13}$**) formulation, I collaborated with Brian Goldsmith in Prof. Baron Peters' group at UCSB. He calculated the structure and energetics of complexes **3.1** and **3.1-*h*$_{13}$** using density functional theory as implemented with the VASP 5.3.5 software.[28-30] The interactions between valence electrons and ions were described using the PAW method.[31] He used two exchange-correlation functionals, PBE[32] and PW91[33], to confirm consistency between different density functional approximations and found that the 12 μ_3-hydride ligands coordinate to the centers of the triangular copper faces (Figure 3.3b), and not to the Cu_P–Cu_N, Cu_{tet}–Cu_N, or Cu_{tet}–Cu_P vertices. Compared to experiment, the average Cu–Cu bond lengths of the calculated **3.1** and **3.1-*h*$_{13}$** structures were slightly elongated, except for the Cu_{tet}–Cu_{tet} distances, which were shorter (Table 3.1). In general, though, the average calculated Cu–Cu bond lengths of **3.1** (Cu_P–Cu_N, Cu_{tet}-Cu_N, and Cu_{tet}-Cu_P) are in closer agreement with experimental values than those of **3.1-*h*$_{13}$**, using either the PBE or PW91 functionals. Furthermore, he calculated that the formation of **3.1** and CH_3Cl from **3.1-*h*$_{13}$** and CH_2Cl_2 is energetically favorable (–188 kJ·mol^{-1} for PBE and –192 kJ·mol^{-1} for PW91). These computational results support the proposed formulation of **3.1**.

To better understand the vibrant color changes that occur during the synthesis of **3.1**, and confirm the source of its chloride counterions, I followed its formation by ^{1}H NMR spectroscopy. Addition of 26 equiv of phen to $[(Ph_3P)CuH]_6$ in CD_2Cl_2 results in formation of a dark red solution. After 5 min, complex **3.1** is observed in the reaction mixture in small amounts, as evidenced by the diagnostic resonance in the ^{1}H NMR spectrum at 3.47 ppm, assignable to the 12 μ_3-H ligands. However, several other hydride-containing complexes are also present in this reaction mixture, as evidenced by broad resonances at 2.13 and 2.75 ppm in the ^{1}H NMR spectrum. Significant amounts of starting material are also present in this sample. After 1 h, the ^{1}H NMR spectrum of the reaction mixture reveals a decrease in the amount of starting material. In addition, the hydride signal at 2.13 ppm decreases in intensity, while those at 3.47 ppm and 2.75 ppm increase. This change occurs concomitant with a color change to green and formation of a dark precipitate. After 17 h, the signals at 2.13 and 2.75 ppm are no longer present in the ^{1}H NMR spectrum, and the only hydride resonance observed in the dark blue solution is that assignable to **3.1**. An *in situ* ^{2}H NMR spectrum of the reaction mixture was also recorded. This spectrum features a broad singlet at 3.27 ppm, which we have assigned to CD_2HCl, the by-product of a CD_2Cl_2 / CuH metathesis reaction,[34] confirming that the Cl^- counterions in **3.1** are derived from dichoromethane. This result also rationalizes the long reaction times required to form **3.1** in high yield, as the hydride metathesis step is likely slow and rate-determining.

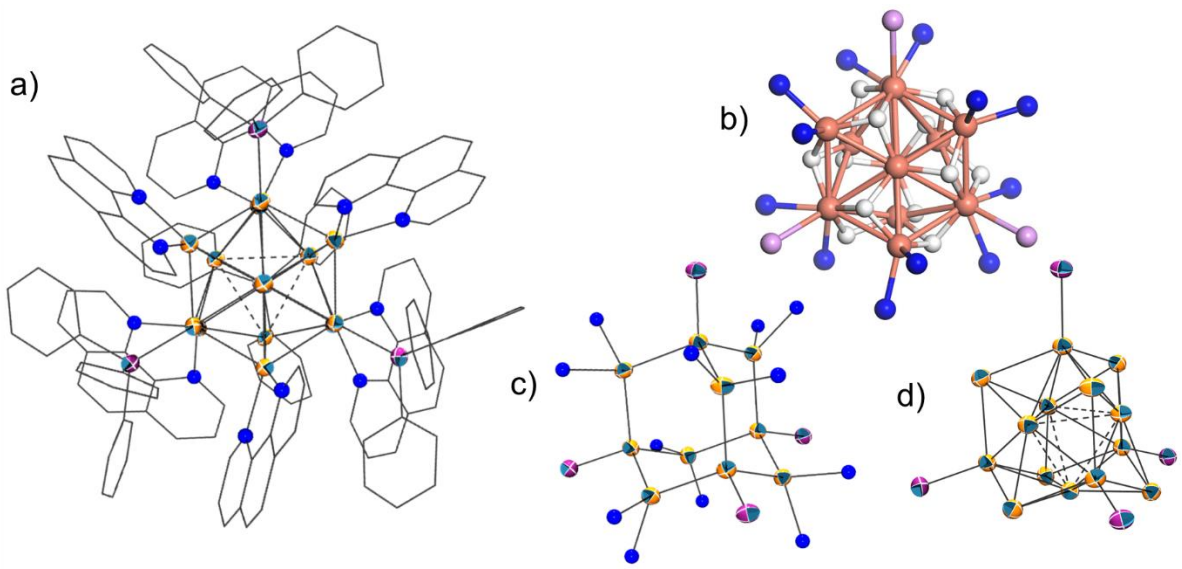

Figure 3.3. Structural diagrams for Cu_{14} a) ORTEP diagram of **3.1** with 50% probability ellipsoids for copper and phosphorus atoms. All hydrogen atoms, two disordered chloride counterions and solvent molecules have been omitted for clarity. b) Optimized structure of $[Cu_{14}H_{12}(phen)_6(PPh_3)_4][Cl]_2$, as determined using the PW91 functional, showing a hexagonal copper face with its three μ_3-H environments. Graphic prepared by Brian Goldsmith. c) Diamondoid arrangement of the outer copper shell in 1, with the $[Cu_4]^{4+}$ core removed. d) ORTEP diagram of 1 with carbon, nitrogen, chloride, and hydrogen atoms removed. Cu_{tet}–Cu_{tet} bonds depicted using dashed lines. Color legend: copper, yellow-orange; hydrogen, white; phosphorus, fuchsia; nitrogen, blue.

To further confirm the importance of a counterion in the formation of the Cu_{14} cluster, I performed the reaction of phen with $[(Ph_3P)CuH]_6$, in the presence of a $[OTf]^-$ source. Thus, addition of MeCN to a vial charged with 1 equiv of $[(Ph_3P)CuH]_6$, 3 equiv of phen, and 1 equiv of $[Cu(MeCN)_4][OTf]$ results in the formation of $[Cu_{14}H_{12}(phen)_6(PPh_3)][OTf]_2$ (**3.2**), which can be isolated as a blue crystalline solid in 41% yield (Scheme 3.1). Importantly, complex **3.2** forms immediately upon mixing of the reagents, as revealed by the rapid color

change to blue. Interestingly, if $[Cu(MeCN)_4][OTf]$ is not added to the reaction mixture, then a brown intractable suspension is formed instead, demonstrating the required presence of a counterion for the formation of **3.2**. Complex **3.2** features similar ^{1}H and ^{31}P NMR spectral parameters as **3.1**. It also features a singlet at -79.33 ppm in its $^{19}F\{^{1}H\}$ NMR spectrum, which is assignable to the OTf^- anion, consistent with our proposed formulation. Complex **3.2** features a signal at *m/z* 1515.96 in its ESI mass spectrum, which corresponds to the parent $[M]^{2+}$ species (calcd *m/z* 1515.94). Finally, **3.2** features a Λ_M of 261.5 $ohm^{-1}\cdot cm^2\cdot mol^{-1}$, also consistent with its formulation as a 2:1 electrolyte.[27]

Complex **3.1** is soluble in CH_2Cl_2 and MeCN, and insoluble in THF, Et_2O and non-polar solvents. It is stable in MeCN for at least 72 h. However, it slowly reacts with CH_2Cl_2 to generate a new species, [(phen)(Ph_3P)CuCl] (**3.3**), along with H_2, copper metal, and other unidentified decomposition products.

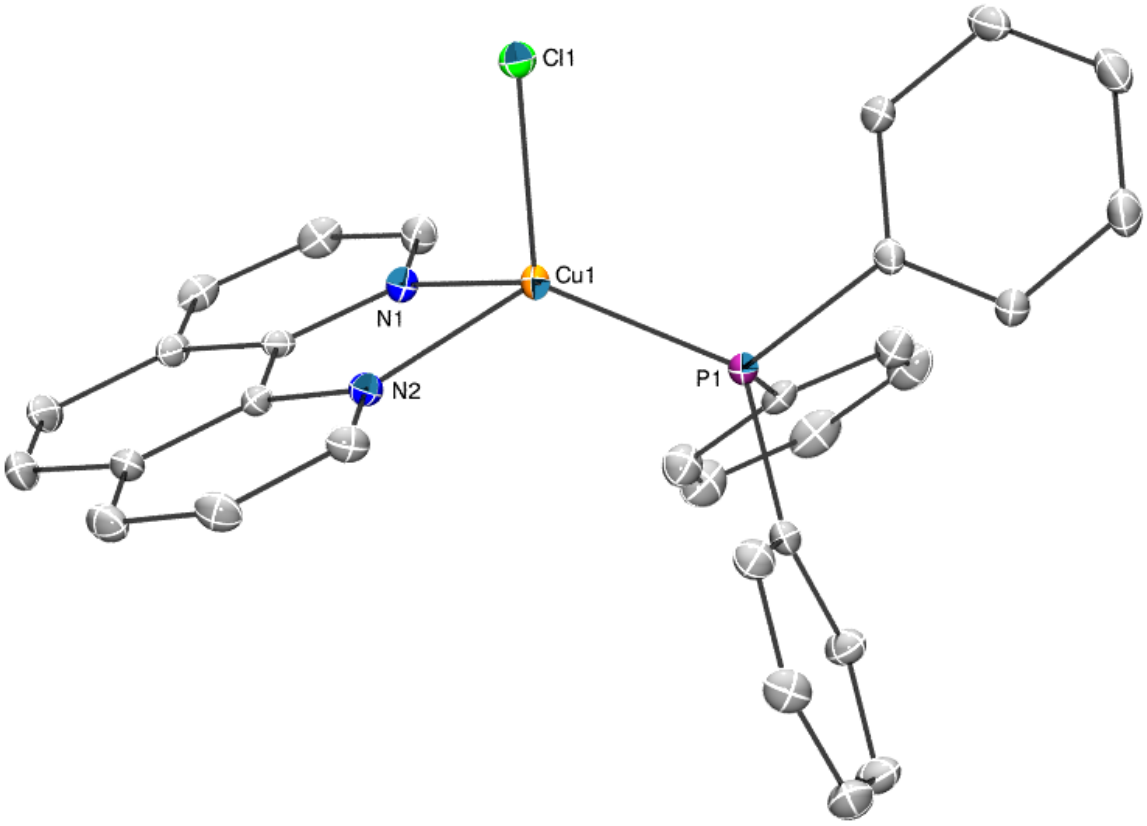

Figure 3.4. Solid-state molecular structure of **3.3** with 50% probability ellipsoids. Hydrogen atoms and a molecule of dichloromethane have been omitted for clarity. Selected bond lengths (Å) and angles (deg): Cu1–Cl1 = 2.3013(6), Cu1–P1 = 2.1731(6), Cu1–N1 = 2.065(2), Cu1–N2 = 2.109(2), ∑(Cl1–Cu1–E) = 327.37.

Presumably, **3.3** is formed via a hydride metathesis with the CH_2Cl_2 solvent. Remarkably, though, in the presence of excess phen, **3.1** is indefinitely stable in CH_2Cl_2, suggesting that the loss of the phen ligand is the first step in its decomposition. Complex **3.1** is air sensitive, and rapidly decomposes upon exposure to air. However, it only slowly reacts with water. Finally, I explored the reactivity of complex **3.1** with CO_2. Several research groups have previously described the reactivity of discrete copper hydrides with CO_2.[9,21,35,36] Of most relevance to my study, Sneeden and co-workers reported that reaction of $[(Ph_3P)CuH]_6$ with

CO_2, in the presence of 6 equiv PPh_3, resulted in the formation of the formate complex, $[(Ph_3P)_2Cu(\kappa^2\text{-}O_2CH)]$ (**3.4**).[35] Similarly, complex **3.1** was reacted with CO_2 in CD_2Cl_2, in the presence of excess PPh_3.[37] Monitoring the reaction by NMR spectroscopy revealed the rapid consumption of **3.1** and the formation of **3.4** in 37% yield (Scheme 3.2), demonstrating that the hydride ligands in **3.1** are accessible to incoming substrates. Complex **3.3** is also formed in this reaction.

Scheme 3.2. Reactivity of complex **3.1**. with CO_2 and CH_2Cl_2

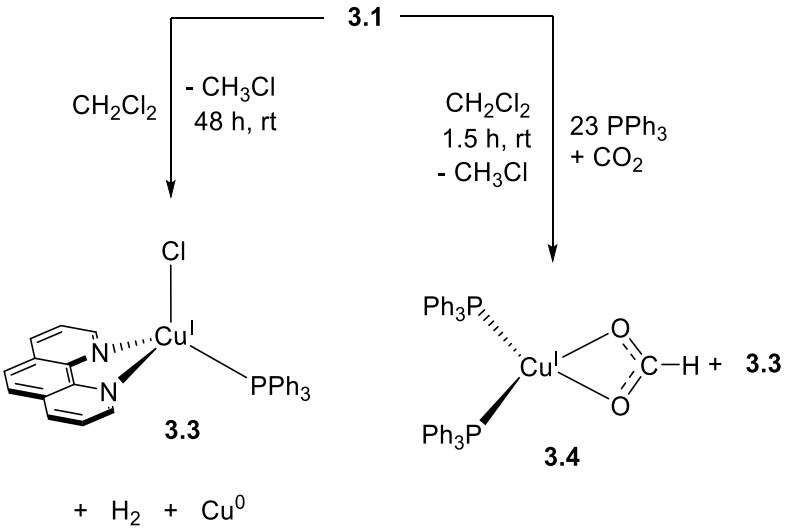

3.3 Summary

In summary, I have isolated and structurally characterized an unusual Cu_{14} hydride cluster. This complex was the largest structurally characterized CuH cluster supported by neutral donor ligands at the time of its publication in 2015. As a consequence, it had a larger H:Cu ratio than other reported high nuclearity clusters. Importantly, the capping hydride ligands in this cluster are accessible to incoming substrates, as demonstrated by its reaction with CO_2. Moreover, the synthesis of complex **3.1** demonstrates that $[(Ph_3P)CuH]_6$ is a viable precursor for the generation of copper hydride clusters with high nuclearity. With the

appropriate choice of co-ligand, even larger Cu nano-crystals may be accessible via this route.

3.4 Experimental

3.4.1 General Procedures

All reactions and subsequent manipulations were performed under anaerobic and anhydrous conditions under an atmosphere of nitrogen. Hexanes, diethyl ether (Et_2O), and toluene were dried using a Vacuum Atmospheres DRI-SOLV Solvent Purification system and stored over 3Å sieves for 24 h prior to use. Dichloromethane, acetonitrile and benzene were degassed and dried over 3Å molecular sieves for 72 h prior to use. Methylene chloride-*d*$_2$ (CD_2Cl_2), acetonitrile-*d*$_3$ (CD_3CN), benzene-*d*$_6$ (C_6D_6), diphenylsilane, diphenylsilane-*d*$_2$ (Sigma-Aldrich, 97 atom % D), and mesitylene were dried over 3Å molecular sieves for 24 h prior to use. All other reagents were purchased from commercial suppliers and used as received.

^{1}H NMR spectra were recorded on an Agilent Technologies 400-MR DD2 spectrometer, a Varian Unity Inova 500 MHz spectrometer, or a Varian Unity Inova A S600 MHz spectrometer. $^{13}C\{^1H\}$ NMR spectra were recorded on an Agilent Technologies 400-MR DD2 spectrometer or a Varian Unity Inova 500 MHz spectrometer. $^{31}P\{^1H\}$, $^{19}F\{^1H\}$ and ^{2}H NMR spectra were recorded on an Agilent Technologies 400-MR DD2 spectrometer. The chemical shifts of all nuclei were referenced indirectly with the ^{1}H resonance of $SiMe_4$ at 0 ppm, according to IUPAC standard,[38,39] or by using the residual solvent peaks (^{1}H and ^{2}H NMR experiments) or the characteristic resonances of the solvent nuclei as internal standards ($^{13}C\{^1H\}$ NMR experiments). IR spectra were recorded on a Nicolet 6700 FT-IR spectrometer with a NXR FT Raman Module. UV-Vis / NIR experiments were performed

on a UV-3600 Shimadzu spectrophotometer. Conductivity measurements were performed using a Fisher Scientific Traceable Expanded Range Conductivity Meter equipped with an instant-response glass probe with platinum electrodes. Mass spectra were collected by the Mass Spectrometry Facility at the University of California, Santa Barbara, using an electrospray ion (ESI) source on positive ion mode with a Waters Micromass QTOF2 Quadrupole/Time-of-Flight Tandem mass spectrometer. Mass spectra were smoothed 4 times using the Savitzky-Golay algorithm with a smooth window of 3 channels. Elemental analyses were performed by the Micro-Mass Facility at the University of California, Berkeley.

3.4.2 Synthesis of $[(Ph_3P)CuH]_6$

$[(Ph_3P)CuH]_6$ was prepared according to a modified procedure based on that previously reported by Yun and coworkers.[40] To a stirring green suspension of Cu(OAc) (148.6 mg, 1.21 mmol) in benzene (1 mL) was added PPh_3 (630.1 mg, 2.40 mmol) as a benzene solution (2 mL). Diphenylsilane (0.115 mL, 0.62 mmol) was then added via syringe. This resulted in a rapid color change to red and dissolution of the green solid. However, a small amount of fine red solid remained undissolved in the reaction mixture. After stirring for 12 h, the reaction mixture was filtered through a Celite column (0.5 cm × 1.5 cm) supported on glass wool. The red filtrate was then layered with acetonitrile (10 mL), and storage of this solution at room temperature for 24 h resulted in the deposition of red crystals, which were isolated by decanting off the supernatant. The solid was washed with acetonitrile (5 × 1 mL) until the washings were colorless, and the solid was dried *in vacuo* (272.5 mg, 69% yield). The NMR spectral data were consistent with those previously reported for $[(Ph_3P)CuH]_6$.[25,40-42] ^{1}H NMR (400 MHz, 25 °C, C_6D_6): δ 3.51 (br s, 6H, hydride H), 6.74 (t,

J_{HH} = 7.5 Hz, 36H, *m*-Ph), 6.95 (t, J_{HH} = 7.4 Hz, 18H, *p*-Ph), 7.67 (m, 36H, *o*-Ph). ^{1}H NMR (400 MHz, 25 °C, CD_2Cl_2): δ 3.10 (br s, 6H, hydride H), 6.70 (t, J_{HH} = 7.2 Hz, 36H, *m*-Ph), 7.04 (t, J_{HH} = 7.1 Hz, 18H, *p*-Ph), 7.34 (m, 36H, *o*-Ph). ^{31}P{^{1}H} NMR (162 MHz, 25 °C, C_6D_6): δ -5.98 (s). ^{31}P{^{1}H} NMR (162 MHz, 25 °C, CD_2Cl_2): δ -6.60 (s).

3.4.3 Synthesis of [(Ph$_3$P)CuD]$_6$

To a stirring suspension of Cu(OAc) (224.6 mg, 1.83 mmol) in benzene (1 mL) was added PPh_3 (951.3 mg, 3.63 mmol) as a benzene solution (3 mL). Diphenylsilane-*d*$_2$ (0.18 mL, 0.97 mmol) was added via syringe. This resulted in a rapid color change to red and dissolution of the green solid. However, a small amount of fine red solid remained undissolved in the reaction mixture. After stirring for 12 h, the reaction mixture was filtered through a Celite column (0.5 cm × 1.5 cm) supported on glass wool. The red filtrate was layered with acetonitrile (10 mL) and storage of this solution at room temperature for 24 h resulted in the deposition of red crystals, which were isolated by decanting off the supernatant. The solid was washed with acetonitrile (5 × 1 mL) until the washings were colorless and subsequently dried *in vacuo* (410.4 mg, 68% yield). The NMR spectral data were consistent with those previously reported for $[(Ph_3P)CuD]_6$.[25] ^{1}H NMR (400 MHz, 25 °C, C_6D_6): δ 6.74 (t, J_{HH} = 7.3 Hz, 36H, *m*-Ph), 6.95 (t, J_{HH} = 7.2 Hz, 18H, *p*-Ph), 7.67 (m, 36H, *o*-Ph). ^{2}H NMR (61 MHz, 25 °C, C_6H_6) δ 3.57 (br s). ^{31}P{^{1}H} NMR (162 MHz, 25 °C, C_6D_6): δ -5.95 (s).

3.4.4 Synthesis of [Cu$_{14}$H$_{12}$(phen)$_6$(PPh$_3$)$_4$][Cl]$_2$ (3.1)

To a vial containing $[(Ph_3P)CuH]_6$ (285.3 mg, 0.145 mmol) was added 1,10-phenanthroline (672.2 mg, 3.73 mmol) as a dichloromethane solution (8 mL). This resulted

in a rapid color change to dark red. After 1h, this solution became dark green concomitant with the deposition of a mixture of colorless needles and green solid. Upon further stirring the solids dissolved, and after 18 h, the solution became dark blue. This solution was subsequently filtered through a Celite column (0.5 cm × 1.5 cm) supported on glass wool. The dark blue filtrate was concentrated *in vacuo* and then layered with toluene (10 mL). Storage of this solution at -25 °C for 12 h resulted in the deposition of dark blue crystals. The dark blue crystals were isolated by decanting off the supernatant, washed with toluene (3 × 3 mL) until the washings were colorless, and dried *in vacuo* (154.7 mg, 80% yield). Anal. Calcd for $C_{144}H_{120}Cl_2Cu_{14}N_{12}P_4$: C, 55.74; H, 3.90; N, 5.42. Found: C, 55.47; H, 4.05; N, 5.05. ^{1}H NMR (500 MHz, 25 °C, CD_2Cl_2): δ 3.45 (s, 12H, μ_3-H), 5.77 (t, J_{HH} = 7.1 Hz, 24H, *m*-Ph on PPh_3), 6.14 (m, 24H, *o*-Ph on PPh_3), 6.67 (dd, J_{HH} = 8.1, 4.7 Hz, 12H, Ar C*H* on phen), 6.72 (t, J_{HH} = 7.3 Hz, 12H, *p*-Ph on PPh_3), 7.88 (s, 12H, Ar C*H* on phen), 8.10 (dd, J_{HH} = 8.1, 1.4 Hz, 12H, Ar C*H* on phen), 8.85 (dd, J_{HH} = 4.7, 1.4 Hz, 12H, Ar C*H* on phen). ^{1}H NMR (400 MHz, 25 °C, CD_3CN): δ 3.44 (s, 12H, μ_3-H), 5.78 (t, J_{HH} = 7.2 Hz, 24H, *m*-Ph on PPh_3), 6.15 (m, 24H, *o*-Ph on PPh_3), 6.69 (t, J_{HH} = 7.3, 12H, *p*-Ph on PPh_3), 6.82 (dd, J_{HH} = 8.1, 4.7 Hz, 12H, Ar C*H* on phen), 7.90 (s, 12H, Ar C*H* on phen), 8.17 (d, J_{HH} = 7.6 Hz, 12H, Ar C*H* on phen), 8.94 (d, J_{HH} = 3.9 Hz, 12H, Ar C*H* on phen). ^{1}H NMR (500 MHz, −80 °C, CD_2Cl_2): δ 3.33 (s, 12H, μ_3-H), 5.69 (br s, 24H, *m*-Ph on PPh_3), 6.09 (br s, 24H, *o*-Ph on PPh_3), 6.48 (dd, J_{HH} = 7.7, 4.6 Hz, 12H, Ar C*H* on phen), 6.73 (t, J_{HH} = 7.3 Hz, 12H, *p*-Ph on PPh_3), 7.87 (s, 12H, Ar C*H* on phen), 8.06 (d, J_{HH} = 7.7 Hz, 12H, Ar C*H* on phen), 8.64 (s, 12H, Ar C*H* on phen). ^{31}P{^{1}H} NMR (162 MHz, 25 °C, CD_2Cl_2): δ -5.35 (br s). ^{31}P{^{1}H} NMR (162 MHz, 25 °C, CD_3CN): δ -5.09 (br s). ^{13}C{^{1}H} NMR (126 MHz, 25 °C, CD_2Cl_2): δ 123.83 (s, Ar *C*H on phen), 126.94 (d, J_{CP} = 8.1 Hz, *m*-*C*H on PPh_3),

127.06 (s, *p*-*C*H on PPh_3), 128.74 (s, Ar *C*H on phen), 129.27 (s, Ar *C* on phen), 133.29 (d, J_{CP} = 13.6 Hz, *o*-*C*H on PPh_3), 135.19 (s, Ar *C*H on phen), 136.42 (d, J_{CP} = 19.5 Hz, 12C, *ipso*-*C* on PPh_3), 143.24 (s, Ar *C* on phen), 150.04 (s, Ar *C*H on phen). ESI-MS: *m/z* 1515.93 $[M]^{2+}$ (Calcd *m/z* 1515.94). IR (KBr pellet, cm^{-1}): 409 (w), 420 (w), 516 (s), 542 (w), 619 (w), 630 (w), 694 (s), 728 (s), 745 (s), 843 (s), 998 (m), 1028 (m), 1045 (m), 1092 (s), 1137 (m), 1182 (m), 1294 (w), 1340 (w), 1422 (s), 1433 (s), 1479 (m), 1493 (m), 1505 (m), 1570 (m), 1585 (m), 1619 (m), 1812 (w), 1955 (w), 1980 (m). Λ_M (25 °C, CH_3CN, 1.07 × 10^{-3} M): 220.5 $ohm^{-1}\cdot cm^2\cdot mol^{-1}$.

3.4.5 Monitoring the formation of $[Cu_{14}H_{12}(phen)_6(PPh_3)_4][Cl]_2$ (3.1) by NMR spectroscopy

$[(Ph_3P)CuH]_6$ (35.7 mg, 0.0182 mmol) was dissolved in CD_2Cl_2 (500 μL) and transferred to a J. Young NMR tube. ^1H and $^{31}P\{^1H\}$ NMR spectra were then recorded. Subsequently, phen (85.2 mg, 0.473 mmol), dissolved in CD_2Cl_2 (500 μL), was added to the J. Young tube, whereupon the bright red solution darkened significantly. After 1.5 h, this solution became dark green concomitant with the deposition of a mixture of colorless needles and green solid. The solids gradually dissolved, and after 18 h, the solution became dark blue. No further changes were observed, even after 70 d. The NMR spectra reveal that although complex **3.1** is formed in small amounts after only 5 min, the reaction is slow and goes through two hydride containing intermediates. Full conversion to **3.1** was only observed after 17 h, after which no further changes were observed in the NMR spectra of the reaction mixture. Also of note, a ^2H NMR spectrum of the reaction mixture after 4d revealed a resonance at 3.27 ppm, which we have assigned to CD_2HCl.[34]

5 min spectra: ^{1}H NMR (400 MHz, 25 °C, CD_2Cl_2): δ 2.13 (br s, hydride H, unidentified intermediate), 2.75 (s, hydride H, unidentified intermediate), 3.14 (br s, 6H, hydride H, $[(Ph_3P)CuH]_6$), 3.47 (br s, 12H, μ_3-H, **3.1**), 4.60 (s, H_2), 5.78 (m, 24H, *m*-Ph on PPh_3, **3.1**), 6.17 (m, 24H, *o*-Ph on PPh_3, **3.1**), 6.58 – 7.49 (m, Ph and phen, overlapping $[(Ph_3P)CuH]_6$, **3.1**, and other unidentified products), 7.57 (dd, J_{HH} = 7.9, 4.3 Hz, 2H, C*H*, uncoordinated phen), 7.72 (s, 2H, C*H*, uncoordinated phen), 7.88 (s, 12H, Ar C*H* on phen, **3.1**), 8.12 (m, 12H, Ar C*H* on phen, **3.1**), 8.19 (d, J_{HH} = 8.0 Hz, 2H, C*H*, uncoordinated phen), 8.88 (m, 12H, Ar C*H* on phen, **3.1**), 9.11 (m, 2H, C*H*, uncoordinated phen). $^{31}P\{^{1}H\}$ NMR (162 MHz, 25 °C, CD_2Cl_2): δ -8.59 (s, unidentified intermediate), -6.58 (s, $[(Ph_3P)CuH]_6$), -5.08 (br s, **3.1**), -1.99 (s, unidentified intermediate).

1 h spectra: ^{1}H NMR (400 MHz, 25 °C, CD_2Cl_2): δ 2.12 (br s, hydride H, unidentified intermediate), 2.74 (s, hydride H, intermediate), 3.13 (br s, 6H, hydride H, $[(Ph_3P)CuH]_6$), 3.47 (br s, 12H, μ_3-H, **3.1**), 4.59 (s, H_2), 5.78 (t, J_{HH} = 7.2 Hz, 24H, *m*-Ph on PPh_3, **3.1**), 6.17 (t, J_{HH} = 8.4 Hz, J_{HP} = 8.4 Hz, 24H, *o*-Ph on PPh_3, **3.1**), 6.34 – 7.45 (m, Ph and phen, overlapping $[(Ph_3P)CuH]_6$, **3.1**, and other unidentified products), 7.57 (dd, J_{HH} = 8.0, 4.3 Hz, 2H, C*H*, uncoordinated phen), 7.73 (s, 2H, C*H*, uncoordinated phen), 7.88 (s, 12H, Ar C*H* on phen, **3.1**), 8.12 (m, 12H, Ar C*H* on phen, **3.1**), 8.19 (d, J_{HH} = 8.0 Hz, 2H, C*H*, uncoordinated phen), 8.87 (d, J_{HH} = 3.7 Hz, 12H, Ar C*H* on phen, **3.1**), 9.11 (m, 2H, C*H*, uncoordinated phen). $^{31}P\{^{1}H\}$ NMR (162 MHz, 25 °C, CD_2Cl_2): δ -8.58 (s, unidentified intermediate), -6.59 (s, $[(Ph_3P)CuH]_6$), -5.21 (br s, **3.1**), -2.93 (br s, unidentified intermediate), -2.00 (s, unidentified intermediate), 2.06 (s, unidentified intermediate).

17 h spectra: ^{1}H NMR (400 MHz, 25 °C, CD_2Cl_2): δ 3.47 (br s, 12H, μ_3-H, **3.1**), 4.59 (s, H_2), 5.78 (t, J_{HH} = 7.2 Hz, 24H, *m*-Ph on PPh_3, **3.1**), 6.17 (t, J_{HH} = 8.4 Hz, J_{HP} = 8.4 Hz,

24H, *o*-Ph on PPh_3, **3.1**), 6.68 (dd, J_{HH} = 8.1, 4.7 Hz, 12H, Ar C*H* on phen, **3.1**), 6.73 (t, J_{HH} = 7.3 Hz, 12H, *p*-Ph on PPh_3, **3.1**), 7.22 – 7.36 (m, Ph on PPh_3, unidentified product), 7.58 (dd, J_{HH} = 8.1, 4.3 Hz, 2H, C*H*, uncoordinated phen), 7.74 (s, 2H, C*H*, uncoordinated phen), 7.88 (s, 12H, Ar C*H* on phen, **3.1**), 8.11 (m, 12H, Ar C*H* on phen, **3.1**), 8.20 (dd, J_{HH} = 8.1, 1.4 Hz, 2H, C*H*, uncoordinated phen), 8.87 (m, 12H, Ar C*H* on phen, **3.1**), 9.09 (m, 2H, C*H*, uncoordinated phen). $^{31}P\{^1H\}$ NMR (162 MHz, 25 °C, CD_2Cl_2): δ -6.30 (s, minor side product), -5.40 (br s, **3.1**), 21.76 (m, unidentified minor side product).

4 d spectra: ^1H NMR (600 MHz, 25 °C, CD_2Cl_2): δ 3.47 (br s, 12H, μ_3-H, **3.1**), 4.59 (s, H_2), 5.78 (t, J_{HH} = 7.3 Hz, 24H, *m*-Ph on PPh_3, **3.1**), 6.17 (t, J_{HH} = 8.4 Hz, J_{HP} = 8.4 Hz, 24H, *o*-Ph on PPh_3, **3.1**), 6.69 (dd, J_{HH} = 8.1, 4.7 Hz, 12H, Ar C*H* on phen, **3.1**), 6.73 (t, J_{HH} = 7.4 Hz, 12H, *p*-Ph on PPh_3, **3.1**), 7.20 – 7.36 (m, Ph on PPh_3, unidentified product), 7.58 (dd, J_{HH} = 8.0, 4.3 Hz, 2H, C*H*, uncoordinated phen), 7.74 (s, 2H, C*H*, uncoordinated phen), 7.88 (s, 12H, Ar C*H* on phen, **3.1**), 8.12 (d, J_{HH} = 8.1 Hz, 12H, Ar C*H* on phen, **3.1**), 8.20 (d, J_{HH} = 7.9 Hz, 2H, C*H*, uncoordinated phen), 8.87 (d, J_{HH} = 4.5 Hz, 12H, Ar C*H* on phen, **3.1**), 9.10 (m, 2H, C*H*, uncoordinated phen). ^2H NMR (61 MHz, 25 °C, CD_2Cl_2): δ 3.27 (br s, C*D*$_2$HCl), 7.87 (s, unidentified deuterated product).

70 d spectra: ^1H NMR (400 MHz, 25 °C, CD_2Cl_2): δ 3.47 (br s, 12H, μ_3-H, **3.1**), 4.59 (s, H_2), 5.78 (t, J_{HH} = 7.2 Hz, 24H, *m*-Ph on PPh_3, **3.1**), 6.16 (t, J_{HH} = 8.4 Hz, J_{HP} = 8.4 Hz 24H, *o*-Ph on PPh_3, **3.1**), 6.68 (dd, J_{HH} = 8.1, 4.7 Hz, 12H, Ar C*H* on phen, **3.1**), 6.73 (t, J_{HH} = 7.4 Hz, 12H, *p*-Ph on PPh_3, **3.1**), 7.19 – 7.37 (m, Ph on PPh_3, unidentified product), 7.58 (dd, J_{HH} = 8.1, 4.3 Hz, 2H, C*H*, uncoordinated phen), 7.74 (s, 2H, C*H*, uncoordinated phen), 7.88 (s, 12H, Ar C*H* on phen, **3.1**), 8.12 (m, 12H, Ar C*H* on phen, **3.1**), 8.21 (m, 2H, C*H*, uncoordinated phen), 8.87 (m, 12H, Ar C*H* on phen, **3.1**), 9.09 (m, 2H, C*H*, uncoordinated

phen). $^{31}P\{^{1}H\}$ NMR (162 MHz, 25 °C, CD_2Cl_2): δ -6.29 (s, unidentified minor side product), -4.95 (br s, **3.1**), 21.76 (m, unidentified minor side product), 26.13 (s, unidentified minor side product), 27.09 (unidentified minor side product).

3.4.6 Synthesis of $[Cu_{14}D_{12}(phen)_6(PPh_3)_4][Cl]_2$ (3.1-d_{12})

To a vial containing $[(Ph_3P)CuD]_6$ (185.6 mg, 0.094 mmol) was added 1,10-phenanthroline (448.3 mg, 2.49 mmol) as a dichloromethane solution (4 mL). This resulted in a rapid color change to dark red. After 1 h, this solution became dark green concomitant with the deposition of a mixture of colorless needles and green solid. Upon further stirring the solids dissolved, and after 18 h, the solution became dark blue. The reaction mixture was filtered through a Celite column (0.5 cm × 1.5 cm) supported on glass wool. The dark blue filtrate was layered with toluene (10 mL) and storage of this solution at -25 °C for 12 h resulted in the deposition of dark blue crystals. The dark blue crystals were isolated by decanting off the green supernatant, washed with toluene (5 × 1 mL) until the washings were colorless, and dried *in vacuo*. The crude product was recrystallized by storage of a dichloromethane solution layered with toluene at -25 °C for 12 h (67.5 mg, 54% yield). ^{1}H NMR (400 MHz, 25 °C, CD_2Cl_2): δ 5.77 (t, J_{HH} = 7.2 Hz, 24H, *m*-Ph on PPh_3), 6.14 (m, 24H, *o*-Ph on PPh_3), 6.67 (dd, J_{HH} = 8.0, 4.7 Hz, 12H, Ar C*H* on phen), 6.72 (t, J_{HH} = 7.2 Hz, 12H, *p*-Ph on PPh_3), 7.88 (s, 12H, Ar C*H* on phen), 8.10 (d, J_{HH} = 7.9 Hz, 12H, Ar C*H* on phen), 8.85 (d, J_{HH} = 4.2 Hz, 12H, Ar C*H* on phen). $^{31}P\{^{1}H\}$ NMR (162 MHz, 25 °C, CD_2Cl_2): δ -5.41 (br s). ^{2}H NMR (61 MHz, 25 °C, CH_2Cl_2): δ 3.58 (s). ^{2}H NMR (61 MHz, 25 °C, CH_3CN): δ 3.55 (s). ESI-MS: *m/z* 1522.04 $[M]^{2+}$ (Calcd *m/z* 1521.98). IR (KBr pellet, cm^{-1}): 403 (w), 421 (m), 516 (s), 542 (m), 619 (m), 630 (m), 694 (s), 728 (s), 745 (s), 842 (s), 998 (w), 1028 (m), 1045 (w), 1092 (s), 1137 (m), 1183 (w), 1219 (w), 1294 (w), 1340

(w), 1422 (s), 1433 (s), 1479 (s), 1492 (w), 1505 (m), 1570 (w), 1585 (m), 1619 (w), 1812 (w), 1954 (w), 1975 (m).

3.4.7 Synthesis of $[Cu_{14}H_{12}(phen)_6(PPh_3)_4][OTf]_2$ (3.2)

To a vial containing $[(Ph_3P)CuH]_6$ (206.2 mg, 0.105 mmol), phen (56.9 mg, 0.316 mmol), and $[Cu(MeCN)_4][OTf]$ (40.8 mg, 0.108 mmol) was added acetonitrile (5 mL). This resulted in the formation of a red suspension. After stirring for 10 min, the solution became dark blue; however, significant amounts of $[(Ph_3P)CuH]_6$ remained undissolved. The reaction mixture was stirred for 18 h, whereupon it was filtered through a Celite column (0.5 cm × 1 cm) supported on glass wool to remove the unreacted $[(Ph_3P)CuH]_6$. The dark blue filtrate was concentrated *in vacuo* and layered with toluene (10 mL). Storage of this solution at -25 °C for 12 h resulted in the deposition of dark blue crystals which were isolated by decanting off the supernatant, washed with toluene (3 × 1 mL) until the washings were colorless and dried *in vacuo* (67 mg, 41% yield). Anal. Calcd for $C_{146}H_{120}Cu_{14}F_6N_{12}O_6P_4S_2$: C, 52.66; H, 3.63; N, 5.05. Found: C, 53.05; H, 3.84; N, 4.68. ^{1}H NMR (400 MHz, 25 °C, CD_3CN): δ 3.45 (s, 12H, μ_3-H), 5.78 (t, J_{HH} = 7.1 Hz, 24H, *m*-Ph on PPh_3), 6.16 (m, 24H, *o*-Ph on PPh_3), 6.69 (t, J_{HH} = 7.3, 12H, *p*-Ph on PPh_3), 6.83 (dd, J_{HH} = 8.1, 4.7 Hz, 12H, Ar C*H* on phen), 7.90 (s, 12H, Ar C*H* on phen), 8.16 (dd, J_{HH} = 8.1, 1.4 Hz, 12H, Ar C*H* on phen), 8.95 (dd, J_{HH} = 4.7, 1.4 Hz, 12H, Ar C*H* on phen). ^{31}P{^{1}H} NMR (162 MHz, 25 °C, CD_3CN): δ -5.26 (br s). ^{19}F{^{1}H} NMR (376 MHz, 25 °C, CD_3CN): δ -79.33 (s). ^{13}C{^{1}H} NMR (126 MHz, 25 °C, CD_3CN): δ 124.49 (s, Ar *C*H on phen), 127.30 (d, J_{CP} = 7.9 Hz, *m*-*C*H on PPh_3), 127.40 (s, *p*-*C*H on PPh_3), 129.16 (s, Ar *C*H on phen), 129.72 (s, Ar *C* on phen), 133.51 (d, J_{CP} = 13.5 Hz, *o*-*C*H on PPh_3), 135.76 (s, Ar *C*H on phen), 136.79 (d, J_{CP} = 19.1 Hz, *ipso*-*C* on PPh_3), 143.55 (s, Ar *C* on phen), 150.65 (s, Ar *C*H on phen). ESI-MS:

m/z 1515.96 $[M]^{2+}$ (Calcd *m/z* 1515.94). IR (KBr pellet, cm^{-1}): 403 (w), 414 (w), 422 (w), 434 (w), 516 (s), 543 (w), 572 (w), 619 (w), 637 (s), 694 (m), 728 (s), 745 (m), 842 (m), 998 (w), 1031 (s), 1092 (w), 1150 (m), 1222 (m), 1272 (s), 1341 (w), 1423 (m), 1434 (m), 1479 (w), 1493 (w), 1508 (w), 1571 (w), 1585 (w), 1621 (w). Λ_M (25 °C, CH_3CN, 1.07×10^{-3} M): 261.5 $ohm^{-1}\cdot cm^2\cdot mol^{-1}$.

3.4.8 Synthesis of [(phen)(PPh_3)CuCl] (3.3)

To a stirring suspension of CuCl (60.6 mg, 0.612 mmol) in dichloromethane (3 mL) was added dropwise a solution of phen (180.21 mg, 0.618 mmol) and PPh_3 (161.1 mg, 0.614 mmol) in dichloromethane (7 mL). This resulted in the rapid dissolution of the solid and a color change to a bright yellow. After stirring for 5 min, the deposition of an orange solid was observed. After 12 h, the reaction mixture was warmed to 40 °C for 5 min to afford a red solution, which was filtered hot through a Celite column (0.5 cm × 1.5 cm) supported on glass wool. The filtrate was allowed to cool and subsequently layered with acetonitrile (8 mL). Storage of this solution at room temperature for 24 h resulted in the deposition of yellow needles, which were isolated by decanting off the yellow supernatant, washed with hexanes (4 × 1 mL) and dried *in vacuo* (199.9 mg, 60% yield). Anal. Calcd for $C_{31}H_{25}Cl_3CuN_2P$: C, 59.44; H, 4.02; N, 4.47. Found: C, 59.91; H, 3.91; N, 4.74. ^{1}H NMR (400 MHz, 25 °C, CD_2Cl_2): δ 7.28 (m, 6H, *m*-Ph on PPh_3), 7.35 (m, 3H, *p*-Ph on PPh_3), 7.47 (m, 6H, *o*-Ph on PPh_3), 7.71 (dd, J_{HH} = 8.1, 4.7 Hz, 2H, Ar C*H* on phen), 7.91 (s, 2H, Ar C*H* on phen), 8.38 (dd, J_{HH} = 8.1, 1.5 Hz, 2H, Ar C*H* on phen), 8.97 (s, 2H, Ar C*H* on phen). $^{31}P\{^1H\}$ NMR (162 MHz, 25 °C, CD_2Cl_2): δ -3.84 (br s). ^{13}C NMR (101 MHz, 25 °C, CD_2Cl_2) δ 125.12 (s, Ar *C* on phen), 127.26 (s, Ar *C* on phen), 128.99 (d, J_{CP} = 8.8 Hz, *m*-*C*H on PPh_3), 129.66 (s, *p*-*C*H on PPh_3), 130.04 (s, Ar *C* on phen), 134.15 (d, J_{CP} = 15.5 Hz,

o-*C*H on PPh_3), 134.91 (d, J_{CP} = 32.1 Hz, *ipso*-*C* on PPh_3), 136.77 (s, Ar *C* on phen), 144.06 (s, Ar *C* on phen), 149.97 (s, Ar *C* on phen). ESI-MS: *m/z* 505.08 $[M - Cl]^+$ (Calcd. *m/z* 505.09). IR (KBr pellet, cm^{-1}): 421 (m), 433 (m), 500 (s), 522 (s), 634 (m), 697 (s), 727 (s), 767 (s), 767 (w), 802 (w), 840 (s), 864 (w), 920 (w), 996 (w), 1028 (w), 1071 (w), 1092 (s), 1136 (w), 1159 (w), 1179 (w), 1221 (w), 1277 (m), 1307 (w), 1338 (w), 1419 (s), 1434 (s), 1478 (m), 1494 (m), 1508 (m), 1572 (w), 1588 (w), 1621 (w).

3.4.9 Reaction of $[Cu_{14}H_{12}(phen)_6(PPh_3)_4][Cl]_2$ with CO_2 in the presence of 23 equiv PPh_3

Complex **3.1** (17 mg, 0.0055 mmol) was dissolved in CD_2Cl_2 (500 μL) and the solution was transferred to a J. Young NMR tube. PPh_3 (32.7 mg, 0.125 mmol) was then added as a CD_2Cl_2 solution (500 μL). Mesitylene (10 μL, 0.072 mmol) was also added via syringe, as an internal standard. The headspace was evacuated and CO_2 (1 atm) was introduced into the tube. Over the course of 20 min, the dark blue solution turned orange brown. After 1.5 h, the ^1H and $^{31}P\{^1H\}$ NMR spectra were recorded. These spectra revealed the complete consumption of the starting material. In addition, an analysis of the ^1H chemical shifts, and comparison of the product peak integrations with those of the internal standard, revealed the *in situ* formation of complex **3.4** in 37% yield. It should be noted that the *in situ* spectral data of complex **3.4** in this sample differ slightly from those recorded for a discrete sample. We believe this difference is due to rapid exchange of PPh_3 between **3.4** and **3.3** in the *in situ* sample, which is evidenced by the observation of only a single $^{31}P\{^1H\}$ signal in this spectrum, despite the simultaneous presence of **3.3**, **3.4**, and free PPh_3. ^1H NMR (400 MHz, 25 °C, CD_2Cl_2): δ 2.27 (s, 9H, C*H*$_3$, mesitylene), 6.80 (s, 3H, C*H*, mesitylene), 7.25 (br s, *m and p*-Ph on PPh_3), 7.33 (*o*-Ph on PPh_3), 7.75 (dd, J_{HH} = 8.1, 4.7 Hz, 2H, Ar C*H* on phen),

8.04 (s, 2H, Ar C*H* on phen), 8.53 (d, J_{HH} = 7.9 Hz, 2H, Ar C*H* on phen), 8.78 (s, 2H, Ar C*H* on phen), 8.84 (s, O_2CH, **3.4**). $^{31}P\{^1H\}$ NMR (162 MHz, 25 °C, CD_2Cl_2): δ -4.19 (br s).

The orange solution was then transferred to a 20 mL vial and subsequently layered with hexanes (3 mL). Storage of this solution at -25 °C for 12 h resulted in the deposition of a mixture of colorless and orange crystals. The crystals were isolated by decanting off the yellow supernatant, washed with Et_2O (2 × 1 mL) and dried *in vacuo* (27.4 mg). The unit cell parameters of the colorless crystals (monoclinic C; *a* = 24.2 Å; *b* = 9.06 Å; *c* = 15.11 Å; α = 90°; β = 115.69°; *γ* = 90°) were consistent with those anticipated for [$(Ph_3P)_2Cu(\kappa^2$-$O_2CH)$] (**3.4**).[43] Similarly, the unit cell parameters of the orange crystals (triclinic; *a* = 9.50 Å; *b* = 12.22 Å; *c* = 13.81 Å; α = 87.53°; β = 71.69°; *γ* = 78.66°) were consistent with those anticipated for [$(phen)(PPh_3)CuCl$] (**3.3**).

3.4.10 Reaction of $[Cu_{14}H_{12}(phen)_6(PPh_3)_4][Cl]_2$ with CD_2Cl_2

Complex **3.1** (27.8 mg, 0.0090 mmol) was dissolved in CD_2Cl_2 (700 μL). The dark blue solution was then transferred to a J. Young NMR tube and monitored by NMR spectroscopy for 48 h. After 24 h, the reaction mixture still appeared dark blue; however, some copper metal had deposited on the walls of the tube. After 48 h, the reaction mixture appeared orange and a brown solid had precipitated from solution. NMR spectra were recorded at both 24 and 48 h. The major decomposition product was identified to be [$(phen)(PPh_3)CuCl$] (**3.3**), by comparison of the spectral data to those of an independently prepared sample. H_2 was also detected in the reaction mixture. *48 hour spectra:* ^1H NMR (400 MHz, 25 °C, CD_2Cl_2): δ 4.60 (s, H_2), 7.29 (m, 6H, *m*-Ph on PPh_3), 7.35 (m, 3H, *p*-Ph on PPh_3), 7.48 (m, 6H, *o*-Ph on PPh_3), 7.70 (dd, J_{HH} = 8.1, 4.6 Hz, 2H, Ar C*H* on phen), 7.88 (s, 2H, Ar C*H* on phen), 8.37 (d, $J_{H\text{-}H}$ = 8.1 Hz, 2H, Ar C*H* on phen), 8.96 (m, 2H, Ar C*H* on phen). $^{31}P\{^1H\}$

NMR (162 MHz, 25 °C, CD_2Cl_2): δ -3.27 (br s, complex **3.3**), 30.75 (s, unidentified minor product).

3.4.11 Reaction of $[Cu_{14}H_{12}(phen)_6(PPh_3)_4][Cl]_2$ with 15 equiv H_2O in CD_3CN

Complex **3.1** (11.3 mg, 0.0036 mmol) was dissolved in CD_3CN (700 μL). The dark blue solution was then transferred to an NMR tube equipped with a rubber septum. Degassed water (1.00 μL, 0.0555 mmol) was then added via microliter syringe. This solution was monitored by NMR spectroscopy for 24 h. After 24 h, the reaction mixture still appeared dark blue, but a very small amount copper metal had deposited on the walls of the tube and a few small yellow cubes (most likely complex **3.3**) had precipitated from solution. The NMR spectra of the reaction mixture revealed that complex **3.1** remained mostly unreacted. ^{1}H NMR (500 MHz, 25 °C, CD_3CN): δ 3.45 (s, 12H, μ_3-H), 5.78 (t, J_{HH} = 7.0 Hz, 24H, *m*-Ph on PPh_3), 6.15 (m, 24H, *o*-Ph on PPh_3), 6.69 (t, J_{HH} = 7.2, 12H, *p*-Ph on PPh_3), 6.82 (dd, J_{HH} = 8.1, 4.6 Hz, 12H, Ar C*H* on phen), 7.90 (s, 12H, Ar C*H* on phen), 8.16 (dd, J_{HH} = 8.2, 1.5 Hz, 12H, Ar C*H* on phen), 8.94 (dd, J_{HH} = 4.8, 1.5 Hz, 12H, Ar C*H* on phen). $^{31}P\{^1H\}$ NMR (162 MHz, 25 °C, CD_3CN): δ -5.09 (br s).

3.4.12 Reaction of $[(Ph_3P)CuH]_6$ with CO_2 in the presence of 7 equiv PPh_3

This reaction has been described previously, by Sneeden and coworkers, to form the formate complex $[(Ph_3P)_2Cu(\kappa^2\text{-}O_2CH)]$ (**3.4**) over the course of 48 h.[35] However, no spectroscopic evidence was provided in the original publication. To a solution of $[(Ph_3P)CuH]_6$ (7.4 mg, 0.0038 mmol) in C_6D_6 (500 μL) was added PPh_3 (7.4 mg, 0.028 mmol) in C_6D_6 (500 μL). This bright red solution was transferred to a J. Young NMR tube. The headspace was evacuated and CO_2 (1 atm) was introduced into the tube. This resulted in

a slow bleaching of the red color. After 4h, the ^{1}H and $^{31}P\{^{1}H\}$ NMR spectra of the colorless solution were recorded. These spectra revealed the complete consumption of the starting material. The colorless solution was then transferred to a glass vial and layered with hexanes (3 mL). Storage of this solution at room temperature for 12 h resulted in the deposition of colorless crystals.[43] The crystals were isolated by decanting off the supernatant, and washed with hexanes (3 × 1 mL), and dried *in vacuo* (11.2 mg, 78% yield). The unit cell parameters of the colorless crystals (Monoclinic C; a = 24.31 Å; b = 9.13 Å; c = 15.17 Å; α = 90°; β = 115.63°; γ = 90°) were consistent with those anticipated for $[(Ph_3P)_2Cu(\kappa^2\text{-}O_2CH)]$ (**3.4**).[43] ^{1}H NMR (500 MHz, 25 °C, CD_2Cl_2): δ 7.27 (t, J_{HH} = 7.4 Hz, 12H, *m*-Ph), 7.33 (m, 12H, *o*-Ph), 7.38 (t, J_{HH} = 7.2 Hz, 6H, *p*-Ph), 8.45 (s, 1H, O_2CH). $^{31}P\{^{1}H\}$ NMR (162 MHz, 25 °C, CD_2Cl_2): δ -3.13 (s). $^{13}C\{^{1}H\}$ NMR (126 MHz, 25 °C, CD_2Cl_2): δ 129.21 (d, J_{CP} = 9.1 Hz, *m*-*C*H), 130.50 (s, 6C, *p*-*C*H), 133.22 (d, J_{CP} = 30.9 Hz, 6C, *ipso*-*C*), 134.31 (d, J_{CP} = 14.9 Hz, 12C, *o*-*C*H), 169.39 (s, O_2CH).

3.4.13 X-ray Crystallography

Data for **3.1**·$3CH_2Cl_2$·C_6H_6 and **3.3**·CH_2Cl_2 were collected on a Bruker KAPPA APEX II diffractometer equipped with an APEX II CCD detector using a TRIUMPH monochromater with a MoKα X-ray source (α = 0.71073 Å). Crystals were mounted on a cryoloop under Paratone-N oil, and all data were collected at 100(2) K using an Oxford nitrogen gas cryostream system. X-ray data for **3.1**·$3CH_2Cl_2$·C_6H_6 were collected utilizing frame exposures of 20 (low angle), 30 (medium angle) and 60 s (high angle). X-ray data for **3.3**·CH_2Cl_2 were collected using frame exposures of 5 s. Data collection and cell parameter determination were conducted using the SMART program.[44] Integration of the data frames and final cell parameter refinement were performed using SAINT software.[45] Absorption

correction of the data were carried out using the multi-scan method SADABS.[46] Subsequent calculations were carried out using SHELXTL.[47] Structure determination was done using direct methods and difference Fourier techniques. All hydrogen atom positions were idealized, and rode on the atom of attachment. The 12 μ_3-hydride ligands on **3.1**·$3CH_2Cl_2$·C_6H_6 were not located in the difference Fourier map due to the high electron density around the copper core. The final refinement included anisotropic temperature factors on Cu and P atoms. Structure solution, refinement, graphics, and creation of publication materials were performed using SHELXTL.[47]

Complex **3.1**·$3CH_2Cl_2$·C_6H_6 exhibits positional disorder of the Cl^- counterions and CH_2Cl_2 solvent molecules. The positional disorder was addressed by modeling the two Cl^- counterions in 8 positions, in a 40:35:35:20:15:20:15:20 ratio and the three CH_2Cl_2 molecules in 6 positions, each with half occupancy. In addition, the C–Cl bonds in CH_2Cl_2 were fixed with the DFIX command. Selected C–C and C–N bonds were also fixed with the DFIX command, while some rings were constrained with the FLAT command.

Table 3.2. X-ray Crystallographic Data for **3.1**·$3CH_2Cl_2$·C_6H_6 and **3.3**·CH_2Cl_2

	3.1·$3CH_2Cl_2$·C_6H_6	**3.3**·CH_2Cl_2
empirical formula	$C_{153}H_{132}Cl_8Cu_{14}N_{12}P_4$	$C_{31}H_{25}Cl_3CuN_2P$
crystal habit, color	block, dark blue	block, yellow
crystal size (mm)	0.25 × 0.15 × 0.10	0.25 × 0.20 × 0.15
crystal system	orthorhombic	triclinic
space group	$P2_12_12_1$	$P\bar{1}$
volume ($Å^3$)	15979.2(9)	1408.72(8)
a (Å)	17.4875(5)	9.2507(3)
b (Å)	29.9969(11)	12.0825(4)
c (Å)	30.4614(9)	13.5382(4)
α (deg)	90.00	88.495(2)
β (deg)	90.00	72.501(2)
γ (deg)	90.00	77.674(2)
Z	4	2
formula weight (g/mol)	3435.75	626.39

density (calculated) (Mg/m^3)	1.428	1.477
absorption coefficient (mm^{-1})	2.044	1.141
F_{000}	6944	640
total no. reflections	72817	21626
unique reflections	31296	5983
final R indices ($I > 2\sigma(I)$]	$R_1 = 0.1268$ $wR_2 = 0.2965$	$R_1 = 0.0452$ $wR_2 = 0.1261$
largest diff. peak and hole ($e^- A^{-3}$)	3.688 and -2.281	2.363 and -1.325
GOF	1.090	0.938

3.5 Appendix

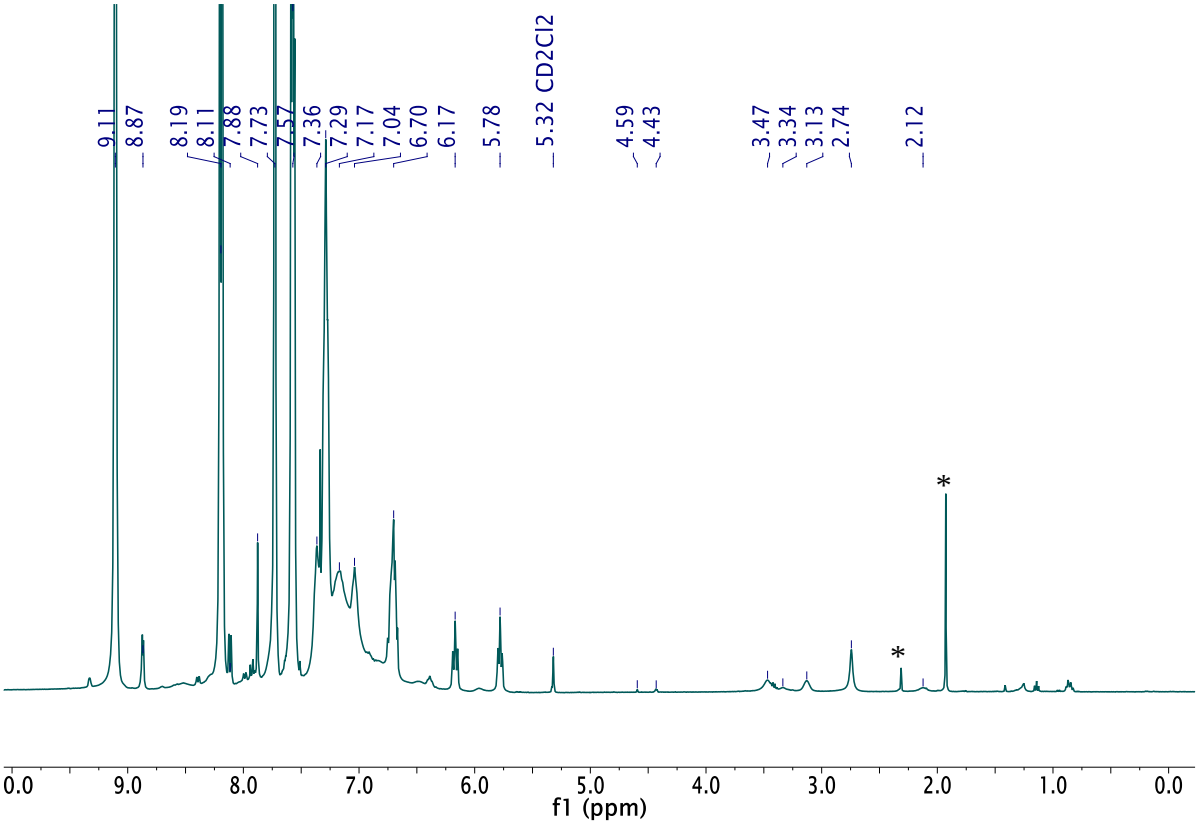

Figure A 3.1. *In situ* ^1H NMR spectrum of the reaction of $[(Ph_3P)CuH]_6$ with 26 equiv of phen after 1 h in CD_2Cl_2. (*) denotes the presence of acetonitrile and toluene.

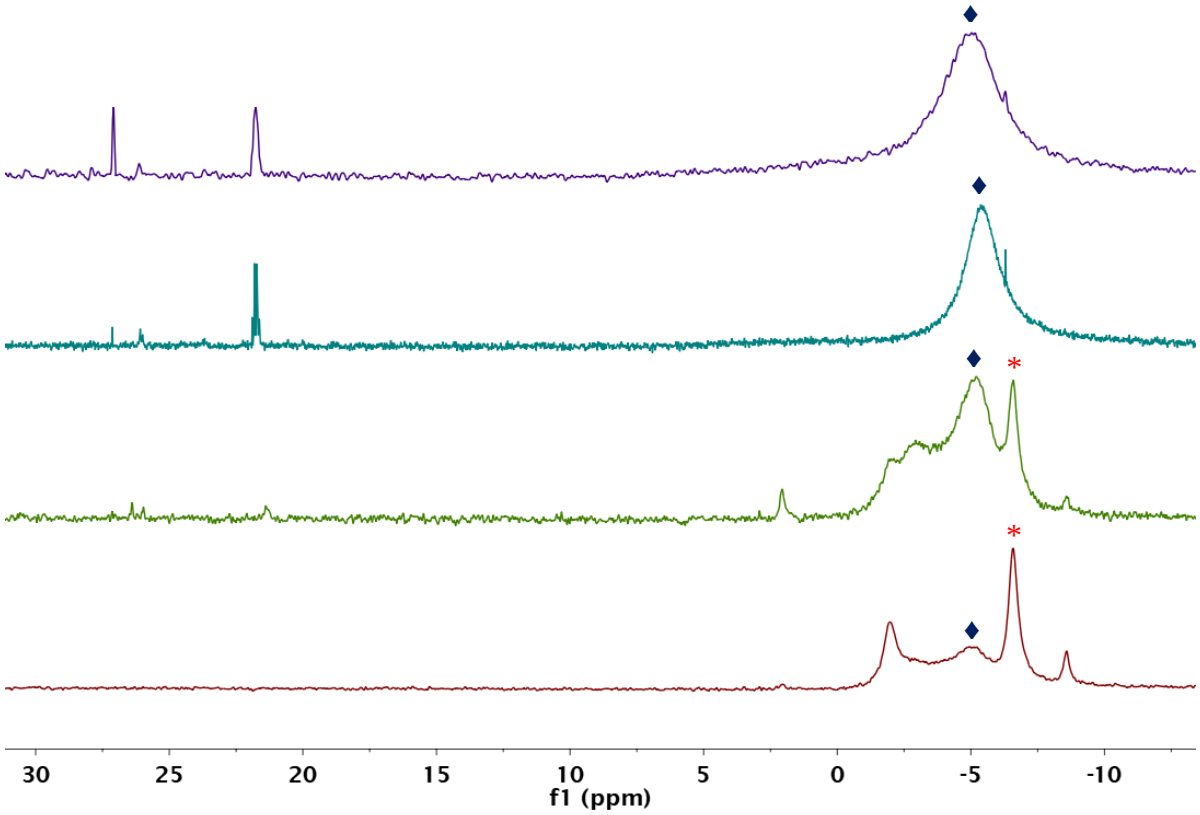

Figure A3.2. *In situ* $^{31}P\{^{1}H\}$ NMR spectra of the reaction of $[(Ph_3P)CuH]_6$ with 26 equiv of phen in CD_2Cl_2. (*) and (♦) indicate the resonances assignable to $[(Ph_3P)CuH]_6$ and $[Cu_{14}H_{12}(phen)_6(PPh_3)_4][Cl]_2$, respectively.

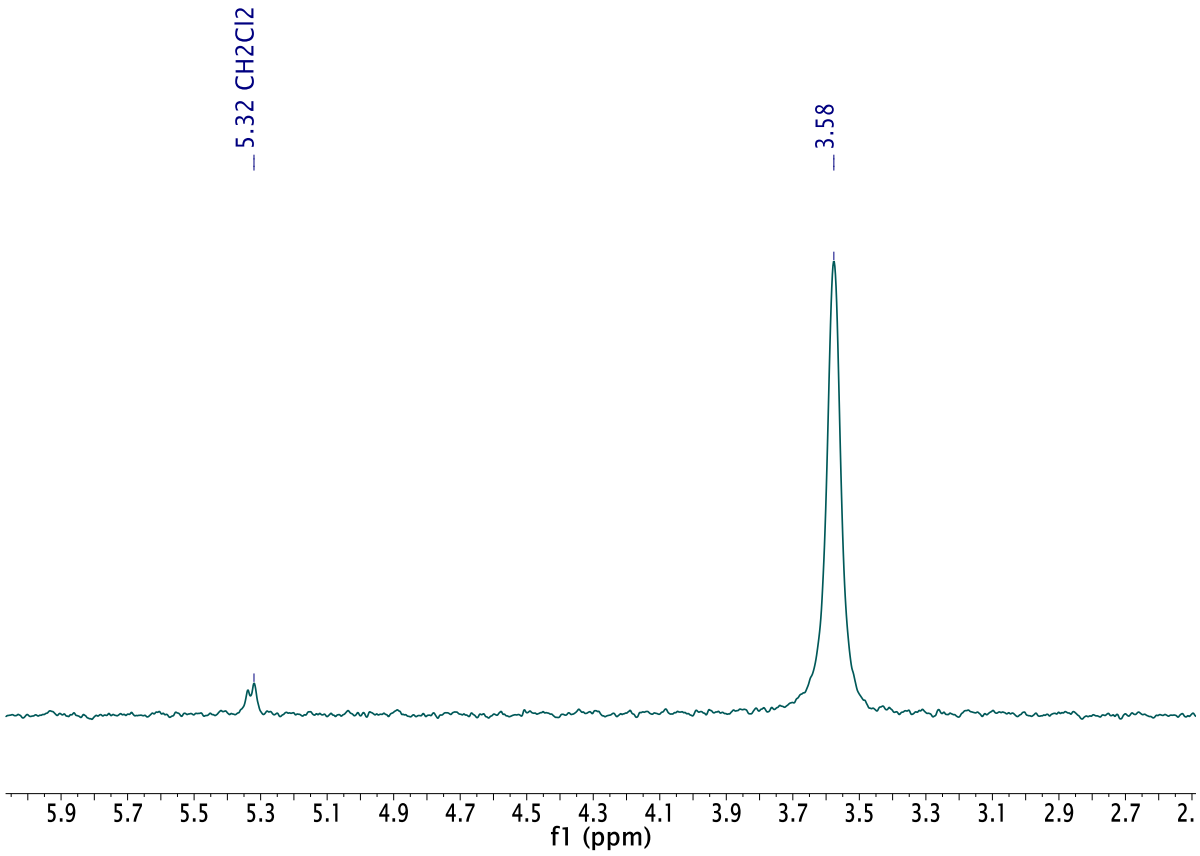

Figure A3.3. ^{2}H NMR spectrum of $[Cu_{14}D_{12}(phen)_6(PPh_3)_4][Cl]_2$ (**3.1-*d*$_{12}$**) in CH_2Cl_2.

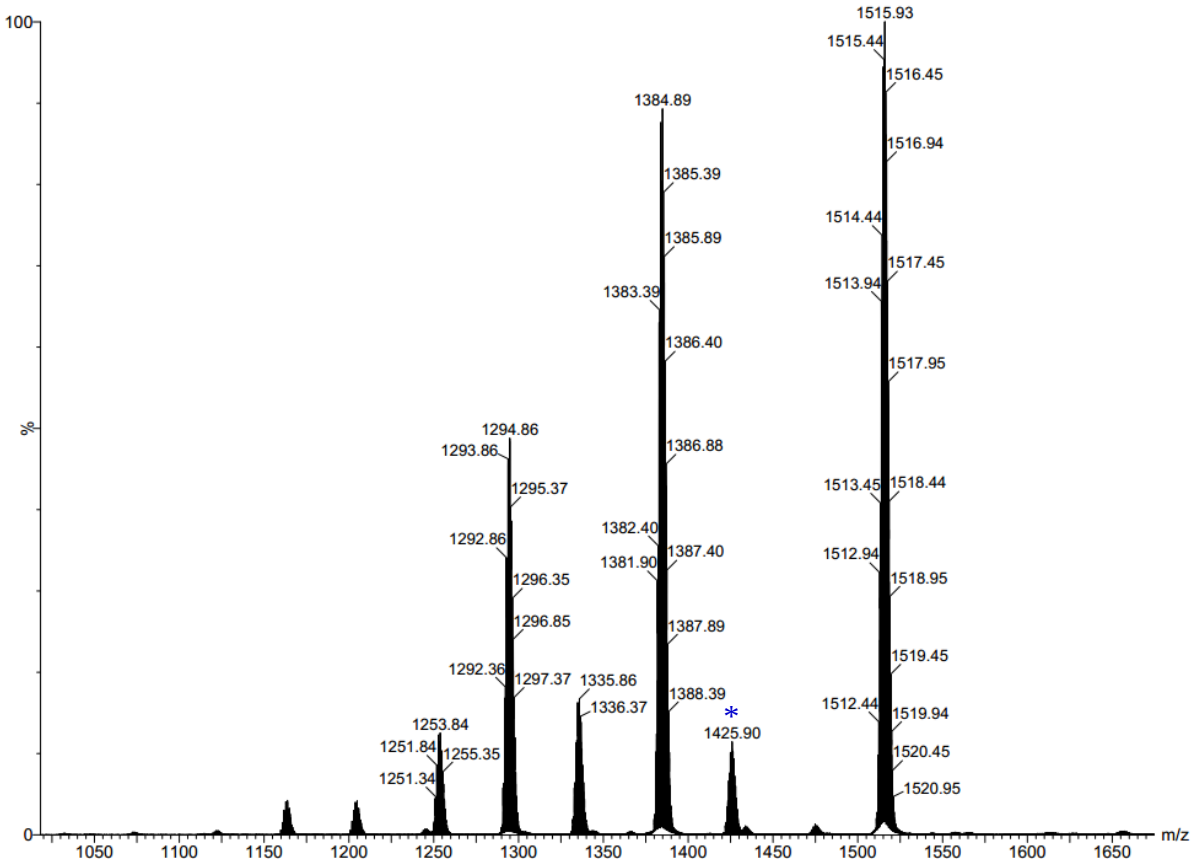

Figure A3.4. ESI-MS of $[Cu_{14}H_{12}(phen)_6(PPh_3)_4][Cl]_2$ (**3.1**) showing the region containing doubly charged peaks assignable to **3.1.** (*) denotes the peak assignable to loss of a phen ligand from **3.1**, $[M-phen]^{2+}$.

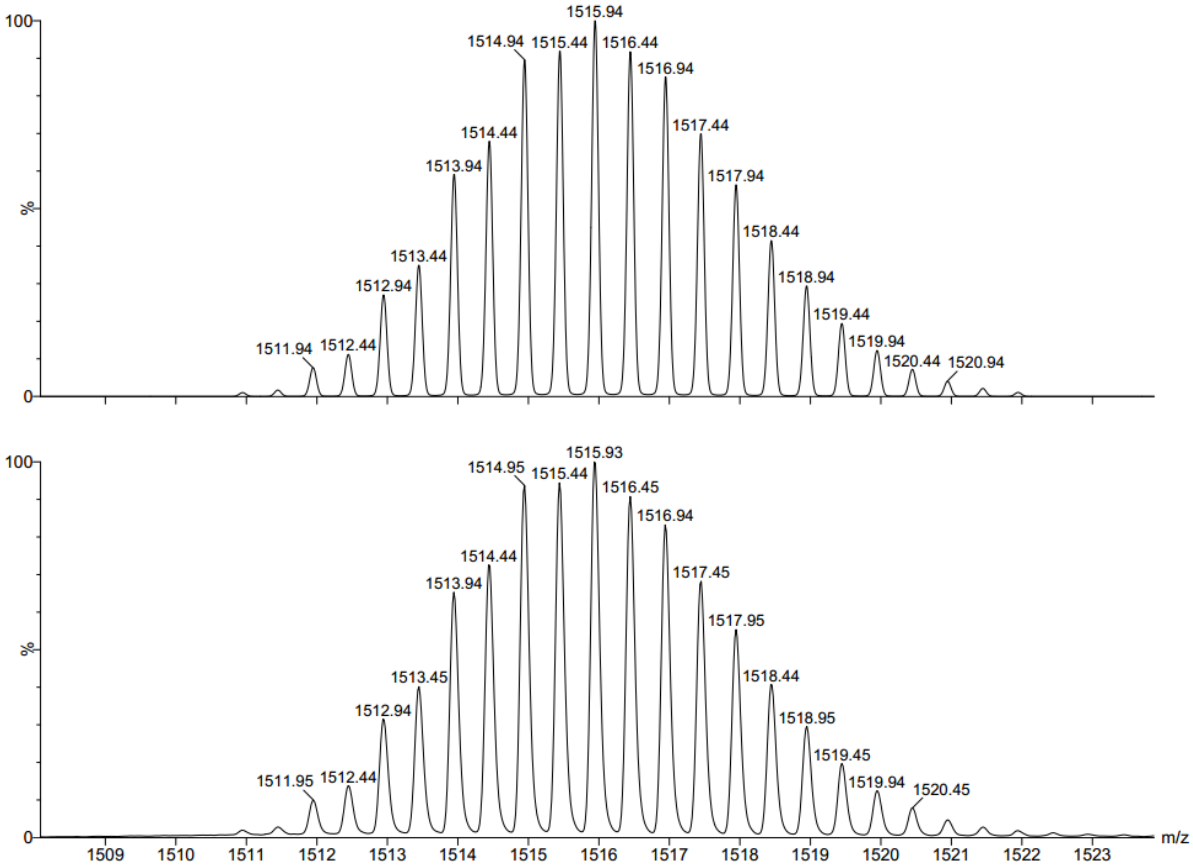

Figure A3.5. Partial ESI-MS of $[Cu_{14}H_{12}(phen)_6(PPh_3)_4][Cl]_2$ (**3.1**). The experimental (bottom) and calculated (top) peaks assignable to $[M]^{2+}$ ion are shown.

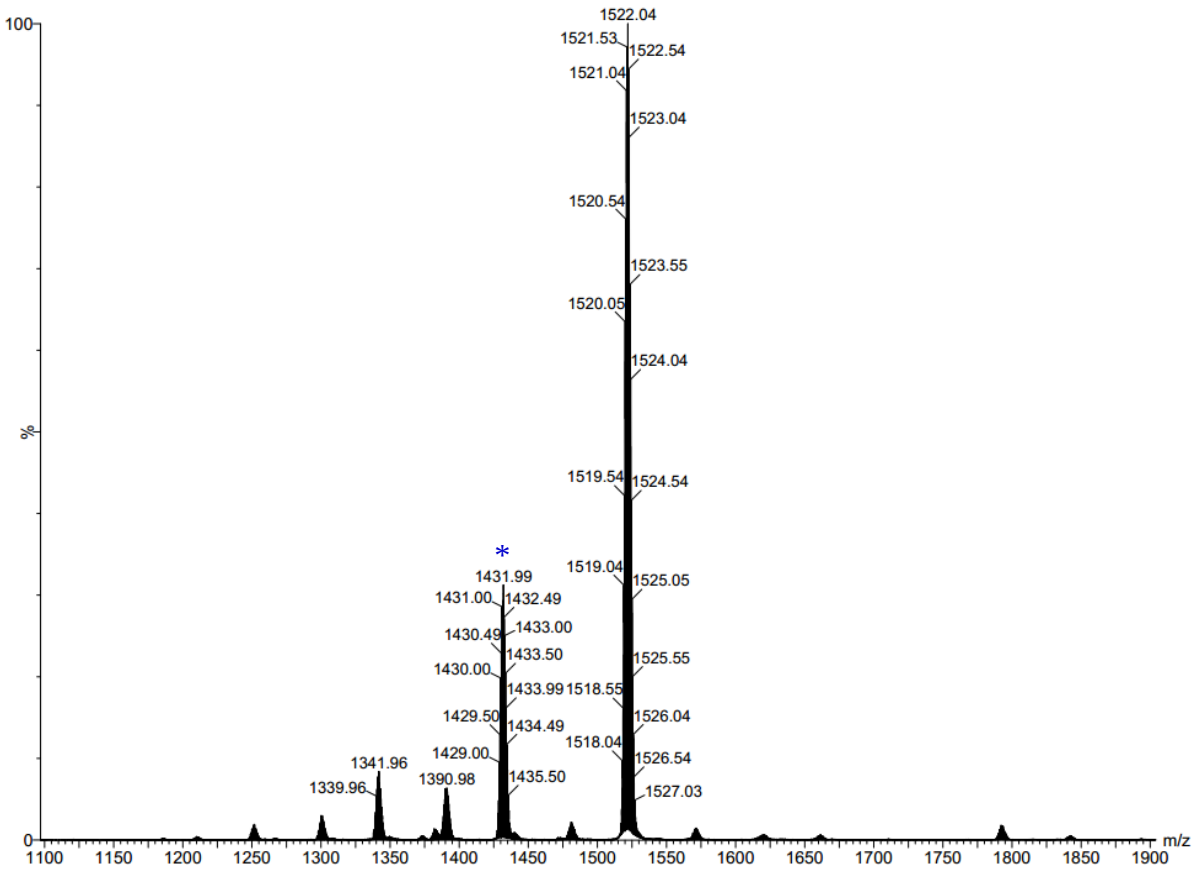

Figure A3.6. ESI-MS of $[Cu_{14}D_{12}(phen)_6(PPh_3)_4][Cl]_2$ (**3.1-*d*$_{12}$**) showing the region containing doubly charged peaks assignable to **3.1-*d*$_{12}$**. (*) denotes the peak assignable to loss of a phen ligand from **3.1-*d*$_{12}$**, $[M-phen]^{2+}$.

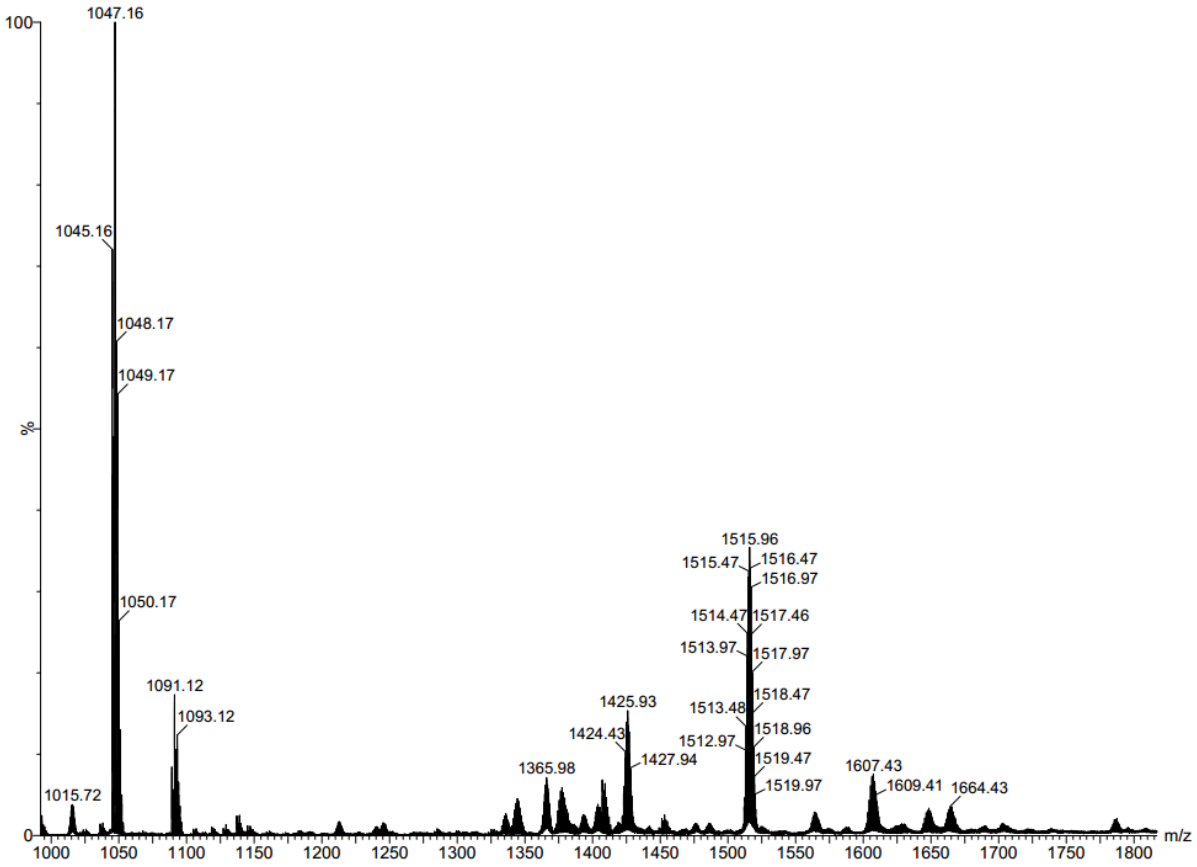

Figure A3.7. ESI-MS of $[Cu_{14}H_{12}(phen)_6(PPh_3)_4][OTf]_2$ (**3.2**) showing the region containing doubly charged peaks assignable to **3.2**.

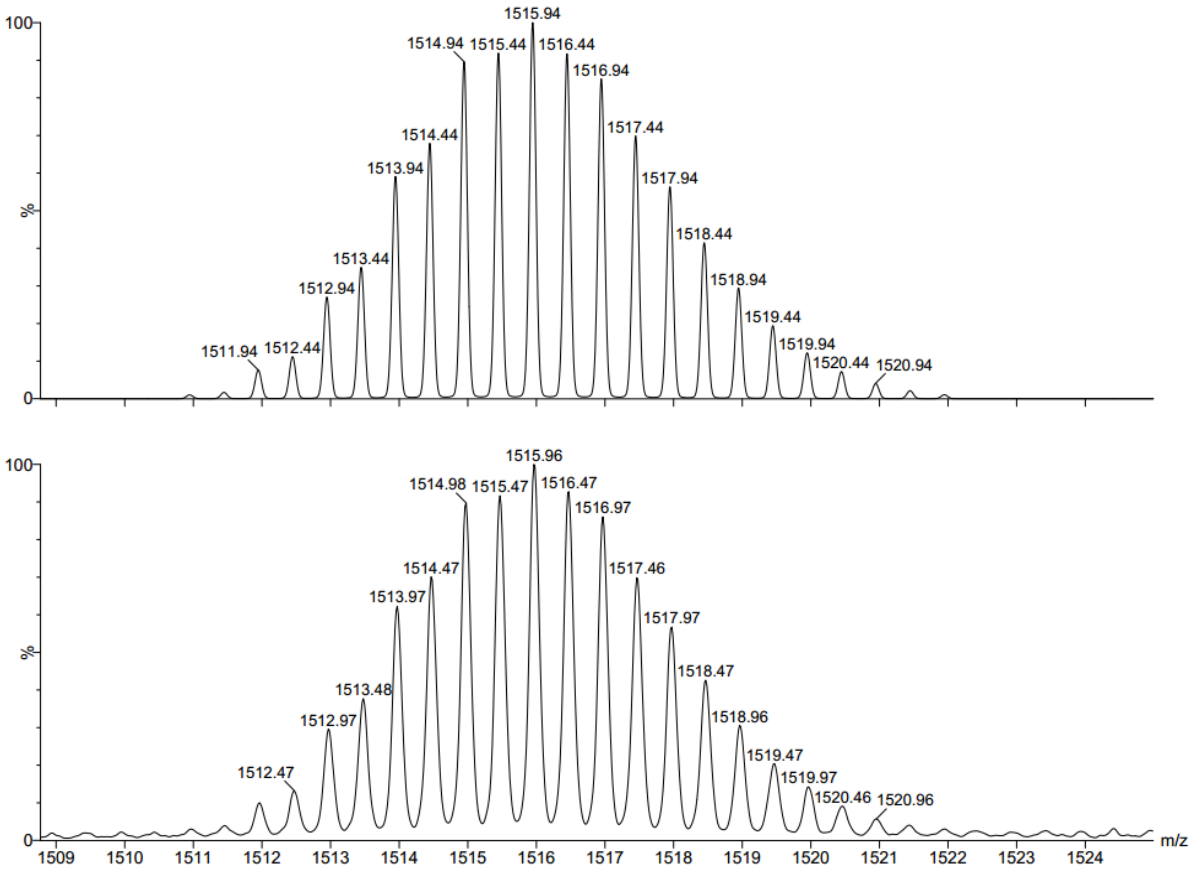

Figure A3.8. Partial ESI-MS of $[Cu_{14}H_{12}(phen)_6(PPh_3)_4][OTf]_2$ (**3.2**). The experimental (bottom) and calculated (top) peaks assignable to $[M]^{2+}$ ion are shown.

3.6 References

(1) Goeden, G. V.; Caulton, K. G. Soluble copper hydrides: solution behavior and reactions related to carbon monoxide hydrogenation. *J. Am. Chem. Soc.* **1981**, *103*, 7354.

(2) Mahoney, W. S.; Brestensky, D. M.; Stryker, J. M. Selective hydride-mediated conjugate reduction of α,β-unsaturated carbonyl compounds using $[(Ph_3P)CuH]_6$. *J. Am. Chem. Soc.* **1988**, *110*, 291.

(3) Yun, J.; Kim, D.; Yun, H. A new alternative to Stryker's reagent in hydrosilylation: synthesis, structure, and reactivity of a well-defined carbene-copper(II) acetate complex. *Chem. Commun.* **2005**, 5181.

(4) Lautens, M.; Ren, Y. Transition Metal Catalyzed Stereospecific Intramolecular [3 + 2] Cycloadditions of Methylenecyclopropanes with Alkynes. *J. Am. Chem. Soc.* **1996**, *118*, 9597.

(5) Baker, B. A.; Bošković, Ž. V.; Lipshutz, B. H. (BDP)CuH: A "Hot" Stryker's Reagent for Use in Achiral Conjugate Reductions. *Org. Lett.* **2007**, *10*, 289.

(6) Ren, Y.; Xu, X.; Sun, K.; Xu, J. A new and effective method for providing optically active monosubstituted malononitriles: selective reduction of α,β-unsaturated dinitriles catalyzed by copper hydride complexes. *Tetrahedron: Asymmetry* **2005**, *16*, 4010.

(7) Osborn, M. E.; Pegues, J. F.; Paquette, L. A. Reduction of α,β-unsaturated nitriles with a copper hydride complex. *J. Org. Chem.* **1980**, *45*, 167.

(8) Daeuble, J. F.; McGettigan, C.; Stryker, J. M. Selective reduction of alkynes to cis-alkenes by hydrometallation using $[(Ph_3P)CuH]_6$. *Tetrahedron Lett.* **1990**, *31*, 2397.

(9) Zhang, L.; Cheng, J.; Hou, Z. Highly efficient catalytic hydrosilylation of carbon dioxide by an N-heterocyclic carbene copper catalyst. *Chem. Commun.* **2013**, *49*, 4782.

(10) Zhang, L.; Hou, Z. N-Heterocyclic carbene (NHC)-copper-catalysed transformations of carbon dioxide. *Chem. Sci.* **2013**, *4*, 3395.

(11) Eberhart, M. S.; Norton, J. R.; Zuzek, A.; Sattler, W.; Ruccolo, S. Electron Transfer from Hexameric Copper Hydrides. *J. Am. Chem. Soc.* **2013**, *135*, 17262.

(12) Kohn, R. D.; Pan, Z.; Mahon, M. F.; Kociok-Kohn, G. Trimethyltriazacyclohexane as bridging ligand for triangular Cu_3 units and C-H hydride abstraction into a Cu_6 cluster. *Chem. Commun.* **2003**, 1272.

(13) Liao, P.-K.; Fang, C.-S.; Edwards, A. J.; Kahlal, S.; Saillard, J.-Y.; Liu, C. W. Hydrido Copper Clusters Supported by Dithiocarbamates: Oxidative Hydride Removal and Neutron Diffraction Analysis of $[Cu_7(H)\{S_2C(\text{aza-15-crown-5})\}_6]$. *Inorg. Chem.* **2012**, *51*, 6577.

(14) Dhayal, R. S.; Liao, J.-H.; Lin, Y.-R.; Liao, P.-K.; Kahlal, S.; Saillard, J.-Y.; Liu, C. W. A Nanospheric Polyhydrido Copper Cluster of Elongated Triangular Orthobicupola Array: Liberation of H_2 from Solar Energy. *J. Am. Chem. Soc.* **2013**, *135*, 4704.

(15) Huertos, M. A.; Cano, I.; Bandeira, N. A. G.; Benet-Buchholz, J.; Bo, C.; van Leeuwen, P. W. N. M. Phosphinothiolates as Ligands for Polyhydrido Copper Nanoclusters. *Chem. Eur. J.* **2014**, *20*, 16121.

(16) Edwards, A. J.; Dhayal, R. S.; Liao, P.-K.; Liao, J.-H.; Chiang, M.-H.; Piltz, R. O.; Kahlal, S.; Saillard, J.-Y.; Liu, C. W. Chinese Puzzle Molecule: A 15 Hydride, 28 Copper Atom Nanoball. *Angew. Chem.* **2014**, *126*, 7342.

(17) Edwards, A. J.; Dhayal, R. S.; Liao, P.-K.; Liao, J.-H.; Chiang, M.-H.; Piltz, R. O.; Kahlal, S.; Saillard, J.-Y.; Liu, C. W. Chinese Puzzle Molecule: A 15 Hydride, 28 Copper Atom Nanoball. *Angew. Chem. Int. Ed.* **2014**, *53*, 7214.

(18) Liao, J.-H.; Dhayal, R. S.; Wang, X.; Kahlal, S.; Saillard, J.-Y.; Liu, C. W. Neutron Diffraction Studies of a Four-Coordinated Hydride in Near Square-Planar Geometry. *Inorg. Chem.* **2014**, *53*, 11140.

(19) Churchill, M. R.; Bezman, S. A.; Osborn, J. A.; Wormald, J. Preparation and crystallographic characterization of a hexameric triphenylphosphinecopper hydride cluster. *J. Am. Chem. Soc.* **1971**, *93*, 2063.

(20) Frey, G. D.; Donnadieu, B.; Soleilhavoup, M.; Bertrand, G. Synthesis of a Room-Temperature-Stable Dimeric Copper(I) Hydride. *Chem. Asian J.* **2011**, *6*, 402.

(21) Wyss, C. M.; Tate, B. K.; Bacsa, J.; Gray, T. G.; Sadighi, J. P. Bonding and Reactivity of a μ-Hydrido Dicopper Cation. *Angew. Chem. Int. Ed.* **2013**, *52*, 12920.

(22) Goeden, G. V.; Huffman, J. C.; Caulton, K. G. A Cu-(μ-H) bond can be stronger than an intramolecular P→Cu bond. Synthesis and structure of $Cu_2(\mu\text{-}H)_2(\eta^2\text{-}CH_3C(CH_2PPh_2)_3)_2$. *Inorg. Chem.* **1986**, *25*, 2484.

(23) Ganesamoorthy, C.; Weßing, J.; Kroll, C.; Seidel, R. W.; Gemel, C.; Fischer, R. A. Der intermetalloide Cluster [(Cp*AlCu)6H4], Stabilisierung eines Cu6-Kerns in einer oktaedrischen Al6-Hülle: molekulare Modellverbindungen für Hume-Rothery-Nanophasen. *Angew. Chem.* **2014**, *126*, 8077.

(24) Ganesamoorthy, C.; Weßing, J.; Kroll, C.; Seidel, R. W.; Gemel, C.; Fischer, R. A. The Intermetalloid Cluster [(Cp*AlCu)6H4], Embedding a Cu6 Core Inside an Octahedral Al6 Shell: Molecular Models of Hume–Rothery Nanophases. *Angew. Chem. Int. Ed.* **2014**, *53*, 7943.

(25) Bennett, E. L.; Murphy, P. J.; Imberti, S.; Parker, S. F. Characterization of the hydrides in Stryker's reagent: $[HCu\{P(C_6H_5)_3\}]_6$. *Inorg. Chem.* **2014**, *53*, 2963.

(26) Mao, Z.; Huang, J.-S.; Che, C.-M.; Zhu, N.; Leung, S. K.-Y.; Zhou, Z.-Y. Unexpected Reactivities of Cu_2(diphosphine)$_2$ Complexes in Alcohol: Isolation, X-ray Crystal Structure, and Photoluminescent Properties of a Remarkably Stable $[Cu_3(\text{diphosphine})_3(\mu_3\text{-}H)]^{2+}$ Hydride Complex. *J. Am. Chem. Soc.* **2005**, *127*, 4562.

(27) Geary, W. J. The use of conductivity measurements in organic solvents for the characterisation of coordination compounds. *Coord. Chem. Rev.* **1971**, *7*, 81.

(28) Kresse, G.; Furthmüller, J. Efficiency of Ab-initio total Energy Calculations for Metals and Semiconductors Using a Plane-wave Basis Set. *Comput. Mat. Sci.* **1996**, *6*, 15.

(29) Kresse, G.; Furthmüller, J. Efficient Iterative Schemes for Ab Initio Total-energy Calculations Using a Plane-wave Basis Set. *Phys. Rev. B* **1996**, *54*, 11169.

(30) Kresse, G.; Hafner, J. Ab Initio Molecular Dynamics for Liquid Metals. *Phys. Rev. B* **1993**, *47*, 558.

(31) Blöchl, P. E. Projector augmented-wave method. *Phys. Rev. B* **1994**, *50*, 17953.

(32) Perdew, J. P.; Burke, K.; Ernzerhof, M. Generalized Gradient Approximation Made Simple. *Phys. Rev. Lett.* **1996**, *77*, 3865.

(33) Perdew, J. P.; Chevary, J. A.; Vosko, S. H.; Jackson, K. A.; Pederson, M. R.; Singh, D. J.; Fiolhais, C. Atoms, molecules, solids, and surfaces: Applications of the generalized gradient approximation for exchange and correlation. *Phys. Rev. B* **1992**, *46*, 6671.

(34) Schrader, A. M.; Schroll, A. L.; Barany, G. Synthetic Routes to, Transformations of, and Rather Surprising Stabilities of (N-Methyl-N-phenylcarbamoyl)sulfenyl Chloride, ((N-Methyl-N-phenylcarbamoyl)dithio)carbonyl Chloride, and Related Compounds. *J. Org. Chem.* **2011**, *76*, 7882.

(35) Beguin, B.; Denise, B.; Sneeden, R. P. A. Hydrocondensation of CO_2 : II. Reaction of carbon dioxide and carbon monoxide with $[HCuPPh_3]_6$. *J. Organomet. Chem.* **1981**, *208*, C18.

(36) Nakamae, K.; Kure, B.; Nakajima, T.; Ura, Y.; Tanase, T. Facile Insertion of Carbon Dioxide into $Cu_2(\mu\text{-}H)$ Dinuclear Units Supported by Tetraphosphine Ligands. *Chem. Asian J.* **2014**, *9*, 3106.

(37) We should also note that complex **3.1** will react with CO_2 in the absence of added PPh_3. However, the addition of extra PPh_3 was found to increase the yield of complex **3.4**.

(38) Harris, R. K.; Becker, E. D.; Cabral De Menezes, S. M.; Goodfellow, R.; Granger, P. NMR Nomenclature. Nuclear Spin Properties and Conventions for Chemical Shifts. *Pure Appl. Chem.* **2001**, *73*, 1795.

(39) Harris, R. K.; Becker, E. D.; Cabral De Menezes, S. M.; Granger, P.; Hoffman, R. E.; Zilm, K. W. Further Conventions for NMR Shielding and Chemical Shifts. *Pure Appl. Chem.* **2008**, *80*, 59.

(40) Lee, D.; Yun, J. Direct synthesis of Stryker's reagent from a Cu(II) salt. *Tetrahedron Lett.* **2005**, *46*, 2037.

(41) Lv, H.; Cai, Y.; Zhang, J. Copper-Catalyzed Hydrodefluorination of Fluoroarenes by Copper Hydride Intermediates. *Angew. Chem. Int. Ed.* **2013**, *52*, 3203.

(42) Chiu, P.; Li, Z.; Fung, K. C. M. An expedient preparation of Stryker's reagent. *Tetrahedron Lett.* **2003**, *44*, 455.

(43) Marsich, N.; Camus, A.; Nardin, G. Reaction of carbon dioxide with arylcopper(I) complexes containing tertiary phosphines. *J. Organomet. Chem.* **1982**, *239*, 429.

(44) *SMART Apex II, Version 2.1*; Bruker AXS Inc.: Madison, WI, 2005.

(45) *SAINT Software User's Guide, Version 7.34a*; Bruker AXS Inc.: Madison, WI, 2005.

(46) Sheldrick, G. M. *SADABS*; University of Göttingen: Göttingen, Germany, 2005.

(47) *SHELXTL PC, Version 6.12*; Bruker AXS Inc.: Madison, WI, 2005.

Chapter 4. **A Cu_{25} Superatom with $N^* = 2$**

Portions of this work were published in:

Thuy-Ai D. Nguyen; Zachary R. Jones; Bryan R. Goldsmith; William R. Buratto; Guang Wu; Susannah L. Scott; Trevor W. Hayton. A Cu_{25} Nanocluster with Partial Cu(0) Character. *J. Am. Chem. Soc*. **2015**, 137, 13319-13324.

4.1 Introduction

Atomically precise, noble metal nanoclusters (NCs) are a relatively new class of materials, with potential applications in catalysis, medicine, and imaging.[1-7] Many examples are now known, including $[Ag_{44}(p\text{-MBA})_{30}]^{4-}$,[8] $[Ag_{21}(S_2P(O^iPr)_2)_{12}]^+$,[9] $[Au_{25}(SCH_2CH_2Ph)_{18}]^-$,[10,11] and $[Au_{102}(p\text{-MBA})_{44}]$.[12,13] Intermetallic Au_mAg_n and Au_mCu_n nanoclusters are also isolable.[14-19] Significantly, their mono-disperse and atomically precise nature has permitted their complete structural characterization, allowing for the development of structure/function relationships for these nanomaterials.[20-23] NCs have also proven to be an excellent testbed for superatom theory, helping to place it upon firm experimental footing.[24]

In contrast, comparable copper NCs have remained elusive. Previous attempts to generate large Cu NCs have produced ill-defined mixtures,[25-28] or required the use of cryogenic matrices.[29,30] Interestingly, several well-defined Cu(I) hydride clusters are known, such as $[Cu_{14}H_{12}(phen)_6(PPh_3)_4]^{2+}$,[31] $[Cu_{18}H_7(1,2\text{-}S(C_6H_4)PPh_2)_{10}(I)]$,[32] $[Cu_{20}H_{11}(S_2P(O^iPr)_2)_9]$,[33,34] $[Cu_{28}H_{15}(S_2CN^nPr_2)_{12}]^+$,[35] and $[Cu_{32}H_{20}\{S_2P(O^iPr)_2\}_{12}]$,[36] but these complexes do not feature a Cu(0) core. Indeed, even Cu(0) coordination complexes are exceptionally rare.[37-40] Relative to the heavier congeners, the enhanced challenge of

generating Cu(0) nanoclusters is due, in part, to the lower M(I)/M(0) half-cell potential of Cu (0.52 V) vs. Ag (0.80 V) and Au (1.69 V).[41] As a consequence, the Cu(I) monomers formed prior to NC aggregation are more resistant to reduction. It also renders any resulting Cu(0) NCs more air-sensitive, which makes their physical isolation more challenging. Despite these challenges, Cu nanomaterials are of intense interest for a variety of catalytic applications, including the electrochemical reduction of CO_2.[42-46] In this regard, the isolation of atomically precise copper nanoclusters would be a significant advance, since they could help address the unanswered mechanistic questions that remain for this transformation.[47,48] Herein, is described the synthesis and structural characterization of a novel Cu_{25} nanocluster that features a Cu_{13} centered-icosahedral core, and probe its electronic structure with X-ray absorption spectroscopy (XAS) and X-ray photoelectron spectroscopy (XPS).

4.2 Results and Discussion

As mentioned above, Cu(I) is more resistant to reduction than either Ag(I) or Au(I). As a result, reduction of a Cu(I) precursor with a hydride source, a common way of making Ag and Au NCs, often only results in the synthesis of stable Cu(I) hydride clusters.[49,50] For example, reduction of Cu(OAc) with diphenylsilane (Ph_2SiH_2), in the presence of excess PPh_3, results in formation of $[(Ph_3P)CuH]_6$ in high yield.[31,51] The failure to observe a Cu(0) nanocluster in this reaction can be rationalized on the basis of the higher stability of copper hydrides vs. silver and gold hydrides. However, I hypothesized that performing the reduction of a Cu(I) salt in a ligand-deficient environment would result in the formation of unstable Cu_xH_x oligomers that could be more amenable to nanocluster growth. Thus, addition of 13 equiv of Ph_2SiH_2 to a slurry containing 24 equiv of Cu(OAc), 1 equiv of

CuCl, and 12 equiv of PPh_3, in C_6H_6, results in a rapid color change from pale green to dark red. With further stirring, this solution undergoes a color change to deep green, concomitant with the deposition of a dark solid. Work-up of this mixture after 14 h resulted in the isolation of two copper hydride clusters, $[Cu_{25}H_{22}(PPh_3)_{12}]Cl$ (**4.1**) and $[Cu_{18}H_{17}(PPh_3)_{10}]Cl$ (**4.2**), in isolated yields of 23 and 14%, respectively (Scheme 4.1). An insoluble dark powder was also isolated, which was subsequently identified to be elemental Cu (17% yield). William Buratto, a former undergraduate student in our lab, helped develop this synthesis and was the first to grow X-ray quality crystals of **4.1**. Complexes **4.1** and **4.2** were separated on the basis of their different solubilities in C_6H_6. Briefly, the reaction mixture was first crystallized from a CH_2Cl_2/hexanes solution. This resulted in deposition of a mixture of dark-green (**4.1**) and yellow (**4.2**) crystalline materials. Extraction of these solids into C_6H_6 resulted in selective dissolution of **4.2**, which permitted its separation from **4.1** by filtration. Complex **4.1** was then extracted into CH_2Cl_2 and crystallized from CH_2Cl_2/hexanes, while complex **4.2** was crystallized separately from $C_6H_6/CH_2Cl_2/Et_2O$. No doubt, this procedure contributed somewhat to the low isolated yields of **4.1** and **4.2**, as both are probably present in higher yields in the crude reaction mixture. The isolation of two different CuH clusters from the reaction can be rationalized by their similar Cu:P ratios (that of complex **4.1** is 2.1:1, while that of complex **4.2** is 1.8:1), both of which are similar to the Cu:P ratio in the original reaction mixture (2.1:1). Alternately, the presence of both **4.1** and **4.2** in the reaction mixture suggests that they have similar thermodynamic stabilities. Interestingly, tractable material cannot be isolated without addition of 1 equiv of CuCl to the reaction mixture, which functions as a Cl^- source. Previously, I elucidated the significance of providing a counter-anion source in the reaction mixture during CuH cluster synthesis.[31]

Importantly, while Ph_2SiH_2 reacts with Cu(OAc), it is unable to reduce CuCl. This orthogonal reactivity permits the two copper salts to play different roles in the reaction.

To better understand the formation of **4.1** and **4.2**, I followed the reaction by ^1H and ^{31}P NMR spectroscopies. A ^1H NMR spectrum of the reaction mixture in C_6D_6, after 18 h, reveals the presence of complexes **4.1** and **4.2**, as evidenced by the distinctive chemical shifts of their hydride ligands (Figure A4.3). In addition, this spectrum also revealed the presence of H_2, which is likely generated during the formation of both complex **4.1** and bulk Cu metal. The presence of **4.1** and **4.2** in the reaction mixture is also supported by the *in situ* ^{31}P NMR spectrum (Figure A4.4a). In addition, a few other copper-containing species are also present in the reaction mixture, as evidenced by singlets at 4.15, -2.62, -4.57, and -6.06 ppm in this spectrum (Figure A4.4a). While these species have eluded isolation thus far, it important to note that they are present as minor components of the reaction mixture. The presence of these other copper-containing complexes in the reaction mixture also helps to account for the low isolated yields of **4.1** and **4.2**.

Scheme 4.1. Synthesis of complexes **4.1** and **4.2**

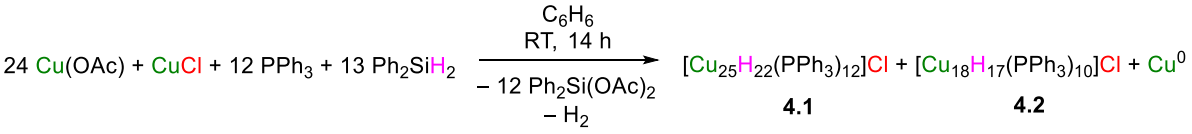

Complex **4.1** crystallizes in the orthorhombic space group Pbca as a hexanes and dichloromethane solvate, **4.1**·$4C_6H_{14}$·$0.5CH_2Cl_2$ (Figure 4.1). In the solid state, **4.1** features a central core of 13 Cu atoms arranged in a distorted centered-icosahedron. The central Cu atom features a coordination number of 12, identical to that observed in bulk Cu metal.[52] An icosahedral Cu_{13} core is predicted computationally in metallic nanoclusters of

intermediate size, although it differs from the *fcc* structure of the bulk metal.[53] The Cu_{13} core is connected, via Cu–Cu bonds, to four triangular $[Cu(PPh_3)]_3$ motifs, which cap the icosahedron in a tetrahedral arrangement. As a result, the cluster occupies the high symmetry *T* point group. The Cu-Cu distances in **4.1** exhibit a large range (2.389(3) - 3.037(3) Å), consistent with the diverse range of Cu coordination environments. The average Cu_{center}–Cu_{icos} bond length (2.635 Å; range: 2.598(3)-2.663(3) Å) is longer than that observed for Cu metal (2.55 Å),[52] but is comparable to those found in other Cu hydride clusters, such as $[CuH(PPh_3)]_6$ (av. 2.630 Å),[54] $[(Me_3\text{-tach})_3Cu_6(\mu_6\text{-H})Cl_4]^{2+}$ (av. 2.580 Å),[55] and the outer Cu–Cu distances in $[Cu_{20}H_{11}(S_2P(O^iPr)_2)_9]$ (2.5284(9)-2.7542(7) Å).[33] More importantly, the Cu_{13} core in **4.1** is similar to M_{13} icosahedral cores found in $[Au_{25}(SCH_2CH_2Ph)_{18}]^-$,[10,11] $[Ag_{21}(S_2P(O^iPr)_2)_{12}]^+$,[9] and $[Au_{13}(PMe_2Ph)_{10}(Cl)_2]^{3+}$,[56] demonstrating for the first time that structurally similar nanoclusters are isolable for all three coinage metals. Finally, the Cu−P distances (av. 2.26 Å) are typical of those found in Cu(I) phosphine complexes,[54,57] while the outer sphere Cl^- counterion was found to be disordered over two positions.

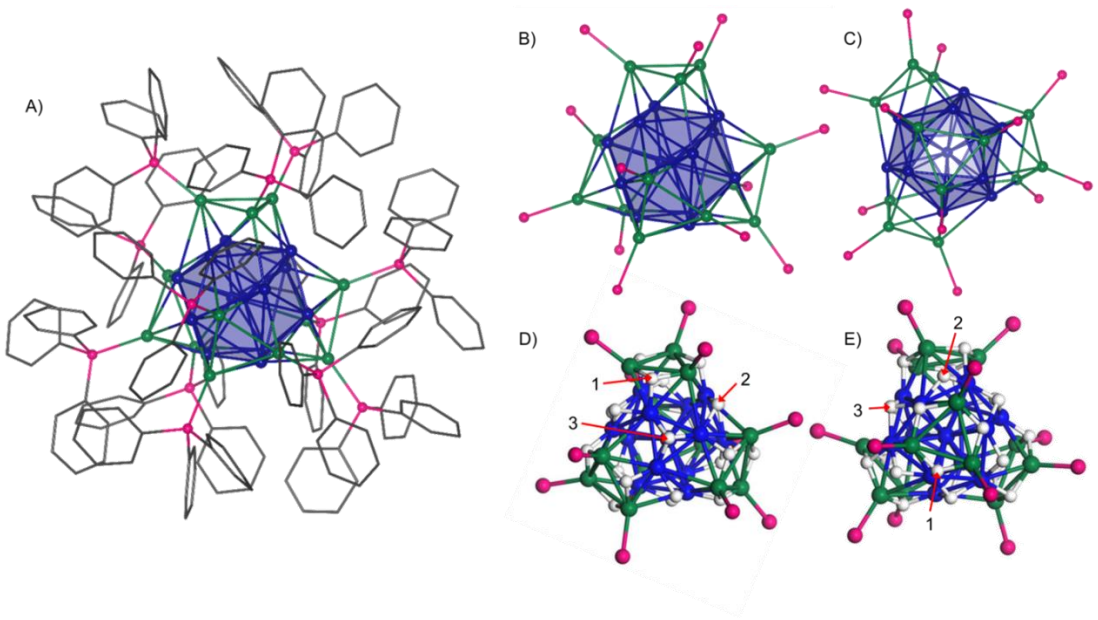

Figure 4.1. Ball and stick diagrams of **4.1**. The Cu_{13} centered-icosahedral core is highlighted in blue. The four $[Cu(PPh_3)]_3$ capping motifs are shown with the Cu atoms in green and P atoms in pink. (A) Side view with carbon atoms depicted in wireframe. All hydrogen atoms, chloride counterion, and solvent molecules have been omitted for clarity. (B) Side view showing only the Cu and P atoms. (C) Top view, looking down the C_3 axis, showing only the Cu and P atoms. (D) and (E) DFT-calculated structure prepared by Brian Goldsmith, optimized using the PW91 functional. Two views of the cluster are shown to facilitate visualization of the hydride ligand positions. The labels 1, 2, and 3 indicate one of the 12 equivalent μ_3-hydrides, one of six equivalent μ_4-hydrides, and one of the four equivalent μ_3-hydrides, respectively.

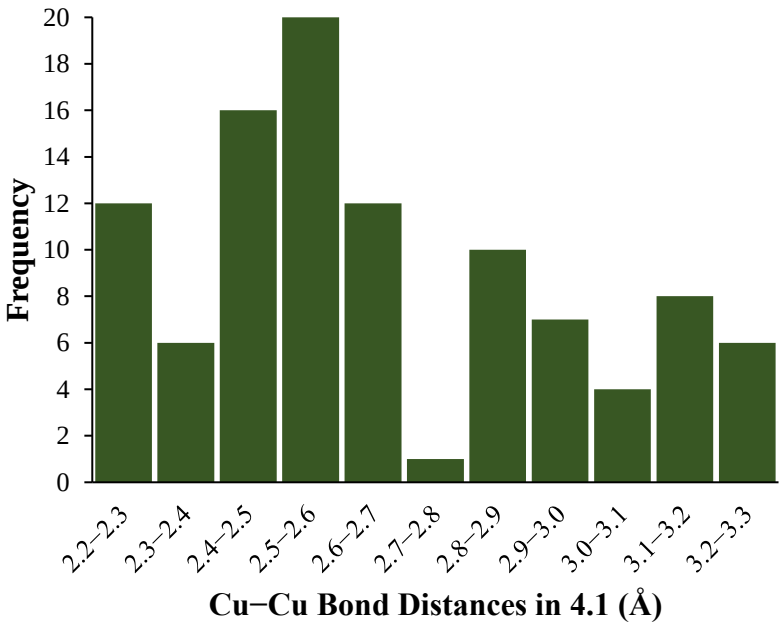

Figure 4.2. Histogram depicting the distribution of Cu–Cu bond distances in complex **4.1**.

Consistent with the high symmetry observed in the solid state, complex **4.1** features a single resonance in its $^{31}P\{^{1}H\}$ NMR spectrum, at -2.96 ppm in CD_2Cl_2. The ^{1}H NMR spectrum of **4.1** features three broad resonances at -0.92, 1.55, and 2.07 ppm, which integrate for 4H, 12H, and 6H, respectively, and are assignable to 22 hydride ligands in three different chemical environments. Interestingly, complex **4.1** features three unique phenyl environments in its ^{1}H NMR spectrum. This observation can be rationalized by assuming that there is no rotation about the Cu–P bonds on the NMR time scale (Figure 4.3)

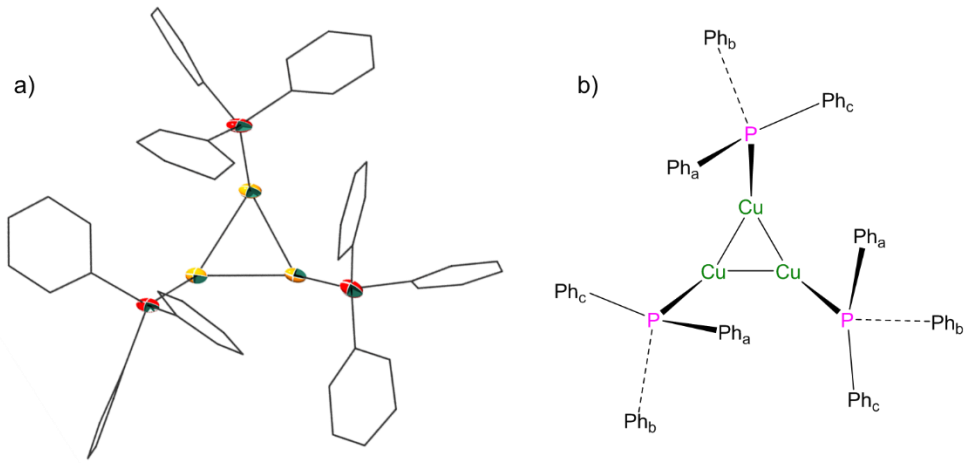

Figure 4.3. Diagrams of $[Cu(PPh_3)]_3$ from **4.1**. a) ORTEP diagram of a $[Cu(PPh_3)]_3$ unit from **4.1** with 50% probability ellipsoids for copper (yellow) and phosphorus (red) atoms. b) Schematic representation of a $[Cu(PPh_3)]_3$ unit in **4.1** depicting the three unique phenyl environments of the Ph_3P ligand. These occur as a result of limited rotation about the Cu–P bonds.

Interestingly, the ^{31}P NMR spectrum of **4.1** in C_6D_6 features many more resonances than the spectrum recorded in CD_2Cl_2. To explain this observation we suggest that its Cl^- counterion forms a contact ion pair in this non-polar solvent, breaking the symmetry of the cluster. Importantly, this transformation is reversible: recovery of this NMR sample and dissolution in CD_2Cl_2 regenerates the high symmetry structure (Figure A4.9). Complex **4.1** features a signal at m/z 4758.61 in its electrospray ionization (ESI) mass spectrum, which corresponds to the parent $[M]^+$ ion (calcd m/z 4758.50).

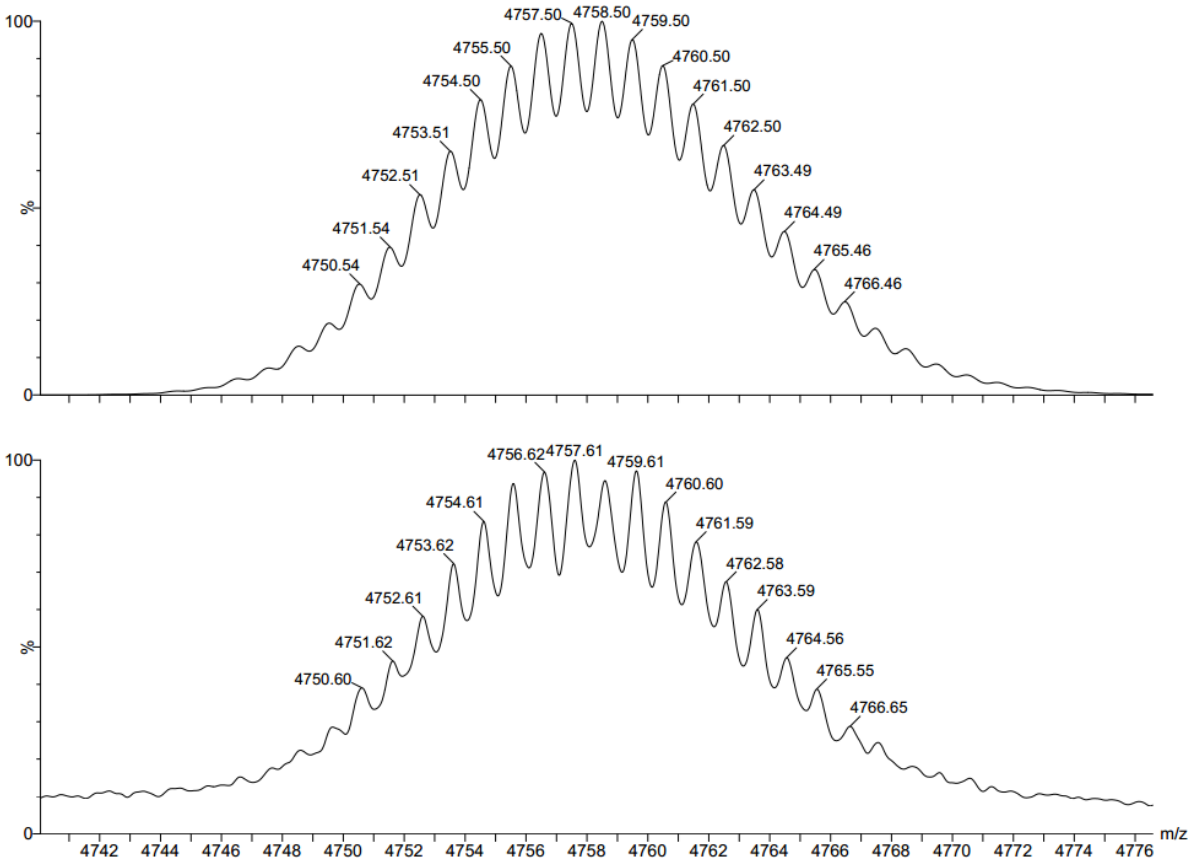

Figure 4.4. Partial ESI-MS of $[Cu_{25}H_{22}(PPh_3)_{12}]Cl$ (**4.1**). The experimental (bottom) and calculated (top) peaks assignable to the $[M]^+$ ion are shown.

Synthesis and characterization of the deuteride analogue, **4.1-*d*$_{22}$**, further supports the proposed formulation. As anticipated, complex **4.1-*d*$_{22}$** features singlets at -0.90, 1.65, and 2.11 ppm in its ^{2}H NMR spectrum, in a 4:12:6 ratio, respectively. In addition, complex **4.1-*d*$_{22}$** features a signal at *m/z* 4780.68 in its ESI mass spectrum, which corresponds to the $[M]^+$ parent ion (calcd. *m/z* 4780.64), a shift of 22 *m/z* versus the signal observed for **4.1-*h*$_{22}$**. Most importantly, with only 22 hydride ligands and one Cl^- counterion, two of the Cu atoms in complex **4.1** must have a formal Cu(0) oxidation state to maintain charge balance, making complex **4.1** the first Cu nanocluster with partial Cu(0) character. Alternately, complex **4.1** can be described as an $N^* = 2$ superatom with closed shell $1S^2$ configuration.[24] Notably,

there are only two other N^* = 2 superatoms known, namely, $Ag_{14}(SC_6H_3F_2)_{12}(PPh_3)_8$ and $Ag_{16}(SC_6H_3F_2)_{14}(DPPE)_8$ (DPPE = 1,2-bis(diphenylphosphino)ethane).[58-60]

Complex **4.2** crystallizes in the monoclinic space group $P2_1\bar{c}$, as a dichloromethane solvate, **4.2**·$4CH_2Cl_2$ (Figure 4.2). In the solid state, **4.2** features a square antiprism $[Cu_8H]^{7+}$ core, which is connected, via Cu–Cu bonds, to two axial $[Cu(PPh_3)]^+$ units and eight equatorial $[Cu(PPh_3)]^+$ units. As a result of this arrangement, the cluster occupies the D_{4d} point group. As was observed for **4.1**, the Cu-Cu bonds in **4.2** exhibit a large range (2.456(4) - 3.044(6) Å). These values are comparable to those exhibited by other CuH clusters, such as $[Cu_{14}H_{12}(phen)_6(PPh_3)_4]^{2+}$ (2.487 (3) – 2.915(3) Å)[31] and $[Cu_{20}H_{11}(S_2P(O^iPr)_2)_9]$ (2.3079 (7) – 2.8595(7) Å).[33] For further comparison, the average Cu-Cu distance in **4.2** (2.639 Å) is intermediate to the Cu−Cu distances reported for solid $[CuH]_x$ (2.85 Å) and Cu metal (2.55 Å).[52,61] The short (av. 2.559 Å) and long (av. 2.893 Å) edges of the square antiprism result in a large internal volume (19.0 $Å^3$), which is occupied by an interstitial hydride ligand (see below). The Cu−P distances (av. 2.24 Å) are similar to those of **4.1** and other Cu(I) phosphine complexes.[54,57] As with complex **4.1**, the outer sphere Cl^- counterion was observed to be disordered over two positions.

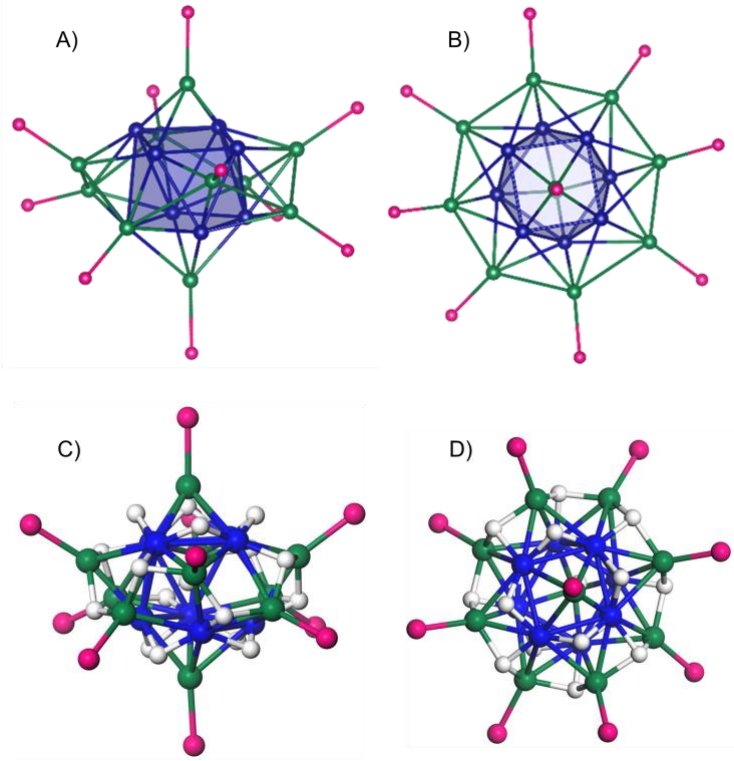

Figure 4.5. Ball and stick diagrams of **4.2**. The square antiprism Cu_8 core is highlighted in blue. The ten $[Cu(PPh_3)]^+$ capping units are shown with the Cu atoms in green and P atoms in pink. The hydride ligands are shown in white. (A) Side view showing only the Cu and P atoms. (B) Top view, looking down the C_4 axis, showing only the Cu and P atoms. (C) Side view of calculated structure, optimized using the PW91 functional. (D) Top view of calculated structure, optimized using the PW91 functional. C) and D) were prepared by Brian Goldsmith.

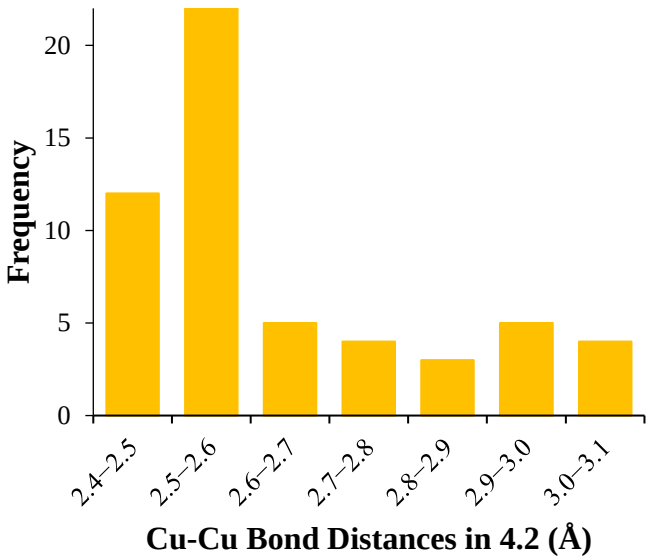

Figure 4.6. Histogram depicting the distribution of Cu–Cu bond distances in complex **4.2**.

Complex **4.2** features two resonances in its $^{31}P\{^{1}H\}$ NMR spectrum at -7.41 and 0.04 ppm in CD_2Cl_2, in a 1:4 ratio, respectively. These resonances are assigned to the two axial and eight equatorial PPh_3 ligands, respectively, and are consistent with the high symmetry observed in the solid state. The ^{1}H NMR spectrum of **4.2** features three broad resonances at 1.17, 2.74, and 10.58 ppm, which integrate for 8H, 8H, and 1H, respectively. These are assignable to 17 hydride ligands in three different chemical environments. As was observed for complex **4.1**, the ^{31}P NMR spectrum of **4.2** in C_6D_6 features more resonances than its spectrum recorded in CD_2Cl_2. In particular, seven resonances are observed, in a 2:2:2:1:1:1:1 ratio. This pattern can be rationalized by assuming that the Cl^- counterion binds to the cluster on a face defined by three equatorial phosphine ligands and one axial phosphine ligand. This interaction is likely quite weak, and probably promoted by the low dielectric constant of C_6D_6. Notably, recovery of this NMR sample and dissolution in

CD_2Cl_2 regenerates the high symmetry structure (Figure A4.11). Complex **4.2** features a signal at *m/z* 3783.80 in its ESI mass spectrum, which corresponds to the parent $[M]^+$ ion (calcd *m/z* 3783.78).

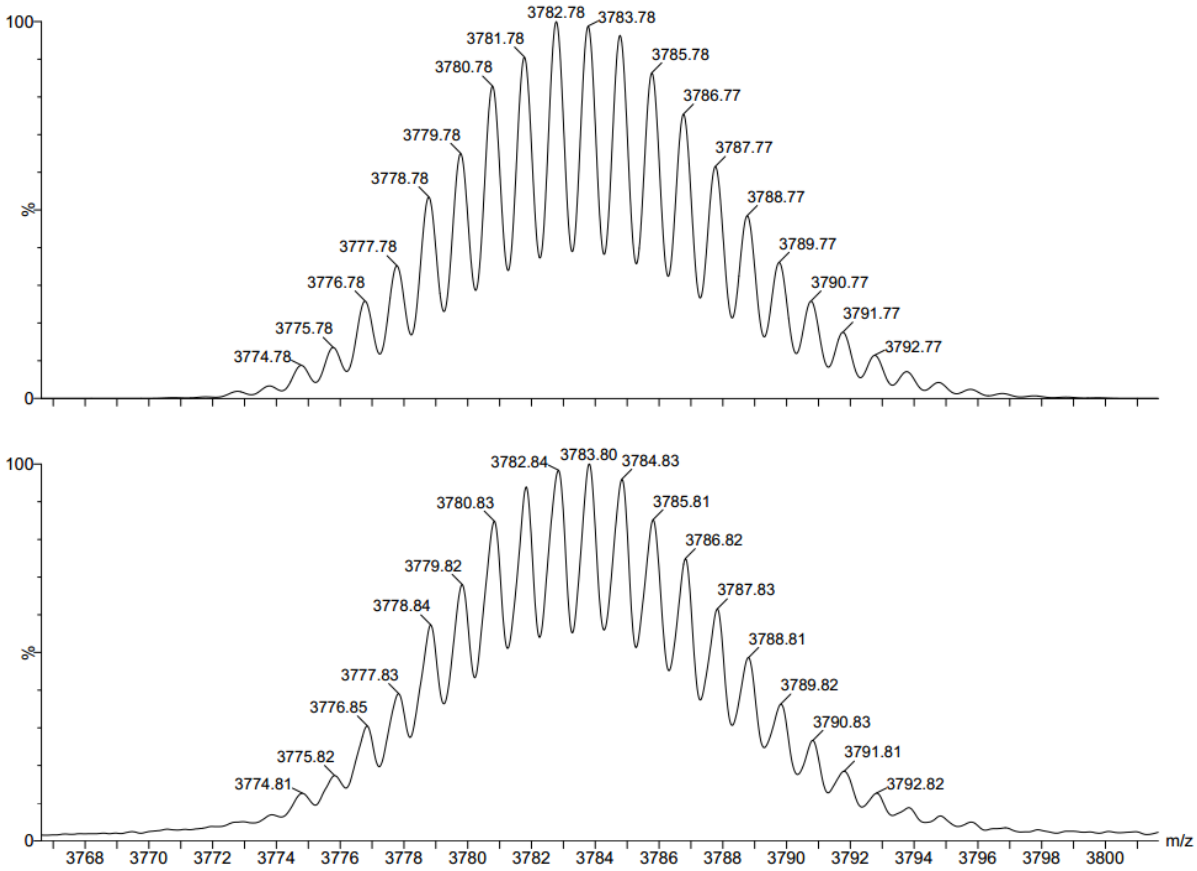

Figure 4.7. Partial ESI-MS of $[Cu_{18}H_{17}(PPh_3)_{10}]Cl$ (**4.2**). The experimental (bottom) and calculated (top) peaks assignable to the $[M]^+$ ion are shown.

Synthesis and characterization of the deuteride analogue, **4.2-*d*$_{17}$**, further supports these spectroscopic assignments. As anticipated, complex **4.2-*d*$_{17}$** features singlets at 1.25, 2.79, and 10.49 ppm in its ^2H NMR spectrum, in an 8:8:1 ratio, respectively. In addition, complex **4.2-*d*$_{17}$** features a signal at *m/z* 3800.95 in its ESI mass spectrum, which corresponds to the $[M]^+$ parent ion (calcd. *m/z* 3800.88), a shift of 17 *m/z* versus the signal observed for **4.2-*h*$_{17}$**.

Unlike complex **4.1**, with 17 hydride ligands and one Cl^- counterion, each Cu atom in **4.2** formally features a Cu(I) oxidation state assignment.

I also briefly probed the chemical properties of complexes **4.1** and **4.2**. Complex **4.1** is soluble in CH_2Cl_2 and THF, partially soluble in C_6H_6 and MeCN, and insoluble in Et_2O and non-polar solvents. It is stable in THF for at least 3 d. However, it very slowly reacts with CD_2Cl_2, generating complex **4.2**, H_2, copper metal, and $(Ph_3P)_3CuCl$ (Scheme 4.2). These products are observed in the reaction mixture after 48 h, according to ^1H and ^{31}P NMR spectroscopies (Figures A4.5 and A4.6). However, this is a very slow transformation, and even after 23 d, small amounts of complex **4.1** are still present in the NMR tube. I suggest that this reaction proceeds via hydride metathesis with the CD_2Cl_2 solvent, as was observed previously in the reaction of $[Cu_{14}H_{12}(phen)_6(PPh_3)_4][Cl]_2$ with CD_2Cl_2.[31] Complex **4.2** is soluble in CH_2Cl_2, partially soluble in C_6H_6, THF, and MeCN, and insoluble in Et_2O and non-polar solvents. Similar to **4.1**, complex **4.2** very slowly reacts with CD_2Cl_2, generating H_2, copper metal, and $(Ph_3P)_3CuCl$. Complex **4.1** is also formed in the reaction. These products are present in small amounts after 48 h, according to ^{31}P NMR spectroscopy (Figure A4.7). It should be noted; however, that even after 25 d, complex **4.2** is still the major component in the NMR sample. Thus it appears that the stability of **4.2** in CD_2Cl_2 is significantly higher than that of complex **4.1**.

Scheme 4.2. Reaction of complex **4.1** with CD_2Cl_2

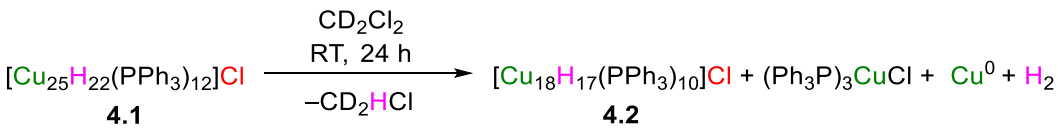

To confirm the proposed formulations, and to predict the locations of the 22 hydride ligands in **4.1**, as well as the 17 hydride ligands in **4.2**, I collaborated with Brian Goldsmith

from Prof. Baron Peters' group at UCSB. He explored their structures using density functional theory, as implemented in VASP 5.3.5.[62-64] The interactions between valence electrons and atoms were described using the PAW method.[65] He used both the PBE[66] and PW91[67] exchange-correlation functionals in order to compare and verify the predictions of different density functional approximations. The lowest energy structure for **4.1** is shown in Figures 4.1D and 4.1E. In this configuration, 12 equivalent hydride ligands are clustered into four groups of three. Each of these hydride ligands bridges two Cu atoms of a triangular $[Cu(PPh_3)]_3$ motif and one Cu atom belonging to the Cu_{13} icosahedron, in an overall μ_3-coordination environment. The six equivalent hydride ligands exhibit asymmetric μ_4-coordination, and are found along the six edges of the tetrahedron defined by the $[Cu(PPh_3)]_3$ motifs. For this environment, three of the Cu-H bond lengths are shorter (1.70 - 1.95 Å), whereas the fourth is much longer (2.3 - 2.5 Å). A similar asymmetry was observed for the μ_5-H environment in $[Cu_{32}H_{20}\{S_2P(O^iPr)_2\}_{12}]$.[36] The four remaining hydride ligands bridge three equivalent Cu atoms belonging to the Cu_{13} icosahedron, in an overall μ_3-coordination mode. Each of these hydride ligands is located directly opposite one of the four triangular $[Cu(PPh_3)]_3$ motifs. Overall, this 12:6:4 arrangement of hydrides is fully consistent with the NMR spectral data. Notably, this structure is calculated to be 0.4 eV lower in energy than the next most stable hydride conformation.

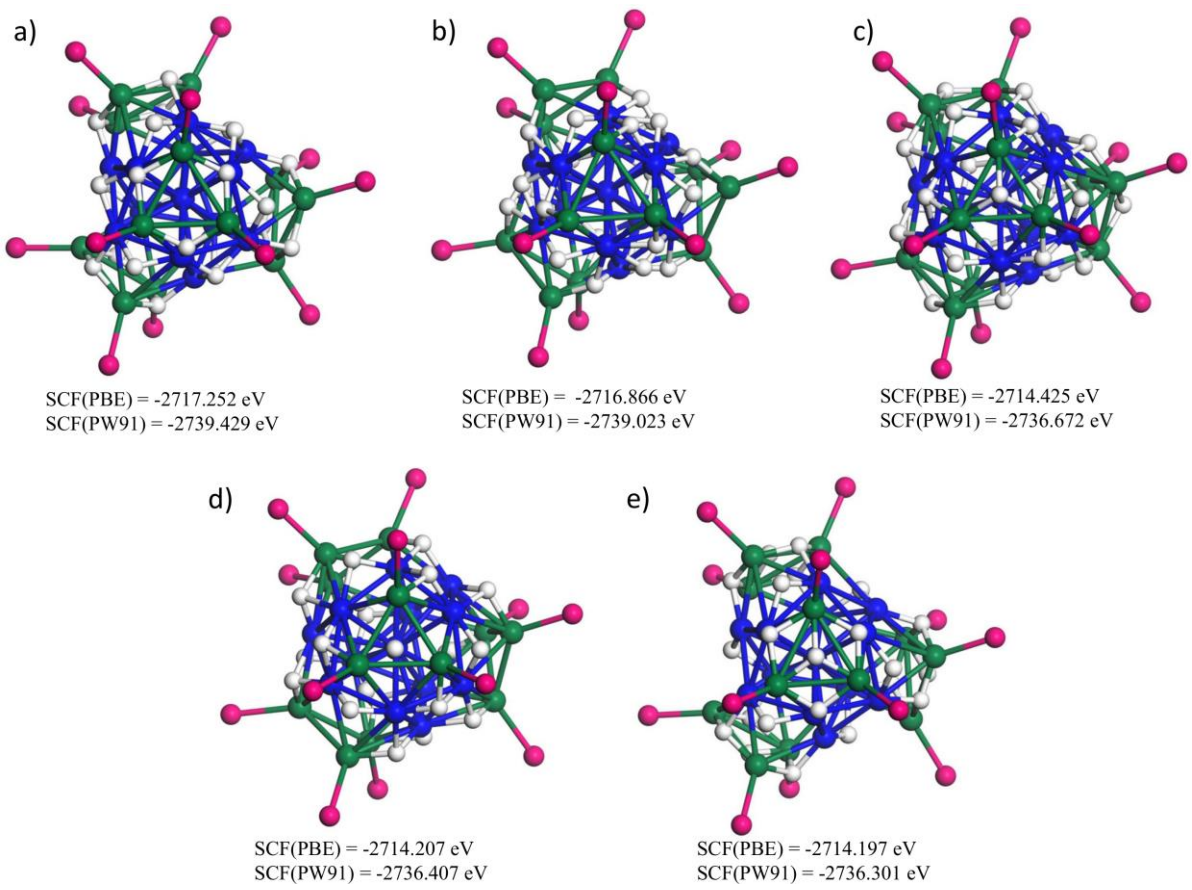

Figure 4.8. Optimized geometries of **4.1** for five different configuration of the 22 hydride ligands consistent with a 12:6:4 ratio. The energetics of each structure is shown, as computed using PBE or PW91. The Ph rings and Cl^- counterion are not shown for clarity. Structure a) is predicted to be most favourable by 0.4 eV compared to the second most stable structure b). Color legend: copper, green or blue; hydrogen, white; phosphorus, fuchsia. Figure prepared by Brian Goldsmith.

The lowest energy computed structure for **4.2** is shown in Figures 4.2C and 4.2D. This structure features eight equivalent hydride ligands, each with a μ_3-coordination mode, that reside along the cluster's equator. Another eight hydride ligands are clustered into two groups of four. These hydride ligands also feature a μ_3-coordination mode, and are located

above and below the equatorial plane. The remaining hydride ligand is positioned within the square antiprism, and features a μ_4-coordination mode, according to calculations. However, to account for the 8:8:1 arrangement of hydride ligands in the ^{1}H NMR spectrum, this interstitial hydride likely exhibits fluxional behavior, allowing it to coordinate equally to all eight Cu atoms of the square antiprism. Several alternate hydride positions were tested computationally for complex **4.2**; however, none of these proved to be minima on the potential energy surface.

Cu K-edge X-ray absorption near-edge spectra (XANES) and extended X-ray absorption fine structure (EXAFS) were acquired by Zach Jones, a graduate student in Prof. Susannah Scott's group at UCSB, to probe the average oxidation state and coordination number of Cu in complex **4.1**. He found that at 8979.6 eV, the edge position of complex **4.1** lies between the values for Cu foil (8979.0 eV) and $[CuH(PPh_3)]_6$ (8980.0 eV) (Table 4.1). This is consistent with an average Cu oxidation state in the cluster that is intermediate between 0 and +1, as the resolution of the spectrum is *ca.* 0.1 eV. Even though the differences in the energies are small, it is important that the edge energy of **4.1** is lower than that of $[CuH(PPh_3)]_6$ because **4.1** has a smaller ratio of PPh_3 ligands to Cu atoms, which should shift the edge energy of **4.1** higher than that of $[CuH(PPh_3)]_6$, assuming identical oxidation states for Cu in the two complexes. For example, the edge energy of $[CuCl(PPh_3)]_4$ (8980.9 eV) is shifted by 1.0 eV, compared to CuCl (8981.9 eV), with only the addition of PPh_3 (Table 4.1). Zach Jones also exctracted the Cu Auger parameter from his XPS spectrum of **4.1**.[68] This parameter can be used to discriminate between Cu(I) and Cu(0) and the value observed for **4.1** (1849.1 eV) lies between that recorded for $[CuH(PPh_3)]_6$ and Cu(0) (Table 4.1). This further supports the XANES K-edge energy assignment of complex **4.1** to an

oxidation state intermediate between Cu(I) and Cu(0). In addition, the Cu:P ratio for **4.1**, as determined by Zach Jones from the XPS, also matches the predicted value (Table 4.3).

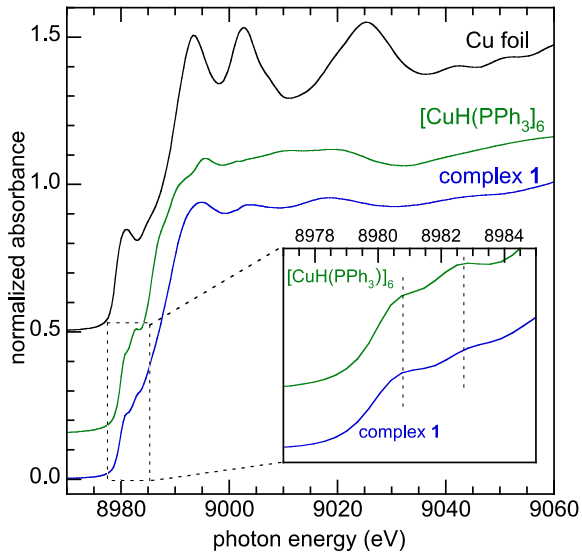

Figure 4.9. Comparison of Cu K-edge XANES profile of complex **4.1** with those of $[CuH(PPh_3)]_6$ and Cu foil standards (vertically offset). Figure prepared by Zach Jones.

Table 4.1. Cu K-edge energies and Auger parameters for selected Cu(0) and Cu(I) compounds. Data collected by Zach Jones.

Material	Edge (eV)	Auger parameter (eV)
Cu foil	8979.0	1851.2[68]
Cu nanoparticles (1-2 nm)	8979.0	1849.8-1850.8[69]
$[Cu_{25}H_{22}(PPh_3)_{12}][Cl]$ (**4.1**)	8979.6	1849.1
$[CuH(PPh_3)]_6$	8980.0	1848.6
$[CuCl(PPh_3)]_4$	8980.9	1847.4
CuCl	8981.9	1847.7

Zach Jones also analyzed the K-edge EXAFS to explore the accuracy of the technique for determining the size of Cu NCs even in the absence of crystal structure data. He was able to obtain a good curvefit of the data using a model with only two single-scattering paths: Cu-P and Cu-Cu. When he fixed the Cu-P degeneracy at 0.5, based on the known

stoichiometry of the cluster, the Cu-Cu coordination number was refined to 7.1 ± 0.9, which is almost identical to 7.2, the exact value obtained from the crystal structure. Even though, the Cu-Cu path (2.52 Å) has a large mean-square displacement, 0.013 $Å^2$, reflecting the large range in Cu-Cu distances (from 2.39 to 3.04 Å, as described above). Since the EXAFS resolution is *ca.* 0.1 Å, Zach Jones incorporated another Cu-Cu single-scattering path into the model. In the fit shown in Figure 4.4, the total Cu-Cu coordination number for both paths, (7.3 ± 1.2), is also consistent with the known value. Thus, we conclude that EXAFS analysis can provide reasonable estimates of coordination number in monodisperse Cu systems, despite the inherent large variation in Cu-Cu distances.

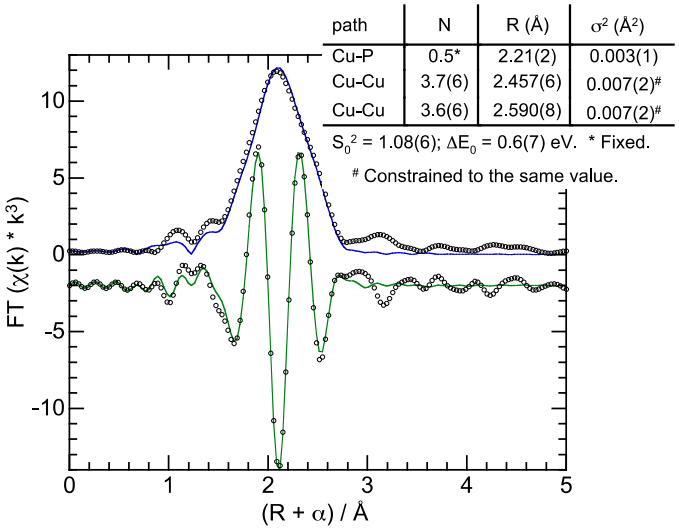

Figure 4.10. Cu K-edge EXAFS of complex 1 (points), in k^3-weighted *R*-space (non-phase-corrected), showing curvefit to the magnitude (blue) and imaginary component (green) of the Fourier transform, as well as the curvefit parameters. Figure prepared by Zach Jones.

4.3 Summary

I have isolated and structurally characterized $[Cu_{25}H_{22}(PPh_3)_{12}]Cl$ (**4.1**), the first copper nanocluster with partial Cu(0) character. This material is built around a Cu_{13} centered-icosahedron, similar to the coordination environment observed in Cu metal (and in agreement with DFT-predicted structures for Cu clusters and nanoparticles). Moreover, the Cu K-edge XANES shows that **4.1** features an edge energy intermediate between those of Cu(0) and Cu(I). The Auger parameter recorded for **4.1** also falls between those measured for Cu(0) and Cu(I). Taken together, these data demonstrate for the first time that NCs with Cu(0) character are isolable for copper. Going forward, I suggest that **4.1** could function as a template for the synthesis of Cu NCs that are larger, and that contain greater Cu(0) character. Furthermore, **4.1** represents a unique opportunity to study the reactivity of Cu nanoclusters, and with this in mind we have begun exploring its activity towards a variety of small molecules.

4.4 Experimental

4.4.1 General Procedures

All reactions and subsequent manipulations were performed under anaerobic and anhydrous conditions under an atmosphere of nitrogen. Hexanes, diethyl ether, and toluene were dried using a Vacuum Atmospheres DRI-SOLV Solvent Purification system and stored over 3Å sieves for 24 h prior to use. Dichloromethane, acetonitrile and benzene were degassed and dried over 3Å molecular sieves for 72 h prior to use. CD_2Cl_2, diphenylsilane, and diphenylsilane-*d*$_2$ (Sigma-Aldrich, 97 atom % D) were dried over 3Å molecular sieves for 24 h prior to use. $[(Ph_3P)CuH]_6$ and $[(Ph_3P)CuCl]_4$ were prepared according to the previously reported procedures.[31,70] Copper(I) acetate, 97% was purchased from Strem

chemicals and used as received. All other reagents were purchased from commercial suppliers and used as received.

All NMR spectra were collected at room temperature. ^{1}H NMR spectra were recorded on an Agilent Technologies 400-MR DD2 400 MHz spectrometer, a Varian Unity Inova 500 MHz spectrometer, or a Varian Unity Inova A S600 MHz spectrometer. ^{13}C{^{1}H} NMR spectra were recorded on an Agilent Technologies 400-MR DD2 400 MHz spectrometer or a Varian Unity Inova 500 MHz spectrometer. ^{31}P{^{1}H} and ^{2}H NMR spectra were recorded on an Agilent Technologies 400-MR DD2 400 MHz spectrometer. The chemical shifts of ^{31}P nuclei were referenced indirectly with the ^{1}H resonance of $SiMe_4$ at 0 ppm, according to IUPAC standard.[71,72] The chemical shifts of the other nuclei were referenced using the solvent peaks (^{1}H, ^{13}C and ^{2}H NMR experiments) as internal standards. IR spectra were recorded on a Nicolet 6700 FT-IR spectrometer with a NXR FT Raman Module. UV-Vis / NIR experiments were performed on a UV-3600 Shimadzu spectrophotometer. Mass spectra were collected by the Mass Spectrometry Facility at the University of California, Santa Barbara, using an electrospray ion (ESI) source on positive ion mode with a Waters Micromass QTOF2 Quadrupole/Time-of-Flight Tandem mass spectrometer. Mass spectra were smoothed 4 times using the mean algorithm with a smooth window of 3 channels. Elemental analyses were performed by the Micro-Mass Facility at the University of California, Berkeley.

4.4.2 Synthesis of $[Cu_{25}H_{22}(PPh_3)_{12}]Cl$ (4.1) and $[Cu_{18}H_{17}(PPh_3)_{10}]Cl$ (4.2)

To a stirring pale green suspension of Cu(OAc) (385.1 mg, 3.14 mmol), CuCl (12.9 mg, 0.13 mmol), and PPh_3 (415.1 mg, 1.58 mmol) in benzene (5 mL) was added diphenylsilane (0.32 mL, 1.7 mmol) via syringe. This resulted in a rapid color change to dark red and

dissolution of the pale green solid. After stirring for 14 h, this solution had become dark green concomitant with the deposition of a dark solid. CH_2Cl_2 (5 mL) was then added to the reaction mixture, which resulted in the dissolution of most of the solid. The green solution was filtered through a pre-weighed 0.2 μm PTFE membrane syringe filter to remove a brown powder. The filter was rinsed with CH_2Cl_2 until the filtrate was colorless then the filter was dried and weighed (35.3 mg, 17% yield of Cu^0 powder). This solid was brought out of the glovebox. Subsequent addition of 0.1 mL of 16 M HNO_3 to this solid resulted in effervescence and formation of a blue solution, consistent with the presence of Cu^{2+}(aq). In the glovebox, the solvent was removed from the filtrate *in vacuo*, and the resulting tacky green residue was redissolved in CH_2Cl_2 (5 mL). This solution was filtered through a Celite column (0.5 cm × 1 cm) supported on glass wool and the resulting dark green filtrate was layered with hexanes (10 mL). Storage of this solution at -25 °C for 72 h resulted in the deposition of a mixture of yellow and dark-green crystalline material, which was isolated by decanting off the supernatant. The solid was washed with hexanes (3 × 1 mL) and dried *in vacuo* (374.2 mg). This mixture was then extracted into benzene (15 mL) and filtered through a Celite column (0.5 cm × 2 cm) supported on glass wool to produce a green-brown filtrate. A dark green plug remained on the column. The green material was then dissolved in CH_2Cl_2 (3 mL) and filtered through the same Celite column into a separate vial. The green CH_2Cl_2 fraction was then layered with hexanes (8 mL), and storage of this solution at -25 °C for 24 h resulted in the deposition of complex **4.1** as a dark green powder, which was isolated by decanting off the brown supernatant. The green powder was washed with hexanes (3 × 1 mL) and dried *in vacuo* (145.4 mg, 23% yield of **4.1**). The benzene fraction was concentrated to ca. 3 mL *in vacuo*, whereupon CH_2Cl_2 (3 mL) was added. This solution

was then layered with Et_2O (10 mL). Storage of this solution at -25 °C for 24 h resulted in the deposition of complex **4.2** as X-ray quality yellow blocks, which were isolated by decanting off the green supernatant. The crystals were washed with Et_2O (3 × 1 mL) and dried *in vacuo* (70.9 mg, 14% yield of **4.2**). X-ray quality crystals of **4.1** were grown from a dilute CH_2Cl_2 solution layered with an equal volume of hexanes, which was stored at -25 °C for 24 h. Complex **4.1**: Anal. Calcd for $C_{216}H_{202}ClCu_{25}P_{12}$: C, 54.12; H, 4.25. Found: C, 54.43; H, 4.26. ^{1}H NMR (400 MHz, 25 °C, CD_2Cl_2): δ -0.91 (s, 4H, hydride), 1.56 (s, 12H, hydride), 2.08 (s, 6H, hydride), 5.84 (t, J_{HH} = 7.3 Hz, 24H, *m*-C*H*), 6.08 (t, J_{HH} = 7.1 Hz, 24H, *m*-C*H*), 6.41−6.52 (m, 36H, *m*-C*H* overlapping with *p*-C*H*), 6.64−6.74 (m, 36H, *o*-C*H* overlapping with *p*-C*H*), 6.82 (t, J_{HH} = 7.2 Hz, 12H, *p*-C*H*), 7.00 (m, 24H, *o*-C*H*), 7.95 (t, J_{HH} = 8.8 Hz, 24H, *o*-C*H*). ^{31}P{^{1}H} NMR (162 MHz, 25 °C, CD_2Cl_2): δ -2.96 (s, *P*Ph$_3$). ^{31}P{^{1}H} NMR (162 MHz, 25 °C, C_6D_6): δ -6.14, -5.74, -5.46, -5.30, -4.92, -4.70, -3.51, -3.08, -2.81, -2.62, 1.48. ^{13}C{^{1}H} NMR (101 MHz, 25 °C, CD_2Cl_2): δ 127.99 (d, J_{CP} = 10.3 Hz, *m*-C), 128.18 (s, *p*-C), 128.44 (d, J_{CP} = 7.7 Hz, *m*-C), 129.04 (s, *p*-C), 129.27 (d, J_{CP} = 9.1 Hz, *m*-C), 130.52 (s, *p*-C), 133.16–133.72 (m, *o*-C overlapping with *ipso*-C), 135.11 (d, J_{CP} = 17.4 Hz, *o*-C), 135.33−136.00 (m, *o*-C overlapping with *ipso*-C), 136.37 (d, J_{CP} = 15.1 Hz, *o*-C). ESI-MS: *m/z* 4758.61 $[M]^+$ (Calcd *m/z* 4758.50). IR (KBr pellet, cm^{-1}): 412 (w), 436 (w), 518 (s), 619 (w), 693 (s), 742 (s), 804 (w), 847 (w), 998 (w), 1027 (m), 1070 (w), 1094 (s), 1157 (w), 1183 (w), 1262 (w), 1310 (w), 1385 (w), 1434 (s), 1479 (m), 1571 (w), 1585 (w), 1813 (w), 1890 (w), 1955 (w). UV-Vis (CH_2Cl_2, 0.035 mM, 25 °C, L·mol^{-1}·cm^{-1}): 450 (ε = 19000), 650 (ε = 7500). Complex **4.2**: Anal. Calcd for $C_{180}H_{167}ClCu_{18}P_{10}$: C, 56.61; H, 4.41. Found: C, 56.38; H, 4.20. ^{1}H NMR (400 MHz, 25 °C, CD_2Cl_2): δ 1.17 (s, 8H, hydride), 2.74 (s, 8H, hydride), 6.39 (t, J_{HH} = 7.0 Hz, 12H, *m*-C*H* axial PPh$_3$), 6.55 (t, J_{HH} =

7.1 Hz, 48H, *m*-C*H* equatorial PPh_3), 6.84 (t, J_{HH} = 7.2 Hz, 6H, *p*-C*H* axial PPh_3), 6.88–6.97 (m, 36H, *p*-C*H* equatorial PPh_3 overlapping with *o*-C*H* axial PPh_3), 7.12 (t, J_{HH} = 8.8 Hz, 48H, *o*-C*H* equatorial PPh_3), 10.58 (s, 1H, interstitial hydride). $^{31}P\{^1H\}$ NMR (162 MHz, 25 °C, CD_2Cl_2): δ -7.41 (s, 2P, axial *P*Ph_3), 0.04 (s, 8P, equatorial *P*Ph_3). ^{31}P NMR (162 MHz, 25 °C, C_6D_6): δ -7.91 (s, 2P), -6.76 (s, 2P), -5.36 (s, 2P), -0.26 (s, 1P), 0.06 (s, 1P), 0.81 (s, 1P), 2.14 (s, 1P). $^{13}C\{^1H\}$ NMR (101 MHz, 25 °C, CD_2Cl_2): δ 128.61−128.98 (m, overlapping *m*-C, axial and equatorial PPh_3), 129.42 (s, *p*-C equatorial PPh_3), 129.60 (s, *p*-C on axial PPh_3), 133.54 (d, J_{CP} = 32.3 Hz, *ipso*-C axial PPh_3), 134.13−134.69 (m, overlapping *o*-C, axial and equatorial PPh_3), 135.13 (d, J_{CP} = 29.0 Hz, *ipso*-C equatorial PPh_3). ESI-MS: *m/z* 3783.80 $[M]^+$ (Calcd *m/z* 3783.78). IR (KBr pellet, cm^{-1}): 413 (w), 441 (w), 518 (s), 619 (w), 693 (s), 742 (s), 803 (w), 845 (w), 998 (w), 1027 (m), 1070 (w), 1093 (m), 1157 (w), 1183 (w), 1262 (w), 1310 (w), 1384 (w), 1434 (s), 1479 (m), 1571 (w), 1585 (w), 1813 (w), 1891 (w), 1957 (w). UV-Vis (CH_2Cl_2, 0.066 mM, 25 °C, $L \cdot mol^{-1} \cdot cm^{-1}$): 450 (sh, ε = 6600).

4.4.3 Synthesis of $[Cu_{25}D_{22}(PPh_3)_{12}]Cl$ (4.1-*d*$_{22}$) and $[Cu_{18}D_{17}(PPh_3)_{10}]Cl$ (4.2-*d*$_{17}$)

To a stirring pale green suspension of Cu(OAc) (359.1 mg, 2.93 mmol), CuCl (12.0 mg, 0.12 mmol) and PPh_3 (382.8 mg, 1.46 mmol) in benzene (5 mL) was added diphenylsilane-*d*$_2$ (0.29 mL, 1.6 mmol) via syringe. This resulted in a rapid color change to dark red, concomitant with dissolution of the pale green solid. After stirring for 12 h, this solution had become dark brown concomitant with the deposition of a dark solid. CH_2Cl_2 (5 mL) was added to the reaction mixture, which resulted in the dissolution of most of the solid. The resulting dark green solution was filtered through a Celite column (0.5 cm × 2 cm) supported on glass wool. The solvent was removed from the filtrate *in vacuo* and the resulting tacky green residue was redissolved in CH_2Cl_2 (5 mL). This solution was filtered

through a Celite column (0.5 cm × 1 cm) supported on glass wool, whereupon the green filtrate was layered with hexanes (15 mL). Storage of this solution at -25 °C for 24 h resulted in the deposition of a mixture of yellow solid and dark green solid, which was isolated by decanting off the supernatant. The solid was washed with pentane (3 × 1 mL) and dried *in vacuo* (346.8 mg). This mixture was then extracted into benzene (15 mL) and filtered through a Celite column (0.5 cm × 2 cm) supported on glass wool to produce a brown filtrate. A dark green plug remained on the column. This dark green solid was then dissolved in CH_2Cl_2 (3 mL) and filtered through the same Celite column into a separate vial. The green CH_2Cl_2 fraction was concentrated and then layered with toluene (12 mL). Storage of this solution at -25 °C for 48 h resulted in the deposition of complex **4.1-*d*$_{22}$** as a dark crystalline solid, which was isolated by decanting off the green supernatant. The solid was washed with benzene (2 mL) then pentane (2 × 1 mL) and dried *in vacuo* (173 mg, 29% yield of **4.1-*d*$_{22}$**). The solvent was removed from the benzene filtrate *in vacuo* and the resulting brown residue was dissolved in CH_2Cl_2 (2 mL). This dark brown solution was layered with Et_2O (10 mL). Storage of this solution at -25 °C for 24 h resulted in the deposition of a brown powder, which was isolated by decanting off the dark green-brown supernatant. This brown powder was again dissolved in CH_2Cl_2 (7 mL) and filtered through a Celite column (0.5 cm × 1 cm) supported on glass wool. The filtrate was then layered with Et_2O (12 mL) and storage of this solution at -25 °C for 24 h resulted in the deposition of complex **4.2-*d*$_{17}$** as a yellow crystalline solid, which was isolated by decanting off the brown supernatant. The solid was washed with Et_2O (3 × 1 mL) and dried *in vacuo* (59.9 mg, 10% yield of **4.2-*d*$_{17}$**). Complex **4.1-*d*$_{22}$**: ^{1}H NMR (400 MHz, 25 °C, CD_2Cl_2): δ 5.83 (t, J_{HH} = 7.2 Hz, 24H, *m*-C*H*), 6.08 (t, J_{HH} = 7.1 Hz, 24H, *m*-C*H*), 6.39−6.51 (m, 36H, *m*-C*H* overlapping

with *p*-C*H*), 6.63−6.74 (m, 36H, *o*-C*H* overlapping with *p*-C*H*), 6.82 (t, J_{HH} = 7.2 Hz, 12H, *p*-C*H*), 7.00 (t, J_{HH} = 9.1 Hz, 24H, *o*-C*H*), 7.95 (t, J_{HH} = 8.8 Hz, 24H, *o*-C*H*). ^{2}H NMR (61 MHz, 25 °C, CH_2Cl_2): δ -0.90 (s, 4D), 1.65 (s, 12D), 2.11 (s, 6D). $^{31}P\{^{1}H\}$ NMR (162 MHz, 25 °C, CD_2Cl_2): δ -3.05 (s, *P*Ph_3). ESI-MS: *m/z* 4780.68 $[M]^+$ (Calcd *m/z* 4780.64). Complex **4.2-*d*$_{17}$**: ^{1}H NMR (400 MHz, 25 °C, CD_2Cl_2): δ 6.39 (t, J_{HH} = 6.9 Hz, 12H, *m*-C*H* axial PPh_3), 6.54 (t, J_{HH} = 7.0 Hz, 48H, *m*-C*H* equatorial PPh_3), 6.85 (t, J_{HH} = 7.4 Hz, 6H, *p*-C*H* axial PPh_3), 6.88–6.96 (m, 36H, *p*-C*H* equatorial PPh_3 overlapping with *o*-C*H* axial PPh_3), 7.11 (t, J_{HH} = 8.7 Hz, 48H, *o*-C*H* equatorial PPh_3). ^{2}H NMR (61 MHz, 25 °C, CD_2Cl_2): δ 1.25 (s, 8D), 2.79 (s, 8D), 10.49 (s, 1D). $^{31}P\{^{1}H\}$ NMR (162 MHz, 25 °C, CD_2Cl_2): δ -7.20 (s, 2P, axial *P*Ph_3), -0.08 (s, 8P, equatorial *P*Ph_3). ESI-MS: *m/z* 3800.95 $[M]^+$ (Calcd *m/z* 3800.88).

4.4.4 Monitoring the formation of $[Cu_{25}H_{22}(PPh_3)_{12}]Cl$ (4.1) and $[Cu_{18}H_{17}(PPh_3)_{10}]Cl$ (4.2) by NMR spectroscopy

A pale green suspension of Cu(OAc) (51.2 mg, 0.42 mmol), CuCl (1.7 mg, 0.017 mmol), and PPh_3 (54.2 mg, 0.21 mmol) in C_6D_6 (1 mL) was transferred to a J. Young NMR tube. Subsequently, Ph_2SiH_2 (40 µL, 0.22 mmol) was added via microsyringe, whereupon the pale green solid dissolved and the solution became dark orange red. Over the course of 3 h, the reaction mixture gradually turned dark brown in color, concomitant with the deposition of a dark solid. After 18 h, the reaction mixture was dark green brown in color and more solid had precipitated. ^{1}H and $^{31}P\{^{1}H\}$ NMR spectra were then recorded. The ^{1}H NMR spectrum reveals the formation of a resonance at 4.46 ppm assignable to H_2 (Figure A4.3), while resonances assignable to complexes **4.1** and **4.2** also appear in the ^{31}P NMR spectra (Figure A4.4a). In addition, several resonances assignable to unidentified PPh_3-

containing products are also present. Note that complex **4.1** partially precipitates under these conditions. As a result, complex **4.2** appears to be the major product.

4.4.5 Monitoring the reaction of 25 equiv of Cu(OAc) with 12 equiv of PPh_3 and 13 equiv of Ph_2SiH_2, with no CuCl present, by NMR spectroscopy

A pale green suspension of Cu(OAc) (14.9 mg, 0.12 mmol) and PPh_3 (15.5 mg, 0.059 mmol) in C_6D_6 (1 mL) was transferred to a J. Young NMR tube. Subsequently, Ph_2SiH_2 (12 µL, 0.065 mmol) was added via microsyringe, whereupon the pale green solid dissolved and the solution became orange in color. The reaction mixture gradually turned dark brown in color over the course of 18 h. A $^{31}P\{^1H\}$ NMR spectrum was then recorded (Figure A4.4b). The NMR spectra reveal the presence of several unidentified products; however, neither complex **4.1** nor **4.2** are present in the sample.

4.4.6 Monitoring the reaction of 25 equiv of CuCl with 15 equiv of PPh_3 and 13 equiv of Ph_2SiH_2, with no Cu(OAc) present, by NMR spectroscopy

A colorless suspension of CuCl (9.3 mg, 0.094 mmol) and PPh_3 (14.7 mg, 0.056 mmol) in C_6D_6 (0.8 mL) was transferred to a J. Young NMR tube. Subsequently, Ph_2SiH_2 (10 µL, 0.054 mmol) was added via microsyringe. No change was observed upon addition of silane to the colorless suspension. This reaction was then monitored by NMR spectroscopy for 20 h. No evidence for the formation of a copper hydride complex was observed during this time.

4.4.7 Reaction of $[Cu_{25}H_{22}(PPh_3)_{12}]Cl$ (4.1) with CD_2Cl_2

Complex **4.1** (7.9 mg, 0.0016 mmol) was dissolved in CD_2Cl_2 (700 µL). The dark green solution was then transferred to a J. Young NMR tube and monitored by NMR spectroscopy

for 23 d. After 30 h, the reaction mixture still appeared dark green; however, a small amount of copper metal had deposited on the walls of the tube. NMR spectra were recorded at 48 h and 23 d. The soluble decomposition products were identified to be complex **4.2**, by comparison of the spectral data to those of an independently prepared sample, and $(Ph_3P)_3CuCl$, by comparison of the spectral data to those of a sample prepared according to literature procedures.[70] H_2 was also detected in the reaction mixture using ^1H NMR spectroscopy. *23 day spectra:* ^1H NMR (400 MHz, 25 °C, CD_2Cl_2): δ -0.91 (s, 4H, hydride, **4.1**), 1.15 (s, 8H, hydride, **4.2**), 1.56 (s, 12H, hydride, **4.1**), 2.08 (s, 6H, hydride, **4.1**), 2.74 (s, 8H, hydride, **4.2**), 4.60 (s, H_2), 5.84 (t, J_{HH} = 7.3 Hz, 24H, *m*-C*H*, **4.1**), 6.08 (t, J_{HH} = 7.8 Hz, 24H, *m*-C*H*, **4.1**), 6.39 (t, J_{HH} = 7.2 Hz, 12H, *m*-C*H* axial PPh_3, **4.2**), 6.42−6.51 (m, 36H, *m*-C*H* overlapping with *p*-C*H*, **4.1**), 6.54 (t, J_{HH} = 7.2 Hz, 48H, *m*-C*H* equatorial PPh_3, **4.2**), 6.65−6.74 (m, 36H, *o*-C*H* overlapping with *p*-C*H*, **4.1**), 6.79−6.88 (m, *p*-C*H* on **4.1** overlapping with *p*-C*H* (axial PPh_3) on **4.2**), 6.88–6.96 (m, 36H, *p*-C*H* equatorial PPh_3 overlapping with *o*-C*H* axial PPh_3, **4.2**), 7.00 (m, 24H, *o*-C*H*, **4.1**), 7.12 (m, 48H, *o*-C*H* equatorial PPh_3, **4.2**), 7.25–7.31 (m, 6H, $(Ph_3P)_3CuCl$)), 7.33–7.41 (m, 9H, $(Ph_3P)_3CuCl$)), 7.95 (m, 24H, *o*-C*H*, **4.1**), 10.59 (s, 1H, interstitial hydride, **4.2**). $^{31}P\{^1H\}$ NMR (162 MHz, 25 °C, CD_2Cl_2): δ -7.41 (s, 2P, axial *P*Ph_3, **4.2**), -4.65 (s, *P*Ph_3, $(Ph_3P)_3CuCl$)), -2.95 (s, *P*Ph_3, **4.1**), 0.05 (s, 8P, equatorial *P*Ph_3, **4.2**).

4.4.8 Reaction of $[Cu_{18}H_{17}(PPh_3)_{10}]Cl$ (4.2) with CD_2Cl_2

Complex **4.2** (7.9 mg, 0.0016 mmol) was dissolved in CD_2Cl_2 (700 µL). The yellow solution was then transferred to a J. Young NMR tube and monitored by NMR spectroscopy for 25 d. After 48 h, the solution became greenish yellow and a small amount of copper metal deposited on the walls of the tube. A small amount of yellow solid, likely complex

4.2, started to precipitate after 20 d. There were no other obvious changes over the course of 25 d. NMR spectra were recorded at 48 h and 23 d. The soluble decomposition products were identified to be complex **4.1**, by comparison of the spectral data to those of an independently prepared sample, and $(Ph_3P)_3CuCl$, by comparison of the spectral data to those of a sample prepared according to literature procedures.[70] H_2 was also detected in the reaction mixture using ^{1}H NMR spectroscopy. *25 day spectra:* ^{1}H NMR (400 MHz, 25 °C, CD_2Cl_2): δ -0.93 (s, 4H, hydride, **4.1**), 1.15 (s, 8H, hydride, **4.2**), 1.56 (s, 12H, hydride, **4.1**), 2.08 (s, 6H, hydride, **4.1**), 2.74 (s, 8H, hydride, **4.2**), 4.60 (s, H_2), 5.83 (t, J_{HH} = 7.1 Hz, 24H, *m*-C*H*, **4.1**), 6.08 (t, J_{HH} = 7.3 Hz, 24H, *m*-C*H*, **4.1**), 6.38 (t, J_{HH} = 7.1 Hz, 12H, *m*-C*H* axial PPh_3, **4.2**), 6.42−6.50 (m, 36H, *m*-C*H* overlapping with *p*-C*H*, **4.1**), 6.54 (t, $J_{H\,H}$ = 7.0 Hz, 48H, *m*-C*H* equatorial PPh_3, **4.2**), 6.64−6.72 (m, 36H, *o*-C*H* overlapping with *p*-C*H*, **4.1**), 6.79−6.87 (m, *p*-C*H* on **4.1** overlapping with *p*-C*H* (axial PPh_3) on **4.2**), 6.87–6.96 (m, 36H, *p*-C*H* equatorial PPh_3 overlapping with *o*-C*H* axial PPh_3, **4.2**), 7.00 (m, 24H, *o*-C*H*, **4.1**), 7.12 (m, 48H, *o*-C*H* equatorial PPh_3, **4.2**), 7.24–7.32 (m, 6H, $(Ph_3P)_3CuCl$)), 7.32–7.41 (m, 9H, $(Ph_3P)_3CuCl$)), 7.95 (m, 24H, *o*-C*H*, **4.1**), 10.59 (s, 1H, interstitial hydride, **4.2**). $^{31}P\{^1H\}$ NMR (162 MHz, 25 °C, CD_2Cl_2): δ -7.42 (s, 2P, axial *P*Ph_3, **4.2**), -4.88 (s, *P*Ph_3, $(Ph_3P)_3CuCl$)), -2.98 (s, *P*Ph_3, **4.1**), 0.03 (s, 8P, equatorial *P*Ph_3, **4.2**).

4.4.9 X-ray Crystallography

Data for **4.1**·$4C_6H_{14}$·$0.5CH_2Cl_2$ and **4.2**·$4CH_2Cl_2$ were collected on a Bruker KAPPA APEX II diffractometer equipped with an APEX II CCD detector using a TRIUMPH monochromater with a MoKα X-ray source (α = 0.71073 Å). Crystals were mounted on a cryoloop under Paratone-N oil, and all data were collected at 100(2) K using an Oxford nitrogen gas cryostream system. X-ray data for **4.1**·$4C_6H_{14}$·$0.5CH_2Cl_2$ were collected

utilizing frame exposures of 10 (low angle) and 30 s (high angle), while data for **4.2**·4CH_2Cl_2 were collected utilizing frame exposures of 5 (low angle) and 10 s (high angle). Data collection and cell parameter determination were conducted using the SMART program.[73] Integration of the data frames and final cell parameter refinement were performed using SAINT software.[74] Absorption correction of the data were carried out using the multi-scan method SADABS.[75] Subsequent calculations were carried out using SHELXTL.[76] Structure determination was done using direct methods and difference Fourier techniques. All hydrogen atom positions were idealized, and rode on the atom of attachment. The final refinement included anisotropic temperature factors on all Cu and P atoms. The remaining atoms were refined isotropically. The 22 hydride ligands on **4.1**·4C_6H_{14}·0.5CH_2Cl_2 and 17 hydride ligands on **4.2**·4CH_2Cl_2 were not located in the difference Fourier maps due to the high electron density around the copper cores. Structure solution, refinement, graphics, and creation of publication materials were performed using SHELXTL.[76]

Complexes **4.1**·4C_6H_{14}·0.5CH_2Cl_2 and **4.2**·4CH_2Cl_2 each exhibit positional disorder of their Cl^- counterions and solvate molecules. The positional disorder of the Cl^- counterion in **4.1**·4C_6H_{14}·0.5CH_2Cl_2 was addressed by modeling it in 2 positions, in a 50:50 ratio. The positional disorder of the four hexanes solvate molecules were addressed by modeling them in 8 positions, each with half occupancy. The CH_2Cl_2 solvate molecule was assigned half occupancy. The positional disorder of the Cl^- counterion in **4.2**·4CH_2Cl_2 was addressed by modelling it in 2 positions, in a 60:40 ratio. The positional disorder of the four CH_2Cl_2 solvate molecules was addressed by modelling them in 8 positions, each with half occupancy. In addition, the C–Cl bonds in the CH_2Cl_2 solvate molecules were fixed with the

DFIX command. Selected C–C bonds within the Ph_3P ligands were also fixed with the DFIX command, while some rings were constrained with the FLAT command.

Table 4.2. X-ray Crystallographic Data for **4.1**·$4C_6H_{14}$·$0.5CH_2Cl_2$ and **4.2**·$4CH_2Cl_2$

	4.1·$4C_6H_{14}$·$0.5CH_2Cl_2$	**4.2**·$4CH_2Cl_2$
empirical formula	$C_{240.5}H_{259}Cl_2Cu_{25}P_{12}$	$C_{184}H_{175}Cl_9Cu_{18}P_{10}$
crystal habit, color	block, dark green	plate, yellow
crystal size (mm)	0.15 × 0.10 × 0.10	0.30 × 0.30 × 0.10
crystal system	orthorhombic	monoclinic
space group	*Pbca*	*P2₁/c*
volume (Å^3)	49752(3)	19021.7(17)
a (Å)	33.3092(11)	28.6582(14)
b (Å)	38.3322(13)	17.4260(10)
c (Å)	38.9657(13)	38.0893(19)
α (deg)	90.00	90.00
β (deg)	90.00	90.095(3)
γ (deg)	90.00	90.00
Z	8	8
formula weight (g/mol)	5180.50	4158.70
density (calculated) (Mg/m^3)	1.383	1.452
absorption coefficient (mm^{-1})	2.230	2.222
F_{000}	21128	8416
total no. reflections	283227	167876
unique reflections	42819	50851
final R indices [I >2σ(I)]	R_1 = 0.2142 wR_2 = 0.2956	R_1 = 0.3191 wR_2 = 0.5838
largest diff. peak and hole (e$^-$ A^{-3})	4.436 and -1.424	9.325 and -3.966
GOF	1.104	1.080

4.4.10 X-ray Absorption Spectroscopy

X-ray absorption near-edge spectra (XANES) and extended X-ray absorption fine structure (EXAFS) at the Cu *K*-edge (8979 eV) were recorded in transmission mode on Beamline 4-1 (bend) at the Stanford Synchrotron Radiation Lightsource (SSRL), which operates at 3.0 GeV with a ring current of 500 mA. X-rays were monochromatized via reflection from a Si(220) double crystal monochromator, φ = 90°, and passed through a 1 × 7 mm entrance slit. The beam was detuned 30 % to reject harmonics. Data were collected with step size of 0.35 eV over the region 40 eV before the edge, and 20 eV after the edge.

This results in a near-edge resolution of ca. 0.1 eV. X-ray absorption data were acquired up to k = 15 Å^{-1}. N_2-filled ionization detectors were mounted in the beam before and after the sample to collect data in transmission mode. A Cu foil was inserted prior to a third ionization chamber, for simultaneous energy calibration. Complex **4.1** and the Cu standards were diluted with boron nitride (99.5% purity, Fischer Scientific) in a N_2 glovebox, to give samples containing ca. 10 wt% Cu to minimize self-absorption effects. The diluted materials were loaded into slotted Al sample plates (slot size 12 × 3 × 0.5 mm) and sealed under N_2, using Kapton tape (5 μm, DuPont). The plates were transferred to a liquid He flow cryostat (Oxford Instruments) and cooled to <15 K. Six scans were recorded and averaged for each sample. Subsequent scans showed no changes, confirming the integrity of each sample under the measurement conditions.

Data processing and analysis were performed using the Demeter software package (0.9.20).[77] The averaged spectra were aligned using the edge energy of the Cu foil spectrum. Absorption edge positions were assigned as the first maximum in the first derivative of the spectrum. A linear pre-edge function was subtracted, and then the data were normalized by the edge height using Athena software. A smooth, third-order polynomial approximating the absorption background of an isolated atom was subtracted to yield $\chi(k)$. The data were then k^3-weighted and Fourier-transformed. EXAFS analysis was conducted with paths generated by FEFF6 from the crystallographic information for complex **4.1** obtained by single crystal X-ray diffraction. The coordination number (N), the distance of the scattering atoms (R), and the mean-squared displacement (σ^2) of the neighboring scatterers, were obtained by non-linear least-squares refinement in R-space using the EXAFS equation. The amplitude reduction factor (S_0^2) and the energy shift parameter (ΔE_0) were refined as global fit

parameters. Their values were then fixed while the values of *R* and σ^2 were refined. Finally, the values of *N* were refined while holding *R* and σ^2 values fixed.

4.4.11 Measurement of Auger parameter

X-ray photoelectron spectroscopy was performed on a Kratos Ultra X-ray photoelectron spectroscopy (XPS) system equipped with an Al-K_α (1559 eV) radiation source. Samples were loaded under a N_2 atmosphere into a custom-built, air-free sample holder. Prior to data collection, a baseline vacuum of 1 x 10^{-8} Torr was achieved. For high resolution scans, a band pass energy of 40 eV was used. Binding energies were calibrated using the C 1*s* peak at 284.6 eV. The peak positions in the Cu 2*p* region and the LMM Auger emission were determined using the Casa XPS software package. The Auger parameter was calculated as the sum of the Cu $2p_{3/2}$ binding energy and the kinetic energy of the LMM Auger line.

4.4.12 X-ray Photoelectron Spectroscopy

P:Cu ratios were also determined by X-ray photoelectron spectroscopy. Survey scans were conducted at a band pass energy of 120 eV. The relative abundance of each element (at%) was calculated from the area of the Cu 2*p*, Cl 2*p*, P 2*p* and C 1*s* peaks. Integrations were performed using the CASA XPS software with Tougaard background correction and Scofield photo-ionization cross-sections.

Table 4.3. XPS Survey Scan Results for Cu Clusters

Complex	Relative abundance (at%)				P:Cu ratio	
	Cu	Cl	C	P	Expt.	Calc.
1	7.1	0.7	89	3.5	0.49	0.48
$[CuH(PPh_3)]_6$	3.9	-	92	4.1	1.1	1
$[CuCl(PPh_3)]_4$	3.9	4.5	88	4.1	1.1	1

4.4.13 Simulation Methodology

The simulation box was specified as a 34.975 × 29.997 × 30.461 *Å* simple cubic cell for $[Cu_{18}H_{17}(PPh_3)_{10}]Cl$ (**4.2**) geometry relaxations while the box size was 37.000 × 37.000 × 37.000 *Å* for $[Cu_{25}H_{22}(PPh_3)_{12}]Cl$ (**4.1**) geometry relaxations. The Kohn−Sham wave functions were expanded by plane waves with a default kinetic energy cutoff as specified in the POTCAR. Standard VASP PAW_GGA pseudopotentials were used [C (08Oct1999), Cl (21Jan2003), Cu (05Jan2001), H (07Jul1998), and P (21Jan2003)] when modeling **2**.[65,78] The same PAW_GGA pseudopotentials were used when modeling **4.1**, except a soft pseudopotential for carbon was employed to increase computational efficiency. The Γ point was used to sample the Brillouin zone. All geometries were relaxed using the conjugate-gradient algorithm until the Hellman−Feynman force on each atom was less than 0.03 eV $Å^{-1}$. All atoms except for the Cu and hydride ligands were fixed in place according to the experimental crystal structure. Relaxing all atoms of the clusters was prohibitively expensive due to their large sizes. All possible structures of **4.2** and **4.1** with 1:8:8 and 12:6:4 equivalent hydrides, respectively, were computed. The most favorable computed geometries of $[Cu_{25}H_{22}(PPh_3)_{12}]Cl$ are shown in Figure 4.8, with structure (a) being the most likely using either PW91 or PBE.

Table 4.4. Comparison of average bond lengths (Å) between **4.1** and its calculated lowest energy molecular structure using the PBE and PW91 functionals

	Expt.	PBE	PW91
Cu_{center}–Cu_{icos}	2.64	2.62	2.63
Cu_{icos}–Cu_{icos}[a]	3.19	3.16	3.17
Cu_{icos}–Cu_{icos}[b]	2.51	2.50	2.50
Cu_{icos}–Cu_P[c]	2.50	2.49	2.50
Cu_{icos}–Cu_P[d]	3.01	3.02	3.02
Cu_P–Cu_P	2.87	2.84	2.84

Cu_P–P	2.26	2.26	2.26

[a]Edges of the icosahedron defined by the Cu_{icos} atoms that interact with the two Cu atoms from the same triangular $[Cu_3(PPh_3)]_3$ unit. [b]Remaining Cu_{icos}–Cu_{icos} edges not included in *a*. [c]Edges formed when a Cu_{icos} atom interacts with the two Cu atoms from the same triangular $[Cu_3(PPh_3)]_3$ unit . [d]Longer Cu_{icos}–Cu_P bonds not included in *c*.

Table 4.5. Comparison of average bond lengths (Å) between **4.2** and its calculated molecular structure using the PBE and PW91 functionals

	Expt.	PBE	PW91
$Cu_{anitprism}$–$Cu_{antiprism}$[a]	2.56	2.56	2.57
$Cu_{anitprism}$–$Cu_{anitprism}$[b]	2.89	2.90	2.93
$Cu_{anitprism}$–$Cu_{P,ax}$	2.52	2.53	2.53
$Cu_{anitprism}$–$Cu_{P,eq}$	2.54	2.54	2.55
$Cu_{P,eq}$–$Cu_{P,eq}$	2.96	2.95	2.95
Cu_P–P	2.24	2.23	2.23

[a]Edges defined by the square faces of the antiprism. [b]Edges defined by the triangular faces of the antiprism.

4.5 Appendix

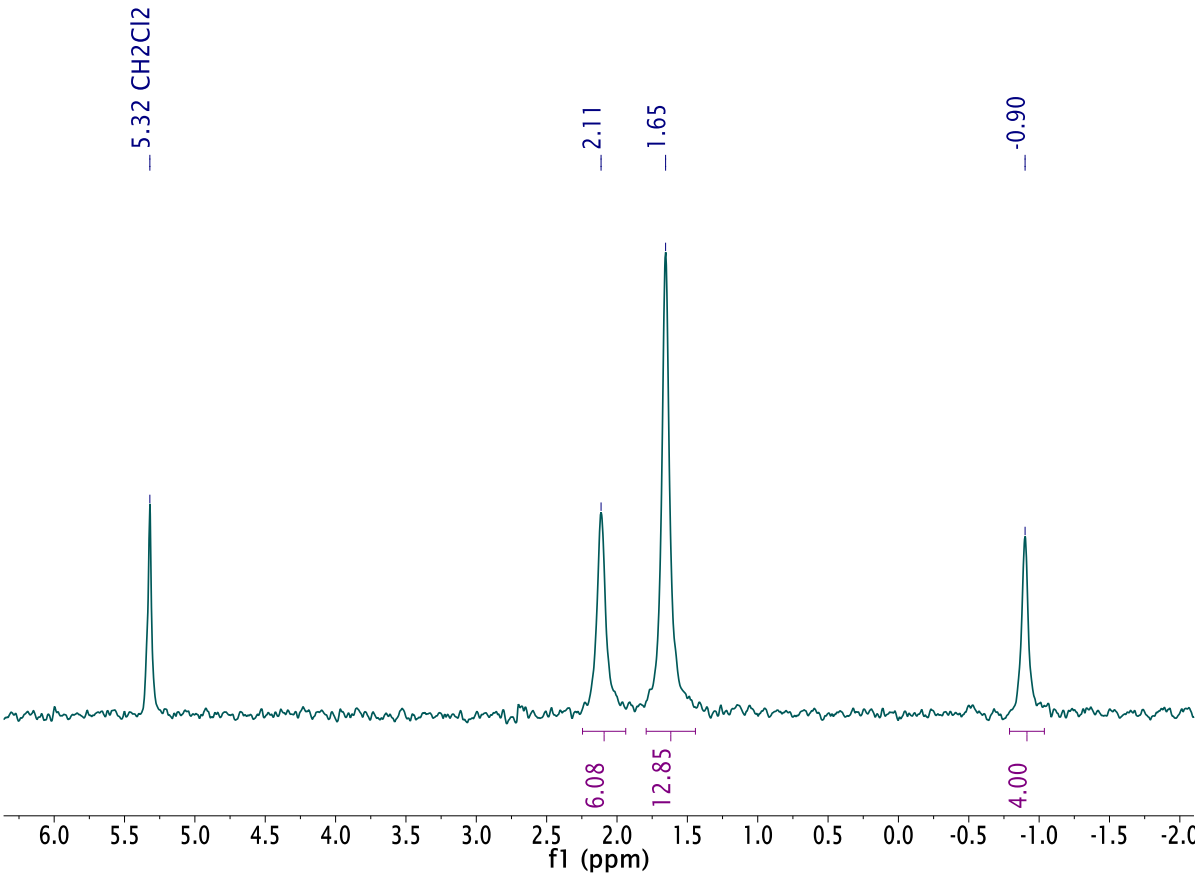

Figure A4.1. ^{2}H NMR spectrum of $[Cu_{25}H_{22}(PPh_3)_{12}]Cl$ (**4.1-*d*$_{22}$**) in CD_2Cl_2.

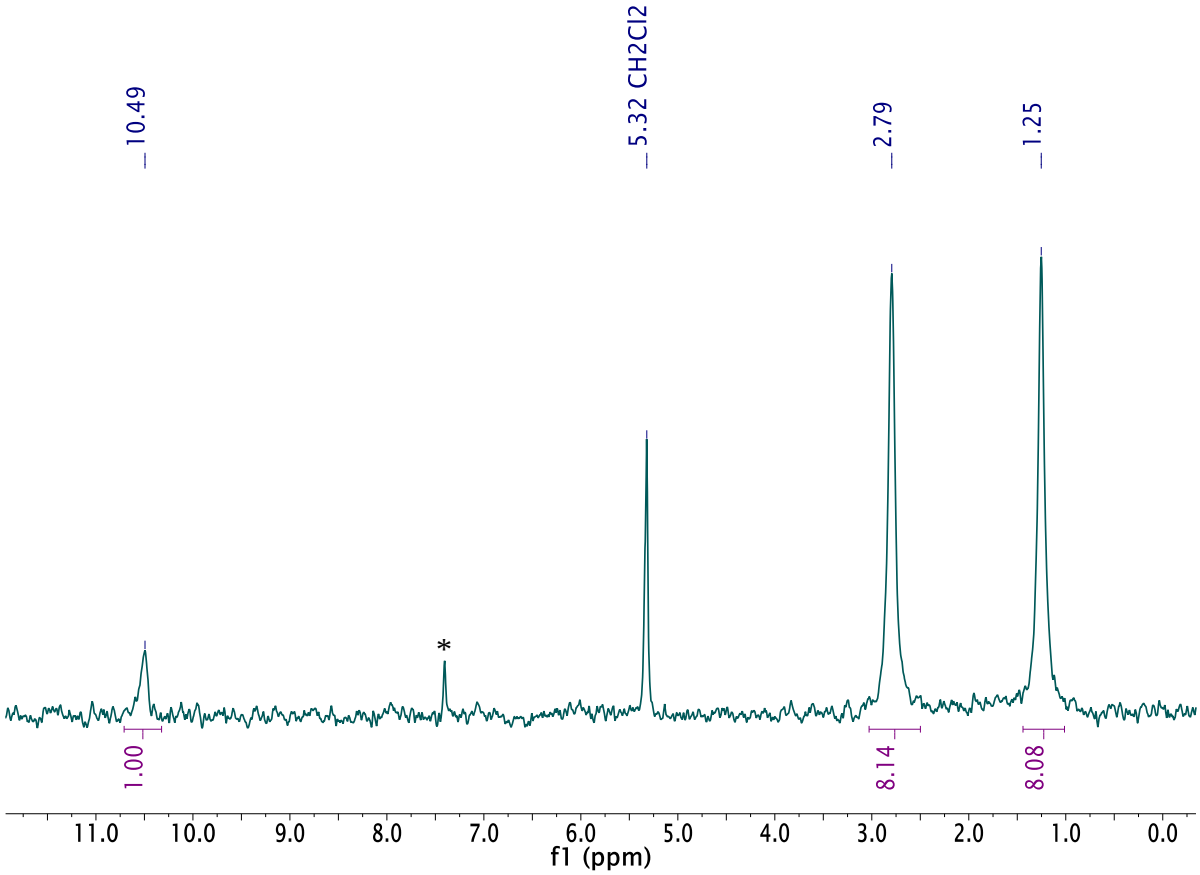

Figure A4.2. ^{2}H NMR spectrum of $[Cu_{18}D_{17}(PPh_3)_{10}]Cl$ (**4.2-*d*$_{17}$**) in CD_2Cl_2. (*) denotes the presence of benzene.

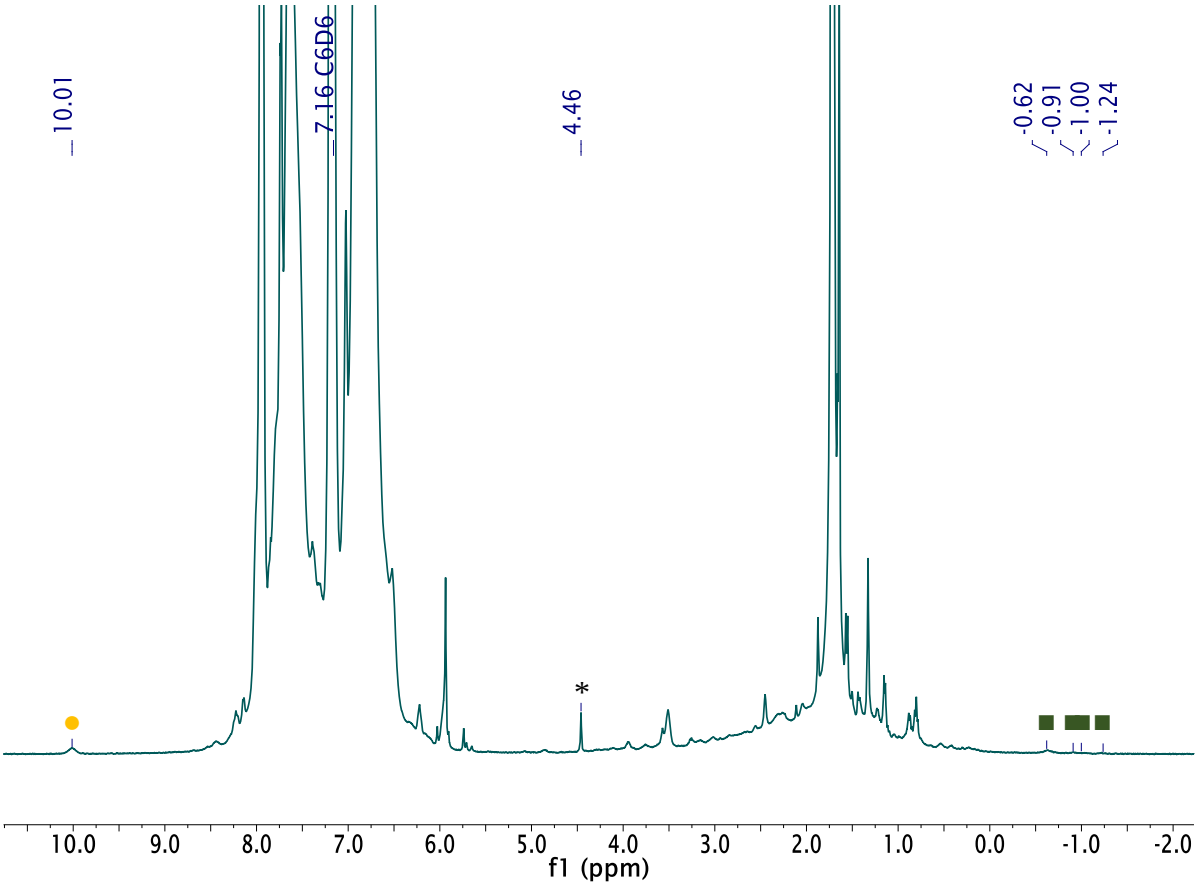

Figure A4.3. *In situ* ^{1}H NMR spectrum of the formation **4.1** and **4.2** after 18 h in C_6D_6. (*) denotes the resonance assignable to H_2, while (■) and (●) indicate hydride resonances assignable to 1 and 2, respectively.

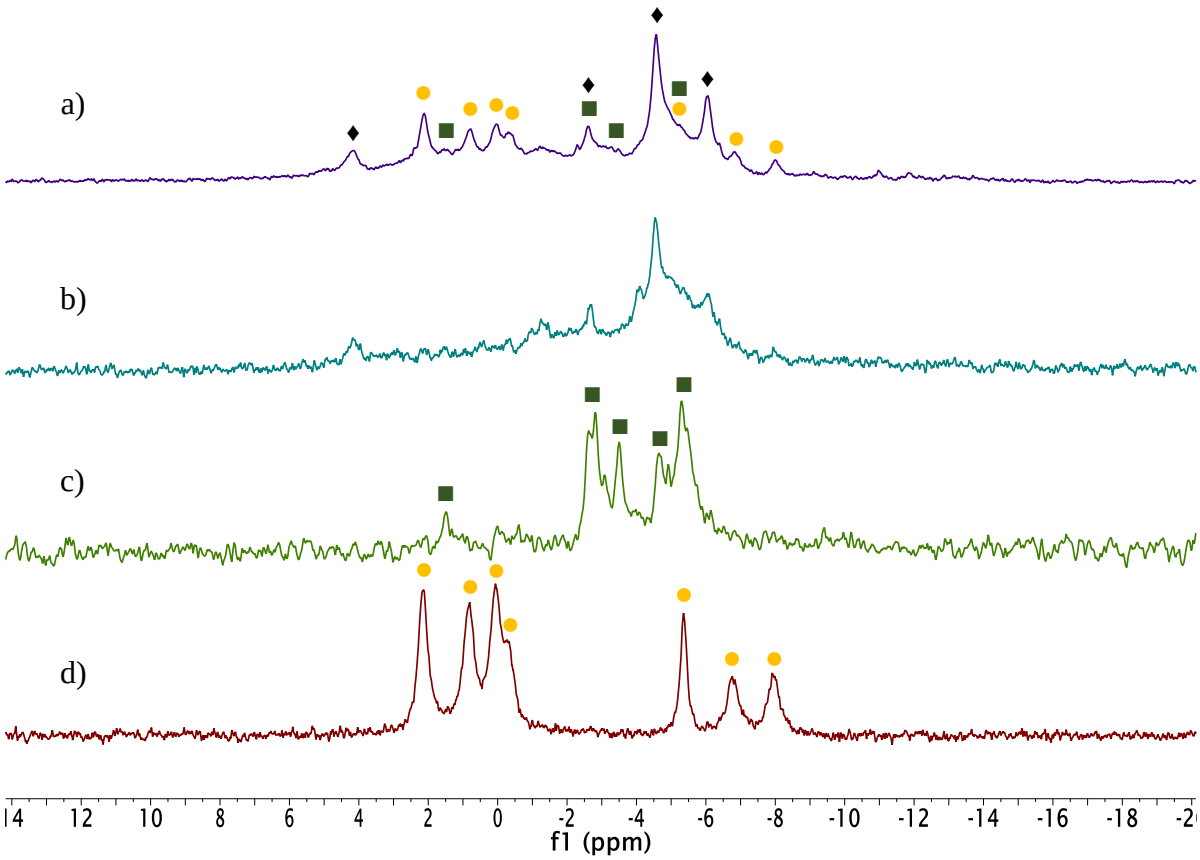

Figure A4.4. Comparison of $^{31}P\{^{1}H\}$ NMR spectra in C_6D_6. a) *In situ* spectrum of the formation $[Cu_{25}H_{22}(PPh_3)_{12}]Cl$ (**4.1**) and $[Cu_{18}H_{17}(PPh_3)_{10}]Cl$ (**4.2**) after 18 h. (Both **4.1** and **4.2** have limited solubility in C_6D_6, but **4.2** is slightly more soluble, which is why **4.2** appears to be the major product). (■) and (●) indicate resonances assignable to **4.1** and **4.2**, respectively, while (♦) denotes the presence of unidentified products. b) *In situ* spectrum of the reaction of 25 equiv of Cu(OAc) with 12 equiv of PPh_3 and 13 equiv of Ph_2SiH_2, with no CuCl present, after 18 h. c) Isolated sample of authentic complex **4.1**. d) Isolated sample of authentic complex **4.2**. Note: the ^{1}H and ^{31}P NMR spectra for both 1 and 2 in C_6D_6 have more resonances than expected, likely because their Cl^- counterions form contact ion pairs in this solvent, breaking the symmetry of the clusters.

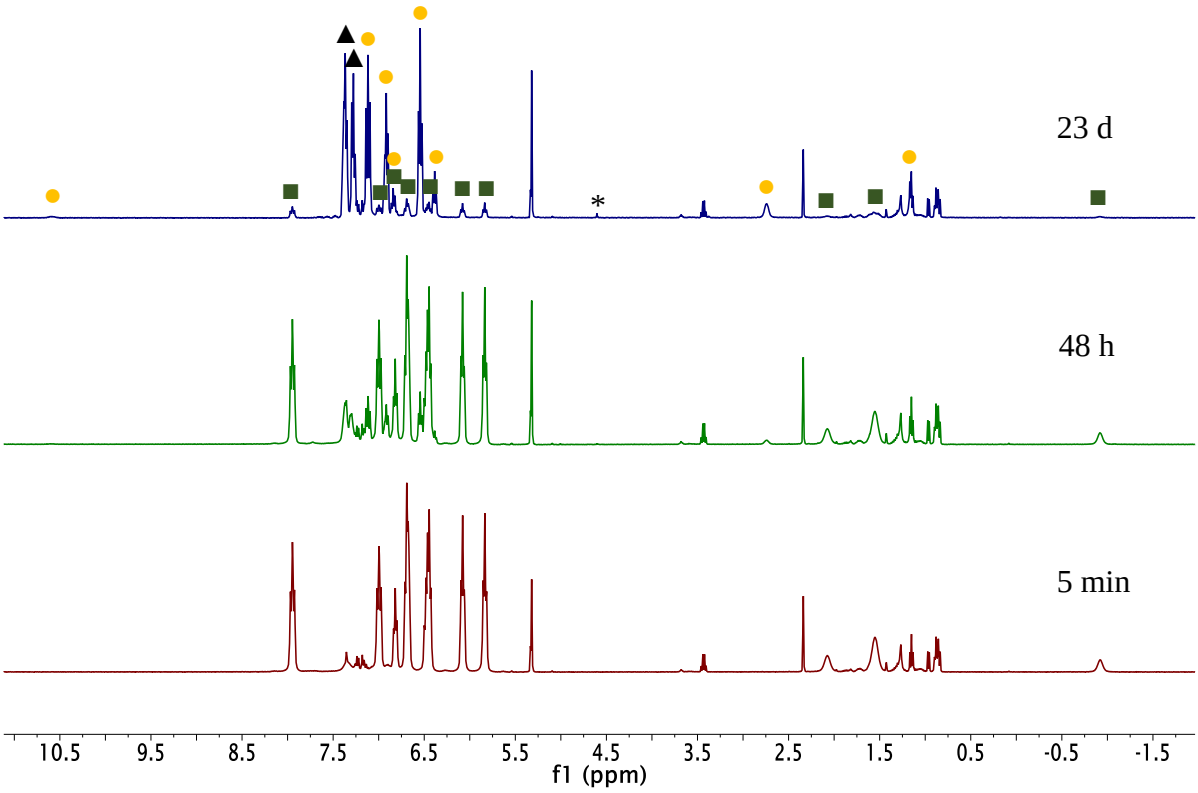

Figure A4.5. *In situ* ^{1}H NMR spectra of the reaction of $[Cu_{25}H_{22}(PPh_3)_{12}]Cl$ (**4.1**) with CD_2Cl_2. (*) denotes the presence of H_2 gas. (■) and (●) indicate resonances assignable to **4.1** and **4.2**, respectively, while (▲) denotes the presence of $(Ph_3P)_3CuCl$.

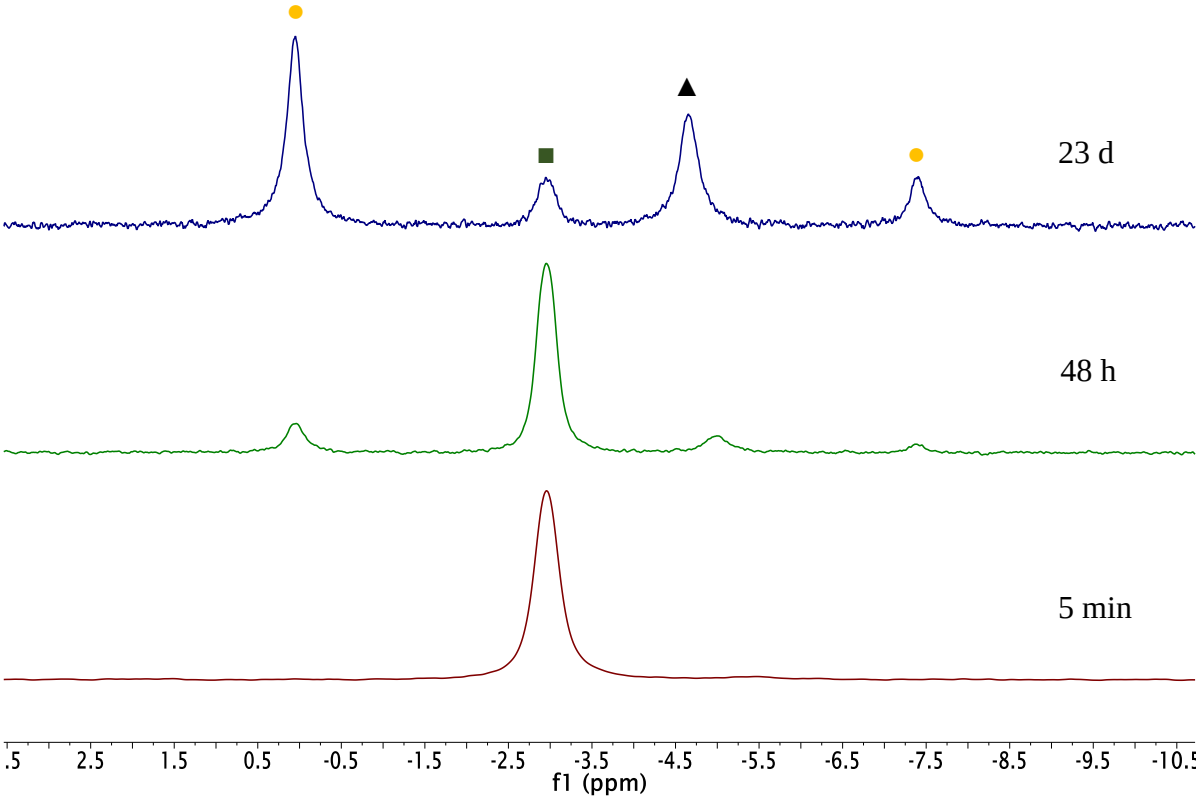

Figure A4.6. *In situ* $^{31}P\{^{1}H\}$ NMR spectra of the reaction of $[Cu_{25}H_{22}(PPh_3)_{12}]Cl$ (**4.1**) with CD_2Cl_2. (■) and (●) indicate resonances assignable to **4.1** and **4.2**, respectively, while (▲) denotes the presence of $(Ph_3P)_3CuCl$.

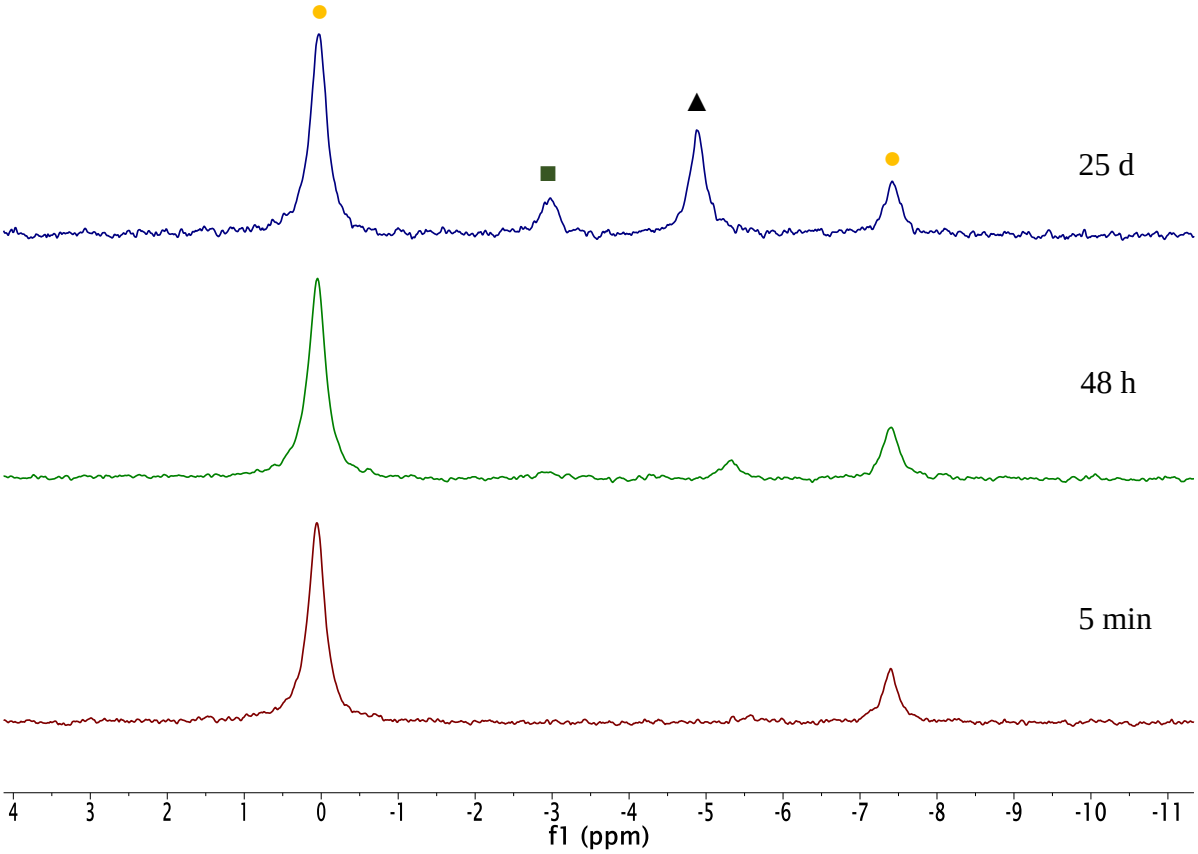

Figure A4.7. *In situ* $^{31}P\{^{1}H\}$ NMR spectra of the reaction of $[Cu_{18}H_{17}(PPh_3)_{10}]Cl$ (**4.2**) with CD_2Cl_2. (■) and (●) indicate resonances assignable to **4.1** and **4.2**, respectively, while (▲) denotes the presence of $(Ph_3P)_3CuCl$.

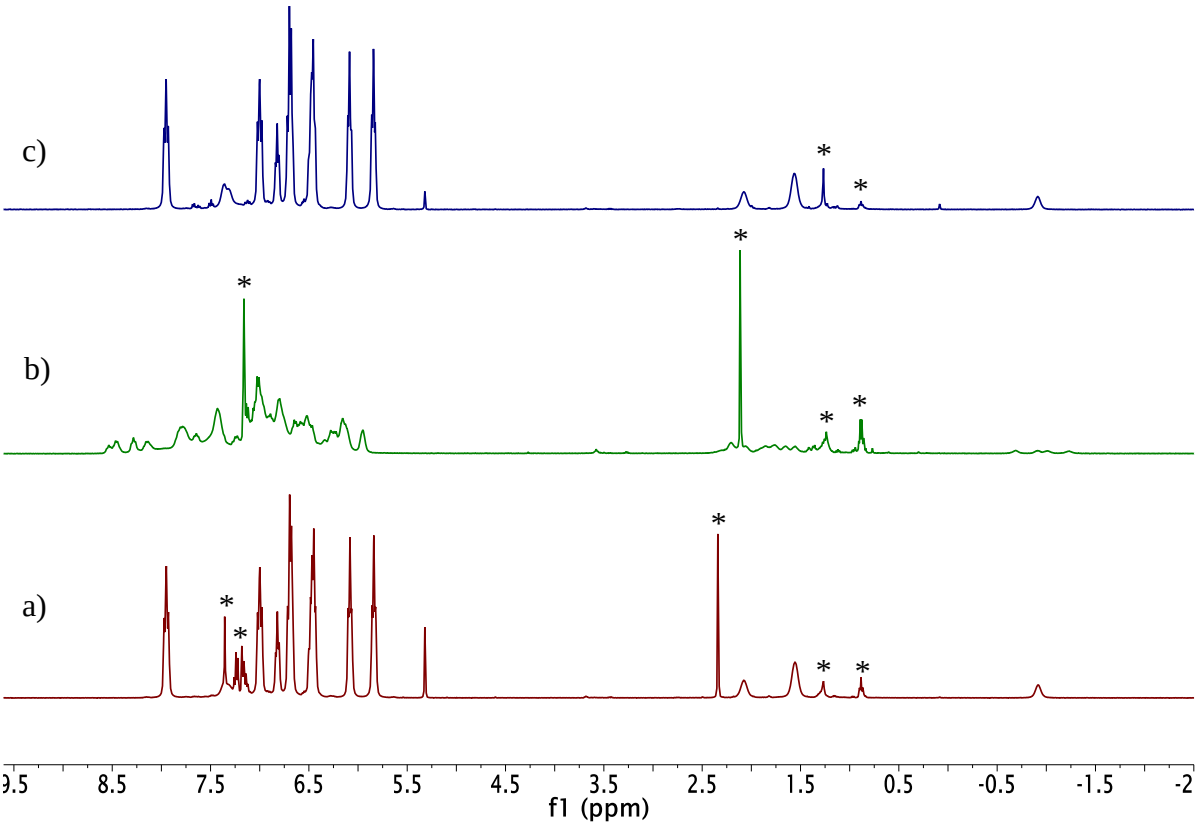

Figure A4.8. ^{1}H NMR spectra of $[Cu_{25}H_{22}(PPh_3)_{12}]Cl$ (**4.1**) in C_6D_6 and CD_2Cl_2. a) ^{1}H NMR spectrum of **4.1** in CD_2Cl_2. b) ^{1}H NMR spectrum of **4.1** in C_6D_6. c) ^{1}H NMR spectrum of sample (b) after removal of the C_6D_6 *in vacuo* and dissolution in CD_2Cl_2. (*) indicate the presence of benzene, toluene and hexanes. **Experimental Details:** Complex **4.1** (13.7 mg, 0.0029 mmol) was dissolved C_6D_6 (0.7 mL), and its NMR spectra were recorded. Note: this sample only partially dissolved, due to its low solubility in C_6D_6. The sample was then returned to the glovebox, where it was transferred to a vial, and the volatiles were removed *in vacuo*. The resulting dark green solid was redissolved in CD_2Cl_2 (0.7 mL) and the NMR spectra were re-recorded. These spectra exhibit resonances consistent with the high symmetry form of **4.1**, demonstrating the reversibility of contact ion pair formation.

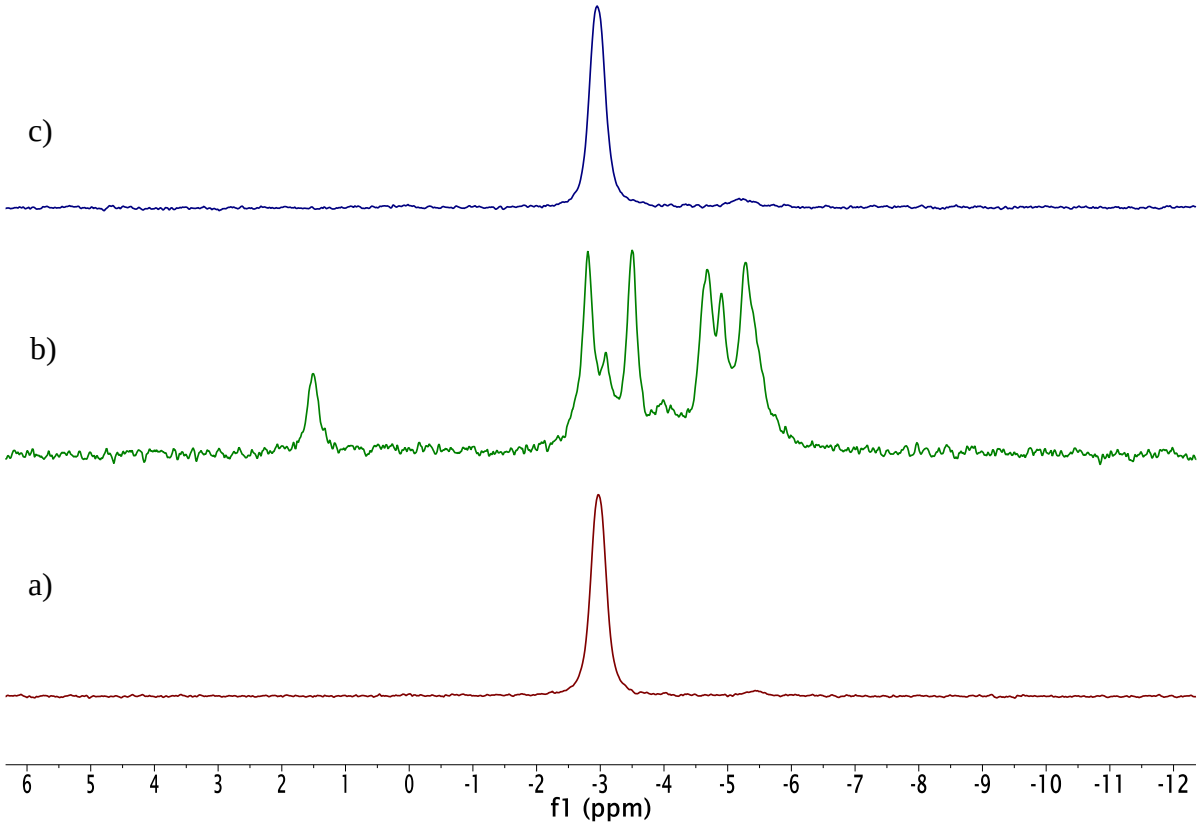

Figure A4.9. $^{31}P\{^{1}H\}$ NMR spectra of $[Cu_{25}H_{22}(PPh_3)_{12}]Cl$ (**4.1**) in C_6D_6 and CD_2Cl_2. a) $^{31}P\{^{1}H\}$ NMR spectrum of **4.1** in CD_2Cl_2. b) $^{31}P\{^{1}H\}$ NMR spectrum of **4.1** in C_6D_6. c) $^{31}P\{^{1}H\}$ NMR spectrum of sample (b) after removal of the C_6D_6 *in vacuo* and dissolution in CD_2Cl_2. See Figure A4.8 for experimental details.

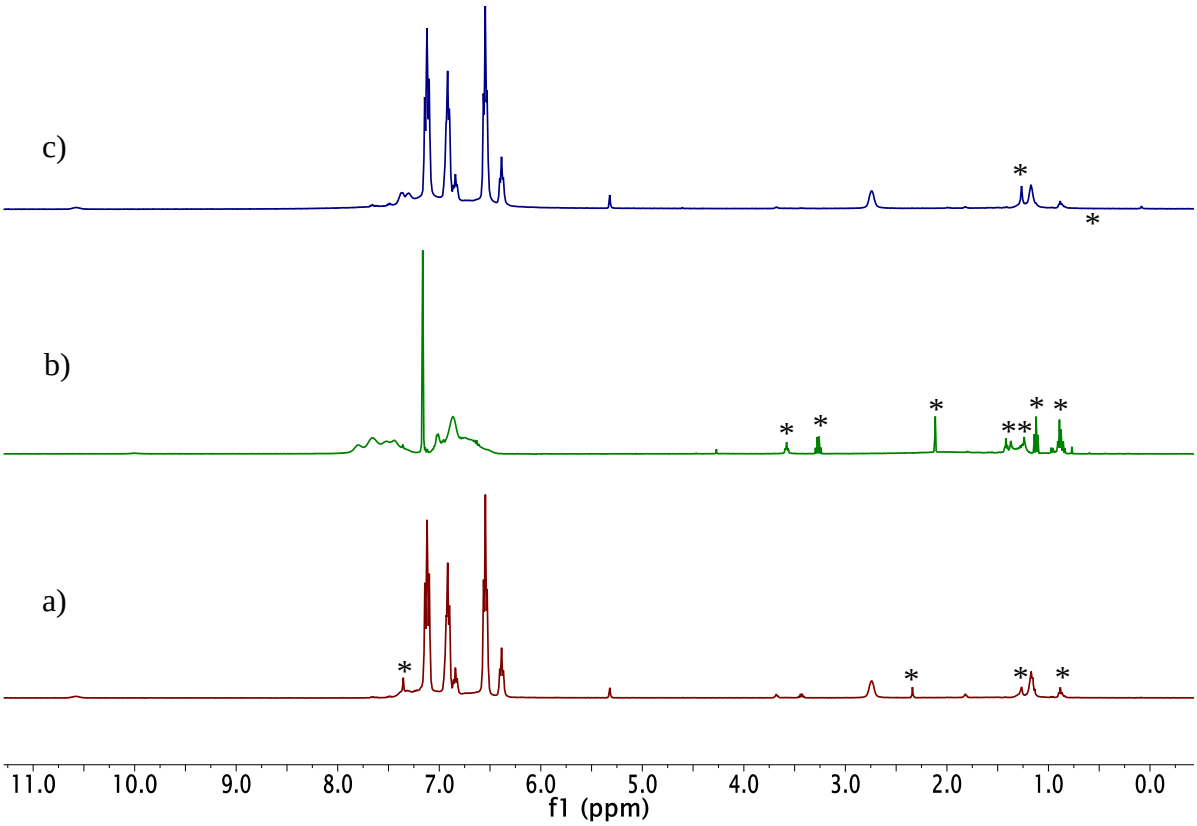

Figure A4.10. ^{1}H NMR experiment of $[Cu_{18}H_{17}(PPh_3)_{10}]Cl$ (**4.2**) in C_6D_6 and CD_2Cl_2. a) ^{1}H NMR spectrum of **4.2** in CD_2Cl_2. b) ^{1}H NMR spectrum of **4.2** in C_6D_6. c) ^{1}H NMR spectrum of sample (b) after removal of the C_6D_6 *in vacuo* and dissolution in CD_2Cl_2 (*) indicate the presence of benzene, toluene, Et_2O, THF, and hexanes. **Experimental Details:** Complex **4.2** (8.8 mg, 0.0023 mmol) was dissolved in C_6D_6 (0.7 mL) and its NMR spectra were recorded. Note: this sample only partially dissolved, due to its low solubility in C_6D_6. The sample was then returned to the glovebox, where it was transferred to a vial, and the volatiles were removed *in vacuo*. The resulting yellow solid was redissolved in CD_2Cl_2 (0.7 mL) and the NMR spectra were re-recorded. These spectra exhibit resonances consistent with the high symmetry form of **4.2**, demonstrating the reversibility of contact ion pair formation.

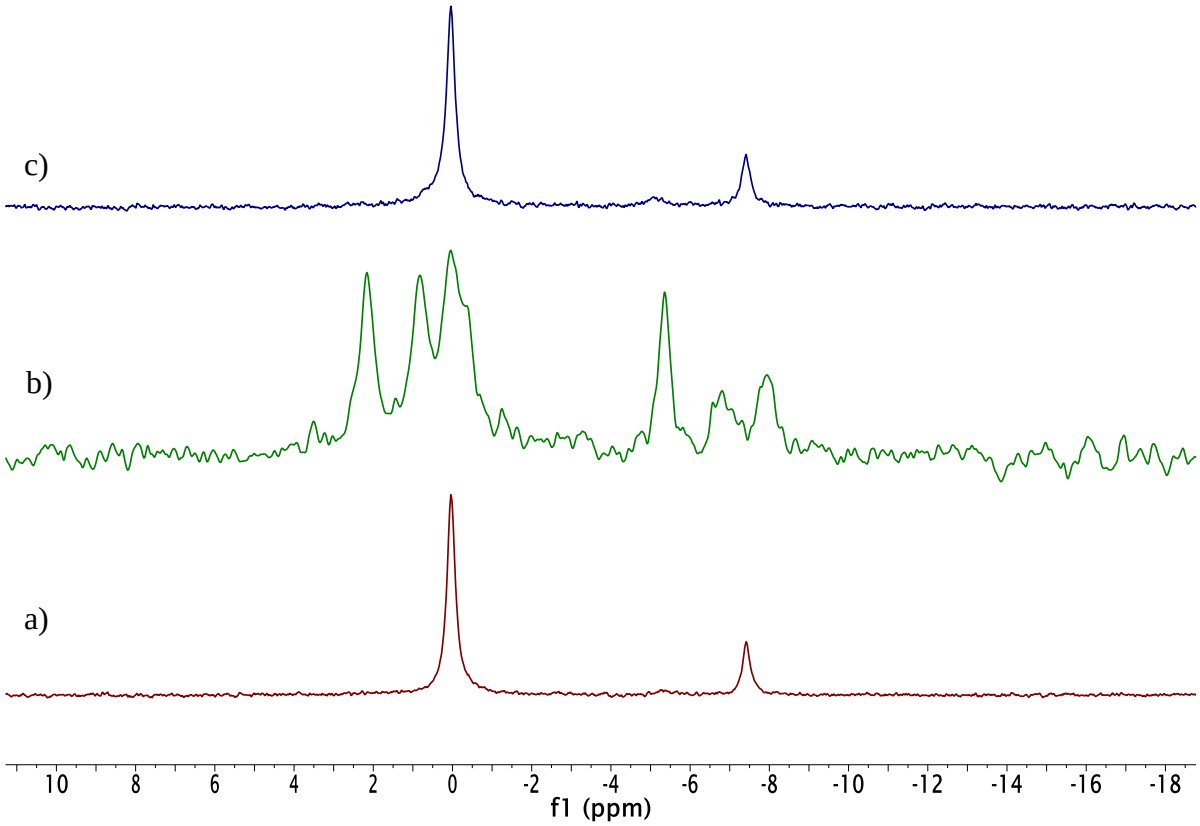

Figure A4.11. $^{31}P\{^{1}H\}$ NMR spectra of $[Cu_{18}H_{17}(PPh_3)_{10}]Cl$ (**4.2**) in C_6D_6 and CD_2Cl_2. a) $^{31}P\{^{1}H\}$ NMR spectrum of **4.2** in CD_2Cl_2. b) $^{31}P\{^{1}H\}$ NMR spectrum of **4.2** in C_6D_6. c) $^{31}P\{^{1}H\}$ NMR spectrum of sample (b) after removal of the C_6D_6 *in vacuo* and dissolution in CD_2Cl_2. See Figure A4.11 for experimental details.

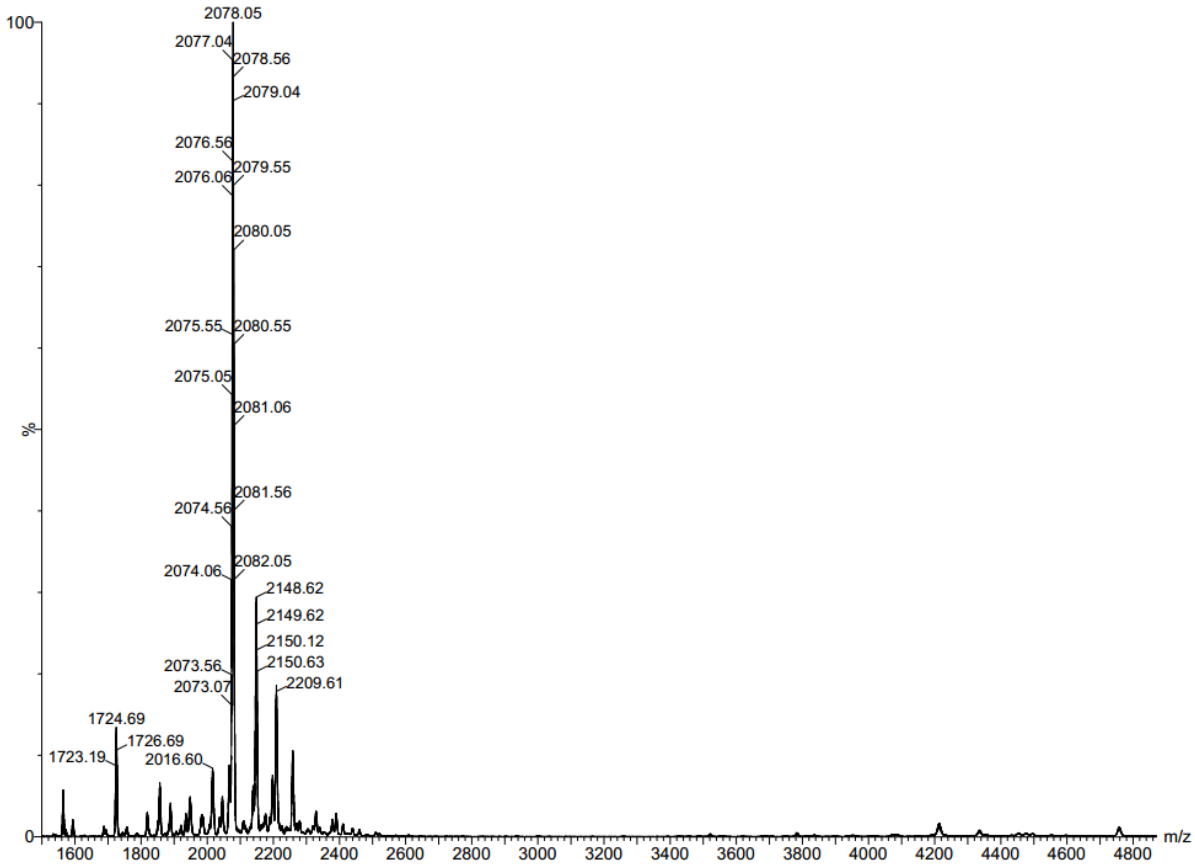

Figure A4.12. ESI-MS of $[Cu_{25}H_{22}(PPh_3)_{12}]Cl$ (**4.1**).

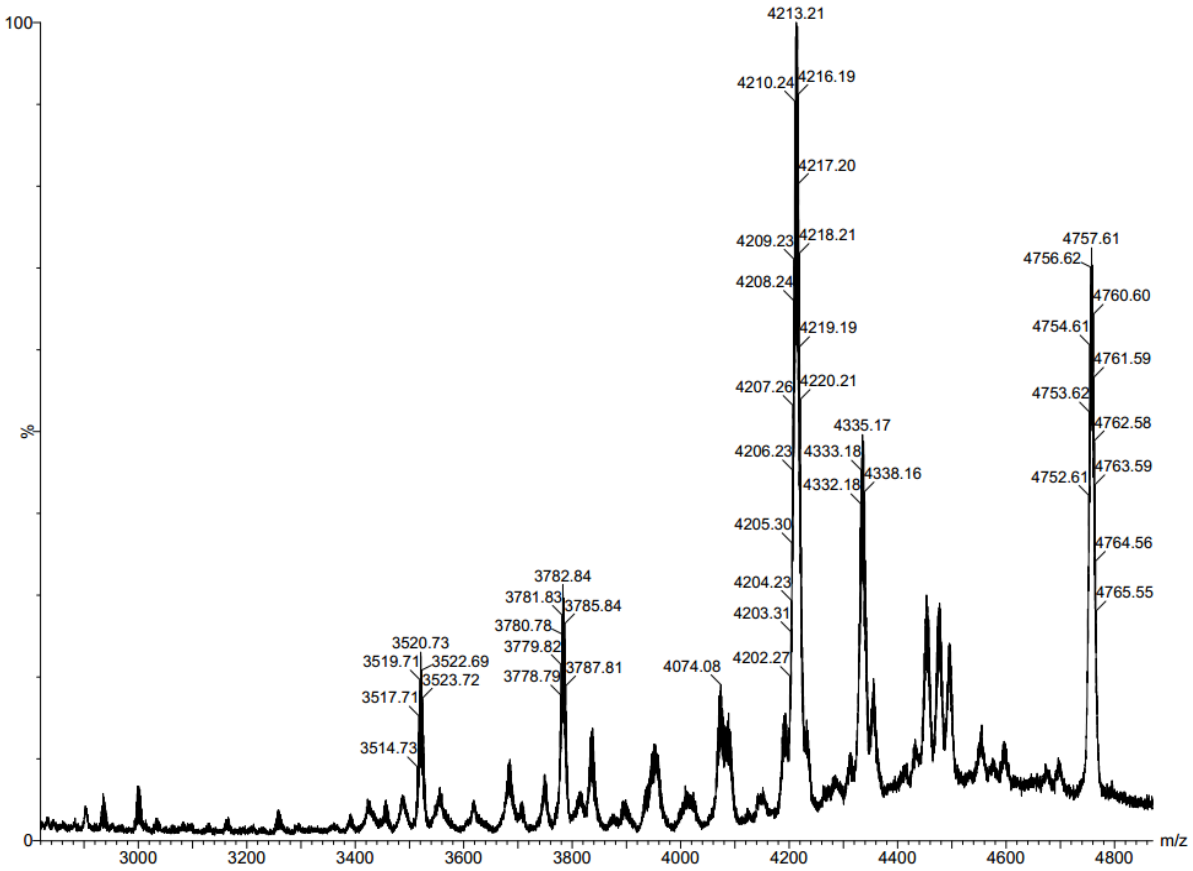

Figure A4.13. Partial ESI-MS of $[Cu_{25}H_{22}(PPh_3)_{12}]Cl$ (**4.1**) showing the region containing singly charged peaks assignable to **4.1**.

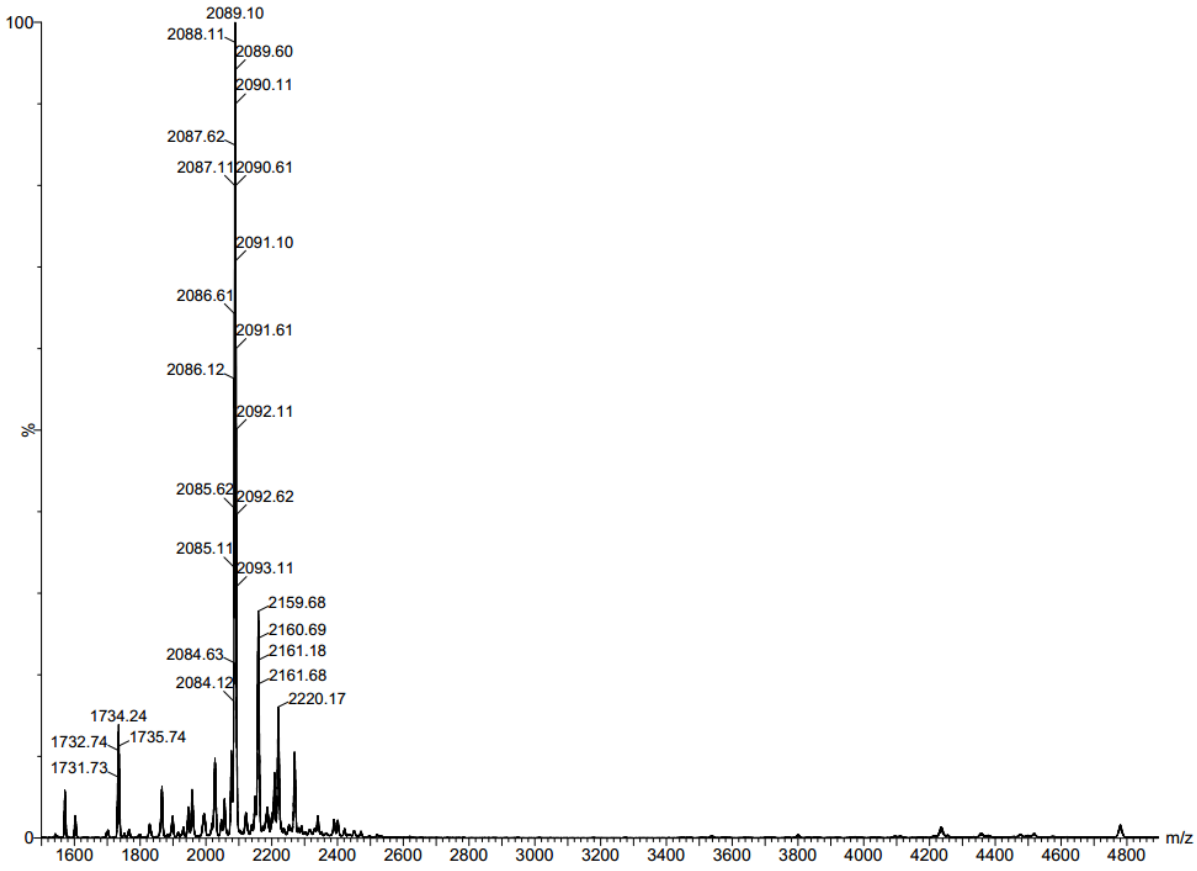

Figure A4.14. ESI-MS of $[Cu_{25}D_{22}(PPh_3)_{12}]Cl$ (**4.1-*d*$_{22}$**).

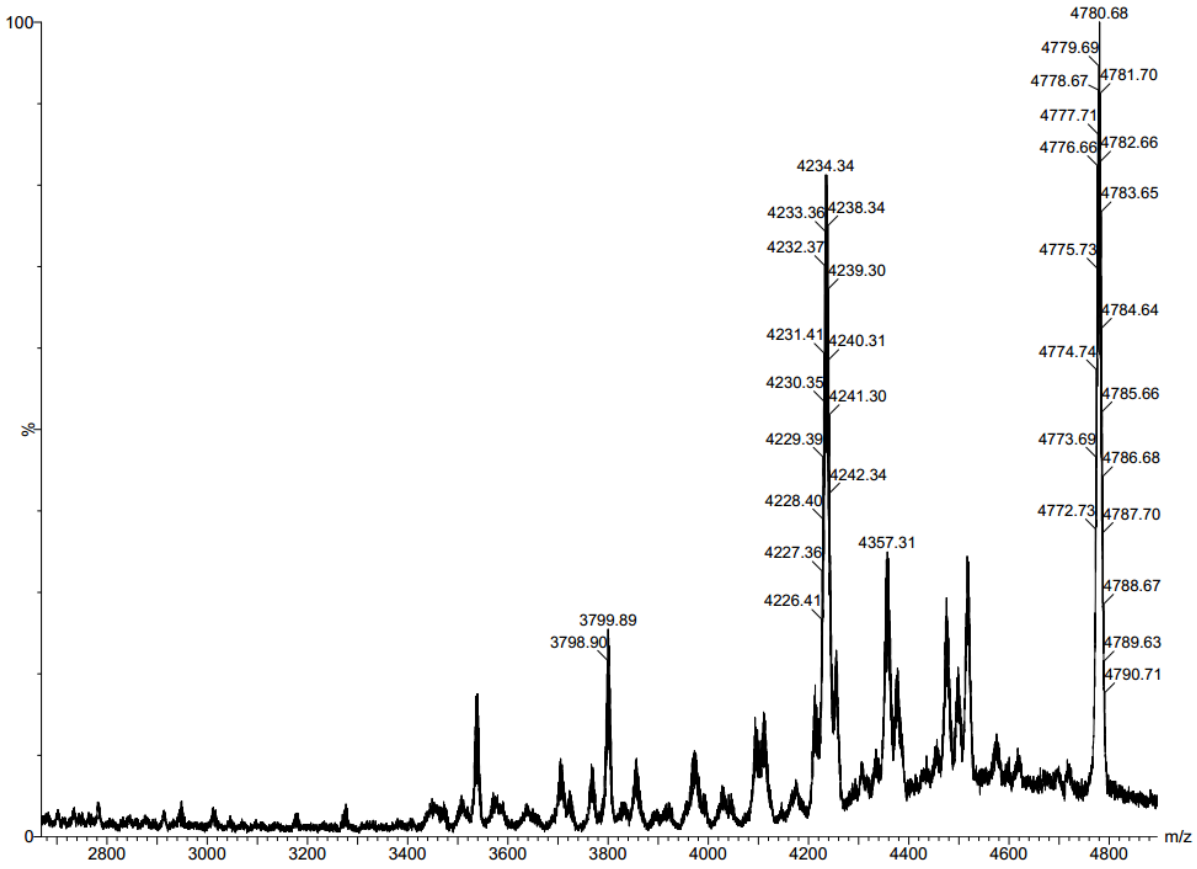

Figure A4.15. Partial ESI-MS of $[Cu_{25}D_{22}(PPh_3)_{12}]Cl$ (**4.1-*d*$_{22}$**) showing the region containing singly charged peaks assignable to **4.1-*d*$_{22}$**.

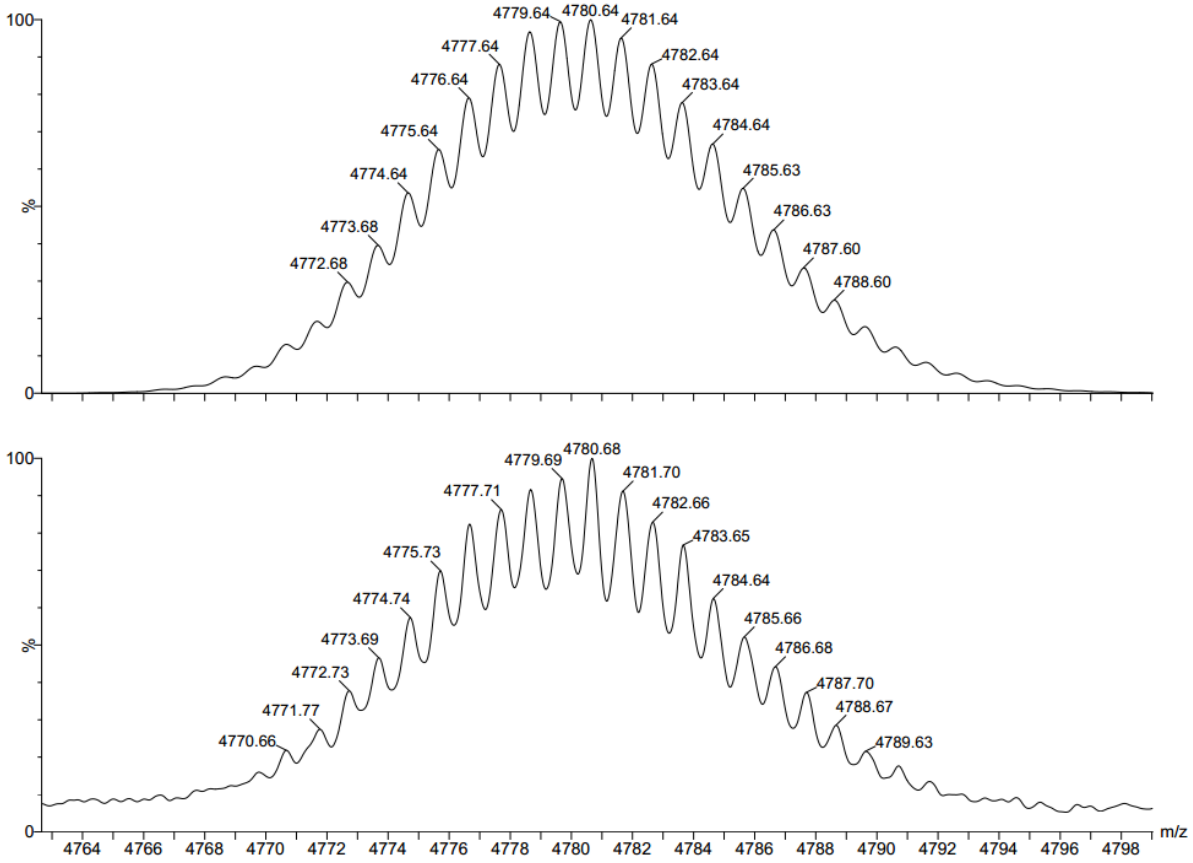

Figure A4.16. Partial ESI-MS of $[Cu_{25}D_{22}(PPh_3)_{12}]Cl$ (**4.1-*d*$_{22}$**). The experimental (bottom) and calculated (top) peaks assignable to the $[M]^+$ ion are shown.

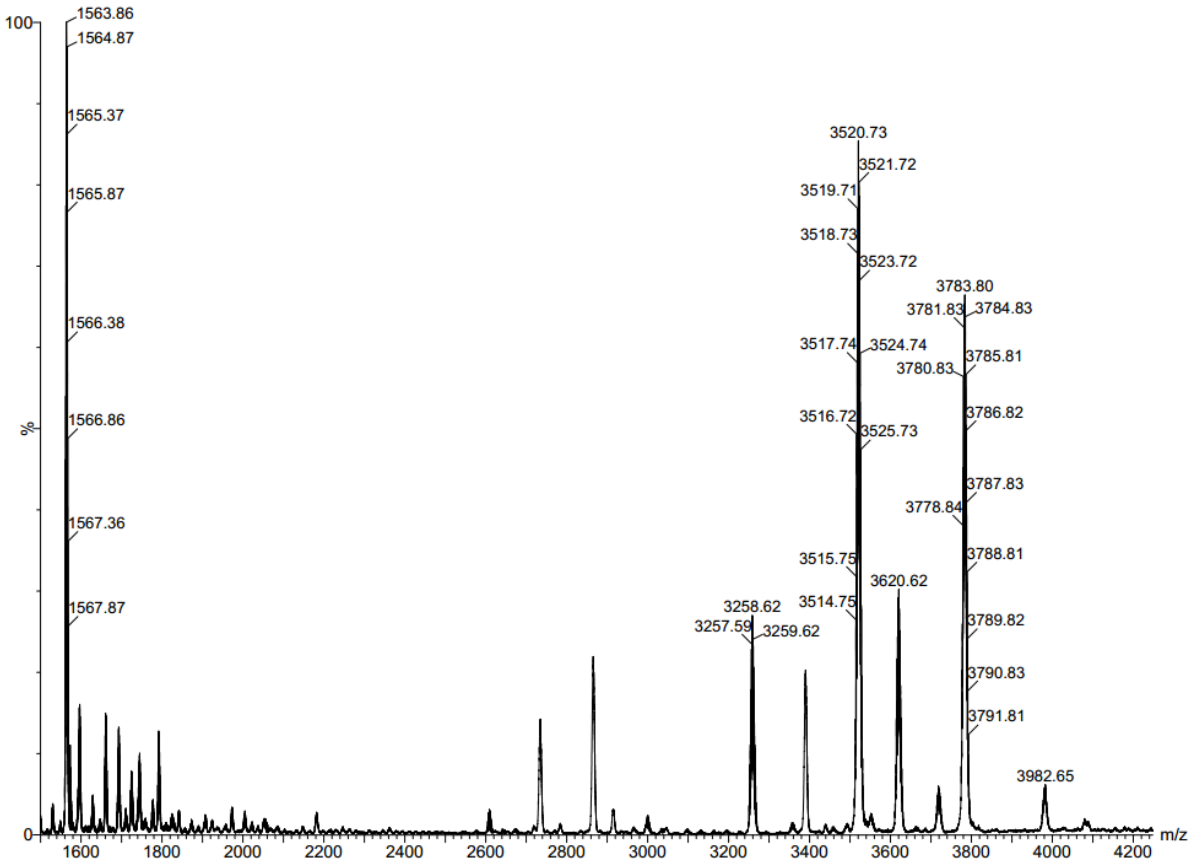

Figure A4.17. ESI-MS of $[Cu_{18}H_{17}(PPh_3)_{10}]Cl$ (**4.2**).

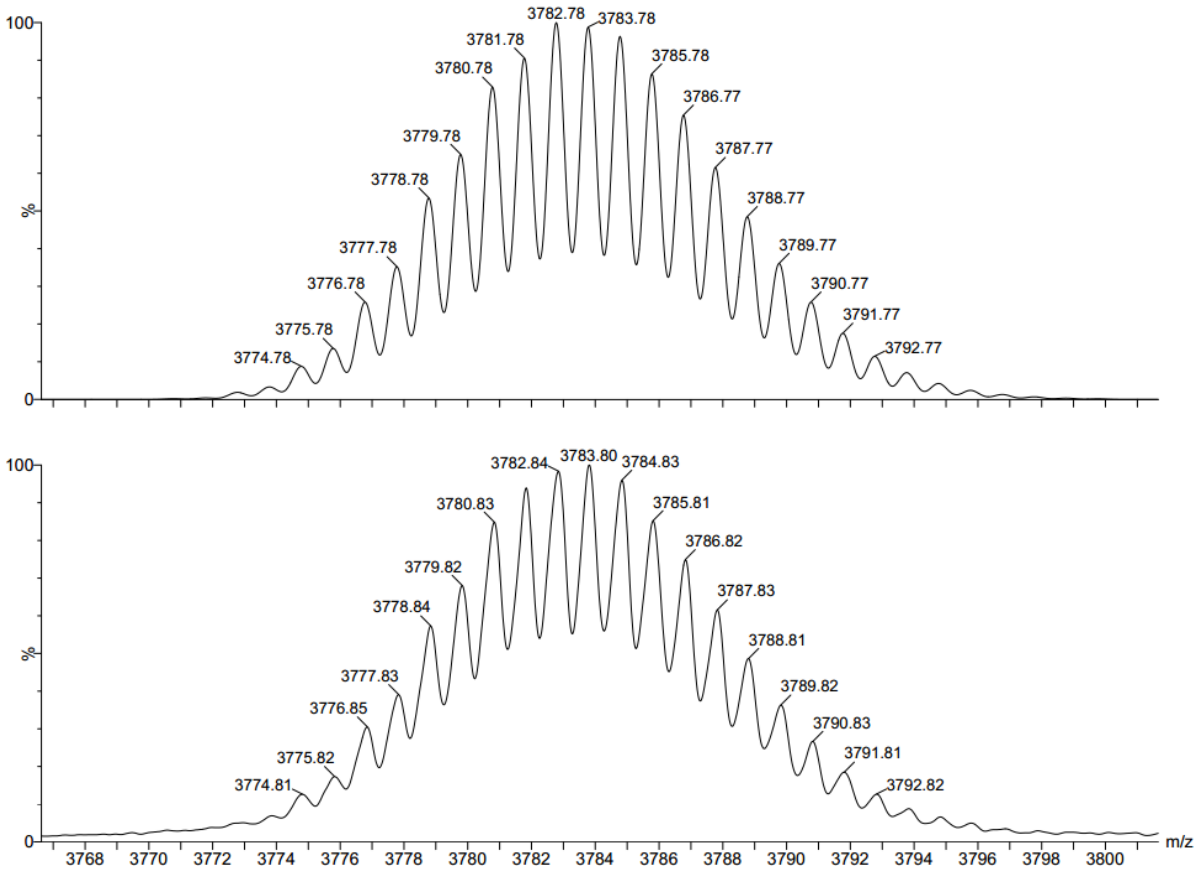

Figure A4.18. Partial ESI-MS of $[Cu_{18}H_{17}(PPh_3)_{10}]Cl$ (**4.2**). The experimental (bottom) and calculated (top) peaks assignable to the $[M]^+$ ion are shown.

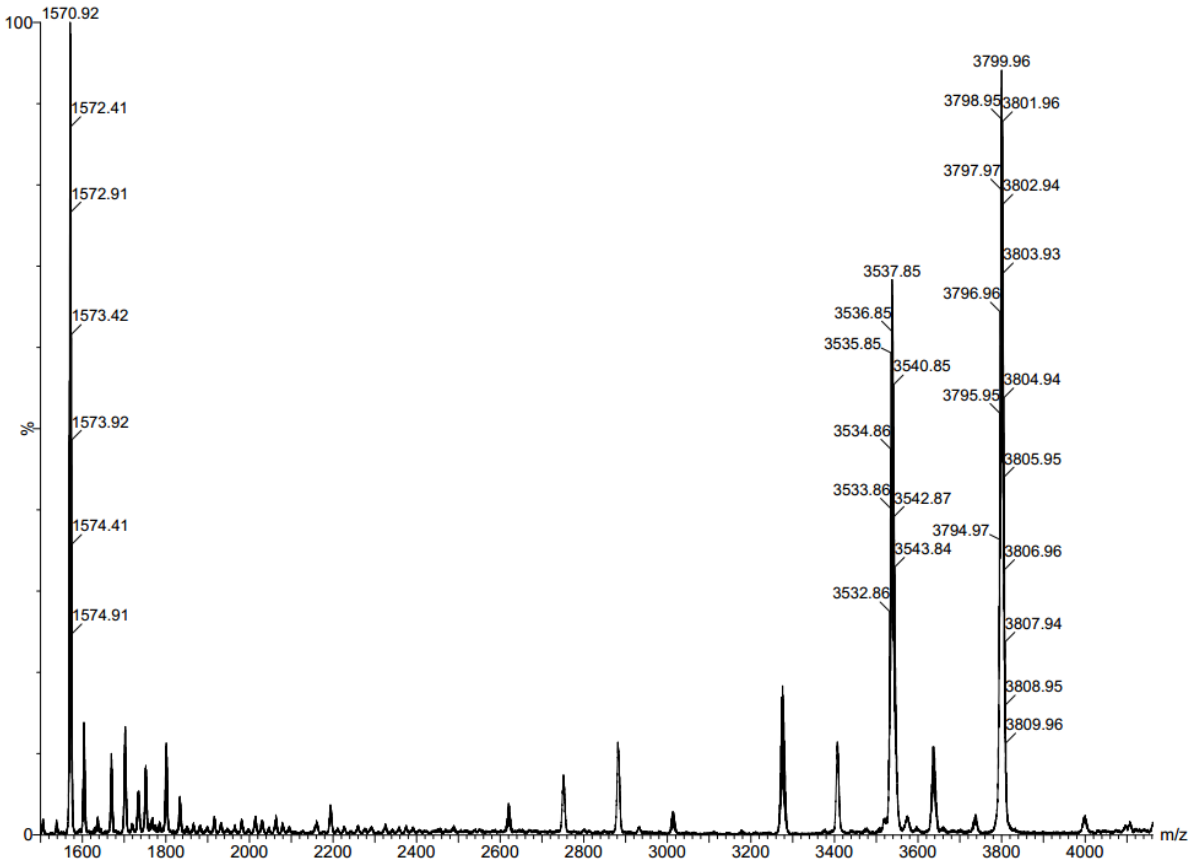

Figure A4.19. ESI-MS of $[Cu_{18}D_{17}(PPh_3)_{10}]Cl$ (**4.2-*d*$_{17}$**).

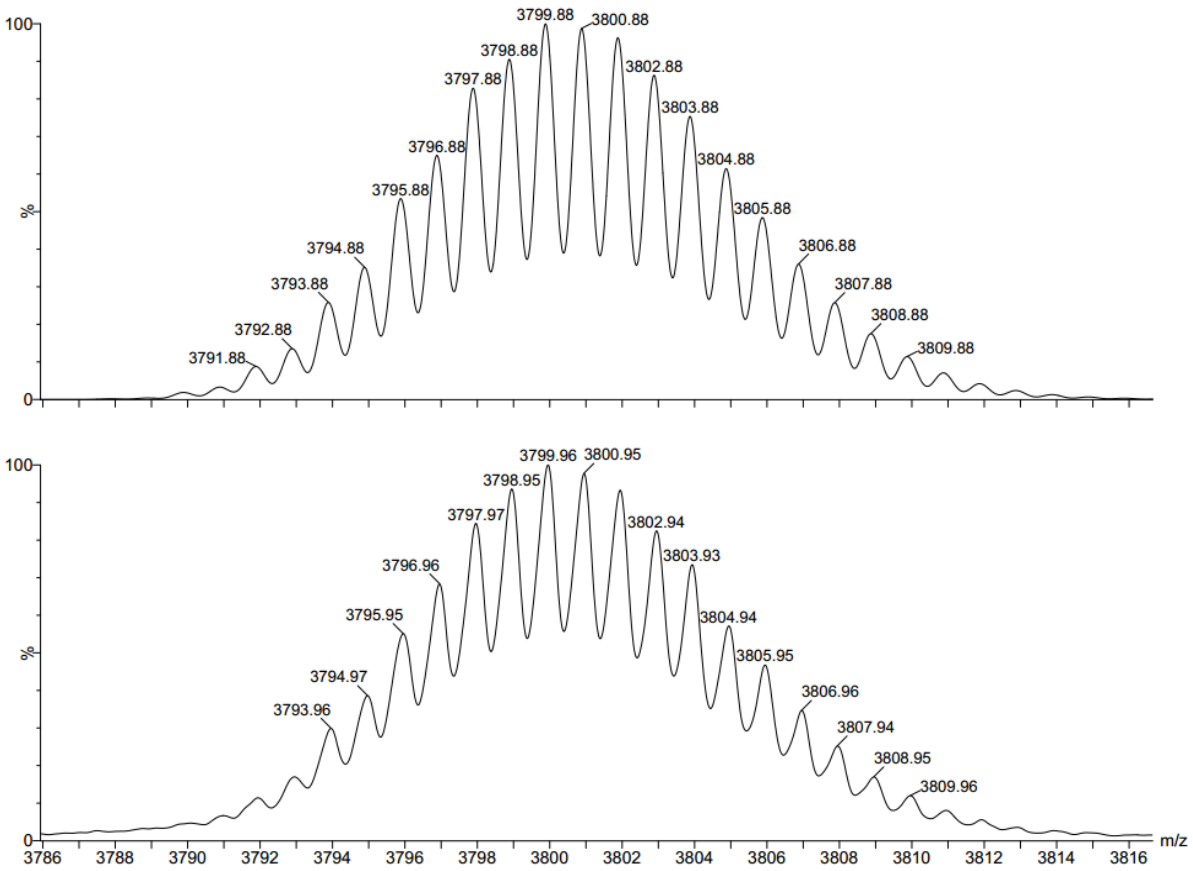

Figure A4.20. Partial ESI-MS of $[Cu_{18}D_{17}(PPh_3)_{10}]Cl$ (**4.2-*d*$_{17}$**). The experimental (bottom) and calculated (top) peaks assignable to the $[M]^+$ ion are shown.

4.6 References

(1) Hakkinen, H. Atomic and electronic structure of gold clusters: understanding flakes, cages and superatoms from simple concepts. *Chem. Soc. Rev.* **2008**, *37*, 1847.

(2) Schmid, G. The relevance of shape and size of Au_{55} clusters. *Chem. Soc. Rev.* **2008**, *37*, 1909.

(3) Yamazoe, S.; Koyasu, K.; Tsukuda, T. Nonscalable Oxidation Catalysis of Gold Clusters. *Acc. Chem. Res.* **2014**, *47*, 816.

(4) Li, G.; Jin, R. Atomically Precise Gold Nanoclusters as New Model Catalysts. *Acc. Chem. Res.* **2013**, *46*, 1749.

(5) Daniel, M.-C.; Astruc, D. Gold Nanoparticles: Assembly, Supramolecular Chemistry, Quantum-Size-Related Properties, and Applications toward Biology, Catalysis, and Nanotechnology. *Chem. Rev.* **2004**, *104*, 293.

(6) Parker, J. F.; Fields-Zinna, C. A.; Murray, R. W. The Story of a Monodisperse Gold Nanoparticle: $Au_{25}L_{18}$. *Acc. Chem. Res.* **2010**, *43*, 1289.

(7) Harkness, K. M.; Tang, Y.; Dass, A.; Pan, J.; Kothalawala, N.; Reddy, V. J.; Cliffel, D. E.; Demeler, B.; Stellacci, F.; Bakr, O. M.; McLean, J. A. $Ag_{44}(SR)_{30}^{4-}$: a silver-thiolate superatom complex. *Nanoscale* **2012**, *4*, 4269.

(8) Desireddy, A.; Conn, B. E.; Guo, J.; Yoon, B.; Barnett, R. N.; Monahan, B. M.; Kirschbaum, K.; Griffith, W. P.; Whetten, R. L.; Landman, U.; Bigioni, T. P. Ultrastable silver nanoparticles. *Nature* **2013**, *501*, 399.

(9) Dhayal, R. S.; Liao, J.-H.; Liu, Y.-C.; Chiang, M.-H.; Kahlal, S.; Saillard, J.-Y.; Liu, C. W. $[Ag_{21}\{S_2P(OiPr)_2\}_{12}]^+$: An Eight-Electron Superatom. *Angew. Chem. Int. Ed.* **2015**, *54*, 3702.

(10) Heaven, M. W.; Dass, A.; White, P. S.; Holt, K. M.; Murray, R. W. Crystal Structure of the Gold Nanoparticle $[N(C_8H_{17})_4][Au_{25}(SCH_2CH_2Ph)_{18}]$. *J. Am. Chem. Soc.* **2008**, *130*, 3754.

(11) Zhu, M.; Aikens, C. M.; Hollander, F. J.; Schatz, G. C.; Jin, R. Correlating the Crystal Structure of A Thiol-Protected Au_{25} Cluster and Optical Properties. *J. Am. Chem. Soc.* **2008**, *130*, 5883.

(12) Levi-Kalisman, Y.; Jadzinsky, P. D.; Kalisman, N.; Tsunoyama, H.; Tsukuda, T.; Bushnell, D. A.; Kornberg, R. D. Synthesis and Characterization of Au_{102}(*p*-MBA)$_{44}$ Nanoparticles. *J. Am. Chem. Soc.* **2011**, *133*, 2976.

(13) Jadzinsky, P. D.; Calero, G.; Ackerson, C. J.; Bushnell, D. A.; Kornberg, R. D. Structure of a Thiol Monolayer-Protected Gold Nanoparticle at 1.1 Å Resolution. *Science* **2007**, *318*, 430.

(14) Teo, B. K.; Keating, K. Novel triicosahedral structure of the largest metal alloy cluster: hexachlorododecakis(triphenylphosphine)-gold-silver cluster $[(Ph_3P)_{12}Au_{13}Ag_{12}Cl_6]^{m+}$. *J. Am. Chem. Soc.* **1984**, *106*, 2224.

(15) Teo, B. K.; Hong, M.; Zhang, H.; Huang, D.; Shi, X. Cluster of clusters: structure of a novel 38-atom cluster (*p*-tolyl$_3$P)$_{12}Au_{18}Ag_{20}Cl_{14}$. *J. Chem. Soc., Chem. Commun.* **1988**, 204.

(16) Nunokawa, K.; Ito, M.; Sunahara, T.; Onaka, S.; Ozeki, T.; Chiba, H.; Funahashi, Y.; Masuda, H.; Yonezawa, T.; Nishihara, H.; Nakamoto, M.; Yamamoto, M. A new 19-metal-atom cluster $[(Me_2PhP)_{10}Au_{12}Ag_7(NO_3)_9]$ with a nearly staggered-staggered M_5 ring configuration. *Dalton Trans.* **2005**, 2726.

(17) Yang, H.; Wang, Y.; Yan, J.; Chen, X.; Zhang, X.; Häkkinen, H.; Zheng, N. Structural Evolution of Atomically Precise Thiolated Bimetallic $[Au_{12+n}Cu_{32}(SR)_{30+n}]^{4-}$ (n = 0, 2, 4, 6) Nanoclusters. *J. Am. Chem. Soc.* **2014**, *136*, 7197.

(18) Wang, Y.; Su, H.; Xu, C.; Li, G.; Gell, L.; Lin, S.; Tang, Z.; Häkkinen, H.; Zheng, N. An Intermetallic $Au_{24}Ag_{20}$ Superatom Nanocluster Stabilized by Labile Ligands. *J. Am. Chem. Soc.* **2015**, *137*, 4324.

(19) Yang, H.; Wang, Y.; Huang, H.; Gell, L.; Lehtovaara, L.; Malola, S.; Häkkinen, H.; Zheng, N. All-thiol-stabilized Ag_{44} and $Au_{12}Ag_{32}$ nanoparticles with single-crystal structures. *Nat. Commun.* **2013**, *4*, 2422.

(20) Yan, N.; Yuan, Y.; Dyson, P. J. Nanometallic chemistry: deciphering nanoparticle catalysis from the perspective of organometallic chemistry and homogeneous catalysis. *Dalton Trans.* **2013**, *42*, 13294.

(21) Zhu, Y.; Qian, H.; Drake, B. A.; Jin, R. Atomically Precise $Au_{25}(SR)_{18}$ Nanoparticles as Catalysts for the Selective Hydrogenation of α,β-Unsaturated Ketones and Aldehydes. *Angew. Chem. Int. Ed.* **2010**, *49*, 1295.

(22) Zhu, Y.; Qian, H.; Jin, R. An Atomic-Level Strategy for Unraveling Gold Nanocatalysis from the Perspective of $Au_n(SR)_m$ Nanoclusters. *Chem. Eur. J.* **2010**, *16*, 11455.

(23) Zhu, Y.; Qian, H.; Jin, R. Catalysis opportunities of atomically precise gold nanoclusters. *J. Mater. Chem.* **2011**, *21*, 6793.

(24) Walter, M.; Akola, J.; Lopez-Acevedo, O.; Jadzinsky, P. D.; Calero, G.; Ackerson, C. J.; Whetten, R. L.; Grönbeck, H.; Häkkinen, H. A unified view of ligand-protected gold clusters as superatom complexes. *Proc. Natl. Acad. Sci.* **2008**, *105*, 9157.

(25) Wei, W.; Lu, Y.; Chen, W.; Chen, S. One-Pot Synthesis, Photoluminescence, and Electrocatalytic Properties of Subnanometer-Sized Copper Clusters. *J. Am. Chem. Soc.* **2011**, *133*, 2060.

(26) Vilar-Vidal, N.; Rey, J. R.; López Quintela, M. A. Green Emitter Copper Clusters as Highly Efficient and Reusable Visible Degradation Photocatalysts. *Small* **2014**, *10*, 3632.

(27) Oyanagi, H.; Sun, Z. H.; Jiang, Y.; Uehara, M.; Nakamura, H.; Yamashita, K.; Orimoto, Y.; Zhang, L.; Lee, C.; Fukano, A.; Maeda, H. Small copper clusters studied by x-ray absorption near-edge structure. *J. Appl. Phys.* **2012**, *111*, 084315.

(28) Oyanagi, H.; Orimoto, Y.; Hayakawa, K.; Hatada, K.; Sun, Z.; Zhang, L.; Yamashita, K.; Nakamura, H.; Uehara, M.; Fukano, A.; Maeda, H. Nanoclusters Synthesized by Synchrotron Radiolysis in Concert with Wet Chemistry. *Sci. Rep.* **2014**, *4*.

(29) Mazalova, V. L.; Soldatov, A. V.; Adam, S.; Yakovlev, A.; Möller, T.; Johnston, R. L. Small Copper Clusters in Ar Shells: A Study of Local Structure. *J. Phys. Chem. C* **2009**, *113*, 9086.

(30) Montano, P. A.; Shenoy, G. K.; Alp, E. E.; Schulze, W.; Urban, J. Structure of Copper Microclusters Isolated in Solid Argon. *Phys. Rev. Lett.* **1986**, *56*, 2076.

(31) Nguyen, T.-A. D.; Goldsmith, B. R.; Zaman, H. T.; Wu, G.; Peters, B.; Hayton, T. W. Synthesis and Characterization of a Cu_{14} Hydride Cluster Supported by Neutral Donor Ligands. *Chem. Eur. J.* **2015**, *21*, 5341.

(32) Huertos, M. A.; Cano, I.; Bandeira, N. A. G.; Benet-Buchholz, J.; Bo, C.; van Leeuwen, P. W. N. M. Phosphinothiolates as Ligands for Polyhydrido Copper Nanoclusters. *Chem. Eur. J.* **2014**, *20*, 16121.

(33) Dhayal, R. S.; Liao, J.-H.; Lin, Y.-R.; Liao, P.-K.; Kahlal, S.; Saillard, J.-Y.; Liu, C. W. A Nanospheric Polyhydrido Copper Cluster of Elongated Triangular Orthobicupola Array: Liberation of H_2 from Solar Energy. *J. Am. Chem. Soc.* **2013**, *135*, 4704.

(34) Liao, J.-H.; Dhayal, R. S.; Wang, X.; Kahlal, S.; Saillard, J.-Y.; Liu, C. W. Neutron Diffraction Studies of a Four-Coordinated Hydride in Near Square-Planar Geometry. *Inorg. Chem.* **2014**, *53*, 11140.

(35) Edwards, A. J.; Dhayal, R. S.; Liao, P.-K.; Liao, J.-H.; Chiang, M.-H.; Piltz, R. O.; Kahlal, S.; Saillard, J.-Y.; Liu, C. W. Chinese Puzzle Molecule: A 15 Hydride, 28 Copper Atom Nanoball. *Angew. Chem. Int. Ed.* **2014**, *53*, 7214.

(36) Dhayal, R. S.; Liao, J. H.; Kahlal, S.; Wang, X.; Liu, Y. C.; Chiang, M. H.; van Zyl, W. E.; Saillard, J. Y.; Liu, C. W. $[Cu_{32}(H)_{20}\{S_2P(O\textit{i}Pr)_2\}_{12}]$: The Largest Number of Hydrides Recorded in a Molecular Nanocluster by Neutron Diffraction. *Chem. Eur. J.* **2015**, *21*, 8369.

(37) Moret, M.-E.; Zhang, L.; Peters, J. C. A Polar Copper–Boron One-Electron σ-Bond. *J. Am. Chem. Soc.* **2013**, *135*, 3792.

(38) Weinberger, D. S.; Amin Sk, N.; Mondal, K. C.; Melaimi, M.; Bertrand, G.; Stückl, A. C.; Roesky, H. W.; Dittrich, B.; Demeshko, S.; Schwederski, B.; Kaim, W.; Jerabek, P.; Frenking, G. Isolation of Neutral Mononuclear Copper Complexes Stabilized by Two Cyclic (Alkyl)(amino)carbenes. *J. Am. Chem. Soc.* **2014**, *136*, 6235.

(39) Jerabek, P.; Roesky, H. W.; Bertrand, G.; Frenking, G. Coinage Metals Binding as Main Group Elements: Structure and Bonding of the Carbene Complexes $[TM(cAAC)_2]$ and $[TM(cAAC)_2]^+$ (TM = Cu, Ag, Au). *J. Am. Chem. Soc.* **2014**, *136*, 17123.

(40) Ganesamoorthy, C.; Weßing, J.; Kroll, C.; Seidel, R. W.; Gemel, C.; Fischer, R. A. The Intermetalloid Cluster $[(Cp^*AlCu)_6H_4]$, Embedding a Cu_6 Core Inside an Octahedral Al_6 Shell: Molecular Models of Hume–Rothery Nanophases. *Angew. Chem. Int. Ed.* **2014**, *53*, 7943.

(41) Bratsch, S. G. Standard Electrode Potentials and Temperature Coefficients in Water at 298.15 K. *J. Phys. Chem. Ref. Data* **1989**, *18*, 1.

(42) Li, C. W.; Ciston, J.; Kanan, M. W. Electroreduction of carbon monoxide to liquid fuel on oxide-derived nanocrystalline copper. *Nature* **2014**, *508*, 504.

(43) Kas, R.; Kortlever, R.; Milbrat, A.; Koper, M. T. M.; Mul, G.; Baltrusaitis, J. Electrochemical CO_2 reduction on Cu_2O-derived copper nanoparticles: controlling the catalytic selectivity of hydrocarbons. *Phys. Chem. Chem. Phys.* **2014**, *16*, 12194.

(44) Tang, W.; Peterson, A. A.; Varela, A. S.; Jovanov, Z. P.; Bech, L.; Durand, W. J.; Dahl, S.; Norskov, J. K.; Chorkendorff, I. The importance of surface morphology in controlling the selectivity of polycrystalline copper for CO_2 electroreduction. *Phys. Chem. Chem. Phys.* **2012**, *14*, 76.

(45) Li, C. W.; Kanan, M. W. CO_2 Reduction at Low Overpotential on Cu Electrodes Resulting from the Reduction of Thick Cu_2O Films. *J. Am. Chem. Soc.* **2012**, *134*, 7231.

(46) Qiao, J.; Jiang, P.; Liu, J.; Zhang, J. Formation of Cu nanostructured electrode surfaces by an annealing–electroreduction procedure to achieve high-efficiency CO_2 electroreduction. *Electrochem. Commun.* **2014**, *38*, 8.

(47) Calle-Vallejo, F.; Koper, M. T. M. Theoretical Considerations on the Electroreduction of CO to C_2 Species on Cu(100) Electrodes. *Angew. Chem. Int. Ed.* **2013**, *52*, 7282.

(48) Schouten, K. J. P.; Qin, Z.; Gallent, E. P.; Koper, M. T. M. Two Pathways for the Formation of Ethylene in CO Reduction on Single-Crystal Copper Electrodes. *J. Am. Chem. Soc.* **2012**, *134*, 9864.

(49) Churchill, M. R.; Bezman, S. A.; Osborn, J. A.; Wormald, J. Preparation and crystallographic characterization of a hexameric triphenylphosphinecopper hydride cluster. *J. Am. Chem. Soc.* **1971**, *93*, 2063.

(50) Albert, C. F.; Healy, P. C.; Kildea, J. D.; Raston, C. L.; Skelton, B. W.; White, A. H. Lewis-base adducts of Group 11 metal(I) compounds. 49. Structural characterization of hexameric and pentameric (triphenylphosphine)copper(I) hydrides. *Inorg. Chem.* **1989**, *28*, 1300.

(51) Lee, D.; Yun, J. Direct synthesis of Stryker's reagent from a Cu(II) salt. *Tetrahedron Lett.* **2005**, *46*, 2037.

(52) Wyckoff, R. W. G. *Crystal Structures*; Second ed.; Interscience Publishers: New York, 1963; Vol. 1.

(53) Yang, M.; Jackson, K. A.; Koehler, C.; Frauenheim, T.; Jellinek, J. Structure and shape variations in intermediate-size copper clusters. *J. Chem. Phys.* **2006**, *124*, 024308.

(54) Bennett, E. L.; Murphy, P. J.; Imberti, S.; Parker, S. F. Characterization of the hydrides in Stryker's reagent: $[HCu\{P(C_6H_5)_3\}]_6$. *Inorg. Chem.* **2014**, *53*, 2963.

(55) Kohn, R. D.; Pan, Z.; Mahon, M. F.; Kociok-Kohn, G. Trimethyltriazacyclohexane as bridging ligand for triangular Cu_3 units and C-H hydride abstraction into a Cu_6 cluster. *Chem. Commun.* **2003**, 1272.

(56) Briant, C. E.; Theobald, B. R. C.; White, J. W.; Bell, L. K.; Mingos, D. M. P.; Welch, A. J. Synthesis and X-ray structural characterization of the centred icosahedral gold cluster compound $[Aul_3(PMe_2Ph)_{10}Cl_2](PF_6)_3$; the realization of a theoretical prediction. *J. Chem. Soc., Chem. Commun.* **1981**, 201.

(57) Mao, Z.; Huang, J.-S.; Che, C.-M.; Zhu, N.; Leung, S. K.-Y.; Zhou, Z.-Y. Unexpected Reactivities of Cu_2(diphosphine)$_2$ Complexes in Alcohol: Isolation, X-ray Crystal Structure, and Photoluminescent Properties of a Remarkably Stable $[Cu_3$(diphosphine)$_3(\mu_3$-H)$]^{2+}$ Hydride Complex. *J. Am. Chem. Soc.* **2005**, *127*, 4562.

(58) Gell, L.; Lehtovaara, L.; Häkkinen, H. Superatomic S^2 Silver Clusters Stabilized by a Thiolate–Phosphine Monolayer: Insight into Electronic and Optical Properties of $Ag_{14}(SC_6H_3F_2)_{12}(PPh_3)_8$ and $Ag_{16}(SC_6H_3F_2)_{14}(DPPE)_4$. *J. Phys. Chem. A* **2014**, *118*, 8351.

(59) Yang, H.; Lei, J.; Wu, B.; Wang, Y.; Zhou, M.; Xia, A.; Zheng, L.; Zheng, N. Crystal structure of a luminescent thiolated Ag nanocluster with an octahedral Ag_6^{4+} core. *Chem. Commun.* **2013**, *49*, 300.

(60) Yang, H.; Wang, Y.; Zheng, N. Stabilizing Subnanometer Ag(0) Nanoclusters by Thiolate and Diphosphine Ligands and their Crystal Structures. *Nanoscale* **2013**, *5*, 2674.

(61) Goedkoop, J. A.; Andresen, A. F. The crystal structure of copper hydride. *Acta Cryst.* **1955**, *8*, 118.

(62) Kresse, G.; Furthmüller, J. Efficiency of Ab-initio total Energy Calculations for Metals and Semiconductors Using a Plane-wave Basis Set. *Comput. Mat. Sci.* **1996**, *6*, 15.

(63) Kresse, G.; Furthmüller, J. Efficient Iterative Schemes for Ab Initio Total-energy Calculations Using a Plane-wave Basis Set. *Phys. Rev. B* **1996**, *54*, 11169.

(64) Kresse, G.; Hafner, J. Ab Initio Molecular Dynamics for Liquid Metals. *Phys. Rev. B* **1993**, *47*, 558.

(65) Blöchl, P. E. Projector augmented-wave method. *Phys. Rev. B* **1994**, *50*, 17953.

(66) Perdew, J. P.; Burke, K.; Ernzerhof, M. Generalized Gradient Approximation Made Simple. *Phys. Rev. Lett.* **1996**, *77*, 3865.

(67) Perdew, J. P.; Chevary, J. A.; Vosko, S. H.; Jackson, K. A.; Pederson, M. R.; Singh, D. J.; Fiolhais, C. Atoms, molecules, solids, and surfaces: Applications of the generalized gradient approximation for exchange and correlation. *Phys. Rev. B* **1992**, *46*, 6671.

(68) Wagner, C. D. Chemical shifts of Auger lines, and the Auger parameter. *Faraday Discuss. Chem. Soc.* **1975**, *60*, 291.

(69) de Crescenzi, M.; Diociaiuti, M.; Lozzi, L.; Picozzi, P.; Santucci, S.; Battistoni, C.; Mattogno, G. Size effects on the linewidths of the Auger spectra of Cu clusters. *Surf. Sci.* **1986**, *178*, 282.

(70) Fife, D. J.; Moore, W. M.; Morse, K. W. Solution equilibria of tertiary phosphine complexes of copper(I) halides. *Inorg. Chem.* **1984**, *23*, 1684.

(71) Harris, R. K.; Becker, E. D.; Cabral De Menezes, S. M.; Goodfellow, R.; Granger, P. NMR Nomenclature. Nuclear Spin Properties and Conventions for Chemical Shifts. *Pure Appl. Chem.* **2001**, *73*, 1795.

(72) Harris, R. K.; Becker, E. D.; Cabral De Menezes, S. M.; Granger, P.; Hoffman, R. E.; Zilm, K. W. Further Conventions for NMR Shielding and Chemical Shifts. *Pure Appl. Chem.* **2008**, *80*, 59.

(73) *SMART Apex II, Version 2.1*; Bruker AXS Inc.: Madison, WI, 2005.

(74) *SAINT Software User's Guide, Version 7.34a*; Bruker AXS Inc.: Madison, WI, 2005.

(75) Sheldrick, G. M. *SADABS*; University of Göttingen: Göttingen, Germany, 2005.

(76) *SHELXTL PC, Version 6.12*; Bruker AXS Inc.: Madison, WI, 2005.

(77) Ravel, B.; Newville, M. ATHENA, ARTEMIS, HEPHAESTUS: data analysis for X-ray absorption spectroscopy using IFEFFIT. *J. Synchrotron Radiat.* **2005**, *12*, 537.

(78) Kresse, G.; Joubert, D. From ultrasoft pseudopotentials to the projector augmented-wave method. *Phys. Rev. B* **1999**, *59*, 1758.

Chapter 5. **Ligand Exchange-Induced Growth of a Cu_{29} Cluster from a Smaller Cluster**

Portions of this work were published in:

Thuy-Ai D. Nguyen; Zachary R. Jones; Domenick F. Leto; Guang Wu; Susannah L. Scott; Trevor W. Hayton. Ligand-Exchange-Induced Growth of an Atomically Precise Cu_{29} Nanocluster from a Smaller Cluster. *Chem. Mater*. **2016**, 28, 8385-8390.

5.1 Introduction

Understanding the mechanisms of nanocluster (NC) formation and growth is an important step toward the tailoring of nanocluster structure and properties.[1,2] An emerging method for controlling the size and structure of nanoclusters involves ligand exchange to induce a transformation from one stable cluster to another.[1,3-6] Although such ligand exchange reactions are commonly used to introduce new functional groups onto the surface of clusters while preserving the original core size, they can also lead to changes in the shape and/or size of the metal core.[3-5,7] For example, exchange of the thiolate ligands in $[Au_{38}(SCH_2CH_2Ph)_{24}]$ upon heating with HSC_6H_4-4-^{t}Bu results in formation of a new, smaller cluster, $[Au_{36}(SC_6H_4\text{-}4\text{-}^tBu)_{24}]$.[8] Similarly, thiolate ligand exchange mediates the conversion of a Ag_{44} cluster into a smaller Ag_{25} cluster.[9] In both of these examples, the change in cluster size likely occurs via thermally-induced disproportionation of an unstable intermediate in the presence of a very large excess of the new ligand, a process which has been called ligand-exchange-induced size/structure transformation (LEIST).[1,10] Generally speaking, however, the mechanisms of ligand exchange and cluster rearrangement are still poorly understood, and researchers are only now beginning to probe these questions.[11]

Nevertheless, the resemblance to reactant-induced Ostwald ripening and disintegration of metal nanoparticles is intriguing.[12,13] Moreover, examples are restricted to less reactive gold and silver NCs; copper NCs with metallic character are significantly rarer due to their much higher susceptibility to oxidation. In fact, before 2016, only two such complexes were known, namely, $[(Cp^*AlCu)_6H_4]$ and $[Cu_{25}H_{22}(PPh_3)_{12}]Cl$ (**4.1**).[14,15]

Herein, I describe the synthesis and structural characterization of the largest copper superatom known to-date, namely, the novel Cu_{29} nanocluster, $[Cu_{29}Cl_4H_{22}(Ph_2phen)_{12}]Cl$ (**5.1**). This material was generated via an unprecedented cluster growth mechanism, involving ligand exchange at room temperature, followed by CuCl monomer dissociation and capture by a previously assembled Cu_{25} core. I also collaborated with the Scott group at UCSB to probe its electronic and geometric structure using X-ray absorption spectroscopy, and assess the rate law for its formation using time-resolved UV-vis spectroscopy.

5.2 Results and Discussion

Addition of 16 equiv of 4,7-diphenyl-1,10-phenanthroline (Ph_2phen) to a dark green solution of $[Cu_{25}H_{22}(PPh_3)_{12}]Cl$ (**4.1**) in CH_2Cl_2 at room temperature causes an immediate color change to dark blue. Work-up of this solution after 15 h resulted in the isolation of a new mixed-valent copper hydride nanocluster, $[Cu_{29}Cl_4H_{22}(Ph_2phen)_{12}]Cl$ (**5.1**), as a deep blue-black crystalline material in 84% yield (Scheme 5.1). While just 12 equiv Ph_2phen are formally required to form **5.1**, according to the stoichiometry of the reaction, the product was isolated in higher purity and yield when the reaction was performed in the presence of a small excess of the ligand. Reaction of **4.1** with 1,10-phenanthroline also yields a deep blue product, which is likely isostructural with **5.1** based on NMR spectral and ESI mass spectrometry data; however, single crystals of this complex were not obtained. In addition,

the reaction does not appear to be as clean as when done with Ph_2phen, and there is at least one other minor hydride-containing product observed in the NMR spectra of the isolated material.

Scheme 5.1. Two synthetic routes for cluster expansion to complex **5.1**

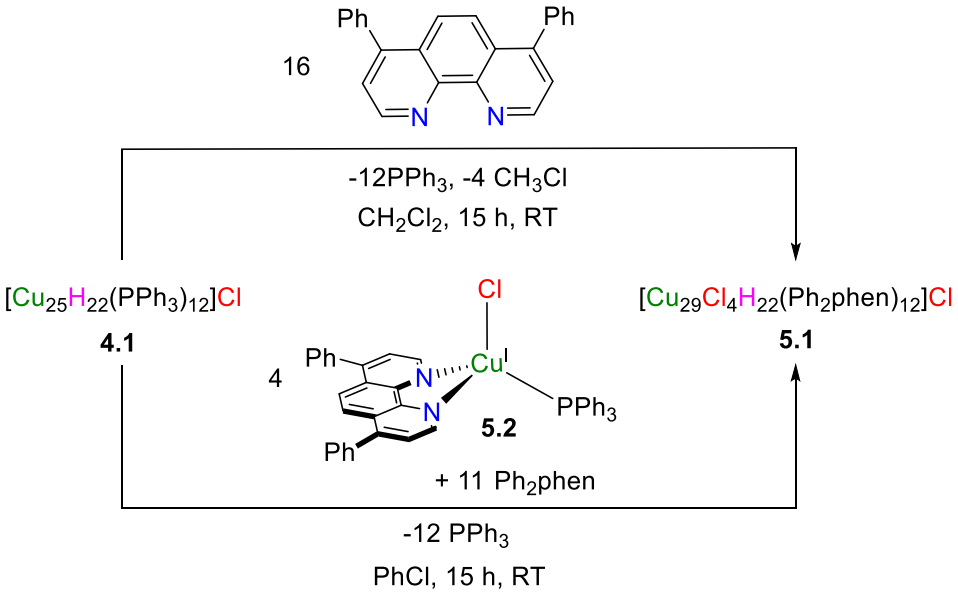

Complex **5.1** crystallizes in the trigonal space group *P*31*c* as a benzene solvate, **5.1**·16.5C_6H_6 (Figure 5.1). In the solid state, it features a central core of 13 Cu atoms arranged in a centered-icosahedron. Notably, this is the same core structure found in the precursor cluster, **4.1**, which also features a central Cu atom with a coordination number of 12.[15] The M_{13} icosahedral core is a common structural motif in nanoclusters, and is also found in $[Au_{25}(SCH_2CH_2Ph)_{18}]^-$,[16,17] $[Ag_{21}(S_2P(O^iPr)_2)_{12}]^+$,[18] $[Au_{13}(PMe_2Ph)_{10}Cl_2]^{3+}$,[19] and $[Ag_{29}(BDT)_{12}(PPh_3)_4]^{3-}$.[20] Comparison of **5.1** with $[Ag_{29}(BDT)_{12}(PPh_3)_4]^{3-}$ is particularly apt, as the two structures feature nearly identical spatial arrangements of their 29 metal atoms, despite very different ligand sets, which suggests that this structural arrangement is particularly stable.

The Cu_{13} core in **5.1** is connected, via Cu-Cu bonds, to four triangular $[Cu_4(Ph_2phen)_3(Cl)]$ motifs, which cap the icosahedron in a tetrahedral arrangement (Figures 5.1d and 5.1e). This arrangement places four [CuCl] units at the vertices of a tetrahedron (Figure 5.1c), while 12 $[Cu(Ph_2phen)]$ units are distributed around the cluster in six π-stacked pairs (Figure 5.1b). The distance between the Ph_2phen ligands is 3.3 Å, in-line with typical π-stacking interactions.[21,22] As was observed for complex **4.1**, complex **5.1** occupies the high symmetry *T* point group. Interestingly, the majority of the Cu-Cu distances in **5.1** exhibit a relatively narrow range (2.537(3)-2.817(3) Å); only four of 96 Cu-Cu bonds (3.286-3.303 Å) fall outside this range (Figure 5.2b). This narrow distribution is reminiscent of the highly ordered structure of the bulk metal, although we note that the average Cu-Cu distance in **5.1** is somewhat longer (av. 2.65 Å) than the distance in bulk Cu (2.556 Å).[23] In contrast, complex **4.1** contains Cu-Cu bond distances that cover a much wider range (2.389(3)-3.037(3) Å) (Figure 5.2b), even though the arrangement of the Cu atoms in both nanoclusters is comparable.[15] Most importantly, the isolation of **5.1** gives credence to the idea that small nanoclusters, such as **4.1**, can be used as templates for larger nanoclusters. Templated growth of nanoclusters has only been observed in a few instances, usually requiring significant thermal activation, and often occurs with major structural rearrangement.[8]

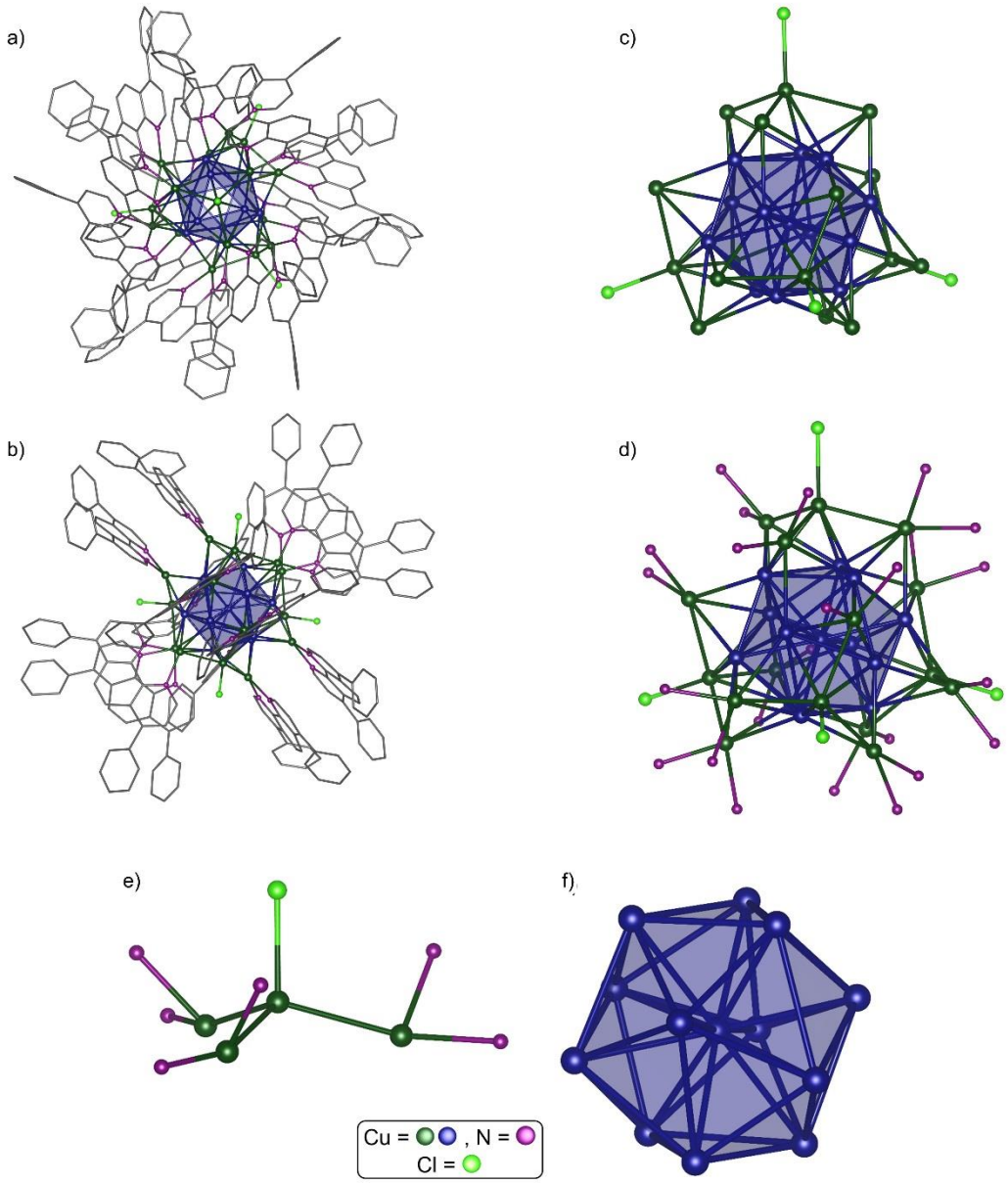

Figure 5.1. Ball and stick diagrams of complex **5.1**. The Cu_{13} centered-icosahedral cores are highlighted in blue. The remaining Cu atoms are shown in dark green. The N atoms are purple, the Cl atoms are lime green. All solvent molecules and outer-sphere counterions have been omitted for clarity. a) View down the C_3 axis, with C atoms depicted in wire frame. b) View down the C_2 axis, highlighting the π-stacking of the Ph_2phen ligands. C atoms are depicted in wireframe. c) Side view showing only the Cu and Cl atoms. d) Side

view showing only the Cu, N, and Cl atoms. e) Triangular [$Cu_4(Ph_2phen)_3(Cl)$] capping motif with carbon atoms omitted for clarity. f) Cu_{13} centered icosahedral core.

In solution, complex **5.1** features a ^{1}H NMR spectrum consistent with the *T* symmetry observed in its solid-state structure, which requires that the six Ph_2phen backbone protons be inequivalent. For example, in CD_2Cl_2, different resonances are assignable to the protons at the 2 and 9 positions of the Ph_2phen ligands, at 9.33 and 10.54 ppm, respectively. The ^{1}H NMR spectrum of **5.1** also features three broad resonances at 2.18, 2.56, and 3.44 ppm, which integrate for 4H, 12H, and 6H, respectively, and are assignable to 22 hydride ligands in three different chemical environments. A similar pattern is observed for **4.1**, and is further evidence that the core structure of complex **5.1** is essentially unchanged from that of **4.1**. This observation also suggests that the hydride positions in **5.1** are close to those predicted for complex **4.1**.[15]

Complex **5.1** features a signal at *m/z* 2979.803 in its electrospray ionization (ESI) mass spectrum, which corresponds to the $[M\text{-}Cl]^{2+}$ ion (Calcd *m/z* 2979.806), and a signal at *m/z* 1974.878 which corresponds to the $[M\text{-}2Cl]^{3+}$ ion (Calcd *m/z* 1974.879). The parent $[M]^+$ ion was not detected, presumably due to the lability of the coordinated chlorides in the gas phase. The synthesis and characterization of the deuteride analog, **5.1-*d*$_{22}$**, also supports our proposed formulation. In particular, complex **5.1-*d*$_{22}$** features singlets at 2.30, 2.71, and 3.69 ppm in its ^{2}H NMR spectrum, in a 4:12:6 ratio, respectively.

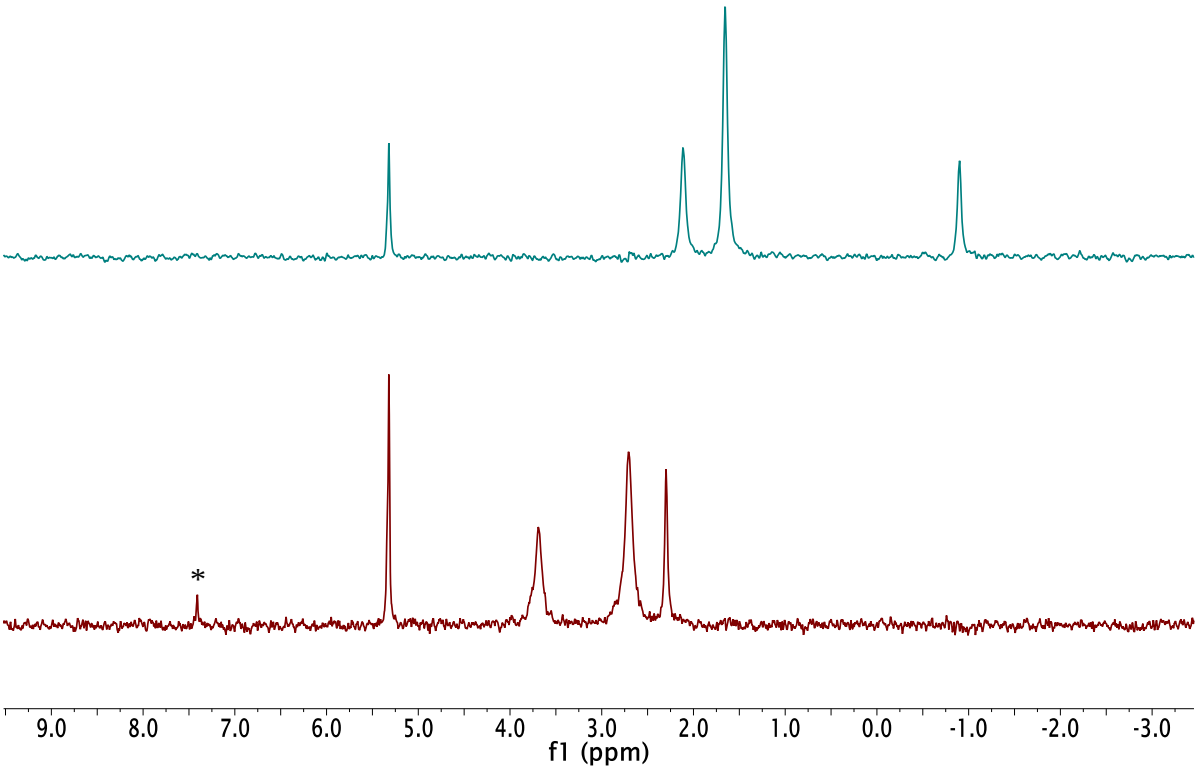

Figure 5.2. Comparison of the ^{2}H NMR spectra of $[Cu_{25}H_{22}(PPh_3)_{12}]Cl$ (**4.1-*d*$_{22}$**, top) $[Cu_{29}Cl_4D_{22}(Ph_2phen)_{12}]Cl$ (**5.1-*d*$_{22}$**, bottom). (*) denotes the presence of benzene.

In addition, complex **5.1-*d*$_{22}$** features a signal at *m/z* 2990.869 in its ESI mass spectrum, which corresponds to the $[M\text{-}Cl]^{2+}$ ion (Calcd *m/z* 2990.875), and a signal at *m/z* 1982.249 which corresponds to the $[M\text{-}2Cl]^{3+}$ ion (Calcd *m/z* 1982.258). These values represent a shift of 22 atomic mass units relative to the signals observed for **5.1-*h*$_{22}$**.

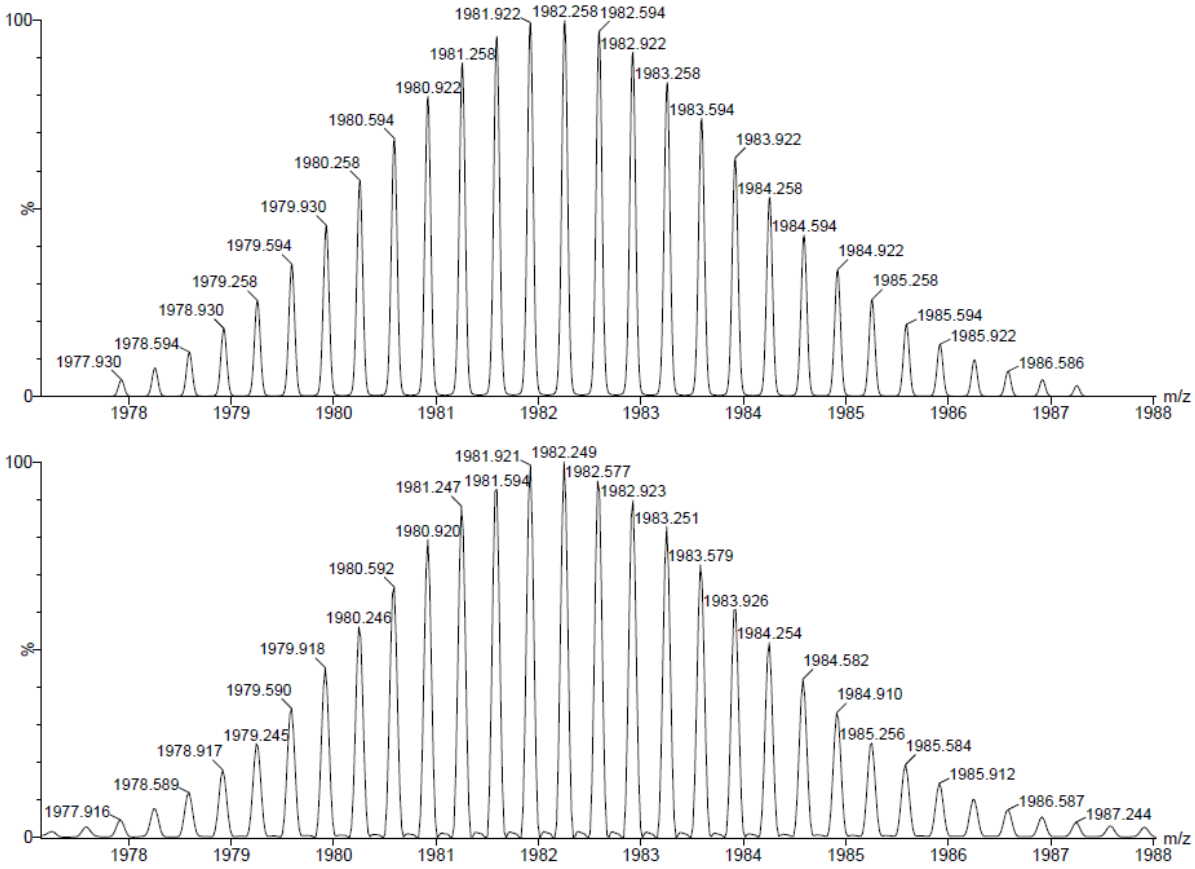

Figure 5.3. Partial ESI-MS of $[Cu_{29}Cl_4D_{22}(Ph_2phen)_{12}]Cl$ (**5.1-*d*$_{22}$**). The experimental (bottom) and calculated (top) peaks assignable to the $[M\text{-}2Cl]^{3+}$ ion are shown.

Finally, two of the Cu atoms in complex **5.1** must have a formal Cu(0) oxidation state to maintain charge balance, making complex **5.1** only the third structurally-characterized Cu nanocluster with partial Cu(0) character.[14,15] Complex **5.1** can also be described as an $N^* = 2$ superatom with a closed-shell $1S^2$ configuration.[24] This is a rare electronic structure with only a handful other well-defined examples, including $Ag_{14}(SC_6H_3F_2)_{12}(PPh_3)_8$, $Ag_{16}(SC_6H_3F_2)_{14}(DPPE)_8$ (DPPE = 1,2-bis(diphenylphosphino)ethane), $Au_{11}(SR)_9$, and $Au_{15}(SR)_{13}$.[2,25-27]

I also briefly probed the chemical properties of complex **5.1**. It is soluble in CH_2Cl_2 and PhCl, sparingly soluble in MeCN, and insoluble in THF, Et_2O, and nonpolar solvents.

Complex **5.1** is stable as a PhCl solution for at least 2 d at room temperature, but solutions of **5.1** in CH_2Cl_2 gradually decompose over the same time period, changing in color from deep blue to dark brown. This is likely due to oxidation by the solvent, which results in formation of copper chloride-containing decomposition products.[6] As a CH_2Cl_2 solution, complex **5.1** is stable in the presence of 40 equiv. of water for at least 5 h, but it is highly O_2-sensitive, and decomposes completely within 10 min upon exposure to air. The enhanced O_2 sensitivity of **5.1**, relative to thiol-passivated Ag and Au NCs, is a consequence of the much higher reactivity of the Cu-H bond,[28] which is partially rooted in the large enthalpic driving force for H_2O formation. While this difference makes copper hydride NCs more challenging to handle, it also provides potential opportunities for catalysis, as copper hydrides are known to promote a wide variety of organic transformations.[28]

Zach Jones from Prof. Susannah Scott's group at UCSB collected Cu K-edge X-ray absorption near-edge spectra (XANES) and extended X-ray absorption fine structure (EXAFS) for complex **5.1**, in order to compare to that previously acquired for **4.1**. The edge position of **5.1** (8979.5 eV) is very close to that of **4.1** (8979.6 eV) and lies between values measured for Cu(0) in the bulk foil (8979.0 eV) and Cu(I) in clusters such as $[CuH(PPh_3)]_6$ (8980.0 eV) and $[CuCl(PPh_3)]_4$ (8980.9 eV).[15] As was the case for **4.1**, this is consistent with an average Cu oxidation state for **5.1** between 0 and +1 (Table 5.1).

Table 5.1. Cu K-edge energies (eV) and Auger parameters (eV) for selected Cu(0) and Cu(I) compounds.

material	K-edge	Auger parameter
Cu foil	8979.0	1851.2
$[Cu_{25}H_{22}(PPh_3)_{12}][Cl]$, **4.1**	8979.6	1849.1
$[Cu_{29}Cl_4H_{22}(Ph_2phen)_{12}][Cl]$, **5.1**	8979.5	1848.9

$[CuH(PPh_3)]_6$	8980.0	1848.6
$[CuCl(PPh_3)]_4$	8980.9	1847.4

Similarly, the Auger parameter that Zach Jones extracted from his XPS spectrum for **5.1**, at 1848.9 eV, is intermediate between values for bulk Cu(0) (1851.2 eV) and those for the $[CuH(PPh_3)]_6$ and $[CuCl(PPh_3)]_4$ Cu(I) clusters (1848.6 and 1847.4 eV, respectively), in agreement with partial Cu(0) character for **5.1**. A similar Auger parameter was previously observed by Zach Jones for **4.1**.[15] In addition, the N:Cu ratio of **5.1** determined by XPS, 0.82, is nearly identical to the expected value of 0.83 based on the crystal structure (Table 5.4).

Interestingly, the narrow range of Cu-Cu distances in complex **5.1** is apparent in its extended X-ray absorption fine structure (EXAFS) featuring a symmetrical narrow peak centered at 2.2 Å (Figure 5.4b; see Figure 5.8 for full EXAFS curves). In contrast, the EXAFS of complex **4.1** has a much more unsymmetrical and broader peak centered at 2.0 Å, which is fully consistent with its wider range of Cu-Cu distances. Zach Jones was able to achieve a satisfactory curvefit to the EXAFS of **5.1** (Figure 5.4c) using only a single Cu-Cu path and a Cu-N path. In contrast, addition of a second Cu-Cu path to the fit for **4.1** yielded a better fit.[15] The curvefit for **5.1** gives an average Cu-Cu single-scattering pathlength of 2.567(3) Å, which is close to the known value derived from the crystal structure (2.65 Å). In addition, the refined average coordination number (N = 6.8 ± 0.6) is close to the expected value (7.5). Thus, XANES and EXAFS are able to distinguish between very closely related nanoclusters.

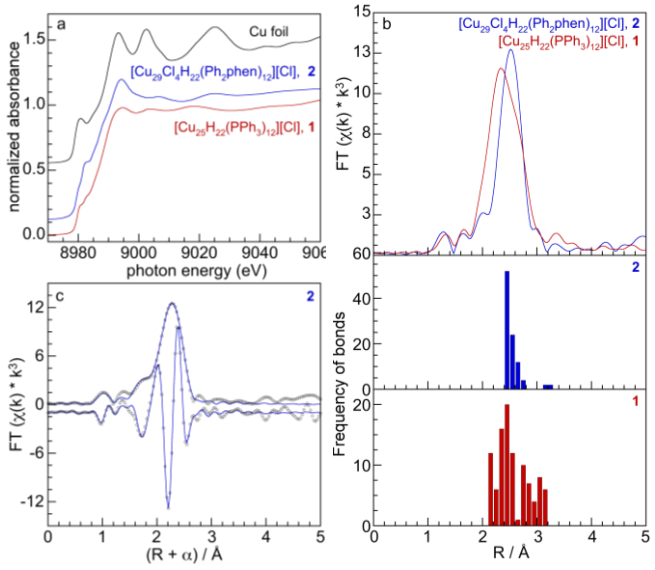

Figure 5.4. Comparison of XANES and EXAFS data for complexes **4.1** and **5.1**. a) Comparison of Cu K-edge XANES profiles for Cu foil and nanoclusters **4.1** and **5.1**. b) Comparison of Cu K-edge EXAFS for nanoclusters **4.1** and **5.1** (phase-corrected FT magnitude: top), as well as distributions of Cu-Cu bond distances based on single-crystal X-ray diffraction (middle and bottom). c) EXAFS curvefit (lines) for **5.1**, showing data (circles) as the FT magnitude and its imaginary component in non-phase-corrected *R*-space. Data for **4.1** taken from Ref. 15. Figure prepared by Zach Jones.

Formation of **5.1** by cluster expansion of **4.1** requires both complete exchange of 12 Ph_3P ligands by 12 Ph_2phen ligands, and addition of four "CuCl" units to the Cu_{25} core. We hypothesize that this process occurs in two stages. First, rapid ligand exchange with Ph_2phen results in formation of $[Cu_{25}H_{22}(PPh_3)_{12-n}(Ph_2phen)_n]Cl$. This unstable intermediate then reacts sequentially with four "CuCl" units to generate complex **5.1**. The "CuCl" units are presumably derived from a reaction between a sacrificial molecule of $[Cu_{25}H_{22}(PPh_3)_{12-n}(Ph_2phen)_n]Cl$ and the CH_2Cl_2 solvent, releasing "CuCl" monomers and forming CH_3Cl. A similar chloride-hydride metathesis process occurs during the formation of

$[Cu_{14}H_{12}(phen)_6(PPh_3)_4][Cl]_2$ from $[(PPh_3)CuH]_6$ and phen in CH_2Cl_2, wherein the solvent provides the required Cl^- counterions, and forms CH_3Cl as a by-product.[6] Importantly, only a small fraction of $[Cu_{25}H_{22}(PPh_3)_{12-n}(Ph_2phen)_n]Cl$ is required to form the required "CuCl" monomers, since just one cluster can supply 25 equiv of "CuCl".

In view of the presence of excess Ph_2phen and un-ligated Ph_3P in the reaction mixture, I hypothesized that a much smaller mixed-ligand Ph_2phen/Ph_3P coordination complex, such as $[(Ph_2phen)(PPh_3)CuCl]$ (**5.2**), acts as the "CuCl" carrier during formation of **5.1**. To confirm its viability in this role, $[(Ph_2phen)(PPh_3)CuCl]$ (**5.2**) was synthesized independently by the reaction of CuCl, PPh_3 and Ph_2phen, and was isolated in 97% yield.

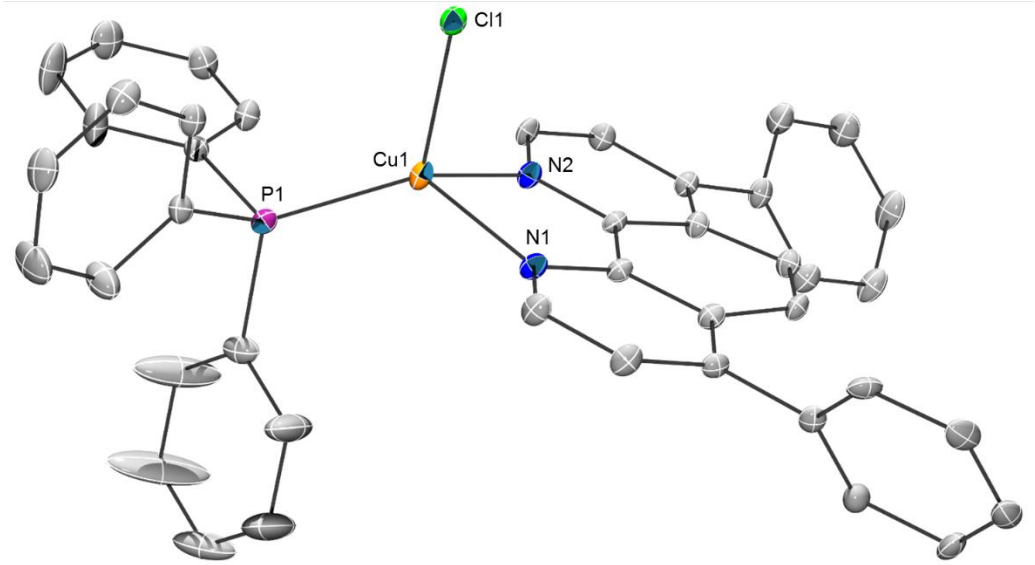

Figure 5.5. Solid-state molecular structure of **5.2**·3THF with 50% probability ellipsoids. Hydrogen atoms and solvate molecules have been omitted for clarity. Selected bond lengths (Å) and angles (deg): Cu1–Cl1 = 2.323(1), Cu1–P1 = 2.180(1), Cu1–N1 = 2.086(4), Cu1–N2 = 2.102(3), ∑(Cl1–Cu1–E) = 318.94.

The self-assembly of complex **5.2** from this mixture, as well as its isolation in nearly quantitative yield, are consistent with the hypothesis that it forms readily *in situ* and can act

as a "CuCl" carrier. In further support of its role in the cluster expansion, reaction of **4.1** with 4 equiv of complex **5.2** and 11 equiv Ph_2phen, in chlorobenzene resulted in formation of complex **5.1**, recovered in 67% yield after work-up (Scheme 5.1). This material is spectroscopically identical to that obtained by the simple ligand exchange method described above; however, the direct use of **5.2** made it possible to form **5.1** in the absence of CH_2Cl_2 as a chloride source.

To further probe the transformation of complex **4.1** to **5.1**, and to test the hypothesis that [$(Ph_2phen)(PPh_3)CuCl$] (**5.2**) is an intermediate in the reaction, I collaborated with Dr. Domenick Leto, a former post-doc in the Scott group at UCSB, to monitor the formation of **5.1** using UV-vis spectroscopy. We collected the data together and then the kinetic analysis was done by Prof. Susannah Scott. Atomically-precise nanoclusters show discrete bands in their UV-vis spectra, unlike typical polydisperse nanoparticles.[10] Complex **4.1** in CH_2Cl_2 features a prominent band at 460 nm, as well as a broad band at 615 nm, with a shoulder at 675 nm (Figure 5.10). Addition of 2, 4 or 8 equiv of **5.2** to 11 equiv of Ph_2phen (both relative to 1 equiv of complex **4.1**, *ca*. 0.05 mM) at 25 °C resulted in a rapid color change of the green solution of **5.2** to blue-black, concomitant with the appearance of overlapping bands at *ca*. 395, 575, 725, and 900 nm (Figure 5.10).

Prof. Scott monitored the kinetics of the conversion of **4.1** to **5.1** using the band at 575 nm (Figure 5.6). In the absence of added monomer **5.2** (black points), she found that the reaction is slow, and pseudo-zeroth-order (Figures 5.6 and 5.11). We propose that ligand exchange (eq 5.1) results in slow extraction of monomer **5.2** from **4.1** to give a less stable nanocluster (e.g., Cu_{24}), via a process that also involves the solvent CH_2Cl_2, eq 5.2.

$$[Cu_{25}H_{22}(PPh_3)_{12}]Cl\ (\mathbf{4.1}) + n\ Ph_2phen \rightleftarrows [Cu_{25}H_{22}(PPh_3)_{12-n}(Ph_2phen)_n]Cl + n\ PPh_3 \quad (5.1)$$

$[Cu_{25}H_{22}(PPh_3)_{12-n}(Ph_2phen)_n]Cl + CH_2Cl_2 + PPh_3 \rightarrow$

$[Cu_{24}H_{21}(PPh_3)_{12-n}[(Ph_2phen)_{n-1}]Cl + [Cu(Ph_2phen)(PPh_3)Cl]$ (**5.2**) + CH_3Cl (5.2)

The rate of the reaction is much faster in the presence of added monomer **5.2**, and accelerates as [**5.2**] increases. Prof. Scott found that the curvefits of the first-order integrated rate equation to the kinetic profiles improves as the [**5.2**]/[**4.1**] ratio increases, as expected since the reaction conditions become closer to pseudo-first-order. The dependence of k_{obs} on [**5.2**] is linear (Figure 5.6 inset and Table 5.6). These results suggest a mechanism in which **4.1** undergoes initial, rapid ligand exchange in a pre-equilibrium step (eq 5.1), followed by association with monomer **5.2** to give a larger nanocluster (i.e., Cu_{26}) in a kinetically relevant capture step such as eq 5.3.

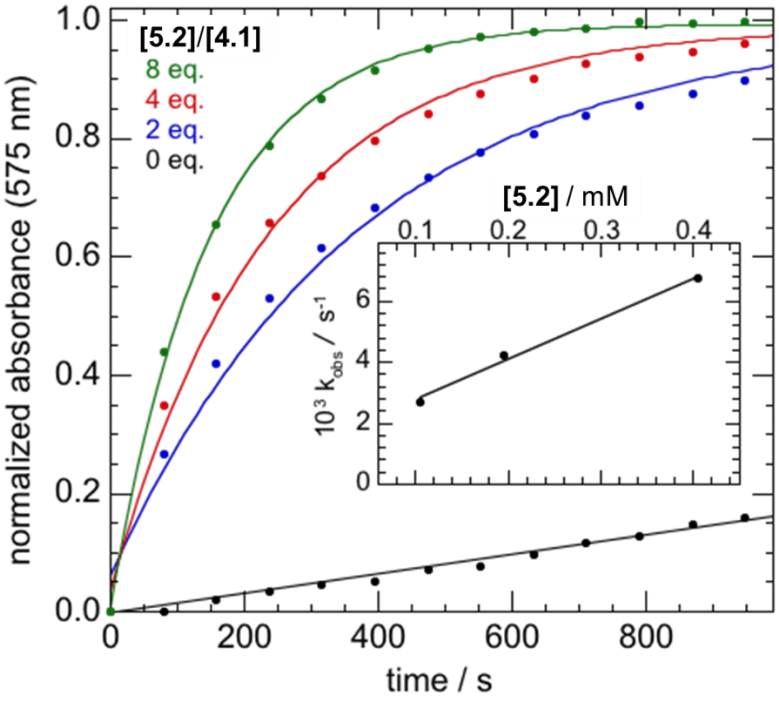

Figure 5.6. Kinetic profiles for the transformation of 0.05 mM **4.1** to **5.1** in CH_2Cl_2 at 25 °C, recorded with 15 equiv Ph_2phen and no added $[Cu(Ph_2phen)(PPh_3)Cl]$ (**5.2**) (black points), or 11 equiv Ph_2phen and variable amounts of added $[Cu(Ph_2phen)(PPh_3)Cl]$ (**5.2**) (colored points). Lines are curvefits to the first-order integrated rate law. The inset shows

the linear dependence of the pseudo-first-order rate constants on the concentration of added **5.2**. Figure prepared by Prof. Susannah Scott.

$[Cu_{25}H_{22}(PPh_3)_{12-n}(Ph_2phen)_n]Cl + [Cu(Ph_2phen)(PPh_3)Cl]$ (**5.2**) → $[Cu_{26}H_{22}Cl(PPh_3)_{12-n}(Ph_2phen)_n]Cl + Ph_2phen + PPh_3$ (5.3)

To determine the reaction order with respect to Ph_2phen, time resolved kinetic profiles were recorded by Dr. Domenick Leto and I, with 8, 14, or 17 equiv of Ph_2phen and a constant amount of **5.2** (4 equiv with respect to **4.1**) at 25 °C. Analysis by Prof. Scott showed that the pseudo-first-order rate constants k_{obs} correlate linearly with the concentration of added Ph_2phen (Figure 5.12 and Table 5.5), indicating that the rate law contains a term that is first-order in both the chelating ligand and the monomer **5.2**. The empirical rate law determined by Prof. Scott is shown in eq 5.4.

$$d[\mathbf{5.1}]/dt = k_0 + k_1[\mathbf{4.1}][\mathbf{5.2}][Ph_2phen] \quad (5.4)$$

5.3 Summary

In summary, I describe the synthesis of a new Cu_{29} nanocluster via a unique mechanism of cluster growth initiated by ligand exchange and involving CuCl monomer formation, transport, and addition. This mechanism could be applicable to other nanocluster systems, and suggests a new strategy to manipulate metal NCs. Additionally, our results reveal the role of a well-defined carrier molecule that mediates the growth process. This study also demonstrates that detailed spectroscopic and kinetic assessments can be obtained for well-defined nanoclusters, and should be highly amenable to first-principles computational analysis.[15] Such studies promise to provide the first quantitative descriptions of nanocluster growth kinetics, in contrast to polydisperse nanoparticle systems whose descriptions remain largely qualitative despite advances in *in situ* observations.[12]

In future studies, X-ray absorption spectroscopy could provide important information about transient species, nanoclusters generated *in situ*, and supported nanoclusters for which single-crystal X-ray diffraction is not possible. More detailed measurements will likely yield information that can be used to understand and predict the driving forces and barriers for cluster rearrangement, and for benchmarking computational models.[29] Ultimately, we expect that a better understanding of cluster behavior and structure will advance the design of nanocluster-based materials for technological applications in sensing, optical imaging, nanomedicine and catalysis.

5.4 Experimental

5.4.1 General Procedures

All reactions and subsequent manipulations were performed under anaerobic and anhydrous conditions under an atmosphere of nitrogen. Hexanes, diethyl ether (Et_2O), tetrahydrofuran (THF), and toluene were dried using a Vacuum Atmospheres DRI-SOLV Solvent Purification system and stored over 3Å sieves for 24 h prior to use. Dichloromethane (CH_2Cl_2), acetonitrile (CH_3CN), benzene (C_6H_6), and chlorobenzene were degassed and dried over 3Å molecular sieves for 72 h prior to use. CD_2Cl_2 was dried over 3Å molecular sieves for 24 h prior to use. $[Cu_{25}H_{22}(PPh_3)_{12}]Cl$ (**4.1**) and $[Cu_{25}H_{22}(PPh_3)_{12}]Cl$ (**4.1-*d*$_{22}$**) were prepared according to the previously reported procedure.[15] All other reagents were purchased from commercial suppliers and used as received.

All NMR spectra were collected at room temperature. NMR spectra were recorded on an Agilent Technologies 400-MR DD2 400 MHz spectrometer. The chemical shifts of ^{31}P nuclei were referenced indirectly with the ^{1}H resonance of $SiMe_4$ at 0 ppm, according to

IUPAC standard.[30,31] The chemical shifts of the other nuclei were referenced using the solvent peaks (^{1}H, ^{13}C and ^{2}H NMR experiments) as internal standards. IR spectra were recorded on a Nicolet 6700 FT-IR spectrometer with a NXR FT Raman Module. UV-Vis / NIR experiments were performed on a UV-3600 Shimadzu spectrophotometer. Mass spectra were collected at the MRL Shared Experimental Facilities at the University of California, Santa Barbara, using an electrospray ion (ESI) source on positive ion mode with a Waters Xevo G2-XS Tof Time-of-Flight mass spectrometer. Mass spectra were smoothed 2 times using the Savitsky-Golay algorithm with a smooth window of 3 channels. Elemental analyses were performed by the Micro-Mass Facility at the University of California, Berkeley.

5.4.2 Synthesis of $[Cu_{29}Cl_4H_{22}(Ph_2phen)_{12}]Cl$ (5.1)

Method A. To a dark green solution of $[Cu_{25}H_{22}(PPh_3)_{12}]Cl$ (**4.1**) (24.1 mg, 0.00503 mmol) in CH_2Cl_2 (1 mL) was added 4,7-diphenyl-1,10-phenanthroline (Ph_2phen, 27.4 mg, 0.0824 mmol) as a CH_2Cl_2 solution (2 mL). This resulted in a rapid color change of the dark green solution to dark blue. After stirring for 15 h, the reaction mixture was filtered through a Celite column (0.5 cm × 1 cm) supported on glass wool. The dark blue filtrate was concentrated *in vacuo* and layered with Et_2O (6 mL). Storage of this solution at -25 °C for 5 h resulted in the deposition of dark blue-black crystalline solid. The solid was isolated by decanting off the supernatant, washing with Et_2O (3 × 1 mL) until the washings were colorless, and drying *in vacuo* (21.9 mg, 84% yield). X-ray quality crystals of **5.1** were grown by slow evaporation of a concentrated C_6H_6 solution at room temperature. Anal. Calcd for $C_{288}H_{214}Cl_5Cu_{29}N_{24}$: C, 57.36; H, 3.58; N, 5.57. Found: C, 57.52; H, 3.56; N, 5.26. ^{1}H NMR (400 MHz, 25 °C, CD_2Cl_2): δ 2.18 (s, 4H, hydride), 2.56 (br s, 12H, hydride), 3.44

(s, 6H, hydride), 6.74 (d, J_{HH} = 4.8 Hz, 12H, 3,8-C*H* on Ph_2phen), 6.80 (d, J_{HH} = 4.6 Hz, 12H, 3,8-C*H* on Ph_2phen), 7.07-7.15 (m, 48H, Ar C*H* on Ph), 7.22 (t, J_{HH} = 7.3 Hz, 24H, Ar C*H* on Ph), 7.30 (t, J_{HH} = 7.5 Hz, 24H, Ar C*H* on Ph), 7.37 (m, 24H, Ar C*H* on Ph), 7.50 (s, 24H, 5,6-C*H* on Ph_2phen), 9.33 (d, J_{HH} = 4.8 Hz, 12H, 2,9-C*H* on Ph_2phen), 10.54 (d, J_{HH} = 4.7 Hz, 12H, 2,9-C*H* on Ph_2phen). $^{13}C\{^1H\}$ NMR (101 MHz, 25 °C, CD_2Cl_2): δ 122.56 (s), 122.62 (s), 122.93 (s), 123.27 (s), 124.34 (s), 125.39 (s), 128.48 (s), 129.54 (s), 129.83 (s), 136.77 (s), 142.84 (s), 143.64 (s), 145.73 (s), 147.00 (s), 149.52 (s), 151.42 (s). Four ^{13}C resonances were not observed. ESI-MS: *m/z* 2979.803 $[M\text{-}Cl]^{2+}$ (Calcd *m/z* 2979.806), 1974.878 $[M\text{-}2Cl]^{3+}$ (Calcd *m/z* 1974.879). IR (KBr pellet, cm^{-1}): 410 (w), 489 (w), 545 (w), 575 (w), 592 (w), 626 (w), 664 (w), 702 (s), 738 (m), 765 (s), 805 (w), 831 (m), 849 (m), 1000 (w), 1019 (m), 1076 (m), 1157 (w), 1180 (w), 1230 (w), 1261 (w), 1386 (w), 1422 (s), 1444 (w), 1491 (m), 1514 (w), 1555 (m), 1590 (w), 1615 (w). UV-Vis / NIR (CH_2Cl_2, 0.024 mM, 25 °C, $L{\cdot}mol^{-1}{\cdot}cm^{-1}$): 410 (sh, ε = 53000), 580 (ε = 47500), 720 (sh, ε = 30500), 900 (ε = 22000). UV-Vis / NIR (CH_2Cl_2, 0.079 mM, 25 °C, $L{\cdot}mol^{-1}{\cdot}cm^{-1}$): 1400 (ε = 1500).

Method B. To a vial containing **4.1** (31.6 mg, 0.00659 mmol), [(Ph_2phen)(PPh_3)CuCl] (**5.2**) (18.8 mg, 0.0.271 mmol), and Ph_2phen (26.5 mg, 0.0797 mmol) was added chlorobenzene (3 mL). This resulted in the formation of a dark blue-black solution. Note that a small amount of complex **4.1** remained undissolved in the reaction mixture. This mixture was stirred for 15 h, which resulted in dissolution of all the solid and formation of a clear dark blue-black solution. The dark blue solution was then filtered through a Celite column (0.5 cm × 1.5 cm) supported on glass wool. The filtrate was concentrated *in vacuo* and layered with toluene (12 mL). Storage of this solution at -25 °C for 24 h resulted in the deposition of dark blue-black crystals which were isolated by decanting off the supernatant, washing with Et_2O (3 × 1.5 mL) until the washings

were colorless, and drying *in vacuo* (26.5 mg, 67% yield). This material was spectroscopically identical to the material prepared by Method A.

5.4.3 Synthesis of [$Cu_{29}Cl_4D_{22}(Ph_2phen)_{12}$]Cl (**5.1-*$d_{22}$***)

To a dark green solution of [$Cu_{25}D_{22}(PPh_3)_{12}$]Cl (**4.1-*$d_{22}$***) (30.8 mg, 0.00640 mmol) in CH_2Cl_2 (2 mL) was added 4,7-diphenyl-1,10-phenanthroline (Ph_2phen, 39.3 mg, 0.118 mmol) as a CH_2Cl_2 solution (1 mL). This resulted in a rapid color change of the dark green solution to an inky dark blue. After stirring for 15 h, the reaction mixture was filtered through a Celite column (0.5 cm × 1 cm) supported on glass wool. The dark blue filtrate was concentrated *in vacuo* and layered with Et_2O (10 mL). Storage of this solution at -25 °C for 5 h resulted in the deposition of dark blue-black crystalline solid. The solid was isolated by decanting off the supernatant, washing with Et_2O (3 × 1 mL) until the washings were colorless, and drying *in vacuo* (22.9 mg, 69% yield). ^{1}H NMR (400 MHz, 25 °C, CD_2Cl_2): δ 6.75 (d, J_{HH} = 4.9 Hz, 12H, 3,8-C*H* on Ph_2phen), 6.83 (m, 3,8-C*H* on Ph_2phen), 7.09-7.16 (m, 48H, Ar C*H* on Ph), 7.23 (t, J_{HH} = 7.5 Hz, 24H, Ar C*H* on Ph), 7.29 (t, J_{HH} = 7.5 Hz, 24H, Ar C*H* on Ph), 7.37 (m, 24H, Ar C*H* on Ph), 7.51 (s, 24H, 5,6-C*H* on Ph_2phen), 9.31 (d, J_{HH} = 4.3 Hz, 12H, 2,9-C*H* on Ph_2phen), 10.54 (d, J_{HH} = 4.7 Hz, 12H, 2,9-C*H* on Ph_2phen). ^{2}H NMR (61 MHz, 25 °C, CD_2Cl_2): δ 2.30 (s, 4D), 2.71 (s, 12D), 3.69 (s, 6D). ESI-MS: *m/z* 2990.869 $[M\text{-}Cl]^{2+}$ (Calcd *m/z* 2990.875), 1982.249 $[M\text{-}2Cl]^{3+}$ (Calcd *m/z* 1982.258).

5.4.4 Synthesis of [(Ph_2phen)(PPh_3)CuCl] (5.2)

To a vial containing CuCl (17.6 mg, 0.178 mmol), PPh_3 (48.6 mg, 0.185 mmol), and Ph_2phen (60.1 mg, 0.181 mmol) was added THF (2 mL) and CH_2Cl_2 (1 mL). This resulted

in the formation of a red solution, which was stirred for 45 min. The red solution was then filtered through a Celite column (0.5 cm × 1 cm) supported on glass wool and the column was rinsed with THF (1 mL). The filtrate was layered with Et_2O (3 mL) and then hexanes (7 mL). Storage of this solution at room temperature for 24 h resulted in the deposition of orange crystals which were isolated by decanting off the supernatant. The solid was washed with hexanes (3 × 1 mL) and dried *in vacuo* (120.1 mg, 97% yield). Anal. Calcd for $C_{42}H_{31}ClCuN_2P$: C, 72.72; H, 4.50; N, 4.04. Found: C, 72.40; H, 4.56; N, 4.16. ^{1}H NMR (400 MHz, 25 °C, CD_2Cl_2): δ 7.28-7.41 (m, 10H, Ph C*H* on Ph_2phen), 7.47-7.62 (m, 15H, C*H* on PPh_3), 7.69 (d, *J* = 4.4 Hz, 2H, 3,8-C*H* on Ph_2phen), 7.96 (s, 2H, 5,6-C*H* on Ph_2phen), 9.02 (m, 2H, 2,9-C*H* on Ph_2phen). ^{31}P{^{1}H} NMR (162 MHz, 25 °C, CD_2Cl_2): δ -3.04 (br s). ^{13}C NMR (101 MHz, 25 °C, CD_2Cl_2) δ 124.95 (s), 125.57 (s), 127.50 (s), 128.99 (d, J_{CP} = 9.1 Hz, *m*-*C*H on PPh_3), 129.32 (s), 129.48 (s), 130.03 (s), 130.15 (s), 134.17 (d, J_{CP} = 15.6 Hz, *o*-*C*H on PPh_3), 134.94 (d, J_{CP} = 27.9 Hz, *ipso*-*C* on PPh_3), 137.55 (s), 144.55 (s), 149.43 (s). One ^{13}C resonance was not observed. IR (KBr pellet, cm^{-1}): 408 (s), 443 (w), 504 (w), 523 (m), 545 (w), 575 (w), 594 (w), 627 (w), 696 (s), 741 (m), 766 (m), 805 (w), 833 (w), 851 (w), 999 (w), 1026 (m), 1071 (m), 1095 (m), 1158 (w), 1181 (w), 1228 (w), 1262 (w), 1385 (w), 1423 (m), 1434 (s), 1479 (m), 1490 (m), 1514 (m), 1556 (m), 1589 (m), 1617 (m). UV-Vis (CH_2Cl_2, 0.10 mM, 25 °C, $L \cdot mol^{-1} \cdot cm^{-1}$): 350 (sh, ε = 5700), 400 (ε = 4800).

5.4.5 X-ray Crystallography

Data for **5.1**·16.5C_6H_6 and **5.2**·3THF were collected on a Bruker KAPPA APEX II diffractometer equipped with an APEX II CCD detector using a TRIUMPH monochromater with a MoKα X-ray source (α = 0.71073 Å). Crystals were mounted on a cryoloop under

Paratone-N oil, and all data were collected at 100(2) K using an Oxford nitrogen gas cryostream system. X-ray data for **5.1**·16.5C_6H_6 were collected utilizing frame exposures of 30 (low angle) and 60 s (medium angle), while data for **5.2**·3THF were collected utilizing frame exposures of 10 (low angle), 15 (medium angle), and 20 s (high angle). Data collection and cell parameter determination were conducted using the SMART program.[32] Integration of the data frames and final cell parameter refinement were performed using SAINT software.[33] Absorption correction of the data were carried out using the multi-scan method SADABS.[34] Subsequent calculations were carried out using SHELXTL.[35] Structure determination was done using direct methods and difference Fourier techniques. All hydrogen atom positions were idealized, and rode on the atom of attachment. The final refinement included anisotropic temperature factors on all non H atoms, except for the solvent C atoms in **5.1**·16.5C_6H_6. The remaining atoms were refined isotropically. The 22 hydride ligands on **5.1**·16.5C_6H_6 were not located in the difference Fourier maps due to the high electron density around the copper cores. Structure solution, refinement, graphics, and creation of publication materials were performed using SHELXTL.[35]

Complex **5.1**·16.5C_6H_6 exhibits positional disorder of one of the C_6H_6 solvate molecules. This disorder was addressed by assigning the molecule half occupancy. In addition, selected C-C bonds within the C_6H_6 solvate molecules were fixed with the DFIX command and constrained with the FLAT command. The EADP command was used to constrain C5, C6, C14, C18, C13, C19, C44 C48, C61, C67, C66, C62, C65, C63, C87, C90, C230 C231 C232 C233 C234, and C235. In complex **5.2**·3THF, two of the THF solvate molecules exhibited minor positional disorder. The C-C and C-O bonds within these THF molecules were fixed with the DFIX command. In addition the C-C bonds within one of the

Ph rings on the PPh_3 ligand were fixed with the DFIX command and constrained with the FLAT command.

Table 5.2. X-ray Crystallographic Data for **5.1**·16.5C_6H_6 and **5.2**·3THF

	5.1·16.5C_6H_6	**5.2**·3THF
empirical formula	$C_{387}H_{291}Cl_5Cu_{29}N_{24}$	$C_{54}H_{55}ClCuN_2O_3P$
crystal habit, color	block, blue-black	block, orange
crystal size (mm)	0.2 × 0.1 × 0.05	0.2 × 0.1 × 0.1
crystal system	trigonal	monoclinic
space group	*P*31*c*	$P2_1/c$
volume (Å^3)	16688.1(16)	4640.2(4)
a (Å)	22.4465(9)	11.6220(6)
b (Å)	22.4465(9)	16.3129(10)
c (Å)	38.2453(18)	24.6222(11)
α (deg)	90	90
β (deg)	90	96.269(3)
γ (deg)	120	90
Z	2	4
formula weight (g/mol)	7297.33	909.96
density (calculated) (Mg/m^3)	1.452	1.303
absorption coefficient (mm^{-1})	1.902	0.609
F_{000}	7414	1912
total no. reflections	41840	28428
unique reflections	14483	10855
final R indices [I >2σ(I)]	R_1 = 0.0697 wR_2 = 0.1578	R_1 = 0.0738 wR_2 = 0.1728
largest diff. peak and hole (e$^-$ A^{-3})	1.513 and -0.572	1.386 and -0.868
GOF	1.019	1.021

5.4.6 X-ray Absorption Spectroscopy

X-ray absorption near-edge spectra (XANES) and extended X-ray absorption fine structure (EXAFS) were recorded at the Cu *K*-edge (8979 eV) on Beamline 4-1 (bend) at the Stanford Synchrotron Radiation Lightsource (SSRL), which operates at 3.0 GeV with a ring current of 500 mA. X-rays were monochromatized via reflection from a Si(220) double crystal monochromator, φ = 90 °, and passed through a 1 × 7 mm entrance slit. The beam was detuned 30 % to reject harmonics. Data were collected with step size of 0.35 eV over

the region 40 eV before the edge, and 20 eV after the edge. This results in a near-edge resolution of ca. 0.1 eV. X-ray absorption data were acquired up to k = 15 Å^{-1}. N_2-filled ionization detectors were mounted in the beam before and after the sample to collect data in transmission mode. The spectrum of a Cu foil was recorded using a third ionization detector, for simultaneous energy calibration. Complex **5.1** and Cu standards were diluted with boron nitride (99.5 %, Fisher Scientific) in a N_2-filled glovebox, to produce samples containing *ca.* 5 wt% Cu in order to minimize self-absorption effects. The dilute materials were loaded into slotted Al sample plates (slot size 12 x 3 x 0.5 mm) and sealed under N_2, using Kapton tape (5 μm, DuPont). The plates were transferred to a liquid He flow cryostat (Oxford Instruments) and cooled to <15 K. Six scans were recorded and averaged for each sample. Subsequent scans showed no changes, confirming the integrity of each sample under the measurement conditions.

Data processing and analysis were performed using the Demeter software package (v. 0.9.20).[36] The averaged spectra were aligned using the edge energy of the Cu foil spectrum. Absorption edge positions were assigned as the first maximum in the first derivative of the spectrum. A linear pre-edge function was subtracted, then the data were normalized by edge height using Athena software. A smooth, third-order polynomial approximating the absorption background of an isolated atom was subtracted to yield $\chi(k)$. The data were then k^3-weighted and Fourier-transformed. EXAFS analysis was conducted with paths generated by FEFF6 from the crystallographic data for complex **4.1** and complex **5.1** obtained by single crystal X-ray diffraction (this work and Ref. 15). Coordination numbers (N), distances of scattering atoms (R) and their mean-squared displacements (σ^2) were obtained by non-linear least-squares refinement in R-space, using the EXAFS equation.

The amplitude reduction factor (S_0^2) and the energy shift parameter (ΔE_0) were refined as global fit parameters. Their values were then fixed while the values of R and σ^2 were refined. Finally, the values of N were refined while holding previously obtained values for R and σ^2 fixed.

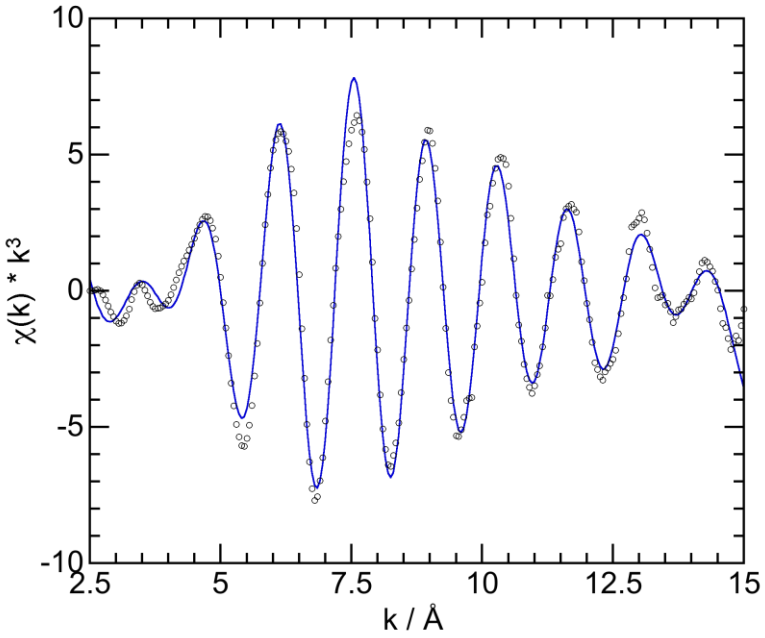

Figure 5.7. Cu K-edge EXAFS of complex **5.1** (points), in k^3-weighted k-space, showing curvefit (solid line) to a 2-path single-scattering model.

Table 5.3. Curvefit parameters for the EXAFS of complex **5.1** (fit shown in Figure 5.4c)

Path	Crystal structure[a]		EXAFS fit[b]		
	N	*d* (Å)[a]	*N*	R (Å)	σ^2 (Å^2)
Cu-N	0.83	2.079	0.8[c]	2.079(6)	0.006(3)
Cu-Cu	7.45	2.65	6.8(6)	2.567(3)	0.008(1)

[a] Determined by single-crystal X-ray diffraction (this work). [b] Global fit parameters: S_o^2 = 0.84(3); ΔE_o = 0.7(4) eV. [c] Fixed at this value (i.e., the known N:Cu ratio).

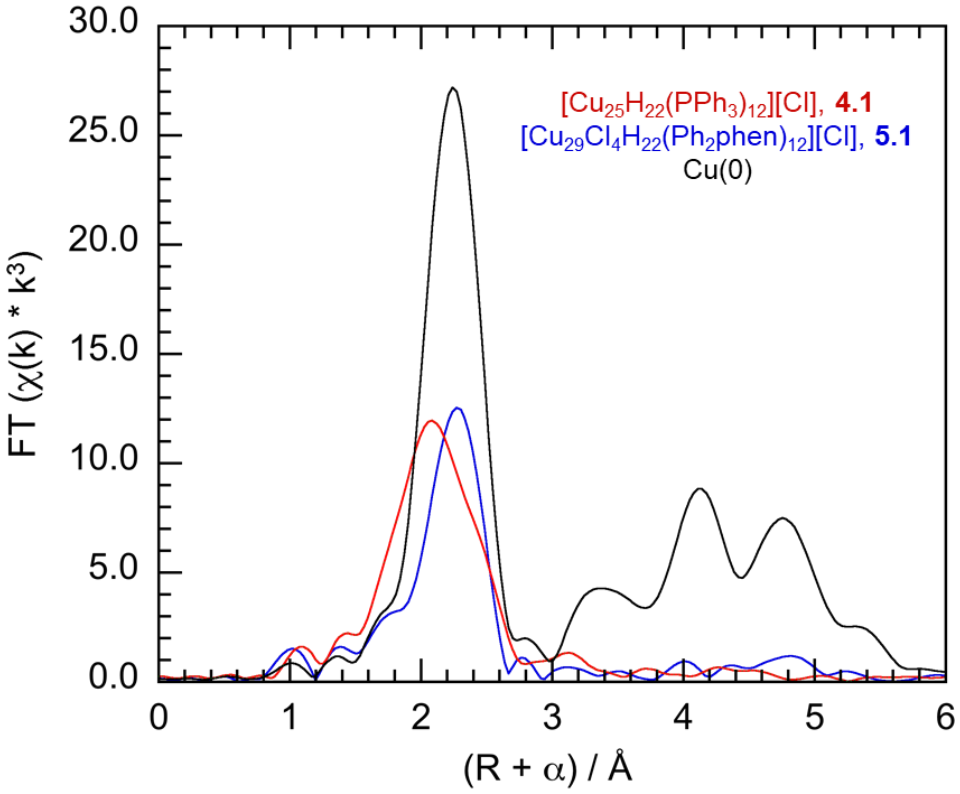

Figure 5.8. Comparison of Cu K-edge EXAFS of Cu nanoclusters **4.1** and **5.1**, and Cu metal.

5.4.7 X-ray Photoelectron Spectroscopy

XPS was performed on a Kratos Ultra system equipped with an Al-Kα (1559 eV) radiation source. Samples were loaded into a custom built air-free sample holder, under a N_2 atmosphere. Prior to data collection, a baseline vacuum of 1 x 10^{-8} Torr was achieved. For

high resolution scans, a band pass energy of 20 eV was used. Binding energies were calibrated using the C 1*s* peak of adventitious carbon at 284.6 eV. Peak positions in the Cu 2*p* and LMM Auger emission regions were determined using the Casa XPS software package. N:Cu ratios were determined from survey scans conducted with a band pass energy of 80 eV. Relative abundances (at%) were calculated from the areas of Cu 2*p*, Cl 2*p*, N 1*s* and C 1*s* peaks. Integrations were performed using the CASA XPS software with Tougaard background correction and Scofield photo-ionization cross-sections.

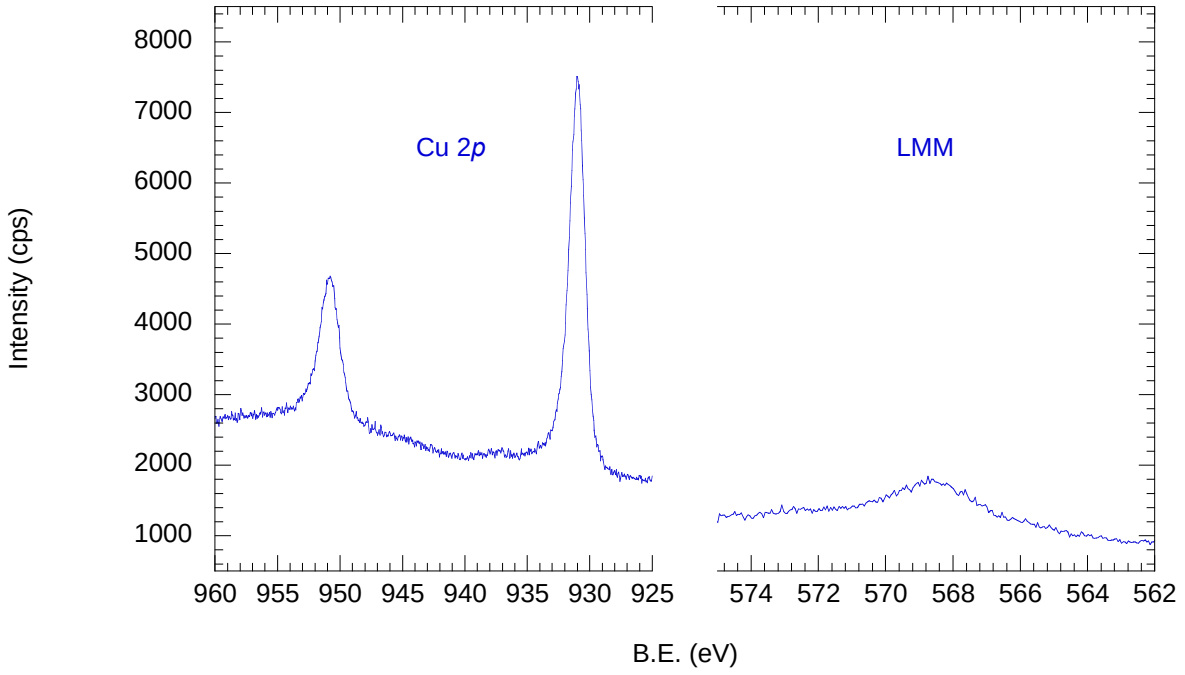

Figure 5.9. High resolution scans of the Cu 2*p* and LMM Auger regions in the X-ray photoelectron spectrum of complex **5.1**.

Table 5.4. XPS Survey Scan Results for complex **5.1**.

Relative abundance (at%)				N:Cu ratio	
Cu	Cl	C	N	Expt.	Calc.
3.5	0.9	93	2.9	0.82	0.83

5.4.8 UV-vis Kinetics

Time-resolved kinetic data for the conversion of **4.1** (ca. 0.05 mM) to **5.1** in CH_2Cl_2 were acquired in a Schlenk-adapted quartz cuvette (1 mm path length), in which the reactants were stored separately prior to initiating the reaction. Spectra were recorded at constant temperature (±0.1 °C) using a Shimadzu UV-2401PC spectrophotometer. Full absorbance spectra (200 – 900 nm) were recorded at a scan rate of 8.9 nm/s with 1 nm resolution. The concentrations of **5.2** and Ph_2phen were varied systematically.

Rate constants were extracted from the kinetic profiles by nonlinear least-squares curve-fitting of the absorbance A_t to the integrated form of the first-order rate equation with three adjustable parameters (A_0, A_∞, k_{obs}), eq 5.5.

$$A_t = A_0 + (A_0 - A_\infty)\,(1 - e^{-kobst}) \qquad (5.5)$$

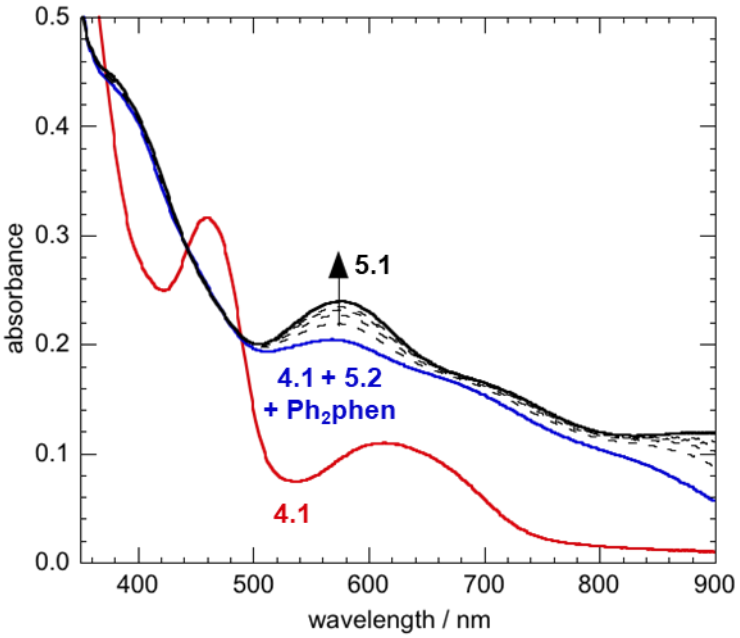

Figure 5.10. UV-vis spectrum of ca. 0.05 mM **4.1** in CH_2Cl_2 (red). Spectra were recorded immediately following the addition of 8 equiv of [(Ph_2phen)(PPh_3)CuCl] (**5.2**) and 11 equiv of Ph_2phen (blue), and during the ensuing conversion to **5.1** (black), at 25 °C.

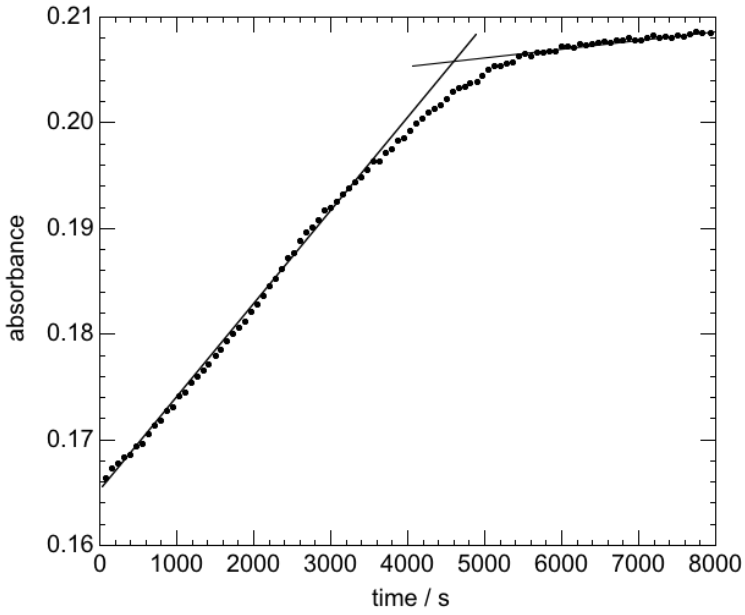

Figure 5.11. Kinetic profile (points) recorded at 575 nm for the conversion of 0.05 mM **4.1** to **5.1** upon addition of 15 equiv Ph_2phen at 25 °C. The approximately linear evolution of the absorbance with time is consistent with pseudo-zeroth-order kinetic behavior.

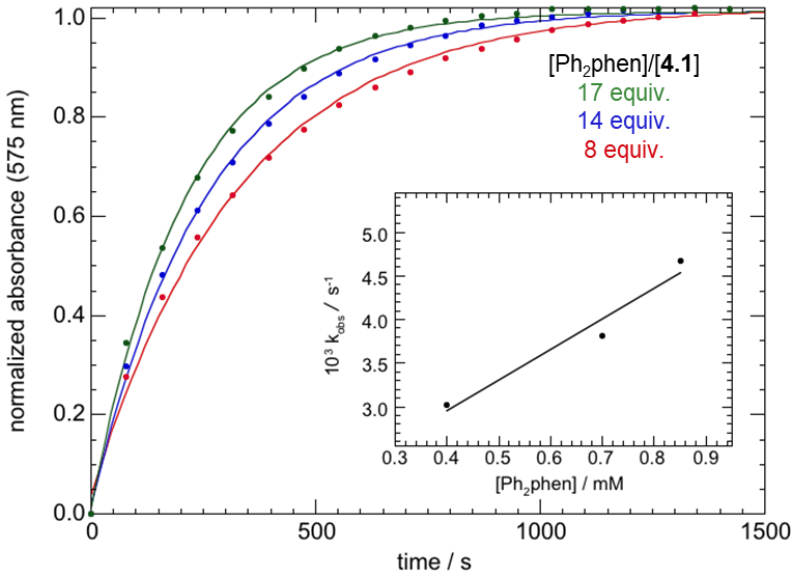

Figure 5.12. Kinetic profiles (points) for the transformation of 0.05 mM **4.1** to **5.1** in CH_2Cl_2 at 25 °C, recorded with variable (excess) amounts of Ph_2phen and 4 equiv of

[Cu(Ph$_2$phen)(PPh$_3$)Cl] (**5.2**). Lines are curvefits to the first-order integrated rate law. The inset shows the linear dependence of the pseudo-first-order rate constants on the concentration of added Ph$_2$phen.

Table 5.5. Pseudo-first-order rate constants for conversion of **4.1** to **5.1** in the presence of variable amounts of added Ph$_2$phen.[a]

Equiv. Ph$_2$phen	[Ph$_2$phen] (mM)	$k_{obs} \times 10^{-3}$ (s^{-1})
8	0.40	3.02 ± 0.06
14	0.70	3.82 ± 0.07
17	0.85	4.67 ± 0.07

[a] Reaction conditions: 0.05 mM **4.1**; 0.195 mM **5.2**, 25 °C in CH_2Cl_2.

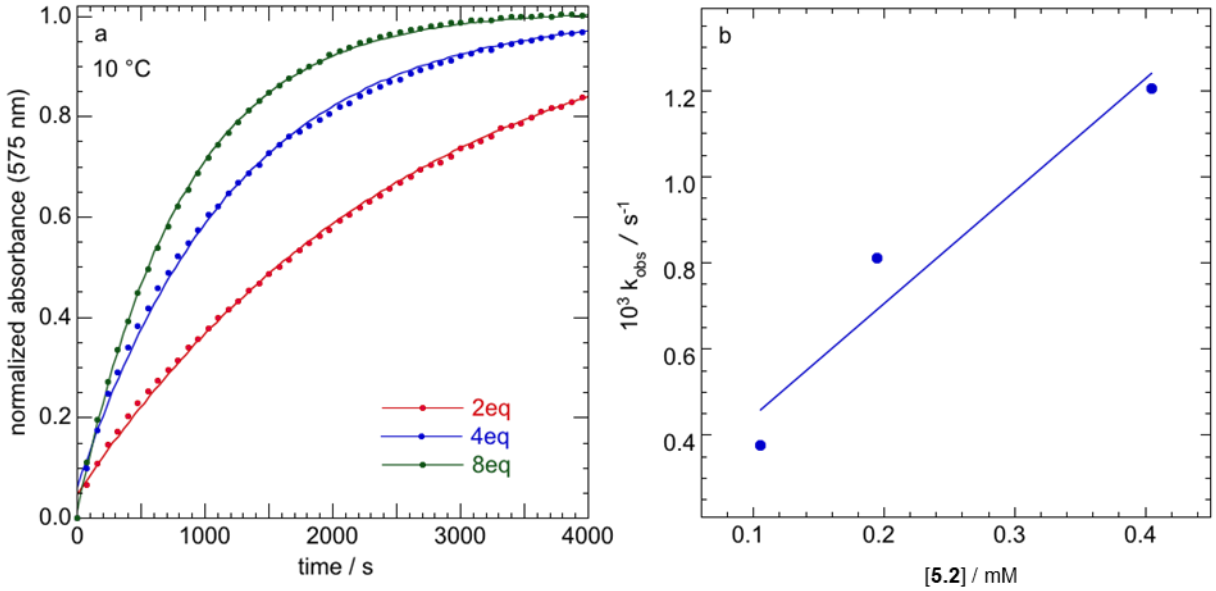

Figure 5.13. (a) Curvefits (lines) of the first-order integrated rate equation to normalized kinetic profiles (points) recorded at 575 nm for the conversion of 0.05 mM **4.1** to **5.1** upon addition of 11 equiv of Ph$_2$phen and either 2, 4, or 8 equiv of [(Ph$_2$phen)(PPh$_3$)CuCl] (**5.2**), at 10 °C. (b) Dependence of k_{obs} on the concentration of added **5.2**.

Table 5.6. Pseudo-first-order rate constants for conversion of **4.1** to **5.1** in the presence of variable amounts of monomer **5.2**.[a]

[(Ph_2phen)(PPh_3)CuCl] (Equiv.)	[(Ph_2phen)(PPh_3)CuCl] (mM)	$k_{obs} \times 10^{-3}$ (s^{-1}) T = 10 °C	$k_{obs} \times 10^{-3}$ (s^{-1}) T = 25 °C
2	0.105	0.378 ± 0.003	2.71 ± 0.05
4	0.195	0.810 ± 0.009	4.25 ± 0.07
8	0.405	1.205 ± 0.007	6.76 ± 0.06

[a] Reaction conditions: 0.05 mM **4.1**; 0.55 mM Ph_2phen; in CH_2Cl_2.

5.5 Appendix

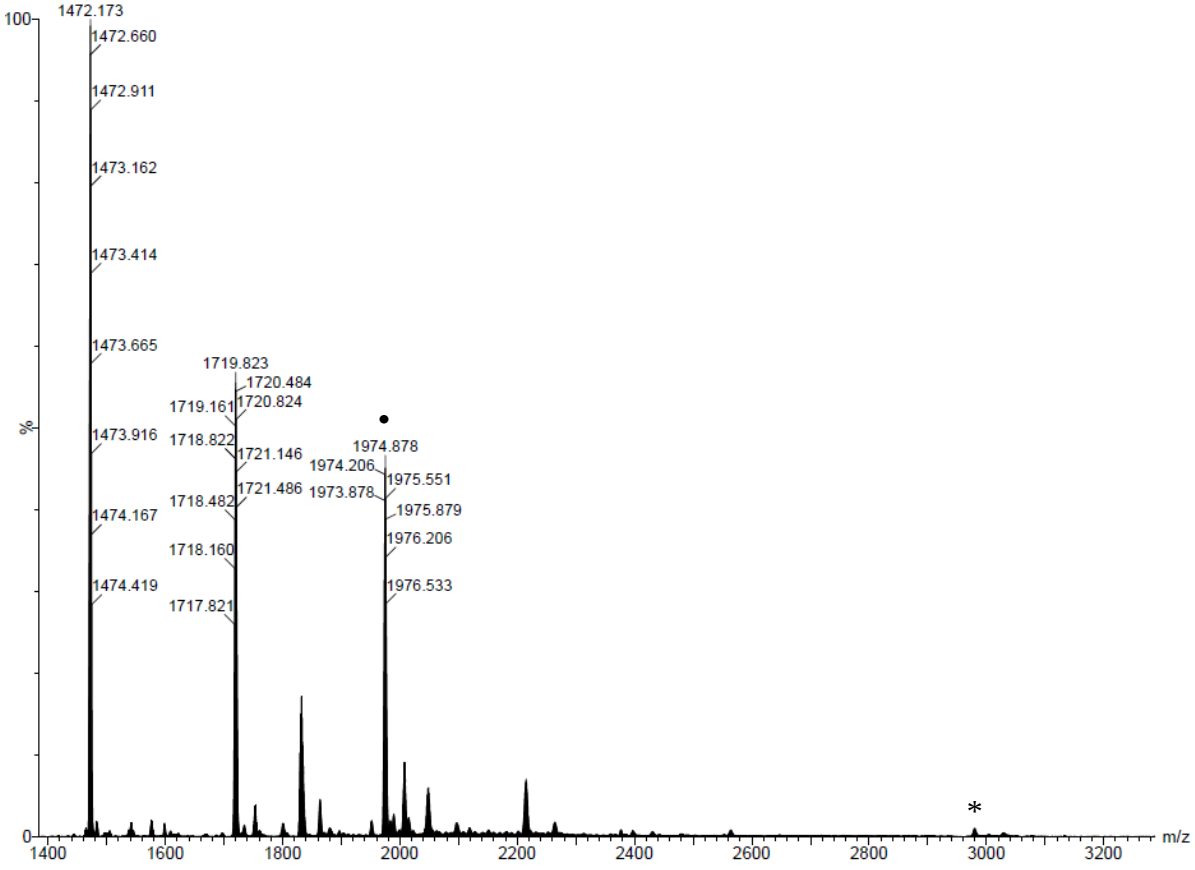

Figure A5.1. ESI-MS of [$Cu_{29}Cl_4H_{22}(Ph_2phen)_{12}$]Cl (**5.1**). (*) denotes the peak assignable to $[M\text{-}Cl]^{2+}$ and (•) denotes the peak assignable to $[M\text{-}2Cl]^{3+}$.

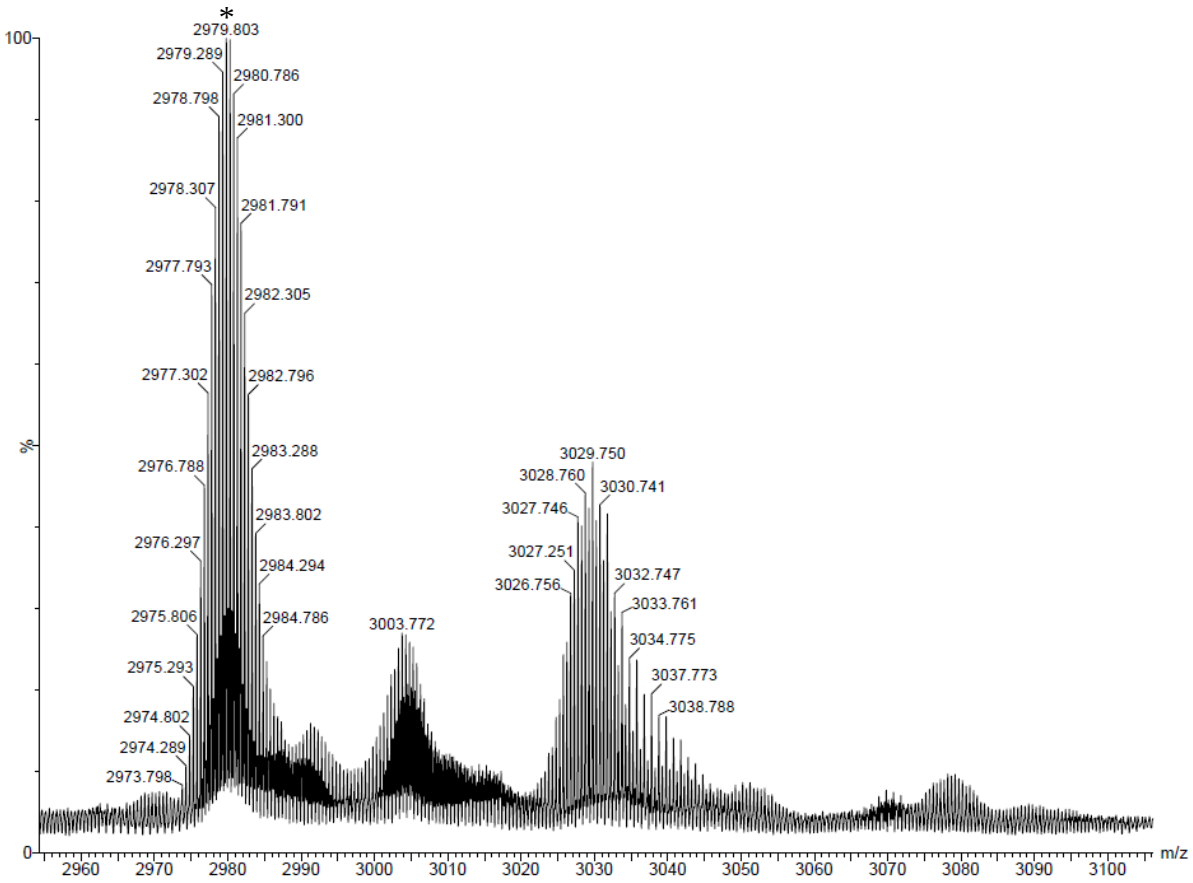

Figure A5.2. Partial ESI-MS of $[Cu_{29}Cl_4H_{22}(Ph_2phen)_{12}]Cl$ (**5.1**), including the $[M\text{-}Cl]^{2+}$ peak (*).

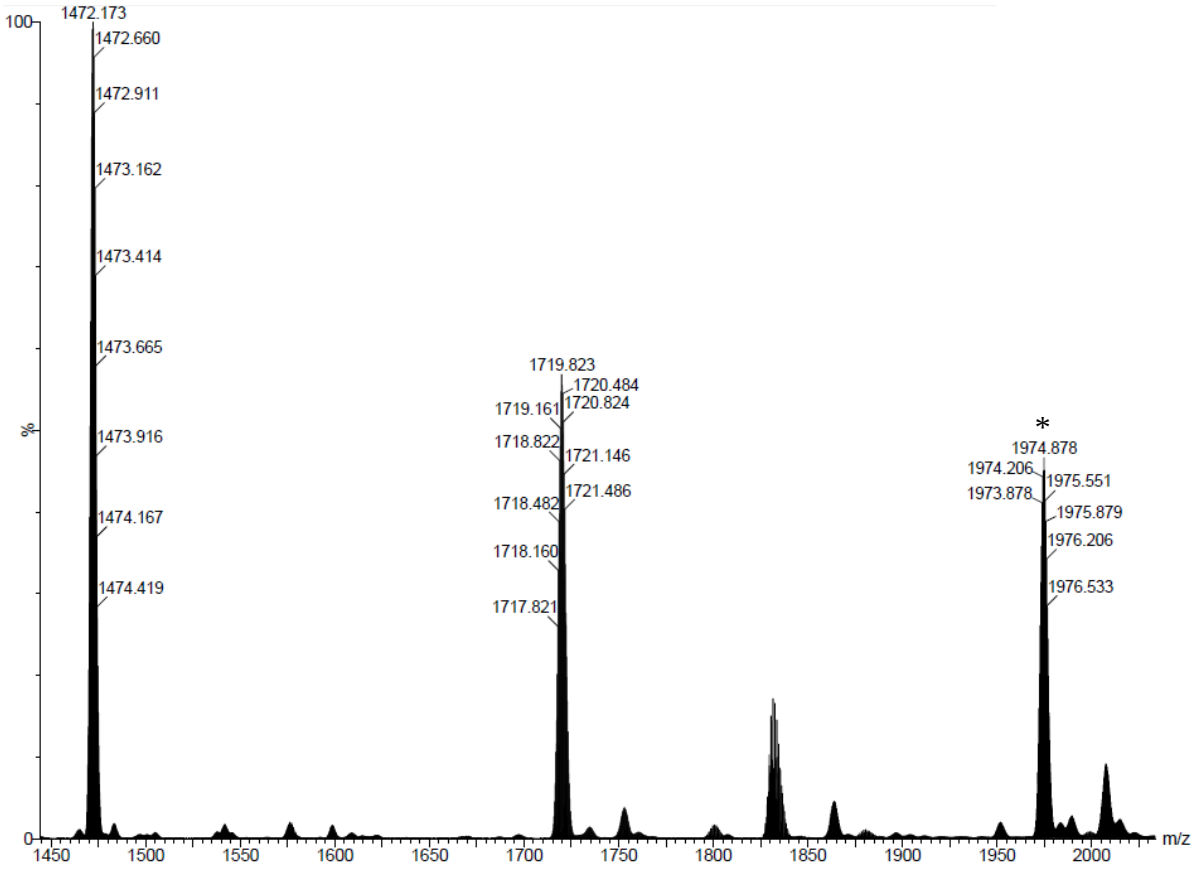

Figure A5.3. Partial ESI-MS of $[Cu_{29}Cl_4H_{22}(Ph_2phen)_{12}]Cl$ (**5.1**), including the $[M-2Cl]^{3+}$ peak (*).

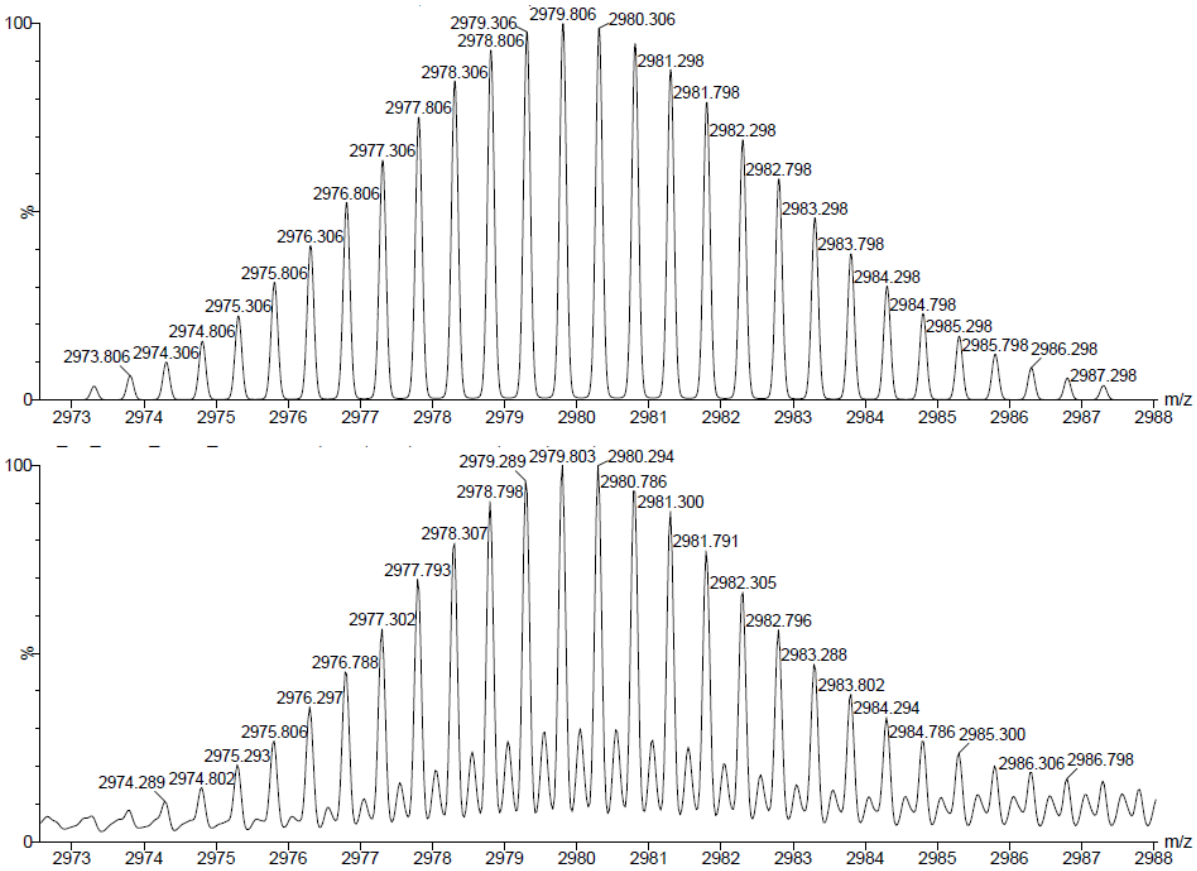

Figure A5.4. Partial ESI-MS of $[Cu_{29}Cl_4H_{22}(Ph_2phen)_{12}]Cl$ (**5.1**). The experimental (bottom) and calculated (top) peaks assignable to the $[M\text{-}Cl]^{2+}$ ion are shown. Note: the $[M\text{-}Cl]^{2+}$ signal overlaps with a small signal that is assignable to a related quadruply charged dimer, $[2M\text{-}2Cl]^{4+}$, that forms in the gas phase (Figure A5.5).

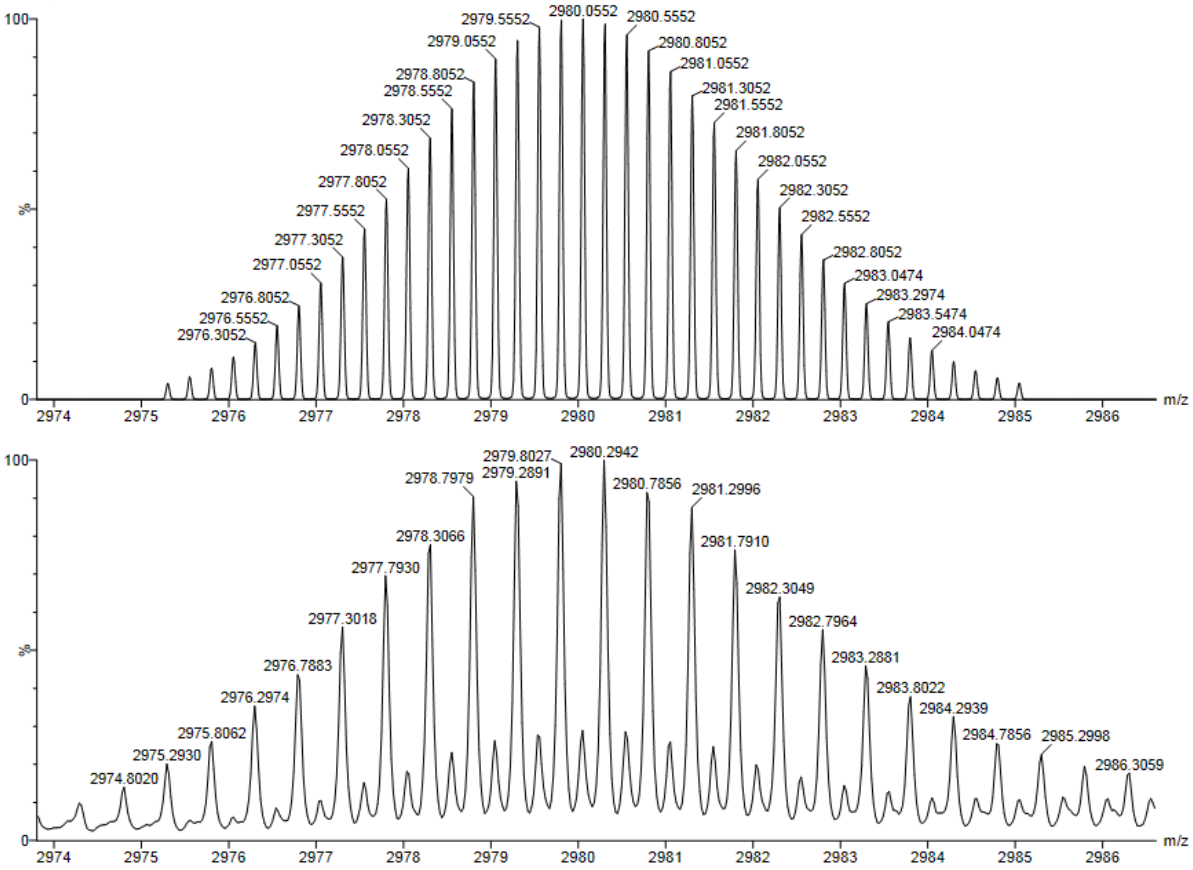

Figure A5.5. Partial ESI-MS of $[Cu_{29}Cl_4H_{22}(Ph_2phen)_{12}]Cl$ (**5.1**). The experimental (bottom) and calculated (top) peaks assignable to the $[2M\text{-}2Cl]^{4+}$ ion are shown. Note: the $[2M\text{-}2Cl]^{4+}$ signal overlaps with a major signal assignable to the $[M\text{-}Cl]^{2+}$ ion (Figure A5.4).

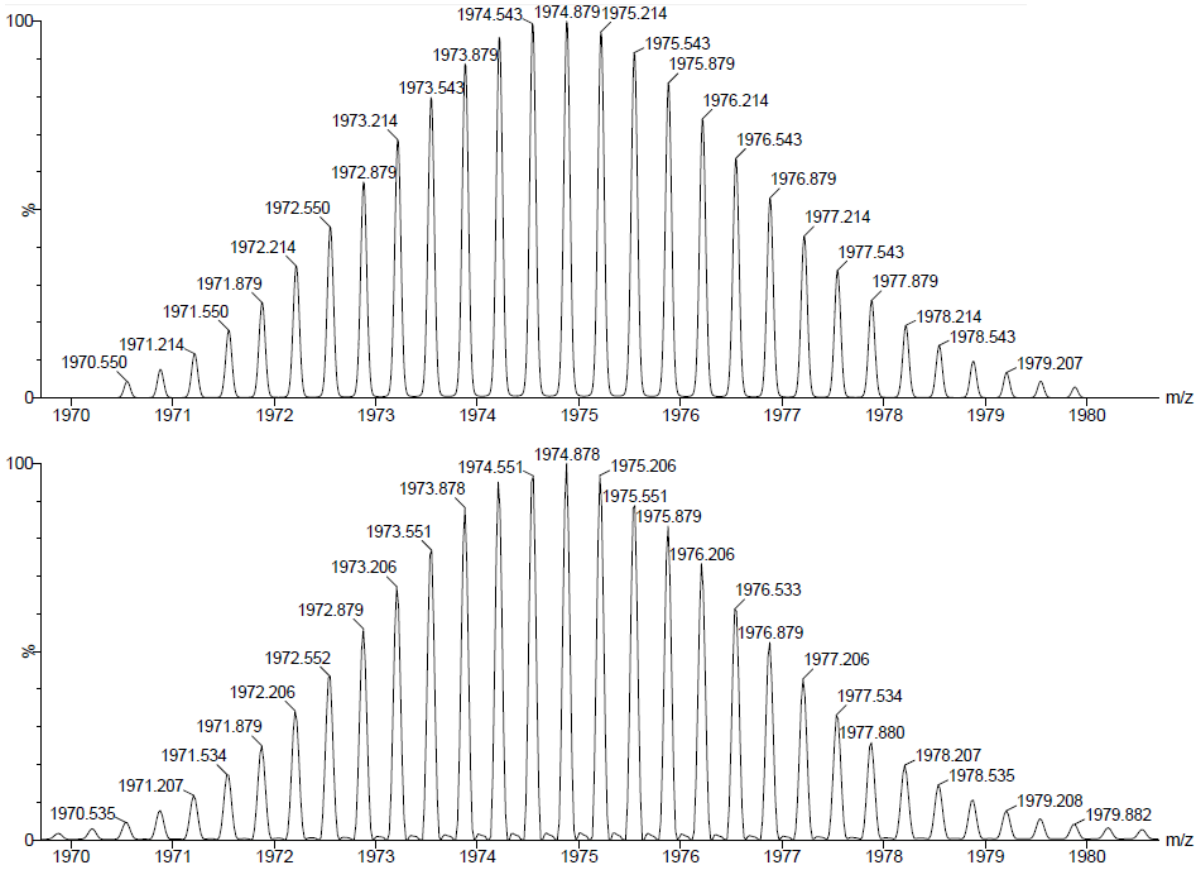

Figure A5.6. Partial ESI-MS of $[Cu_{29}Cl_4H_{22}(Ph_2phen)_{12}]Cl$ (**5.1**). The experimental (bottom) and calculated (top) peaks assignable to the $[M\text{-}2Cl]^{3+}$ ion are shown.

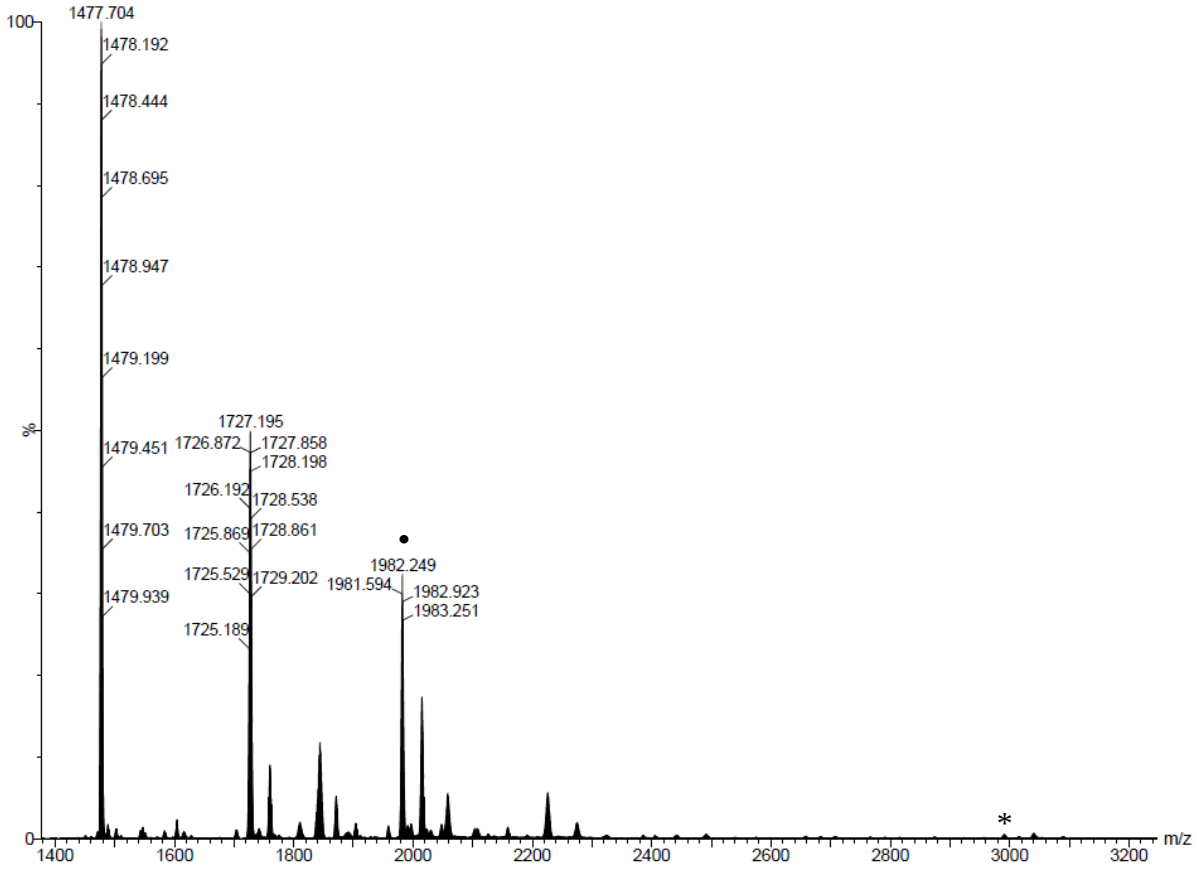

Figure A5.7. ESI-MS of $[Cu_{29}Cl_4D_{22}(Ph_2phen)_{12}]Cl$ (**5.1-*d*$_{22}$**). (*) denotes the peak assignable to $[M\text{-}Cl]^{2+}$ and (•) denotes the peak assignable to $[M\text{-}2Cl]^{3+}$.

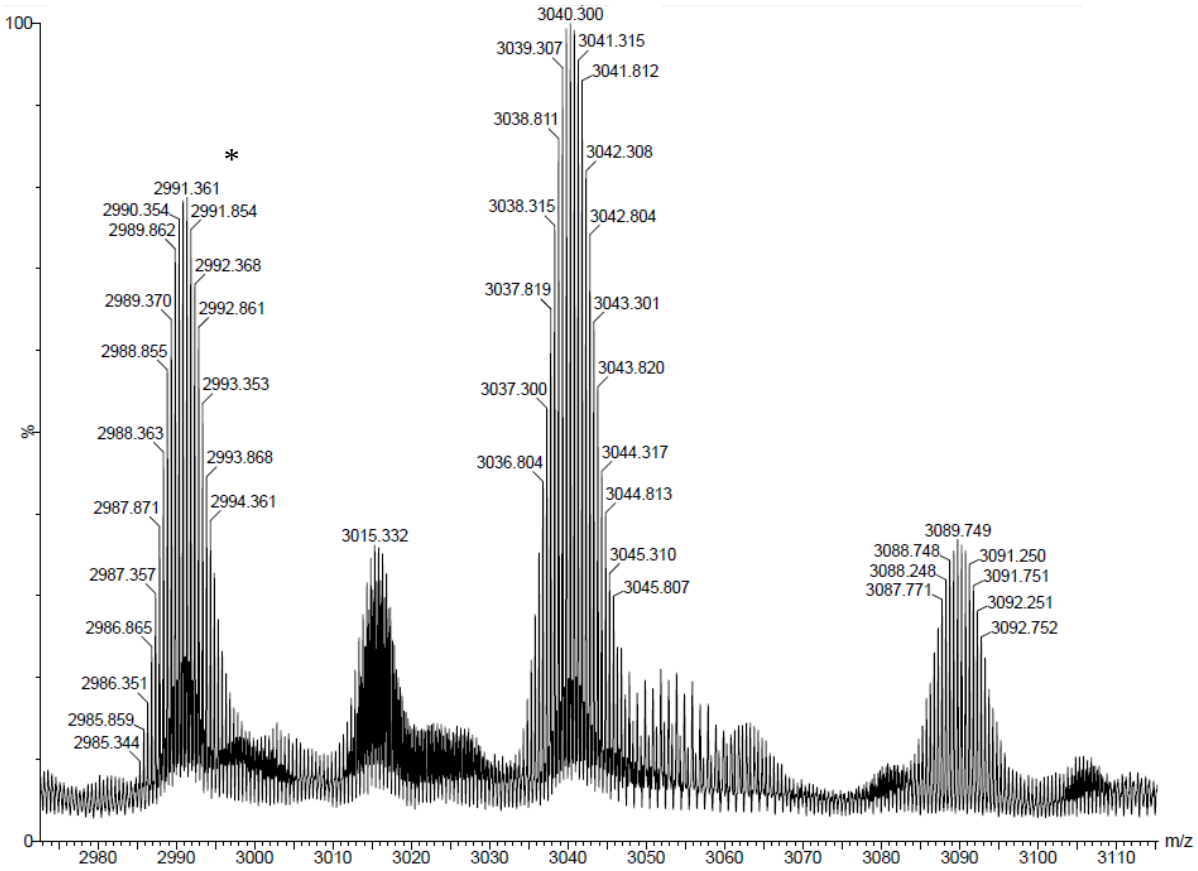

Figure A5.8. Partial ESI-MS of $[Cu_{29}Cl_4D_{22}(Ph_2phen)_{12}]Cl$ (**5.1-*d*$_{22}$**), including the $[M-Cl]^{2+}$ peak (*).

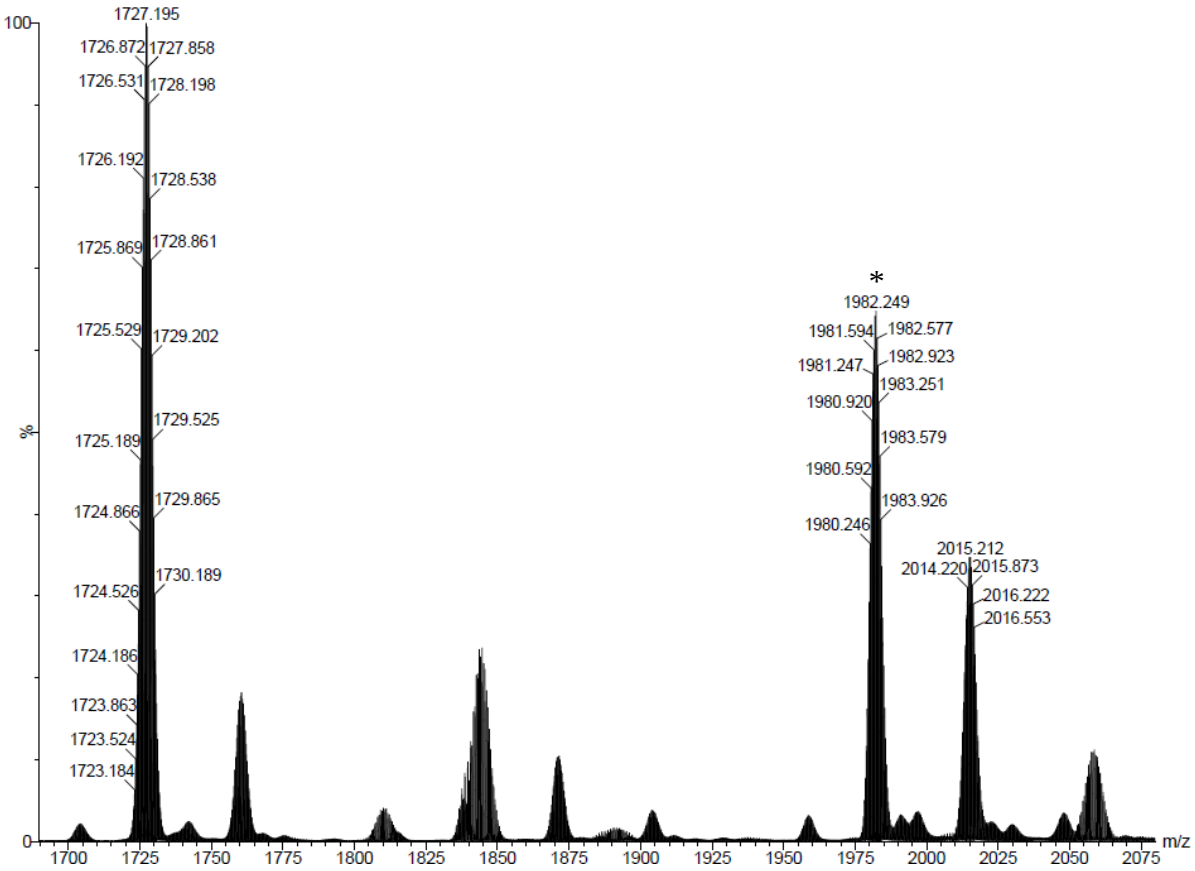

Figure A5.9. Partial ESI-MS of $[Cu_{29}Cl_4D_{22}(Ph_2phen)_{12}]Cl$ (**5.1-*d*$_{22}$**), including the $[M-2Cl]^{3+}$ peak (*).

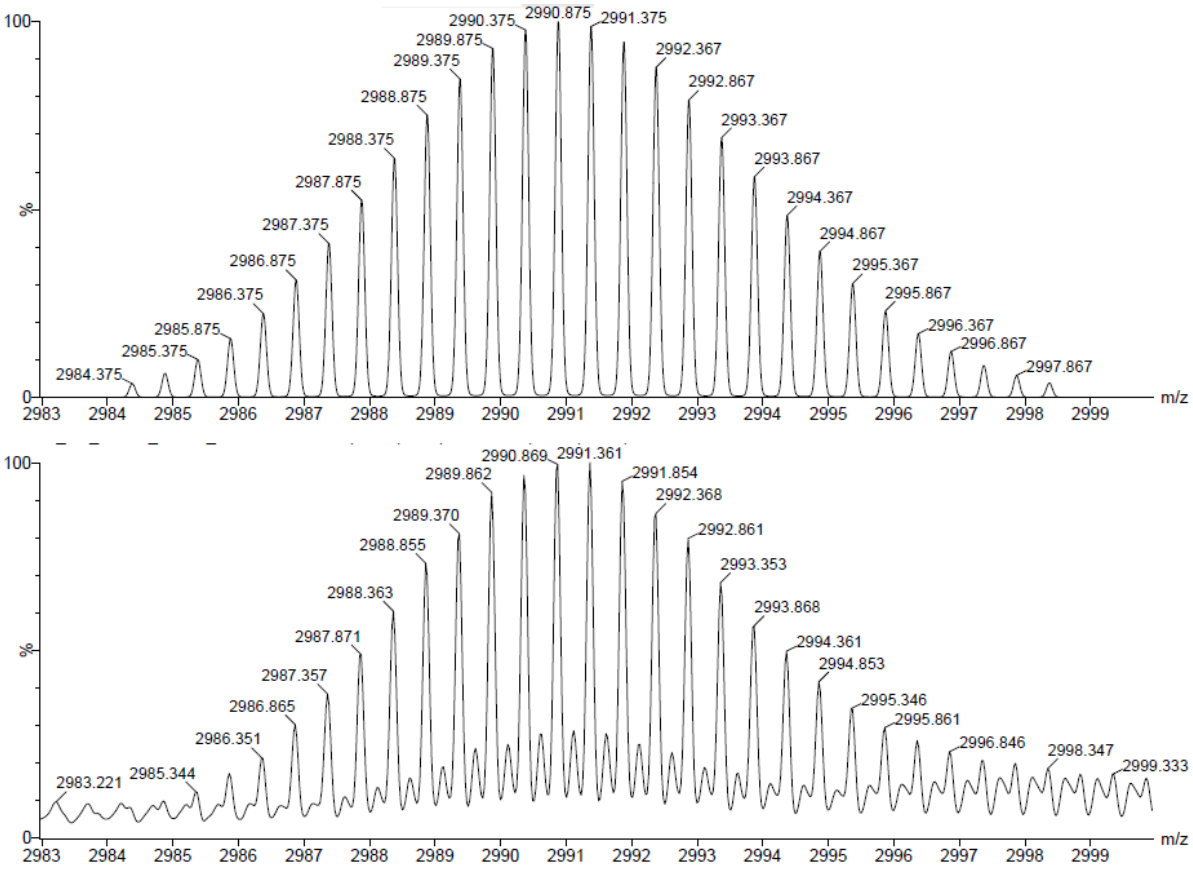

Figure A5.10. Partial ESI-MS of $[Cu_{29}Cl_4D_{22}(Ph_2phen)_{12}]Cl$ (**5.1-*d*$_{22}$**). The experimental (bottom) and calculated (top) peaks assignable to the $[M\text{-}Cl]^{2+}$ ion are shown. Note: the $[M\text{-}Cl]^{2+}$ signal overlaps with a small signal that is assignable to a related quadruply charged dimer, $[2M\text{-}2Cl]^{4+}$, that forms in the gas phase (Figure A5.11).

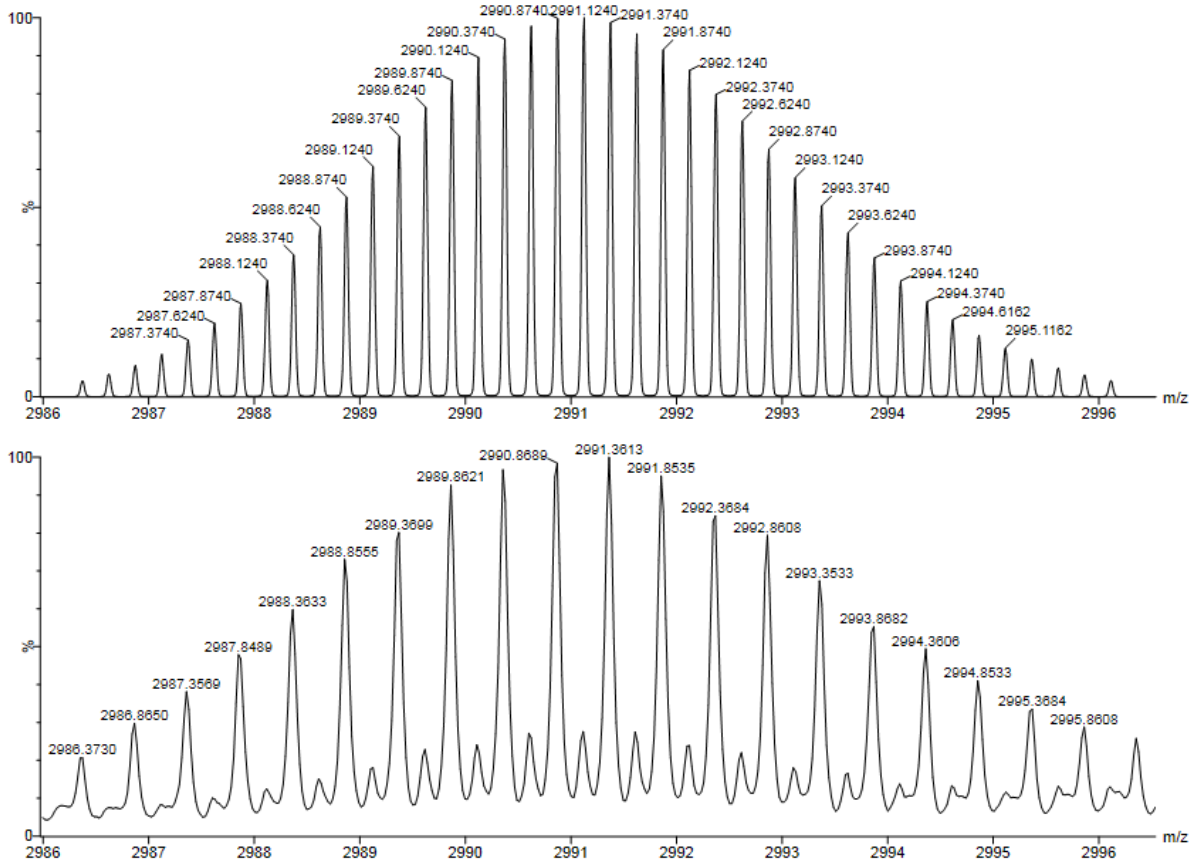

Figure A5.11. Partial ESI-MS of $[Cu_{29}Cl_4D_{22}(Ph_2phen)_{12}]Cl$ (**5.1-*d*$_{22}$**). The experimental (bottom) and calculated (top) peaks assignable to the $[2M\text{-}2Cl]^{4+}$ ion are shown. Note: the $[2M\text{-}2Cl]^{4+}$ signal overlaps with a major signal assignable to the $[M\text{-}Cl]^{2+}$ ion (Figure A5.10).

5.6 References

(1) Zeng, C.; Chen, Y.; Das, A.; Jin, R. Transformation Chemistry of Gold Nanoclusters: From One Stable Size to Another. *J. Phys. Chem. Lett.* **2015**, *6*, 2976.

(2) Luo, Z.; Nachammai, V.; Zhang, B.; Yan, N.; Leong, D. T.; Jiang, D.-e.; Xie, J. Toward Understanding the Growth Mechanism: Tracing All Stable Intermediate Species from Reduction of Au(I)–Thiolate Complexes to Evolution of Au_{25} Nanoclusters. *J. Am. Chem. Soc.* **2014**, *136*, 10577.

(3) Kamei, Y.; Shichibu, Y.; Konishi, K. Generation of Small Gold Clusters with Unique Geometries through Cluster-to-Cluster Transformations: Octanuclear Clusters with Edge-sharing Gold Tetrahedron Motifs. *Angew. Chem. Int. Ed.* **2011**, *50*, 7442.

(4) AbdulHalim, L. G.; Kothalawala, N.; Sinatra, L.; Dass, A.; Bakr, O. M. Neat and Complete: Thiolate-Ligand Exchange on a Silver Molecular Nanoparticle. *J. Am. Chem. Soc.* **2014**, *136*, 15865.

(5) Heinecke, C. L.; Ni, T. W.; Malola, S.; Mäkinen, V.; Wong, O. A.; Häkkinen, H.; Ackerson, C. J. Structural and Theoretical Basis for Ligand Exchange on Thiolate Monolayer Protected Gold Nanoclusters. *J. Am. Chem. Soc.* **2012**, *134*, 13316.

(6) Nguyen, T.-A. D.; Goldsmith, B. R.; Zaman, H. T.; Wu, G.; Peters, B.; Hayton, T. W. Synthesis and Characterization of a Cu_{14} Hydride Cluster Supported by Neutral Donor Ligands. *Chem. Eur. J.* **2015**, *21*, 5341.

(7) McKenzie, L. C.; Zaikova, T. O.; Hutchison, J. E. Structurally Similar Triphenylphosphine-Stabilized Undecagolds, $Au_{11}(PPh_3)_7Cl_3$ and $[Au_{11}(PPh_3)_8Cl_2]Cl$, Exhibit Distinct Ligand Exchange Pathways with Glutathione. *J. Am. Chem. Soc.* **2014**, *136*, 13426.

(8) Zeng, C.; Liu, C.; Pei, Y.; Jin, R. Thiol Ligand-Induced Transformation of $Au_{38}(SC_2H_4Ph)_{24}$ to $Au_{36}(SPh\text{-}t\text{-}Bu)_{24}$. *ACS Nano* **2013**, *7*, 6138.

(9) Bootharaju, M. S.; Joshi, C. P.; Alhilaly, M. J.; Bakr, O. M. Switching a Nanocluster Core from Hollow to Nonhollow. *Chem. Mater.* **2016**, *28*, 3292.

(10) Jin, R.; Zeng, C.; Zhou, M.; Chen, Y. Atomically Precise Colloidal Metal Nanoclusters and Nanoparticles: Fundamentals and Opportunities. *Chem. Rev.* **2016**, *116*, 10346.

(11) Niihori, Y.; Kikuchi, Y.; Kato, A.; Matsuzaki, M.; Negishi, Y. Understanding Ligand-Exchange Reactions on Thiolate-Protected Gold Clusters by Probing Isomer Distributions Using Reversed-Phase High-Performance Liquid Chromatography. *ACS Nano* **2015**, *9*, 9347.

(12) Hansen, T. W.; DeLaRiva, A. T.; Challa, S. R.; Datye, A. K. Sintering of Catalytic Nanoparticles: Particle Migration or Ostwald Ripening? *Acc. Chem. Res.* **2013**, *46*, 1720.

(13) Wang, F.; Richards, V. N.; Shields, S. P.; Buhro, W. E. Kinetics and Mechanisms of Aggregative Nanocrystal Growth. *Chem. Mater.* **2014**, *26*, 5.

(14) Ganesamoorthy, C.; Weßing, J.; Kroll, C.; Seidel, R. W.; Gemel, C.; Fischer, R. A. The Intermetalloid Cluster $[(Cp^*AlCu)_6H_4]$, Embedding a Cu_6 Core Inside an Octahedral Al_6 Shell: Molecular Models of Hume–Rothery Nanophases. *Angew. Chem. Int. Ed.* **2014**, *53*, 7943.

(15) Nguyen, T.-A. D.; Jones, Z. R.; Goldsmith, B. R.; Buratto, W. R.; Wu, G.; Scott, S. L.; Hayton, T. W. A Cu_{25} Nanocluster with Partial Cu(0) Character. *J. Am. Chem. Soc.* **2015**, *137*, 13319.

(16) Heaven, M. W.; Dass, A.; White, P. S.; Holt, K. M.; Murray, R. W. Crystal Structure of the Gold Nanoparticle $[N(C_8H_{17})_4][Au_{25}(SCH_2CH_2Ph)_{18}]$. *J. Am. Chem. Soc.* **2008**, *130*, 3754.

(17) Zhu, M.; Aikens, C. M.; Hollander, F. J.; Schatz, G. C.; Jin, R. Correlating the Crystal Structure of A Thiol-Protected Au_{25} Cluster and Optical Properties. *J. Am. Chem. Soc.* **2008**, *130*, 5883.

(18) Dhayal, R. S.; Liao, J.-H.; Liu, Y.-C.; Chiang, M.-H.; Kahlal, S.; Saillard, J.-Y.; Liu, C. W. $[Ag_{21}\{S_2P(OiPr)_2\}_{12}]^+$: An Eight-Electron Superatom. *Angew. Chem. Int. Ed.* **2015**, *54*, 3702.

(19) Briant, C. E.; Theobald, B. R. C.; White, J. W.; Bell, L. K.; Mingos, D. M. P.; Welch, A. J. Synthesis and X-ray structural characterization of the centred icosahedral gold cluster compound $[Au_3(PMe_2Ph)_{10}Cl_2](PF_6)_3$; the realization of a theoretical prediction. *J. Chem. Soc., Chem. Commun.* **1981**, 201.

(20) AbdulHalim, L. G.; Bootharaju, M. S.; Tang, Q.; Del Gobbo, S.; AbdulHalim, R. G.; Eddaoudi, M.; Jiang, D.-e.; Bakr, O. M. $Ag_{29}(BDT)_{12}(TPP)_4$: A Tetravalent Nanocluster. *J. Am. Chem. Soc.* **2015**, *137*, 11970.

(21) Delhaes, P. *Graphite and Precursors*; Taylor & Francis, 2000.

(22) Holligan, B. M.; Jeffery, J. C.; Ward, M. D. The Co-ordination Chemistry of Mixed Pyridine-Phenol and Phenanthroline-Phenol Ligands; Effects of π-Stacking Interactions and Ligand Rigidity on Complex Structures. *J. Chem. Soc., Dalton Trans.* **1992**, 3337.

(23) Wyckoff, R. W. G. *Crystal Structures*; Second ed.; Interscience Publishers: New York, 1963; Vol. 1.

(24) The superatom number for **5.1** was calculated in the following way: $N^* = 29$ (Cu 4s) – 22 (H^-) – 4 (Cl^-) - 1 (cluster charge) = 2.

(25) Gell, L.; Lehtovaara, L.; Häkkinen, H. Superatomic S^2 Silver Clusters Stabilized by a Thiolate–Phosphine Monolayer: Insight into Electronic and Optical Properties of $Ag_{14}(SC_6H_3F_2)_{12}(PPh_3)_8$ and $Ag_{16}(SC_6H_3F_2)_{14}(DPPE)_4$. *J. Phys. Chem. A* **2014**, *118*, 8351.

(26) Yang, H.; Lei, J.; Wu, B.; Wang, Y.; Zhou, M.; Xia, A.; Zheng, L.; Zheng, N. Crystal structure of a luminescent thiolated Ag nanocluster with an octahedral Ag_6^{4+} core. *Chem. Commun.* **2013**, *49*, 300.

(27) Yang, H.; Wang, Y.; Zheng, N. Stabilizing Subnanometer Ag(0) Nanoclusters by Thiolate and Diphosphine Ligands and their Crystal Structures. *Nanoscale* **2013**, *5*, 2674.

(28) Jordan, A. J.; Lalic, G.; Sadighi, J. P. Coinage Metal Hydrides: Synthesis, Characterization, and Reactivity. *Chem. Rev.* **2016**, *116*, 8318.

(29) Bligaard, T.; Bullock, R. M.; Campbell, C. T.; Chen, J. G.; Gates, B. C.; Gorte, R. J.; Jones, C. W.; Jones, W. D.; Kitchin, J. R.; Scott, S. L. Toward Benchmarking in Catalysis Science: Best Practices, Challenges, and Opportunities. *ACS Catal.* **2016**, *6*, 2590.

(30) Harris, R. K.; Becker, E. D.; Cabral De Menezes, S. M.; Goodfellow, R.; Granger, P. NMR Nomenclature. Nuclear Spin Properties and Conventions for Chemical Shifts. *Pure Appl. Chem.* **2001**, *73*, 1795.

(31) Harris, R. K.; Becker, E. D.; Cabral De Menezes, S. M.; Granger, P.; Hoffman, R. E.; Zilm, K. W. Further Conventions for NMR Shielding and Chemical Shifts. *Pure Appl. Chem.* **2008**, *80*, 59.

(32) *SMART Apex II, Version 2.1*; Bruker AXS Inc.: Madison, WI, 2005.

(33) *SAINT Software User's Guide, Version 7.34a*; Bruker AXS Inc.: Madison, WI, 2005.

(34) Sheldrick, G. M. *SADABS*; University of Göttingen: Göttingen, Germany, 2005.

(35) *SHELXTL PC, Version 6.12*; Bruker AXS Inc.: Madison, WI, 2005.

(36) Ravel, B.; Newville, M. ATHENA, ARTEMIS, HEPHAESTUS: data analysis for X-ray absorption spectroscopy using IFEFFIT. *J. Synchrotron Radiat.* **2005**, *12*, 537.

Chapter 6. **A Cu_{26} Superatom with $N^* > 2$**

6.1 Introduction

The controlled synthesis of atomically precise nanoclusters (NCs) is an emerging area of nanoscience. NCs differ from traditional nanoparticles because they are stoichiometrically defined, and are perfectly uniform in both composition and structure. They are also smaller than nanoparticles, ranging in size from about 10-300 metal atoms. There is intense fundamental interest in NCs for their unique electronic properties, and they also have practical appeal due to their potential use in any nanoparticle-based systems that require more particle size and structure uniformity than is possible in conventional nanoparticle synthesis.[1-7] Despite this interest, there are many challenges in this area. Firstly, the identification and thorough characterization of NCs is limited by the ability to obtain an accurate crystal structure, as imaging techniques typically used for nanoparticles such as transmission electron microscopy (TEM) and scanning electron microscopy (SEM), cannot determine the number or location of the capping ligands, which is essential for understanding NCs. Unfortunately, it is significantly more challenging to grow an X-ray quality crystal of a NC, compared to most inorganic/organometallic complexes, due to their large sizes.

Secondly, except in rare cases, mixtures of NCs are usually formed during these reactions, which are difficult to separate and purify. Some very robust NCs can be purified using techniques such as high-resolution polyacrylamide gel electrophoresis (PAGE), enabling the separation of complex mixtures of NCs.[8] However, the copper NCs protected by neutral phosphine ligands that we are exploring are much more susceptible to decomposition during chromatography and are unsuitable for PAGE separations. Therefore,

it is critical to design syntheses for copper NCs that produce a limited number of clusters in one reaction.

Thirdly, there is currently only a preliminary understanding of the mechanisms for NC assembly, and thus, there is a shortage of effective and rational synthetic methods.[9] Inspiration can be drawn from the NCs that have already been characterized in order to design new syntheses. There is a relationship in gold thiolate NCs between the metal to ligand ratio and size of the cluster (Figure 6.1), which is a consequence of the relationship between the surface-to-volume ratio and the cluster radius.[9] This relationship is particularly sensitive for gold thiolate NCs with a core of *ca.* 75 atoms or less, as demostrated by the slope of the trendline in Figure 6.1, which is steepest below 75 atoms. .

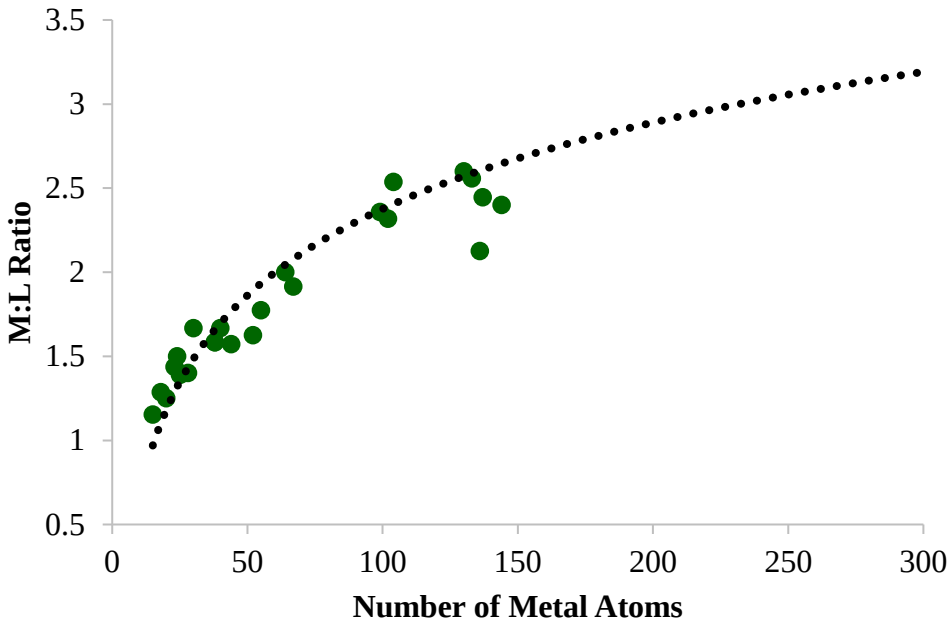

Figure 6.1. The relationship between cluster size and the metal to ligand ratio for gold thiolate clusters. Green dots represent known NCs, while the black dotted line is the trendline. Larger NCs have a higher metal to ligand ratio. Data for this graph was taken from Ref. 9, Table 1.

Given this relationship, I propose that manipulation of the stoichiometric ratio of the Cu(I) salt and the ligand, will allow for control of the size of the resulting products. For example, the successful synthesis of the superatom $[Cu_{25}H_{22}(PPh_3)_{12}]Cl$ (**4.1**) demonstrated that the formation of **4.1** is sensitive to the stoichiometry of the Cu(I) salt and ligand, and the Cu:L ratio of 2.1:1 used in the reaction is retained in the major product. In addition, performing the reduction of Cu(OAc) in this ligand-deficient environment allowed for partial reduction of the product to a mixed valent Cu(I)/Cu(0) complex (N^* = 2).[10] I hypothesized that increasing the Cu:L ratio of the reaction further would result in formation of even larger nanoclusters, with magic numbers $N^* \leq 2$. This would be a significant result as, for copper, only a handful of NCs are presently known, all featuring N^* = 2, including, $[Cu_{25}H_{22}(PPh_3)_{12}][Cl]$ (**4.1**),[10] $[Cu_{29}Cl_4H_{22}(Ph_2phen)_{12}][Cl]$ (**5.1**),[11] and $[Cu_{13}\{S_2CN^nBu_2\}_6(C{\equiv}CR)_4]^+$ (R = C(O)OMe, C_6H_4F).[12]

6.2 Results and Discussion

Addition of 13 equiv of Ph_2SiH_2 to a slurry containing 26 equiv of Cu(OAc) and 10 equiv of PPh_3 in C_6H_6, which corresponds to a Cu:L ratio of 2.6:1, results in a rapid color change from pale green to dark red. Upon further stirring, this solution undergoes a color change to dark brown. Work-up of this solution after 15 h resulted in the isolation of two copper hydride clusters, which have been tentatively formulated as $[Cu_{26}H_{17}(PPh_3)_9(OAc)_3]$ (**6.1**) and $[Cu_{26}H_{22}(PPh_3)_{10}(OAc)_2]$ (**6.2**), in isolated yields of 18 % and <1 %, respectively (Scheme 6.1). An insoluble dark powder, which was likely elemental Cu, was also produced in the reaction, however, its yield was not determined. Complexes **6.1** and **6.2** were separated on the basis of their different solubilities in toluene and CH_2Cl_2 after a recrystallization of the crude solid from a THF/Et_2O solution. Briefly, the reaction mixture

was first crystallized from a C_6H_6/THF solution that was layered with hexanes. This resulted in deposition of a dark brown powder that is composed primarily of **6.1** and **6.2**. Crystallization of this solid from a THF solution layered with Et_2O that was allowed to stand undisturbed for 3 d in the freezer typically results in the deposition of **6.1** as a fine dark brown powder and **6.2** as larger red particles. This size difference is crucial for the successful separation of the two because the larger red particles dissolve more slowly in toluene than the fine brown powder, permitting their separation by selective dissolution. Unfortunately, a large amount of material is always sacrificed in this process because **6.1** is slightly soluble in Et_2O and a significant amount of product remained in solution after crystallization, even after 3 d in the freezer. In addition, the growth of large particles of **6.2** is somewhat unreliable and often forms powders instead, which then cannot be separated from **6.1**. The toluene solution of **6.1** can then layered with Et_2O and stored in the freezer, resulting in the deposition of **6.1** as a dark brown powder (using MeCN instead of Et_2O for this step also works well). The remaining undissolved **6.2** can then be washed with CH_2Cl_2 to remove residual **6.1**, extracted with THF, and crystallized from THF/Et_2O. Similar to the reaction that generates both $[Cu_{25}H_{22}(PPh_3)_{12}]Cl$ and $[Cu_{18}H_{17}(PPh_3)_{10}]Cl$,[10] the isolation of two different CuH clusters from this reaction can be rationalized by their similar Cu:P ratios (that of complex **6.1** is 2.9:1, while that of complex **6.2** is 2.6:1), both of which are similar to the Cu:P ratio in the original reaction mixture (2.6:1). The formation of two products also suggests that they have similar thermodynamic stabilities. Interestingly, addition of more than *ca*. 13 equiv of Ph_2SiH_2 to the reaction mixture results in unidentified new products, presumably from further exchange of the remaining acetate ligands for hydride. Complex **6.1** is very soluble in C_6H_6, toluene, THF, CH_2Cl_2, insoluble in hexanes and acetonitrile, and

has extremely low solubility in Et_2O. Complex **6.2** is soluble in THF, C_6H_6 and toluene, however, once crystalline, it is most readily dissolved in THF. It has low solubility in CH_2Cl_2 and is insoluble in hexanes, Et_2O, or acetonitrile.

Scheme 6.1. Synthesis of $[Cu_{26}H_{17}(PPh_3)_9(OAc)_3]$ (**6.1**) and $[Cu_{26}H_{22}(PPh_3)_{10}(OAc)_2]$ (**6.2**)

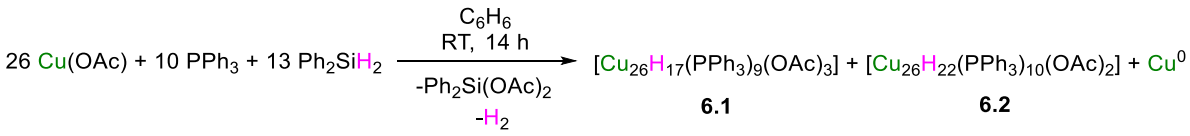

Complex **6.1** crystallizes in the monoclinic space group C2/c. Crystals were grown by slow concentration of a C_6H_6/CH_2Cl_2 solution of **6.1** stored at −25 °C, in the glovebox freezer. The slow concentration was achieved by diffusion of the solvent from this solution into an outer vial of toluene. Unfortunately, these crystals diffracted poorly, so only a preliminary solid state molecular structure was achieved. Only the location of the Cu and P atoms were determined, and none of the C and H atoms, acetate ligands, or solvate molecules were located. The cluster occupies the D_{3d} point group. In the solid state, complex **6.1** features a triangular core of three copper atoms, surrounded by a cage of 23 copper atoms connected via Cu–Cu bonds that form an oblate sphere. Nine of the copper atoms in this cage form a belt on the equatorial plane of the cluster, while the remaining 14 copper atoms make up the top and bottom faces of the oblate sphere, arranged in a distorted centered hexagon. Each of the three copper atoms in the triangular core features a coordination number of 12, identical to that observed in bulk Cu metal.[13] This unusual architecture has not been observed previously in any other group 11 NCs. The outer cage of 23 copper atoms is protected by nine PPh_3 ligands, three of which are distributed equally

among the nine copper atoms on the equatorial plane of the cluster, and the other two equivalent sets of three PPh_3 ligands are arranged axially on the top and bottom faces of the cluster (Figure 6.2). While the three acetate ligands were not located in the solid state molecular structure, the ^1H NMR spectra of **6.1** indicate that they are all chemically equivalent. They are likely coordinated within the equatorial plane, in a κ^2 fashion, each bridging one of the three pairs of copper atoms that are in the belt of nine copper atoms and not coordinated by PPh_3. The Cu–Cu distances in **6.1** exhibit a large range (2.30 – 3.25 Å), consistent with a diverse range of Cu coordination environments within the Cu_{26} core (Figure 6.2d). Interestingly, the three shortest Cu–Cu bonds are between the three central atoms in the core of the cluster (2.30 – 2.40 Å), which is shorter than that found in Cu metal (2.55 Å).[13] The average Cu–Cu bond length (2.64 Å) in complex **6.1** is comparable to those found in other Cu hydride clusters, such as $[CuH(PPh_3)]_6$ (av. 2.630 Å),[14] $[Cu_{25}H_{22}(PPh_3)_{12}]Cl$ (**4.1**) (2.389(3) – 3.037(3) Å),[10] and $[Cu_{29}Cl_4H_{22}(Ph_2phen)_{12}]Cl$ (**5.1**) (2.537(3) –3.303(3) Å).[11] Finally, the Cu–P distances (av. 2.20 Å) are typical of those found in Cu(I) phosphine complexes,[10,11,14,15]

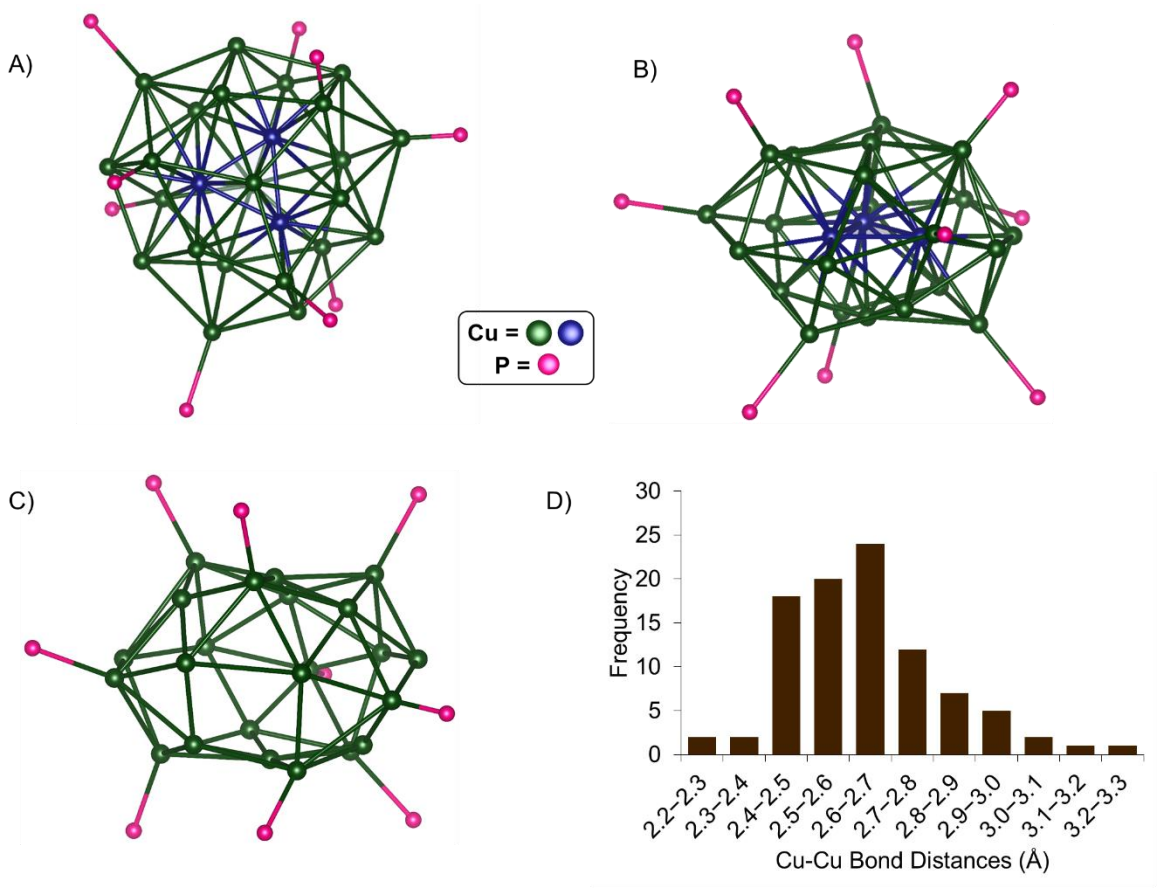

Figure 6.2. Ball and stick diagrams and Cu-Cu bond distance histogram for [$Cu_{26}H_{17}(PPh_3)_9(OAc)_3$] (6.1). The three core Cu atoms are highlighted in blue. The remaining Cu atoms are shown in green, while the P atoms are shown in pink. No other atoms were found in this preliminary structure. (A) Top view with all Cu and P atoms shown. (B) Side view with all Cu and P atoms shown. (C) Side view showing only the outer layer of Cu atoms and the P atoms. (D) Histogram depicting the distribution of Cu-Cu bond distances.

Complex **6.1** features two resonances in its $^{31}P\{^1H\}$ NMR spectrum, at -4.54 and 4.16 ppm in C_6D_6, in a 6:3 ratio, respectively. These resonances are assigned to the six axial and three equatorial PPh_3 ligands, respectively, and are consistent with the high symmetry observed in the solid state. Notably, these resonances correspond to two of the previously

unidentified resonances (4.15 and −4.57 ppm, C_6D_6) observed in the *in situ* $^{31}P\{^1H\}$ NMR spectrum of the reaction to form **4.1** (Figure A4.4a).[10] However, in that reaction, **6.1** was a minor product. The ^1H NMR spectrum of **6.1** features a broad resonance at 1.71 ppm, which integrates for 17H, and is tentatively assigned to 17 hydride ligands. The broadness of this peak suggests that there is fast exchange of the hydride ligands in multiple chemical environments at room temperature. A ^1H NMR spectrum of 6.1 at −40 °C shows that the single hydride resonance resolves into at least three separate environments. There is a sharp resonance at 1.34 ppm in the ^1H NMR spectrum of **6.1** that integrates to 9H, and is assignable to three acetate ligands. NMR spectra of **6.1** were also recorded in THF-d_8, and these spectra were virtually identical to those recorded in C_6D_6.

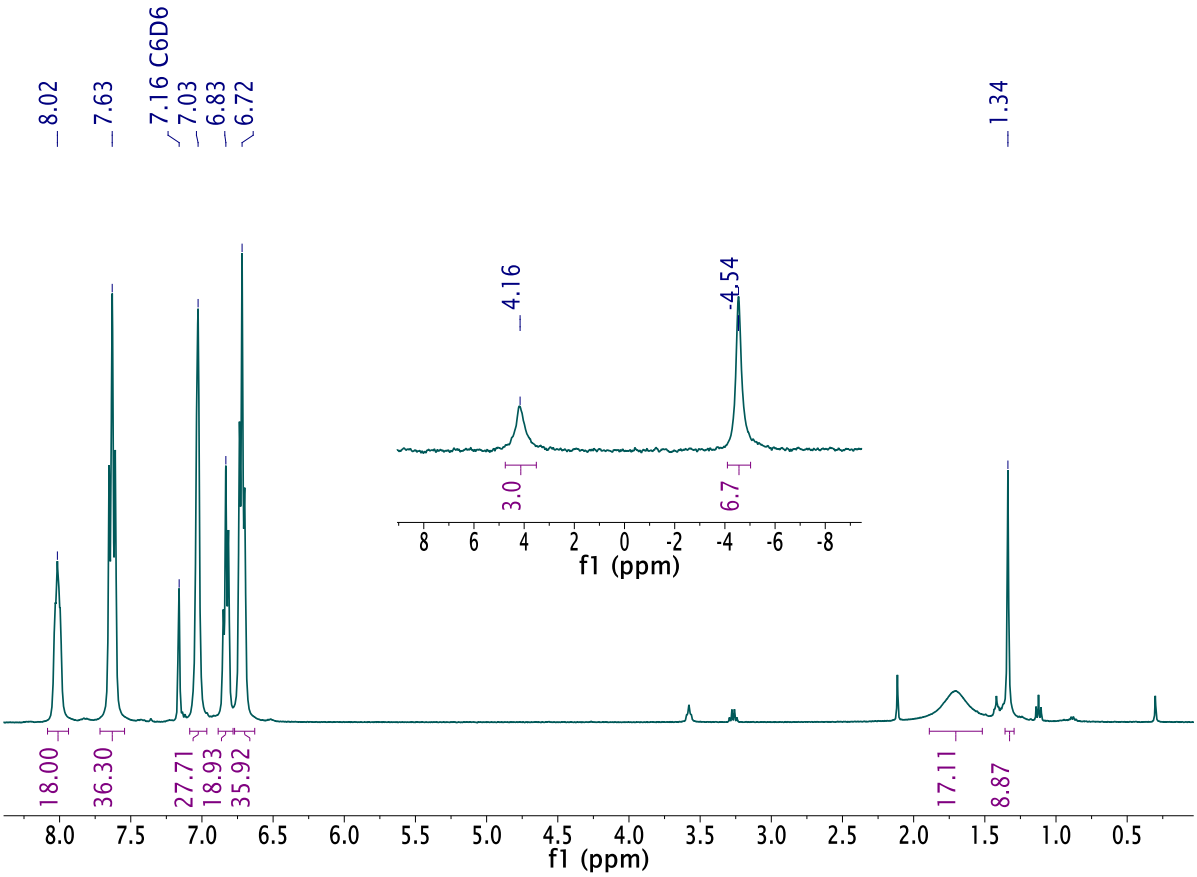

Figure 6.3. ^{1}H NMR spectrum and ^{31}P{^{1}H} NMR spectrum (inset) of $[Cu_{26}H_{17}(PPh_3)_9(OAc)_3]$ (**6.1**) in C_6D_6.

An electrospray ionization (ESI) mass spectrum of complex **6.1** in THF does not feature any signals that correspond to an obvious parent peak, such as $[[Cu_{26}H_{17}(PPh_3)_9(OAc)_3] - OAc]^+$ or $[[Cu_{26}H_{17}(PPh_3)_9(OAc)_3] + Na]^+$. Although unfortunate, this is not unusual as a neutral cluster is typically more challenging to characterize with this technique than a charged cluster. There are signals between *ca*. 2400 and 4800 *m/z* that are assignable to at least several singly charged CuH clusters with varying numbers of PPh_3 ligands. The deuteride analogue **6.1-*d*$_{17}$** was synthesized and characterized in an effort to interpret the ESI mass spectrum and the ^{1}H NMR spectrum. As anticipated, the ^{1}H NMR spectrum of complex **6.1-*d*$_{17}$** in C_6D_6 is nearly identical to that for **6.1**. It has two different phenyl

environments in the aryl region, assignable to the PPh_3 ligands, and it has a sharp resonance at 1.31 ppm that integrates to 9H, confirming the assignment of this peak to three acetate ligands. However, the ^{1}H NMR spectrum does not have a broad peak at 1.71 ppm where the resonance assignable to hydride was. Instead, complex **6.1-*d*$_{17}$** features a broad singlet at 1.72 ppm in its ^{2}H NMR spectrum. In addition, a ^{2}H NMR spectrum of this material at –40 °C in toluene-d_8 reveals the presence of approximately three hydride chemical environments in what appears to be a 2:9:6 ratio. The signals are small, not fully resolved and overlapping with solvent peaks as there were difficulties collecting a high quality spectrum due to the small amount of pure material available. Interestingly, the ESI mass spectrum of **6.1-*d*$_{17}$** features singly charged peaks in the region between *ca*. 2400 and 4800 *m/z* that are shifted either 17 or 21 *m/z* from those observed for **6.1**. While these spectra cannot be used to definitively determine the number of hydride ligands in **6.1**, because none of the signals have been assigned, it is not unreasonable to say that they support the tentative 17 hydride formulation of complex **6.1** . Although calculations have not been done to determine probable locations for the 17 hydrides, one possibility is that two hydrides are located within the Cu_{26} core, specifically above and below the triangular core, while six cap the top and bottom faces of the cluster, and the remaining nine hydrides are distributed along the equatorial plane of the cluster.

Complex **6.2** crystallizes in the monoclinic space group $P2_1/n$ upon crystallization from a C_6H_6/toluene/Et_2O solution at −25 °C. As with **6.1**, only a preliminary solid state molecular structure was determined. While the Cu and P atoms were successfully located, none of the C and H atoms, acetate ligands, or solvate molecules were located. The cluster occupies the C_2 point group. In the solid state, complex **6.2** features a central core of two copper atoms,

surrounded by a cage of 14 Cu atoms and an outer layer of ten Cu(PPh_3) units. Each of the two copper atoms in the core features a coordination number of 12, identical to that observed in bulk Cu metal.[13] Similar to **6.1**, this is also an unprecedented architecture that has not been observed previously in any other group 11 NCs. As was observed for **6.1**, the Cu–Cu bonds in **6.2** exhibit a large range (2.26 – 3.05 Å). These values are comparable to those exhibited by other CuH clusters such as **6.1** (2.30 – 3.25 Å), $[Cu_{14}H_{12}(phen)_6(PPh_3)_4]^{2+}$ (2.487 (3)–2.915(3) Å),[16] $[Cu_{25}H_{22}(PPh_3)_{12}]Cl$ (**4.1**) (2.389(3) – 3.037(3) Å),[10] and $[Cu_{29}Cl_4H_{22}(Ph_2phen)_{12}]Cl$ (**5.1**) (2.537(3) –3.303(3) Å).[11] For further comparison, the average Cu–Cu distance in **6.2** (2.61 Å) is intermediate to the Cu−Cu distances reported for solid $[CuH]_x$ (2.85 Å) and Cu metal (2.55 Å).[13,17] Finally, the Cu–P distances (av. 2.36 Å) are in the range of those typically found in Cu(I) phosphine complexes,[10,11,14,15]

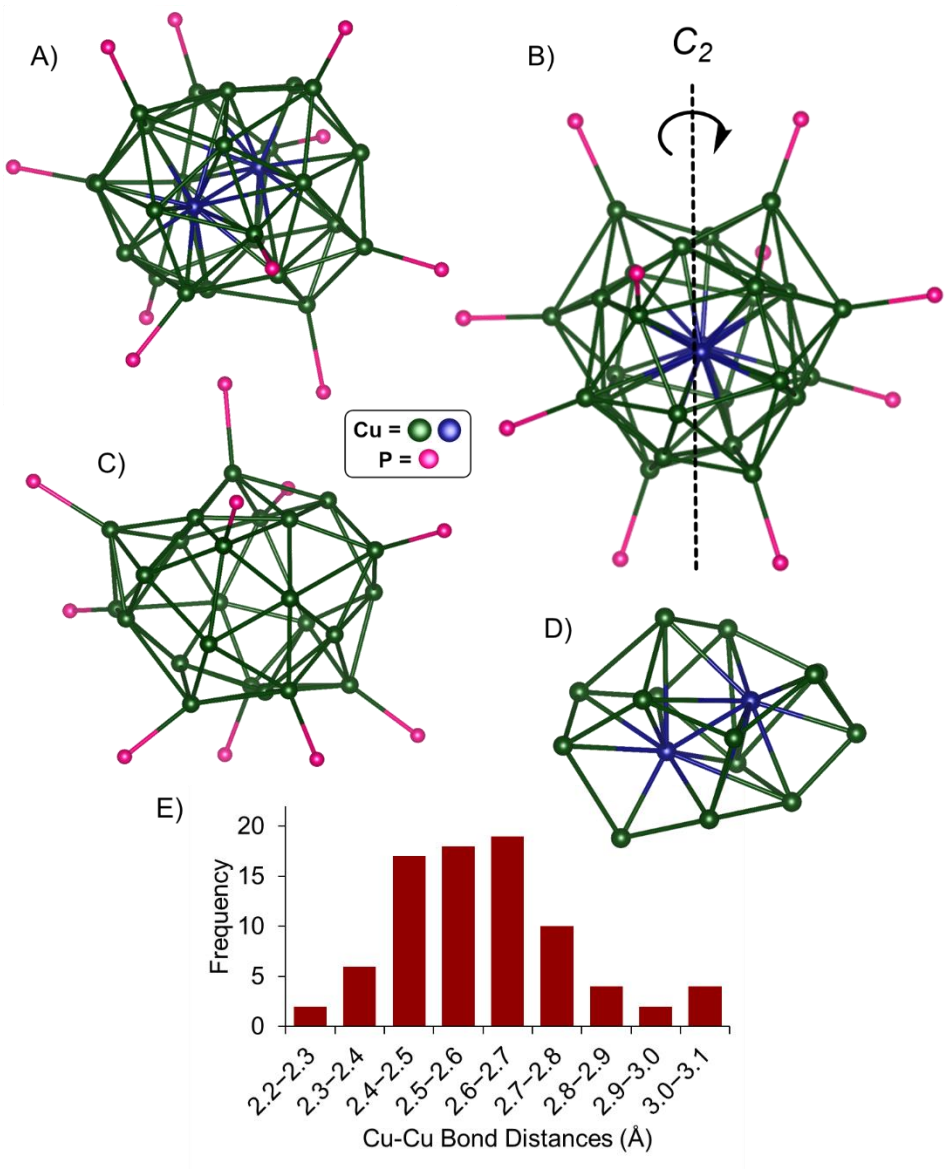

Figure 6.4. Ball and stick diagrams and Cu-Cu bond distance histogram for $[Cu_{26}H_{22}(PPh_3)_{10}(OAc)_2]$ (**6.2**). The two central Cu atoms are highlighted in blue. The remaining Cu atoms are shown in green, while the P atoms are shown in pink. No other atoms were found in this preliminary structure. (A) Full Structure. (B) Full structure showing the C_2 axis. (C) Structure shown without the two central Cu atoms (Blue). (D) Structure shown without the P atoms and the Cu atoms bonded to P. (E) Histogram depicting the distribution of Cu-Cu bond distances.

Complex **6.2** features five resonances in its $^{31}P\{^1H\}$ NMR spectrum at -11.17, -6.44, -3.20, 1.40, and 2.04 ppm in C_6D_6 in a 1:1:1:1:1 ratio. These resonances are assigned to five

pairs of PPh_3 ligands in unique environments, which is expected based on the C_2 point group of this cluster. The ^1H NMR spectrum of **6.2** in C_6D_6 features seven broad resonances at 0.22, 0.41, 0.53, 1.77, 1.99, 2.64, and 4.87 ppm, as well as several more that overlap with solvent, which are assigned to hydride ligands. The aryl region in the ^1H NMR spectrum is unusually broad, and unlike in the $^{31}P\{^1H\}$ NMR spectrum, 5 distinct phenyl environments from PPh_3 cannot be distinguished. However, a resonance assigned to an ortho CH environment at 8.43 ppm is set to integrate to 6H because it does not overlap with any other peaks. It is set to only one PPh_3 because doing so allows the entire aryl region, minus the benzene solvent peak, to integrate to about 150H, which is the expected number for 10 PPh_3 ligands. In addition, there is a sharp resonance at 1.68 ppm integrating for 6H, which I have tentatively assigned to two acetate ligands. Unfortunately, the resonances assignable to hydride are small and overlapping with solvent peaks, making them impossible to integrate reliably. However, based on the presence of 2 acetate ligands, I hypothesize that the cluster has either 22 or 24 hydride ligands, making it either an N^* = 2, or a Cu(I) cluster, respectively. As was observed for complex **6.1**, an ESI mass spectrum of **6.2**, recorded in THF, does not feature any signals that correspond to an obvious parent species, such as $[[Cu_{26}H_{22}(PPh_3)_{10}(OAc)_2] - OAc]^+$ or $[[Cu_{26}H_{22}(PPh_3)_{10}(OAc)_2] + Na]^+$. In fact, this spectrum features the same signals between *ca*. 2400 and 4800 *m/z* as was observed for **6.1** (Figure A6.9), which is further evidence that the two Cu_{26} clusters are closely related. The deuteride analogue **6.2-*d*$_{22}$** was also synthesized and characterized. As anticipated, the ^1H NMR spectrum of complex **6.2-*d*$_{22}$** in C_6D_6 is nearly identical to that for **6.2**. It has a broad phenyl region, assignable to the PPh_3 ligands, that integrates to about 150H if the resonance at 8.42 ppm is set to 6H, and it has a sharp resonance at 1.67 ppm that integrates to 6H,

confirming the assignment of this peak to two acetate ligands. This ^{1}H NMR spectrum does not feature any of the small broad peaks previously assigned to hydride. Instead, the ^{2}H NMR spectrum features about 10 resonances between 0.31 and 5.01 ppm that are assignable to deuteride ligands (Figure A6.8). Unfortunately, the peaks in the spectrum are weak and cannot be reliably integrated due to the low solubility of **6.2-*d*$_{22}$** in C_6H_6 and because of how they overlap. Unsurprisingly, because the ESI mass spectra of **6.1** and **6.2** were virtually identical, an ESI mass spectrum of the deuterated material also features signals that are shifted either 17 or 21 *m/z* from the non-deuterated cluster. Thus, I tentatively suggest that there are 22 hydrides on the basis that there are stable clusters in the ESI mass spectrum with 21 hydrides, which is very close to 22 and can easily be rationalized by the loss of one hydride ligand for a positively charged cluster. Although, it is still also possible that there are 24 hydride ligands in the cluster. Most importantly, with 22 hydride ligands and 2 acetate ligands, two of the Cu atoms in complex **6.2** must have a formal Cu(0) oxidation state to maintain charge balance and **6.2** can then be described as an $N^* = 2$ superatom with closed shell $1S^2$ configuration, which is significant as an odd number of N^* electrons (e.g. 21 hydrides instead of 22) is much less likely and would result in a paramagnetic complex, which is not consistent with our data.[18] Nonetheless, more work must be done to determine the number of hydrides in **6.2**.

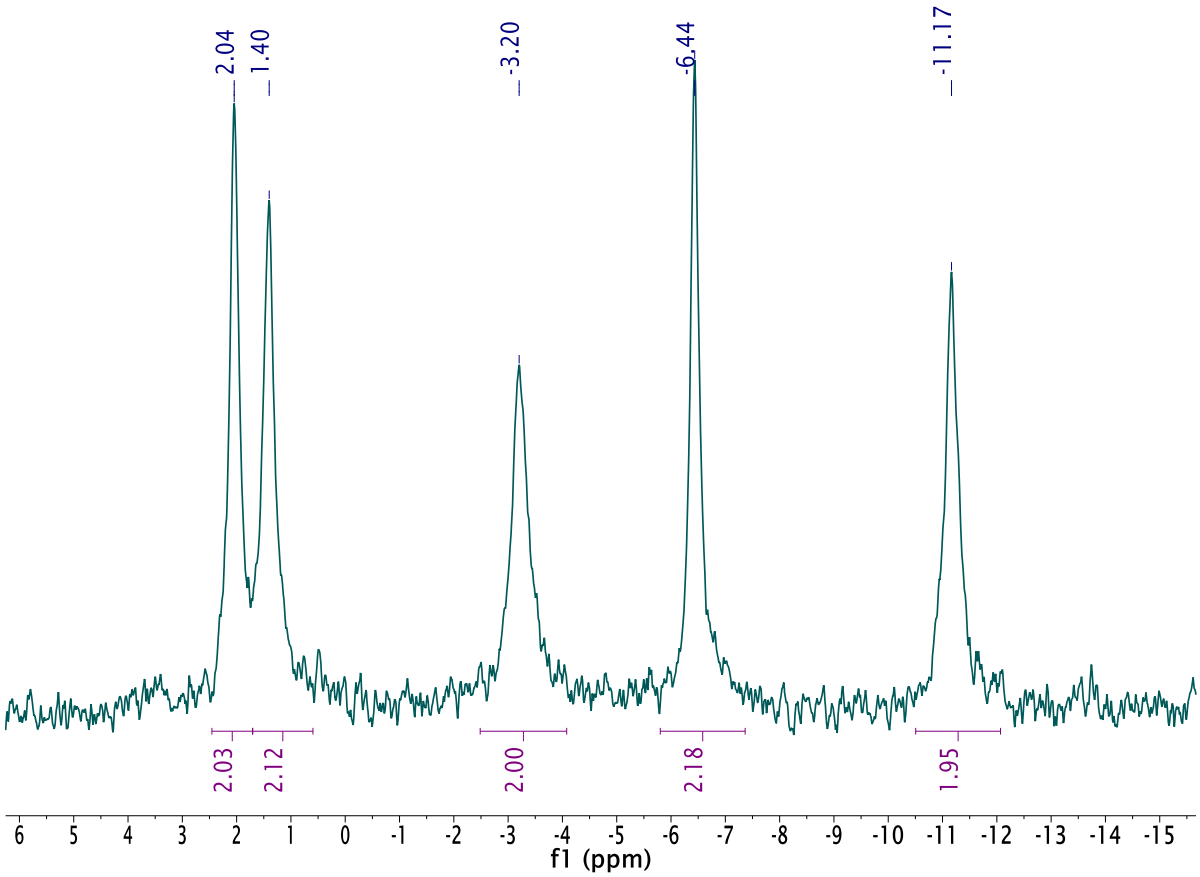

Figure 6.5. $^{31}P\{^{1}H\}$ NMR spectrum of $[Cu_{26}H_{22}(PPh_3)_{10}(OAc)_2]$ (**6.2**) in C_6D_6.

My collaboration with Zach Jones in Prof. Susannah Scott's group at UC Santa Barbara previously established that Cu K-edge X-ray absorption near-edge spectra (XANES) can be used to probe the average oxidation state of nanoclusters such as $[Cu_{25}H_{22}(PPh_3)_{12}][Cl]$ (**4.1**) and $[Cu_{29}Cl_4H_{22}(Ph_2phen)_{12}]Cl$ (**5.1**).[10,11] Zach collected data for a series of Cu(0) and Cu(I) materials and determined that for the N^* = 2 clusters, **4.1** and **5.1**, the edge position is sensitive enough to detect an average Cu oxidation state that is intermediate between 0 and +1, even though these clusters have minimal Cu(0) character. These studies provided a benchmark for using XANES to probe oxidation state because the exact composition of the clusters, including the number of hydrides, was experimentally confirmed through multiple techniques. Given the *ca*. 0.1 eV resolution of the spectra, XANES should be able to

determine if **6.1**, which we have assigned as an N^* = 6 cluster, features more metallic character than the N^* = 2 clusters, even though the number of hydrides in the cluster was not conclusively confirmed. In the same manner, the edge energy for **6.2** should also be consistent with an N^* = 2 cluster. At 8979.3 eV, the edge energy of complex **6.1** lies between the values for Cu foil (8970.0 eV) and $[Cu_{25}H_{22}(PPh_3)_{12}][Cl]$ (**4.1**) (8979.6 eV), and is consistent with an average Cu oxidation state in the cluster that is intermediate between a fully reduced Cu(0) oxidation state, such as in bulk metal, and N^* = 2, which supports the assignment of **6.1** as an N^* = 6 cluster. Interestingly, 6 is not a typical magic number in the jellium model for superatoms (N^* = 2, 8, 18, 34…).[18] However, it should be noted that the jellium model assumes a perfectly spherical cluster when predicting superatomic orbitals, and thus the number of electrons needed for a closed shell structure.[19] Complex **6.1** deviates away from spherical with the triangular core and may still be described as a closed shell, stable superatom. While the difference in edge energy is small, it is notable that the edge energy of **6.1** is lower than that of **4.1**, because **6.1** has a smaller ratio of PPh_3 ligands to Cu atoms, which should shift the edge energy of **6.1** higher than that of **4.1**, given identical oxidation states for Cu in the two complexes. This is because the Cu K-edge energy is greatly affected by coordination of electron-donating PPh_3 to Cu, which is evidenced by how the energy of $[CuCl(PPh_3)]_4$ (8980.9 eV) is shifted by 1.0 eV, compared to CuCl (8981.9 eV), with only the addition of PPh_3 (Table 4.1). By the same logic, at 8980.0 eV, the edge energy of complex **6.2** supports its assignment as an N^* = 2 cluster. It has a significantly smaller ratio of PPh_3 ligands to Cu atoms compared to $[CuH(PPh_3)]_6$ (8980.0 eV), which should result in a larger edge energy. Yet, they are the same, which suggests that the average oxidation state of **6.2** is less than Cu(I). In addition, **6.2** has a smaller ratio of

PPh_3 ligands to Cu atoms as compared to **4.1**, so if they are both $N^* = 2$, **6.2** (8980.0 eV) should have a higher edge energy than **4.1** (8979.6 eV), which is indeed the case.

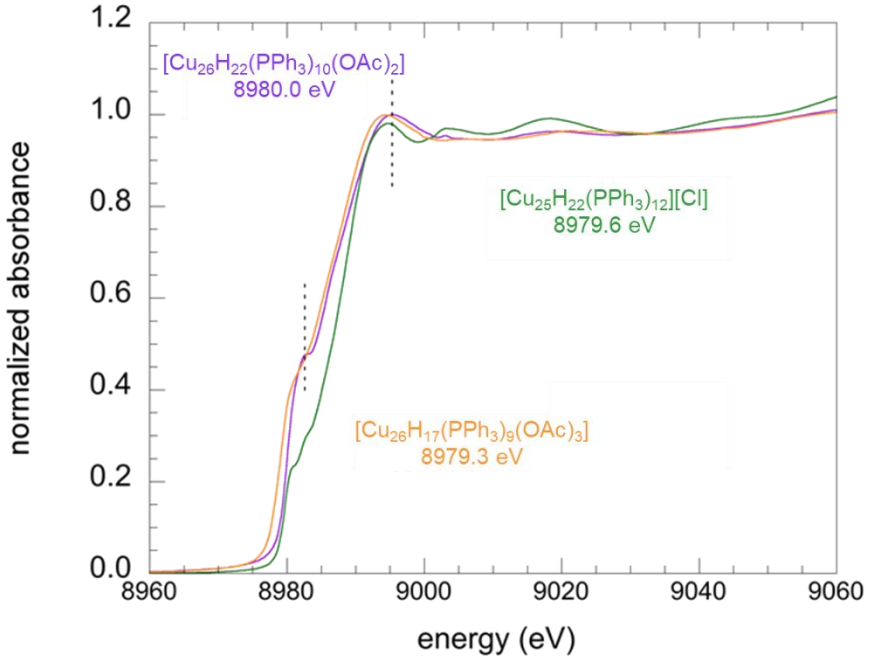

Figure 6.6. Comparison of Cu K-edge XANES profile of $[Cu_{25}H_{22}(PPh_3)_{12}][Cl]$ (**4.1**), $[Cu_{26}H_{17}(PPh_3)_9(OAc)_3]$ (**6.1**), and $[Cu_{26}H_{22}(PPh_3)_{10}(OAc)_2]$ (**6.2**). Figure prepared by Zach Jones.

Table 6.1. Cu K-edge energies (eV) and Auger parameters (eV) for selected Cu(0) and Cu(I) compounds. Data collected by Zach Jones.

Material	K-edge (eV)	Oxidation state
Cu foil[10]	8979.0	0
Cu nanoparticles (1-2 nm)[10]	8979.0	0
$[Cu_{26}H_{17}(PPh_3)_9(OAc)_3]$, **6.1**	8979.3	$N^* = 6$
$[Cu_{25}H_{22}(PPh_3)_{12}][Cl]$, **4.1**[10]	8979.6	$N^* = 2$
$[Cu_{29}Cl_4H_{22}(Ph_2phen)_{12}][Cl]$, **5.1**[11]	8979.5	$N^* = 2$
$[Cu_{26}H_{22}(PPh_3)_{10}(OAc)_2]$, **6.2**	8980.0	$N^* = 2$
$[CuH(PPh_3)]_6$[10]	8980.0	1

$[Cu_{18}H_{17}(PPh_3)_{10}]Cl$, **4.2**[10]	8980.5	1
$[CuCl(PPh_3)]_4$[10]	8980.9	1
CuCl[10]	8981.9	1

6.3 Summary

I have isolated and characterized $[Cu_{26}H_{17}(PPh_3)_9(OAc)_3]$ (**6.1**), the first copper nanocluster with a magic number greater than 2. This material is built around an unusual core of three Cu centers arranged in a triangle, each of which have a coordination environment of 12 other Cu atoms, similar to that observed in Cu metal. Complex **6.1** has proven challenging to characterize and thus, the exact number of hydride ligands present in the cluster is inconclusive. However, structurally, this cluster appears to have more metallic character than other nanoclusters such as **4.1** and **5.1**, which are built around a Cu_{13} centered-icosahedron with only 1 Cu atom with a coordination number of 12. Moreover, the Cu-K edge XANES shows that **6.1** features an edge energy intermediate between those of Cu(0) and $N^* = 2$ copper nanoclusters. Taken together with the NMR spectral data, the ESI-MS, and a structural analysis, these data support the assignment of **6.1** as an $N^* = 6$ superatom, containing 17 hydride ligands. Demonstrating for the first time that an $N^* > 2$ superatom is isolable for copper. In order to complete this work, good crystal structures for both **6.1** and **6.2** must be obtained, at least to confirm the number and location of acetate ligands. The number of hydride ligands must also be more reliably determined. Ideally, parent peaks would be found in the ESI mass spectra. While this has not yet been done, it is not clear whether this is inherently impossible because of the nature of the complexes, or if they are decomposing in the instrument, before detection. Lastly, a good single crystal neutron diffraction study would experimentally determine both the number and location of

the hydrides. However, this is likely to be extremely challenging as currently, even a crystal suitable for an adequate X-ray crystal structure is out of reach. That said, my development of this series of NCs supported by PPh_3 has resulted in the ability to reliably probe the oxidation state of new related NCs using XANES, and although the X-ray absorption fine structure (EXAFS) data for **6.1** and **6.2** has not yet been analyzed, that can also be used to determine average coordination number and size of a NC, which will be instrumental when a crystal structure is not available, such as during *in situ* catalytic experiments or for supported NCs.

6.4 Experimental

6.4.1 General Methods

All reactions and subsequent manipulations were performed under anaerobic and anhydrous conditions under an atmosphere of nitrogen. Hexanes, diethyl ether, benzene, dichloromethane, and toluene were dried using a Vacuum Atmospheres DRI-SOLV Solvent Purification system and stored over 3Å sieves for 24 h prior to use. Acetonitrile was degassed and dried over 3Å molecular sieves for 72 h prior to use. CD_2Cl_2, diphenylsilane, and diphenylsilane-d_2 (Sigma-Aldrich, 97 atom % D) were dried over 3Å molecular sieves for 24 h prior to use. Copper(I) acetate, 97% was purchased from Strem chemicals and used as received. All other reagents were purchased from commercial suppliers and used as received.

All NMR spectra were collected at room temperature. ^{1}H NMR spectra were recorded on an Agilent Technologies 400-MR DD2 400 MHz spectrometer, a Varian Unity Inova 500 MHz spectrometer, or a Varian Unity Inova A S600 MHz spectrometer. $^{13}C\{^1H\}$ NMR spectra were recorded on an Agilent Technologies 400-MR DD2 400 MHz spectrometer or a

Varian Unity Inova 500 MHz spectrometer. $^{31}P\{^{1}H\}$ and ^{2}H NMR spectra were recorded on an Agilent Technologies 400-MR DD2 400 MHz spectrometer. The chemical shifts of ^{31}P nuclei were referenced indirectly with the ^{1}H resonance of $SiMe_4$ at 0 ppm, according to IUPAC standard.[20,21] The chemical shifts of the other nuclei were referenced using the residual solvent peaks (^{1}H, ^{13}C and ^{2}H NMR experiments) as internal standards. IR spectra were recorded on a Nicolet 6700 FT-IR spectrometer with a NXR FT Raman Module. UV-Vis experiments were performed on a Shimadzu UV-2401PC spectrophotometer. Mass spectra were collected by the Mass Spectrometry Facility at the University of California, Santa Barbara, using an electrospray ion (ESI) source on positive ion mode with a Waters Micromass QTOF2 Quadrupole/Time-of-Flight Tandem mass spectrometer. Mass spectra were smoothed 4 times using the mean algorithm with a smooth window of 3 channels. Elemental analyses were performed by the Micro-Mass Facility at the University of California, Berkeley.

6.4.2 Synthesis of $[Cu_{26}H_{17}(PPh_3)_9(OAc)_3]$ (6.1) and $[Cu_{26}H_{22}(PPh_3)_{10}(OAc)_2]$ (6.2)

To a stirring pale green suspension of Cu(OAc) (302.6 mg, 2.47 mmol) and PPh_3 (250.4 mg, 0.95 mmol) in benzene (2 mL) was added diphenylsilane (0.24 mL, 1.3 mmol) via syringe. This resulted in a rapid color change to dark red and dissolution of the pale green solid. After stirring for 15 h, this solution had become dark brown. This solution was filtered through a Celite column (0.5 cm × 1.5 cm) supported on glass wool and the filter was rinsed with THF (2 mL). The resulting dark brown filtrate was layered with hexanes (10 mL). Storage of this solution at -25 °C for 72 h resulted in the deposition of a dark brown material, which was isolated by decanting off the supernatant. The solid was washed with hexanes (3 × 1 mL) and dried *in vacuo* (439.3 mg). This solid was redissolved in THF

(8mL) and filtered through a Celite column (0.5 cm × 1.5 cm) supported on glass wool, to remove a small amount of undissolved brown solid. The resulting dark brown filtrate was concentrated to *ca.* 5 mL *in vacuo* and layered with Et_2O (15 mL). Storage of this solution at -25 °C for 72 h resulted in the deposition of a dark brown material, which was isolated by decanting off the supernatant. The solid was washed with hexanes (3 × 1 mL) and dried *in vacuo* (173.0 mg). This solid was then extracted into toluene (7 mL) and filtered through a Celite column (0.5 cm × 2 cm) supported on glass wool to produce a dark brown filtrate. A brown plug remained on the column. The plug was rinsed with CH_2Cl_2 (1 mL) to reveal a red plug, which was then dissolved in THF (2 mL) and filtered through the same Celite column into a separate vial. The brown toluene fraction was then concentrated to *ca*. 3 mL *in vacuo* and layered with Et_2O (13 mL), and storage of this solution at -25 °C for 5 d resulted in the deposition of complex **6.1** as a dark brown powder, which was isolated by decanting off the brown supernatant. The brown powder was washed with Et_2O (3 × 1 mL) and dried *in vacuo* (71.6 mg, 18% yield of **6.1**). The red THF fraction was layered with Et_2O (5 mL). Storage of this solution at -25 °C for 24 h resulted in the deposition of complex **6.2** as a red crystalline material, which was isolated by decanting off the supernatant. The solid was washed with Et_2O (2 × 1 mL) and dried *in vacuo* (3.0 mg, <1 % yield of **6.2**). Complex **6.1**: Anal. Calcd for $C_{168}H_{162}Cu_{26}O_6P_9$: C, 47.95; H, 3.88. Found: C, 49.20; H, 3.82. ^{1}H NMR (400 MHz, 25 °C, C_6D_6): δ 1.34 (s, 9H, OAc^-), 1.71 (s, 17H, hydride), 6.72 (t, *J* = 7.2 Hz, 36H, *m*-C*H* on axial PPh_3), 6.83 (t, *J* = 7.2 Hz, 18H, *p*-C*H* on axial PPh_3), 7.03 (m, 27H, *m*-C*H* overlapping with *p*-C*H* on equatorial PPh_3), 7.63 (t, *J* = 8.6 Hz, 36H, *o*-C*H* on axial PPh_3), 8.02 (m, 18H, *o*-C*H* on equatorial PPh_3). $^{31}P\{^1H\}$ NMR (162 MHz, 25 °C, C_6D_6): δ -4.54 (s, 6P, axial *P*Ph_3), 4.16 (s, 3P, equatorial *P*Ph_3). Complex **2**: ^{1}H NMR (400 MHz, 25

°C, C_6D_6): δ 0.22 (s, hydride), 0.41 (s, hydride), 0.53 (s, hydride), 0.78 (s, hydride), 1.05 (s, hydride), 1.68 (s, 6H, OAc^-), 1.77 (s, hydride), 1.99 (s, hydride), 2.64 (s, hydride), 4.87 (s, hydride), 5.96 (s, 6H), 6.19-8.07 (m), 8.43 (s, 6H). ^{31}P NMR (162 MHz, 25 °C, C_6D_6): δ -11.17 (s, 2P), -6.44 (s, 2P), -3.20 (s, 2P), 1.40 (s, 2P), 2.04 (s, 2P). IR (KBr pellet, cm^{-1}): 442 (w), 458 (w), 518 (s), 619 (w), 693 (s), 742 (m), 1028 (w), 1094 (m), 1183 (w), 1385 (w), 1409 (m), 1434 (s), 1479 (m), 1561 (m), 1585 (w).

6.4.3 Synthesis of $[Cu_{26}D_{17}(PPh_3)_9(OAc)_3]$ (6.1-d_{17}) and $[Cu_{26}D_{22}(PPh_3)_{10}(OAc)_2]$ (6.2-d_{22})

To a stirring pale green suspension of Cu(OAc) (115.6 mg, 0.94 mmol) and PPh_3 (97.0 mg, 0.37 mmol) in benzene (2 mL) was added diphenylsilane (90 µL, 0.48 mmol) via syringe. This resulted in a rapid color change to dark red and dissolution of the pale green solid. After stirring for 16 h, this solution had become dark brown. This solution was filtered through a Celite column (0.5 cm × 1.5 cm) supported on glass wool and the filter was rinsed with THF (3 mL). The resulting dark brown filtrate was layered with hexanes (10 mL). Storage of this solution at -25 °C for 10 d resulted in the deposition of a dark brown material, which was isolated by decanting off the supernatant. The solid was washed with hexanes (3 × 1 mL) and dried *in vacuo* (137.8 mg). This solid was redissolved in THF (8 mL) and filtered through a Celite column (0.5 cm × 1.5 cm) supported on glass wool. The resulting dark brown filtrate was concentrated to *ca.* 3 mL *in vacuo* and layered with Et_2O (17 mL). Storage of this solution at -25 °C for 14 d resulted in the deposition of a dark brown material, which was isolated by decanting off the supernatant. The solid was washed with Et_2O (3 × 1 mL) and dried *in vacuo* (54.5 mg). This solid was then extracted into toluene (3 mL) and filtered through a Celite column (0.5 cm × 2 cm) supported on glass

wool to produce a dark brown filtrate. A brown plug remained on the column. The plug was rinsed with CH_2Cl_2 (1 mL) to reveal a red plug, which was then dissolved in THF (3 mL) and filtered through the same Celite column into a separate vial. The brown toluene fraction was then layered with Et_2O (12 mL), and storage of this solution at -25 °C for 4 d resulted in the deposition of complex **6.1-*d*$_{17}$** as a dark brown powder, which was isolated by decanting off the brown supernatant. The brown powder was washed with Et_2O (3 × 1 mL) and dried *in vacuo* (18.4 mg, 12% yield of **6.1-*d*$_{17}$**). The red THF fraction was layered with Et_2O (17 mL). Storage of this solution at -25 °C for 24 h resulted in the deposition of complex **6.2** as a red crystalline material, which was isolated by decanting off the supernatant. The solid was washed with Et_2O (2 × 1 mL) and dried *in vacuo* (14.2 mg, 9% yield of **6.2-*d*$_{22}$**). Complex **6.1 -*d*$_{17}$**: ^{1}H NMR (400 MHz, 25 °C, CD_2Cl_2): 1.31 (s, 9H, OAc^-), 6.71 (t, *J* = 7.1 Hz, 36H, *m*-C*H* on axial PPh_3), 6.83 (t, *J* = 7.1 Hz, 18H, *p*-C*H* on axial PPh_3), 7.02 (m, 27H, *m*-C*H* overlapping with *p*-C*H* on equatorial PPh_3), 7.62 (t, *J* = 8.6 Hz, 36H, *o*-C*H* on axial PPh_3), 8.03 (m, 18H, *o*-C*H* on equatorial PPh_3). ^{2}H NMR (61 MHz, 25 °C, CH_2Cl_2): δ 1.72 (s). ^{31}P{^{1}H} NMR (162 MHz, 25 °C, C_6D_6): δ -4.71 (s, 6P, axial *P*Ph_3), 4.06 (s, 3P, equatorial *P*Ph_3). Complex **6.2-*d*$_{22}$**: ^{1}H NMR (400 MHz, 25 °C, CD_2Cl_2): δ 1.67 (s, 6H, OAc^-), 5.97 (s, 6H), 6.23-8.04 (m), 8.42 (s, 6H). ^{31}P NMR (162 MHz, 25 °C, C_6D_6): δ -11.17 (s, 2P), -6.44 (s, 2P), -3.20 (s, 2P), 1.40 (s, 2P), 2.04 (s, 2P). ^{2}H NMR (61 MHz, 25 °C, C_6D_6): δ 0.31 (s). 0.44 (s), 0.56 (s), 0.82 (s), 1.20 (s), 1.30 (s), 1.75 (s), 2.04 (s), 2.64 (s), 5.01 (s).

6.4.4 X-Ray Crystallography

Data for **6.1** was collected on a Bruker KAPPA APEX II diffractometer equipped with an APEX II CCD detector using a TRIUMPH monochromater with a MoKα X-ray source (α = 0.71073 Å). Data for **6.2** was collected on a Bruker Proteum2 diffractometer equipped with

a PLATINUM CCD detector using multilayer optics with a CuKα X-ray source (α = 1.4178 Å). Crystals were mounted on a cryoloop under Paratone-N oil, and all data were collected at 100(2) K using an Oxford nitrogen gas cryostream system. X-ray data for **6.1** were collected utilizing frame exposures of 10 (low angle) and 20 s (high angle), while data for **6.2** were collected utilizing frame exposures of 10 s. Data collection and cell parameter determination were conducted using the SMART program.[22] Integration of the data frames and final cell parameter refinement were performed using SAINT software.[23] Absorption correction of the data were carried out using the multi-scan method SADABS.[24] Subsequent calculations were carried out using SHELXTL.[25] Structure determination was done using direct methods and difference Fourier techniques. Due to the low quality of the data, only the Cu and P atoms on complexes **6.1** and **6.2** were located. The final refinement for complex **6.1** included anisotropic temperature factors on all Cu and P atoms, while the Cu and P atoms in complex **6.2** were refined isotropically. Structure solution, refinement, graphics, and creation of publication materials were performed using SHELXTL.[25]

Table 6.2. X-ray crystallographic Data for **6.1** and **6.2**

	6.1	**6.2**
empirical formula	$C_{168}H_{161}Cu_{26}O_6P_9$	$C_{184}H_{178}Cu_{26}O_4P_{10}$
crystal habit, color	block, dark brown	plate, red
crystal size (mm)	0.15 × 0.10 × 0.10	0.20 × 0.10 × 0.025
crystal system	monoclinic	monoclinic
space group	C2/c	$P2_1/n$
volume ($Å^3$)	52648(34)	19280(6)
a (Å)	69.79(2)	27.212(5)
b (Å)	23.425(11)	25.775(4)
c (Å)	36.793(11)	27.921(5)
α (deg)	90.00	90.00
β (deg)	118.919(18)	100.102(11)
γ (deg)	90.00	90.00
Z	12	4

formula weight (g/mol)	4207.09	4415.38
density (calculated) (Mg/m^3)	1.724	1.454
absorption coefficient (mm^{-1})	3.570	3.580
F_{000}	26292	8588
total no. reflections	65653	14485
unique reflections	24827	7720
final R indices [I >2σ(I)]	R_1 = 0.6403 wR_2 = 0.6106	R_1 = 0.4875 wR_2 = 0.6789
largest diff. peak and hole ($e^- A^{-3}$)	2.487 and -3.179	2.394 and -1.793
GOF	1.950	3.235

6.5 Appendix

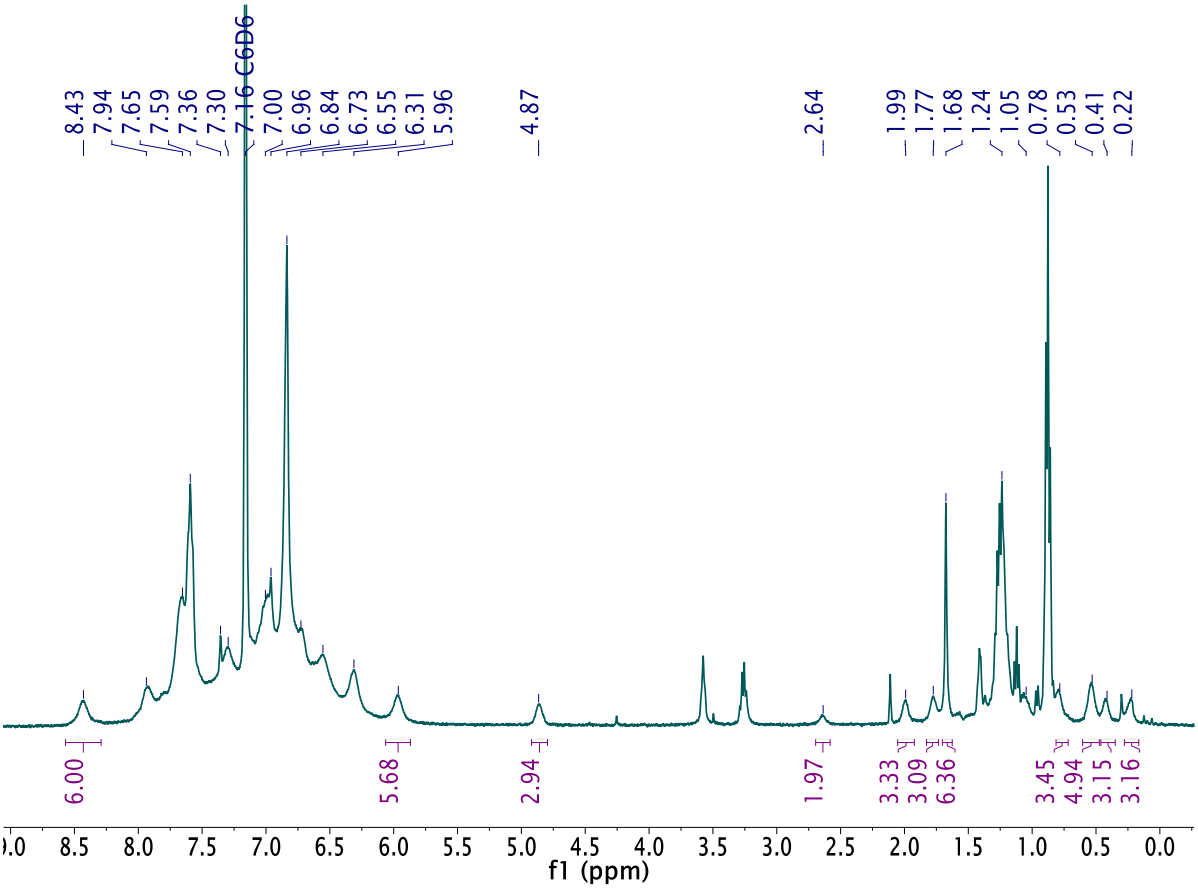

Figure A6.1. ^1H NMR spectrum of $[Cu_{26}H_{22}(PPh_3)_{10}(OAc)_2]$ (**6.2**) in C_6D_6.

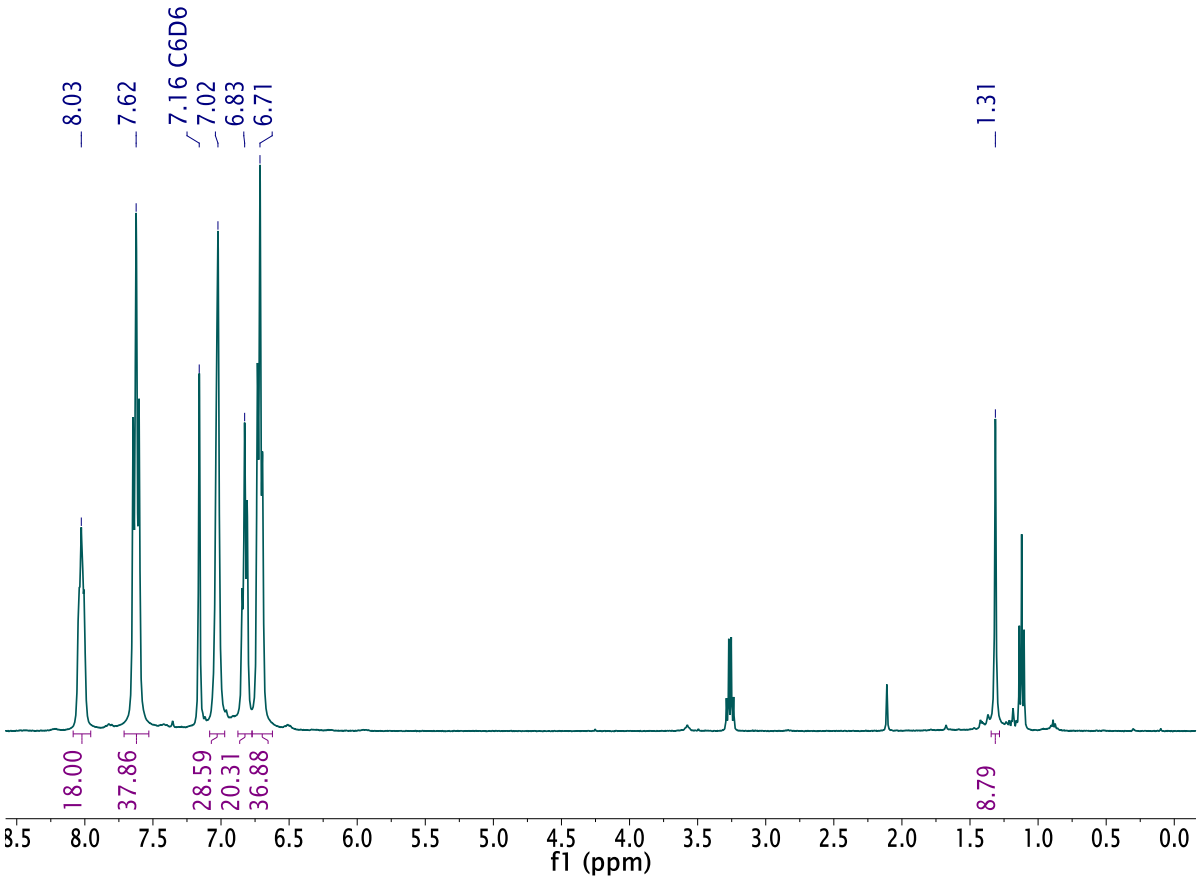

Figure A6.2. ^{1}H NMR spectrum of $[Cu_{26}D_{17}(PPh_3)_9(OAc)_3]$ (**6.1-*d*$_{17}$**) in C_6D_6.

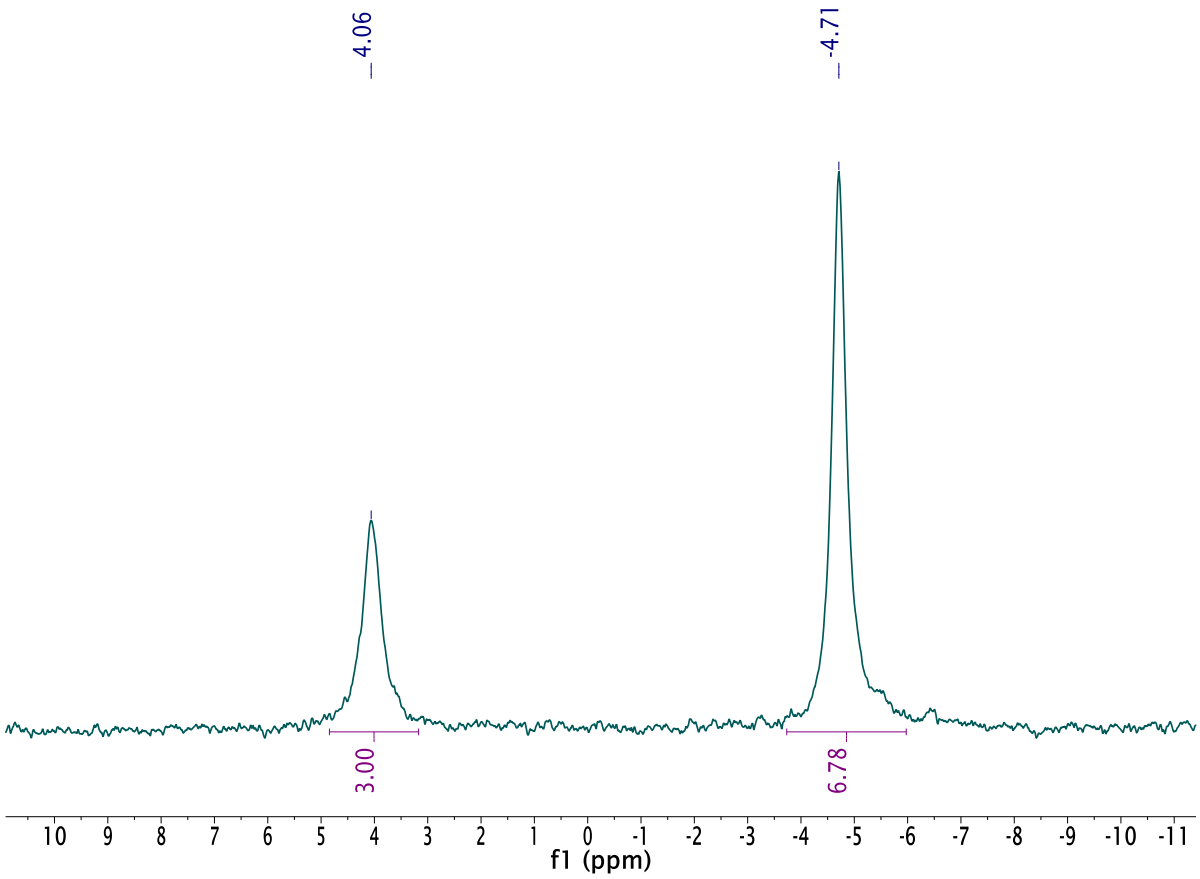

Figure A6.3. $^{31}P\{^{1}H\}$ NMR spectrum of $[Cu_{26}D_{17}(PPh_3)_9(OAc)_3]$ (**6.1-*d*$_{17}$**) in C_6D_6.

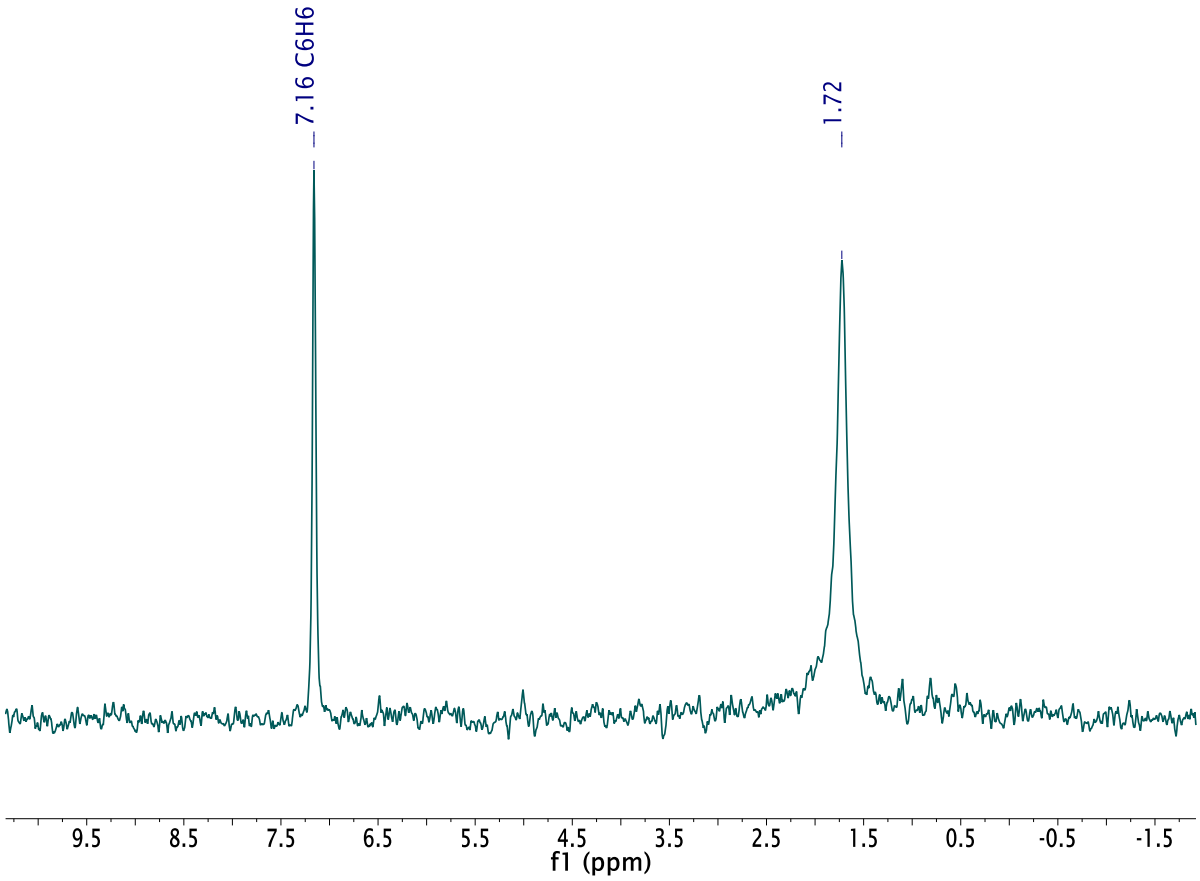

Figure A6.4. ^{2}H NMR spectrum of $[Cu_{26}D_{17}(PPh_3)_9(OAc)_3]$ (**6.1-*d*$_{17}$**) in C_6H_6.

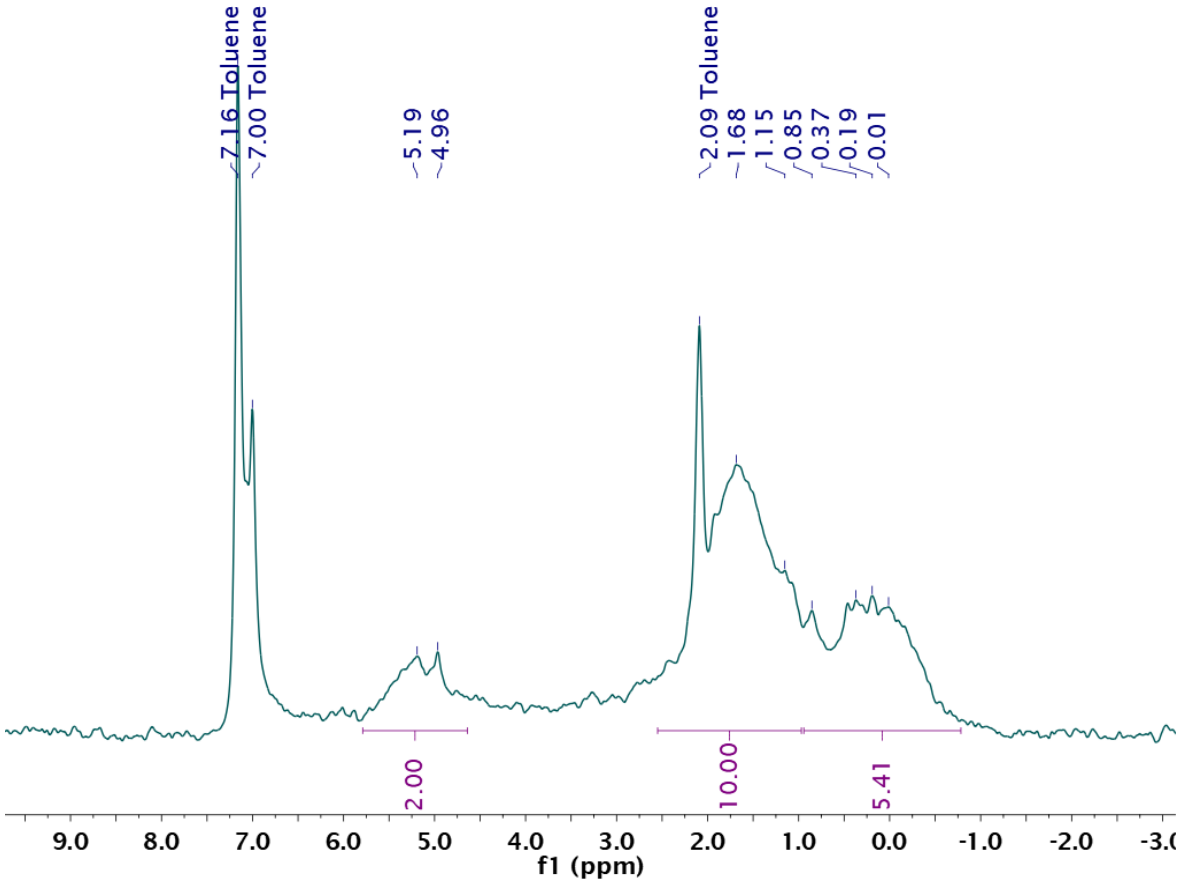

Figure A6.5. ^{2}H NMR spectrum of $[Cu_{26}D_{17}(PPh_3)_9(OAc)_3]$ (**6.1-*d*$_{17}$**) in C_6H_6 at –40 °C.

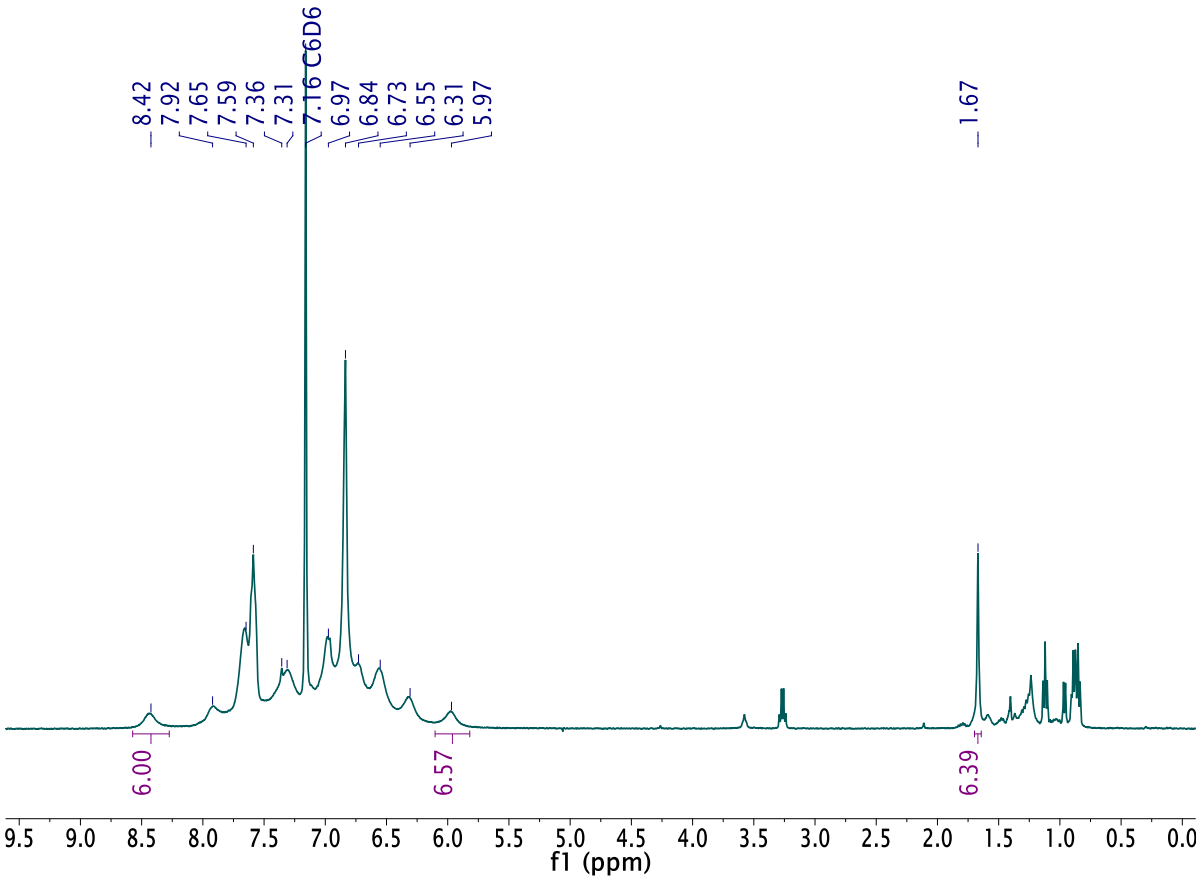

Figure A6.6. ^{1}H NMR spectrum of $[Cu_{26}D_{22}(PPh_3)_{10}(OAc)_2]$ (**6.2-*d*$_{22}$**) in C_6D_6.

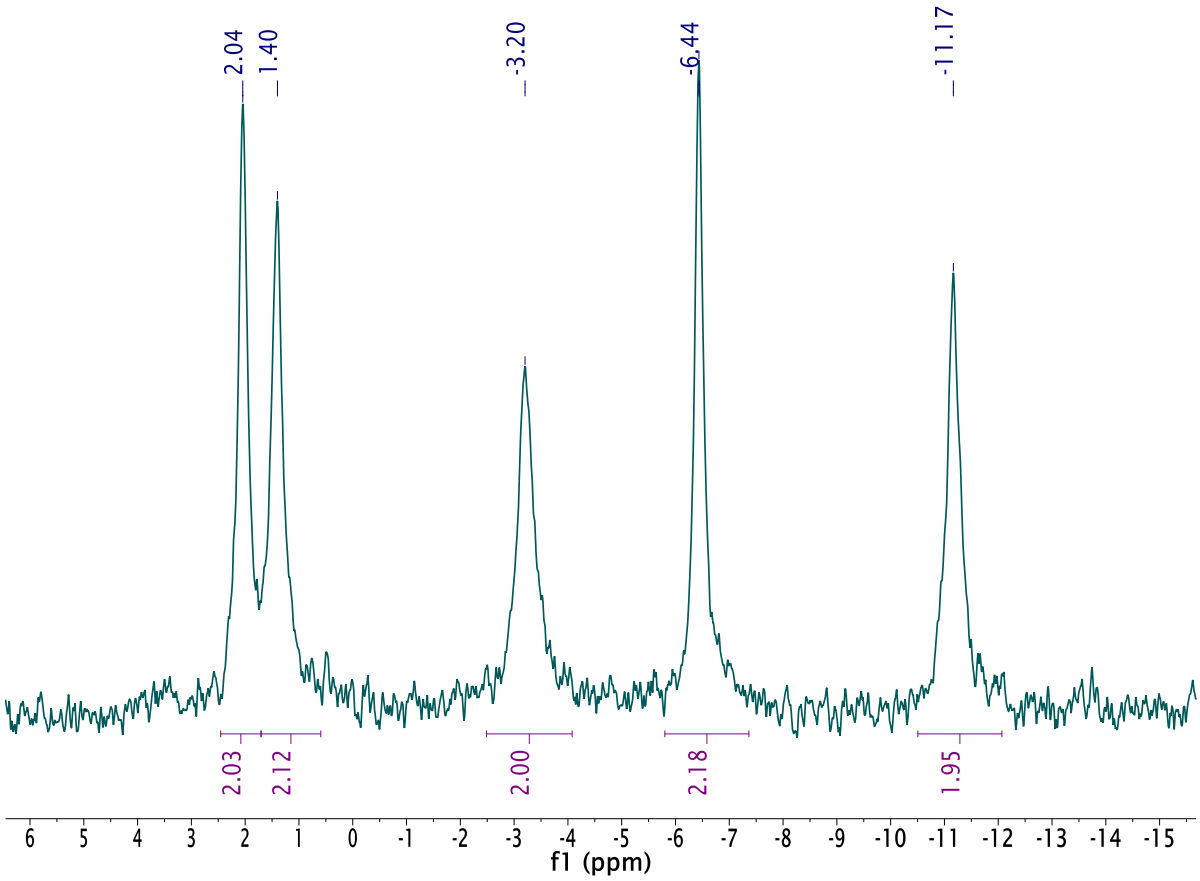

Figure A6.7. $^{31}P\{^{1}H\}$ NMR spectrum of $[Cu_{26}D_{22}(PPh_3)_{10}(OAc)_2]$ (**6.2-*d*$_{22}$**) in C_6D_6.

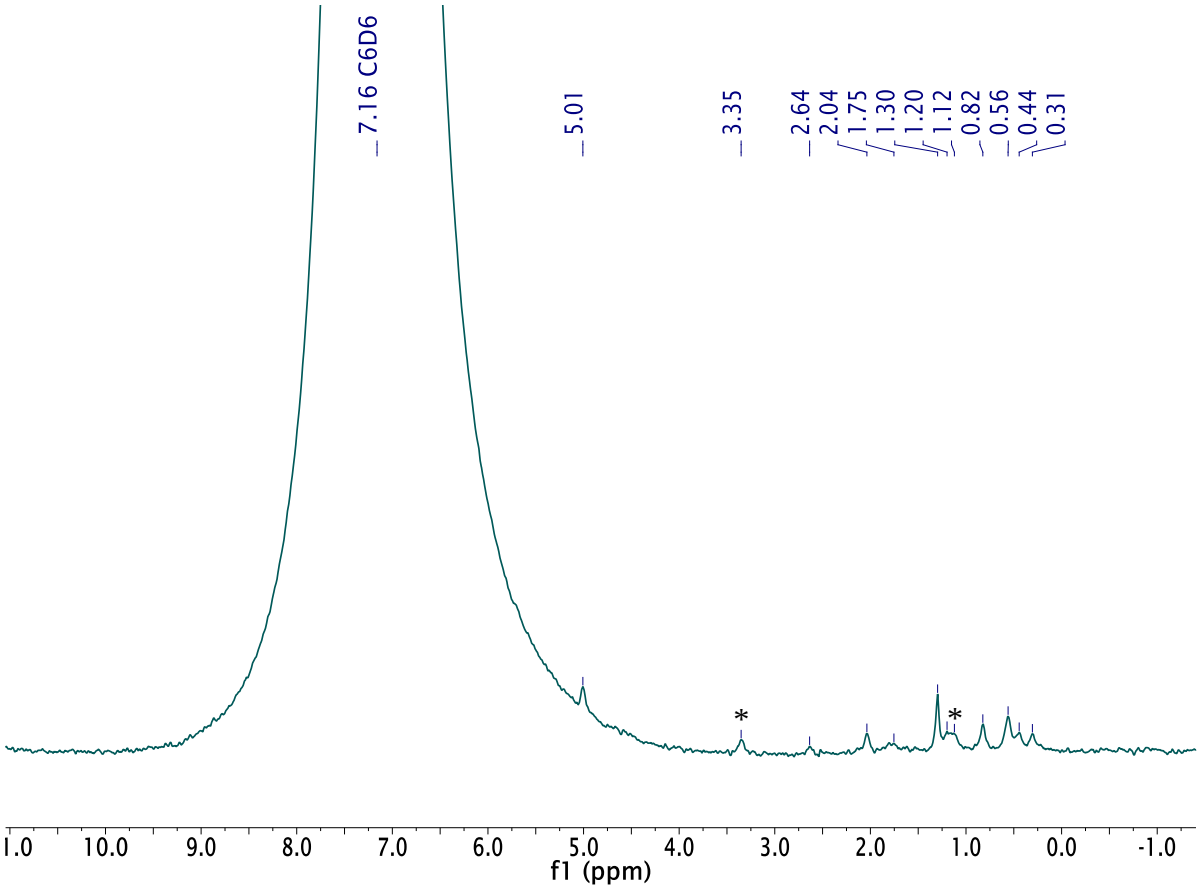

Figure A6.8. ^{2}H NMR spectrum of $[Cu_{26}D_{22}(PPh_3)_{10}(OAc)_2]$ (**6.2-*d*$_{22}$**) in C_6H_6 and a few drops of C_6D_6. (*) denotes the presence of Et_2O.

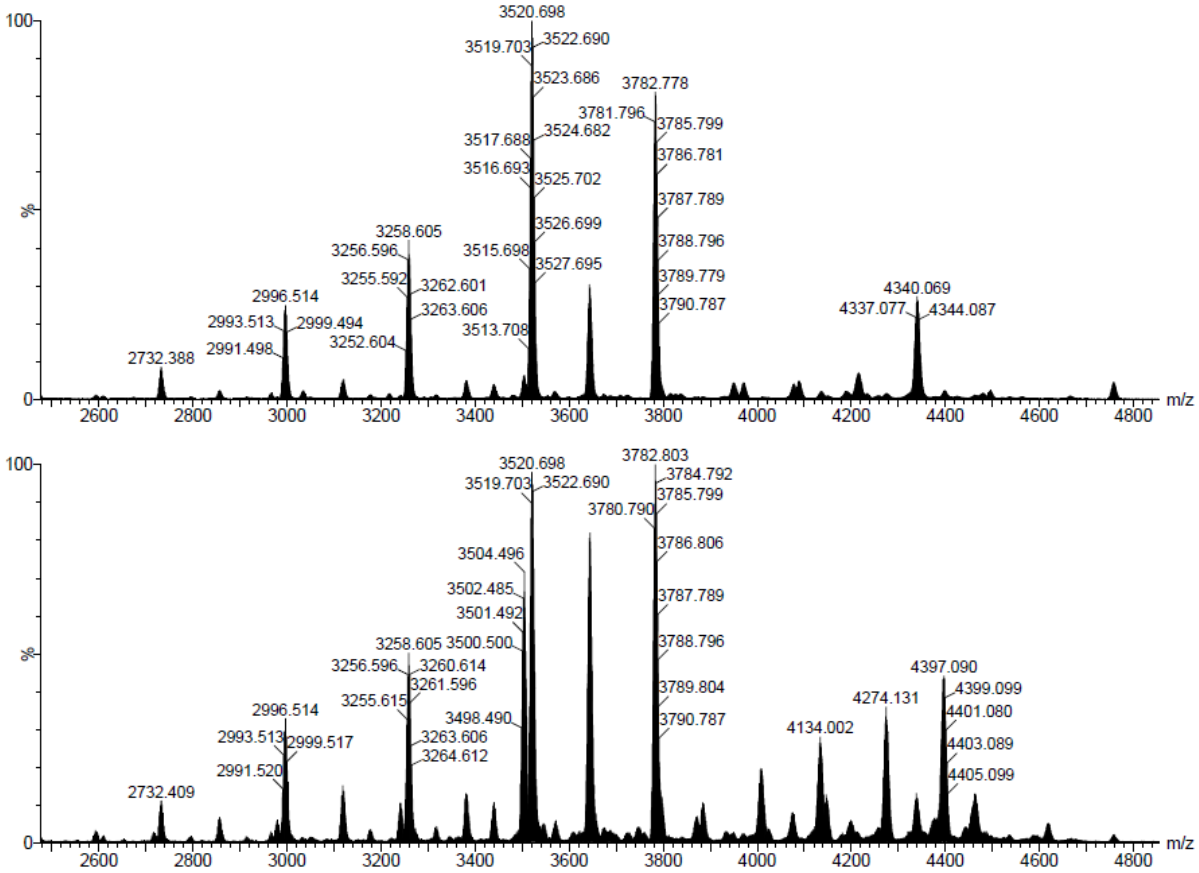

Figure A6.9. Partial ESI-MS of **6.1** (bottom) and **6.2** (top).

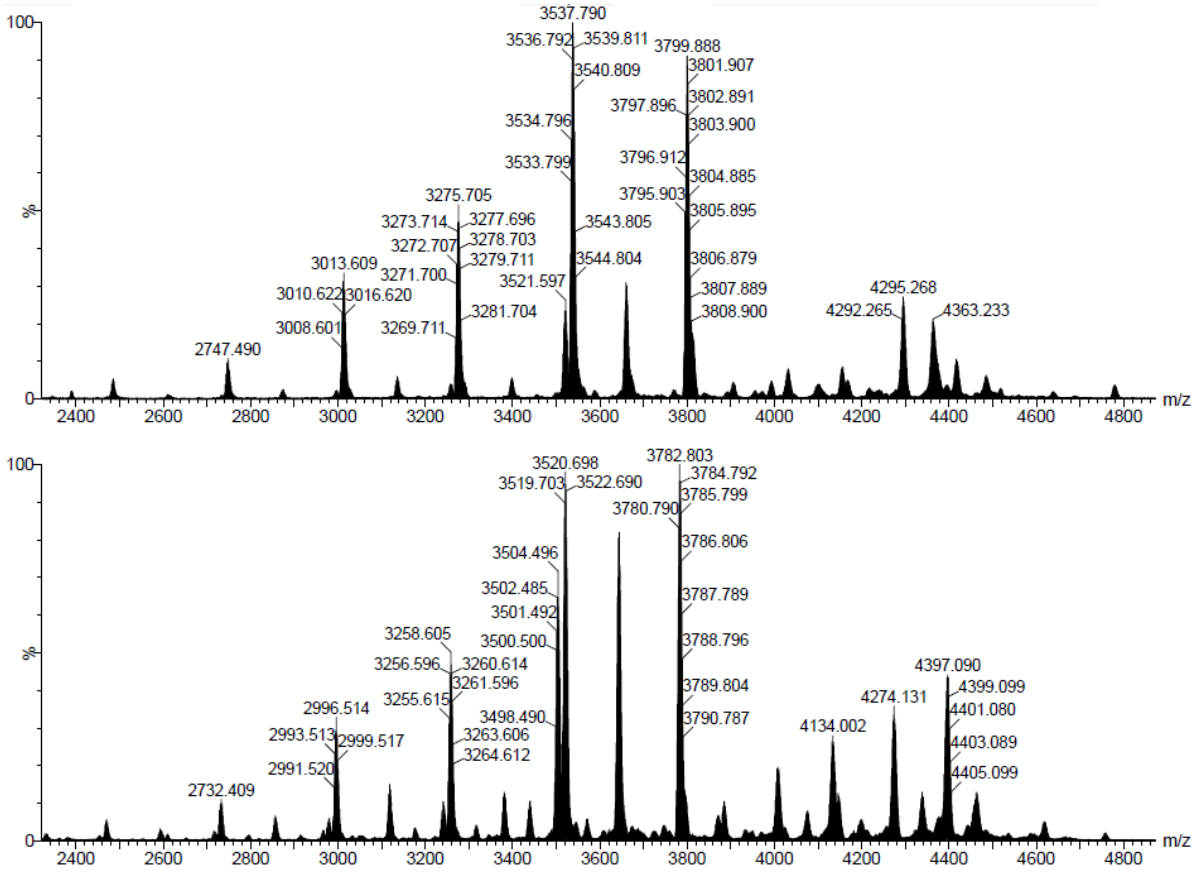

Figure A6.10. Partial ESI-MS of **6.1** (bottom) and **6.1-*d*$_{17}$** (top).

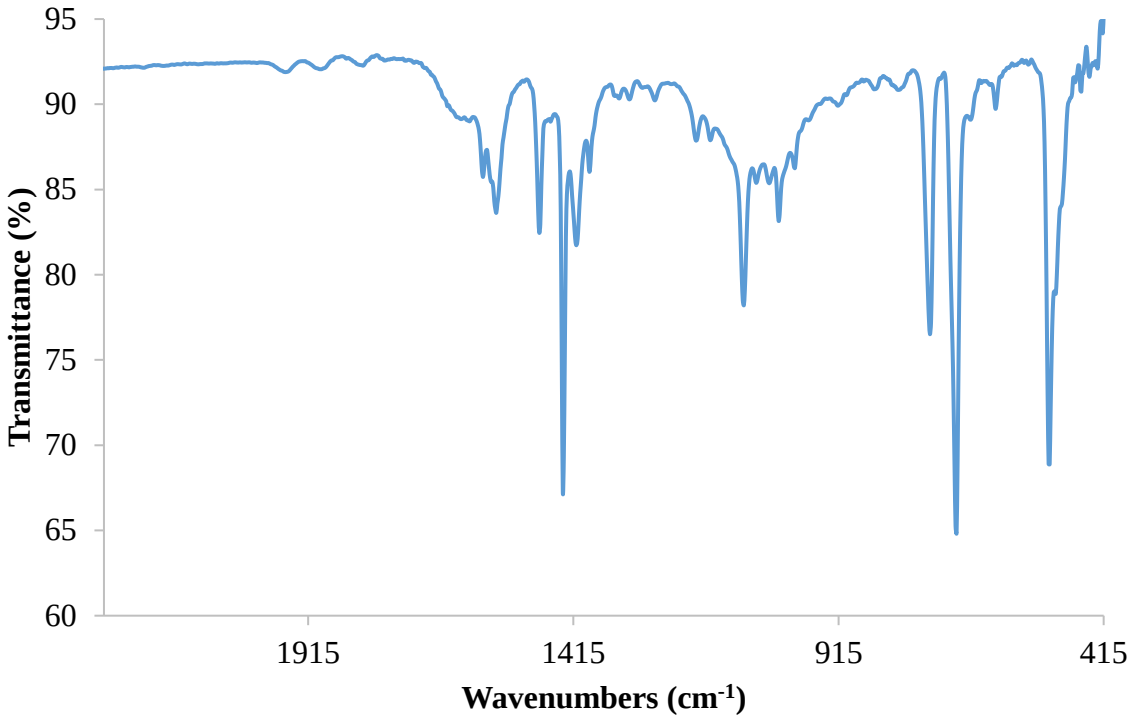

Figure A6.11. Partial IR spectrum of $[Cu_{26}H_{22}(PPh_3)_{10}(OAc)_2]$ (**6.2**) (KBr pellet).

6.6 References

(1) Hakkinen, H. Atomic and electronic structure of gold clusters: understanding flakes, cages and superatoms from simple concepts. *Chem. Soc. Rev.* **2008**, *37*, 1847.

(2) Schmid, G. The relevance of shape and size of Au_{55} clusters. *Chem. Soc. Rev.* **2008**, *37*, 1909.

(3) Yamazoe, S.; Koyasu, K.; Tsukuda, T. Nonscalable Oxidation Catalysis of Gold Clusters. *Acc. Chem. Res.* **2014**, *47*, 816.

(4) Li, G.; Jin, R. Atomically Precise Gold Nanoclusters as New Model Catalysts. *Acc. Chem. Res.* **2013**, *46*, 1749.

(5) Daniel, M.-C.; Astruc, D. Gold Nanoparticles: Assembly, Supramolecular Chemistry, Quantum-Size-Related Properties, and Applications toward Biology, Catalysis, and Nanotechnology. *Chem. Rev.* **2004**, *104*, 293.

(6) Parker, J. F.; Fields-Zinna, C. A.; Murray, R. W. The Story of a Monodisperse Gold Nanoparticle: $Au_{25}L_{18}$. *Acc. Chem. Res.* **2010**, *43*, 1289.

(7) Harkness, K. M.; Tang, Y.; Dass, A.; Pan, J.; Kothalawala, N.; Reddy, V. J.; Cliffel, D. E.; Demeler, B.; Stellacci, F.; Bakr, O. M.; McLean, J. A. $Ag_{44}(SR)_{30}^{4-}$: a silver-thiolate superatom complex. *Nanoscale* **2012**, *4*, 4269.

(8) Jin, R. Quantum sized, thiolate-protected gold nanoclusters. *Nanoscale* **2010**, *2*, 343.

(9) Jin, R.; Zeng, C.; Zhou, M.; Chen, Y. Atomically Precise Colloidal Metal Nanoclusters and Nanoparticles: Fundamentals and Opportunities. *Chem. Rev.* **2016**, *116*, 10346.

(10) Nguyen, T.-A. D.; Jones, Z. R.; Goldsmith, B. R.; Buratto, W. R.; Wu, G.; Scott, S. L.; Hayton, T. W. A Cu_{25} Nanocluster with Partial Cu(0) Character. *J. Am. Chem. Soc.* **2015**, *137*, 13319.

(11) Nguyen, T.-A. D.; Jones, Z. R.; Leto, D. F.; Wu, G.; Scott, S. L.; Hayton, T. W. Ligand-Exchange-Induced Growth of an Atomically Precise Cu_{29} Nanocluster from a Smaller Cluster. *Chem. Mater.* **2016**, *28*, 8385.

(12) Chakrahari, K. K.; Liao, J.-H.; Kahlal, S.; Liu, Y.-C.; Chiang, M.-H.; Saillard, J.-Y.; Liu, C. W. $[Cu_{13}\{S_2CN^nBu_2\}_6(acetylide)_4]^+$: A Two-Electron Superatom. *Angew. Chem. Int. Ed.* **2016**, *55*, 14704.

(13) Wyckoff, R. W. G. *Crystal Structures*; Second ed.; Interscience Publishers: New York, 1963; Vol. 1.

(14) Bennett, E. L.; Murphy, P. J.; Imberti, S.; Parker, S. F. Characterization of the hydrides in Stryker's reagent: $[HCu\{P(C_6H_5)_3\}]_6$. *Inorg. Chem.* **2014**, *53*, 2963.

(15) Mao, Z.; Huang, J.-S.; Che, C.-M.; Zhu, N.; Leung, S. K.-Y.; Zhou, Z.-Y. Unexpected Reactivities of Cu_2(diphosphine)$_2$ Complexes in Alcohol: Isolation, X-ray Crystal Structure, and Photoluminescent Properties of a Remarkably Stable $[Cu_3$(diphosphine)$_3(\mu_3$-H)$]^{2+}$ Hydride Complex. *J. Am. Chem. Soc.* **2005**, *127*, 4562.

(16) Nguyen, T.-A. D.; Goldsmith, B. R.; Zaman, H. T.; Wu, G.; Peters, B.; Hayton, T. W. Synthesis and Characterization of a Cu_{14} Hydride Cluster Supported by Neutral Donor Ligands. *Chem. Eur. J.* **2015**, *21*, 5341.

(17) Goedkoop, J. A.; Andresen, A. F. The crystal structure of copper hydride. *Acta Cryst.* **1955**, *8*, 118.

(18) Walter, M.; Akola, J.; Lopez-Acevedo, O.; Jadzinsky, P. D.; Calero, G.; Ackerson, C. J.; Whetten, R. L.; Grönbeck, H.; Häkkinen, H. A unified view of ligand-protected gold clusters as superatom complexes. *Proc. Natl. Acad. Sci.* **2008**, *105*, 9157.

(19) Cheng, L.; Ren, C.; Zhang, X.; Yang, J. New insight into the electronic shell of $Au_{38}(SR)_{24}$: a superatomic molecule. *Nanoscale* **2013**, *5*, 1475.

(20) Harris, R. K.; Becker, E. D.; Cabral De Menezes, S. M.; Goodfellow, R.; Granger, P. NMR Nomenclature. Nuclear Spin Properties and Conventions for Chemical Shifts. *Pure Appl. Chem.* **2001**, *73*, 1795.

(21) Harris, R. K.; Becker, E. D.; Cabral De Menezes, S. M.; Granger, P.; Hoffman, R. E.; Zilm, K. W. Further Conventions for NMR Shielding and Chemical Shifts. *Pure Appl. Chem.* **2008**, *80*, 59.

(22) *SMART Apex II, Version 2.1*; Bruker AXS Inc.: Madison, WI, 2005.

(23) *SAINT Software User's Guide, Version 7.34a*; Bruker AXS Inc.: Madison, WI, 2005.

(24) Sheldrick, G. M. *SADABS*; University of Göttingen: Göttingen, Germany, 2005.

(25) *SHELXTL PC, Version 6.12*; Bruker AXS Inc.: Madison, WI, 2005.

Chapter 7. **Subnanometer-Sized Copper Clusters: A Critical Reevaluation of the Synthesis and Characterization of $Cu_8(MPP)_4$**

Portions of this work were published in:

Thuy-Ai D. Nguyen; Andrew W. Cook; Guang Wu; Trevor W. Hayton. Subnanometer-Sized Copper Clusters: A Critical Reevaluation of $Cu_8(MPP)_4$ (HMPP = 2-Mercapto-5-*n*-propylpyrimidine). *Inorg. Chem*. **2017**, 56, 8390-8396.

7.1 Introduction

Atomically precise nanoclusters have recently received considerable attention for their unique properties and potential use in a wide variety of applications.[1-5] Due to their mono-dispersity and solubility in a wide range of solvents, complete characterization of these materials is often possible, including analysis by X-ray crystallography.[5] That said, nanoclusters have often proven harder to characterize than typical coordination complexes, on account of their large sizes and low yielding syntheses, which leads to challenges in generating analytically pure material.[5] In this regard, examples abound in the chemical literature of mischaracterized nanoclusters.[5,6] For example, the gold nanocluster, $[Au_{36}(SCH_2CH_2Ph)_{24}]$, was re-formulated to $[Au_{25}(SCH_2CH_2Ph)_{18}]^-$, on the basis of ESI-MS data.[6] Similarly, $[Ag_{28}(SG)_{16}]$ (HSG = glutathione) was re-formulated to $[Au_{25}(SG)_{18}]^-$ after further characterization.[7] In other examples, $Au_{144}(SR)_{59}$ was re-formulated to $Au_{144}(SR)_{60}$,[8] while $Au_{38}(SR)_{22}$ was later re-formulated to $Au_{38}(SR)_{24}$.[9] In each of these examples, mass spectrometry was the critical technique used to establish the correct formula, demonstrating its importance for the characterization of nanoclusters.

In 2011, Chen and co-workers reported the synthesis of "stable Cu_n ($n \leq 8$) nanoclusters by a simple one-pot chemical reduction" in the *Journal of the American Chemical Society*.[10] These clusters were stabilized by ligation to 2-mercapto-5-*n*-propylpyrimidine (HMPP). Within these samples, $Cu_8(MPP)_4$ was claimed to be the "dominant Cu-containing component."[10] This claim was made on the basis of ESI-MS characterization. We found the formulation of this complex to be particularly intriguing. First, it represents an exceptionally rare example of a low-valent (Cu oxidation state < 1) copper coordination complex.[11-14] To our knowledge, there are only a handful of confirmed examples of authentic Cu^0-containing complexes in the literature, including $[(Cp^*AlCu)_6H_4]$, which was reported by Fischer and co-workers in 2014, $[Cu_{25}H_{22}(PPh_3)_{12}]Cl$ and $[Cu_{29}Cl_4H_{22}(Ph_2phen)_{12}]Cl$ (Ph_2phen = 4,7-diphenyl-1,10-phenanthroline), which were both recently reported by our group, and $[Cu_{13}\{S_2CN^nBu_2\}_6(C{\equiv}CC(O)OMe)_4]^+$, which was reported by Liu and co-workers in 2016.[14-18] Second, according to superatom theory,[19] $Cu_8(MPP)_4$ would possess a superatom number of $N^* = 4$. This value is not a magic number, and while complexes with non-magic values of N^* are known for Ag and Au,[20-24] they are nonetheless rare, and more importantly, they are unprecedented for copper.

Given my interest in copper nanoclusters and superatoms, I endeavored to re-synthesize $Cu_8(MPP)_4$, in an effort to further explore the properties of this intriguing material. Herein, I report a critical reinvestigation of the synthesis and characterization of $Cu_8(MPP)_4$. Importantly, I establish that there is limited experimental evidence to support the existence of $Cu_8(MPP)_4$ in the reaction mixture. Instead, I suggest that the material generated in the prior synthesis is a complex mixture containing $[N(C_8H_{17})_4]^+$, Br^-, NO_3^-, 2-mercapto-5-*n*-

propyl-1,6-dihydropyrimidine (H_2MPP*), along with small amounts of the Cu(I) coordination polymer, $[Cu(MPP)]_n$.

7.2 Results and Discussion

7.2.1 Attempt to Repeat the Original Synthesis

In the original report, the synthesis of $Cu_8(MPP)_4$ was achieved via a modified Brust-Schiffrin protocol (Scheme 7.1).[10,25] Specifically, an ethanolic solution of $Cu(NO_3)_2$ and 4 equiv of $[N(C_8H_{17})_4][Br]$ was prepared. In-line with my understanding of the Brust-Schiffrin mechanism, I presume that this step results in formation of $[N(C_8H_{17})_4]_2[Cu(NO_3)_2Br_2]$.[25] This solution was heated to 80 °C for 30 min, and then cooled to 0 °C with an ice bath. 5 equiv of HMPP was then added to this solution, and after vigorous stirring for 6 h, an ethanolic solution of $NaBH_4$ (12 equiv) was added to the reaction mixture. After stirring for a further 7 h, a maize precipitate was reported to form, which was collected by centrifugation. A yield was not reported.

Scheme 7.1. Original synthetic procedure used to prepare $Cu_8(MPP)_4$

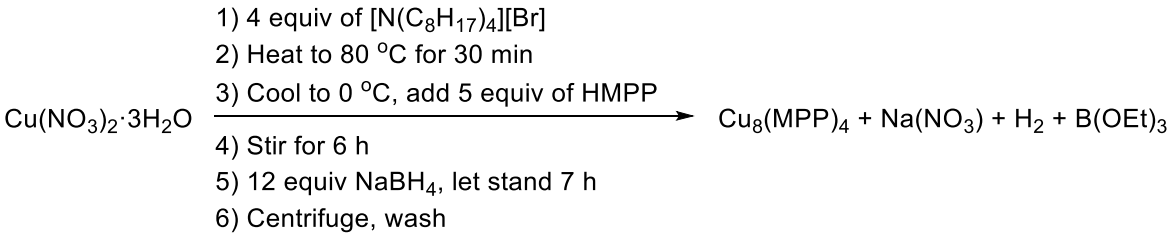

The maize precipitate was characterized by ESI-MS, IR spectroscopy, UV-vis spectroscopy, and XPS. The only experimental support for the $Cu_8(MPP)_4$ formulation comes from the ESI-MS data, in particular, identification of a parent ion peak, $[Cu_8(MPP)_4 + H]^+$, at 1120 *m/z*.[26] The original report also assigns peaks at 1015, 995, 978, and 968 *m/z* to

the fragmentation products $[Cu_8(MPP)_3 + 2Na]^+$, $[Cu_6L_4 + 2H]^+$, $[Cu_5L_4 + 2Na]^+$, and $[Cu_8L_3 + H]^+$, respectively. However, close inspection of the experimental isotope patterns of these peaks does not reveal good matches with simulated patterns (see Figure S2 in ref 10). Also of note is a peak observed at *ca*. 465 *m/z* (Figure S1b in ref 10). This peak, which is the highest intensity peak in the spectrum, is assigned to the $[Cu_5(MPP)]^+$ fragment. As will be discussed in detail in the following paragraphs, I believe these assignments are incorrect.

I attempted to repeat the original procedure as closely as possible, under an atmosphere of nitrogen. In my hands, addition of EtOH to 1 equiv of $Cu(NO_3)_2$ and 4 equiv of $[N(C_8H_{17})_4][Br]$ results in the formation of a homogenous yellow solution. Heating of this solution to 80 °C results in a deepening of the yellow color, but cooling to 0 °C results in reformation of the original color (see Figure A7.1 for photographs). Addition of HMPP to this solution results in formation of an orange suspension; HMPP is only sparingly solution in ethanol. After 15 h of stirring, 12 equiv of $NaBH_4$, dissolved in ethanol, was added to the reaction mixture. This resulted in complete dissolution of the undissolved orange solid, and formation of a homogenous red-orange solution, concomitant with significant H_2 evolution. To our chagrin, however, after stirring for a further 7 h no precipitate was observed to form, even after concentration and cooling of the reaction mixture. Removal of the volatiles *in vacuo* led to formation of an inhomogeneous mixture of orange and white solids.

An ESI-MS (in EtOH) of this mixture, recorded in positive-ion mode, features major peaks at 466.782, 1014.000, and 1086.121 *m/z*, and minor peaks at 968.039 and 995.062 *m/z* (Figure A7.8). These peaks are assignable to $[N(C_8H_{17})_4]^+$, $[2N(C_8H_{17})_4 + Br]^+$, $[2[N(C_8H_{17})_4] + MPP]^+$, $[2[N(C_8H_{17})_4] + Cl]^+$, and $[2[N(C_8H_{17})_4] + NO_3]^+$, respectively.

Importantly, the peaks at 466.528, 1014.000, 968.039, and 995.062 *m/z* were also observed in the original ESI-MS (Figures S1 and S2 in Ref 10), and were originally assigned to $[Cu_5(MPP)]^+$, $[Cu_8(MPP)_3 + 2Na]^+$, $[Cu_8(MPP)_3 + H]^+$, and $[Cu_6(MPP)_4 + 2H]^+$, respectively. Clearly, the original assignments are wrong. To confirm my assignments of the peaks at 466.782 and 1014.000 *m/z*, I recorded an ESI-MS, in positive-ion mode, of commercially purchased $[N(C_8H_{17})_4][Br]$ (Figure A7.16). Both peaks are present in this spectrum, thereby verifying our hypothesis. To confirm the assignment of the peak at 1086.121 *m/z* as $[2[N(C_8H_{17})_4] + MPP]^+$, an ESI-MS of a 1:1 solution of Na(MPP) and $[N(C_8H_{17})_4][Br]$ was recorded (Figure A7.24). This spectrum features a peak at 1086.137 *m/z*, again confirming our assignment. Finally, to confirm our assignment of the peak at 995.062 *m/z*, I independently prepared $[N(C_8H_{17})_4][NO_3]$ by the literature procedure.[27] An ESI-MS, in positive-ion mode, of this material features a peak at 995.070 *m/z* (Figure A7.20), thereby verifying this assignment.

Of note, and in contrast to the original report, I did not observe peaks at 1120 or 978 *m/z* in our ESI mass spectrum, so these peaks remain unassigned. However, note that the calculated isotope pattern for $[2[N(C_8H_{17})_4] + EtO]^+$, which appears at 978 *m/z* (Figure A7.27), is a better match to the experimental isotope pattern than the assignment provided in the original report (e.g., $[Cu_6(MPP)_4 + 2H]^+$). Accordingly, I prefer the new assignment for this peak over that provided in the original manuscript.

To better understand this transformation, I recorded a ^1H NMR spectrum of the inhomogeneous orange and white solid. A ^1H NMR spectrum of this material in CD_3OD revealed the presence of resonances assignable to Na(MPP), $[N(C_8H_{17})_4]^+$, and unreacted $[BH_4]^-$ (Figure A7.2). In addition, this spectrum features resonances at 1.94, 3.84, and 5.78

ppm, which I have assigned to 2-mercapto-5-*n*-propyl-1,6-dihydropyrimidine (H_2MPP*). This product is formed by reduction of the pyrimidine ring in HMPP by $NaBH_4$ (see below). H_2MPP* and Na(MPP) are present in an approximately 2:1 ratio and are the only observed products that are derived from HMPP. In fact, H_2MPP* appears to be the major product of the reaction, according to NMR spectroscopy. No other products, including HMPP, appear to be present in this spectrum. The ^{1}H NMR spectrum of this material recorded in 1,2-dichloroethane-d_4 was essentially identical to that recorded in CD_3OD.

To assist my efforts, Andrew Cook, a graduate student in our lab, also monitored the reaction of $Cu(NO_3)_2{\cdot}3H_2O$ with HMPP and $NaBH_4$, in CD_3OD, by ^{1}H NMR spectroscopy. A ^{1}H NMR spectrum of this mixture after 24 h reveals resonances assignable to H_2MPP* and Na(MPP) (Figure A7.3), consistent with the bulk synthesis. Interestingly, however, he also observed resonances at 8.39 and 8.06 ppm, which we have assigned to the *meta* proton environments of the pyrimidine ring of a new MPP-derived material. He also recorded a ^{1}H NMR spectrum of this sample in 1,2-dichloroethane-d_4 (Figure A7.4). The *meta* proton environments of this new material appear at 8.14 and 7.97 ppm in this solvent.

7.2.2 Rational Synthesis of the HMPP Reduction Product, H_2MPP*

To corroborate my hypothesis that HMPP is reduced under the reaction conditions described in the original report, I monitored the reaction of HMPP with $NaBH_4$ in the absence of both $[N(C_8H_{17})_4][Br]$ and a copper source. Thus, reaction of 1 equiv of HMPP with 2.4 equiv of $NaBH_4$, in EtOH, for 18 h resulted in deposition of a colorless powder. Re-crystallization of this solid from THF resulted in isolation of 2-mercapto-5-*n*-propyl-1,6-dihydropyrimidine (H_2MPP*), as a colorless crystalline solid in 51% yield.

Scheme 7.2. Synthesis of H_2MPP*

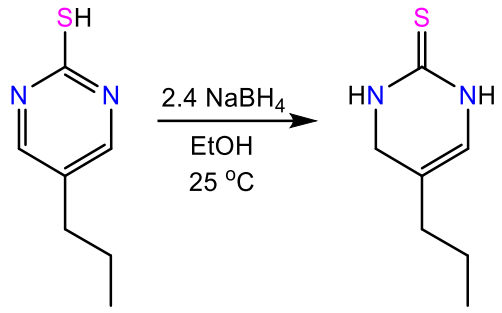

(HMPP) **(H_2MPP*)**

A ^{1}H NMR spectrum of this material in py-d_5, at room temperature, features resonances at 6.07 and 3.95 ppm, in a 1:2 ratio, respectively. These are assignable to the proton environments at the 4- and 6-positions of the pyrimidine ring, respectively, and confirm the 2e$^-$ reduction of the ring system. Importantly, these resonances are nearly identical to those observed in the crude reaction mixture, confirming that H_2MPP* is formed during the reaction of $Cu(NO_3)_2$ and HMPP with $NaBH_4$. Additionally, the IR spectrum of H_2MPP* features a sharp band at 1696 cm^{-1} (Figure A7.50), which we have tentatively assigned to the ν(C=C) mode. Importantly, this mode is not observed in IR spectra of HMPP, Na(MPP), or $[Cu(MPP)]_n$ (see below), but it is observed in the IR spectrum of $[Cu(HMPP*)]_n$ (see below), and it may be present in the IR spectrum provided in the original report for the isolated nanocluster (see Figure S5 in ref 10). Specifically, that spectrum features a sharp absorption in the same spectral region, suggesting that the originally isolated material may have also contained H_2MPP*. Interestingly, H_2MPP* appears to be ESI-MS silent, but it could be characterized by FI-MS. Using this technique I observe a peak at 156.06 *m/z*, which is assignable to the $[H_2MPP*]^{\bullet+}$ ion. I also characterized H_2MPP* by X-ray crystallography.

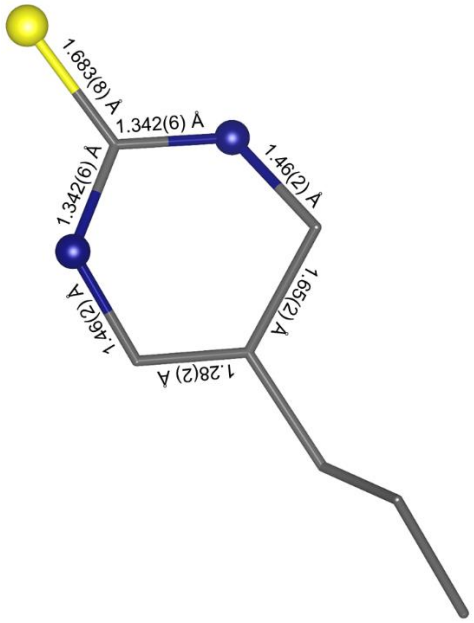

Figure 7.1. Ball and stick diagram of H_2MPP* with the carbon atoms shown in wireframe. S atoms, yellow; N atoms, blue. The hydrogen atoms and a second orientation of the molecule have been omitted for clarity.

7.2.3 Ligation of H_2MPP* to Cu(I)

Given the facile formation of H_2MPP* during the reaction of $Cu(NO_3)_2$ with HMPP and $NaBH_4$, I speculated that the yellow material described in the original report may have been a copper H_2MPP* complex. Accordingly, I endeavored to design a rational synthesis of $[Cu(HMPP^*)]_n$, and ultimately decided on a protonolysis protocol. Thus, reaction of 0.25 equiv of yellow $[Cu(N=C^tBu_2)]_4$[28] with 1 equiv of colorless H_2MPP*, in THF, results in immediate formation of a colorless solution. Work-up of the reaction mixture lead to the isolation of $[Cu(HMPP^*)]_n$ as a colorless crystalline solid in 90% yield (Scheme 7.3).

Scheme 7.3. Syntheses of $[Cu_2(MPP^*)]_n$ and $[Cu(HMPP^*)]_n$

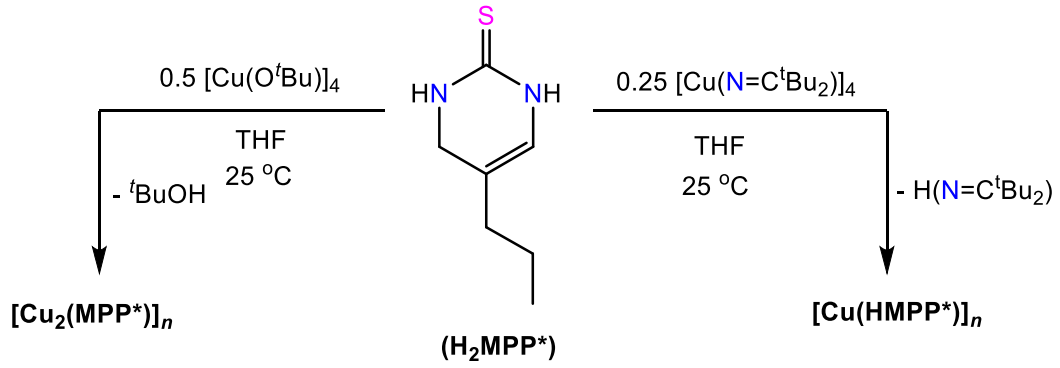

$[Cu(HMPP^*)]_n$ crystallizes in the monoclinic space group C2/c as a tetramer, $[Cu(HMPP^*)]_4 \cdot 2THF$, and its solid state molecular structure is shown in Figure 7.1a. In the solid state, $[Cu(HMPP^*)]_4$ adopts a distorted tetrahedral arrangement of its four Cu atoms. Each Cu atom is coordinated by two S atoms and an N atom, which are provided by the HMPP* ligands. The Cu-Cu distances within the tetrahedral core feature a large range (2.5934(4) – 2.9742(6) Å), but are within the parameters typically observed for Cu(I) cluster complexes.[29-39] The average Cu-N and Cu-S bond lengths (1.99 and 2.27 Å, respectively) are also typical of Cu clusters decorated with anionic *S*,*N* chelates.[29-39] In addition, the N-C and C-C bond lengths within the ring support the presence of the dihydropyrimidine moiety. For example, the C11-C10 (1.354(4) Å) and C9-C10 (1.442(4) Å) bond lengths are consistent with double and single bonds, respectively (Figure 7.1b). Additionally, the oxygen atom of the THF solvate molecule appears to form a hydrogen bond with an amide proton on N4 (O1-N4 = 2.07 Å), which also supports presence of the dihydropyrimidine moiety. Although $[Cu(HMPP^*)]_4$ is colorless and thus is unlikely to be the product described in the original report, it is insoluble in EtOH, which matches the reported solubility for that material. It is also insoluble in nonpolar solvents, CH_2Cl_2, CH_3CN, and 1,2-dichloroethane. It is soluble in THF, but only immediately after its formation. Once

isolated, it is no longer soluble in this solvent, presumably because of oligomerization during the isolation process. However, it is soluble in pyridine, which allowed for its characterization by NMR spectroscopy.

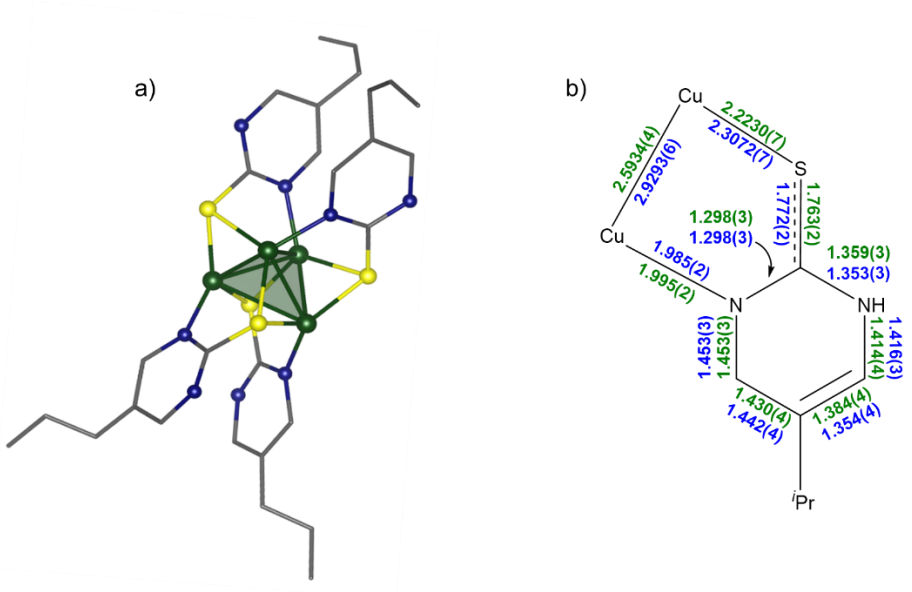

Figure 7.2. Diagrams of $[Cu(HMPP^*)]_4$ a) Ball and stick diagram of $[Cu(HMPP^*)]_4 \cdot 2THF$ with the carbon atoms shown in wireframe. Cu atoms, green; S atoms, yellow; N atoms, blue. All hydrogen atoms and THF solvate molecules are omitted for clarity. Half of the molecule is generated by symmetry. b) Partial structural diagram of $[Cu(HMPP^*)]_4 \cdot 2THF$, showing the bond lengths (Å) of the two crystallographically independent HMPP* ligands in green and blue.

A ^1H NMR spectrum of $[Cu(HMPP^*)]_4$ in pyridine-d_5, at room temperature, features resonances at 6.13 and 6.01 ppm, in an approximately 1:1 ratio (Figure A7.6). These resonances are assignable to the proton at the 4-position of the pyrimidine ring in two different chemical environments, suggesting of the presence of two major HMPP*-containing products. These two HMPP*-containing products are most likely oligomers of

different length, and I suggest that one of these species is $[Cu(HMPP^*)]_4$ on the basis of our X-ray crystallographic analysis. Also of note, there is only one resonance assignable to the NH protons of the pyrimidine ring, despite the presence of two different HMPP*-containing products, which is likely due to fast proton exchange. An IR spectrum of this material features a sharp vibrational mode at 1697 cm^{-1}, which we have assigned to the ν(C=C) mode. A similar mode is observed in the IR spectrum of free H_2MPP^*. The ESI-MS of $[Cu(HMPP^*)]_n$, recorded in THF in positive ion mode, is consistent with its oligomeric structure, revealing peaks assignable to clusters of several different sizes (Figure A7.28). The major peaks are assignable to $[Cu_n(HMPP^*)_n + Cu]^+$ (n = 3, 4, 5, 6, 7) and $[Cu_4(HMPP^*)_4 + H]^+$.

Given the presence of two acidic protons in H_2MPP^*, I rationalized that this ligand could also form a 2:1 complex with the Cu^+ ion, and that this product corresponds to the maize-colored material isolated in the prior synthesis. Thus, reaction of 0.5 equiv of pale yellow $[Cu(O^tBu)]_4$ with 1 equiv of colorless H_2MPP^*, in THF, results in formation of an orange solution. Work-up of the reaction mixture led to the isolation of $[Cu_2(MPP^*)]_n$, as a yellow powder in 77% yield (Scheme 7.3).[40] This complex is insoluble in EtOH, MeOH, CH_2Cl_2, CH_3CN, DMSO, acetone, H_2O and non-polar solvents, consistent with the formation of an oligomeric material.[25] However, it is soluble in THF when prepared *in situ* in that solvent, presumably because it is only partially oligomerized at short reaction times. A ^1H NMR spectrum of freshly prepared $[Cu_2(MPP^*)]_n$ in THF-d_8 reveals broad resonances at 5.74 and 4.10 ppm, in a 1:2 ratio, respectively (Figure A7.7). These resonances are assignable to the proton environments at the 4- and 6-positions of the pyrimidine ring. A resonance assignable to an NH proton was not observed, confirming the double deprotonation of the H_2MPP^*

ligand. The UV-vis spectrum of $[Cu_2(MPP^*)]_n$, also prepared *in situ* in THF, features a broad shoulder at 300 nm (ε = 14400 $L \cdot mol^{-1} \cdot cm^{-1}$).

I was unable to grow X-ray quality crystals of $[Cu_2(MPP^*)]_n$, nor was I able to observe a signal for $[Cu_2(MPP^*)]_n$ in its ESI mass spectrum. Nonetheless, I suggest that $[Cu_2(MPP^*)]_n$ could be a component of the material isolated in 2011. I believe this assertion is reasonable, given that H_2MPP^* is a major product of the reaction, and given that $[Cu_2(MPP^*)]_n$ is a similar color, and has similar solubility properties (i.e., insoluble in EtOH), to those reported for $Cu_8(MPP)_4$. Finally, it is intriguing to note that $Cu_8(MPP^*)_4$ would exhibit a parent ion peak at 1122.65 *m/z* ($[Cu_8(MPP^*)_4 - H]^+$) in its mass spectrum, which is similar to the 1120 *m/z* peak mentioned in the original report, suggesting that this peak could be reassigned to an $[MPP^*]^{2-}$ coordination polymer.

7.2.4 Ligation of HMPP to Cu(I)

Finally, I endeavored to determine if the simple Cu(I) MPP coordination polymer, $[Cu(MPP)]_n$, was also a product in the reaction of $Cu(NO_3)_2$ with HMPP and $NaBH_4$. In this regard, we note that Chen and co-workers recently reported the synthesis of a copper(I) mercaptobenzoxazole cluster, $[Cu(SR)]_6$ (R = NOC_7H_4),[41] via a synthetic procedure similar to that reported for $Cu_8(MPP)_4$. Moreover, several copper mercaptopyrimidine complexes are known, and they often adopt oligomeric or polymeric structures.[42-44] I adopted a similar protonolysis protocol as was employed for $[Cu(HMPP^*)]_4$. Thus, reaction of 0.3 equiv of $[Cu(N{=}C^tBu_2)]_4$ with 1 equiv of HMPP, in THF, resulted in immediate deposition of $[Cu(MPP)]_n$, which can be isolated in 94% yield as a pale yellow powder (Scheme 7.4). This material is insoluble in EtOH, MeOH, THF, CH_2Cl_2, CH_3CN, and non-polar solvents, consistent with the formation of oligomeric Cu(I) thiolate species.[25] Interestingly,

$[Cu(MPP)]_n$ is soluble in hot 1,2-dichloroethane, and, conveniently, it does not immediately precipitate from 1,2-dichloroethane upon cooling back to room temperature, giving me a means to characterize this material in solution. Most likely, the oligomeric structure of $[Cu(MPP)]_n$ is disrupted upon warming in 1,2-dichloroethane, which improves its solubility. A ^{1}H NMR spectrum of this material in 1,2-dichloroethane-d_4, at room temperature, features resonances at 7.94 and 8.16 ppm, in a 1.8:1 ratio, respectively (Figure A7.5). These are assignable to the *meta* proton environments of the pyrimidine ring in two different chemical environments, suggesting the presence of two major MPP-containing products. These two MPP-containing products are most likely oligomers of different length, and I suggest that one of these species is $[Cu(MPP)]_6$ on the basis of our X-ray crystallographic analysis (see below). Importantly, the chemical shifts of these ^{1}H NMR resonances are essentially identical to those observed in the ^{1}H NMR spectrum of the material generated during reaction of $Cu(NO_3)_2$ with HMPP and $NaBH_4$ in CD_3OD (Figures A7.3 and A7.4), demonstrating that $[Cu(MPP)]_n$ was formed during our *in situ* monitoring experiment. An ESI-MS of $[Cu(MPP)]_n$, in positive ion mode, is consistent with its oligomeric structure (Figure A7.35). The major peaks observed in the mass spectrum are assignable to $[Cu_n(MPP)_n + H]^+$ (n = 4, 6) and $[Cu_n(MPP)_{n-1}]^+$ (n = 4, 6, 7, 8, 10, 11, 12, 14). Again, none of these peaks are observed in the originally reported spectra, nor in any of the ESI mass spectra we recorded of the material formed by reaction of $Cu(NO_3)_2$ with HMPP with $NaBH_4$ in ethanol. Nonetheless, given the presence of $[Cu(MPP)]_n$ in our *in situ* synthesis, in combination with its yellow color, I believe that this complex was present in the material isolated by Chen and co-workers.

Scheme 7.4. Synthesis of $[Cu(MPP)]_n$

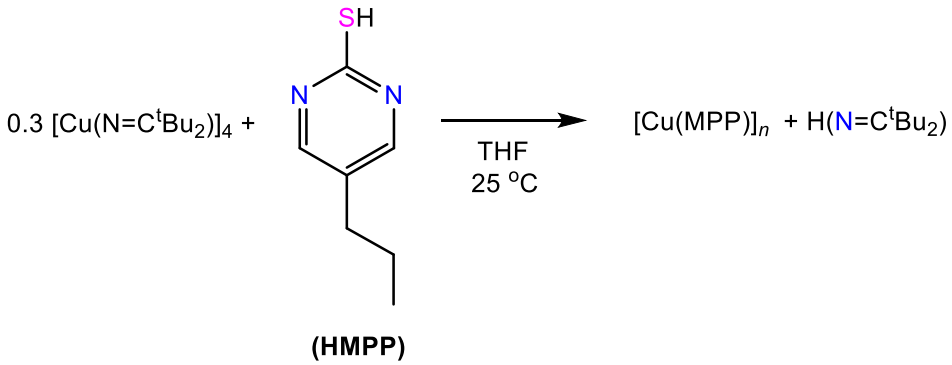

(HMPP)

Cooling of a 1,2-dichloroethane/Et_2O solution of $[Cu(MPP)]_n$ to -25 °C for 24 h resulted in deposition of small yellow crystals. An X-ray crystallographic analysis of this material revealed it to be $[Cu(MPP)]_6$. The solid state molecular structure of $[Cu(MPP)]_6$ is shown in Figure 7.2. In the solid state, it features a central core of six Cu atoms arranged in a distorted octahedron. Each Cu atom is coordinated by two S atoms and an N atom, which are provided by the MPP ligand. Notably, this is the same core structure found in a number of Cu_6 complexes with anionic *S*,*N* chelating ligands,[30-32,34-39] such as $[Cu\{\mu_2\text{-}SC(=NPh)(OC_6H_4\text{-}4\text{-}Me)\}]_6$ and $[Cu(Hmna)]_6$ (H_2mna = 2-mercapto nicotinic acid).[29,33] The range of Cu-Cu distances in $[Cu(MPP)]_6$ (2.6282(2) – 3.072 (2) Å) is comparable to those observed in complexes with the same core structure (2.711 – 3.465 Å).[29-39] In addition, the N-C and C-C bond lengths within the pyrimidine ring are consistent with the presence of an intact aromatic ring (Figure 7.3b), and are notably different from the intra-ring distances observed for $[Cu(HMPP^*)]_4$. The average Cu-N and Cu-S bond lengths (2.04 and 2.25 Å, respectively) are also typical of Cu_6 complexes decorated with anionic *S*,*N* chelates (Cu-N: 1.99-2.04 Å; Cu-S: 2.24-2.25 Å).

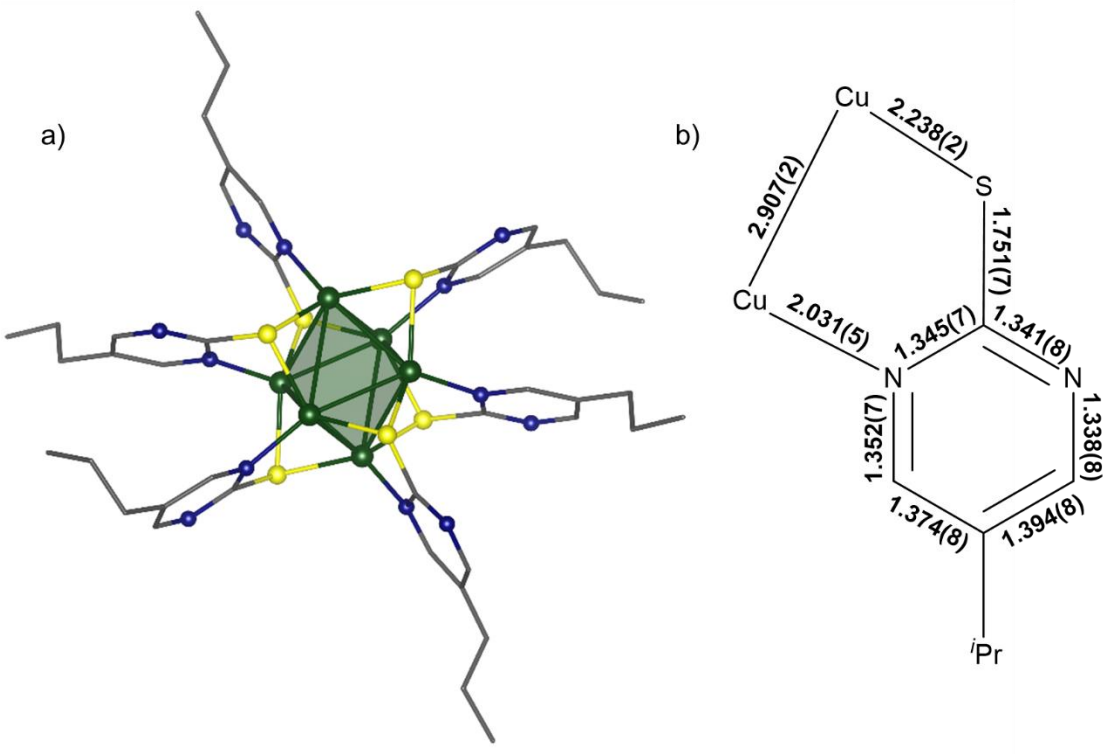

Figure 7.3. Diagrams of[Cu(MPP)]$_6$. a) Ball and stick diagram of [Cu(MPP)]$_6$ with the carbon atoms shown in wireframe. Cu atoms, green; S atoms, yellow; N atoms, blue. All hydrogen atoms are omitted for clarity. Half of the molecule is generated by symmetry. Selected bond lengths (Å): Cu-Cu = 2.682(2)-3.072(2), avg Cu-S = 2.25, avg Cu-N = 2.04, avg S-C = 1.75. b) Partial structural diagram of [Cu(MPP)]$_6$, showing the bond lengths (Å) of one of the three crystallographically independent [MPP]$^-$ ligands.

7.3 Summary

I have re-evaluated the synthesis of the maize-colored copper nanocluster, $Cu_8(MPP)_4$, which was originally generated by reaction of $Cu(NO_3)_2$ with HMPP and $NaBH_4$ in ethanol. Despite repeated efforts, under a variety of conditions, and use of a broad range of analytical techniques, we were unable to confirm the presence of $Cu_8(MPP)_4$ in the reaction mixture. That said, my ESI mass spectrum reproduces several key features found in the originally

reported ESI mass spectrum. However, these features do not support the presence of $Cu_8(MPP)_4$ in the reaction mixture. Instead, these results, in combination with NMR spectroscopic analysis, demonstrate that the material formed in this reaction is a complex mixture containing $[N(C_8H_{17})_4]^+$, Br^-, NO_3^-, Na(MPP), and 2-mercapto-5-*n*-propyl-1,6-dihydropyrimidine (H_2MPP*), and $[Cu(MPP)]_n$. In addition, this mixture may also contain small amounts of $[Cu_2(MPP^*)]_n$, which is yellow in color, and could conceivably be formed under the reaction conditions. Ultimately, my re-assignment of the original ESI-MS data, along with my inability to reproduce the prior results, calls into question the existence of the $Cu_8(MPP)_4$ nanocluster.

Perhaps more importantly, my reinvestigation highlights the importance of using a wide variety of complementary characterization techniques to assay both the purity and formulations of nanoclusters.[45,46] In examples where X-ray quality crystals are not accessible, ESI-mass spectrometry has proven to be an extremely useful characterization technique;[5] however, caution should be employed when using this technique alone, as some compounds are not easily ionizable (e.g., H_2MPP*). Additionally, because gas phase abundance does not necessarily correlate with abundance in a solid state or solution sample, this method cannot assess bulk purity. This work also emphasizes the utility of NMR spectroscopy for the characterization of nanoclusters. This technique, in particular, is well suited for the identification of impurities (e.g., $[N(C_8H_{17})_4]^+$) in the isolated material.

7.4 Experimental

7.4.1 General Procedures

All reactions and subsequent manipulations were performed under anaerobic and anhydrous conditions under an atmosphere of nitrogen. Hexanes, diethyl ether (Et_2O), and

tetrahydrofuran (THF) were dried using a Vacuum Atmospheres DRI-SOLV Solvent Purification system and stored over 3Å sieves for 24 h prior to use. Acetonitrile (CH_3CN) and 1,2-dichloroethane were degassed and dried over 3Å molecular sieves for 72 h prior to use. Rossville Gold Shield 200 proof ethanol from Gold Shield Chemical Co. was used as received. Pyridine-d_5, 1,2-dichloroethane-d_4, and CD_3OD were dried over 3Å molecular sieves for 24 h prior to use. $[Cu(N{=}C^tBu_2)]_4$, $[Cu(O^tBu)]_4$ and $[TOA][NO_3]$ were prepared according to the previously reported procedures.[27,28,47] All other reagents were purchased from commercial suppliers and used as received.

NMR spectra were recorded on an Agilent Technologies 400-MR DD2 400 MHz spectrometer at room temperature. ^1H NMR spectra were referenced to external $SiMe_4$ using the residual protio solvent peaks as internal standards. $^{13}C\{^1H\}$ NMR spectra were referenced indirectly with the ^1H resonance of $SiMe_4$ at 0 ppm, according to IUPAC standard,[48,49] using the residual solvent peaks as internal standards. IR spectra were recorded on a Nicolet 6700 FT-IR spectrometer with a NXR FT Raman Module. UV-Vis experiments were performed on a Shimadzu UV-2401PC spectrophotometer. ESI Mass spectra were collected at the MRL Shared Experimental Facilities at the University of California, Santa Barbara, using an electrospray ion (ESI) source in positive ion mode with a Waters Xevo G2-XS Tof Time-of-Flight mass spectrometer. All other mass spectra were collected by the Mass Spectrometry Facility in the Department of Chemistry and Biochemistry at the University of California, Santa Barbara. Elemental analyses were performed by the Micro-Mass Facility at the University of California, Berkeley.

7.4.2 Replication of the literature procedure of Chen and co-workers[10]

A yellow solution of $Cu(NO_3)_2{\cdot}3(H_2O)$ (25.3 mg, 0.105 mmol), tetra-*n*-octylammonium bromide (135.8 mg, 0.421 mmol), and a magnetic stir bar, in EtOH (25 mL), in a 50 mL round bottom Schlenk flask was heated to 80 °C for 30 min with stirring. The solution became dark yellow upon heating (see Figure A7.1 for photographs). Upon cooling to 0 °C, the reaction mixture returned to the original yellow color. HMPP (78.3 mg, 0.508 mmol) was then added to the reaction mixture to generate an orange suspension. After stirring for 15 h, an EtOH solution (5 mL) of $NaBH_4$ (50.7 mg, 1.34 mmol) was added dropwise to the reaction mixture. The addition of $NaBH_4$ resulted in the dissolution of the orange solid and formation of a red-orange solution, concomitant with vigorous bubbling. The pressure within the reaction flask was kept at 1 atm via an open connection to a dual manifold vacuum line connected to an oil bubbler. After the addition of $NaBH_4$ was completed, the stirring was stopped and the solution was allowed to stand undisturbed for 7 h. While the reaction mixture did continue to bubble, no obvious changes were observed over this time. An aliquot of the reaction mixture was collected for ESI-MS analysis. The solvent was then removed *in vacuo* to provide an inhomogeneous solid that contained a mixture of both orange and white material. A ^{1}H NMR spectrum of this material was recorded in CD_3OD. A small amount of yellow solid remained undissolved in the NMR solution. ^{1}H NMR (400 MHz, 25 °C, CD_3OD): δ Na(MPP): 0.94 (m, 3H, CH_3, overlaps with a large resonance assignable to $[N(C_8H_{17})_4][Br]$), 1.56 (m, 2H, CH_2), 2.41 (t, J = 7.6 Hz, 2H, CH_2), 8.03 (s, 2H, CH); $[N(C_8H_{17})_4][Br]$: 0.91 (m, 12H, CH_3), 1.27-1.43 (m, 40H, CH_2), 1.67 (m, 8H, CH_2), 3.23 (m, 8H, CH_2); $NaBH_4$: -0.14 (m, BH_4); H_2MPP*: 1.43 (2H, CH_2, partially overlaps with a large resonance assignable to $[N(C_8H_{17})_4][Br]$), 1.94 (t, J = 7.4 Hz, 2H,

C*H*$_2$), 3.84 (s, 2H, C*H*$_2$), 5.78 (s, 1H, C*H*). The CH_3 resonance for H_2MPP* was not observed due to overlap with a large resonance assignable to [N(C_8H_{17})$_4$][Br]. ESI-MS (in EtOH): *m/z* 354.413 [N(C_8H_{17})$_3$ + H]$^+$ (Calcd *m/z* 354.410), 466.528 [N(C_8H_{17})$_4$]$^+$ (Calcd *m/z* 466.535), 968.047 [2N(C_8H_{17})$_4$ + Cl]$^+$ (Calcd *m/z* 968.039), 995.062 [2N(C_8H_{17})$_4$ + (NO_3)]$^+$ (Calcd *m/z* 995.058), 1014.000 [2N(C_8H_{17})$_4$ + Br]$^+$ (Calcd *m/z* 1013.989), 1086.121 [2N(C_8H_{17})$_4$+MPP]$^+$ (Calcd *m/z* 1086.119). IR (KBr pellet, cm^{-1}): 418 (w), 446 (w), 513 (w), 639 (w), 661 (w), 691 (w), 723 (w), 753 (w), 807 (w), 836 (w), 866 (w), 924 (w), 999 (s), 1077 (s), 1115 (s), 1151 (m), 1214 (w), 1238 (w), 1386 (s), 1467 (m), 1513 (w), 1588 (w), 1655 (w), 1696 (w, ν(C=C), H_2MPP*), 2226 (w), 2293 (w), 2320 (w), 2724 (w), 2862 (m), 2924 (s), 2961 (s), 3235 (w), 3439 (w).

7.4.3 Synthesis of H_2MPP*

To a Schlenk flask containing HMPP (446.4 mg, 2.894 mmol) and $NaBH_4$ (261.4 mg, 6.910 mmol) was added EtOH (10 mL). After addition of EtOH, the resulting bright yellow suspension bubbled vigorously. The mixture was stirred for 18 h at room temperature, which resulted in consumption of the yellow solid and the deposition of a colorless precipitate. The pressure within the reaction flask was kept at 1 atm via an open connection to a dual manifold vacuum line connected to an oil bubbler. The solid was allowed to settle and the colorless solution was removed via cannula filtration. The white solid was then dried *in vacuo* and brought into the glovebox. The solid was dissolved in THF (5 mL) and the resulting solution was filtered through a Celite column (0.5 cm × 2 cm) supported on glass wool. The colorless filtrate was concentrated *in vacuo* to *ca*. 4 mL and layered with hexanes (16 mL). Storage of this solution at -25 °C for 24 h resulted in the deposition of a white solid. The solid was isolated by decanting off the supernatant, and was then washed with

hexanes (4 × 1 mL) and dried *in vacuo* (192.5 mg, 51% yield). Anal. Calcd for $C_7H_{12}N_2S$: C, 53.81; H, 7.74; N, 17.93. Found: C, 53.59; H, 7.93; N, 17.67. ^{1}H NMR (400 MHz, 25 °C, pyridine-d_5): δ 0.79 (t, J = 7.3 Hz, 3H, CH_3), 1.26 (m, 2H, CH_2), 1.79 (t, J = 7.4 Hz, 2H, CH_2), 3.95 (s, 2H, CH_2), 6.07 (s, 1H, CH), 10.14 (s, 2H, NH). ^{13}C{^{1}H} NMR (101 MHz, 25 °C, pyridine-d_5): δ 14.07 (s, CH$_3$), 20.48 (s, CH$_2$), 34.06 (s, CH$_2$), 44.86 (s, CH$_2$), 111.75 (s, C=C), 119.94 (s, C=C), 177.03 (s, C=S). FI-MS: *m/z* 156.06 $[H_2MPP^*]^{\bullet+}$ (Calcd *m/z* 156.07). IR (KBr pellet, cm^{-1}): 443 (w), 494 (w), 578 (w), 638 (m), 688 (m), 726 (m), 795 (w), 838 (w), 875 (w), 900 (w), 1003 (w), 1082 (w), 1112 (m), 1202 (s), 1271 (m), 1294 (m), 1367 (w), 1426 (w), 1464 (m), 1512 (s), 1570 (s), 1696 (m, ν(C=C)), 2837 (m), 2866 (m), 2927 (m), 2954 (m), 3230 (s, br).

7.4.4 Synthesis of [Cu(HMPP*)]$_n$

To a yellow THF solution (1 mL) of $[Cu(N{=}C^tBu_2)]_4$ (31.2 mg, 0.0383 mmol) was added a colorless THF solution (2 mL) of H_2MPP* (24.3 mg, 0.156 mmol). The yellow solution lightened slightly upon addition. After stirring for 20 min, the slightly cloudy, pale yellow solution was filtered through a Celite column (0.5 cm × 2 cm) supported on glass wool. The filtrate was then layered with hexanes (9 mL). Storage of this solution at -25 °C for 24 h resulted in the deposition of a nearly colorless microcrystalline solid. The solid was isolated by decanting off the supernatant, and was then washed with hexanes (3 × 1 mL) and dried *in vacuo* (32.6 mg, 90% yield). Anal. Calcd for $C_7H_{11}CuN_2S{\cdot}0.5C_4H_8O$: C, 42.42; H, 5.93; N, 10.99. Found: C, 43.09; H, 6.03; N, 10.62. ^{1}H NMR (400 MHz, 25 °C, pyridine-d_5): δ 0.71-0.77 (m, 3H, CH_3), 1.07-1.21 (m, 2H, CH_2), 1.56-1.68 (m, 2H, CH_2), 3.96 (s, 2H, CH_2, isomer A), 4.25 (s, 2H, CH_2, isomer B), 6.01 (s, 1H, CH, isomer B), 6.13 (s, 1H, CH, isomer A), 9.89 (s, 1H, NH). ESI-MS (THF): *m/z* 718.9066 $[Cu_3(HMPP^*)_3 + Cu]^+$ (Calcd

m/z 718.9113), 874.9782 $[Cu_4(HMPP^*)_4 + H]^+$ (Calcd *m/z* 874.9834), 938.8978 $[Cu_4(HMPP^*)_4 + Cu]^+$ (Calcd *m/z* 938.9052), 1156.8914 $[Cu_5(HMPP^*)_5 + Cu]^+$ (Calcd *m/z* 1156.8990), 1374.8868 $[Cu_6(HMPP^*)_6 + Cu]^+$ (Calcd *m/z* 13.74.8929), 1594.8907 $[Cu_7(HMPP^*)_7 + Cu]^+$ (Calcd *m/z* 1594.8790). IR (KBr pellet, cm^{-1}): 446 (w), 636 (w), 678 (w), 835 (w), 896 (w), 1045 (w), 1111 (w), 1203 (s), 1257 (m), 1290 (m), 1333 (w), 1377 (w), 1464 (s), 1492 (s), 1530 (m), 1582 (w), 1656 (w), 1697 (m, ν(C=C)), 2826 (m), 2869 (m), 2927 (m), 2956 (s), 3314 (s).

7.4.5 Synthesis of $[Cu_2(MPP^*)]_n$

To a yellow suspension of $[Cu(O^tBu)]_4$ (159.8 mg, 0.292 mmol) in THF (2 mL) was added a colorless THF solution (2 mL) of H_2MPP^* (82.6 mg, 0.529 mmol). This resulted in the immediate dissolution of the solid, concomitant with a color change to orange. After stirring for 2 h, the orange solution was filtered through a Celite column (1 cm × 2 cm) supported on glass wool and the filtrate was concentrated *in vacuo* to *ca.* 3 mL. Et_2O (3 mL) and then pentane (10 mL) were added to the orange filtrate, which resulted in the deposition of a yellow powder. The solid was collected on a glass frit, washed with pentane (2 × 3 mL) and Et_2O (2 × 3 mL), and then dried *in vacuo* to give an orange powder (114.8 mg, 77% yield). Anal. Calcd for $[C_7H_{10}Cu_2N_2S]_n$: C, 29.89; H, 3.58; N, 9.96. Found: C, 29.08; H, 3.85; N, 8.12. IR (KBr pellet, cm^{-1}): 457 (w), 659 (w), 851 (w), 899 (w), 994 (w), 1046 (m), 1076 (m), 1114 (m), 1200 (m), 1271 (s), 1305 (s), 1391 (s), 1456 (m), 1514 (s), 1584 (w), 1662 (m, ν(C=C)), 2824 (m), 2868 (s), 2925 (s), 2955 (s), 3435 (w). No signal was observed in the ESI mass spectrum of this material (in either THF, THF/MeCN, THF/1,2-dichoroethane, or THF/EtOH).

7.4.6 In Situ Characterization of $[Cu_2(MPP^*)]_n$ by NMR and UV-vis Spectroscopies

THF-d_8 (1.0 mL) was added to a mixture of $[Cu(O^tBu)]_4$ (20.1 mg, 0.037 mmol) and H_2MPP^* (11.2 mg, 0.0717 mmol) in a 20 mL glass scintillation vial. The resulting orange solution was transferred to a J-Young NMR tube and a ^1H NMR spectrum was recorded. The sample was returned to the glovebox and transferred to a 20 mL glass scintillation vial, whereupon the solution was diluted to 0.05 mM by addition of 2 μL of the solution to THF (3 mL). A UV-vis spectrum of this solution was then recorded. ^1H NMR (400 MHz, 25 °C, THF-d_8): δ 0.89 (br s, 3H, CH_3), 1.14 (s, 9H, CH_3, ^{t}BuOH), 1.30 (s, CH_3, $[Cu(O^tBu)]_4$), 1.39 (br s, 2H, CH_2), 1.73 (br s, 2H, CH_2, overlapping with THF), 3.22 (s, 1H, OH, ^{t}BuOH), 4.10 (br s, 2H, CH_2), 5.74 (br s, 1H, CH). UV-Vis (THF, 0.05 mM assuming n = 1, 25 °C, $L \cdot mol^{-1} \cdot cm^{-1}$): 300 (sh, ε = 12600).

7.4.7 Synthesis of $[Cu(MPP)]_n$

To a bright yellow slurry of HMPP (139.3 mg, 0.903 mmol) in THF (3 mL) was added dropwise a yellow THF solution (6 mL) of $[Cu(N{=}C^tBu_2)]_4$ (223.4 mg, 0.274 mmol). This resulted in the rapid deposition of a fine pale yellow powder. The mixture was stirred for 2 h at room temperature, which resulted in deposition of more yellow solid and the complete consumption of the HMPP. Hexanes (8 mL) was then added to the yellow reaction mixture, which resulted in further deposition of yellow solid. The solid was collected on a glass frit, washed with hexanes (5 mL), and dried *in vacuo* (184.3 mg, 94% yield). Single crystals of $[Cu(MPP)]_6$ suitable for X-ray diffraction were grown from a 1,2-dichloroethane solution (5 mL) layered with Et_2O (10 mL) and stored at -25 °C for 5 d. Anal. Calcd for $[C_7H_9CuN_2S]_n$: C, 38.79; H, 4.19; N, 12.92. Found: C, 38.76; H, 4.11; N, 12.83. ^1H NMR (400 MHz, 25 °C,

1,2-dichloroethane-d_4): δ 0.74 (t, J = 7.3 Hz, 3H, CH_3, isomer A), 0.83 (t, J = 7.3 Hz, 3H, CH_3, isomer B), 1.33 (m, 2H, CH_2, isomer A), 1.47 (m, 2H, CH_2, isomer B), 2.19 (t, J = 7.6 Hz, 2H, CH_2, isomer A), 2.35 (m, 2H, CH_2, isomer B), 7.94 (s, 2H, CH, isomer A), 8.16 (s, 2H, CH, isomer B). ESI-MS (1,2-dichloroethane): *m/z* 712.894 $[Cu_4(MPP)_3]^+$ (Calcd *m/z* 712.864), 866.957 $[Cu_4(MPP)_4 + H]^+$ (Calcd *m/z* 866.921), 1146.877 $[Cu_6(MPP)_5]^+$ (Calcd *m/z* 1146.821), 1300.931 $[Cu_6(MPP)_6 + H]^+$ (Calcd *m/z* 1300.877), 1363.863 $[Cu_7(MPP)_6]^+$ and $[Cu_{14}(MPP)_{12}]^{2+}$ (Calcd *m/z* 1363.807 and 1363.798), 1580.853 $[Cu_8(MPP)_7]^+$ and $[Cu_{16}(MPP)_{14}]^{2+}$ (Calcd *m/z* 1580.770 and 1580.777), 2012.818 $[Cu_{10}(MPP)_9]^+$ (Calcd *m/z* 2012.726), 2230.805 $[Cu_{11}(MPP)_{10}]^+$ and $[Cu_{22}(MPP)_{20}]^{2+}$ (Calcd *m/z* 2230.704 and 2230.704), 2446.801 $[Cu_{12}(MPP)_{11}]^+$ (Calcd *m/z* 2446.682), 2880.764 $[Cu_{14}(MPP)_{13}]^+$ (Calcd *m/z* 2880.638). IR (KBr pellet, cm^{-1}): 409 (w), 464 (w), 526 (w), 642 (w), 667 (w), 684 (w), 740 (w), 769 (w), 832 (w), 896 (w), 937 (w), 1053 (w), 1094 (w), 1153 (s), 1244 (s), 1341 (m), 1391 (s), 1456 (m), 1536 (s), 1586 (s), 2867 (m), 2928 (m), 2956 (s), 3031 (m), 3452 (w). UV-Vis (1,2-dichloroethane, 0.05 mM assuming n = 1, 25 °C, $L \cdot mol^{-1} \cdot cm^{-1}$): 300 (ε = 14800).

7.4.8 Synthesis of NaMPP

A mixture of HMPP (257.8 mg, 1.671 mmol) and $NaN(SiMe_3)_2$ (312.6 mg, 1.705 mmol) was suspended in CH_3CN (3 mL). The mixture was stirred for 15 h at room temperature, which resulted in consumption of the yellow solid and the deposition of a colorless precipitate. The volatiles were then removed *in vacuo* and the resulting solid was dissolved in THF (3 mL). The very pale yellow solution was filtered through a Celite column (0.5 cm × 1 cm) supported on glass wool. The pale yellow filtrate was then layered with Et_2O (4 mL), and storage of this solution at room temperature for 24 h resulted in the deposition of

an off white solid. The solid was isolated by decanting off the supernatant, and was then washed with hexanes (3 × 1 mL) and dried *in vacuo* (278 mg, 94% yield). Anal. Calcd for $C_7H_9N_2NaS$: C, 47.71; H, 5.15; N, 15.90. Found: C, 47.42; H, 5.06; N, 15.90. ^{1}H NMR (400 MHz, 25 °C, CD_3OD): δ 0.89 (t, *J* = 7.3 Hz, 3H, C*H*$_3$), 1.53 (m, 2H, C*H*$_2$), 2.36 (t, *J* = 7.5 Hz, 2H, C*H*$_2$), 7.98 (s, 2H, C*H*). ESI-MS (EtOH): *m/z* 727.149 $[Na_5(MPP)_4]^+$ (Calcd *m/z* 727.143). IR (KBr pellet, cm^{-1}): 662 (w), 776 (w), 1172 (s), 1235 (m), 1387 (s), 1463 (w), 1525 (s), 1592 (s), 2870 (w), 2928 (m), 2957 (m), 3421 (w).

7.4.9 X-ray Crystallography

Data for $[Cu(MPP)]_6$, H_2MPP^*, and $[Cu(HMPP^*)]_4\cdot 2THF$ were collected on a Bruker KAPPA APEX II diffractometer equipped with an APEX II CCD detector using a TRIUMPH monochromater with a MoKα X-ray source (α = 0.71073 Å). Crystals were mounted on a cryoloop under Paratone-N oil, and all data were collected at 100(2) K using an Oxford nitrogen gas cryostream system. X-ray data for $[Cu(MPP)]_6$, H_2MPP^*, and $[Cu(HMPP^*)]_4\cdot 2THF$ were collected utilizing frame exposures of 15 s, except for the low angle data for $[Cu(HMPP^*)]_4\cdot 2THF$, which were collected utilizing frame exposures of 10 s. Data collection and cell parameter determination were conducted using the SMART program.[50] Integration of the data frames and final cell parameter refinement were performed using SAINT software.[51] Absorption correction of the data was carried out using the multi-scan method SADABS.[52] Subsequent calculations were carried out using SHELXTL.[53] Structure determination was done using direct methods and difference Fourier techniques. Structure solution, refinement, graphics, and creation of publication materials were performed using SHELXTL.[53]

H_2MPP* crystallizes in two superimposed orientations, which are related by a C_2 rotation about the C-S vector. This disorder was addressed by modelling the molecule over two positions in a 50:50 ratio. The final refinements included anisotropic temperature factors on all non-H atoms, except for C2, C2B and C3. Additionally, hydrogen atoms on C2 and C2B were not located due to the positional disorder.

Table 7.1. X-ray Crystallographic Data for $[Cu(MPP)]_6$, H_2MPP*, and $[Cu(HMPP^*)]_4 \cdot 2THF$

	$[Cu(MPP)]_6$	H_2MPP*	$[Cu(HMPP^*)]_4 \cdot 2THF$
empirical formula	$C_{42}H_{54}Cu_6N_{12}S_6$	$C_7H_{12}N_2S$	$C_{36}H_{60}Cu_4N_8O_2S_4$
crystal habit, color	plate, orange	block, colorless	block, colorless
crystal size (mm)	0.15 × 0.1 × 0.05	0.1 × 0.1 × 0.05	0.1 × 0.1 × 0.08
crystal system	monoclinic	orthorhombic	monoclinic
space group	$P2_1/n$	$Fddd$	$C2/c$
volume ($Å^3$)	2488(2)	3304.0(5)	4211.2(5)
a (Å)	11.821(6)	8.6311(7)	13.740(1)
b (Å)	13.032(6)	15.172(1)	15.376(1)
c (Å)	16.384(8)	25.230(2)	20.500(1)
α (deg)	90	90	90
β (deg)	99.725(15)	90	103.500(6)
γ (deg)	90	90	90
Z	4	16	4
formula weight (g/mol)	1300.56	156.25	1019.32
density (calculated) (Mg/m^3)	1.736	1.256	1.608
absorption coefficient (mm^{-1})	2.816	0.319	2.234
F_{000}	1320	1344	2112
total no. reflections	20602	6639	34821
unique reflections	5129	926	10072
final R indices [I >2σ(I)]	R_1 = 0.0546 wR_2 = 0.0781	R_1 = 0.1149 wR_2 = 0.2625	R_1 = 0.0475 wR_2 = 0.1263
largest diff. peak and hole ($e^- A^{-3}$)	0.858 and -0.661	0.925 and -0.738	1.429 and -1.416
GOF	0.929	1.254	0.885

7.5 Appendix

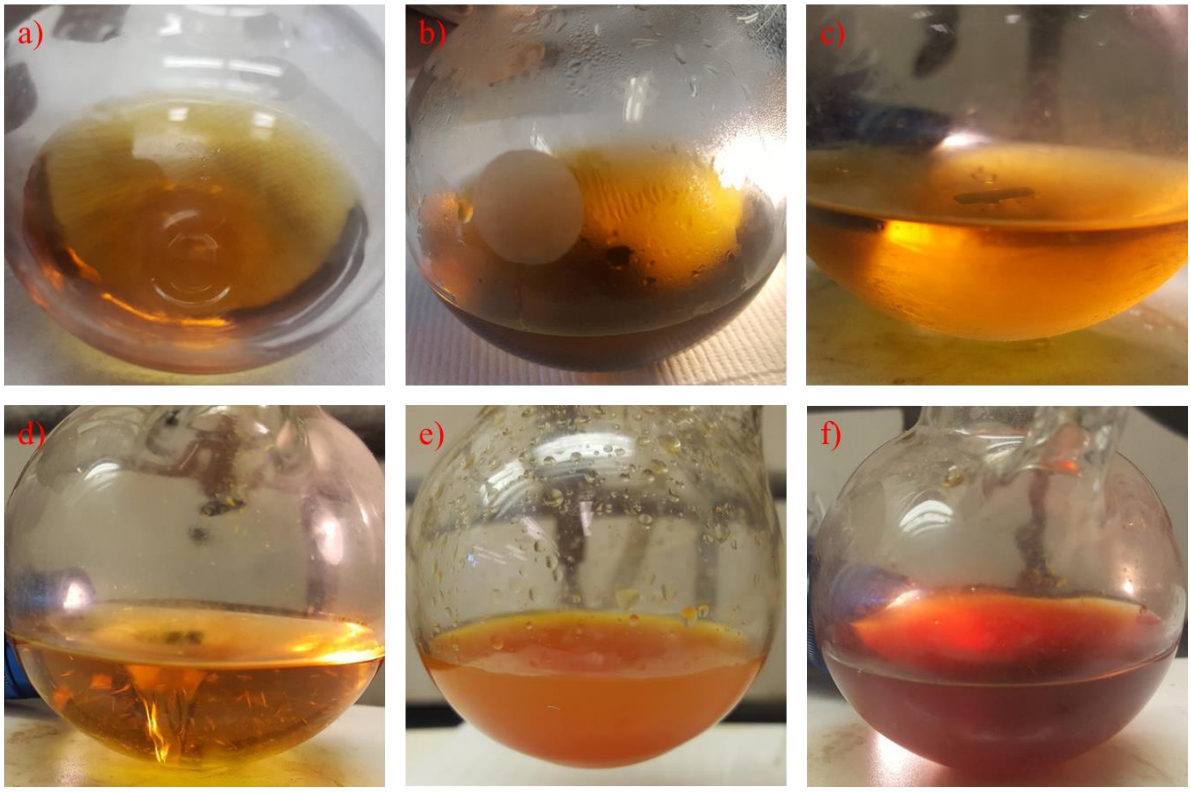

Figure A7.1. Photographs at various stages of the reaction of $Cu(NO_3)_2$ with HMPP and $NaBH_4$ in the presence of $[N(C_8H_{17})_4][Br]$, in EtOH, following the literature procedure described by Chen and co-workers.[10] a) Yellow solution of $Cu(NO_3)_2 \cdot 3(H_2O)$ and $[N(C_8H_{17})_4][Br]$. b) Darker yellow solution after 30 min at 80 °C. c) Yellow solution after cooling to 0 °C. d) Yellow slurry immediately after addition of yellow HMPP crystals. e) Orange suspension, 30 min after addition of HMPP. f) Red-orange solution immediately after addition of a $NaBH_4$ solution to the orange suspension.

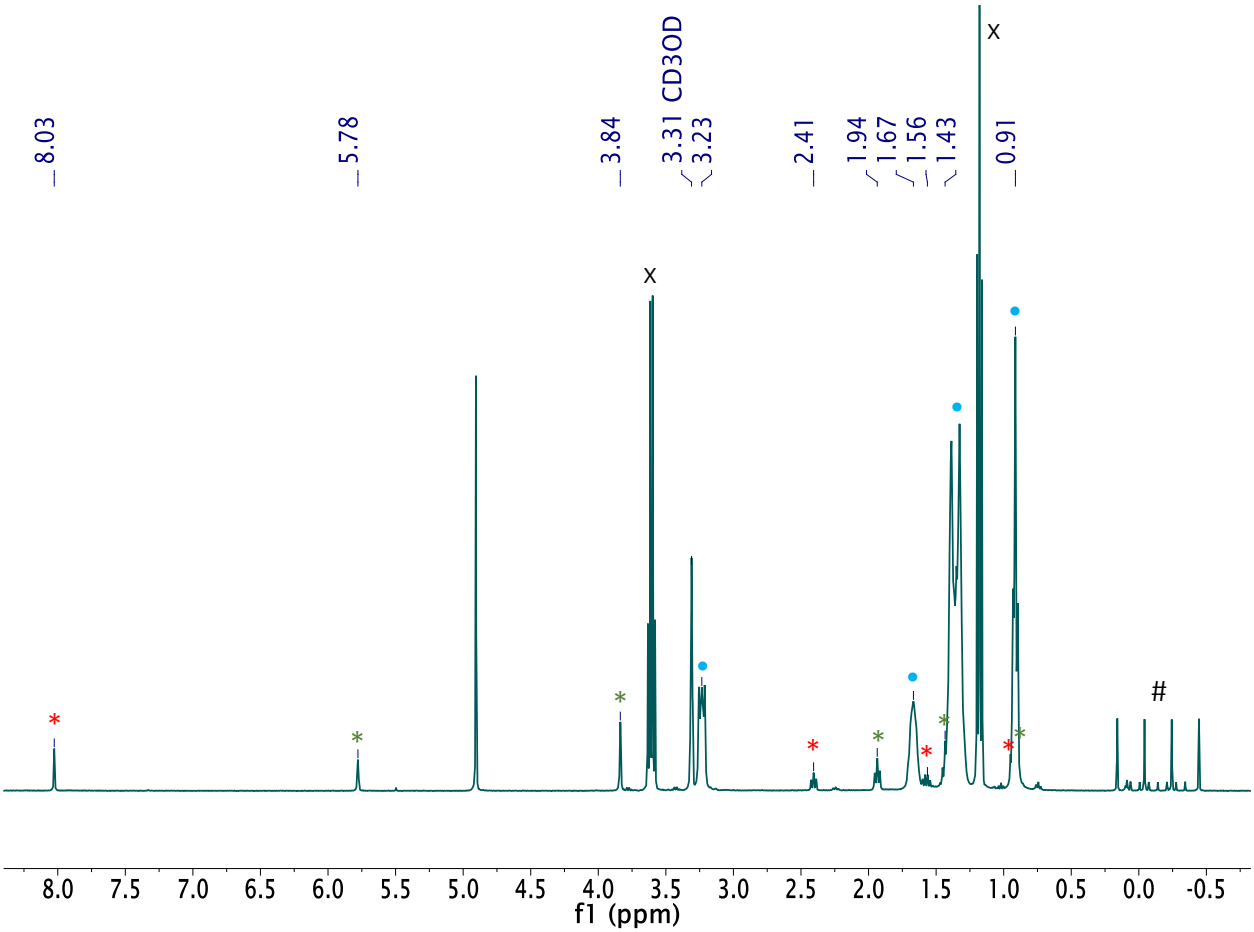

Figure A7.2. ^{1}H NMR spectrum in CD_3OD of the inhomogeneous mixture of orange and white material generated by following the literature procedure of Chen and co-workers.[10] Note: a small amount of yellow solid remained undissolved in this sample. The red (*) indicate resonances assignable to Na(MPP), the green (*) indicate resonances assignable to H_2MPP*, the blue (•) indicate resonances assignable to $[N(C_8H_{17})_4][Br]$, the black (#) indicates the resonance assignable to $NaBH_4$, the black (x) indicates the resonances assignable to EtOH.

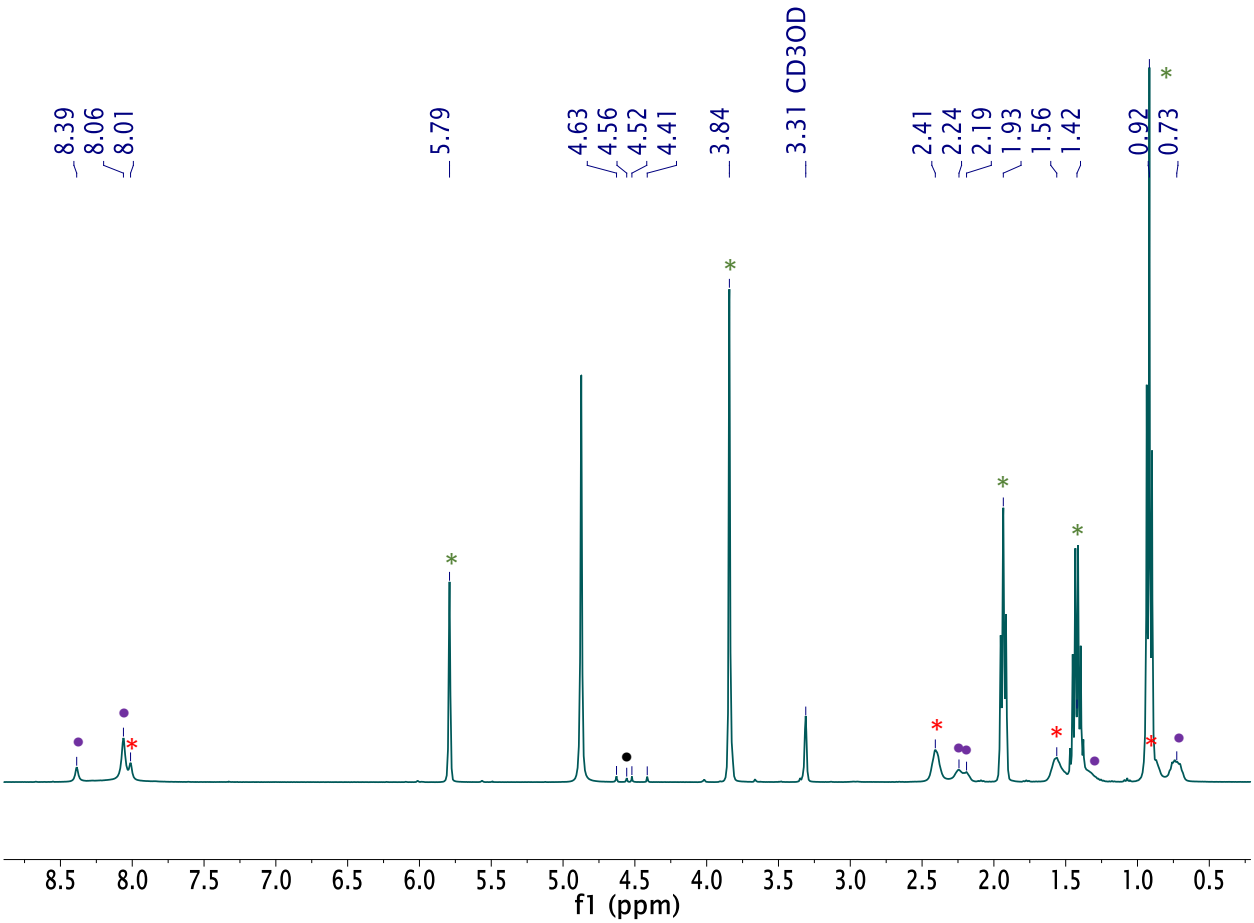

Figure A7.3. ^{1}H NMR spectrum in CD_3OD of the *in situ* reaction of $Cu(NO_3)_2 \cdot 3H_2O$ with HMPP and $NaBH_4$ after 24 h at room temperature. **Experimental Details**: A J. Young NMR tube equipped with a Teflon rotoflow valve was charged with $Cu(NO_3)_2 \cdot 3H_2O$ (5 mg, 0.02 mmol), HMPP (26 mg, 0.17 mmol), and CD_3OD (1 mL). This resulted in formation of a dark orange solution, with some undissolved HMPP, as well as considerable amounts of a fine pale yellow powder. A ^{1}H NMR spectrum was taken of this mixture. The sample was brought back into the glovebox, whereupon $NaBH_4$ (10 mg, 0.26 mmol) was added as a solid, and the tube was promptly sealed. The addition of $NaBH_4$ resulted in the dissolution of the undissolved HMPP and formation of a yellow-orange solution, concomitant with vigorous bubbling. The sample was brought out of the glovebox, connected to a dual-

manifold vacuum line, and the headspace gases were removed *in vacuo*. The reaction was monitored intermittently by ^{1}H NMR spectroscopy over the course of 24 h. A small amount of off-white solid remained undissolved in the NMR solution, even after 24 h of reaction time. The red (*) indicate resonances assignable to Na(MPP), the green (*) indicate resonances assignable to H_2MPP*, the purple (•) indicate resonances assignable to $[Cu(MPP)]_n$, while the black (•) indicates the resonances assignable to H_2 and HD.

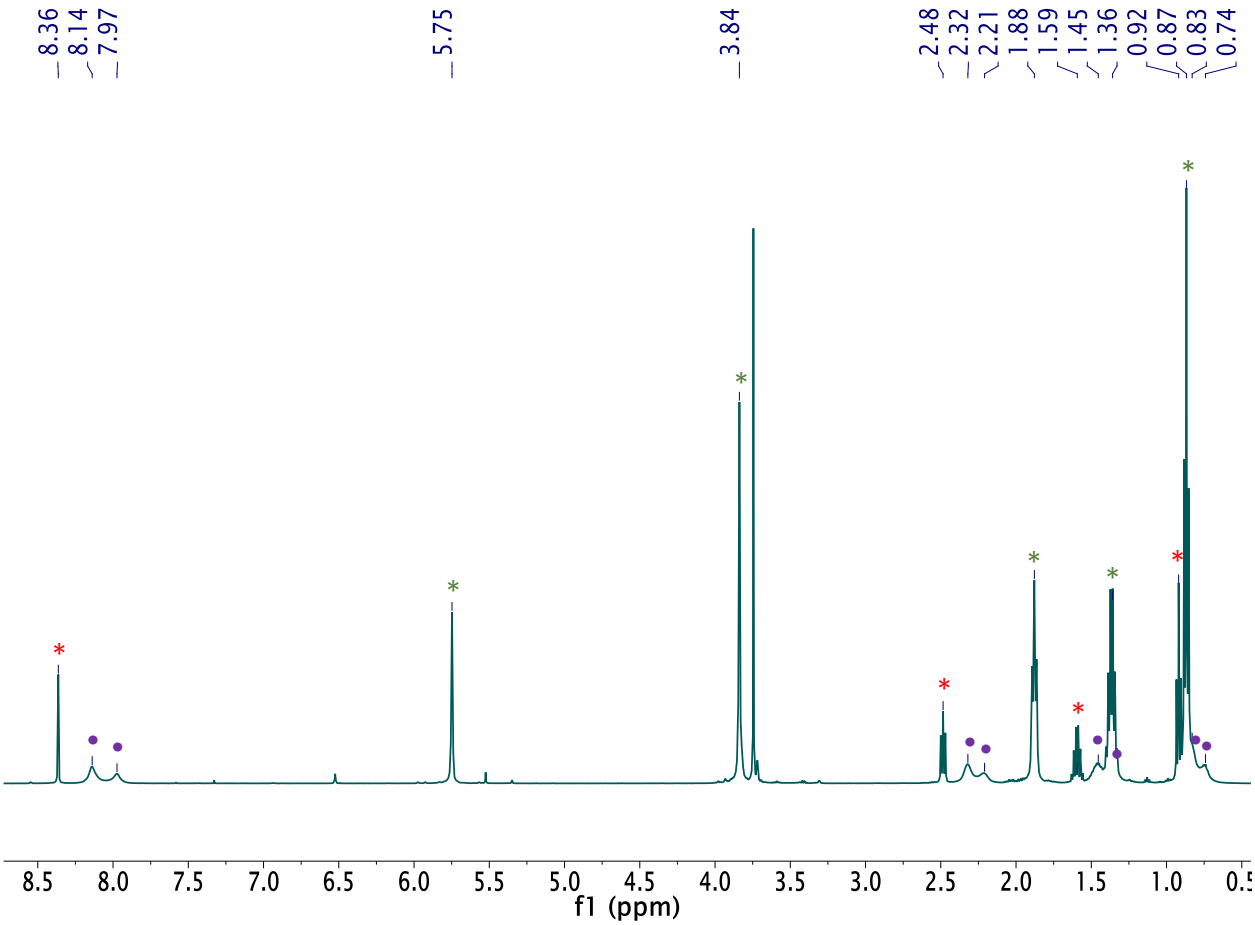

Figure A7.4. ^{1}H NMR spectrum in 1,2-dichlorethane-d_4 of the *in situ* reaction of $Cu(NO_3)_2 \cdot 3H_2O$ with HMPP and $NaBH_4$. **Experimental Details:** After completion of the *in situ* monitoring experiment (see Figure A7.3 for details), the volatiles were removed from the J. Young NMR tube *in vacuo*. The resulting solid was suspended in 1,2-dichlorethane-d_4

(0.75 mL) and the tube was gently warmed in a hot water bath (75 °C) for 15 min. This resulted in dissolution of the solid and formation of an orange solution. A ^{1}H NMR spectrum was then recorded. Note that a small amount of off-white solid remained undissolved in the NMR solution, even after heating. The red (*) indicate resonances assignable to Na(MPP), the green (*) indicate resonances assignable to H_2MPP*, the purple (•) indicate resonances assignable to [Cu(MPP)]$_n$.

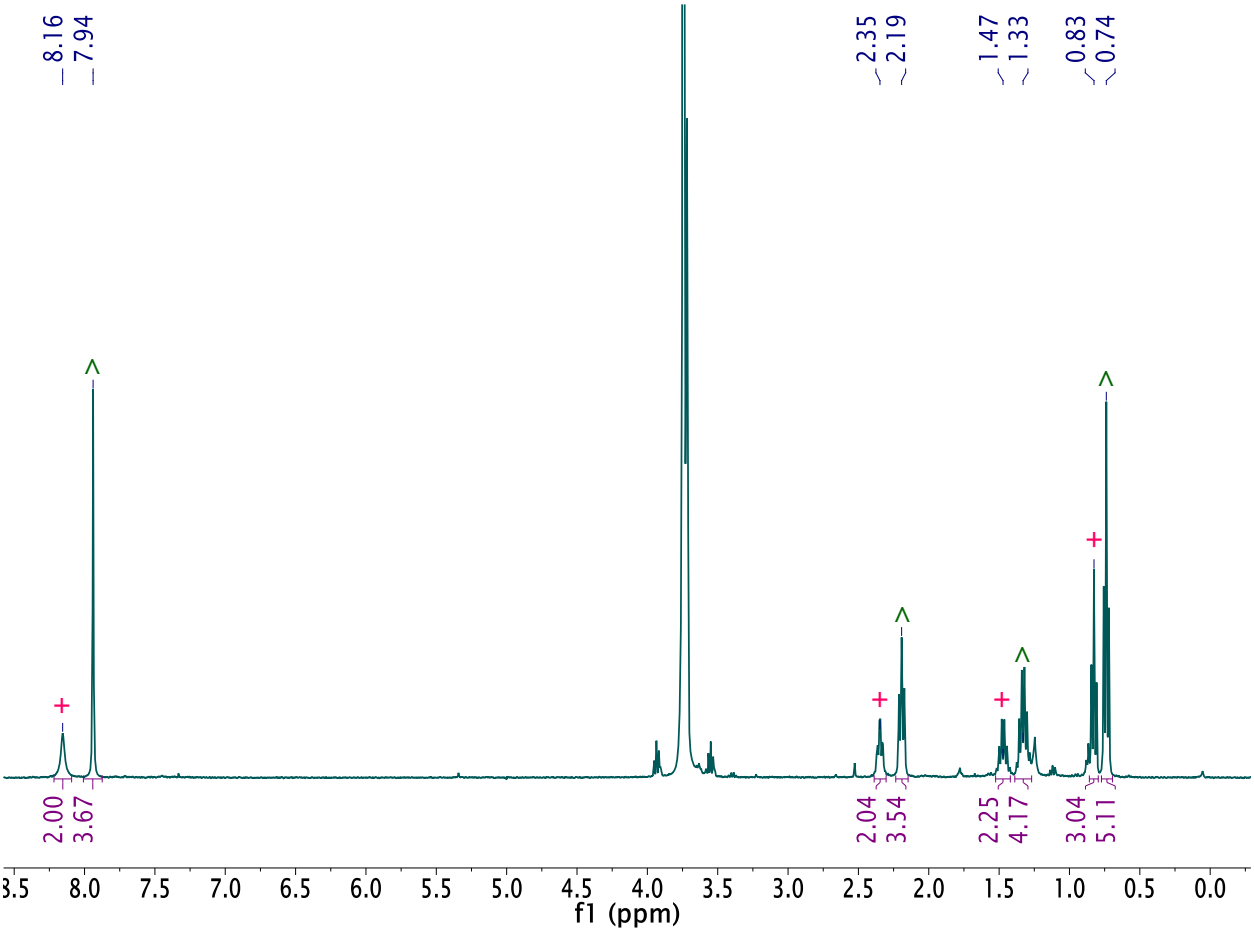

Figure A7.5. ^{1}H NMR spectrum of [Cu(MPP)]$_n$ in 1,2-dichloroethane-d_4. The pink (+) are assignable to one [MPP]$^-$ environment, while the green (^) are assignable to a second [MPP]$^-$ environment.

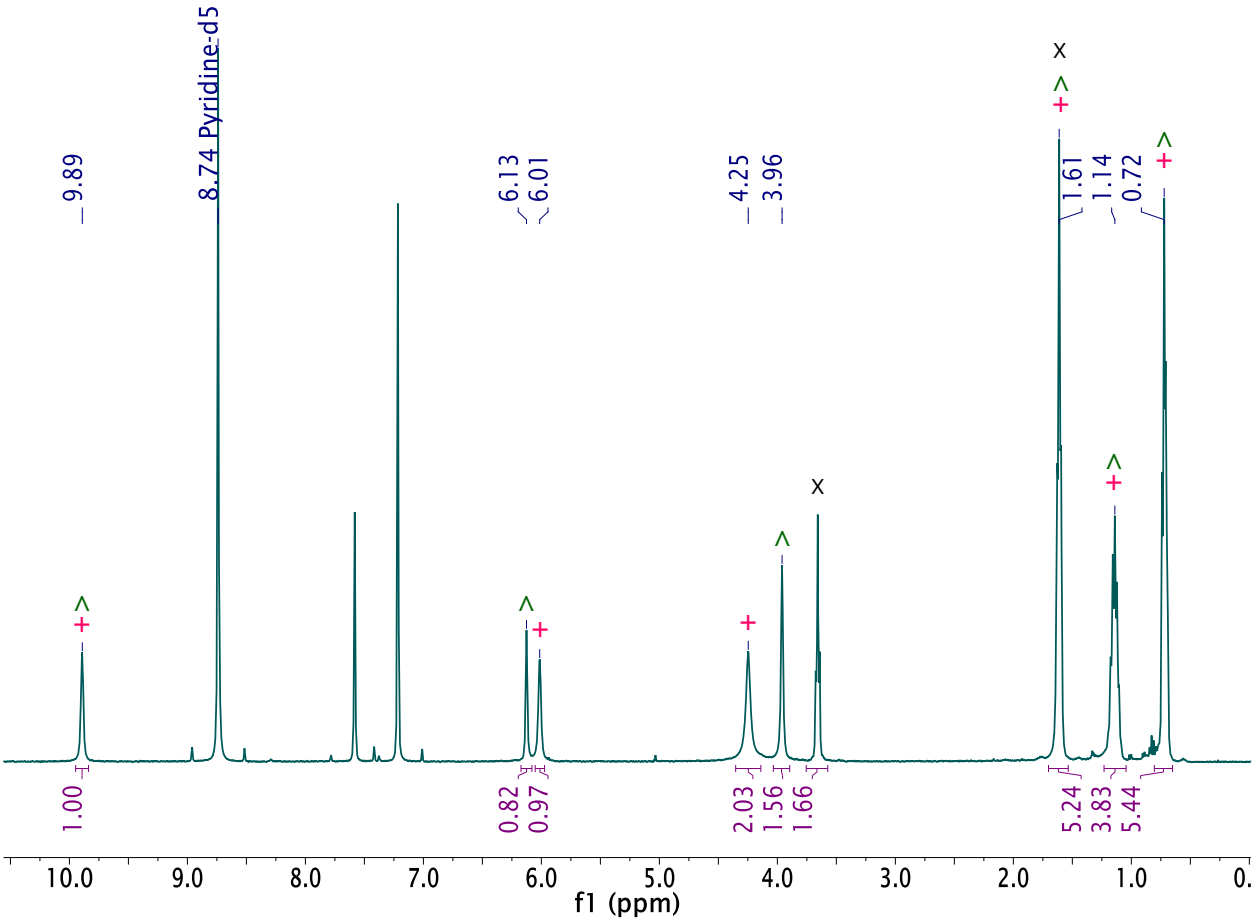

Figure A7.6. ^{1}H NMR spectrum of $[Cu(HMPP^*)]_n$ in pyridine-d_5. The pink (+) are assignable to one $[HMPP^*]^-$ environment, while the green (^) are assignable to a second $[HMPP^*]^-$ environment. Note that the NH and propyl resonances of these two environments overlap. The black (x) are assignable to THF solvent. The signal at 1.61 ppm overlaps with the THF solvent.

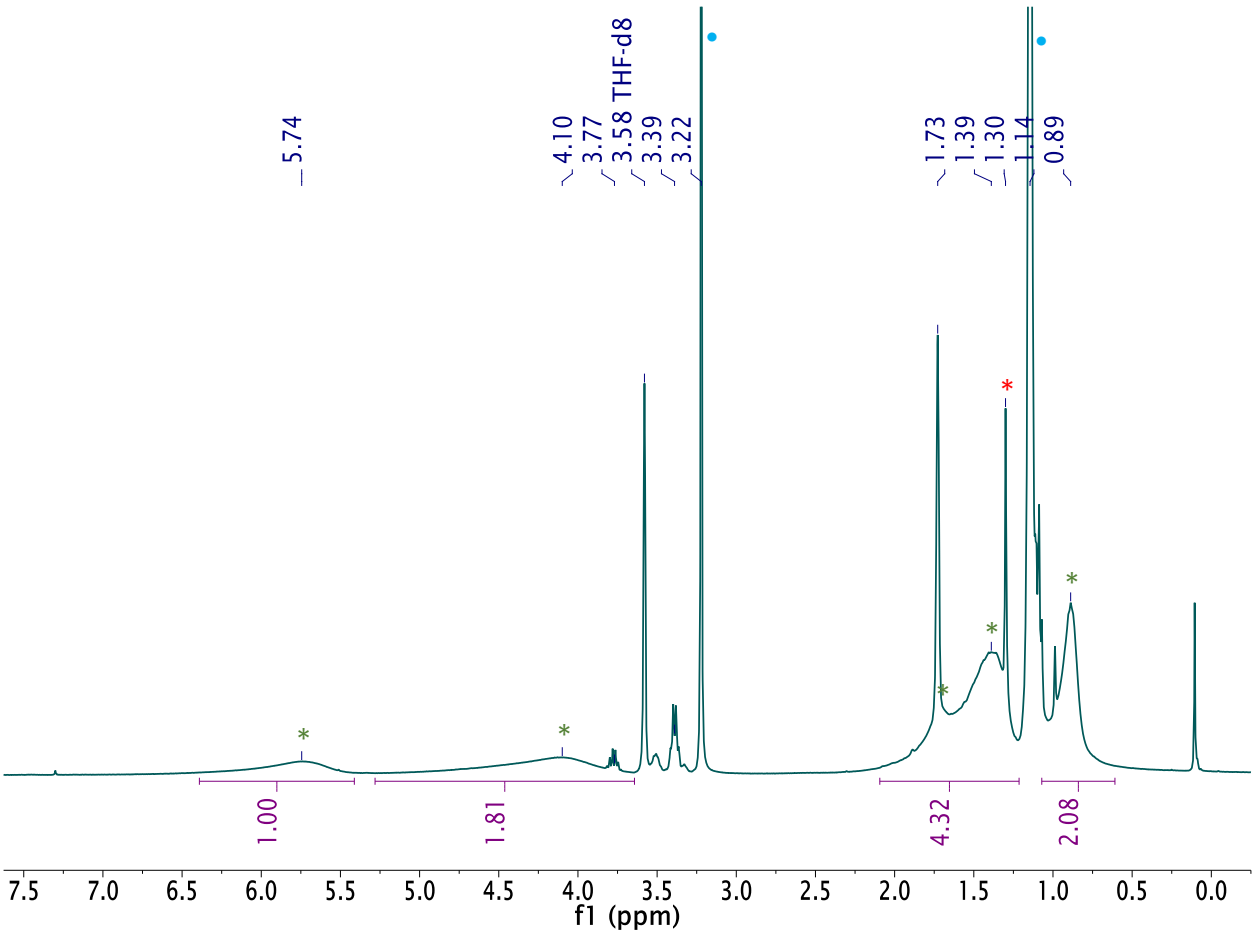

Figure A7.7. *In situ* ^{1}H NMR spectrum in THF-d_8 of the reaction of 0.5 equiv of $[Cu(O^tBu)]_4$ with 1 equiv of H_2MPP^* to generate $[Cu_2(MPP^*)]_n$ and ^{t}BuOH. The green (*) indicate resonances assignable to $[Cu_2(MPP^*)]_n$, the blue (•) indicate resonances assignable to ^{t}BuOH, and the red (*) indicates the resonance assignable to $[Cu(O^tBu)]_4$ starting material.

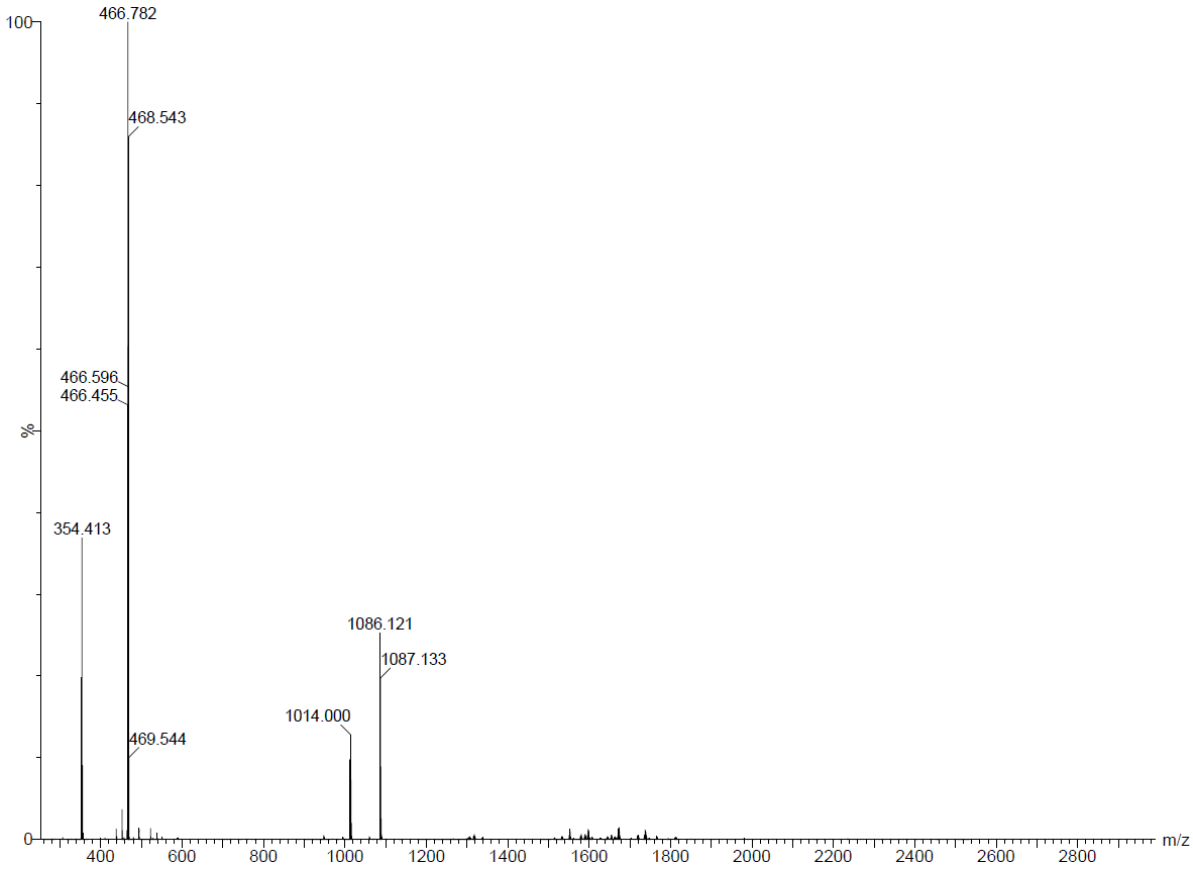

Figure A7.8. ESI-MS of an aliquot, in EtOH, of the reaction mixture generated by following the literature procedure of Chen and co-workers.[10]

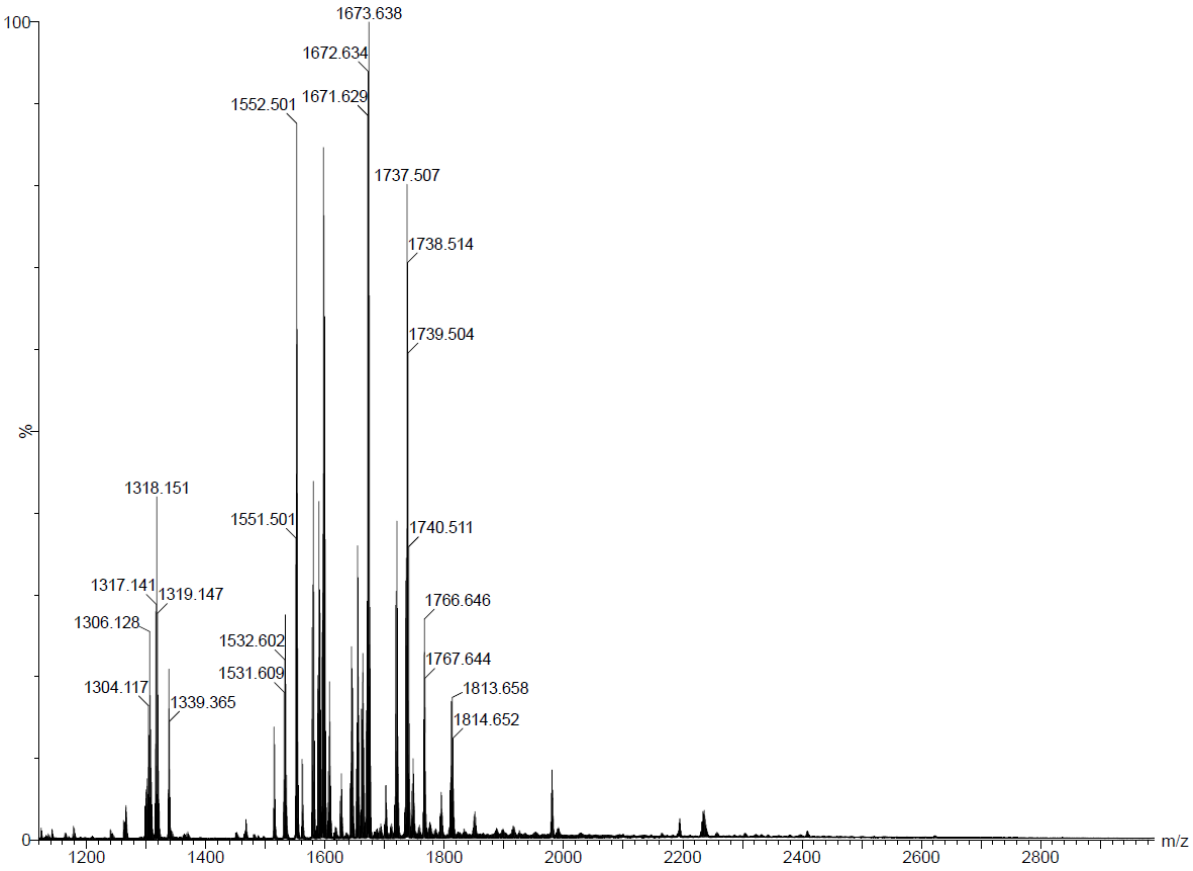

Figure A7.9. Partial ESI-MS of an aliquot, in EtOH, of the reaction mixture generated by following the literature procedure of Chen and co-workers.[10]

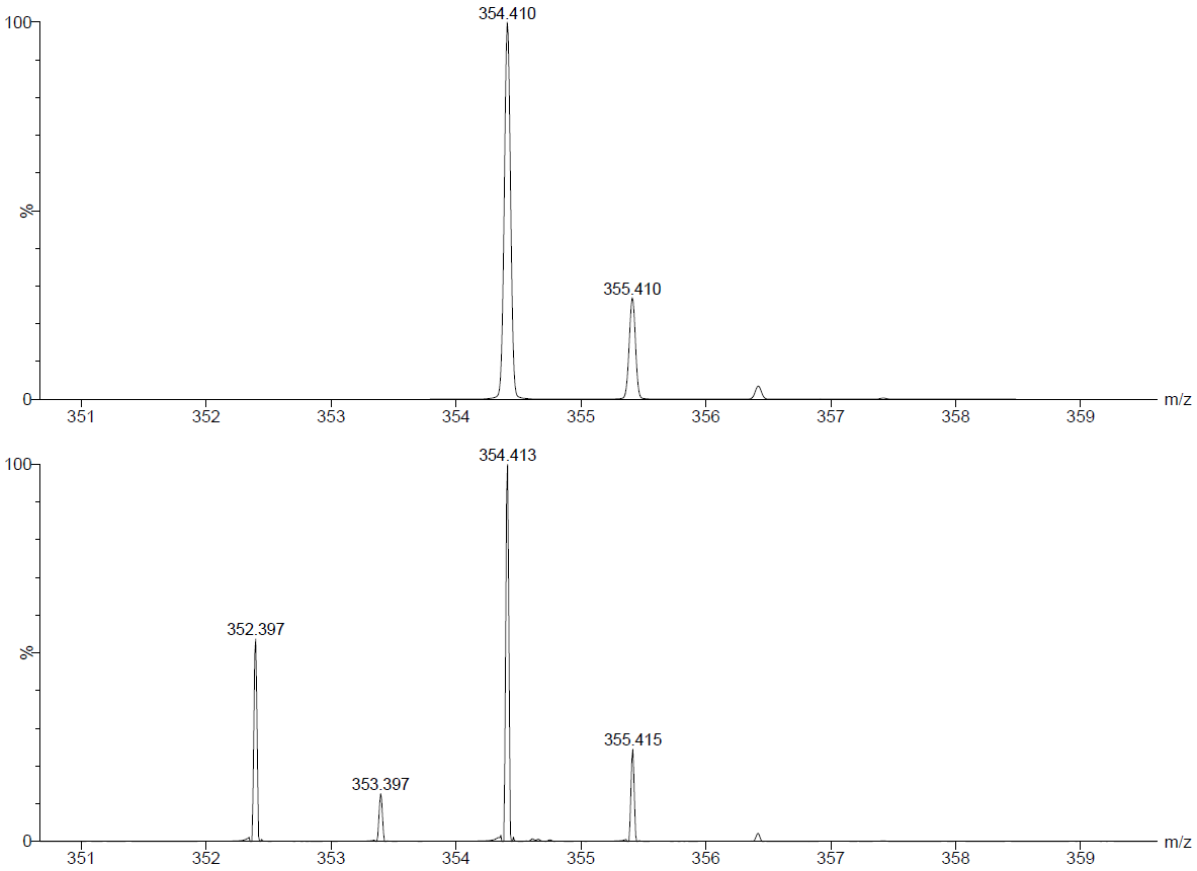

Figure A7.10. Partial ESI-MS of an aliquot, in EtOH, of the reaction mixture generated by following the literature procedure of Chen and co-workers.[10] The experimental (bottom) and calculated (top) peaks are assignable to the $[N(C_8H_{17})_3 + H]^+$ ion. The extra peaks in the

experimental spectrum are assignable to $[N(C_8H_{17})_3 - H]^+$.

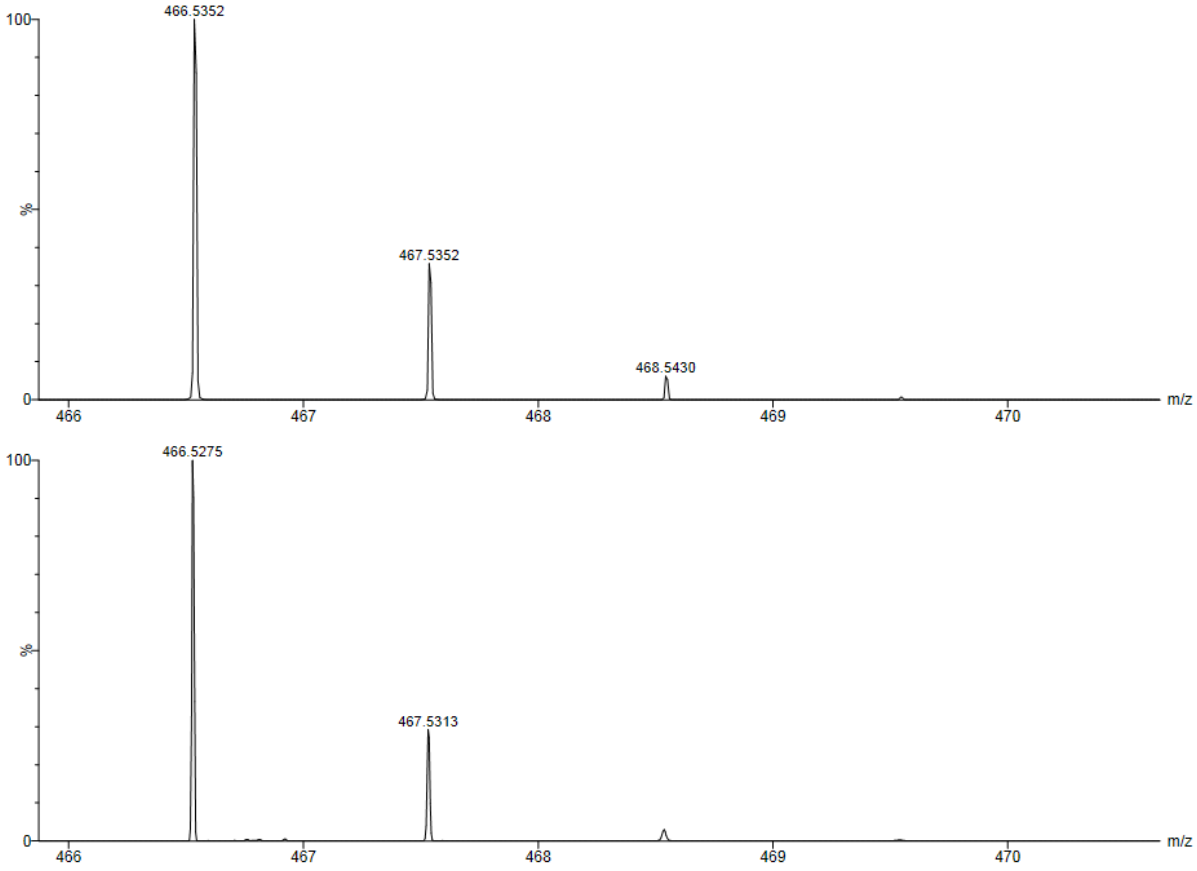

Figure A7.11. Partial ESI-MS of an aliquot, in EtOH, of the reaction mixture generated by following the literature procedure of Chen and co-workers.[10] The experimental (bottom)

and calculated (top) peaks are assignable to the $[N(C_8H_{17})_4]^+$ ion.

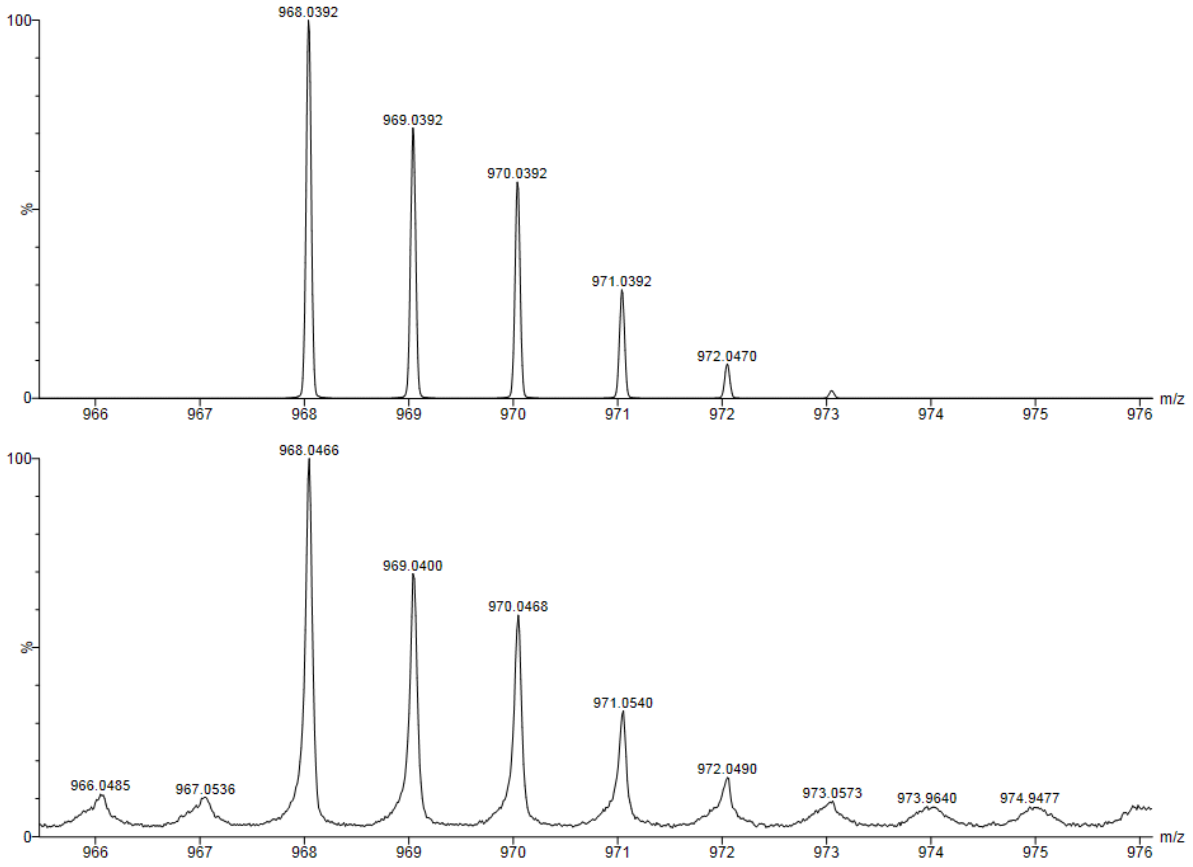

Figure A7.12. Partial ESI-MS of an aliquot, in EtOH, of the reaction mixture generated by following the literature procedure of Chen and co-workers.[10] The experimental (bottom)

and calculated (top) peaks are assignable to the $[2[N(C_8H_{17})_4] + Cl]^+$ ion.

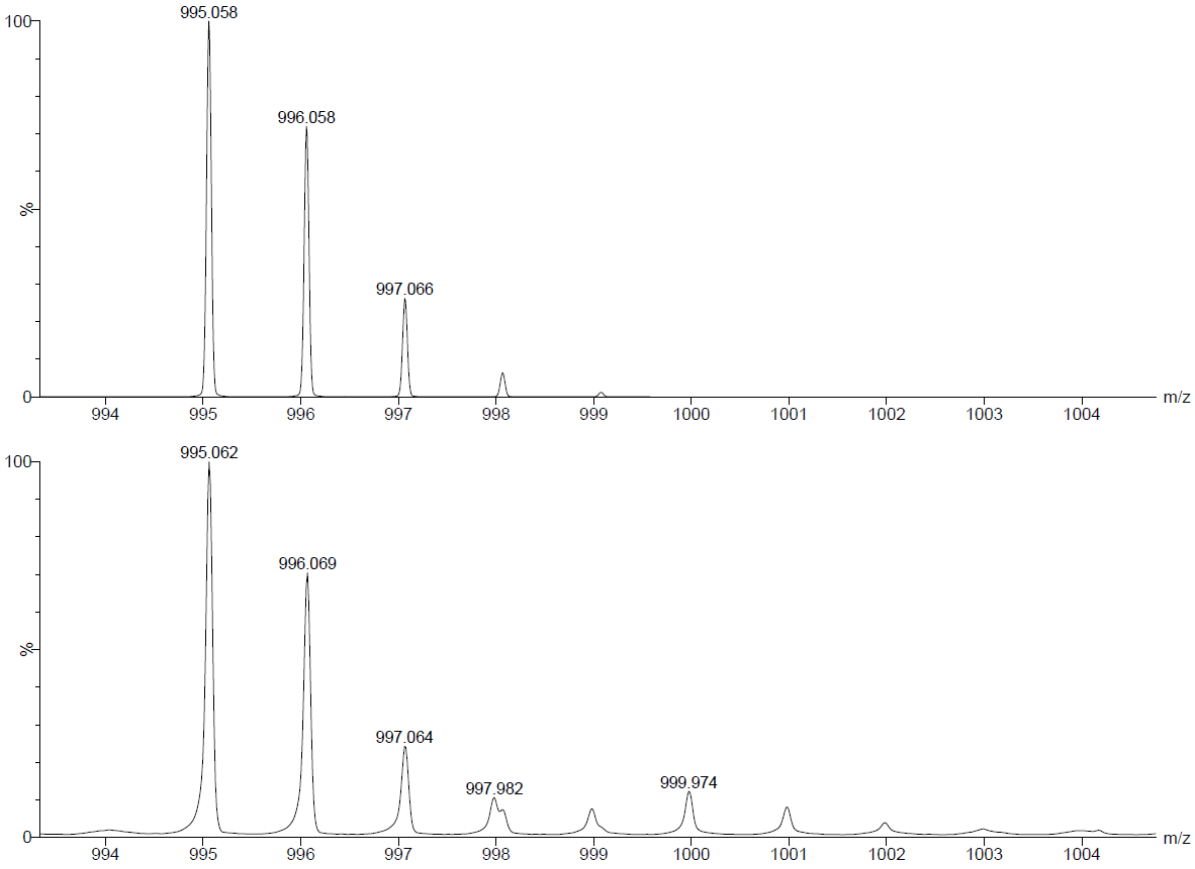

Figure A7.13. Partial ESI-MS of an aliquot, in EtOH, of the reaction mixture generated by following the literature procedure of Chen and co-workers.[10] The experimental (bottom)

and calculated (top) peaks are assignable to the $[2[N(C_8H_{17})_4] + (NO_3)]^+$ ion.

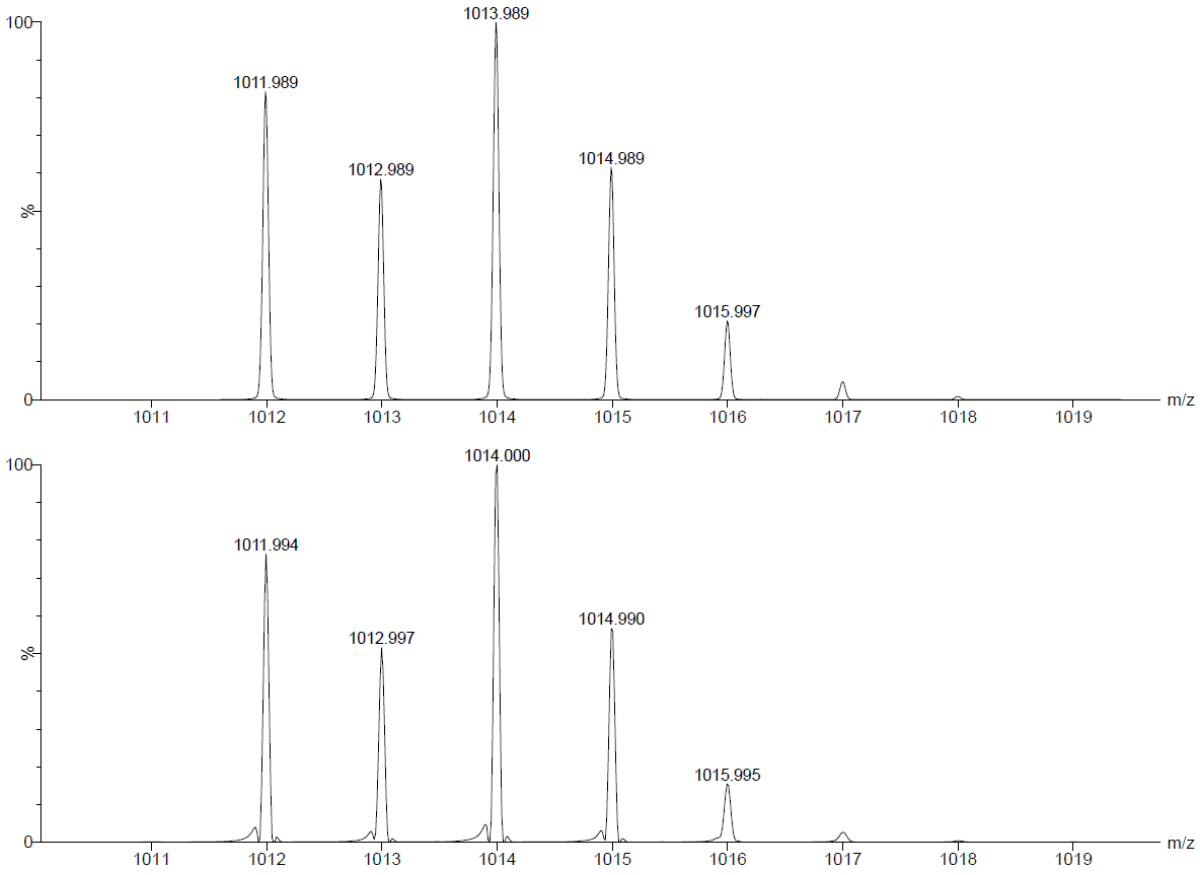

Figure A7.14. Partial ESI-MS of an aliquot, in EtOH, of the reaction mixture generated by following the literature procedure of Chen and co-workers.[10] The experimental (bottom) and calculated (top) peaks are assignable to the $[2[N(C_8H_{17})_4] + Br]^+$ ion. The identity of the ion responsible for the minor peaks at ca. 1011.9, 1012.9, 1013.9, and 1014.9 *m/z* is

unknown.

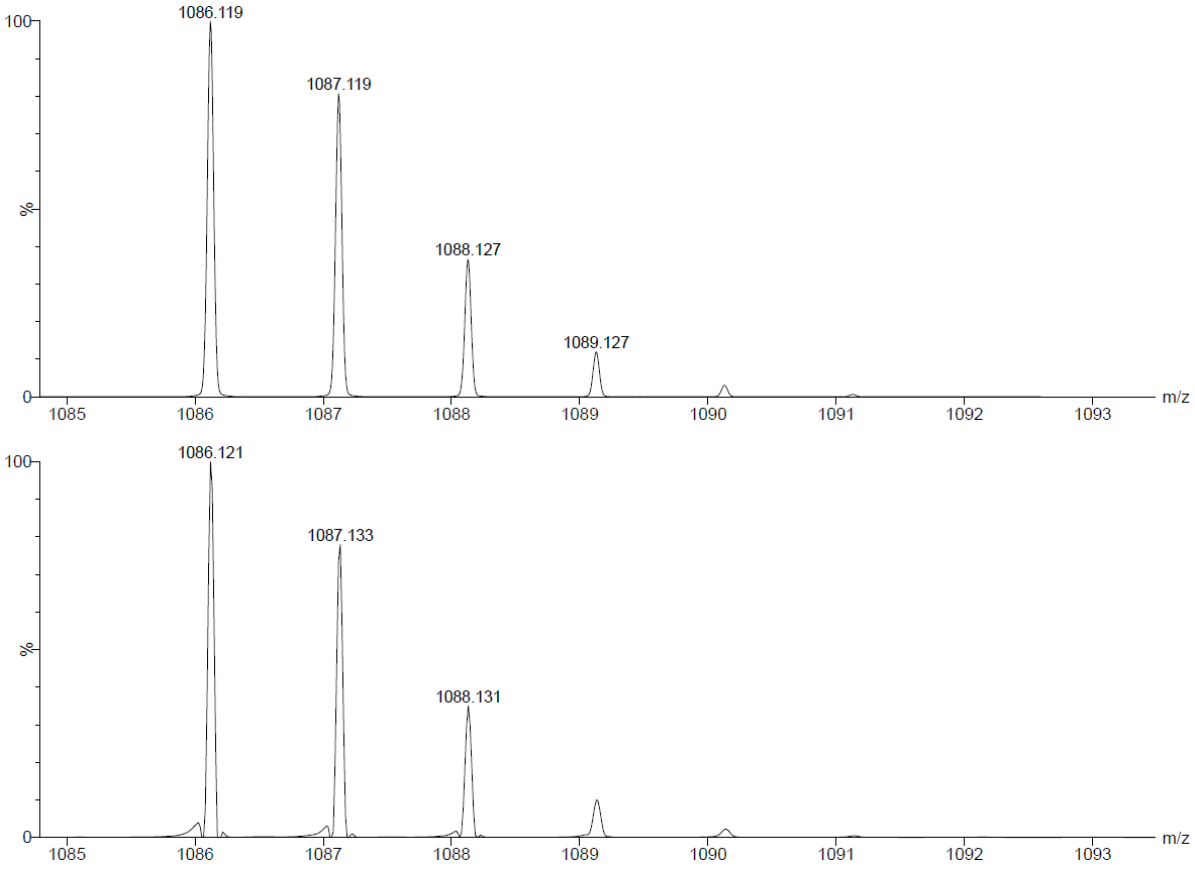

Figure A7.15. Partial ESI-MS of an aliquot, in EtOH, of the reaction mixture generated by following the literature procedure of Chen and co-workers.[10] The experimental (bottom) and calculated (top) peaks are assignable to the $[2[N(C_8H_{17})_4] + MPP]^+$ ion. The identity of

the ion responsible for the minor peaks at ca. 1086.0, 1087.0, and 1088.0 *m/z* is unknown.

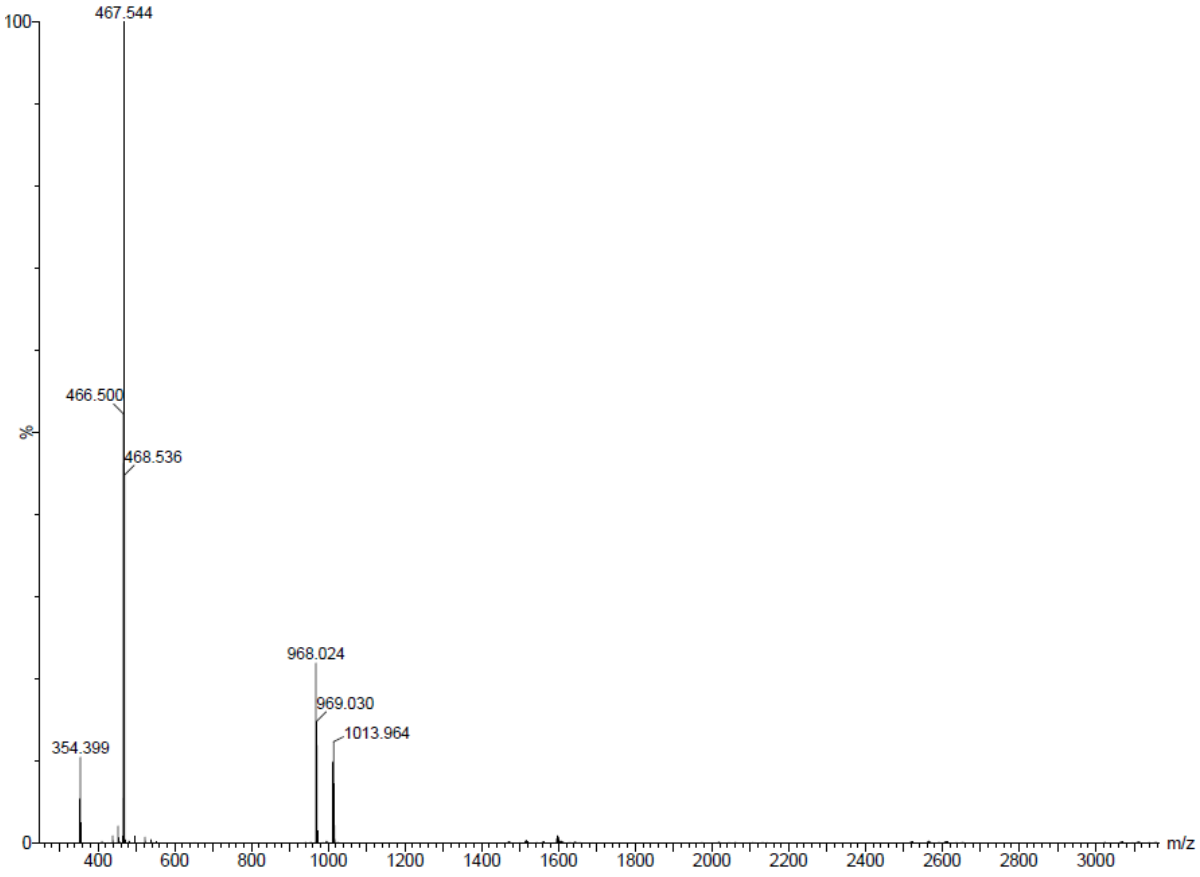

Figure A7.16. ESI-MS of $[N(C_8H_{17})_4][Br]$ in 1,2-dichloroethane. **Assignments**: *m/z*: 354.399 $[N(C_8H_{17})_3 + H]^+$ (Calcd *m/z* 354.410), 466.542 $[N(C_8H_{17})_4]^+$ (Calcd *m/z* 466.535), 968.024 $[2N(C_8H_{17})_4 + Cl]^+$ (Calcd *m/z* 968.039), 1013.964 $[2N(C_8H_{17})_4 + Br]^+$ (Calcd *m/z* 1013.989).

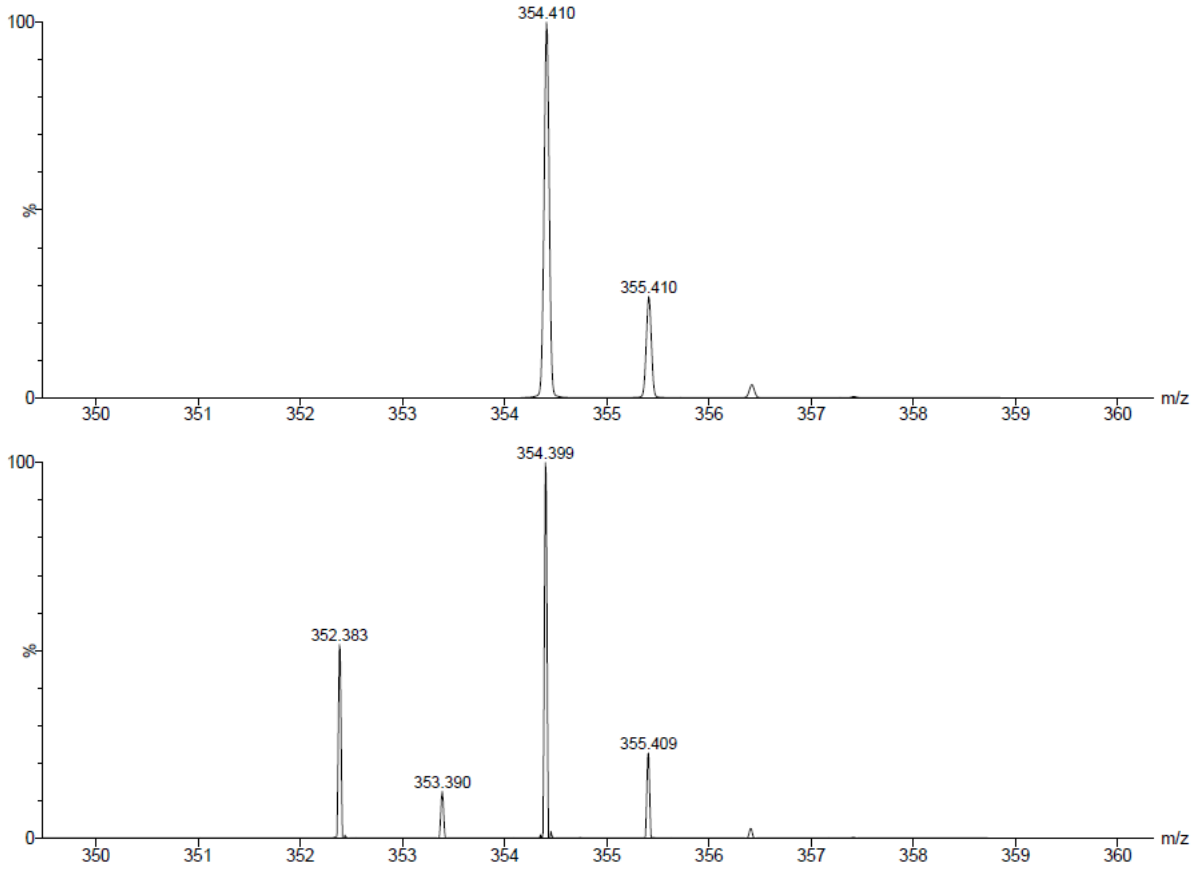

Figure A7.17. Partial ESI-MS of $[N(C_8H_{17})_4][Br]$ in 1,2-dichloroethane. The experimental (bottom) and calculated (top) peaks are assignable to the $[N(C_8H_{17})_3 + H]^+$ ion. The extra peaks in the experimental spectrum are assignable to $[N(C_8H_{17})_3 - H]^+$.

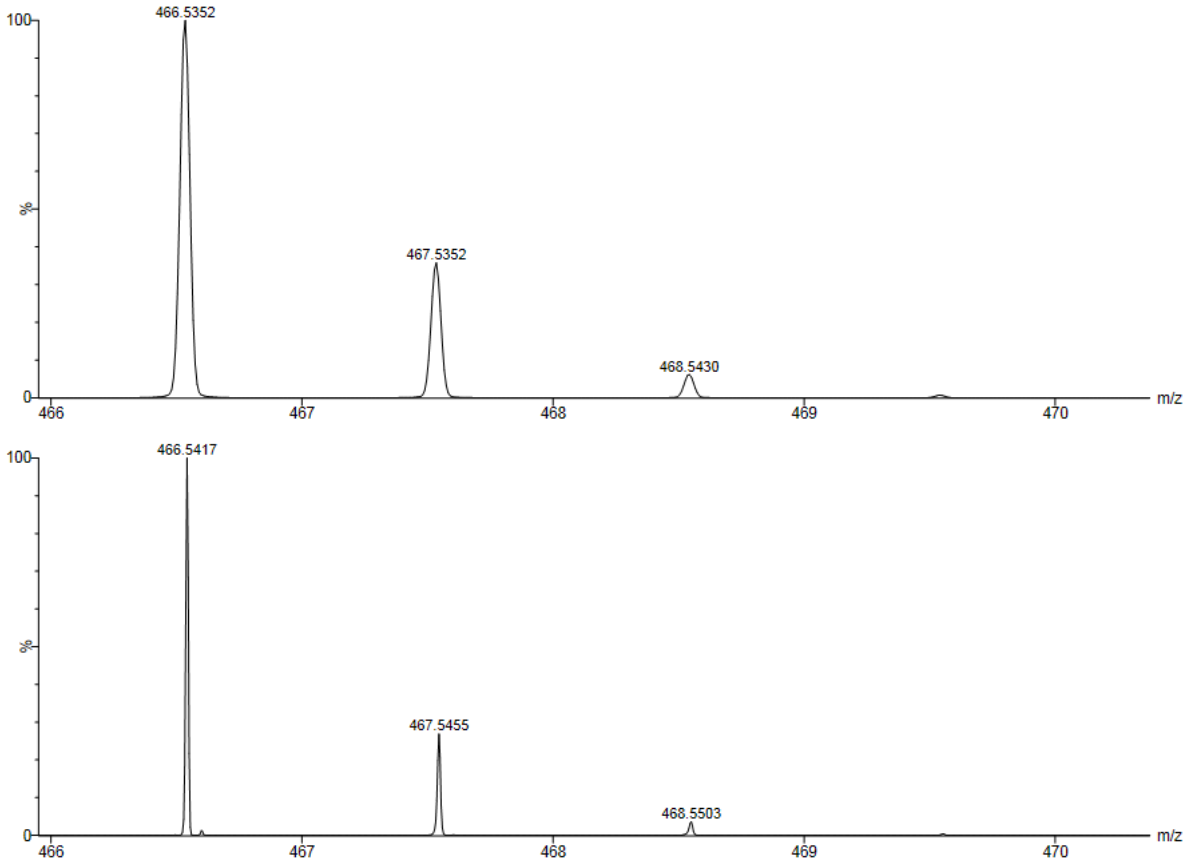

Figure A7.18. Partial ESI-MS of $[N(C_8H_{17})_4][Br]$ in 1,2-dichloroethane. The experimental (bottom) and calculated (top) peaks are assignable to the $[N(C_8H_{17})_4]^+$ ion.

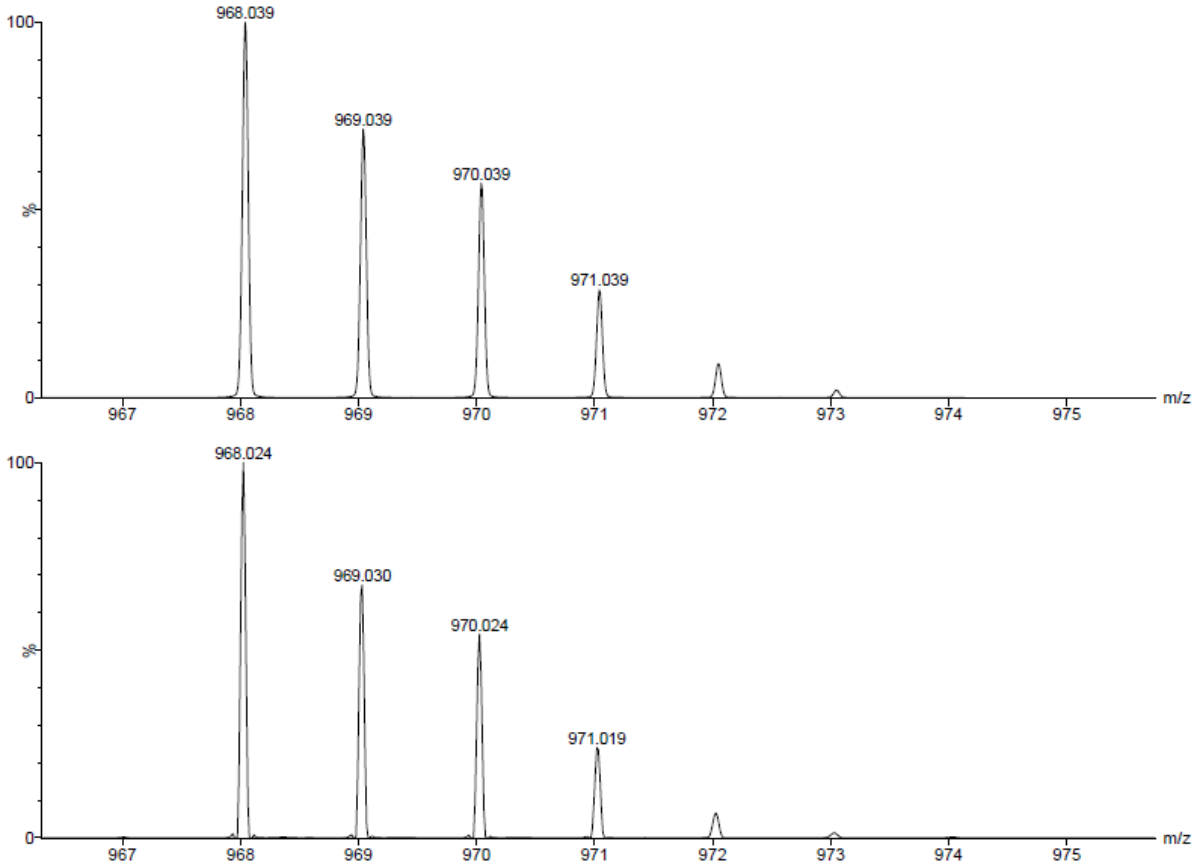

Figure A7.19. Partial ESI-MS of $[N(C_8H_{17})_4][Br]$ in 1,2-dichloroethane. The experimental (bottom) and calculated (top) peaks are assignable to the $[2N(C_8H_{17})_4 + Cl]^+$ ion. This peak likely appears due to Cl^- exchange with the solvent.

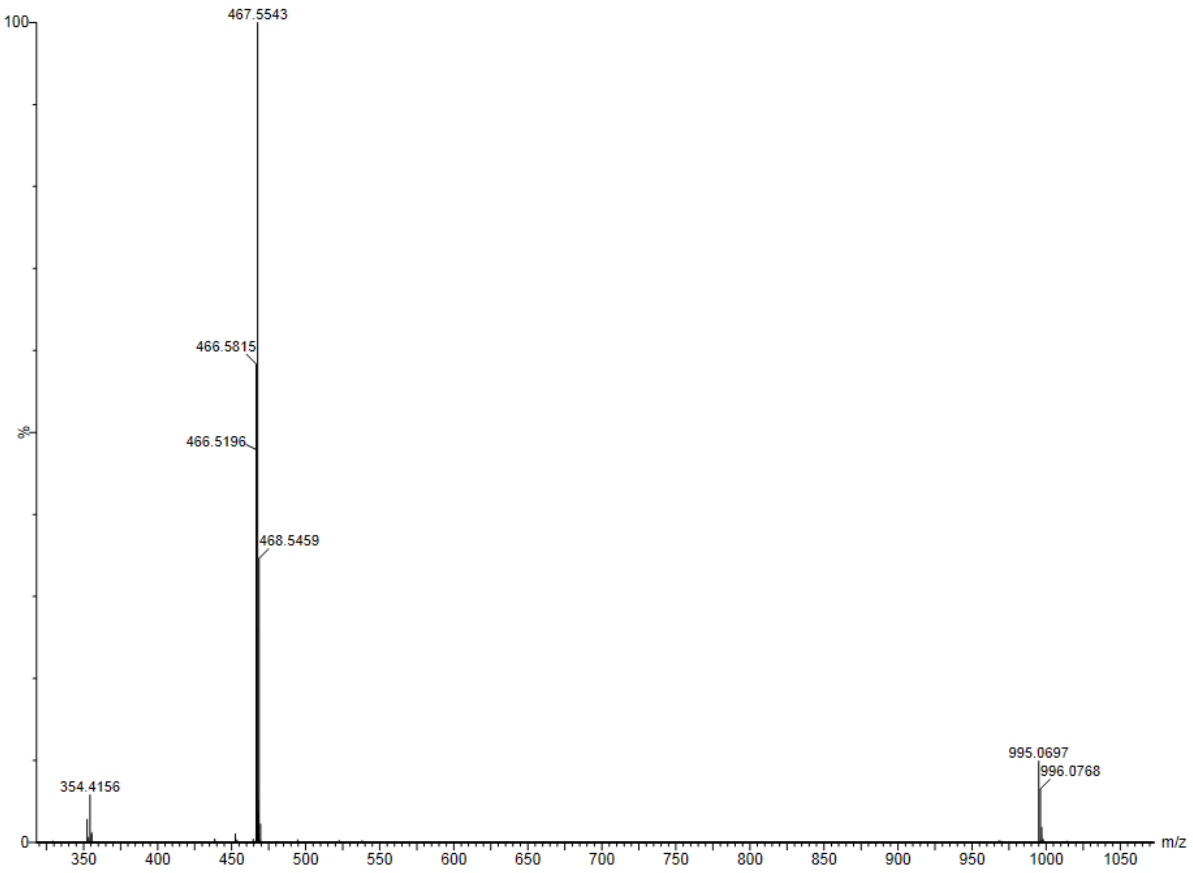

Figure A7.20. ESI-MS of $[N(C_8H_{17})_4][NO_3]$ in 1,2-dichloroethane. **Assignments**: *m/z* 995.070 $[2N(C_8H_{17})_4 + (NO_3)]^+$ (Calcd *m/z* 995.058).

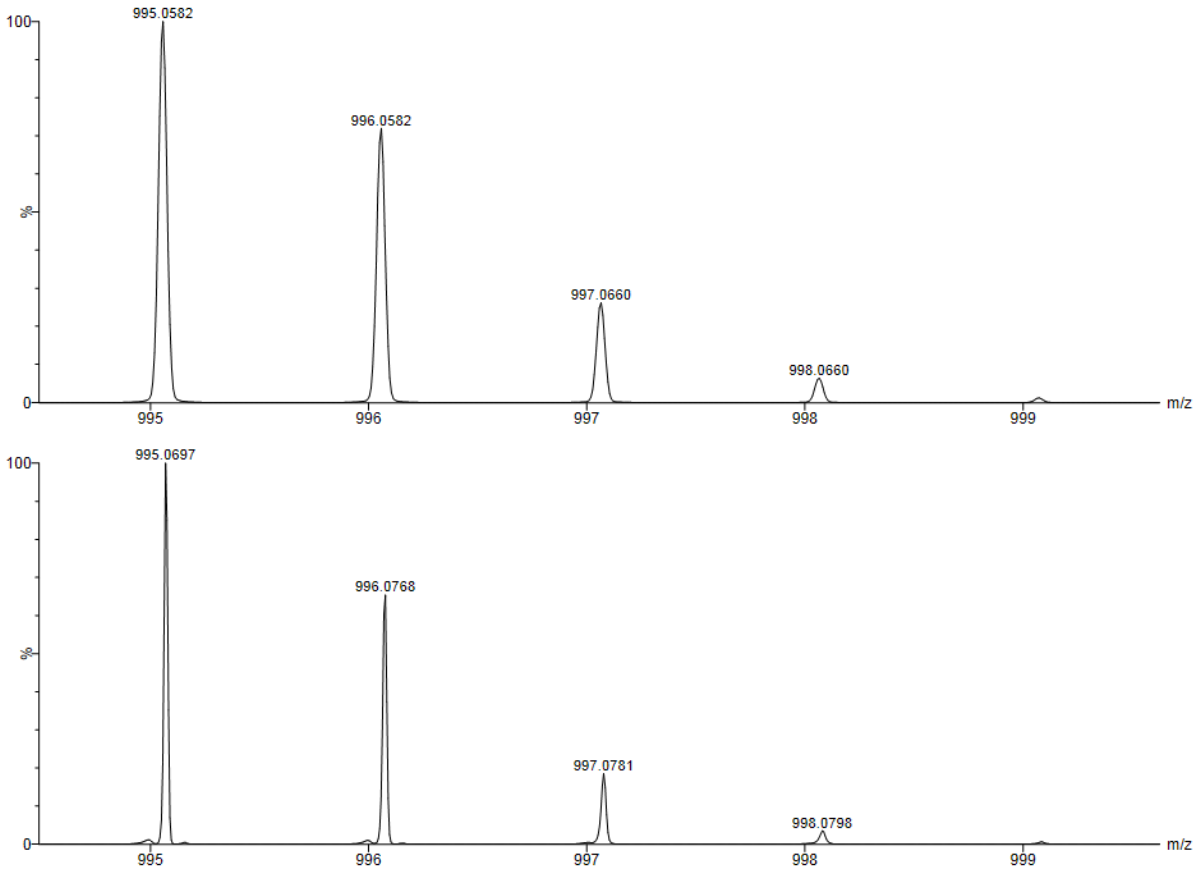

Figure A7.21. Partial ESI-MS of $[N(C_8H_{17})_4][NO_3]$ in 1,2-dichloroethane. The experimental (bottom) and calculated (top) peaks are assignable to the $[2N(C_8H_{17})_4 + (NO_3)]^+$ ion.

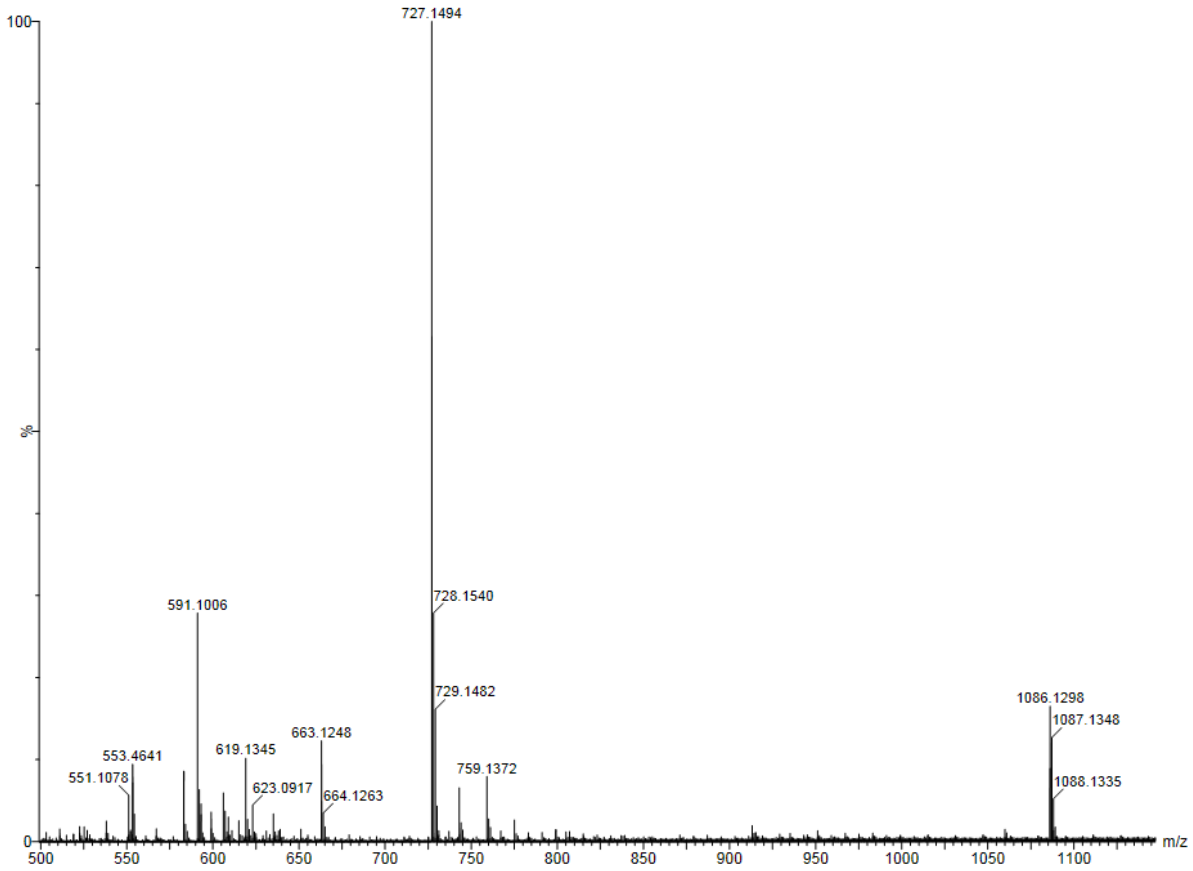

Figure A7.22. ESI-MS of Na(MPP) in EtOH. **Assignments**: *m/z* 727.149 $[Na_5(MPP)_4]^+$ (Calcd *m/z* 727.143), *m/z* 1086.130 $[2N(C_8H_{17})_4 + MPP]^+$ (Calcd *m/z* 1086.119).

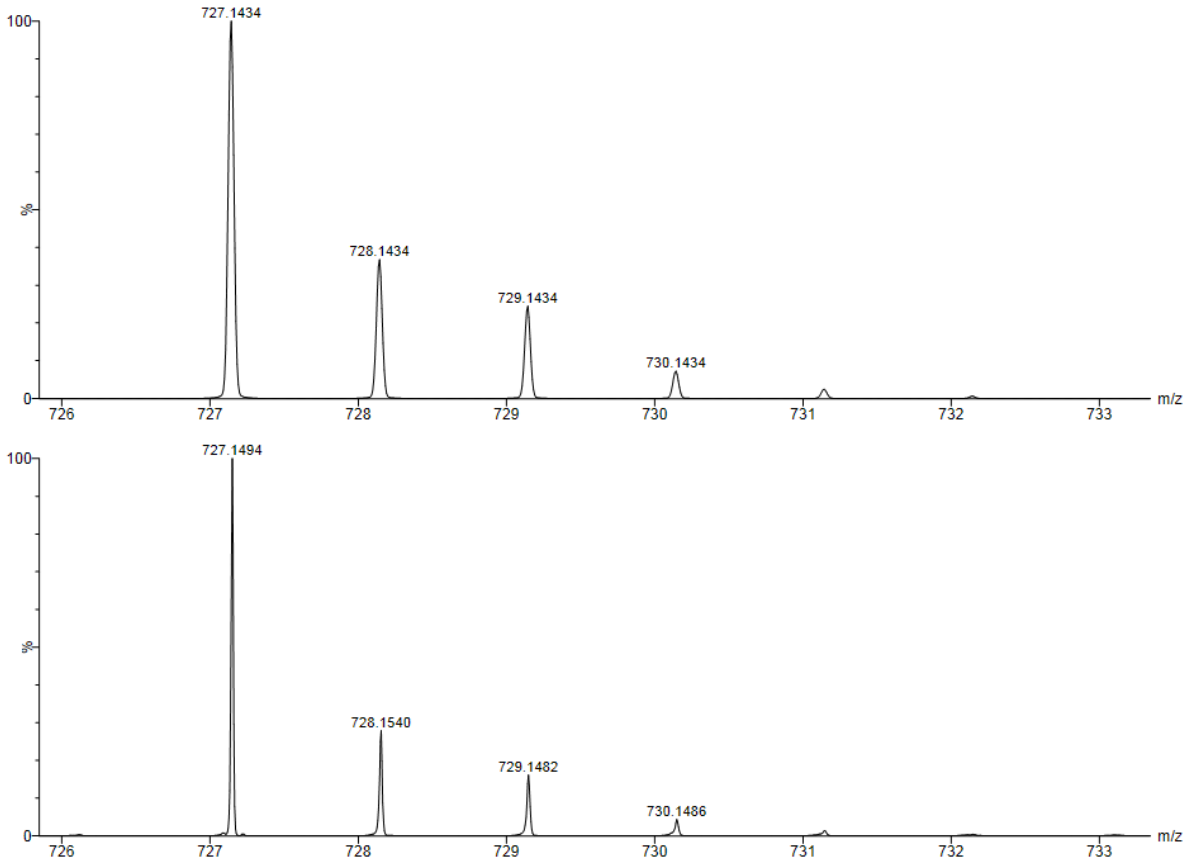

Figure A7.23. Partial ESI-MS of Na(MPP) in EtOH. The experimental (bottom) and calculated (top) peaks are assignable to the $[Na_5(MPP)_4]^+$ ion.

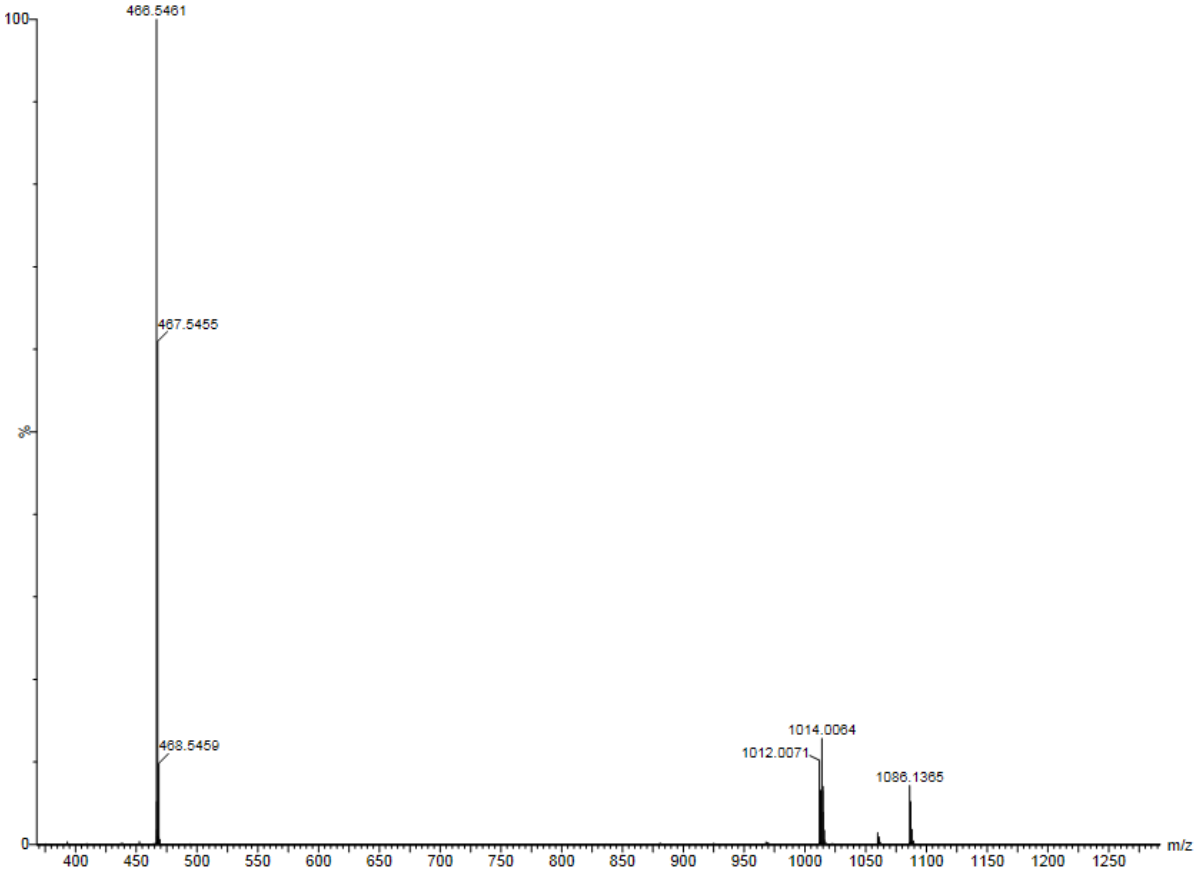

Figure A7.24. ESI-MS of a 1:1 mixture of Na(MPP) and $[N(C_8H_{17})_4][Br]$ in EtOH. **Experimental details**: Na(MPP) (5.0 mg, 0.028 mmol) and $[N(C_8H_{17})_4][Br]$ (9.2 mg, 0.028 mmol) were dissolved in EtOH to generate a pale yellow stock solution. The stock solution was then diluted with EtOH and an ESI mass spectrum was collected. **Assignments**: *m/z* 1086.137 $[2N(C_8H_{17})_4 + MPP]^+$ (Calcd *m/z* 1086.119).

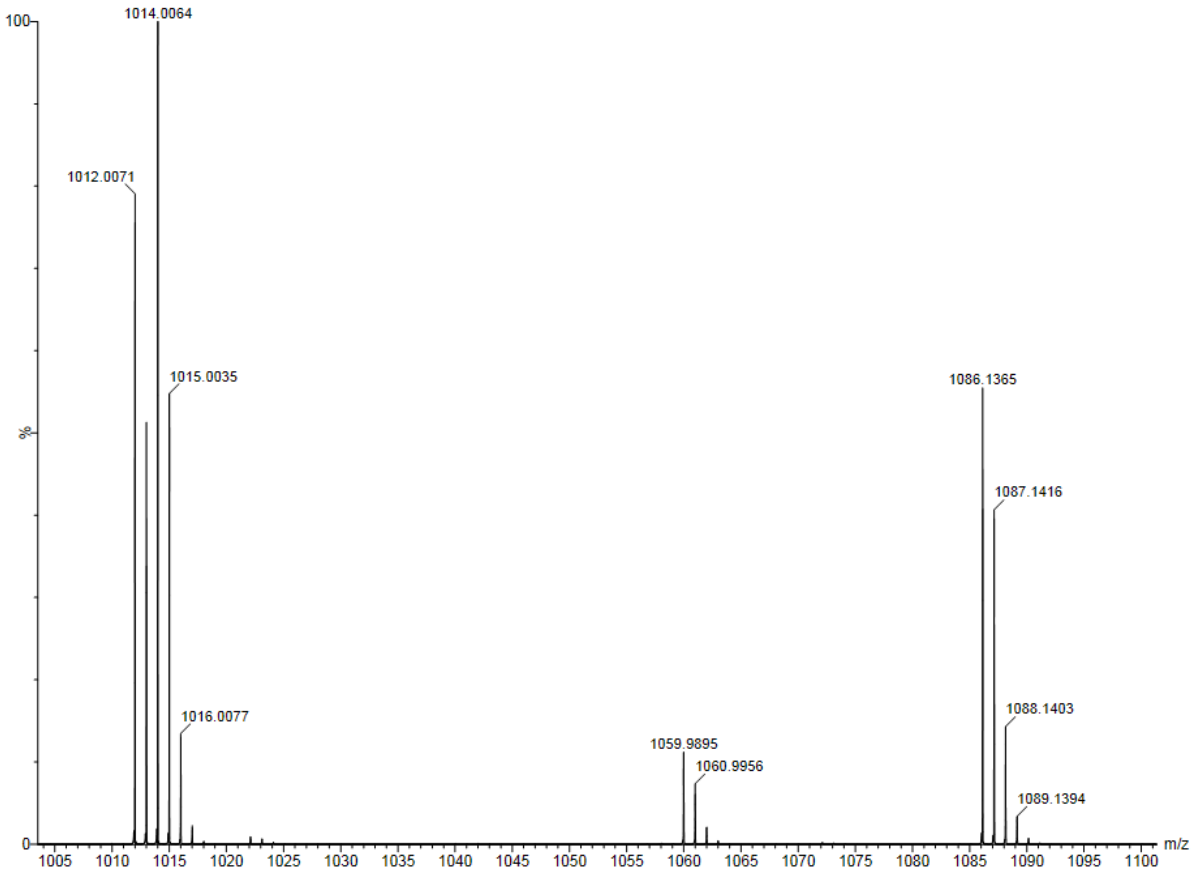

Figure A7.25. Partial ESI-MS of a 1:1 mixture of Na(MPP) and $[N(C_8H_{17})_4][Br]$ in EtOH.

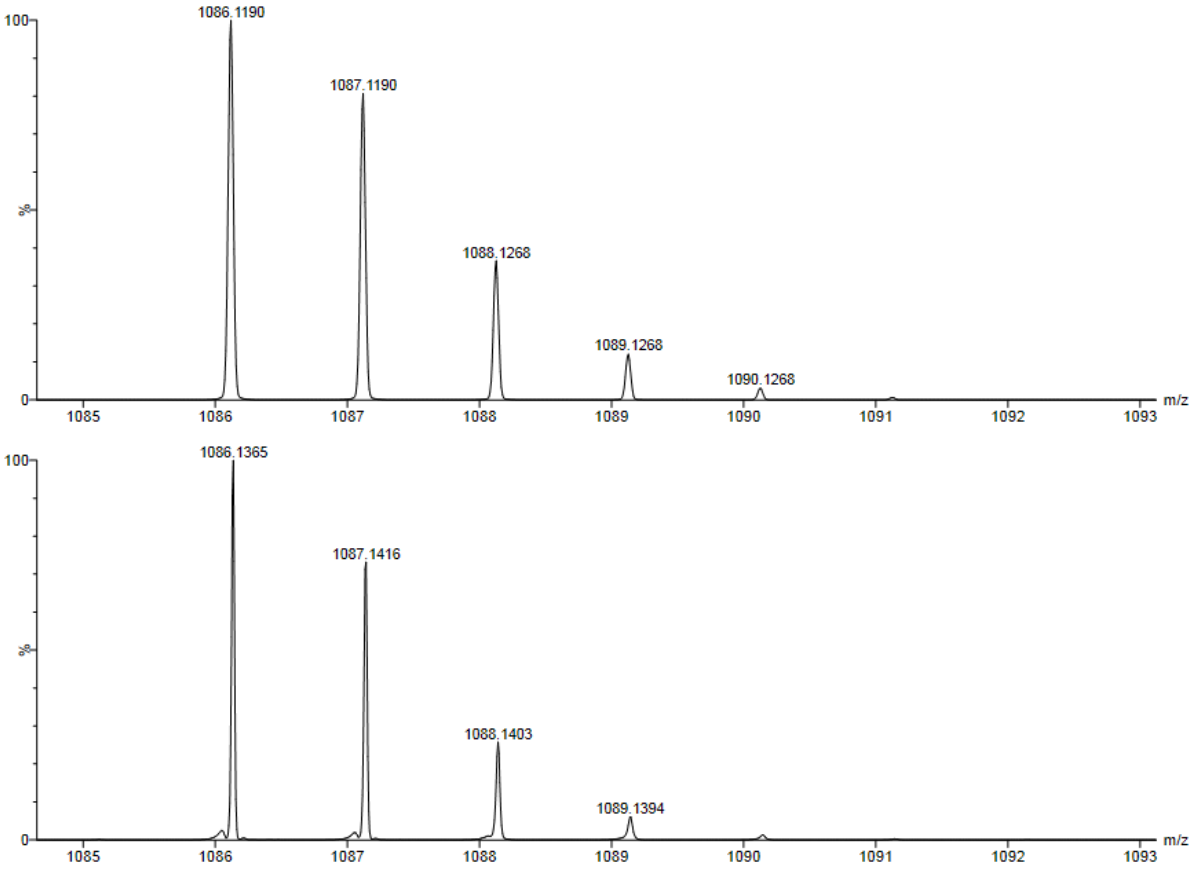

Figure A7.26. Partial ESI-MS of a 1:1 mixture of Na(MPP) and $[N(C_8H_{17})_4][Br]$ in EtOH. The experimental (bottom) and calculated (top) peaks are assignable to the $[2[N(C_8H_{17})_4] + MPP]^+$ ion.

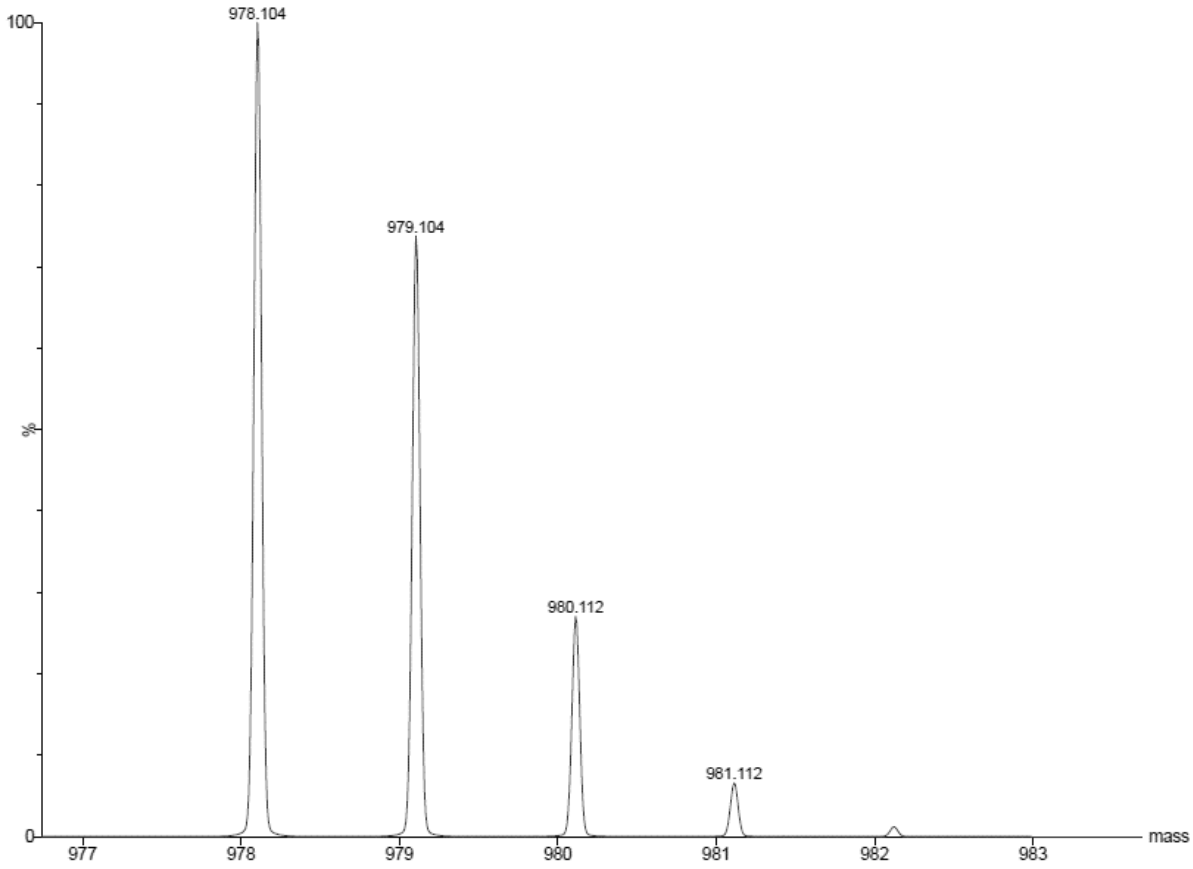

Figure A7.27. Calculated ESI mass spectrum for the $[2[N(C_8H_{17})_4] + EtO]^+$ ion.

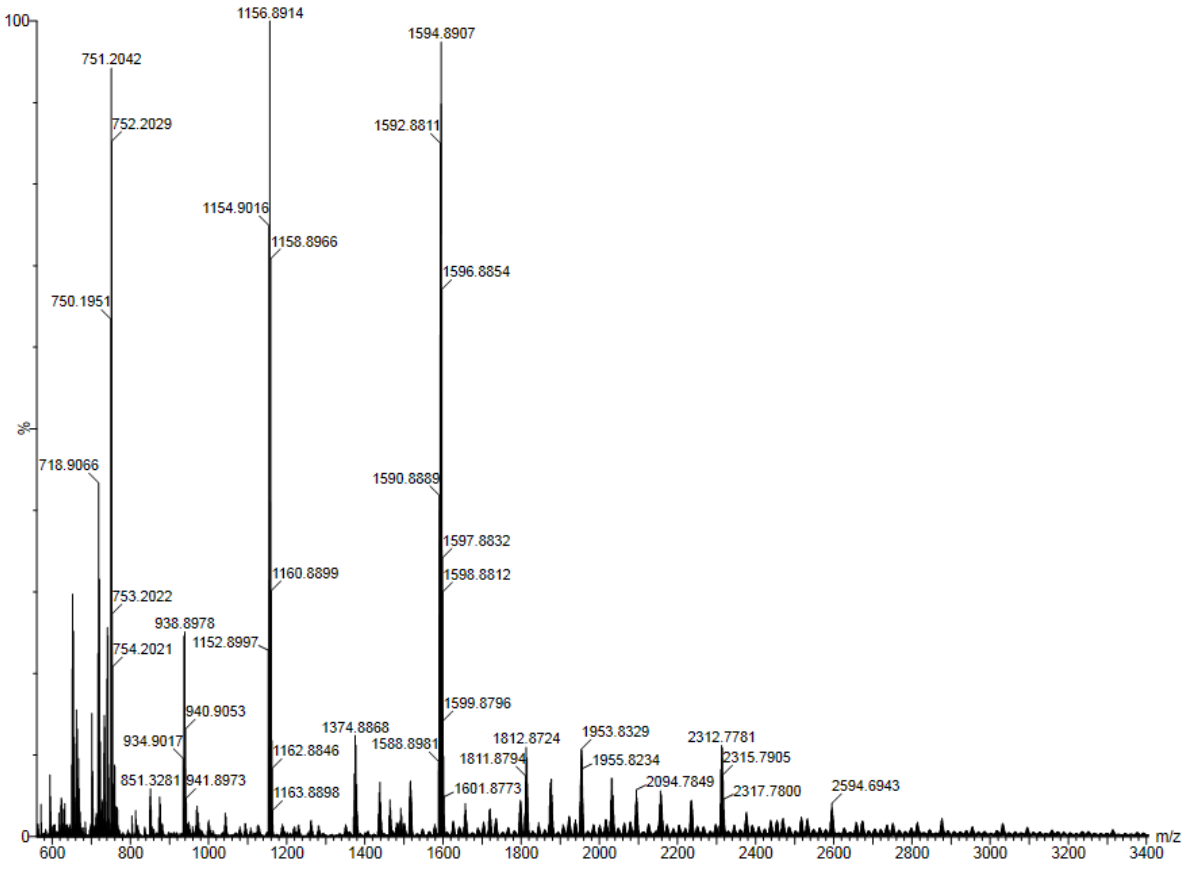

Figure A7.28. ESI-MS of [Cu(HMPP*)]$_n$ in THF.

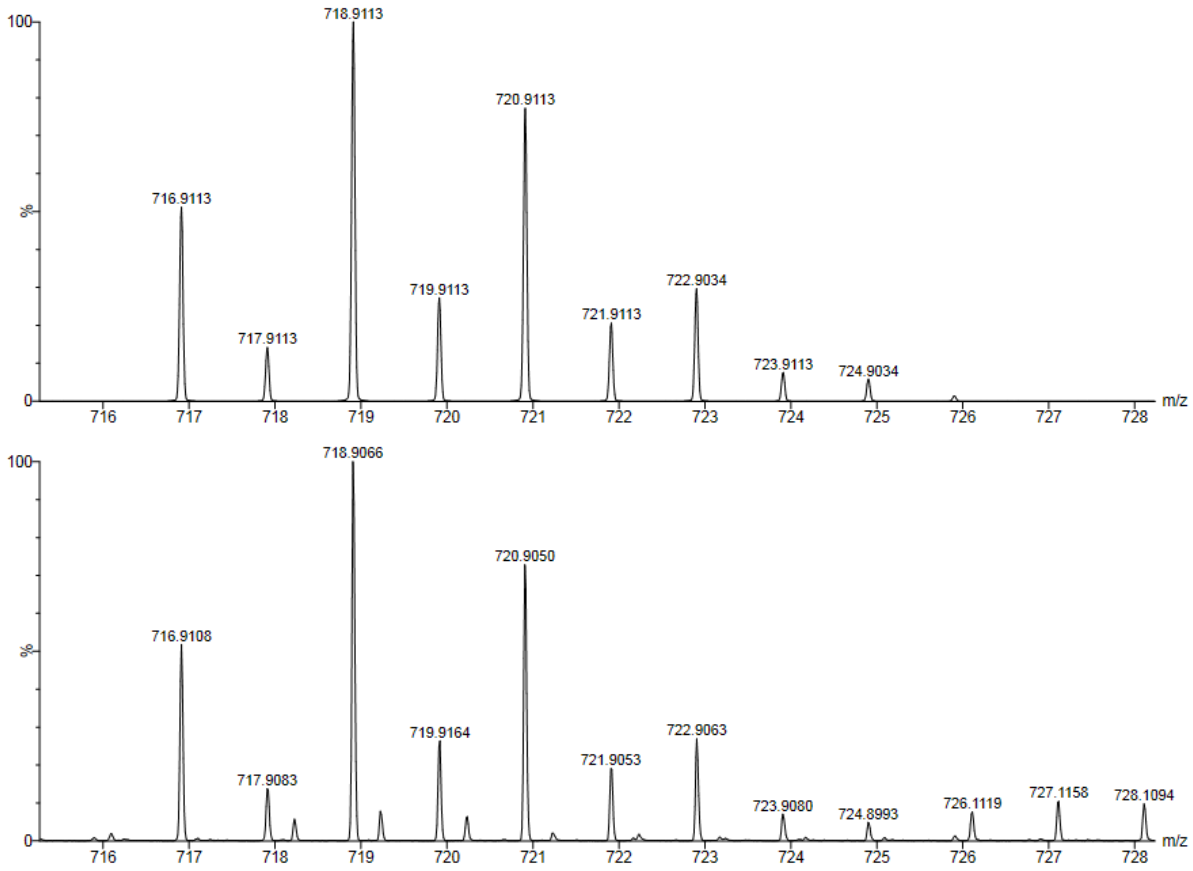

Figure A7.29. Partial ESI-MS of $[Cu(HMPP^*)]_n$ in THF. The experimental (bottom) and calculated (top) peaks are assignable to the $[Cu_3(HMPP^*)_3 + Cu]^+$ ion. The identity of the ion responsible for the minor peaks at ca. 718.2, 719.2, 720.2, and 721.2 *m/z* is unknown.

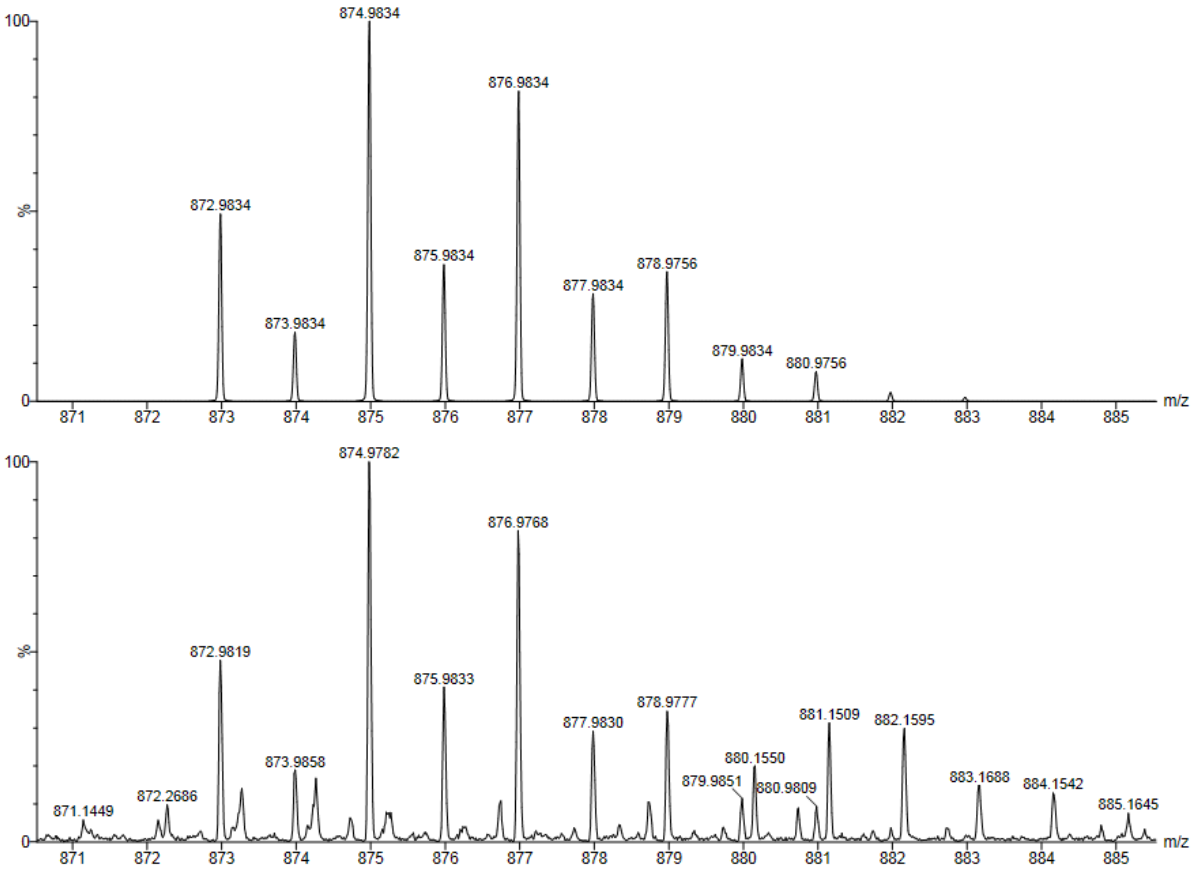

Figure A7.30. Partial ESI-MS of $[Cu(HMPP^*)]_n$ in THF. The experimental (bottom) and calculated (top) peaks are assignable to the $[Cu_4(HMPP^*)_4 + H]^+$ ion. The identity of the ion (or ions) responsible for the minor peaks observed in this spectrum is unknown.

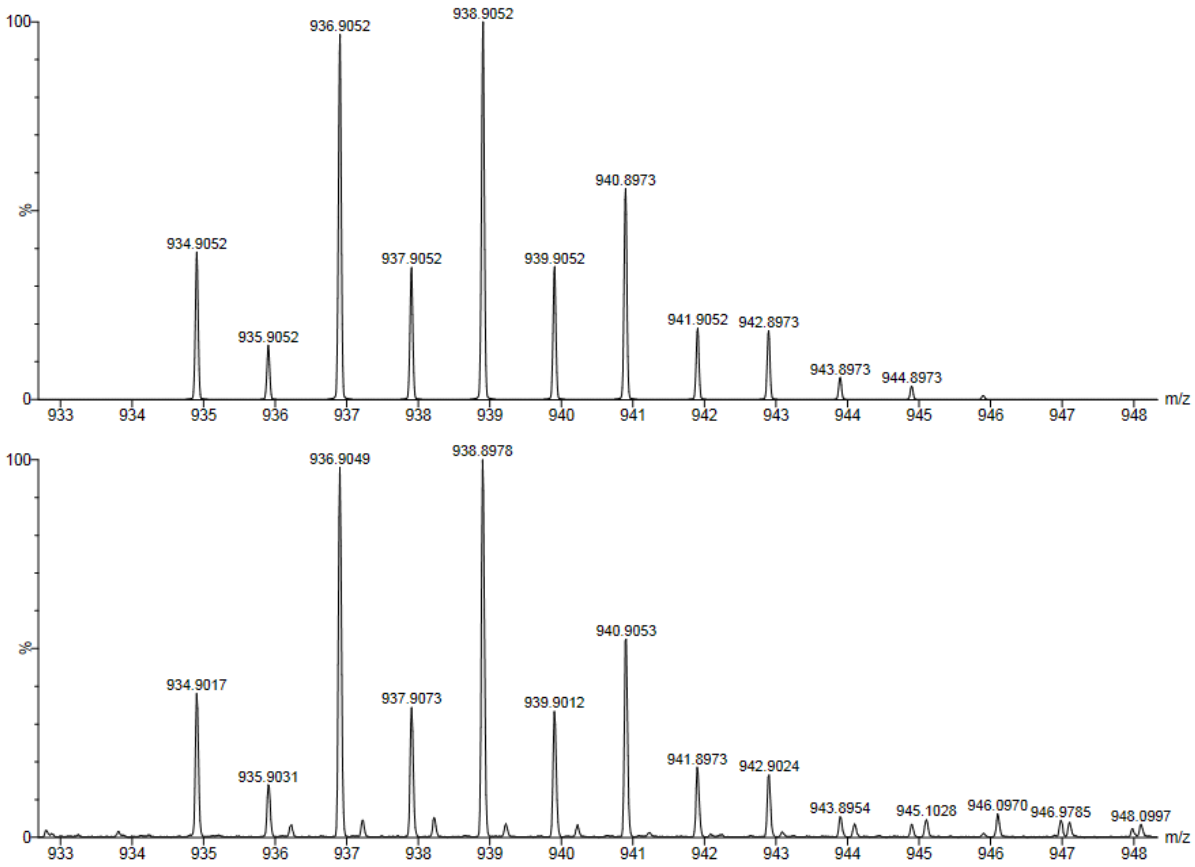

Figure A7.31. Partial ESI-MS of $[Cu(HMPP^*)]_n$ in THF. The experimental (bottom) and calculated (top) peaks are assignable to the $[Cu_4(HMPP^*)_4 + Cu]^+$ ion.

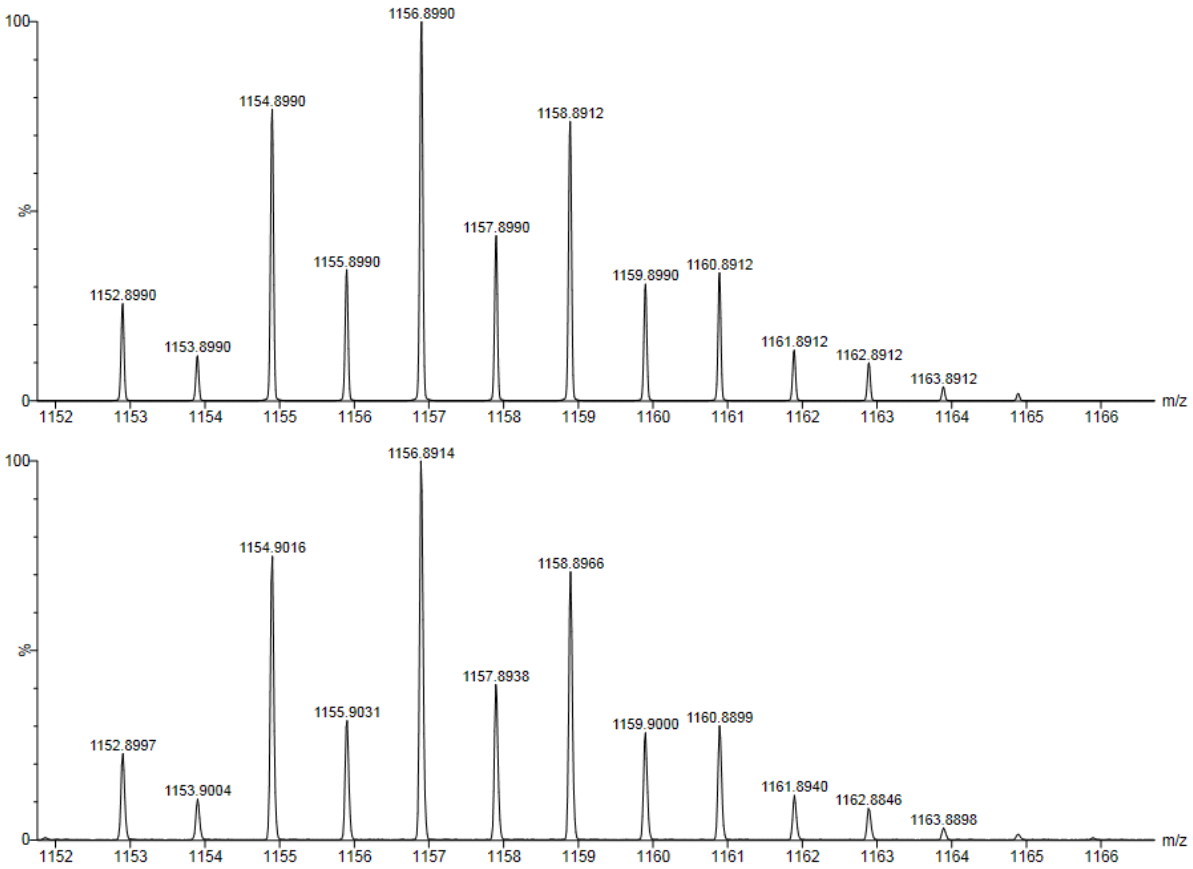

Figure A7.32. Partial ESI-MS of $[Cu(HMPP^*)]_n$ in THF. The experimental (bottom) and calculated (top) peaks are assignable to the $[Cu_5(HMPP^*)_5 + Cu]^+$ ion.

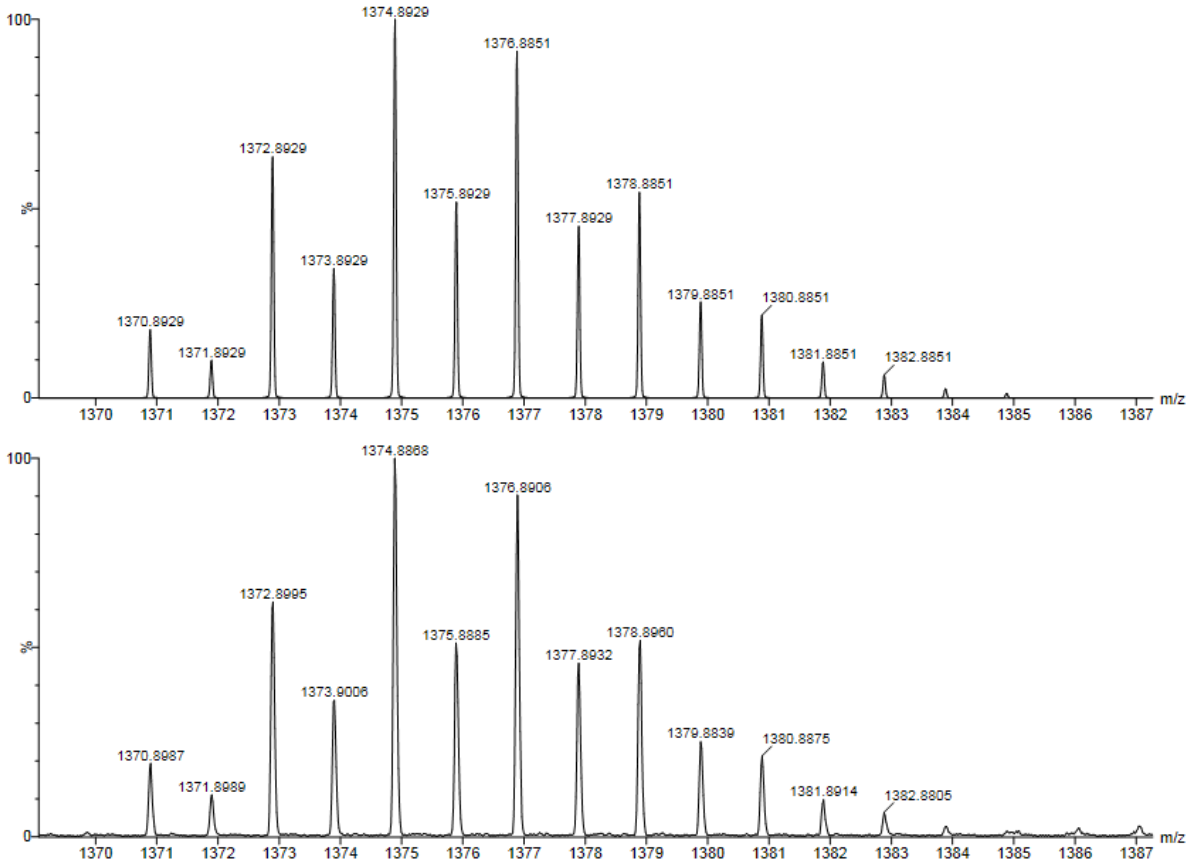

Figure A7.33. Partial ESI-MS of $[Cu(HMPP^*)]_n$ in THF. The experimental (bottom) and calculated (top) peaks are assignable to the $[Cu_6(HMPP^*)_6 + Cu]^+$ ion.

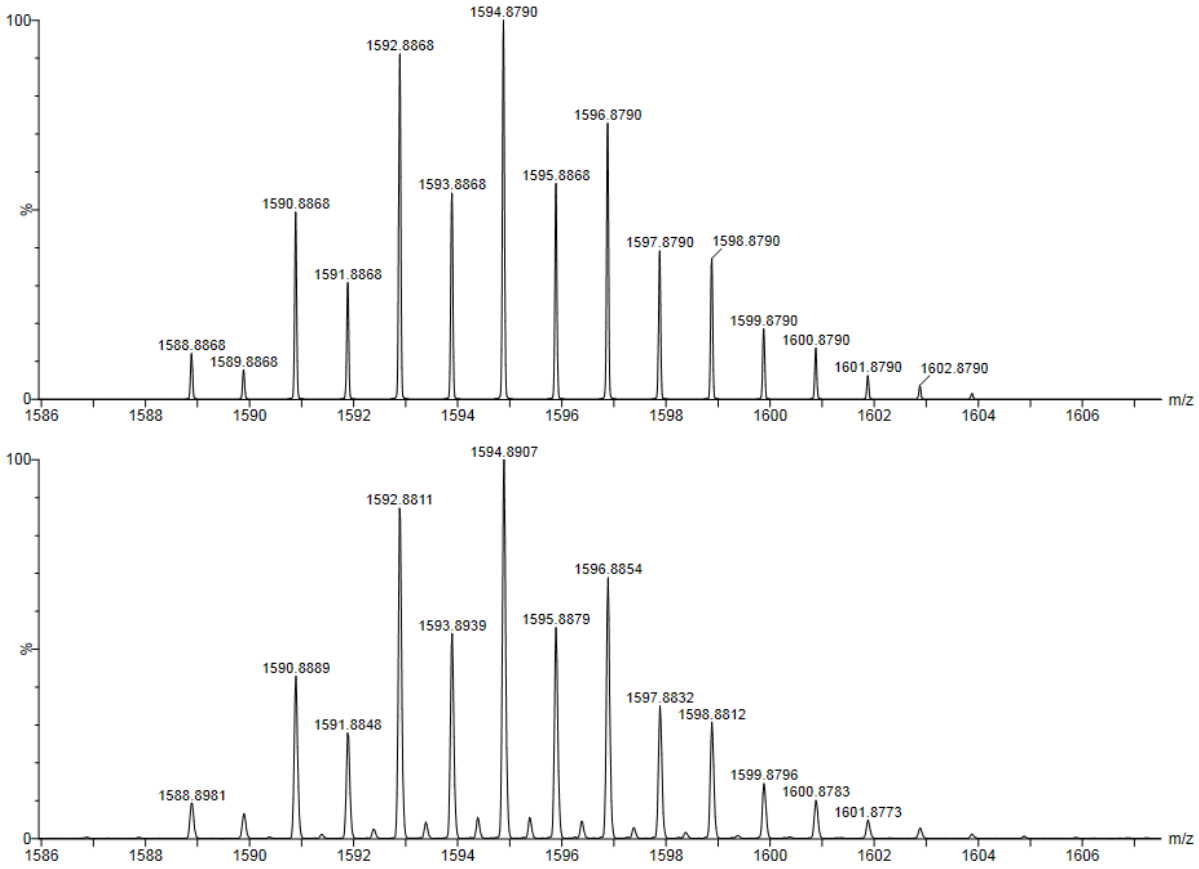

Figure A7.34. Partial ESI-MS of $[Cu(HMPP^*)]_n$ in THF. The experimental (bottom) and calculated (top) peaks are assignable to the $[Cu_7(HMPP^*)_7 + Cu]^+$ ion. The minor peaks in this spectrum are assignable to the doubly charged dimer, $[Cu_{16}(HMPP^*)_{14}]^{2+}$.

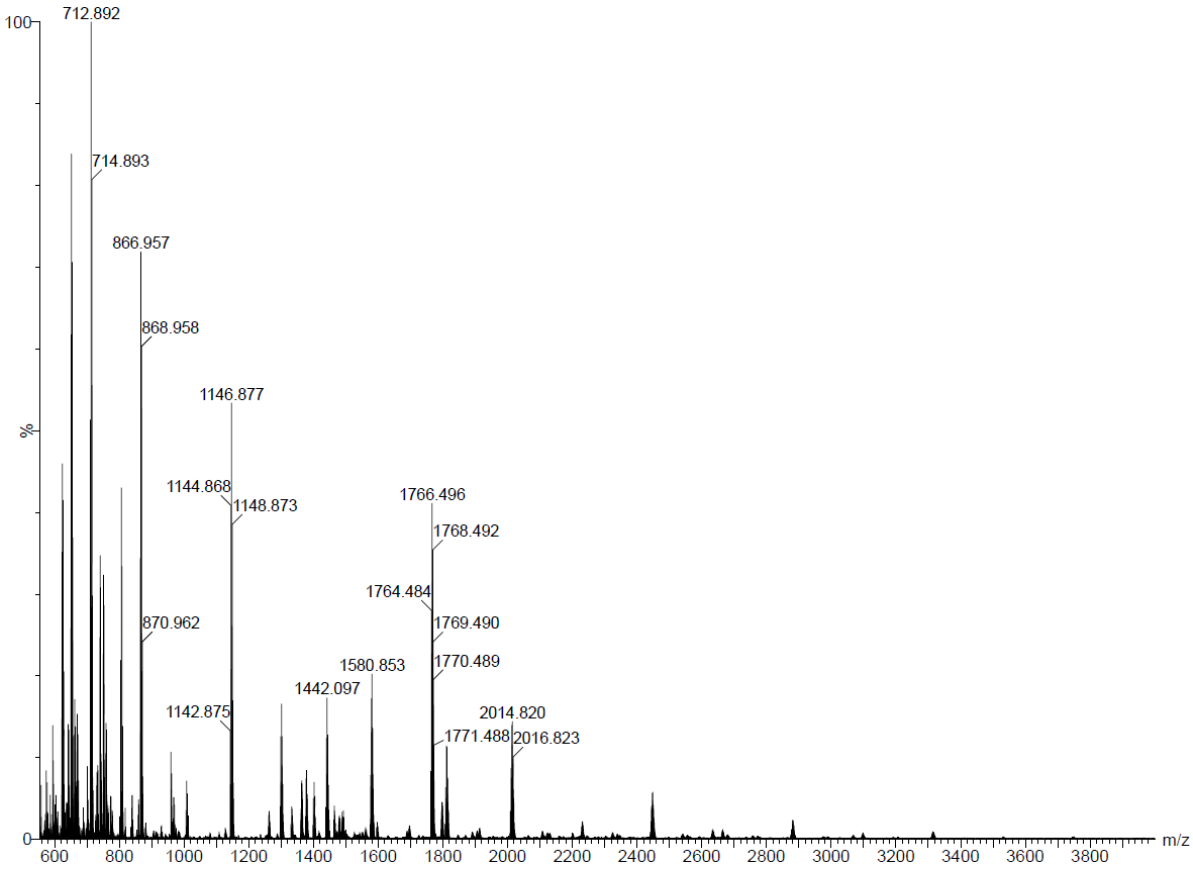

Figure A7.35. ESI-MS of [Cu(MPP)]$_n$ in 1,2-dichloroethane.

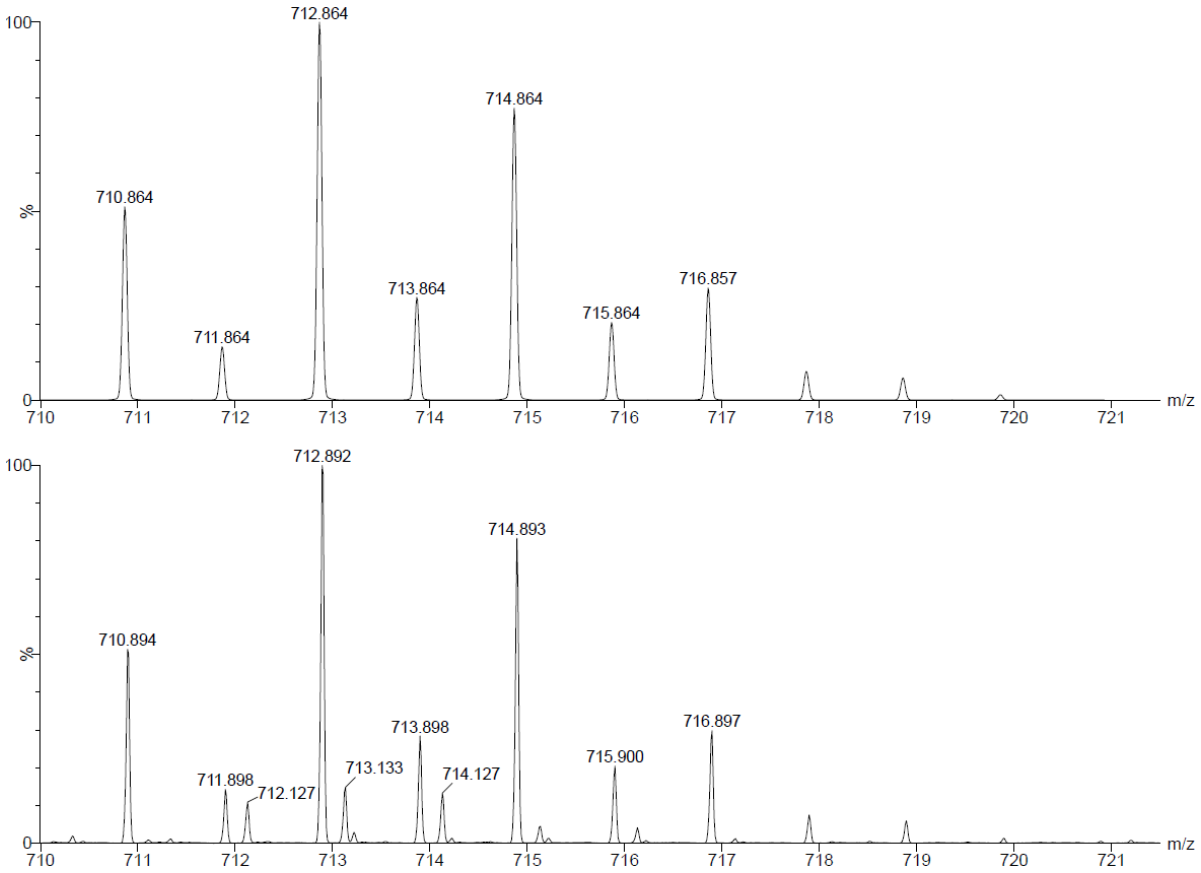

Figure A7.36. Partial ESI-MS of $[Cu(MPP)]_n$ in 1,2-dichloroethane. The experimental (bottom) and calculated (top) peaks are assignable to the $[Cu_4(MPP)_3]^+$ ion. The identity of the ion responsible for the minor peaks at ca. 712.1, 713.1, and 714.1 *m/z* is unknown.

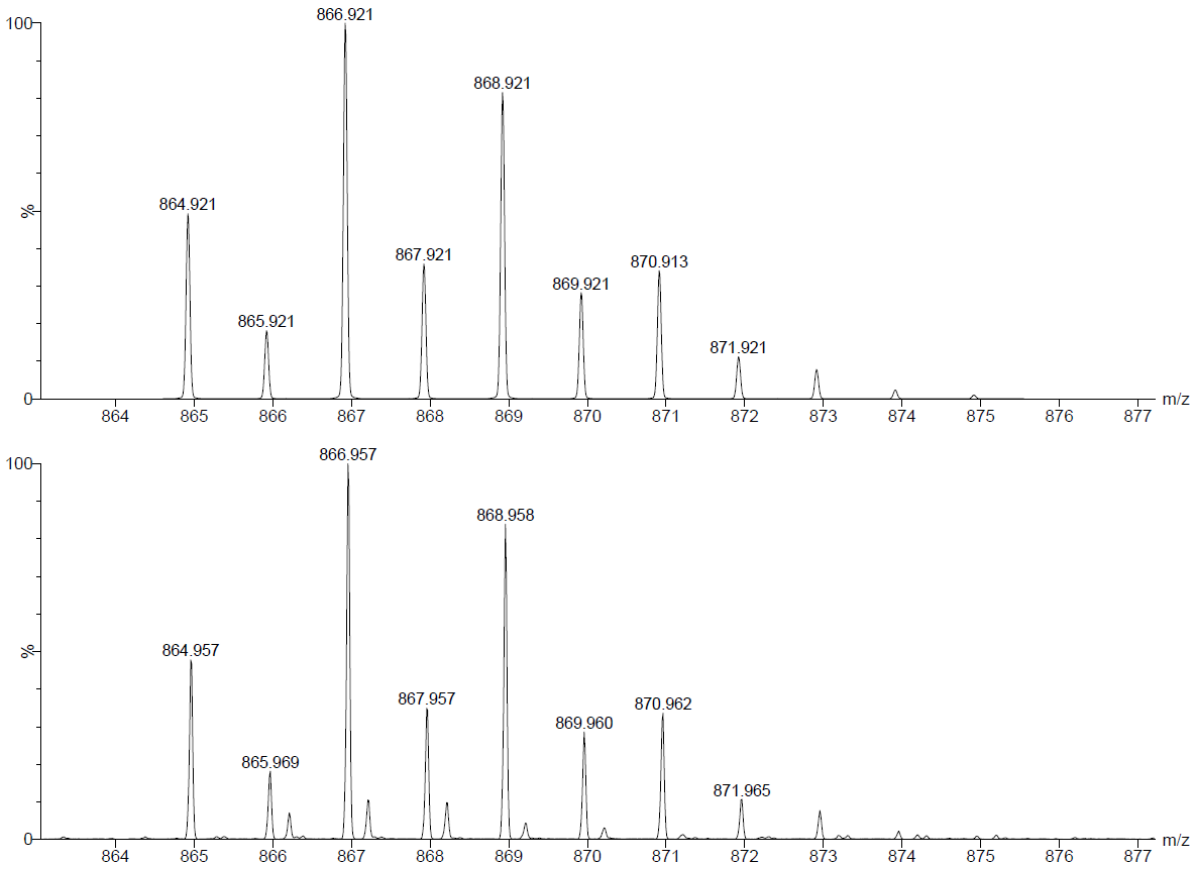

Figure A7.37. Partial ESI-MS of $[Cu(MPP)]_n$ in 1,2-dichloroethane. The experimental (bottom) and calculated (top) peaks are assignable to the $[Cu_4(MPP)_4 + H]^+$ ion. The identity of the ion responsible for the minor peaks at ca. 866.2, 867.2, 868.2 and 869.2 *m/z* is unknown.

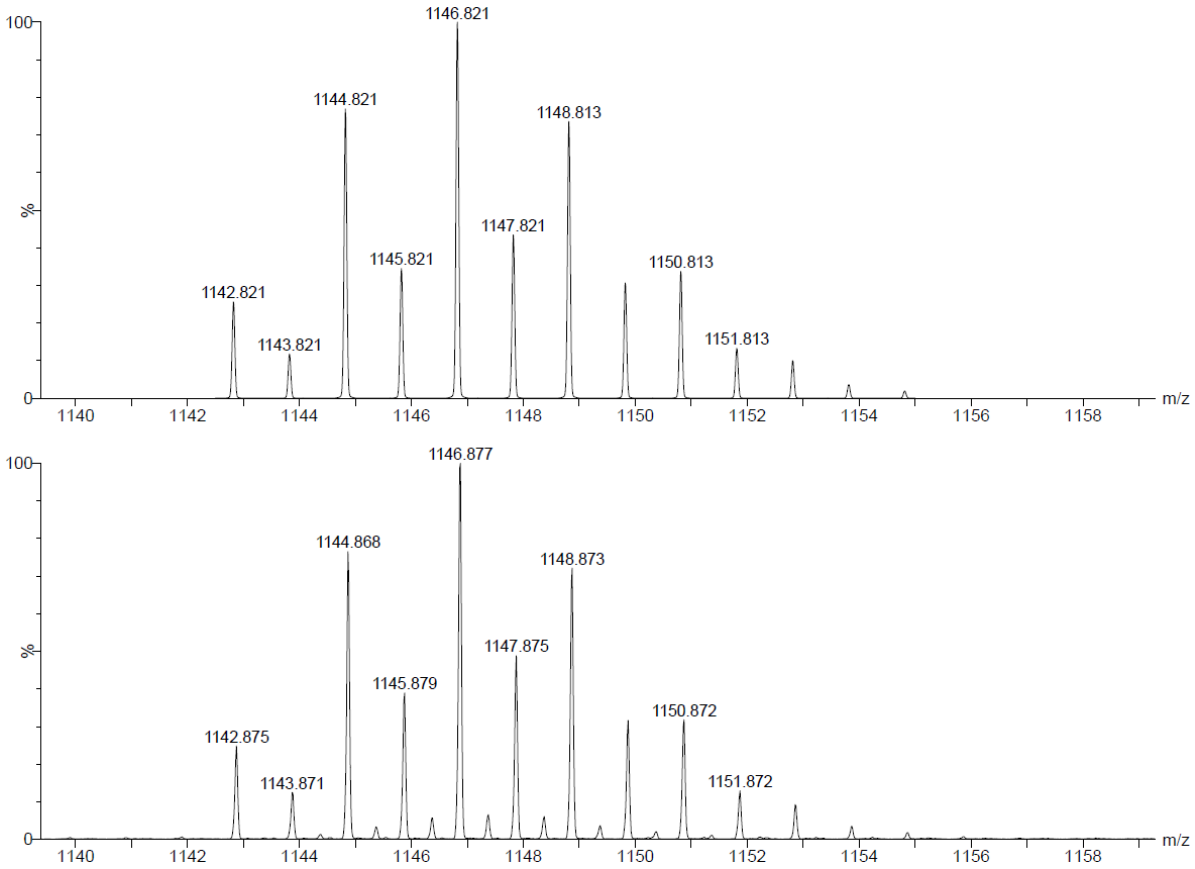

Figure A7.38. Partial ESI-MS of $[Cu(MPP)]_n$ in 1,2-dichloroethane. The experimental (bottom) and calculated (top) peaks are assignable to the $[Cu_6(MPP)_5]^+$ ion. The minor peaks in this spectrum are assignable to the doubly charged dimer, $[Cu_{12}(MPP)_{10}]^{2+}$.

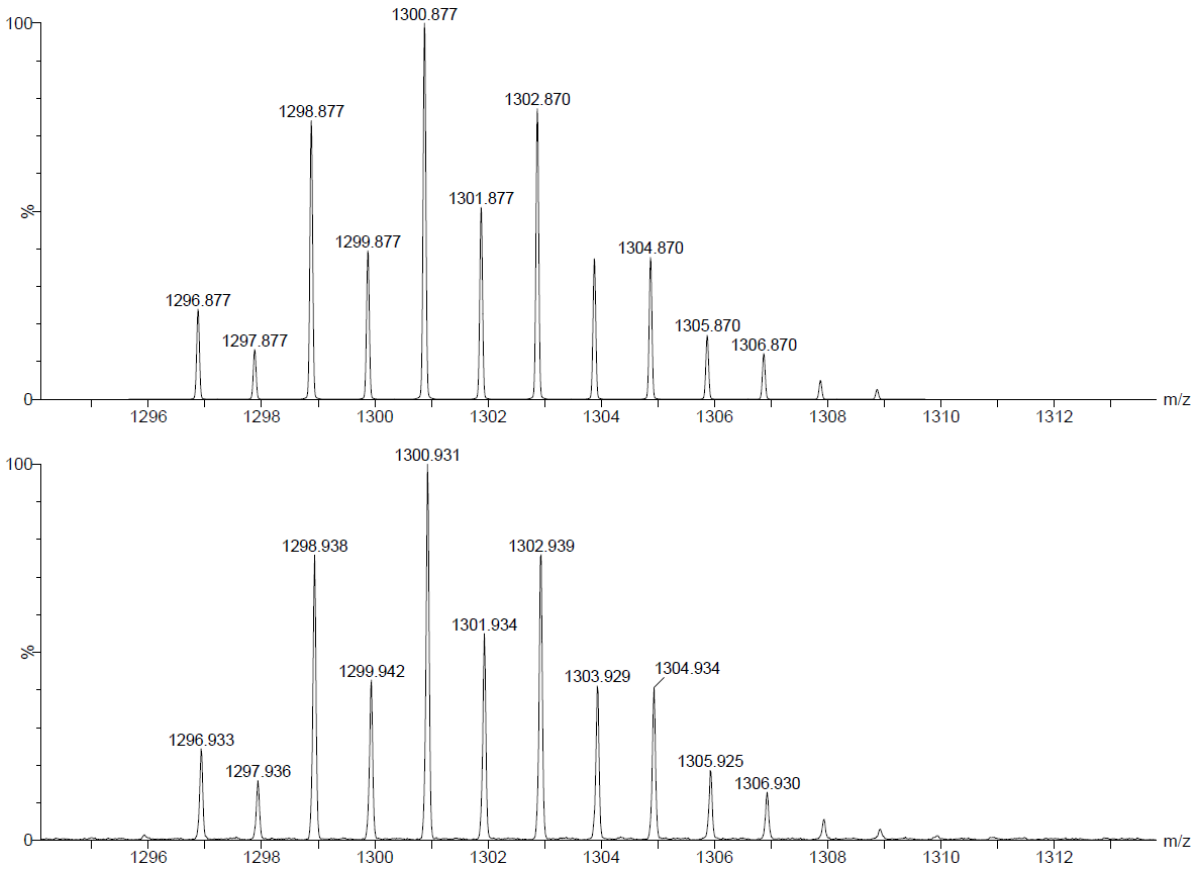

Figure A7.39. Partial ESI-MS of $[Cu(MPP)]_n$ in 1,2-dichloroethane. The experimental (bottom) and calculated (top) peaks are assignable to the $[Cu_6(MPP)_6 + H]^+$ ion.

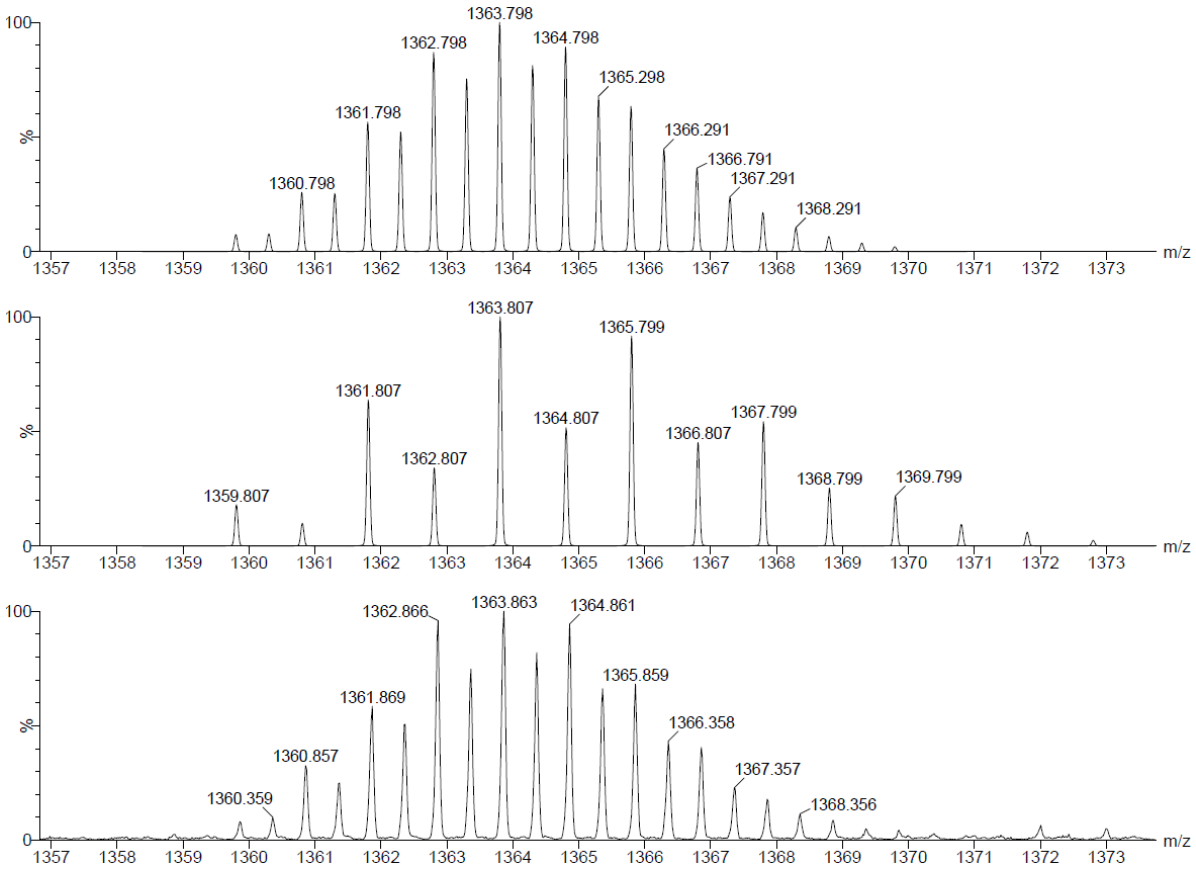

Figure A7.40. Partial ESI-MS of $[Cu(MPP)]_n$ in 1,2-dichloroethane. The experimental (bottom) peak is assignable to overlapping signals from $[Cu_7(MPP)_6]^+$ (middle = calculated) and the related doubly charged dimer, $[Cu_{14}(MPP)_{12}]^{2+}$ (top = calculated).

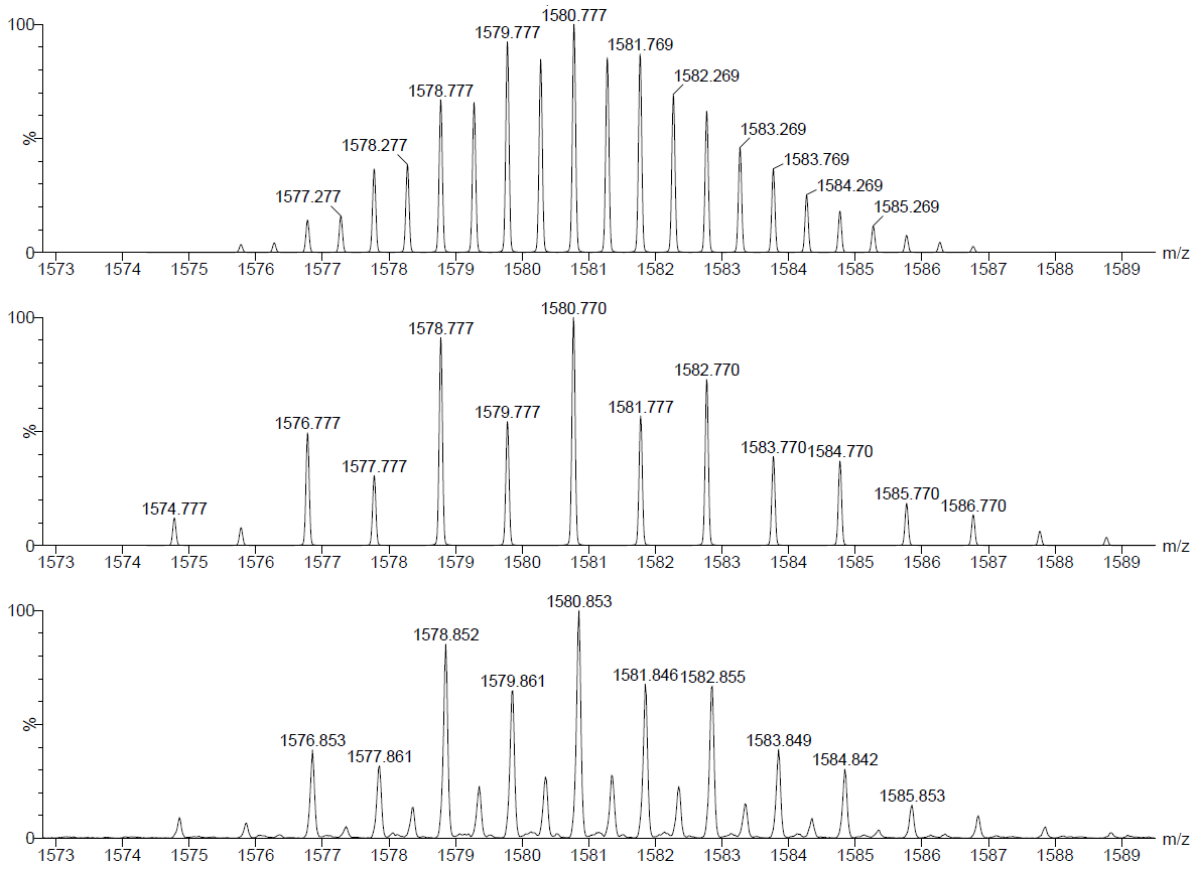

Figure A7.41. Partial ESI-MS of $[Cu(MPP)]_n$ in 1,2-dichloroethane. The experimental (bottom) peak is assignable to overlapping signals from $[Cu_8(MPP)_7]^+$ (middle = calculated) and the related doubly charged dimer, $[Cu_{16}(MPP)_{14}]^{2+}$ (top = calculated).

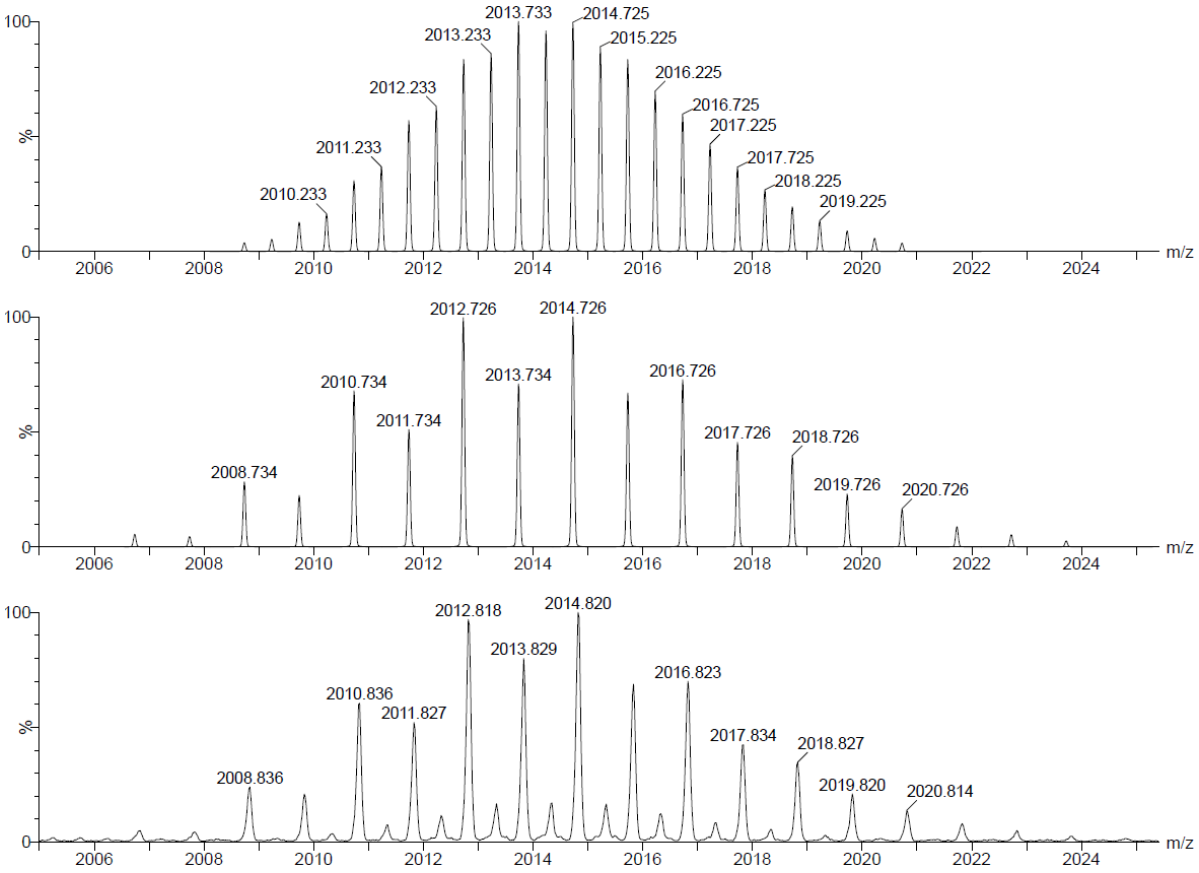

Figure A7.42. Partial ESI-MS of $[Cu(MPP)]_n$ in 1,2-dichloroethane. The experimental (bottom) peak is assignable to overlapping signals from $[Cu_{10}(MPP)_9]^+$ (middle = calculated) and the related doubly charged dimer, $[Cu_{20}(MPP)_{18}]^{2+}$ (top = calculated).

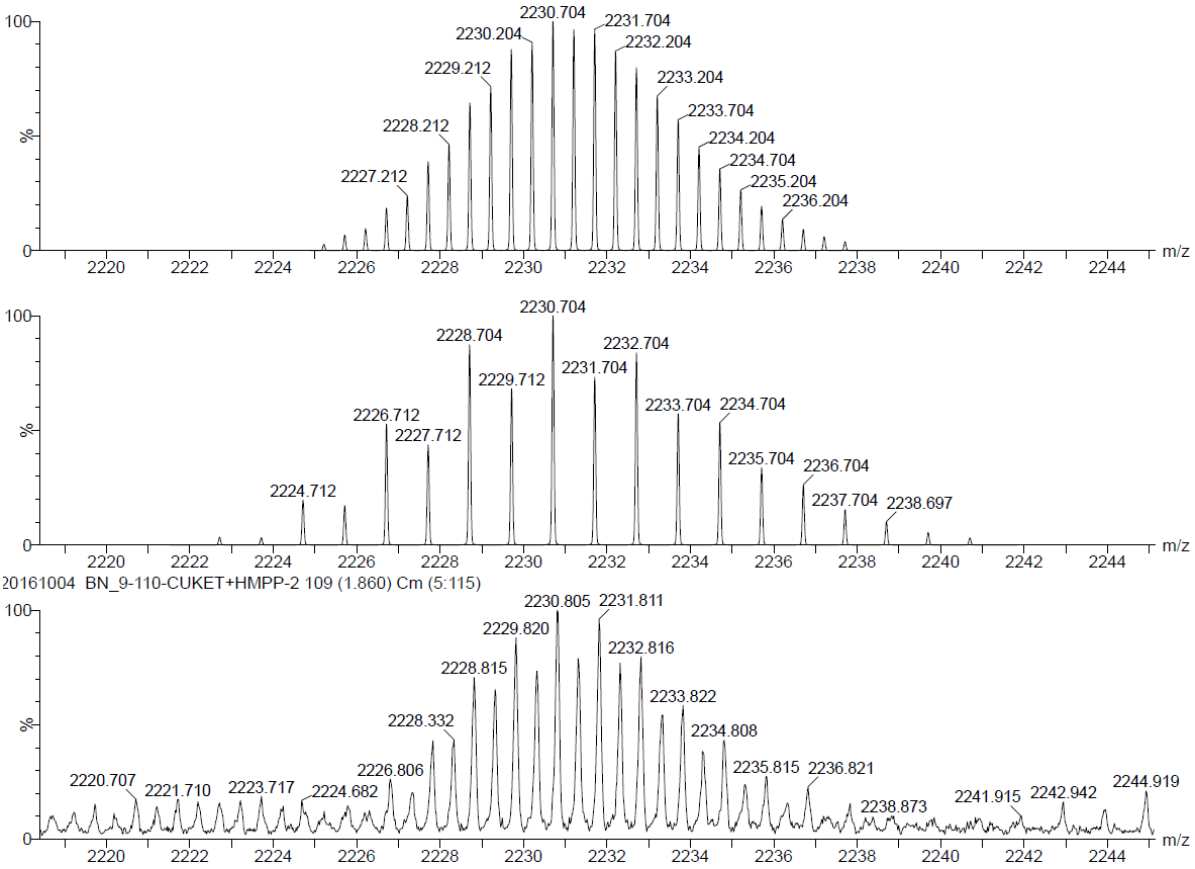

Figure A7.43. Partial ESI-MS of [Cu(MPP)]$_n$ in 1,2-dichloroethane. The experimental (bottom) peak is assignable to overlapping signals from $[Cu_{11}(MPP)_{10}]^+$ (middle = calculated) and the related doubly charged dimer, $[Cu_{22}(MPP)_{20}]^{2+}$ (top = calculated).

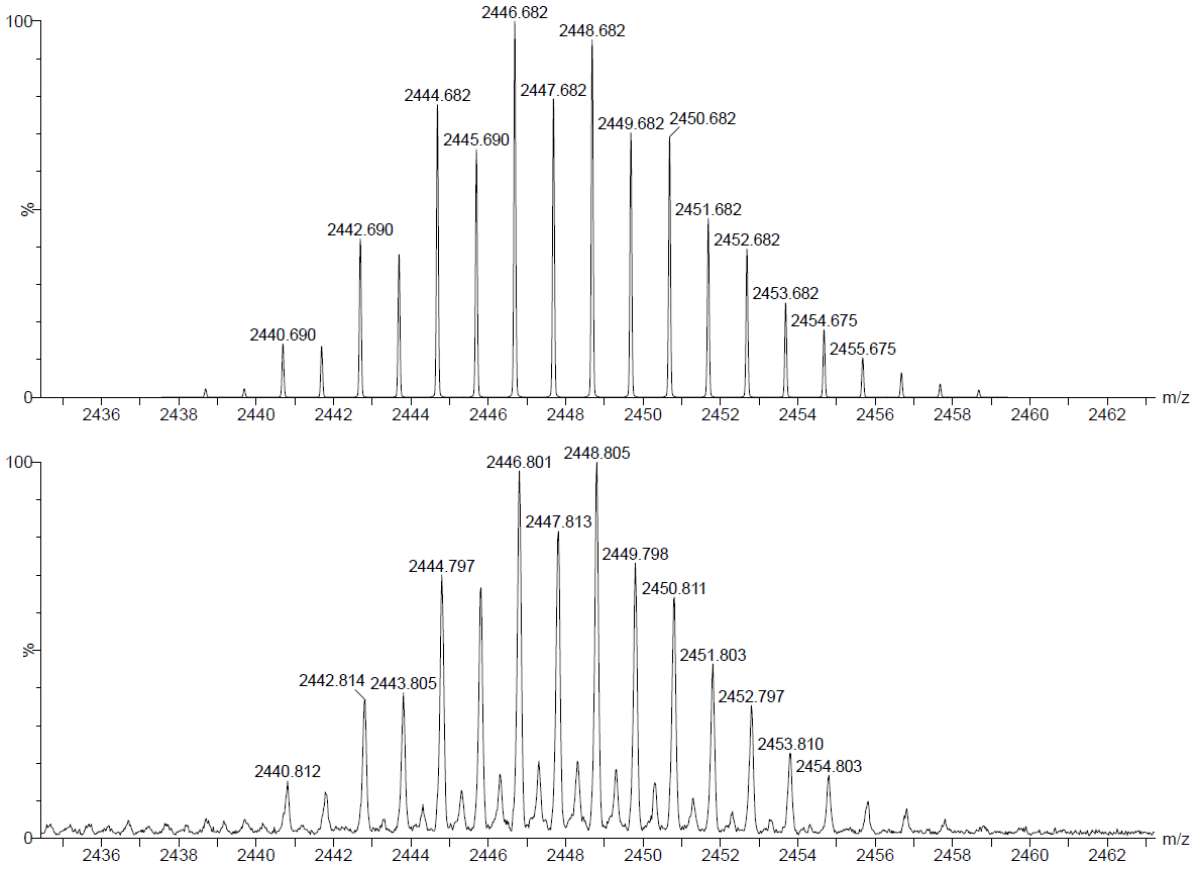

Figure A7.44. Partial ESI-MS of $[Cu(MPP)]_n$ in 1,2-dichloroethane. The experimental (bottom) and calculated (top) peaks are assignable to the $[Cu_{12}(MPP)_{11}]^+$ ion.

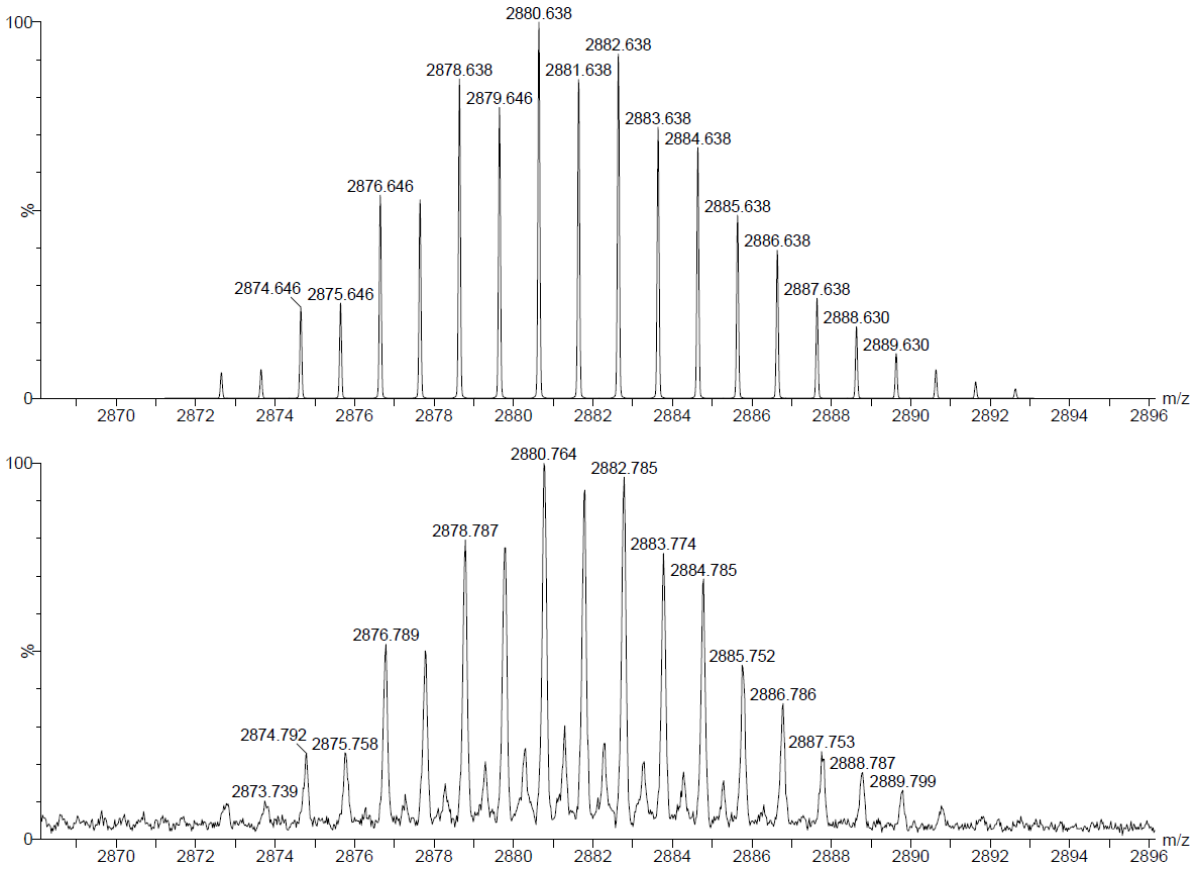

Figure A7.45. Partial ESI-MS of $[Cu(MPP)]_n$ in 1,2-dichloroethane. The experimental (bottom) and calculated (top) peaks are assignable to the $[Cu_{14}(MPP)_{13}]^+$ ion.

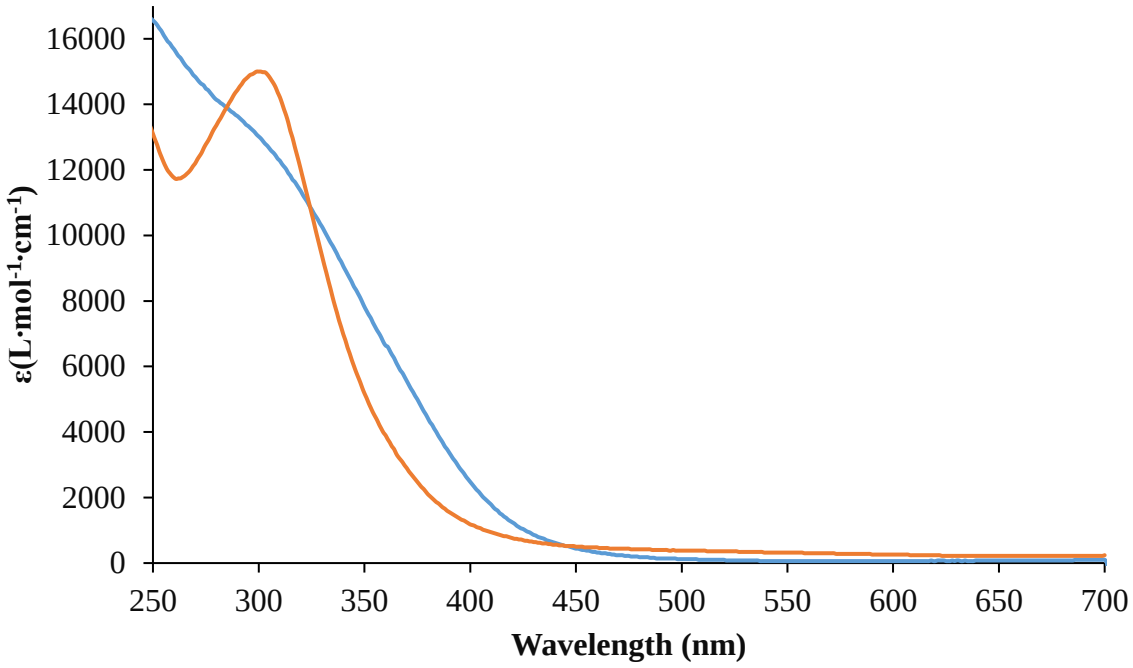

Figure A7.46. UV-vis spectra of $[Cu(MPP)]_n$ (0.05 mM assuming n = 1, 1,2-dichloroethane, orange line) and $[Cu_2(MPP^*)]_n$ generated *in situ* from the reaction of 0.5 equiv of $[Cu(O^tBu)]_4$ and 1 equiv of H_2MPP^* (0.05 mM (assuming n = 1), THF, blue line).

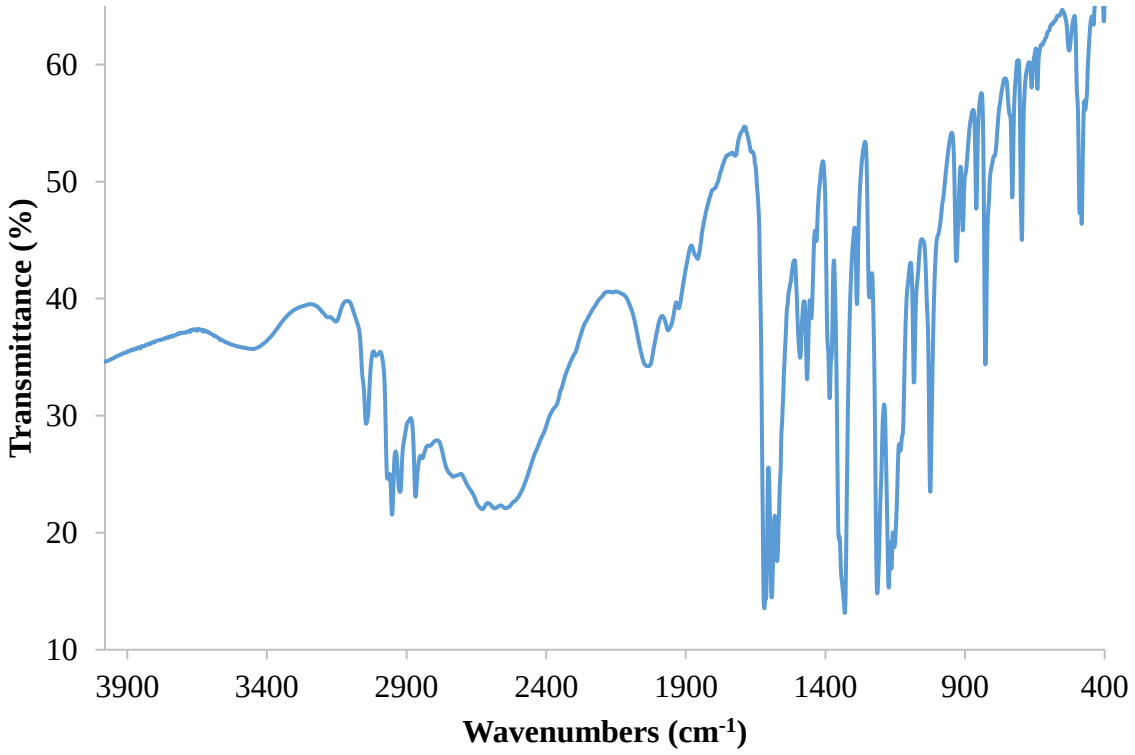

Figure A7.47. IR spectrum of HMPP (KBr pellet, cm^{-1}): 403 (w), 440 (w), 469 (w), 482 (w), 489 (w), 527 (w), 641 (w), 661 (w), 697 (w), 731 (w), 827 (m), 860 (w), 908 (w), 931 (w), 1025 (m), 1083 (m), 1153 (s), 1164 (s), 1173 (s), 1214 (s), 1242 (w), 1287 (w), 1331 (s), 1385 (m), 1432 (w), 1451 (w), 1466 (w), 1491 (w), 1573 (s), 1592 (s), 1619 (s), 1858 (w), 1963 (w), 2036 (m), 2629 (m), 2868 (m), 2923 (m), 2952 (s), 3044 (m), 3153 (w), 3448 (w).

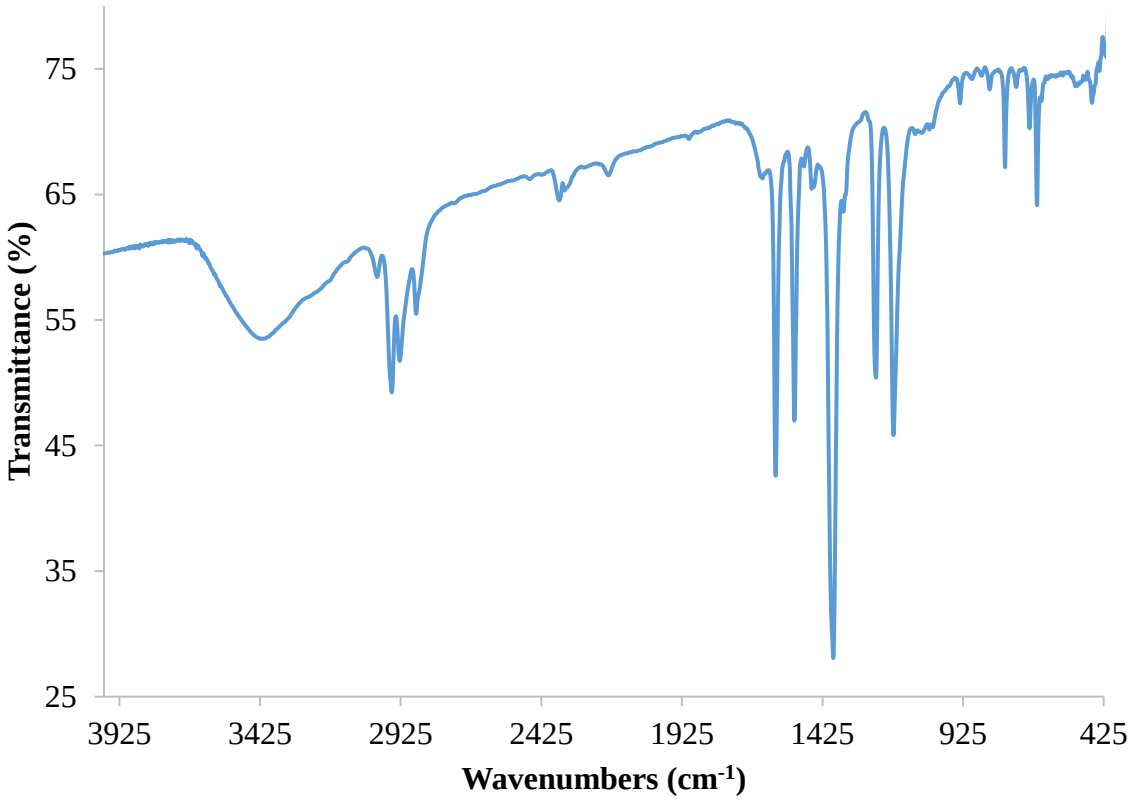

Figure A7.48. IR spectrum of Na(MPP) (KBr pellet).

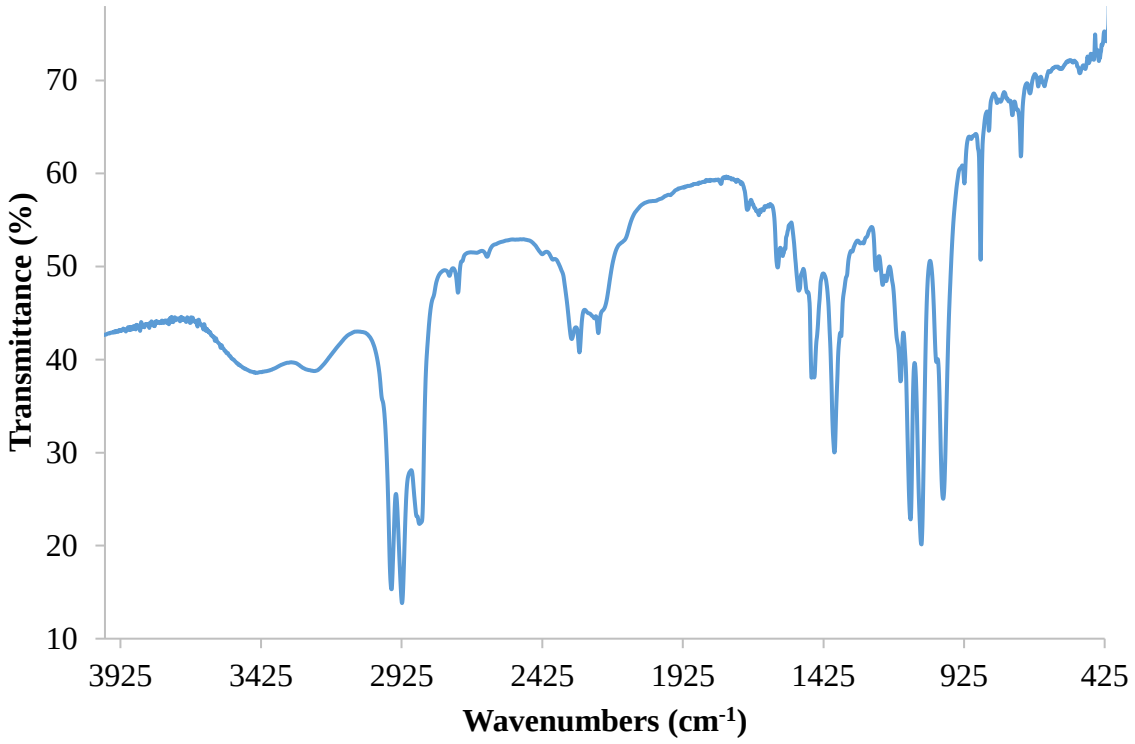

Figure A7.49. IR spectrum of inhomogeneous white and orange solid generated by following the literature procedure of Chen and co-workers (KBr pellet).[10]

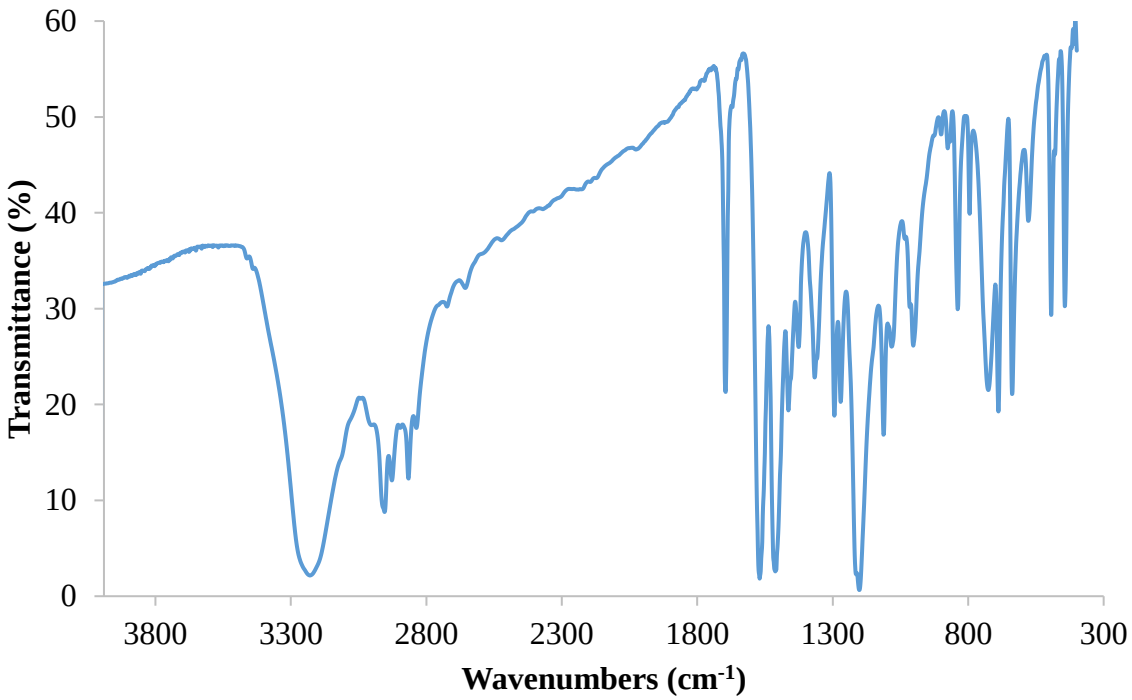

Figure A7.50. IR spectrum of H_2MPP* (KBr pellet).

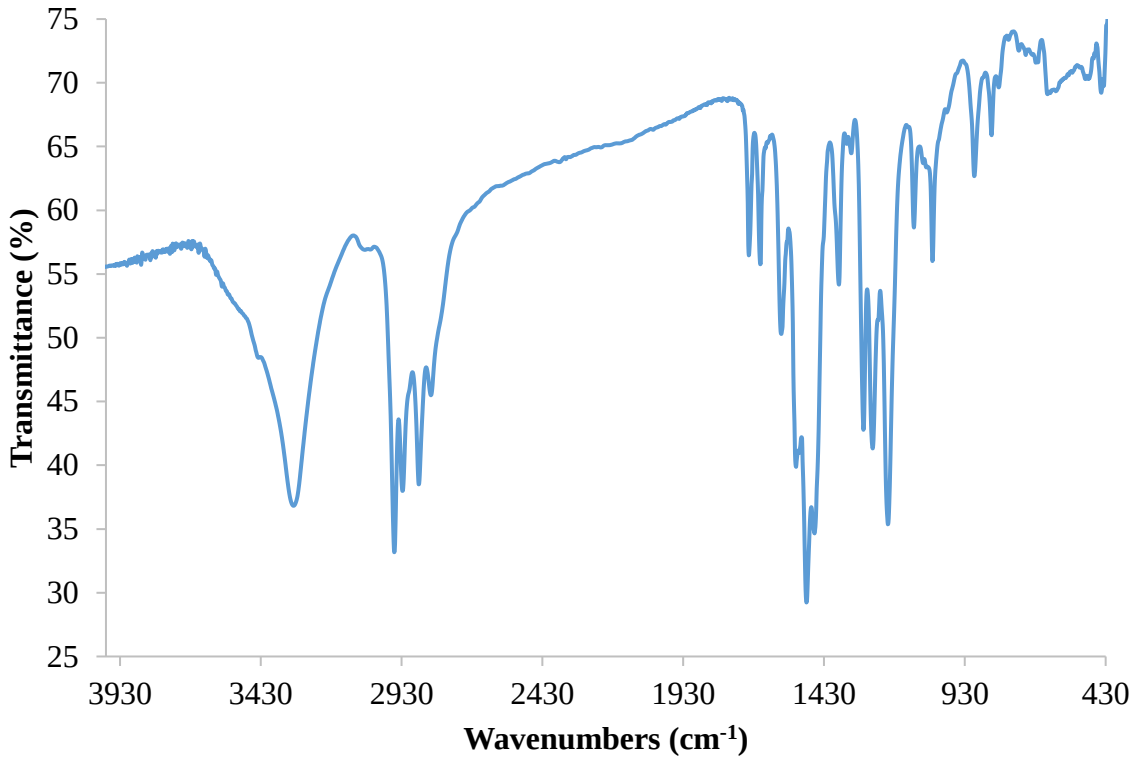

Figure A 7.51. IR spectrum of $[Cu(HMPP^*)]_n$ (KBr pellet).

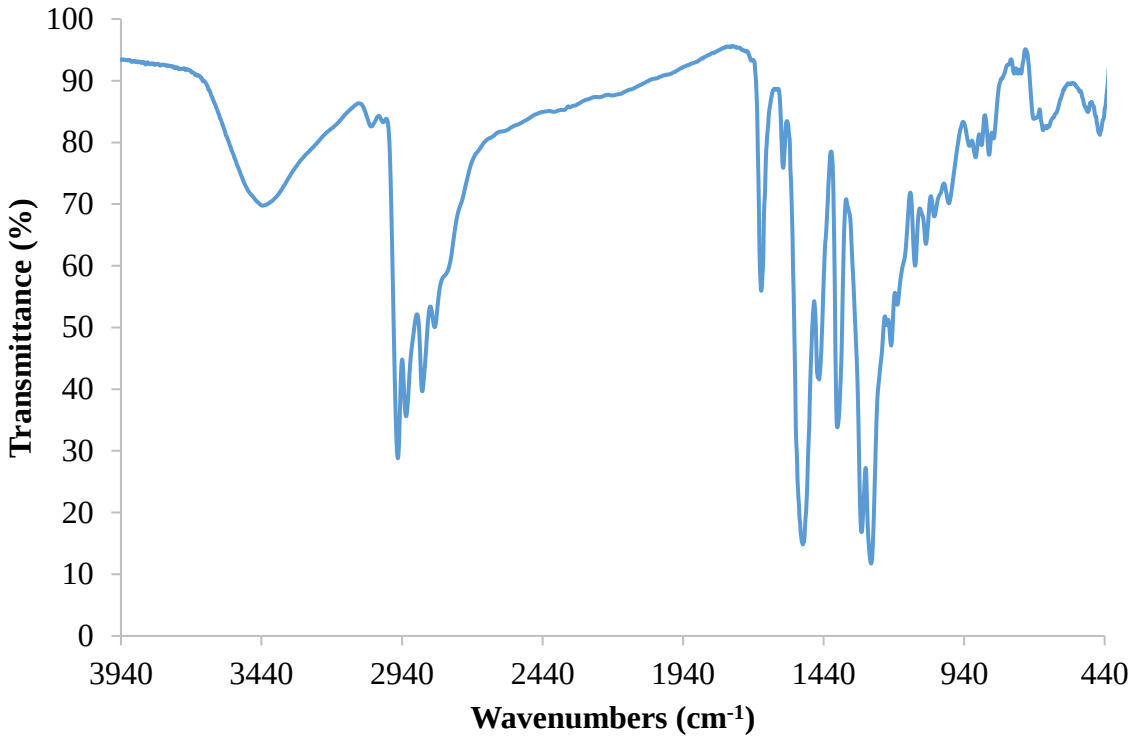

Figure A7.52. IR spectrum of $[Cu_2(MPP^*)]_n$ (KBr pellet).

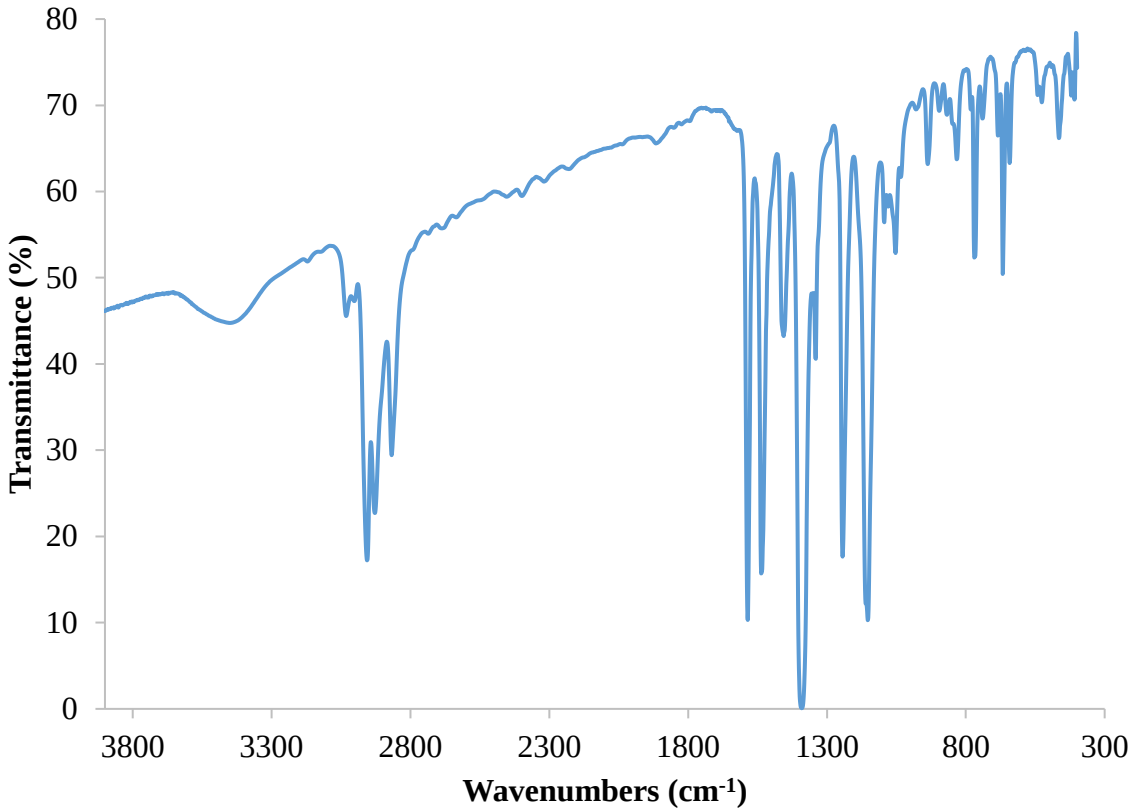

Figure A7.53. IR spectrum of $[Cu(MPP)]_n$ (KBr pellet).

7.6 References

(1) Daniel, M.-C.; Astruc, D. Gold Nanoparticles: Assembly, Supramolecular Chemistry, Quantum-Size-Related Properties, and Applications toward Biology, Catalysis, and Nanotechnology. *Chem. Rev.* **2004**, *104*, 293.

(2) Li, G.; Jin, R. Atomically Precise Gold Nanoclusters as New Model Catalysts. *Acc. Chem. Res.* **2013**, *46*, 1749.

(3) Templeton, A. C.; Wuelfing, W. P.; Murray, R. W. Monolayer-Protected Cluster Molecules. *Acc. Chem. Res.* **2000**, *33*, 27.

(4) Jin, R. Quantum sized, thiolate-protected gold nanoclusters. *Nanoscale* **2010**, *2*, 343.

(5) Jin, R.; Zeng, C.; Zhou, M.; Chen, Y. Atomically Precise Colloidal Metal Nanoclusters and Nanoparticles: Fundamentals and Opportunities. *Chem. Rev.* **2016**, *116*, 10346.

(6) Tracy, J. B.; Crowe, M. C.; Parker, J. F.; Hampe, O.; Fields-Zinna, C. A.; Dass, A.; Murray, R. W. Electrospray Ionization Mass Spectrometry of Uniform and Mixed Monolayer Nanoparticles: $Au_{25}[S(CH_2)_2Ph]_{18}$ and $Au_{25}[S(CH_2)_2Ph]_{18-x}(SR)_x$. *J. Am. Chem. Soc.* **2007**, *129*, 16209.

(7) Tracy, J. B.; Kalyuzhny, G.; Crowe, M. C.; Balasubramanian, R.; Choi, J.-P.; Murray, R. W. Poly(ethylene glycol) Ligands for High-Resolution Nanoparticle Mass Spectrometry. *J. Am. Chem. Soc.* **2007**, *129*, 6706.

(8) Qian, H.; Jin, R. Controlling Nanoparticles with Atomic Precision: The Case of $Au_{144}(SCH_2CH_2Ph)_{60}$. *Nano Lett.* **2009**, *9*, 4083.

(9) Chaki, N. K.; Negishi, Y.; Tsunoyama, H.; Shichibu, Y.; Tsukuda, T. Ubiquitous 8 and 29 kDa Gold:Alkanethiolate Cluster Compounds: Mass-Spectrometric Determination of Molecular Formulas and Structural Implications. *J. Am. Chem. Soc.* **2008**, *130*, 8608.

(10) Wei, W.; Lu, Y.; Chen, W.; Chen, S. One-Pot Synthesis, Photoluminescence, and Electrocatalytic Properties of Subnanometer-Sized Copper Clusters. *J. Am. Chem. Soc.* **2011**, *133*, 2060.

(11) Moret, M.-E.; Zhang, L.; Peters, J. C. A Polar Copper–Boron One-Electron σ-Bond. *J. Am. Chem. Soc.* **2013**, *135*, 3792.

(12) Weinberger, D. S.; Amin Sk, N.; Mondal, K. C.; Melaimi, M.; Bertrand, G.; Stückl, A. C.; Roesky, H. W.; Dittrich, B.; Demeshko, S.; Schwederski, B.; Kaim, W.; Jerabek, P.; Frenking, G. Isolation of Neutral Mononuclear Copper Complexes Stabilized by Two Cyclic (Alkyl)(amino)carbenes. *J. Am. Chem. Soc.* **2014**, *136*, 6235.

(13) Jerabek, P.; Roesky, H. W.; Bertrand, G.; Frenking, G. Coinage Metals Binding as Main Group Elements: Structure and Bonding of the Carbene Complexes $[TM(cAAC)_2]$ and $[TM(cAAC)_2]^+$ (TM = Cu, Ag, Au). *J. Am. Chem. Soc.* **2014**, *136*, 17123.

(14) Ganesamoorthy, C.; Weßing, J.; Kroll, C.; Seidel, R. W.; Gemel, C.; Fischer, R. A. The Intermetalloid Cluster $[(Cp^*AlCu)_6H_4]$, Embedding a Cu_6 Core Inside an Octahedral Al_6 Shell: Molecular Models of Hume–Rothery Nanophases. *Angew. Chem. Int. Ed.* **2014**, *53*, 7943.

(15) Nguyen, T.-A. D.; Jones, Z. R.; Goldsmith, B. R.; Buratto, W. R.; Wu, G.; Scott, S. L.; Hayton, T. W. A Cu_{25} Nanocluster with Partial Cu(0) Character. *J. Am. Chem. Soc.* **2015**, *137*, 13319.

(16) Nguyen, T.-A. D.; Jones, Z. R.; Leto, D. F.; Wu, G.; Scott, S. L.; Hayton, T. W. Ligand-Exchange-Induced Growth of an Atomically Precise Cu_{29} Nanocluster from a Smaller Cluster. *Chem. Mater.* **2016**, *28*, 8385.

(17) Chakrahari, K. K.; Liao, J.-H.; Kahlal, S.; Liu, Y.-C.; Chiang, M.-H.; Saillard, J.-Y.; Liu, C. W. $[Cu_{13}\{S_2CN^nBu_2\}_6(acetylide)_4]^+$: A Two-Electron Superatom. *Angew. Chem. Int. Ed.* **2016**, *128*, 14924.

(18) Freitag, K.; Banh, H.; Gemel, C.; Seidel, R. W.; Kahlal, S.; Saillard, J.-Y.; Fischer, R. A. Molecular brass: Cu_4Zn_4, a ligand protected superatom cluster. *Chem. Commun.* **2014**, *50*, 8681.

(19) Walter, M.; Akola, J.; Lopez-Acevedo, O.; Jadzinsky, P. D.; Calero, G.; Ackerson, C. J.; Whetten, R. L.; Grönbeck, H.; Häkkinen, H. A unified view of ligand-protected gold clusters as superatom complexes. *Proc. Natl. Acad. Sci.* **2008**, *105*, 9157.

(20) Kamei, Y.; Shichibu, Y.; Konishi, K. Generation of Small Gold Clusters with Unique Geometries through Cluster-to-Cluster Transformations: Octanuclear Clusters with Edge-sharing Gold Tetrahedron Motifs. *Angew. Chem. Int. Ed.* **2011**, *50*, 7442.

(21) Shichibu, Y.; Zhang, M.; Kamei, Y.; Konishi, K. $[Au_7]^{3+}$: A Missing Link in the Four-Electron Gold Cluster Family. *J. Am. Chem. Soc.* **2014**, *136*, 12892.

(22) Zeng, C.; Chen, Y.; Iida, K.; Nobusada, K.; Kirschbaum, K.; Lambright, K. J.; Jin, R. Gold Quantum Boxes: On the Periodicities and the Quantum Confinement in the Au_{28}, Au_{36}, Au_{44}, and Au_{52} Magic Series. *J. Am. Chem. Soc.* **2016**, *138*, 3950.

(23) Chen, S.; Xiong, L.; Wang, S.; Ma, Z.; Jin, S.; Sheng, H.; Pei, Y.; Zhu, M. Total Structure Determination of $Au_{21}(S\text{-}Adm)_{15}$ and Geometrical/Electronic Structure Evolution of Thiolated Gold Nanoclusters. *J. Am. Chem. Soc.* **2016**, *138*, 10754.

(24) Albano, V. G.; Grossi, L.; Longoni, G.; Monari, M.; Mulley, S.; Sironi, A. Synthesis and characterization of the paramagnetic $[Ag_{13}Fe_8(CO)_{32}]^{4-}$ tetraanion: a cuboctahedral Ag_{13} cluster stabilized by $Fe(CO)_4$ groups behaving as 4-electron donors. *J. Am. Chem. Soc.* **1992**, *114*, 5708.

(25) Goulet, P. J. G.; Lennox, R. B. New Insights into Brust−Schiffrin Metal Nanoparticle Synthesis. *J. Am. Chem. Soc.* **2010**, *132*, 9582.

(26) Note that the experimental isotope pattern for the parent ion and a comparison to the simulated mass spectrum was not provided in the original report.

(27) Schlenk, S.; Wasserscheid, P.; Rijksen, C.; Noti, C.; Hanselmann, P., Method for preparation of mononitrated aromatic compounds. Google Patents: 2013; WO2012156540 A3.

(28) Soriaga, R. A. D.; Javed, S.; Hoffman, D. M. Synthesis of Copper(I) Complexes with Ketimide and Hydrazide Ligands. *Clust. Sci.* **2010**, *21*, 567.

(29) Narasimhamurthy, N.; Samuelson, A. G.; Manohar, H. Reaction of copper(I) phenoxide with PhNCS: formation and X-ray structure of a novel copper(I) hexameric complex. *J. Chem. Soc., Chem. Commun.* **1989**, 1803.

(30) Wycliff, C.; Samuelson, A. G.; Nethaji, M. Reversible Insertion of Methyl Isothiocyanate into Copper(I) Aryloxides. *Inorg. Chem.* **1996**, *35*, 5427.

(31) Kuroda-Sowa, T.; Munakata, M.; Miyazaki, M.; Maekawa, M. Syntheses and structures of tetranuclear and hexanuclear copper(I) complexes with iminomethanethiolato bridges derived from isothiocyanate. *Polyhedron* **1995**, *14*, 1003.

(32) Bai, Y.; He, G.-j.; Zhao, Y.-g.; Duan, C.-y.; Dang, D.-b.; Meng, Q.-j. Porous material for absorption and luminescent detection of aromatic molecules in water. *Chem. Commun.* **2006**, 1530.

(33) Kundu, T.; Jana, A. K.; Natarajan, S. Stepwise Crystallization: Illustrative Examples of the Use of Metalloligands $[Cu_6(mna)_6]^{6-}$ and $[Ag_6(Hmna)_2(mna)_4]^{4-}$ (H_2mna = 2-Mercapto Nicotinic Acid) in the Formation of Heterometallic Two- and Three-Dimensional Assemblies with *brucite*, *pcu*, and *sql* Topologies. *Cryst. Growth Des.* **2014**, *14*, 4531.

(34) Kitagawa, S.; Kawata, S.; Nozaka, Y.; Munakata, M. Synthesis and crystal structures of novel copper(I) co-ordination polymers and a hexacopper(I) cluster of quinoline-2-thione. *J. Chem. Soc., Dalton Trans.* **1993**, 1399.

(35) Castro, R.; Duran, M. L.; Garcia-Vazquez, J. A.; Romero, J.; Sousa, A.; Castellano, E. E.; Zukerman-Schpector, J. Copper(I) complexes with 4,6-dimethylpyrimidine-2-thione (Hdmpymt); the crystal and molecular structure of $[Cu_6(dmpymt)_6]$. *J. Chem. Soc., Dalton Trans.* **1992**, 2559.

(36) Singh, A.; Bharty, M. K.; Bharati, P.; Bharti, A.; Singh, S.; Singh, N. K. Synthesis, spectral, thermal and structural characterization of a hexanuclear copper(I) cluster and a cobalt(III) complex of 1-ethyl-3-phenyl-thiourea. *Polyhedron* **2015**, *85*, 918.

(37) Su, B.-Q.; Xian, L.; Zhang, B.; Song, H.-B. Synthesis and characterisation of a hexanuclear copper (I) cluster coordination compound. *J. Chem. Res.* **2005**, *2005*, 101.

(38) Kitagawa, S.; Nozaka, Y.; Munakata, M.; Kawata, S. Synthesis and crystal structures of tetra- and hexanuclear copper(I) complexes of pyrimidine derivatives, $[Cu_4(C_4H_8N_2S)_4](ClO_4)_4$ and $[Cu_6(C_5H_5N_2S)_6]$. *Inorg. Chim. Acta* **1992**, *197*, 169.

(39) Kitagawa, S.; Munakata, M.; Shimono, H.; Matsuyama, S.; Masuda, H. Synthesis and crystal structure of hexanuclear copper(I) complexes of μ_3-pyridine-2-thionate. *J. Chem. Soc., Dalton Trans.* **1990**, 2105.

(40) $[Cu(O^tBu)]_4$ was used as the Cu(I) source for this reaction instead of $[Cu(N{=}C^tBu_2)]_4$, because NMR spectra of the material generated upon reaction of $[Cu(N{=}C^tBu_2)]_4$ with H_2MPP* revealed the presence of a persistent impurity related to $H(N{=}C^tBu_2)$.

(41) Gao, X.; He, S.; Zhang, C.; Du, C.; Chen, X.; Xing, W.; Chen, S.; Clayborne, A.; Chen, W. Single Crystal Sub-Nanometer Sized $Cu_6(SR)_6$ Clusters: Structure, Photophysical Properties, and Electrochemical Sensing. *Adv. Sci.* **2016**, 1600126.

(42) Ramaprabhu, S.; Lucken, E. A. C. Crystal Structure and NQR of Two Copper(I) Complexes of 4,6-Dimethylpyrimidine-2-thione. *Z. Naturforsch* **1994**, *49a*, 193.

(43) Seth, S.; Das, A. K.; Mak, T. C. W. Distant Copper-Copper Interactions in a Metal-Organic Compound in the Solid State: Hexakis[(μ_3-4,6-dimethylpyrimidine-2-thiolato-*N:S:S*)copper(I)] Dihydrate. *Acta Cryst.* **1995**, *C51*, 2529.

(44) Han, L.; Hong, M.; Wang, R.; Wu, B.; Xu, Y.; Lou, B.; Lin, Z. Red luminescent polymeric cuprous organosulfide generated by solvothermal redox reaction. *Chem. Commun.* **2004**, 2578.

(45) Zhang, Y.; Hu, Q.; Paau, M. C.; Xie, S.; Gao, P.; Chan, W.; Choi, M. M. F. Probing Histidine-Stabilized Gold Nanoclusters Product by High-Performance Liquid Chromatography and Mass Spectrometry. *J. Phys. Chem. C* **2013**, *117*, 18697.

(46) Paau, M. C.; Hu, Q.; Zhang, Y.; Choi, M. M. F. Role of UHPLC in evaluating as-synthesised ligand-protected gold nanoparticles products. *Anal. Methods* **2015**, *7*, 2452.

(47) Lemmen, T. H.; Goeden, G. V.; Huffman, J. C.; Geerts, R. L.; Caulton, K. G. Alcohol elimination chemistry of tetrakis(tert-butoxocopper). *Inorg. Chem.* **1990**, *29*, 3680.

(48) Harris, R. K.; Becker, E. D.; Cabral De Menezes, S. M.; Goodfellow, R.; Granger, P. NMR Nomenclature. Nuclear Spin Properties and Conventions for Chemical Shifts. *Pure Appl. Chem.* **2001**, *73*, 1795.

(49) Harris, R. K.; Becker, E. D.; Cabral De Menezes, S. M.; Granger, P.; Hoffman, R. E.; Zilm, K. W. Further Conventions for NMR Shielding and Chemical Shifts. *Pure Appl. Chem.* **2008**, *80*, 59.

(50) *SMART Apex II, Version 2.1*; Bruker AXS Inc.: Madison, WI, 2005.

(51) *SAINT Software User's Guide, Version 7.34a*; Bruker AXS Inc.: Madison, WI, 2005.

(52) Sheldrick, G. M. *SADABS*; University of Göttingen: Göttingen, Germany, 2005.

(53) *SHELXTL PC, Version 6.12*; Bruker AXS Inc.: Madison, WI, 2005.